FLOW BOILING OF R134A IN VERTICAL MINI-DIAMETER TUBES

A thesis submitted for the degree of Doctor of Philosophy

By

Mohamed M. Mahmoud M.

Mechanical Engineering Department
School of Engineering and Design
Brunel University
West London, Uxbridge, UB8 3PH

March 2011

Abstract

The current study is a part of a long term experimental project devoted to investigate flow boiling heat transfer, pressure drop and flow visualization of R134a in small to mini/micro-diameter tubes. The experimental facility was first designed and constructed by X. Huo (2005) with the contribution of L. Chen (2006). In the present study, the experimental facility was upgraded by changing the heating system from AC to DC heating and also upgrading the logging system through using a faster data logger and developing a new Labview program. The objectives of the current study include (i) contribute in identifying the reasons behind the wide scatter in the published flow boiling heat transfer results, (ii) contribute in understanding the fundamentals of flow boiling heat transfer in mini/micro-diameter tubes and (iii) evaluation of the existing heat transfer and pressure drop prediction methods. Two sizes of stainless steel tubes were investigated in the current study; 0.52 mm and 1.1 mm diameter. In the current study, the 0.52 mm tube was roughly called a "micro-tube" whilst the 1.1 mm tubes were called "mini-tubes".

The present study proposes two possible reasons for the scatter in the published heat transfer results. The first reason is the variations in the heated length from one study to another–there is no criterion for choosing the heated length. The second reason is the variations in the inner surface characteristics of the channels from one study to another. These two important parameters were not taken into consideration by researchers in the past studies. Accordingly, the effect of the heated length was investigated in the current study using a seamless cold drawn tube with diameter of 1.1 mm and heated length ranging from 150 to 450 mm. The effect of the tube inner surface was also tested here by conducting the test in two stainless steel tubes with diameter of 1.1 mm and manufactured by two different processes. The first tube was manufactured by welding technique whilst the second tube was a seamless cold drawn tube. Both tubes were identical in design and dimensions. The inner surface of each tube was examined first using SEM analysis and demonstrated that, the surface morphology is completely different. The local heat transfer coefficient was determined through measuring the local wall temperature using 14 K-type thermocouples attached to the wall using thermally conducting but electrically insulating epoxy supplied by Omega. Pressure drop was measured directly across the heated section and a high speed camera was used for the

flow visualization at 1000 frames/s. All measurements were recorded after the system attained steady state. The experimental conditions include mass flux range of 100 – 500 kg/m^2 s, system pressure range of 6 – 10 bar, inlet sub-cooling of about 5K and exit quality up to about 0.9.

The most frequently observed flow regimes in the 0.52 mm tube were found to be slug (elongated bubble), transition to annular and annular flow regimes. In the 1.1 mm tube, the observed regimes were found to be slug, churn and annular. The transition from slug flow to annular flow in the 0.52 mm tube occurred smoothly with little disturbances at the liquid vapour interface compared to the 1.1 mm tube. Additionally, increasing the heated length of the 1.1 mm tube was found to shift the transition to annular flow to occur at lower vapour quality.

The heat transfer results demonstrated that the behaviour of the local heat transfer coefficient in the 0.52 mm diameter tube is different compared to that in the 1.1 mm tubes. Also, the tube inner surface characteristics and the heated length were found to strongly influence the local behaviour of the heat transfer coefficient. Flow boiling hysteresis was investigated and the results indicated that hysteresis exists only at very low heat fluxes near the boiling incipience.

Existing heat transfer and pressure drop correlations were examined using the results of the 0.52 and 1.1 mm seamless cold drawn tubes. The pressure drop data were predicted very well using the Muller-Stienhagen and Heck (1986) correlation, the homogeneous flow model and the correlation of Mishima and Hibiki (1996). On the contrary, all macro and microscale heat correlations failed to predict the current experimental data. The mechanistic models failed to predict the data of all tubes with the same accuracy. Accordingly, two heat transfer correlations were proposed in the current study. The first correlation is based on dimensionless groups whilst the second is based on the superposition model of Chen (1966). Both correlations predicted the current experimental data and the data of Huo (2005) and Shiferaw (2008) very well.

Declaration

The research presented in this thesis is the original work of the author except where otherwise specified, or where acknowledgements are made by references. This project was carried out at the School of Engineering and Design, Brunel University, under the supervision of Prof. T. G. Karayiannis and Prof. D.B.R. Kenning.

The work has not been submitted for another degree or award to any other institution.

Acknowledgements

I would like to express my gratitude to my supervisors Professor T.G. Karayiannis and Professor D.B.R. Kenning for all their support, guidance and encouragement throughout this work. Without their fruitful discussions and comments through very regular research meetings, this work would not have been possible. They never forced me to follow their personal viewpoints but everything was open for discussions.

I would also like to thank my colleague and my friend Dr. D. Shiferaw for passing me his knowledge about the experimental facility and offering his kind and useful advice.

I am grateful to the technician Mr. C. Xanthos for his support and help in the preparation of the investigated test sections.

I would like to acknowledge the Egyptian Ministry of Higher Education for granting me a full time and fully funded scholarship.

To my parents and my family, words fail to express my gratitude; you all have done a lot for me. I am very thankful for your constant praying for me.

I would like to thank my lovely wife for her constant patience and support all the time.

Above all, I would like to thank “Allah” the Almighty God for granting me the power to accomplish this work. Without the willing of Allah, nothing is possible.

Contents

List of Figures

three zone pressure drop model of Shiferaw et al. (2002) for (a) D = 0.52 mm, (b) D = 1.1 mm, L = 150 mm and (c) D = 1.1 mm, L = 450 mm.

List of Tables

Nomenclature

Latin

Symbol	*Parameter*	*SI unit*
A	Cross sectional area	m^2
A	Constant in Eq. (5.52)	-
AC	Alternating current	-
Bo	Boiling number, q/Gh_{fg}	-
Bd	Bond number, Eq. (1.1)	-
B_X	Systematic uncertainty in a measured parameter X	
C	Chisholm parameter	-
C_L	Single phase heat loss coefficient	$W\ K^{-1}$
Ca	Capillary number, $\mu U/\sigma$	-
C_0	Distribution parameter in Eq. (2.13)	-
$C_{\delta 0}$	Constant for initial film thickness	-
CHF	Critical Heat Flux	$W\ m^{-2}$
Co	Confinement number, $[\sigma/g\Delta\rho]^{0.5}/D$	-
COP	Coefficient of performance	-
c_P	Specific heat capacity	$J\ kg^{-1}\ K^{-1}$
D	Tube diameter	m
D_b	Bubble diameter	m
D_h	Hydraulic diameter, $4A/P_e$	m
DC	Direct current	-
DFM	Drift Flux Model	
EDL	Electric double layer	-
$Eö$	Eötvös number, $4\pi^2\sigma/D^2\Delta\rho g$	-
G	Mass flux, $\dot{m}/A$	$kg\ m^{-2}\ s^{-1}$

Symbol	*Parameter*	*SI unit*
Gz	Graetz number	
g	Gravitational acceleration	$\mathrm{m\ s^{-2}}$
E	Energy	-
F	Convective boiling enhancement factor	-
f	Fanning friction coefficient	-
f_b	Bubble frequency	Hz
F_b	Buoyancy force	N
F_D	Drag force	N
F_C	Capillary force	
F_{fl}	Fluid-Surface parameter	-
F_i	Inertia force	N
F_L	Left force	N
F_{nb}	Nucleate boiling factor, Eq. (5.5)	-
F_s	Surface tension force	N
Fr	Froude number	-
h_{sp}	Single phase heat transfer coefficient	$Wm^{-2}K^{-1}$
h	Heat transfer coefficient	$Wm^{-2}K^{-1}$
h	Specific enthalpy	$\mathrm{J\ kg^{-1}}$
h_{fg}	Latent heat of vaporization	$\mathrm{J\ kg^{-1}}$
HFM	Homogeneous Flow Model	
I	Electrical current	Ampere
$\overline{J}$	Total volumetric flux	$\mathrm{m\ s^{-1}}$
J	Volumetric flux	$\mathrm{m\ s^{-1}}$
J_a	Jakob number	-
k	Thermal conductivity	$Wm^{-1}K^{-1}$
L	Length	m
L_B	Bubble length	m

Symbol	*Parameter*	*SI unit*
L_{dry}	Dryout length	m
L_{film}	Film length	m
L_p	Pair (tripplet) length	m
La	Laplace constant	m
M	Maranzana number, $q_{axial\ conduction} / q_{forced\ convection}$	-
M	Mass	kg
MW	Molecular weight	kg kmol^{-1}
MAE	Mean Absolute Error	-
$\dot{m}$	Mass flow rate	kg s^{-1}
N	Number of samples	-
N_{Co}	Convection number	-
Nu	Nusselt number, hD/k	-
ONB	Onset of nucleate boiling	-
P	Pressure	Pa
P_e	Perimeter	m
P_r	Reduced pressure	-
Po	Poiseulle number, f Re	-
Pr	Pradtl number, $\mu c_p / k$	-
q	Heat flux	W m^{-2}
Q_{Loss}	Heat loss	W
Q_V	Heat generation rate per unit volume	W m^{-3}
r	Radial coordinate	-
r_c	cavity radius	m
R	Tube radius	m
R_B	Slug bubble radius	m
Re	Reynolds number	-
Re_{LO}	Liquid only Reynolds number, GD/μ_L	

Symbol	*Parameter*	*SI unit*
Re_L	Liquid Reynolds number, $(1-x)GD/\mu_L$	
R_G	Gas constant	J mol^{-1} K^{-1}
s	Wall thickness in Eq. (3.2)	m
S	Slip ratio	-
S	Nucleate boiling suppression factor	-
S_X	Standard deviation	-
S_{BX}	Standard deviation of the systematic uncertainty	
SFM	Separated Flow Model	
T	Temperature	^{0}C
T^*	Dimensionless temperature, Eq. (3.1)	-
t	Time	s
t_{dry}	Time for dry vapour to pass a fixed location	s
$t_{dry\ film}$	Time required for film to dry out	s
t_{film}	Residence time for liquid film	s
t_{95}	95 % confidence limit	-
U	Velocity	m s^{-1}
U	Overall uncertainty in a measured variable	
U_{GS}	Gas superficial velocity	
U_{LS}	Liquid superficial velocity	
U_B	Slug bubble velocity	m s^{-1}
U_H	Homogeneous velocity	m s^{-1}
u_{random}	Random error	-
U_{sys}	Systematic error	
V	Voltage	Volts
v	Specific volume	$\mathrm{m}^3 kg^{-1}$
V_L	Liquid volumetric flow rate	$m^3 s^{-1}$
V_g	Gas volumetric flow rate	$m^3 s^{-1}$

We	Weber number, $G^2 D / \rho\sigma$	-
X	Martinelli parameter, $\left[(dp/dz)_L/(dp/dz)_g\right]^{0.5}$	-
$\overline{X}$	The mean value	
x	Vapour quality	-
x_{cr}	Quality at critical heat flux	-
x_e	Exit quality	-
z	Axial coordinate	-
Z_N	Axial position of bubble nose	-

Greek

Symbol	*Parameter*	*SI unit*
α	Area void fraction	-
h_{film}	Heat transfer coefficient during the passage of a confined bubble with liquid film.	$W\ m^{-2}\ K^{-1}$
β	Surface area density	$m^2 m^{-3}$
β	Homogeneous (volumetric) void fraction	-
β	Percentage of data within ±30 %	-
δ_{tb}	Thermal boundary layer thickness	m
δ_0	Initial film thickness	m
δ_{dryout}	Film thickness at which dryout occurs	m
δ_{end}	End film thickness	m
δ^*	Non-dimensional film thickness	-
ΔP	Pressure drop	Pa
ΔT	Temperature difference	K
ϕ	Two phase multiplier	-
k	Conductivity	$W\ m^{-1}\ K^{-1}$
μ	Viscosity	$N\ s\ m^{-2}$
v	Specific volume	$m^3\ kg^{-1}$
ω	Angular frequency	Hz
τ	Time	s
θ	Inclination angle	rad
θ	Contact angle	rad
ρ	Density	$kg\ m^{-3}$
σ	Surface tension	$N\ m^{-1}$
τ	Shear stress	$N\ m^{-2}$
τ_b	Bubble generation period	s
τ_i	Interfacial shear stress	$N\ m^{-2}$

Subscripts

Symbol	*Meaning*
a	Annular
acc	Acceleration
B	Bubble
c	Coalesence
cv	Convective
CH	Chisholm
crit	Critical
Exp	Experimental value
fb	Fluid bulk
f	Friction
film	Film
g	Gas
g	Gravitational
go	Gas-only
h, *fd*	Hydrodynamically fully developed
H	Homogeneous
h	Heated
i	Internal
in	Inlet
L	Liquid
Lo	Liquid only
Lv	Liquid to vapour change
LM	Lockhart-Martinelli
m	Measured
max	Maximum
min	Minimum

o	Outer
ONB	Onset of nucleate boiling
p	Pair
Pool	Nucleate pool boiling
Pred	Predicted
ref	Reference
sat	Saturation
sp	Single phase
sub	Subcooled
sup	Superheat
tp	Two phase
sp	Single phase
v	Vapour
w	Wall
wi	Inner wall
wo	Outer wall

Dimensionless Groups

Group	Definition	Expression
Biot number, *Bi*	$\frac{\textit{The internal thermal resistance of a solid}}{\textit{The boundary layer thermal resistance}}$	$\frac{hL}{k}$
Bond number, *Bd* Eotvos number, *Eo*	$\frac{\textit{Buoyancy force}}{\textit{Surface tension force}}$	$\frac{g\Delta\rho D^2}{\sigma}$
Boiling number, *Bo*	A heat flux non-dimensionalized with the latent heat and mass flux	$\frac{q}{Gh_{fg}}$
Capillary number, *Ca*	$\frac{\textit{Viscous force}}{\textit{Surface tension force}}$	$\frac{\mu V}{\sigma}$
Froude number, *Fr*	$\frac{\textit{Inertia force}}{\textit{Gravitational force}}$	$\frac{V^2}{gD}$
Martinelli parameter, X^2	$\frac{\textit{Frictional pressure gradient of liquid}}{\textit{Frictional pressure drop of gas}}$	$\frac{[dp/dz]_{f,L}}{[dp/dz]_{f,g}}$
Weber number, *We*	$\frac{\textit{Inertia force}}{\textit{Surface tension force}}$	$\frac{\rho V^2 D}{\sigma}$

Chapter 1

Introduction

1.1 Background

Microchannels heat exchangers are expected to play a vital role in the fields of process intensification, improving energy efficiency and cooling high and ultrahigh heat flux systems. The benefits of using microchannels heat exchangers over conventional ones include: (i) large heat transfer surface area per unit volume; (ii) Higher laminar and turbulent single phase heat transfer coefficients. This can be deduced simply from the well-known single phase relations provided that they are still valid at the microscale, e.g. $Nu = 4.36$ for fully developed laminar flow under constant heat flux boundary condition and $Nu = 0.023Re^{0.8}Pr^{0.4}$ for turbulent flow. However, the high single phase heat transfer coefficients in microchannels may influence boiling incipience through affecting the thickness of the thermal boundary layer next to the wall. As the single phase heat transfer coefficient increases, the thermal boundary layer thickness decreases ($\delta_{tb} = k_L / h_{sp}$) with a steep temperature gradient next to the wall. This affects the thermal equilibrium conditions required for bubble growth and delays boiling incipience to occur at very high wall superheat; (iii) Fewer number of flow patterns with well-defined liquid/vapour interface. The frequently observed flow boiling patterns in microchannels are isolated bubble, confined bubble/slug and annular as reported by Kandlikar (2002). Also, Thome (2004) reported that, the elongated bubble regime can be sustained in microchannels up to vapour quality values of 0.6 – 0.7. This feature may encourage researchers on developing mechanistic models, which is still a challenge; (iv) Much higher two phase flow boiling heat transfer coefficient compared to conventional channels. In microchannels, the nucleating bubble grows until it fills the entire channel

cross section before leaving the nucleation site and undergoes some axial growth with the formation of a thin liquid film around the bubble. The presence of an evaporating thin liquid film around the nucleating bubble results in a very high heat transfer coefficient. Some researchers such as Saitoh et al. (2005), Consolini and Thome (2009) and Karayiannis et al. (2008) found that the flow boiling heat transfer coefficient increases when the diameter decreases; (v) The effect of orientation is insignificant in case of microchannels heat exchangers due to the prevailing of surface tension force over buoyancy and gravity forces as reported by Suo and Griffith (1964), Fukano and Karaiyasaki (1993), Chen et al. (2002) and Akbar et al. (2003). Despite the abovementioned benefits, microchannels heat exchangers still have some limitations that are worth mentioning. These include high pressure drop, high local pressure fluctuations induced by single bubble growth as reported by Wen and Kenning (2004), flow instability, flow mal-distribution, difficulty of triggering stable boiling, deterioration of heat transfer at high heat fluxes due to intermittent dryout and the lack of accurate prediction methods for safe design and operation; all calling for more research in this area. Another encouraging feature for microchannels heat exchangers is the advances in fabrication technologies. Kandlikar and Grande (2003) discussed the different micro-fabrication technologies and concluded that fabricating channels with hydraulic diameters down to 0.1 μm is possible. Historically, microchannels heat exchangers of 0.7 – 1.5 mm hydraulic diameters are commercially available by Heatric Company (www.heatric.com) since 1985, especially for offshore gas applications. The company called these exchangers Printed Circuit Heat Exchangers (PCHEs) because their manufacturing process is similar to the manufacturing process of electronic circuits. Pua and Rumbold (2003) detailed the manufacturing process, features and applications of PCHEs. Other commercial examples include the brazed micro heat exchangers produced by The Institut fur Microtechnik-Mainz (IMM) (www.imm-mainz.de) with hydraulic diameter of 0.75 mm, the micro heat exchangers produced by Danfos Company (www.danfos.com) and the micro evaporators and condensers produced by Delphi Company (www.delphi.com).

This chapter is organized as follows: section 1.2 presents a brief summary on some of the possible future applications of microchannels heat exchangers, section 1.3 presents

the motivations behind the current research, section 1.4 presents the objectives of the current study and finally the outline of the thesis is presented in section 1.5

1.2 Applications of microchannels heat exchangers

Micro heat exchangers may be used in many applications such as cooling of gas turbine components, cooling of mechanical seals and bearings, in condensers and evaporators and cooling of electronic equipment. Kelly et al. (2001) have described the manufacturing process used to fabricate these micro heat exchangers for these different applications. Another application for the micro heat exchangers is cooling high and ultra-high heat flux systems. Mudawar (2001) classified the heat fluxes into two ranges based on the magnitude of heat dissipation. The first is a high heat flux range with cooling requirements in the order of 1–10 MW/m^2 and is encountered in high performance supercomputers, power devices, electric vehicles and advanced military avionics. The second is an ultra-high heat flux range with cooling requirements of 10–10^3 MW/m^2 and is found in applications such as fusion reactors, magnetrons used for short pulse laser and radars and synchrotron sources that deliver x-ray beams. In the coming sub-sections, the potential applications of microchannels heat exchangers in electronics and refrigeration and air conditioning industries will be discussed.

1.2.1 Electronics Cooling

Electronic systems are encountered in several fields such as computers, information technology, avionics, marines, vehicles and high power devices. These systems keep advancing every year due to the demand on increasing processing speed and miniaturization. Increasing processing speed requires increasing the density of electronic elements on the chip, e.g. transistors and electronic switches. Since each element has its own resistance and current and also their size is about few nanometres, hot spots or huge local heat fluxes are created inside the chip. These local heat fluxes exceeded values of 5 MW/m^2, 10 MW/m^2 and 15 MW/m^2 for microprocessors as reported by Zhou et al. (2004), Yang et al. (2007) and Wei (2008), respectively. Moreover, Zhirnov et al. (2003) predicted an astronomic value of 5×10^4–10^5 MW/m^2 to be dissipated from electronics components in the future. This huge value of heat flux can be attained only if the technology can reduce the size of the electronic element to 1.5 nm (the size will decrease to 22 nm by 2016 as reported by ITRS (2001)). As a

result, the design target is to keep the hottest location in the chip below the design temperature (< 100 ^{0}C) otherwise malfunction and failure will occur. Nnanna et al. (2009) reported that every 10 K rise in junction temperature increases the failure rate by a factor of two while Yang et al. (2007) reported that processor speed decreases by 10 – 15 % as a result of the local hot spots. Consequently, thermal management of electronic equipment has become a critical issue in the recent years and the lack of having an appropriate and efficient cooling technique may impede the rapid advances in electronics industry.

Before discussing the applicability of microchannels heat exchangers in electronics cooling, it is appropriate here to briefly shed the light on the other cooling techniques. It is well known that, air cooling using conventional fan system is the most commonly used technique. Unfortunately, this technique is about to attain its upper cooling limit. Zhou et al. (2004) and Webb (2005) reported that this technique could not dissipate more than 1–1.5 MW/m^2. In addition to that, it is a noisy technique. Another cooling scheme is the thermoelectric cooling module that has the advantages of noise free, compactness and no fluid flow. However, Yang et al. (2007) reported that they have very low cooling capacity of 0.05– 0.1 MW/m^2 for the best commercially available conventional one and up to 1 MW/m^2 for the miniaturized one. Additionally, Simons and Chu (2000) reported that, thermoelectric modules have a lower COP compared to the vapour compression refrigeration. Since the cooling performance of thermoelectric coolers improves when the contact area with the hot surface decreases, Prasher et al. (2005) proposed cooling the die locally at the hot spots using Thin Film Thermoelectric Cooler (TFTEC). This may lead to a reduction in the total average power dissipation from the other locations. However, they reported that the thermal performance is still not reasonable and some practical challenges are still required. Recently, Nnanna et al. (2009) experimentally investigated the thermal augmentation of a thermoelectric module using a nanofluid-based micro heat exchanger. With this module, the measured thermal resistance was 0.12 K/W. However, this value is equivalent to dissipating heat flux value of 1.5 MW/m^2 for a microprocessor footprint area of 18 × 18 mm^2 and chip temperature rise of 60 K. Another cooling scheme that may be used is the direct liquid cooling by jet impingement using single or array of micro-jets. This technique dissipated 2.5 MW/m^2 using water as reported by Natarajan and Bezama (2007) and 3.1 MW/m^2 using water and FC-40 as reported by Fabbri and Dhir (2005). With the advent

of laptops, heat pipes were used as a cooling scheme. Nevertheless, Jiang et al. (2002) reported that they are not optimum for chip power in excess of few tens of Watts due to the limitations in the wick thickness and the expected increase in cross section area. For example, Singh et al. (2007) and Zimbeck et al. (2008) attained heat flux values of 0.5 MW/m^2 using loop heat pipe. Even with a pulsating heat pipe, which is considered as an advanced one, the heat dissipated was 2.5 MW/m^2 as reported by Zuo et al. (2000).

Since the aforementioned cooling techniques could not attain heat fluxes above 10 MW/m^2, microchannels single phase liquid cooling scheme has been introduced by some investigators such as Tuckerman and Pease (1981), Zhou et al. (2004), Zhang et al. (2005), Wei et al. (2007), Kang et al. (2007) and Xie et al. (2009). Thirty years ago in 1981, Tuckerman and Pease tested a water-cooled silicon microchannels heat sink for cooling very large-scale integrated circuits (VLSI). This heat sink has channels with hydraulic diameter of 98.6 μm and achieved thermal resistance of 0.09 K/W and power dissipation up to 7.9 MW/m^2. This high value of power dissipation was accompanied by high pressure drop, which was in the order of 1.2 bar. Zhou et al. (2004) presented a prototype for an electro-kinetic microchannel cooling system for desktop computers using water as a fluid. Their cooling system was consisting of a microchannel heat exchanger with hydraulic diameter of 30 – 100 μm, electro-kinetic pump and liquid-air heat exchanger. Their configuration managed to remove an average heat flux value of 2.5 MW/m^2 and local peak value of 3.6 W/cm^2 with a thermal resistance of 0.37 K/W at liquid flow rate of 300 ml/min. Zhang et al. (2005) developed a liquid cooling apparatus for microchips using an aluminium microchannels heat sink of 0.38 mm hydraulic diameter and water as a test fluid. They measured thermal resistances of 0.44 – 0.32 K/W for 12 × 12 mm chip and 0.59 – 0.44 K/W for 10 × 10 mm chip. These values of resistance indicate that heat flux values over 1.3 MW/m^2 can be dissipated for a temperature rise of 60 K and pressure drop in the order of 0.2 bar. Wei et al. (2007) experimentally evaluated the thermal performance of liquid cooling module developed for cooling microelectronic devices and consisting of a stacked microchannels (multilayer) heat sink of 90.7 μm hydraulic diameter and de-ionized water as a test fluid. This system achieved thermal resistance of 0.09 $K/W.cm^2$ over chip area of 1 cm^2. Kang et al. (2007) proposed a prototype for a closed loop liquid cooling for high performance computer systems. This cooling system was designed for cooling the CPU and GPU in a Dell Dimension 9100 commercial PC and it consists of a DC pump, cold

plates, heat exchangers (D_h = 4.17 mm), flexible tubing and coolant. The authors reported that, this system managed to dissipate a heat flux of 5 MW/m^2. Xie et al. (2009) numerically optimised the configuration of a microchannel heat sink for cooling electronics components and found that a heat flux value of 2.56 MW/m^2 can be achieved at a pumping power of 0.205 W.

Though microchannel liquid cooling managed to remove heat fluxes up to 7.9 MW/m^2, it still has some drawbacks. One problem is the linear temperature rise of wall temperature in the stream wise direction – something which is not desirable in electronics systems. A second problem is the required high mass flow rate to meet a certain cooling demand, which requires higher pumping power. Accordingly, phase change cooling such as immersion cooling, i.e. pool boiling, and flow boiling were proposed to alleviate the very high heat fluxes and keep moderate changes in the chip temperature. In immersion cooling technique, the electronic component is immersed in a saturated or sub-cooled pool of inert non-flammable dielectric liquid. It has the advantages of suitability for multichip cooling, no pump, no hoses and little danger of short circuit due to liquid leakage. One of the problems of this technique is that, it is only limited for a few number of fluids, i.e. dielectric fluids, which unfortunately have poor thermal transport properties compared to other coolants such as water. Another drawback of this technique is the danger of damaging the chip by thermal shock at the onset of nucleate boiling due to vigorous boiling and temperature excursion as addressed by Mudawar (2001). Moreover, dielectric fluids have a very small contact angle, which means that the large cavities will flood and vapour embryos will be trapped in a micro-cavity within the large cavity. As a result, high wall superheat will be required to trigger nucleation, a value that reached 46 K for FC-72 as reported by Mudawar (2001). El-Genk et al. (2003) experimentally investigated pool boiling of HFE-7100 from 1 cm^2 smooth copper surface simulating a high performance computer chip. Their results demonstrated that only up to 0.245 MW/m^2 could be removed. Geisler et al. (2004) investigated an immersion cooling module for military electronics using FC-72 as a fluid and reported heat removal from the chip in excess of 0.2 MW/m^2. Even with surface enhancements, the CHF increased from 1.05 MW/m^2 to 1.6 MW/m^2 in saturated and sub-cooled FC-72 liquid as reported by Mudawar (2001), which are still far away from the required cooling demand.

Two phase flow boiling heat sinks have the advantage of requiring much lower mass flow rate than single phase heat sinks for the same thermal duty and consequently low pumping power. Additionally, due to phase change, the hot surface temperature remains approximately uniform at values slightly higher than saturation temperature and also it does not vary significantly with the variations in the applied load (sudden jump or drop in the heat flux). This advantage is desirable for reducing the thermal stresses and consequently prolonging the life of the device. Jiang et al. (2002), Faulkner et al. (2003), Agostini et al. (2008a) and Lee and Mudawar (2009) investigated two phase cooling of high heat flux electronic equipment. Jiang et al. (2002) developed a closed loop two phase micro-channels cooling system using electro-osmotic pumping for cooling VLSI using de-ionized water as a test fluid. The heat sink was a plasma-etched silicon multichannel with hydraulic diameter of 0.1 mm and directly attached to a $1cm^2$ chip. This system achieved thermal resistance of 0.1 K/W and removed only 0.38 MW/m^2. Faulkner et al. (2003) experimentally investigated sub-cooled and saturated boiling of water in a microchannel heat sink and found that up to 1.25 MW/m^2 and 2.8 MW/m^2 for saturated and sub-cooled boiling, respectively, can be removed. Agostini et al. (2008a) experimentally investigated the performance of a two phase cooling system for a chip at very high heat flux using R236fa. The heat sink was composed of 134 parallel channels 67 × 680 μm and 20 mm length. Their module managed to keep the junction temperature below 52 ^0C while dissipating 2.55 MW/m^2. With some kind of extrapolation they concluded that, two phase cooling is able to cool the chip 13K lower than single phase liquid cooling for the same pumping power at heat flux value of 3.5 MW/m^2. Lee and Mudawar (2009) discussed the benefits of cooling Defense electronics using direct and indirect refrigeration cooling system. In the direct cooling system, a micro-channel heat sink served as an evaporator in a vapour compression cycle using R134a as a fluid. In the indirect cooling system, HFE7100 was used to cool the heat sink in a primary pumped liquid loop that rejects heat to a secondary refrigeration loop. In the direct system, the fluid undergoes saturated flow boiling while in the indirect one it was under highly sub-cooled boiling. They concluded that, indirect cooling system is more effective than the direct one where indirect system yielded cooling heat fluxes as high as 8.4 MW/m^2 at G = 16765 kg/m^2 s without attaining the critical heat flux. Recently, Sung and Mudawar (2009) combined the benefits of two phase micro-channels heat sinks and the two phase impinging jets in a hybrid cooling technique with the aim of increasing the critical heat flux. The micro-channels heat sink was horizontal

and the fluid HFE7100 was introduced into the channels through a series of micro jets located on the top surface of each channel. After impinging, the fluid gets out from both sides of the channel into the outlet plena. This module removed heat flux values as high as 11.27 MW/m^2, which is the highest value ever achieved from a dielectric fluid at near atmospheric pressure. The trend of the measured pressure drop in this system was contrary to trends found in most flow boiling situations. The pressure drop decreased with increasing heat flux and reached its minimum value just before the critical heat flux. They attributed this to the different nature of nucleate boiling encountered in the hybrid system compared to conventional micro-channels. In conventional micro-channels the void fraction increases monotonically along the channel, which increases both frictional and acceleration components of pressure drop. In the hybrid configuration, the void fraction increases gradually between jets before it greatly decreases due to condensation beneath the jet and consequently the void fraction undergoes mild changes along the channel resulting in lower pressure drop. However, from their graphs the measured values of pressure drop exceeded 2 bar, which is significantly high.

Nnanna (2006) experimentally investigated the performance of R134a vapour compression refrigeration for cooling high heat flux electronics and computers. The author was interested in investigating the transient response of the evaporator to the variation in the applied load. The evaporator was directly attached to the heating surface, which simulates the electronic device. It was observed that the temperature highly oscillated at the early stage of cooling, which was attributed to the adjustments made in the thermostatic expansion valve to compensate the variations in the applied load. These temperature oscillations are not desirable in electronics, which could lead to thermal stress and failure. Also, the temperature at the exit of the evaporator was the highest one as a result of the existence of vapour phase, i.e. dryout. Truttasanawin et al. (2006) developed and experimentally examined R134a mini-refrigeration system for electronics cooling applications. They found that the most significant energy losses were in the compressor, which calls for a better compressor design to achieve better performance with electronics cooling. The compressor failed after 400 hr of operation. Thus, the challenge in applying miniature refrigeration system to cool electronics equipments is the efficiency and reliability of the compressor. This system was able to

dissipate heat fluxes in the order of 0.4–0.75 MW/m^2 and keep the junction temperature below 85 ^{0}C.

It can be concluded from the above studies that, having a reliable and efficient cooling technique for high and ultrahigh heat flux systems is still a big challenge. Single phase liquid cooling and jet impingement may be good options for dissipating high heat fluxes but on the expense of pressure drop. Also, the high pressure drop, flow mal-distribution and flow reversal in saturated flow boiling heat sinks may add some limitations on the maximum heat flux. Most studies reported values below 5 MW/m^2, which is still far away from the cooling demand of at least 10 MW/m^2. On the other hand, sub-cooled flow boiling may be a good option for combining dissipating high heat fluxes with low pressure drop. But, sub-cooled boiling heat sinks require working at high system pressure in order to increase the sub-cooling degree. This may require a more safe and rigid system, which represents another issue in electronics systems. In addition to that, using a miniature vapour compression refrigeration system for electronics cooling is another big challenge.

1.2.2 Refrigeration and air conditioning

The use of microchannels heat exchangers in refrigeration and air conditioning industry has several benefits. Reay (2002) summarized the benefits of using compact heat exchangers in the refrigeration industry as follows: (i) high coefficient of performance (COP) due to their high effectiveness and close temperature approach, (ii) easier retrofitting and lower fluid inventory due to the smaller volume and weight, (iii) lower installation cost and improved safety as a result of the reduced fluid inventory and (iv) better system control due to their fast response. Another important benefit of using micro heat exchangers in refrigeration and air conditioning industry is the ability to reduce global warming and ozone layer depletion. Petterson et al. (1998) reported that, the annual emission of refrigerants is likely to exceed 100,000 tonnes, which corresponds to the impact of more than 150 million tonnes CO_2. This figure is expected to decrease if compact heat exchangers are used.

Hrnjak and Litch (2008) carried out an experimental study on a prototype for ammonia chiller with an air-cooled condenser and flat evaporator with the aim of charge reduction and compactness. They evaluated two aluminium air-cooled condensers. The

first one was a single serpentine macro-tube condenser (D = 4.06 mm) and the second was a parallel microchannels condenser (D_h = 0.7 mm). They reported that, microchannels condensers reduced the specific charge by 76 % (18 g/kW) compared to the serpentine macro-tube condenser. Additionally, the overall heat transfer coefficient in the microchannels condenser was 60 – 80 % higher than that of the serpentine one. Qi et al. (2010) reported some enhancements in the performance of automotives air conditioning system due to using microchannels heat exchangers. They have tested two systems; one was composed of the normal heat exchangers used in the current market (laminated evaporators and parallel flow condensers) as a baseline while the second was composed of the new parallel microchannels heat exchangers. Their results demonstrated that, microchannels heat exchangers resulted in: (i) 17.2 % and 15.1 % volume reduction and 2.8 % and 14.9 % weight reduction for the evaporator and condenser respectively and (ii) 5 % and 8 % enhancement in the cooling capacity and COP respectively. Park and Hrnjak (2008) experimentally and numerically investigated the effect of condenser type on the performance of R410A residential air conditioning system. They carried out a comparison between two similar systems but with different condenser type where one was a microchannel condenser while the other was a round tube condenser. They reported significant performance improvement with the microchannels condenser where the COP increased by 13.1 %, condensation temperature decreased by 2.5 K, pressure drop decreased by 66 % and charge was reduced by 9.2 %. Poggi et al. (2008) discussed the different strategies of reducing refrigerant charge in refrigeration systems. Amongst these strategies was to use compact heat exchangers for evaporators and condensers. On doing so, they found that the specific charge was reduced to 17 – 29 g/kW compared to that of the conventional evaporators and condensers, which was 400 – 1000 g/kW.

Although having compact refrigeration units is promising, there are still some practical limitations. Jeong (2004) discussed the difficulties of having micro-refrigerators in light of the second law of thermodynamics by estimating the entropy changes for each component in a vapour compression refrigerator. The author reported that, the mechanical compressor is the most difficult component to be miniaturized in a micro-refrigerator. Thus, to have a micro vapour compression refrigerator a great deal of effort must be made to have a workable micro-compressor, as mentioned earlier with reference to the result of Truttasanawin et al. (2006). Another practical problem with

micro-channels evaporators is the mal-distribution of the fluid. Shao et al. (2010) investigated the performance of a commercial heat pump using microchannels heat exchangers as an evaporator compared to the performance of the conventional finned tube heat exchangers under frost conditions. Their results showed that the performance of the microchannel heat pump could be improved provided that refrigerant distribution in the channels is uniform.

In addition to using microchannels heat exchangers in the field of electronics cooling and refrigeration and air condition industry, automotives industry is another important future market. The only current application of phase change microchannels heat exchangers in automotives industry is limited to the air conditioning system. However, other future applications are possible especially with the development of the fuel cell vehicles. One of the major challenges with this type of vehicles is the availability of hydrogen required to feed the cell. Since storing hydrogen on board is a big problem, one proposed solution is to have on-board fuel reformer that converts the current gasoline or diesel fuel into hydrogen rich gas. Accordingly, microchannels heat exchangers will be required at that point for the reforming system, cooling the fuel cell and cooling the power transmission motors.

1.3 Research motivations

It is clear from the aforementioned discussion that microchannels heat exchangers are promising in vapour compression refrigeration, electronics cooling, automotives, energy savings and environment. However, several fundamental issues at microscale were raised by the research community. These issues may be divided into single phase and two phase issues as discussed below.

1.3.1 Single phase issues

It is known that, the two phase flow boiling correlations are usually developed as a function of single phase parameters, i.e. single phase heat transfer coefficient and friction factor. These parameters are calculated from the commonly used conventional single phase correlations. However, some recent single phase experimental studies reported some size effects on single phase parameters and thus single phase correlations

should be used with some caution. Accordingly, in this section, some of the important single phase issues will be discussed.

1. The first issue is the dependence of the *Poiseulle's* number *(Po = fRe)* on *Re* in the laminar flow regime. This has been observed by Mala and Li (1999) and Li et al. (2003) for de-ionized water flow in micro-tubes of diameters ranging from 50 to 1570 μm. Conventionally, this number equals 16 for circular channels and does not change with *Re*.
2. The second issue is the measured value of the friction factor. Some researchers measured higher values than conventional theory but keeping the same trend, i.e. the *Poiseulle's* number remains constant but higher than theory. This trend has been reported by Tang et al. (2007) and Li et al. (2003). Other researchers such as Choi et al. (1991) found that for a tube having an inner diameter of 10 μm the *Poiseulle's* number was lower than the conventional value by a factor of 17.2 %. Even for turbulent flow, Hegab et al. (2001) found that the friction factor of R134a was 9 – 23 % less than theory.
3. The third issue is the early transition from laminar to turbulent flow regime reported by Mala and Li (1999), Guo and Li (2003), Yang et al. (2003), Hsieh et al. (2004) and Liu et al. (2007) at Re values of 300 – 900, 1000, 1200, 240 and 1100 – 1500, respectively.
4. The fourth issue is the channel diameter at which departure from single phase conventional theory occurs. For example, Mala and Li (1999), Li et al. (2003), Li et al. (2007), Liu et al. (2007) and Celata et al. (2002) found deviation occurred at diameters 150 μm, 129 μm, 373 μm, 168 μm and 130 μm, respectively. However, Hetsroni et al. (2005) carried out a review on fluid flow in microchannels and concluded that the conventional theory is valid at least up to channel diameter of 50 μm.
5. The fifth issue is the dependence of *Nu* on *Re* in the fully developed laminar flow that was found by Choi et al. (1991) and Lee et al. (2005). Conventionally, *Nu* does not depend on *Re* and equals 4.36 under constant heat flux boundary conditions. However, Qu et al. (2000) found that the Nu number had a similar trend to the classical theory but its value was much lower than the theoretical value of 4.36.

6. The sixth issue that must be mentioned is the measured value of the heat transfer coefficient. For example, Choi et al. (1991), Hegab et al. (2001), Adams et al. (1998), Qu et al. (2000) and Lee et al. (2005) found differences larger than the experimental error between their measured single phase heat transfer coefficient and the theory.
7. In addition, the next issue is the significant effect of surface roughness in laminar flow that is conventionally negligible. This factor was assessed by Mala and Li (1999), Qu et al. (2000) and Kandlikar et al. (2001). Mala and Li (1999) included the increase in fluid viscosity due to surface roughness in the momentum equation, which was ignored at macro scale. On doing so, their numerical solution agreed quite well with the measured values which confirmed the significance of surface roughness. Kandlikar et al. (2001) experimentally investigated the effect of surface roughness using tubes with diameters of 0.62 and 1.032 mm. The roughness was changed by etching the surface with an acid solution. It was found that, the effect of roughness on the heat transfer coefficient for the larger tube was insignificant while for the smaller tube with $\varepsilon > 0.003$ the heat transfer coefficient increased with roughness. Consequently, a new threshold value for the significance of relative roughness at microscale was introduced compared to the macro scale value of 5 %. The new threshold value ranged from less than 1 to 1.5 % according to the work of Mala and Li (1999), Li et al. (2007), and Wang and Wang (2007). However, Hrnjak and Tu (2007) experimentally showed that relative roughness may not be the best criterion for explaining the departure from theory. Since the departure from the theory occurred with the tube that has lower relative roughness, they believed that the shape and distribution of roughness element is the most important parameter.

Despite the discrepancy and departure from theory reported above, many investigators did not find any size effect on fluid flow and heat transfer in micro-channels, Agostini et al. (2002), Li and Cui (2003), Lelea et al. (2004), Owahib and Palm (2004), Hwang and Kim (2006), Li et al. (2007), Hrnjak and Tu (2007), Hao et al. (2007) and Lin and Yang (2007). Researchers who reported a size effect on heat transfer and fluid flow at microscale attributed this to the effect of surface roughness, the effect of ionic concentration in the fluid, viscous heat dissipation and axial heat conduction. Mala et al. (1997) studied theoretically the effect of the electric double layer (EDL) on the friction

constant. They introduced the friction constant *(fRe)* as a function of the surface potential and some dimensionless parameters. It was concluded that, as the surface potential increases, i.e. the electrostatic charge at the surface increases, the friction constant increases above the conventional value of 24 for rectangular channels. Maranzana et al. (2004) and Li et al. (2007) studied numerically conjugate heat transfer and proposed a dimensionless number M to estimate the significance of axial heat conduction. Maranzana et al. (2004) reported that if $M < 0.01$, axial heat conduction can be neglected while Li et al. (2007) found that for axial heat conduction to be neglected M should be in the order of 10^{-5}. Recently, Rosa et al. (2009) carried out a review of single phase heat transfer and placed emphasis on the importance of scaling effects. They concluded that standard theories and correlations "are suitable to describe heat transfer in micro-channels, once cross-section geometry, scaling effects and measurement uncertainties are carefully considered." The following scaling effects were considered important: entrance effects, temperature dependence of the fluid properties, rarefaction effects (gases only) compressibility effects (gases only), conjugate heat transfer, viscous heating and EDL effects. The surface effect was considered not to have a major effect. Another important parameter that might result in a deviation from the conventional theory is the accuracy of measuring the channel diameter. For example, the fanning friction factor depends on D^5 for circular channels, which means that any small error in diameter measurement may lead to high deviations in the measured friction factor.

1.3.2 Flow boiling issues

Though the number of flow boiling studies at microscale has increased in the last decade, still there is no agreement between researchers on several issues and there is a wide scatter in the published results.

1. The first issue is the threshold diameter at which the channel may be regarded as small, mini and micro. Some people such as Shah and Sekulic (2003) used the surface area density (β) to differentiate between conventional, compact, meso and micro heat exchangers. Heat exchangers were regarded as compact when $\beta \geq 700$ m^2/m^3, meso when $\beta \geq 3000$ m^2/m^3 and micro when $\beta \geq 15000$ m^2/m^3. When these values of β are converted into hydraulic diameter, similar ranges to those given by Mehendale et al. (2000) will result. These ranges are: $D > 6$ mm for macro exchangers, $D = 1 - 6$ mm for compact exchangers, $D =$

0.1 – 1 mm for meso exchangers and *D = 0.001 – 0.1* mm for micro exchangers. Kandlikar and Grande (2003) proposed other different ranges based on the applications. They have considered the exchangers as conventional when *D > 3* mm, mini when *D = 0.2 – 3* mm and micro when *D = 0.01 – 0.2* mm. If the threshold diameter is defined as the one at which the phenomenon changes, the previous classifications seem to be not representative because it does not consider the physical mechanisms and other flow effects. The absence of stratified flow in horizontal microchannels and hence the fact that channel orientation has no effect on two phase flow pattern indicates the predominance of surface tension force over gravity and buoyancy forces. Consequently, a number of attempts to define macro to micro transition have used surface tension as a base to formulate a non-dimensional criterion. These include Eotvös number (Eö >1) recommended by Brauner and Maolem-Maron (1992), confinement number (*Co* = 0.5) by Cornwell and Kew (1993), Bond number ($Bd^{0.5} \leq 0.3$) by Su and Griffith (1964) and Laplace constant, *La = D* by Triplett et al. (1999). Thome (2004) reviewed flow boiling in microchannels and discussed the use of bubble departure diameter as a preliminary criterion. He also mentioned the effect of shear on bubble departure diameter and reduced pressure on bubble size that needed to be considered in addition to surface tension forces. Applying these criteria given by eqns. (1.1–1.4) on R134a at 8 bar, the threshold diameter values will be 0.24, 5.1, 1.63 and 0.81 mm, respectively. In conclusion, the aforementioned diameter ranges and even the physics-based criteria reflect the discrepancy about the definition of macro, mini and microchannels.

$$Bd = D\left[\frac{\sigma}{g\Delta\rho}\right]^{-0.5} = 0.3 \tag{1.1}$$

$$\text{Eö} = \frac{(2\pi)^2\sigma}{\Delta\rho g D^2} = 1 \tag{1.2}$$

$$Co = \frac{1}{D}\sqrt{\frac{\sigma}{g\Delta\rho}} = 0.5 \tag{1.3}$$

$$La = \left[\frac{\sigma}{g\Delta\rho}\right]^{0.5} = D \tag{1.4}$$

where, $\Delta\rho = \rho_L - \rho_g$

2. The second issue is the prevailing heat transfer mechanism. There is no common agreement between researchers on the dominant heat transfer mechanism at micro-scale. In large diameter channels, it is known that nucleate boiling dominates at low vapour qualities and convective boiling dominates at high vapour qualities. Conventionally, nucleate boiling dominates when the heat transfer coefficient depends on heat flux but does not change with vapour quality and mass flux. Whereas convective boiling dominates when the heat transfer coefficient depends on mass flux and vapour quality but does not change with heat flux. However a large number of experimental studies were conducted at micro-scale, various conclusions were drawn on the dominant heat transfer mechanism. For example, one group such as Lazarek and Black (1982), Wambsganss et al. (1993), Tran et al. (1996), Bao et al. (2000), Agostini and Bontemps (2005), Marín-Callizo et al. (2007), Del Col et al. (2008) and Bertsh et al. (2009) concluded the dominance of nucleate boiling mechanism. A second group such as Sumith et al. (2003), Lee and Lee (2001) and Lee and Mudawar (2005b) concluded convective boiling mechanism. In addition, a third group such as Yan and Lin (1998), Lin et al. (2001a), Saitoh et al. (2005) and Chin and Thome (2009) concluded nucleate and convective boiling mechanisms. Thome (2004) and Thome et al. (2004) argued that the prevailing heat transfer mechanism in micro tubes is the transient thin film evaporation in the elongated bubble regime rather than nucleate boiling. This point was the basis of the three zone evaporation model that was developed by them for slug flow in micro tubes. In fact, there is no full understanding whether heat transfer occurs by film evaporation or nucleation. Some investigators such as Kasza et al. (1997) observed small nucleating bubbles in the liquid film around the vapour slug during water flow boiling in a narrow rectangular channel. Also, Haririchian and Garimella (2009) observed small nucleating bubbles in the liquid film of the wispy-annular flow during flow boiling of FC77 in rectangular microchannels. In conclusion, the heat transfer mechanism at micro scale is not clear. Additionally, there is a wide scatter on the local behaviour of the heat transfer

coefficient as summarized by Agostini and Thome (2005) in Fig. 1.1 The figure is divided into two rows and four columns. The first row depicts the effect of heat flux while the second one shows the effect of mass flux with X1 and X2 does not show any heat and mass flux effects. Unfortunately, the reasons behind this wide discrepancy in these trends are not yet understood.

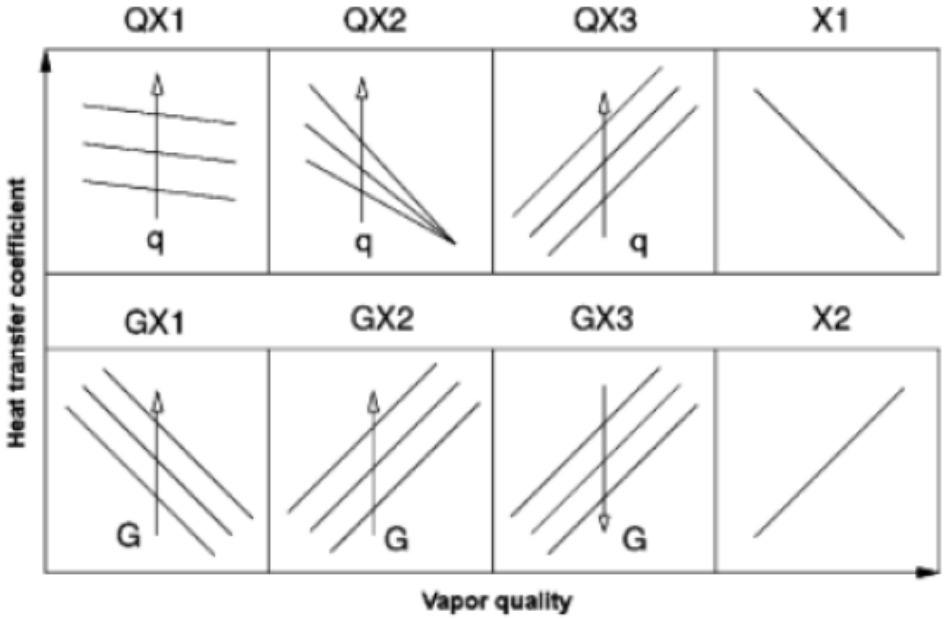

Fig. 1.1 The trends of the local heat transfer coefficient versus vapour quality as a function of heat and mass fluxes, Agostini and Thome (2005)

3. The third issue is the flow boiling hysteresis. This issue is very important and must be investigated in microchannels due to the expected few number of nucleation sites per unit length. Only, few experimental studies have examined this phenomenon. Chin and Thome (2009) observed only boiling hysteresis that is associated with boiling incipience only. They reported high temperature undershoot of 17 K for R134a and 1.09 mm diameter tube. By contrast, Bertsh et al. (2009a) did not observe any temperature undershoot for R134a in microchannels with hydraulic diameters of 0.54 and 1.09 mm. Marín-Callizo et al. (2007) observed for R134a and tubes of diameters 0.83, 1.22 and 1.7 mm a temperature undershoot of 18 K with the presence of nucleation hysteresis.

4. The fourth issue is the applicability of macro scale models and correlations at microscale level. Many researchers evaluated the macro scale correlations using experimental data collected using small to micro diameter channels and found very poor agreement. Even the recent micro scale correlations that were developed based on certain experimental data failed to predict the data from other laboratories. The lack of validated design correlations represents a major barrier to the wide spread commercial applications of compact evaporators as reported by Watel et al. (2003). They mentioned that the current design advancement is made based on the basis of experience and experimentation on prototypes. Having accurate design correlations requires more accurate experimental database, the corresponding flow regimes and the controlling heat transfer mechanism.

1.4 Objectives

It is clear from the aforementioned issues that flow boiling fundamentals at microscale level are still unclear and require more research. Accordingly, an experimental facility was carefully designed and constructed by X. Huo (2005) with the contribution of L. Chen (2006) for a long term experimental project to investigate flow boiling patterns, pressure drop and heat transfer in small to micro diameter vertical metallic tubes. Only single tubes were investigated to exclude the effects of uneven flow distribution encountered in multi-channels and the effects of channel corners in case of non-circular channels. X. Huo studied heat transfer and pressure drop in 4.26 and 2.01 mm diameter tubes while L. Chen (2006) carried out an extensive flow visualization study using four tubes of diameters 4.26, 2.88, 2.01 and 1.1 mm. D. Shiferaw (2008) extended the heat transfer and pressure drop experiments to include diameters of 2.88, 1.1 and 0.52 mm tubes. Thus, the effect of tube diameter on flow boiling characteristics was investigated and clarified.

All test sections investigated in the above studies were seamless cold drawn stainless steel tubes and were directly heated by AC current that was supplied by a high current transformer and controlled by a variac. The experimental results of the 0.52 mm diameter tube showed different behaviour compared to the other investigated tubes. Additionally, partial dryout was found to occur early at heat fluxes corresponding to

exit quality in the order of 0.5, i.e. intermediate heat fluxes. In some cases partial dryout started more early at local qualities in the order of 0.3 especially in the 1.1 mm tubes. This behaviour is not desirable and represents a big limitation on using small diameter tubes heat exchangers for dissipating high heat fluxes. As a result, the objectives of the current study include:

1. Investigate flow boiling heat transfer and pressure drop for the 0.52 and 1.1 mm tubes using DC heating instead of AC with the simultaneous recording of flow patterns. As will be discussed later in Chapter 3, heating the tube using AC current has insignificant effect as long as the tube wall is thick enough. Since the wall thickness of the 0.52 is smaller than the other tubes, DC heating was used to avoid any effect for AC current.
2. Investigate flow boiling hysteresis in the examined tubes by conducting the tests in both directions, i.e. increasing and decreasing heat fluxes. This phenomenon was investigated by few researchers and it is still not clarified. Investigating hysteresis is important due to the possibility of only few nucleation sites per unit length at micro scale.
3. Study the effect of varying the heated length on flow boiling characteristics. There is no criterion for selecting the length of the examined heated sections in the open literature. Some researchers examined too short test sections while some others examined too long ones. If the micro evaporator is too short, the heat flux required to attain exit quality of about one will be too high. This intensive heating may cause local thermal non equilibrium resulting in vigorous boiling which may cause partial dryout. If the evaporator is too long the flow patterns may keep developing along the channel and thus the heat transfer mechanism may vary along the heated length. Accordingly, investigating this parameter may contribute in explaining the wide scatter in the published heat transfer results.
4. Evaluate the existing heat transfer and pressure drop correlations and models.
5. Investigate the effect of inner surface characteristics on the local heat transfer behaviour. This will be carried out through testing two tubes of similar dimensions but manufactured by two different methods: seamless cold drawn and welded. This may greatly contribute in interpreting the wide scatter in the local heat transfer behaviour reported in the open literature.

1.5 Outlines of the thesis

The current thesis is organised as follows. Chapter 2 presents an overview on the previous experimental studies in small, mini and microchannels. The review in this chapter covers several topics such as flow patterns in adiabatic and heated channels, void fraction and bubble dynamics, experimental heat transfer and pressure drop, flow instability and prediction approaches. Chapter 3 gives a detailed description for the experimental facility, measurement system, single phase validation and uncertainty analysis. Chapter 4 presents and discusses the flow patterns and heat transfer results. In chapter 5 a detailed evaluation of the existing heat transfer models and correlation is presented. Chapter 6 presents the pressure drop results as well as the evaluation of pressure drop models and correlations. Chapter 7 gives the conclusions and recommendations for future work.

Chapter 2

Review of Flow Boiling Studies at Microscale

2.1 Introduction

The term “microscale” is simply used herein as a general term referring to small/mini/micro channels as there is no agreement on the threshold diameter value between macro and small/mini/micro. On the other hand, the term “macroscale” is used for conventional large diameter channels. As discussed in Chapter 1, flow boiling in microchannels is very promising for cooling high and ultra-high heat flux systems. However, the fundamentals of flow boiling at microscale are still unclear. Therefore, more research was directed towards investigating flow boiling at microscale. This research has covered several topics such as flow boiling patterns, boiling incipience, critical heat flux and dryout, heat transfer characteristics and two phase pressure drop. This chapter presents a detailed review for theses topics.

The chapter is organized as follows: Section 2.2 provides a review of the typically observed flow patterns at microscale while section 2.3 presents the flow pattern maps. Section 2.4 presents the studies covering two phase flow pressure drop and section 2.5 presents the pressure drop prediction methods. Section 2.6 reviews bubble dynamics and void fraction. Section 2.7 reviews the liquid film thickness measurement in slug flow. Section 2.8 gives a review of flow boiling heat transfer characteristics at microscale (nucleation, boiling incipience and hysteresis). Section 2.9 reviews the characteristics of the measured flow boiling heat transfer coefficient. Section 2.10 presents the prediction methods used for predicting the flow boiling heat transfer coefficient. Section 2.11 presents the studies covering the critical heat flux CHF and

dryout phenomena. Section 2.12 gives a review of the flow boiling instability and finally section 2.13 summarizes the findings of this chapter.

2.2 Flow patterns: experimental observation

Flow patterns in macrochannels can be identified using either integral or local techniques as reported by Bergles et al. (1981). In the integral techniques, the flow is directly visualized in a transparent section using a high speed camera. In the local techniques, a certain probe is locally inserted into the flow to detect the changes in a certain physical parameter and the flow patterns are deduced from the statistical properties of this parameter, e.g. power spectrum of the parameter. The integral techniques are more qualitative compared to the local techniques, which are more quantitative. In microchannels, using local techniques is difficult due to the big difficulties of inserting a probe without disturbing the flow. Recently, Revellin et al. (2006) used an optical technique for identifying the flow patterns of R134a in an adiabatic glass tube of 0.5 mm diameter. This technique aimed at determining flow patterns characteristics such as bubble velocity, bubble length and frequency. The features of the typically observed flow patterns in macro and microchannels are reviewed in the following sub-sections.

2.2.1 Flow patterns in macrochannels

The most commonly agreed and observed adiabatic flow patterns in macrochannels are presented herein for the purpose of comparison with those observed in microchannels. Figure 2.1 shows a schematic drawing for the generally recognized flow patterns in both vertical and horizontal large diameter tubes taken from Collier and Thome (1994). It is clear from the figure that, the flow patterns in vertical tubes differ from those in horizontal ones due to the effect of gravity and buoyancy forces. The qualitative description and features of the patterns shown in Fig. 2.1 can be found in Hewitt and Hall-Taylor (1970) and Collier and Thome (1994). In vertical co-current up flow, five flow patterns were identified namely: bubbly, slug, churn, wispy-annular and annular. In bubbly flow, the bubbles are smaller than channel diameter and may have the shape of a sphere or a cap with a flat tail. In slug flow, the bubbles are cylindrical in shape with size approaching the tube diameter, have a hemi-spherical head, surrounded by a

liquid film and separated from each other by a liquid slug that may contain tiny bubbles or may not. Churn flow is formed as a result of the breakdown of large bubbles in slug flow when gas velocity is high enough. This pattern is an unstable one where liquid phase moves up and down in an oscillatory motion while gas phase flows in a chaotic manner. In small diameter channels, the oscillation motion may disappear and smooth transition to annular flow may occur as reported by Hewitt and Hall-Taylor (1970). This pattern is sometimes called semi-annular or slug-annular flow. Wispy-annular flow occurs at high mass fluxes and is characterized by the relatively thick liquid film, existence of small gas bubbles in the film and large concentration of liquid droplets entrain to the gas core, which agglomerate and form long irregular wisps or lumps. In annular flow, the channel wall is covered with a liquid film, which may be smooth or wavy, while gas flows through the channel core with or without liquid entrainments.

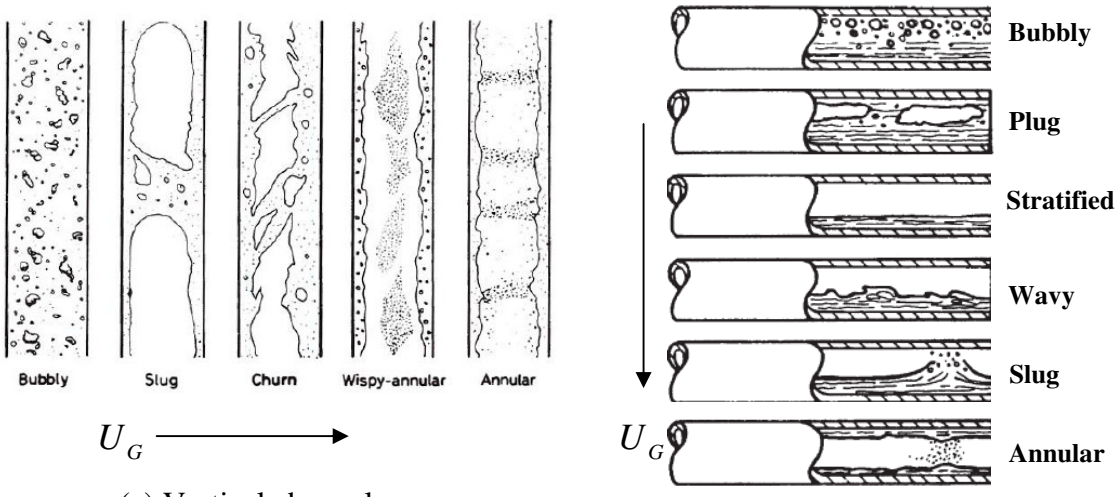

(a) Vertical channels

(b) Horizontal channels

Figure 2.1 The flow patterns in macro channels, Collier and Thome, (1994).

In co-current horizontal two phase flow, flow patterns were classified into four major patterns: dispersed (bubbly, dispersed bubbly), intermittent (slug, plug), stratified (wavy, smooth) and annular. Bubbly flow is similar to that observed in vertical channels except that the bubbles tend to travel in the upper section of the tube. However, at high mass velocities the bubbles tend to disperse uniformly in the tube due to the dominance of shear force and the pattern is sometimes called froth flow. Plug flow (elongated bubble flow) is similar to slug flow in vertical tubes with a thicker liquid layer at the bottom than at the top. Stratified smooth flow occurs only at very low liquid and vapour

velocities where the two phases flow separately with a smooth interface. Stratified wavy flow develops from stratified smooth flow with further increase in gas velocity such that the interface becomes disturbed with a wave travelling in the direction of flow. Slug flow develops from wavy flow when the summit of the wave reaches the upper surface of the channel. Further increase in gas velocity leads to the formation of a gas core with liquid film wetting the surface whose thickness at the bottom is greater than that at the top surface of the channel.

2.2.2 Flow patterns in adiabatic microchannels

There is an argument about using the adiabatic flow patterns in explaining the flow boiling heat transfer and pressure drop characteristics. Thus, the adiabatic studies are segregated from the flow boiling studies to clarify whether there is any difference or not. Compared to macrochannels, the flow patterns observed in microchannels are different as reported by Watel (2003). As channel size decreases, surface tension force dominates over gravity and buoyancy forces and therefore the effect of channel orientation becomes insignificant; Suo and Griffith (1964), Fukano and Karaiyasaki (1993), Chen et al. 2002 and Akbar et al. (2003). Hence, new patterns/features may appear or some of the conventional patterns may diminish. For instance, the conventional stratified flow pattern diminishes in microchannels, see Triplett et al. (1999), Coleman and Garimella (1999), Kawahara et al. (2002), Serizawa et al. (2002), Chen et al. (2002), Chung and Kawaji (2004), Hayashi et al. (2007), Xiong and Chung (2007), Yeom et al. (2007), Saisorn and Wongwises (2008), Weinmueller et al. (2009), and Saisorn and Wongwises (2010). Bubbly and churn flows were not observed in the experimental studies of Kawahara et al. (2002), Hayashi et al. (2007) and Xiong and Chung (2007). Three of the major conventional patterns namely bubbly, churn and annular flows were not observed in the experimental study of Chung and Kawaji (2004) in 50 and 100 μm diameter tubes where slug flow was the prevailing flow pattern.

Mishima and Hibiki (1996) and Wang and Bao (2009) conducted flow visualization studies in vertical tubes while Triplett et al. (1999), Coleman and Garimella (1999), Yang and shieh (2001) and Chen et al. (2002) carried out their studies in co-current horizontal tubes. Additionally, Fukano and Karaiyasaki (1993) investigated gas-liquid two phase flow in both horizontal and vertical tubes including upward and downward

orientations. Mishima and Hibiki (1996) investigated air/de-ionized water flow in four Pyrex glass tubes of diameters 1.05, 2.05, 3.12 and 4.08 mm. Superficial gas velocity was varied from 0.09 to 79.3 m/s and superficial liquid velocity was varied from 0.012 to 1.67 m/s. All conventional patterns were observed namely: bubbly, slug, churn, annular and annular-mist flow. Additionally, the 1.05 mm diameter tube demonstrated new features as seen in Fig. 2.2. The new features are: (i) in bubbly flow, the bubbles aligned along the centreline of the tube without coalescence forming either spiral train in case of very small bubbles or intermittent bubble train in case of relatively larger bubbles, (ii) in slug flow, the bubbles were relatively longer with a better defined spherical head and a thinner liquid film with the presence of small oscillating bubbles at the tail and (iii) in churn flow, the head of the long bubble was highly deformed with the appearance of a number of tiny bubbles moving rapidly in the liquid slug. It is worth mentioning that, the long slug with distortion at head and tail that appeared in the 1.05 mm tube was called churn flow.

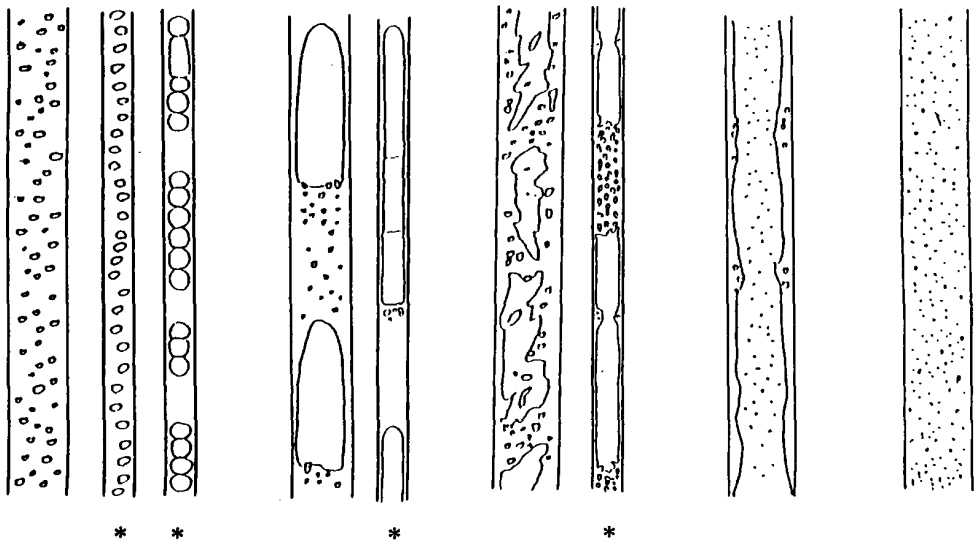

Figure 2.2 Sketch of the air-water flow patterns in co-current vertical tubes of diameter 1.05 – 4.08 mm (the asterisks refer to the special flow patterns observed in the 1.05 mm tube); Mishima and Hibiki, (1996).

Wang and Bao (2009) performed a flow visualization study for a mixture of nitrogen gas and aqueous CuO nano-fluid (0.2 – 2 % wt concentration) in a Pyrex glass tube of 1.6 mm diameter. The superficial gas velocity ranged from 0.1 to 40 m/s and the

superficial liquid velocity ranged from 0.04 to 4 m/s. In addition to that, they have conducted experiments using pure water and did not find any difference in the observed flow patterns between water and nano-fluid solution. The observed flow patterns included bubbly, slug, churn and annular as seen in Fig. 2.3. It is worth noting that, their description of churn flow was similar to that of the conventional wavy annular flow. Although the experimental conditions in the study of Wang and Bao and Mishima and Hibiki are almost similar, the features of bubbly, slug and churn flows are different as seen in Fig. 2.2 and Fig. 2.3. The differences in churn flow are not feature-related but it is a subjectivity problem. Mishima and Hibiki defined churn flow as long slugs with distortions at the head and tail whereas Wang and Bao defined churn flow as a wavy film flow. On the other hand, the different features of bubbly and slug flow may be due to the following reasons. First, the difference in inlet conditions, i.e. gas-liquid mixture entered the channel by different means. In the study of Mishima and Hibiki, the gas was injected co-axially into the channel using a micro nozzle of less than 0.5 mm inner diameter. This configuration may explain the concentration of the bubbles at the centreline of the 1.05 mm tube. On the other hand, Wang and Bao used a mixing chamber before the tube inlet that was packed with fine plastic meshes to enhance the mixing process. Second, the difference in physical properties of the liquid phase, i.e. de-ionised water versus aqueous CuO solution. Wang and Bao reported that the nano-particles decreased the surface tension of distilled water by around 63 % (However, as mentioned above, they did not report differences between this experiment and that with pure water).

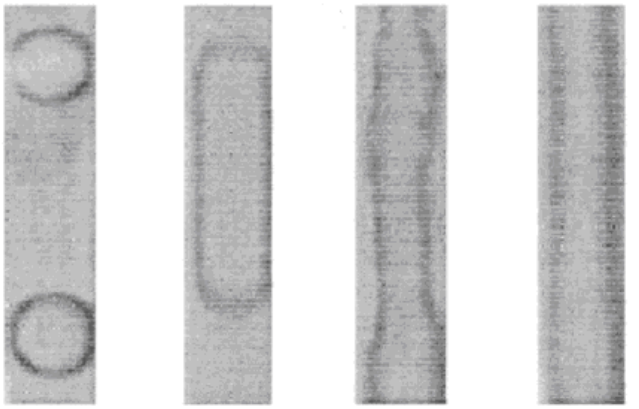

Figure 2.3 The flow patterns of N_2-aqueous CuO nanofluids in a 1.6 mm tube, Wang and Bao (2009).

Triplett et al. (1999) carried out a visualization study for air-water flow in two circular horizontal tubes of diameters 1.1 and 1.45 mm. The gas superficial velocity was varied from 0.02 to 80 m/s and the liquid superficial velocity was varied from 0.02 to 8 m/s. They identified five flow patterns namely: bubbly, slug, churn, slug-annular and annular as seen in Fig. 2.4. The definition of slug flow included both smooth confined bubbles with nice spherical head and tail and long slugs with flat tail and wavy liquid film interface. The liquid film at the bottom was found to be slightly thicker than that at the top and no tiny bubbles were observed either in the film or in the liquid slugs. Churn flow was found to appear in some cases as elongated bubbles, which are unstable near their trailing ends leading to their disruption. In some other cases, it appeared as flooding-type churning waves periodically disrupted. Slug-annular flow established at relatively low superficial liquid velocities as a result of the merging of elongated bubbles. In this pattern, long segment of the channel supported wavy-annular flow and were interrupted by large amplitude solitary wave, which was not sufficient to block the flow path. This wave disappeared with further increase in superficial gas velocity and thus annular flow establishes. Although the channel was horizontal, stratified flow was not observed within their experimental ranges, which confirms the predominance of surface tension.

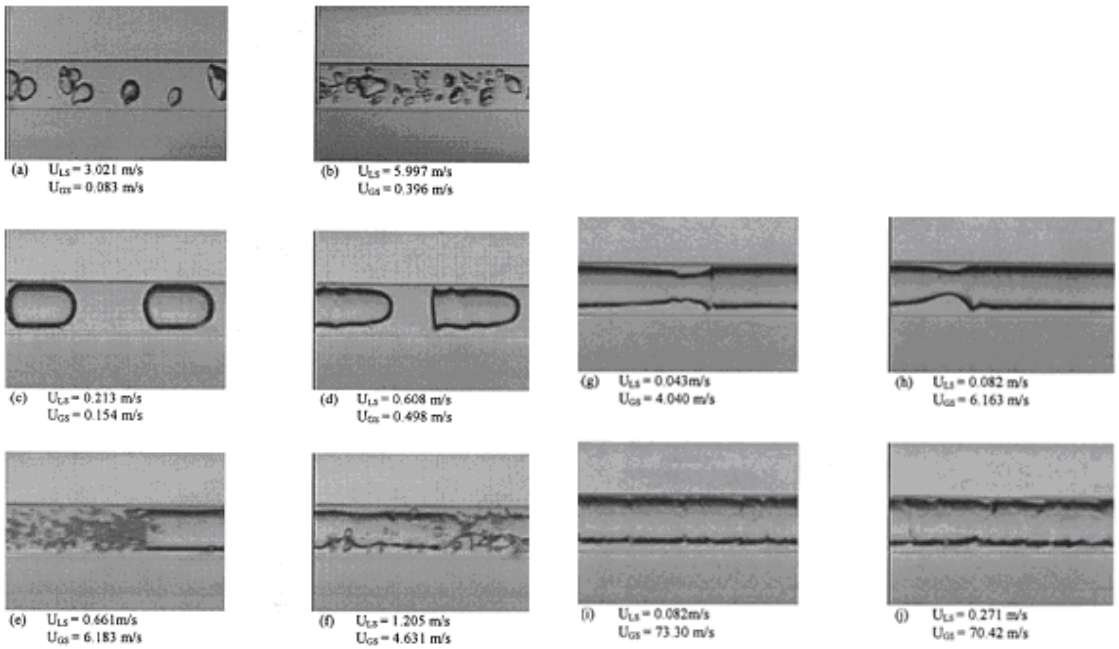

Figure 2.4 The flow patterns in the 1.097 mm diameter circular test section: (a), (b) bubbly, (c), (d) slug, (e), (f) churn, (g), (h) slug-annular, (i), (j) annular, Tripplet et al. (1999).

Coleman and Garimella (1999) investigated air-water two phase flow in horizontal tubes of diameters ranging from 1.3 to 5.5 mm. Gas superficial velocity ranged from 0.1 to 100 m/s and liquid superficial velocity ranged from 0.01 to 10 m/s. All conventional flow patterns were observed except the diminishing of stratified flow in channels with diameters less than 5.5 mm. Yang and Shieh (2001) investigated flow patterns of air-water flow in 1, 2 and 3 mm diameter tubes. Gas superficial velocity was varied from 0.21 to 75 m/s and liquid superficial velocity was varied from 0.014 to 1.34 m/s. They did not report any new features and all the conventional patterns were observed except the absence of wavy stratified flow in the 1 mm tube. Chen et al. (2002) performed flow visualization study for nitrogen-water flow in two capillary tubes of diameters 1 and 1.5 mm. Superficial gas and liquid velocities ranged from 0.5 – 11 and 4 – 3.5 m/s respectively. They identified five flow patterns: bubbly, slug, bubble-train slug flow, churn and annular flow as shown in Fig. 2.5. The liquid film in the slug flow was not smooth but had some ripples that were attributed to the significant difference in curvature at the front and rear of the bubble. This difference in curvature was believed to arise from the higher liquid pressure at the bubble front compared to that at the rear while the gas pressure inside the bubble is uniform. Consequently, the authors stated that radius of curvature at the front is expected to be smaller than that at rear according

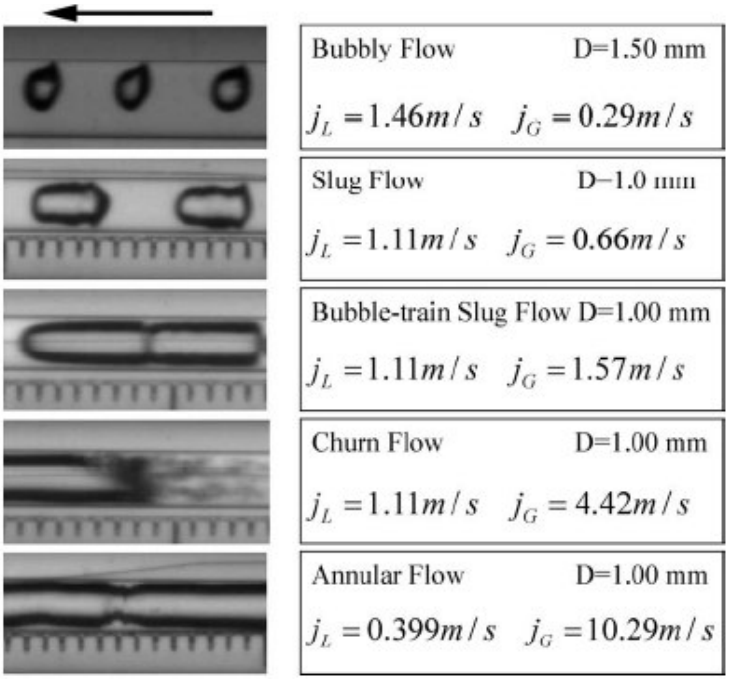

Figure 2.5 The flow patterns of N_2-water in 1.5 and 1 mm horizontal tube, Chen et al., (2002).

to the Young-Laplace equation. They also reported that, bubble-train slug flow is unique in microchannels and only appears in conventional channels under micro-gravity conditions. In this pattern, a number of bubbles align in contact, like a train, with a clear interface between the connected bubbles. The presence of the interface or membrane between the consecutive bubbles was attributed to the balance between inertia and surface tension forces where the Weber number was found to be around unity. Fukano and Karaiyasaki (1993) conducted a flow visualization study for air-water flow in three tubes of 1, 2.4 and 4.9 mm inner diameter and orientations including horizontal, vertical upward and vertical downward. The test sections had an enlarged section at the inlet, which acted as a mixer where the air was injected into this section through three holes of 0.3 or 0.5 mm diameter distributed at 120 degree intervals on the circumference. They have observed some specific features in the capillary tubes compared to the conventional ones. The first feature was the insignificant effect of flow direction in vertical flow. The second feature was that the liquid film became thinner and uniform and the flow tended to be axi-symmetric when the diameter decreases.

In the above studies, the diameter of the investigated channels ranged from 1 to 5 mm and some new features were observed at diameter value of about 1 mm. With further reduction in channel diameter below 1 mm size, some researchers reported further changes in the observed patterns. Kawahara et al. (2002) examined two phase flow of nitrogen and de-ionized water in a horizontal fused silica tube of 0.1 mm diameter. The gas superficial velocity was varied from 0.1 to 60 m/s and the liquid superficial velocity was varied from 0.02 to 4 m/s. Nitrogen and water were mixed in a mixing section with geometry shown in Fig. 2.6. The dominant flow patterns were intermittent and semi-annular flows while bubbly, stratified and churn flows were not observed. The observed patterns were classified based on the interfacial configuration into “liquid alone or liquid-slug”, “gas core with a smooth thin liquid film”, “gas core with a ring shaped liquid film”, “gas core with a smooth thick liquid film” and “gas core with a deformed interface” as seen in Fig. 2.6. The ring-shaped liquid film and the smooth-thin liquid film were both axi-symmetrically distributed around the channel inner wall, which indicated negligible gravity effect. Moreover, they reported that both serpentine-like gas core and ring-shaped liquid film patterns are unique for microchannels. Additionally, in some cases the liquid film was found to be thicker than the diameter of the gas core and

also small liquid droplets were sometimes observed in the flowing gas core. The absence of bubbly and churn flows was attributed to the laminar nature of liquid flow in microchannels, i.e. no enough turbulence to break up the gas phase into small bubbles.

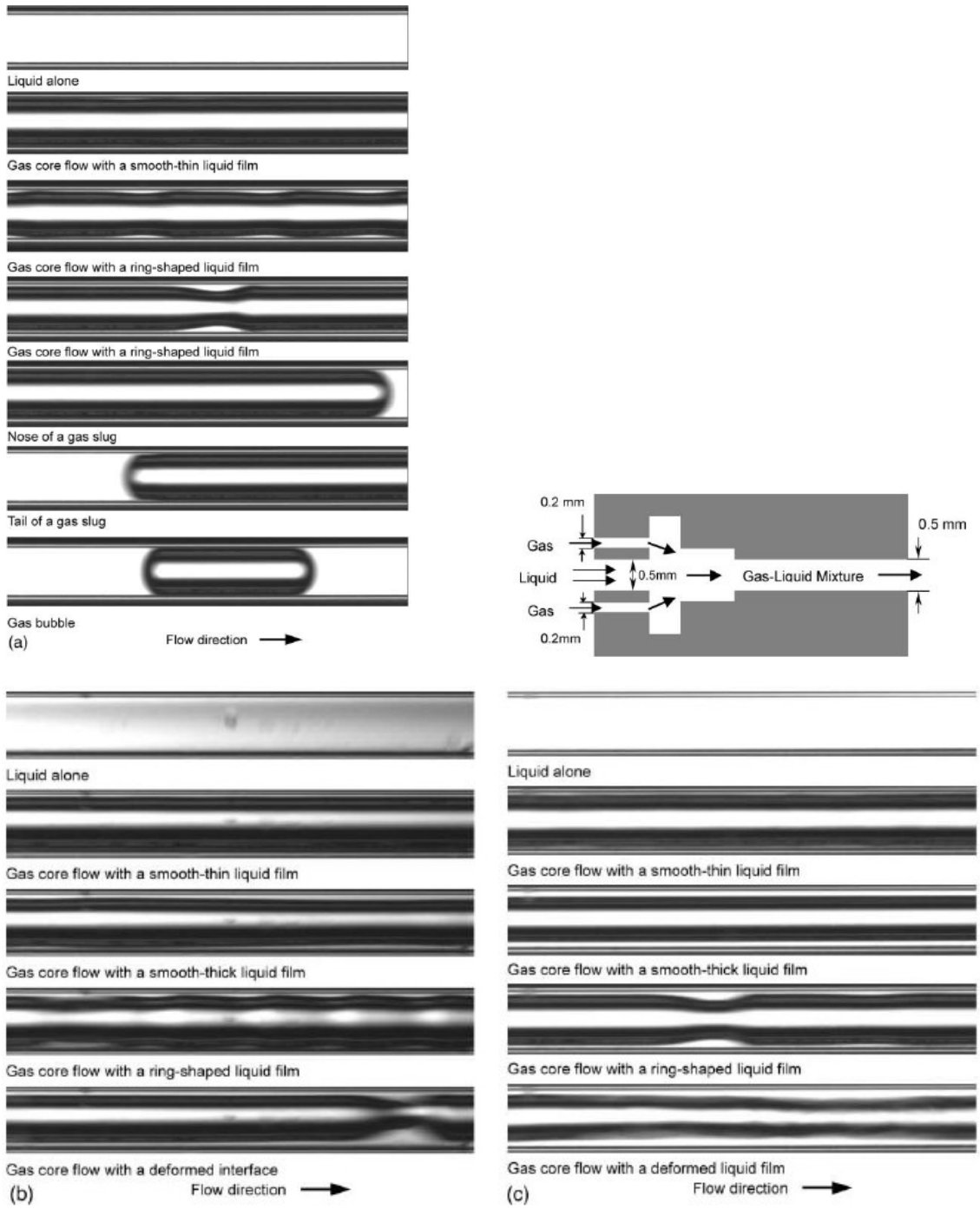

Figure 2.6 The flow patterns of nitrogen-water two phase flow in 0.1 mm diameter tube at (a) low liquid and intermediate gas flow rates, (b) intermediate liquid and high gas flow rates (c) high liquid and gas flow rates, Kawahara et al., (2002).

Serizawa et al. (2002) conducted a flow visualization study on air-water flow in three tubes of 20, 25 and 100 μm inner diameter and steam-water flow in a 50 μm diameter tube. The gas superficial velocity was varied from 0.0012 to 295.3 m/s and the liquid superficial velocity from 0.003 to 17.52 m/s. The gas was injected co-axially while the liquid was introduced peripherally into the air-water mixer shown in Fig. 2.7. The observed flow patterns of air-water flow in the 25 μm tube were: dispersed bubbly flow (at very low gas velocities 0.0083 m/s), slug flow, liquid ring flow and liquid lump flow. They reported that slug flow was not formed due to the coalescence mechanism because of the high rigidity of the fine bubbles in micro tubes. Instead, they believed that it was formed due to the inlet conditions when the flow rate of the gas at the channel inlet was high and the speed of the long bubble was not sufficient to overcome the liquid bridge between the consecutive bubbles. Liquid ring flow developed from slug flow when the gas flow rate was increased to the extent at which liquid slugs become too short to support a stable liquid bridge between the consecutive gas slugs. Liquid lump flow developed from liquid-ring flow when the gas velocity increased further where the high speed core gas entrains the liquid and forms liquid lumps sliding on the wall. Additionally, they reported that a dry zone may form underneath the bubble which was believed to arise from: (i) the high pressure drop induced by slug flow that suppresses the sliding motion between the bubble and the wall, (ii) the strong effect of surface tension which prevents the liquid from dispersing into a film and (iii) the very small size of the gas slug that creates sufficient interfacial pressure difference to push the gas into the whole cross section. In case of steam-water flow, they observed similar flow patterns to that observed in air-water flow with few exceptions. First, in slug flow some small liquid droplets were observed to stick on tube wall, which was considered as evidence on the absence of liquid film. Second, stable liquid ring flow appeared with thinner liquid film distributed uniformly at tube wall. In liquid lump flow, the lumps were moving in partially continuous films instead of separate discrete lumps. Figure 2.7 shows the new flow patterns observed by Serizawa et al. (2002).

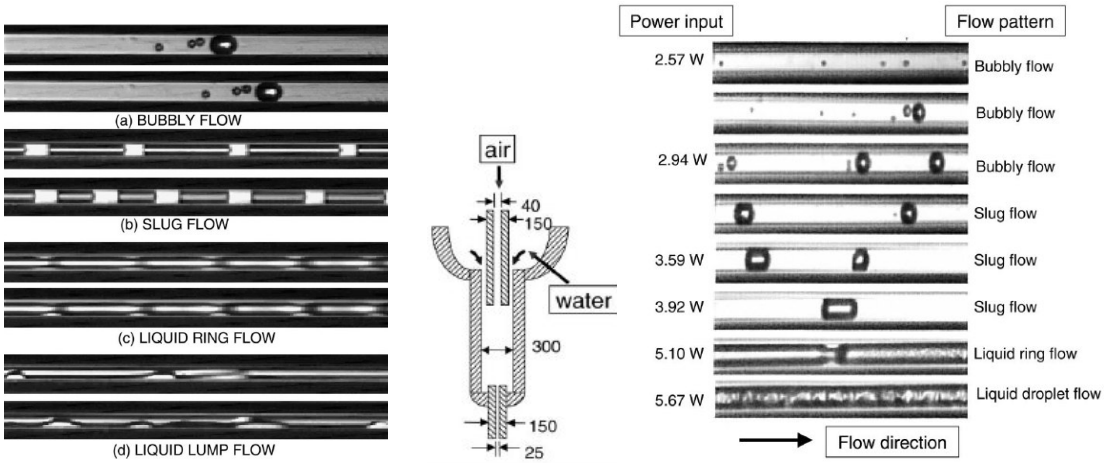

(a) (b)

Figure 2.7 The flow patterns of (a) Air-water flow in 25 μm and (b) Steam-water flow in 50 μm with the used gas-liquid mixer, Serizawa et al., (2002).

In addition to that, Serizawa et al. (2002) observed some interesting features when they cleaned the 100 μm tube using ultrasonic vibration in a pool of high purity distilled water, ethanol and dilute hydrogen chloride solution. Figure 2.8 shows the observed flow patterns before and after cleaning. This figure shows interesting features due to cleaning. In bubbly flow, tiny bubbles flowed in a discrete way without coalescence while before cleaning the bubble size was larger. In slug and annular flows, the liquid droplets observed before cleaning disappeared after cleaning. Additionally, a new pattern appeared after cleaning, which they called “skew flow” as shown in picture d in Fig. 2.8. In this pattern, several bubbles were connected in series by the gas stems located at the centreline of the tube. Also, wispy annular flow was more obvious after cleaning where small bubbles were trapped within the thin liquid film. This special behaviour that occurred after cleaning was attributed to the enhancement in surface wet-ability, which was found to significantly influence flow patterns in micro tubes.

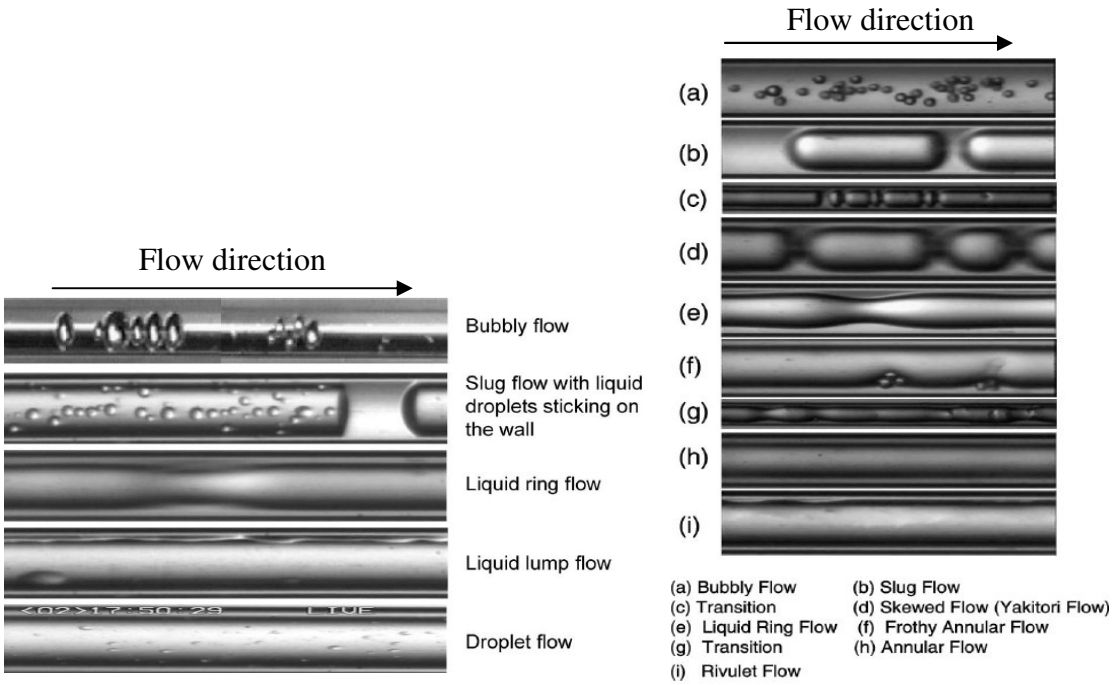

(a) before cleaning (b) after cleaning

Figure 2.8 The effect of surface contamination (wet-ability) on flow patterns of air-water flow in a 100 μm quartz tube; Serizawa et al. (2002).

Chung and Kawaji (2004) performed a flow visualization study using nitrogen-water flow in four horizontal micro tubes of 530, 250, 100 and 50 μm diameters. Water flowed co-axially through 0.5 mm diameter tube while nitrogen was introduced peripherally though a 0.2 mm annular gap. They classified the observed flow patterns in the two largest tubes using the same names proposed by Triplett et al. (1999) whilst they used the names proposed by Kawahara et al. (2002) for classifying the patterns in the two smallest tubes. The observed flow patterns in the 530 and 250 μm tubes were bubbly, slug, churn, slug-annular and annular flow regimes as seen in Fig. 2.9(i). They considered the flow regime in pictures c and d of Fig. 2.9(i) as a kind of churn flow. For the two smallest tubes, bubbly, churn, slug-annular and annular flow regimes were not observed as seen in Fig. 2.9 (ii). The absence of these patterns was attributed to the greater viscous and surface tension effects, which suppress the turbulence and agitation of gas-liquid interface. The authors reported that, the absence of the highly irregular gas-liquid interface in churn flow that was observed in the two largest tubes reflects the high level of mixing between the phases.

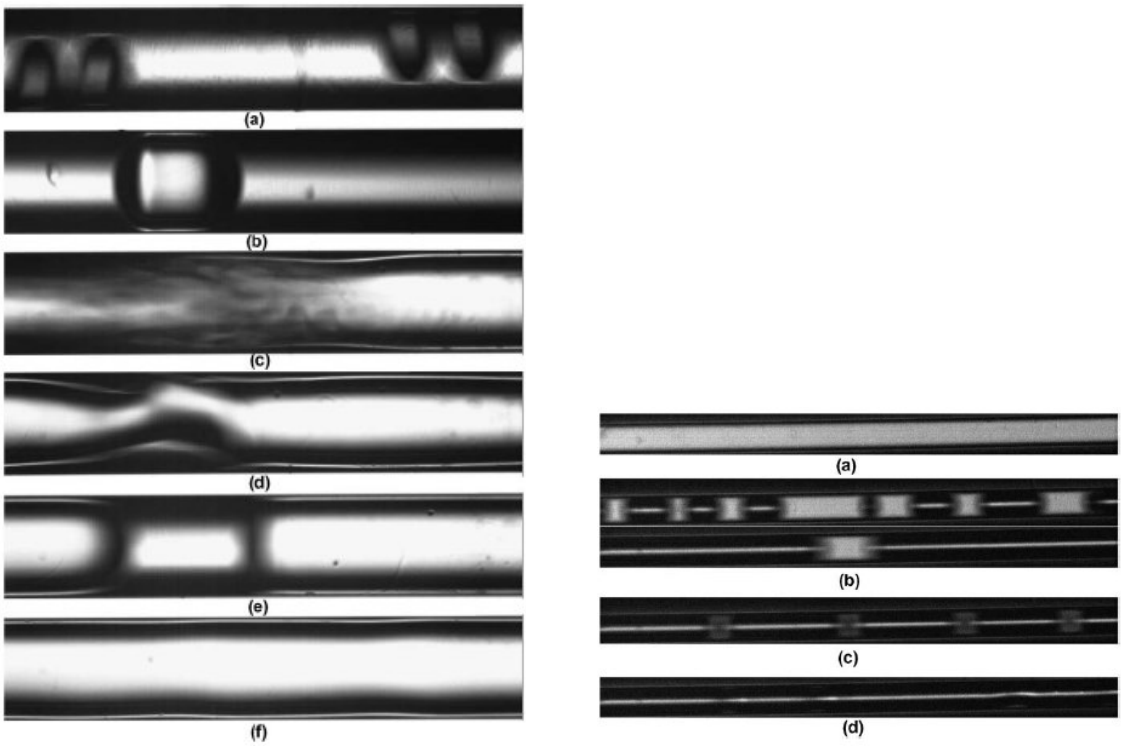

(i) D = 250 µm
(a) bubbly, (b) slug, (c) swirling pattern in churn flow, (d) serpentine-like gas core in churn flow, (e) liquid bridge in slug-annular flow, (f) annular flow

(ii) D = 50 µm
(a) single phase liquid flow, (b) gas slugs with thin-smooth liquid film, (c) gas slug with ring-shaped liquid film, (d) serpentine-like gas core

Figure 2.9 The flow patterns of nitrogen-water in (i) 250 µm and (ii) 50 µm, Chung and Kawaji, (2004).

The presence of the edges or corners in non-circular channels may keep the channel wall covered with liquid all the time and consequently may influence the features of the gas-liquid interface. Xu et al. (1999) investigated flow patterns of air-water flow in rectangular vertical channels of 0.3, 0.6 and 1 mm mini gaps and constant width of 12 mm. All conventional flow patterns were observed in channels of 0.6 and 1 mm gaps. On the contrary, the patterns observed in the channel with the smallest gap of 0.3 mm were different as seen in Fig. 2.10. Bubbly flow was not observed even at very low gas flow rates. At high liquid flow rates and low gas flow rates, cap bubbly flow appeared due to the squeeze and merge of the very small bubbles. The shape of the bubbles was almost half circle at the nose with a flat bottom and the distance between any consecutive bubbles was almost the same. Slug-droplet flow appeared at low gas and liquid flow rates. In this pattern the slug was elongated and has a half circular nose with

flat rectangular tail. Some isolated liquid droplets were observed on the wall surface and were pushed by the moving elongated slugs. Xu et al. stated that, the adhesion of these droplets to the wall surface occurred due to the increased influence of surface tension and friction shear stress in the minichannels. In annular-droplet flow, isolated liquid droplets were observed on the wall and were pushed by the flowing gas core even though the liquid film still existing, i.e. the source of these droplets was not the disintegration of the liquid film.

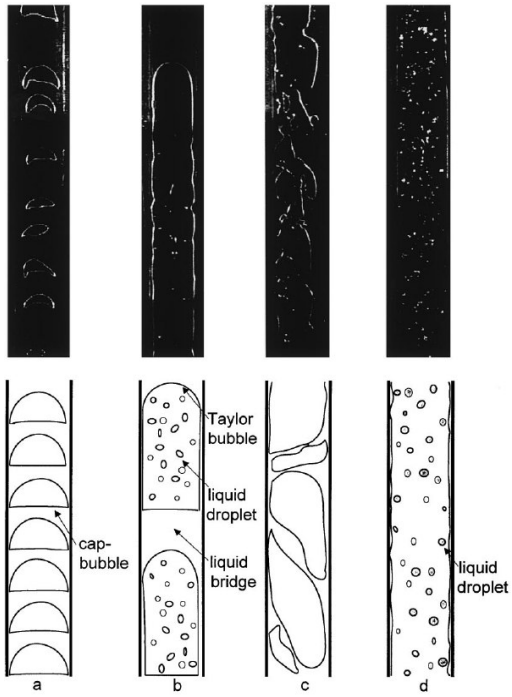

Figure 2.10 The flow patterns in channel with a gap of 0.3 mm or D_h = 0.58 mm, Xu et al. (1999).

Triplett et al. (1999) investigated two phase flow patterns of air-water flow in horizontal semi-triangular channels (triangular with one corner smoothed) of 1.09 and 1.49 mm diameters. The observed flow patterns were similar to those observed in circular channels shown in Fig. 2.4 (bubbly, slug, churn, slug-annular and annular) without stratified flow. Zhao and Bi (2001) conducted flow visualization for co-current air-water flow in vertical triangular channels of 2.886, 1.443 and 0.866 mm hydraulic diameters. They have found that the flow patterns observed in the two largest channels were similar to those observed in conventional vertical circular channels. However, two peculiar phenomena were observed in the smallest one. The first was the diminishing of

dispersed bubbly flow while the second was the appearance of new-featured bubbly flow called “capillary bubbly flow”. Figure 2.11 shows the observed flow patterns in the smallest channel with the simultaneous pressure drop signal. They characterized the

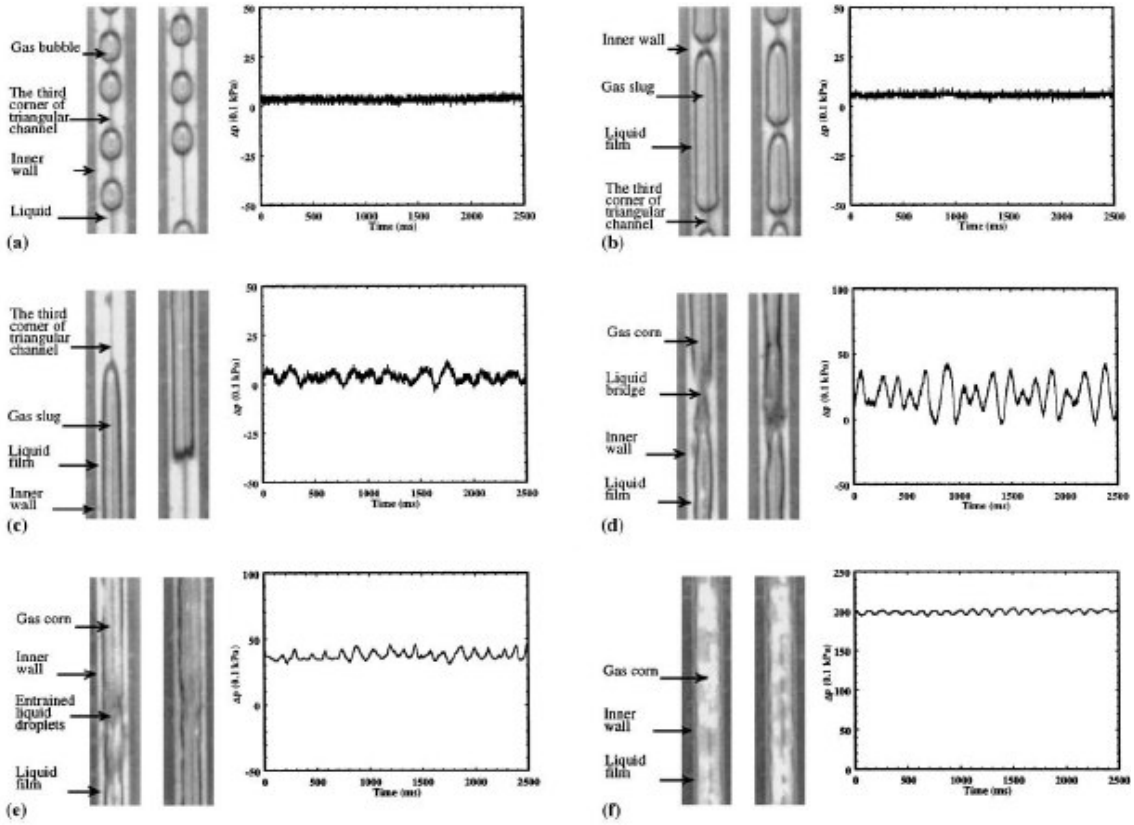

Figure 2.11 The flow patterns of air-water in equilateral triangular channel of 0.866 mm hydraulic diameter, (a) Capillary bubble flow, (b), (c) slug flow, (d) Churn flow, (e), (f) annular flow; Zhao and Bi (2001).

capillary bubbly flow as a train of ellipsoidal bubbles regularly distributed in the liquid phase along the axis of the channel and span the whole cross section. Moreover, liquid phase was found to be continuous though the bubble covered all channel cross section and made the wall partially dried. This was attributed to the strong effect of surface tension, which pulled the liquid towards channel corners. The pressure drop signal in Fig. 2.11 demonstrated that, in capillary bubbly flow, the pressure drop fluctuates with extremely high frequency but with relatively small fluctuation amplitude. On the other hand, churn flow showed the highest pressure drop fluctuation amplitude with relatively lower frequency. In the two largest channels bubble shape was irregular compared to the regular one in circular channels. This irregularity was attributed to the difference in

superficial velocities at which dispersed bubbles form. In triangular channels, dispersed bubbles were found to appear at very low gas velocity and very high liquid velocity compared to circular channels.

2.2.3 Flow boiling patterns in microchannels

In adiabatic two phase flow studies, the inlet geometry strongly affects the bubble formation as reported by Hayashi et al. (2007) whereas in boiling it might be influenced by the stability of nucleation sites. In macrochannels, the commonly observed flow boiling patterns are bubbly, slug, churn, annular and mist flow; Collier and Thome (1994) whilst Kandlikar (2002) reported that isolated bubble, confined bubble/slug and annular flow are prevailing in microchannels. Also, Thome (2004) reported that elongated bubble regime sustains in microchannels even at vapour quality values as high as 0.6 – 0.7. Additionally, many researchers such as Kuznetsov and Shamirazaev (1999), Shuai et al. (2003), Sobierska et al., (2006), Revellin et al. (2006), Revellin and Thome (2007a), Sobierska et al., (2007) and Huh and Kim (2006) reported the diminishing churn flow during flow boiling in microchannels. Flow boiling patterns in metallic tubes are usually observed in a glass section located immediately after the heated section. The observed patterns in this case are not fully adiabatic or fully non-adiabatic, and some researchers such as Revellin and Thome (2007b) called it diabatic flow patterns. In contrast, the flow boiling patterns in non-circular channels were directly visualized by making one side of the channel of glass. Owhaib et al. (2007) proposed another technique for directly visualizing boiling flow patterns in micro tubes. They conducted flow boiling tests in a vertical quartz glass tube of 1.33 mm inner diameter with the outer surface coated with a transparent resistive coating of Indium Tin Oxide (ITO), which acted as a heater. However, boiling in glass tube may result in different heat transfer characteristics compared to metallic tubes due to the different surface characteristics. This section presents the typically observed flow boiling patterns in some of the past experimental studies.

Kew and Cornwell (1997) investigated flow boiling of R141b in metallic tubes of diameters ranging from 1.39 to 3.69 mm. They observed three patterns namely: isolated bubble, confined bubble and annular-slug flow. Isolated bubble regime was similar to bubble flow in large diameter channels. In confined bubble regime, one bubble filled the

whole channel cross section with a liquid film between the bubble and the wall. They believed that, the formation of the confined bubble is due to the growth of the nucleating bubble to channel size before leaving the cavity or due to the coalescence of isolated bubbles. Additionally, they reported that the formation of the confined bubble regime is accompanied with significant pressure fluctuations at channel inlet. The formation of the annular-slug flow was attributed to the expansion of the confined bubbles that forces all liquid in the slugs between the consecutive bubbles to flow as a liquid film. Saitoh et al. (2005) investigated flow boiling of R134a in three horizontal metallic tubes having inner diameters of 0.51, 1.12 and 3.1 mm. They observed only two patterns namely: intermittent (plug and slug flow) and annular flow without observing bubbly and stratified flow patterns. In the smallest tube, slug flow was formed at low vapour qualities while annular flow developed at high qualities. Also, they have found that the vapour quality at which slug-annular flow occurs increases with decreasing diameter and mass flux. Chen et al. (2006) investigated flow boiling patterns of R134a in four vertical metallic tubes having inner diameters of 4.26, 2.88, 2.01 and 1.1 mm and observed seven flow patterns; dispersed bubble, bubbly, confined, slug, churn, annular and mist flow as seen in Fig. 2.12. Mist flow was only observed in the largest tube. They found that, the flow patterns of the two largest tubes are almost similar to those observed in conventional ones. When the diameter was decreased to 2.01 mm, the flow patterns experienced “small tube characteristics” where the liquid film around the long bubble became thinner and the liquid vapour interface in churn flow became less chaotic. Also, in the 2.01 mm tube, confined bubbles appeared first at 6 bar system pressure and established at all pressures 6 – 14 bar when the diameter was decreased further to 1.1 mm. Since the 2.01 mm tube showed both small tube characteristics and conventional tube characteristics, they concluded that the threshold diameter between small and conventional tubes may be in the order of 2 mm.

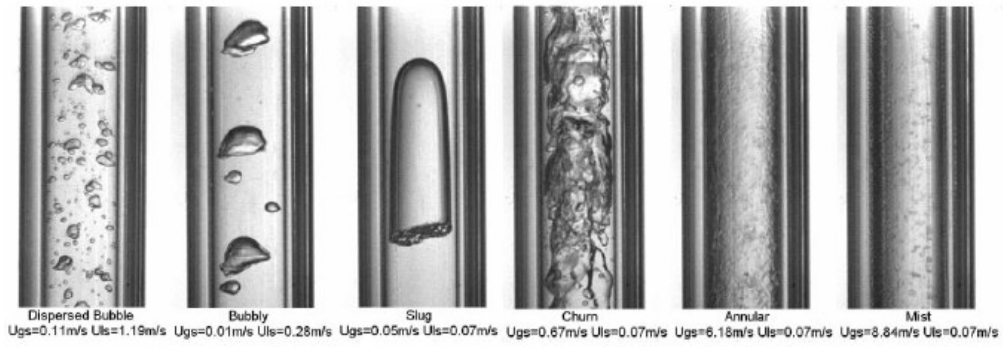

(a) 4.26 mm

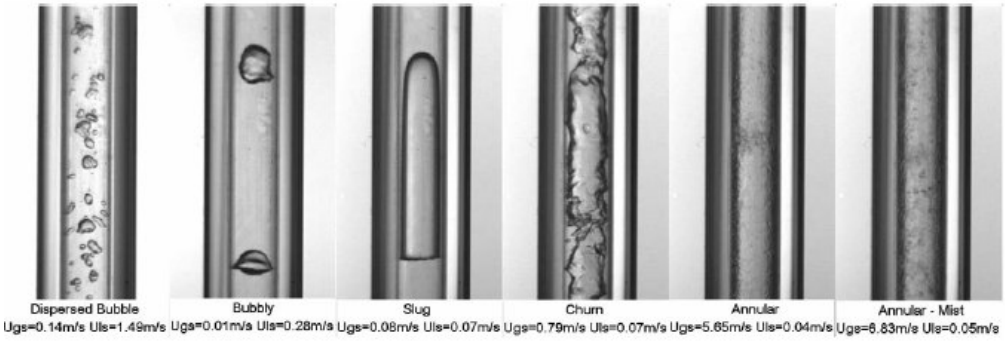

(b) 2.88 mm

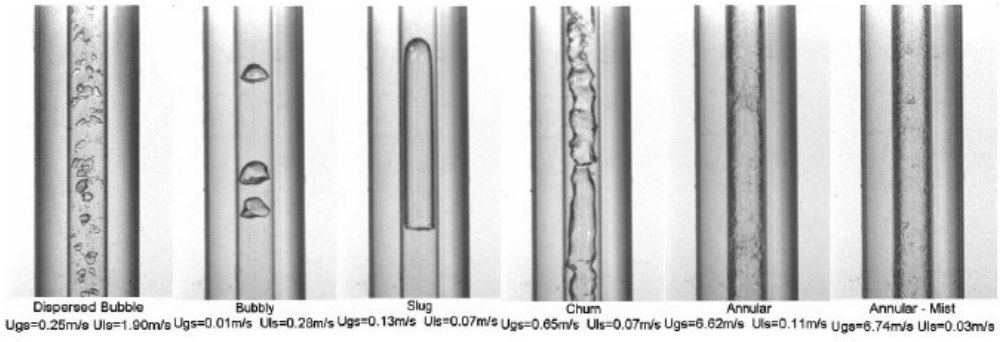

(c) 2.01 mm

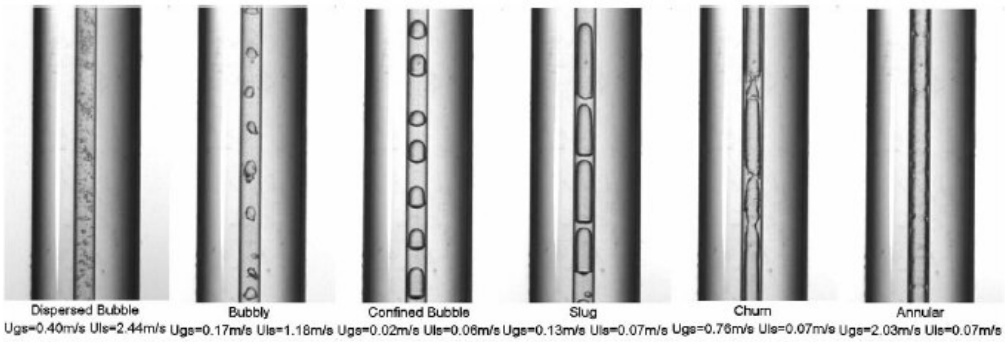

(d) 1.1 mm

Figure 2.12 The flow boiling patterns of R134a at 10 bar in small to mini diameter tubes; Chen et al. (2006).

Revellin and Thome (2007a) identified four major flow patterns for R134a and R245fa in two horizontal metallic tubes having inner diameters 0.5 and 0.8 mm. The observed regimes were: bubbly, slug, semi-annular and annular with two transition patterns namely: bubbly/slug and slug/semi-annular as shown in Fig. 2.13. Bubbly flow was found to cover a very small range of vapour quality and is more or less absent at high mass fluxes. In slug flow, the bubble was found to have a hemispherical cap and variable length. In semi-annular flow, liquid slugs disappeared and continuous liquid film formed at the wall while the gas flowed in the core with the presence of churning liquid zone.

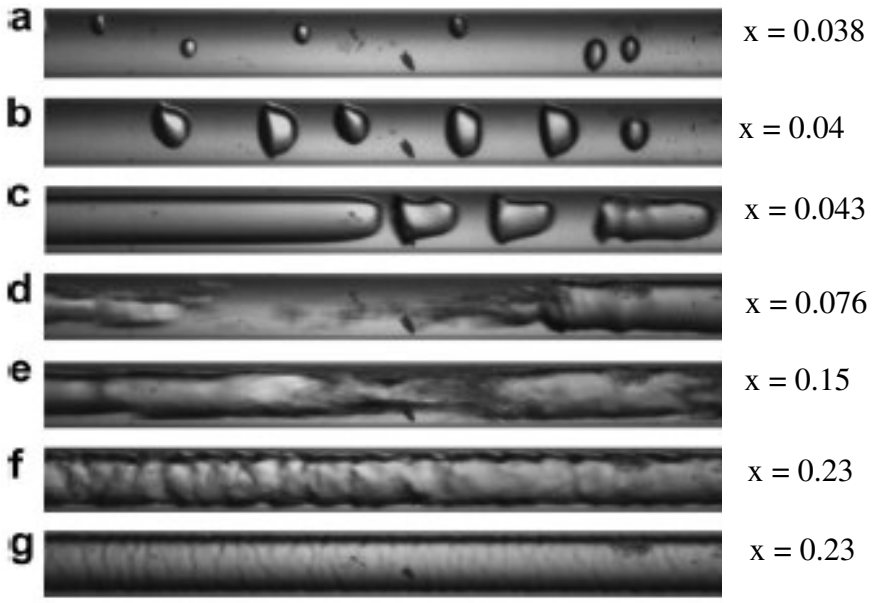

Figure 2.13 The flow patterns of R245fa in a 0.5 mm diameter tube at 500 kg/m^2 s and T_{sat} = 35 ^{0}C as a function of exit quality; (a) bubbly, (b) bubbly/slug, (c) slug, (c) slug/semi-annular, (d) semi-annular, (e) wavy annular, (f) smooth annular, Revellin and Thome (2007).

Fu et al. (2008) observed four flow patterns namely bubbly, slug, churn and annular flows during flow boiling of liquid nitrogen in a vertical metallic tube of inner diameter 1.931 mm as seen in Fig. 2.14. They have observed some interesting features in bubbly flow. At very small gas and liquid superficial velocities the bubbles accumulated close to channel wall and formed what they called “wall-peaking bubbly flow”. In this pattern, bubbles were almost attaching to the wall with the same span and almost identical in size. The interesting thing in this pattern was the appearance of a tip like a

neck, which is similar to the shape of a bubble departing from the nucleation site. Moreover, the size of these bubbles was comparable to the bubble departure diameter (~ 0.62 mm). They attributed the formation of this pattern to the absence of coalescence at very small gas and liquid flow rates and to the probability of bubble nucleation, growth and departure from the same nucleation site before flowing into the adiabatic observation section. One important result from their study was the early appearance of annular flow at qualities greater than 0.15.

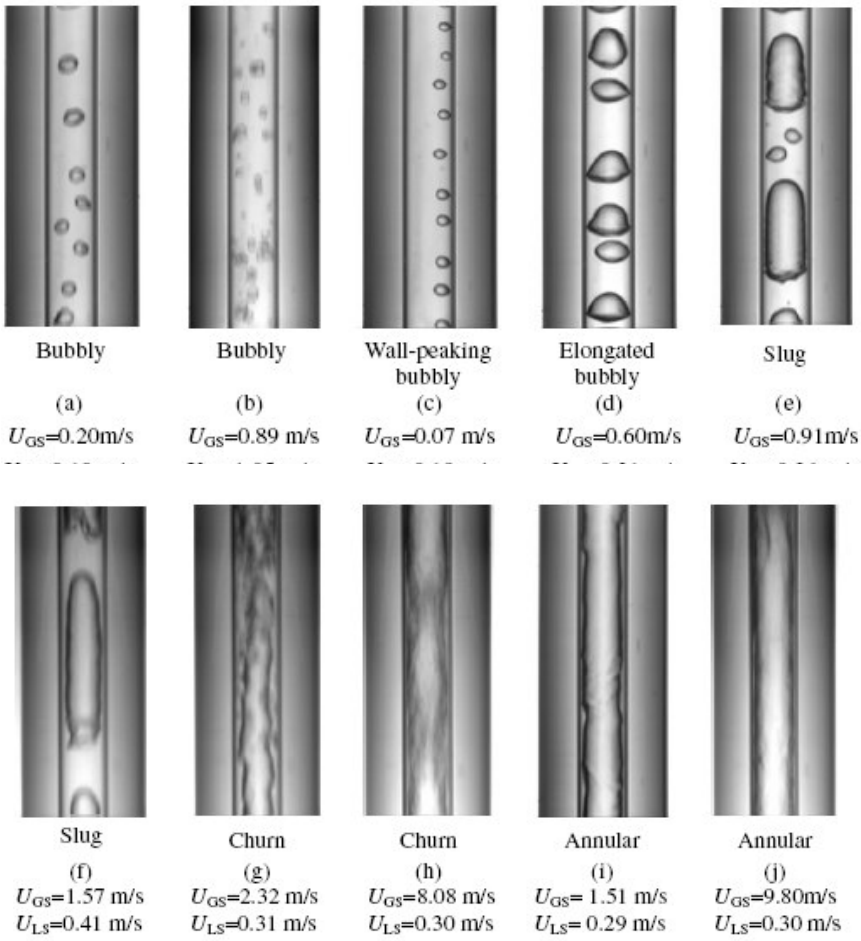

Figure 2.14 The flow boiling patterns of nitrogen in a vertical tube of D = 1.931 mm; (a), (b), (c), (d) bubbly flow; (e), (f) slug flow; (g), (h) churn flow; (i), (j) annular flow; Fu et al. (2008).

Shiferaw (2008) investigated flow boiling heat transfer of R134a in a vertical 0.52 mm diameter tube. The flow patterns were recorded simultaneously with the heat transfer data. Five flow regimes were observed in this tube namely, bubbly, elongated bubble (slug), liquid ring flow, wavy annular and annular flow. The details and pictures of

these flow patterns will be presented later in chapter 4. Chen and Garimella (2006) investigated flow boiling of FC-77 in a multi-channel heat sink with channel dimensions of 389 × 389 μm. Flow patterns were presented at two conditions: low heat flux or before flow reversal and high heat flux or after the incipience of flow reversal. Before flow reversal and at very low heat fluxes, small bubbles were observed to nucleate on the channel walls, detach and move downstream when they reach a certain size without coalescence. Further increase in heat flux resulted in the development of slug flow due to bubble coalescence and in between the passing slugs small bubbles were observed to nucleate and grow violently at the wall. When the heat flux was increased further, flow reversal was observed to commence with flow patterns alternating between churn and wispy-annular flow. This alternating pattern was observed to continue with increasing heat flux until dryout occurs. Sobierska et al. (2007) investigated flow boiling of de-ionized, de-gassed water in a vertical rectangular microchannel of hydraulic diameter 0.48 mm (0.807 × 0.346 mm). Three flow patterns were observed namely bubbly, slug and annular and annular flow was found to develop at very small quality ~ 0.05. Harirchian and Garimella (2009a) experimentally investigated the effects of channel dimensions, mass flux and heat flux on flow boiling patterns of FC-77 in microchannels. Six different silicon heat sinks with parallel microchannels of widths ranging from 100 to 5850 μm and fixed depth of 400 μm were investigated. The observed flow patterns were: bubbly, slug, churn, wispy-annular, annular and inverted annular flow. Figure 2.15 shows a typical images as well as a sketch for the commonly observed flow patterns in the examined channels. Bubbly flow was characterized by small isolated bubbles, which nucleate on the channel wall, detach after growing and move in the flow direction. With increasing heat flux, the bubble generation frequency increased resulting in high coalescing rate and thus the development of slug flow with the presence of tiny bubbles in the liquid slug. Churn flow consisted of vapour chunks flowing in the upstream direction with large nucleating bubble was seen at the wall. In wispy-annular flow, the vapour core was separated from the wall by a thick unstable liquid film with irregular shaped droplet entrainment into the vapour core as well as the existence of few nucleating bubbles in the liquid film. In annular flow, the film remained wavy and thin with the disappearance of the tiny bubbles and liquid entrainments observed in the wispy-annular flow. It was also found that, when channel width was decreased to a value below 400 μm: (i) bubbly flow was not established and instead slug flow appeared immediately after boiling incipience, (ii)

as heat flux increased, the tail of the slug broke up and so did the liquid film at the location of nucleating bubbles and (iii) in annular flow the liquid film was discontinuous due to bubble nucleation without observing any liquid droplets in the core. Also, it was observed for all tested channels that bubble nucleation in the film stopped at certain heat flux.

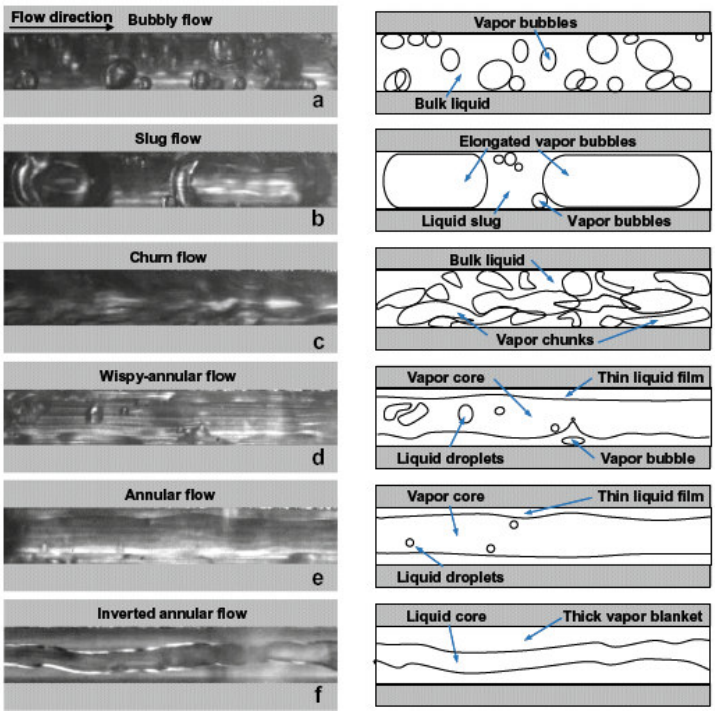

Figure 2.15 The flow patterns of FC-77 in rectangular silicon microchannels, Harirchian and Garimella (2009a).

Martin-Callizo et al. (2010) conducted a direct visualization study for the flow boiling of R134a in a vertical circular channel with an inner diameter of 1.33 mm and heated length of 235 mm. the tube was made of quartz and covered with a thin layer of Indium Tin Oxide acting as a heater. Accordingly, the flow patterns were visualized directly in the heated section rather than observing the flow patterns at the exit of the heated section as was the case in most studies. They identified seven flow patterns namely: isolated bubbly flow, confined bubbly flow, slug flow, churn flow, slug-annular flow, annular flow and mist flow as seen in Fig. 2.16. It is worth mentioning that, they observed the flow patterns at eight axial locations along the heated section. It was found that the transition to annular flow occurs either through the slug-annular regime or the

churn flow. The slug-annular transition occurred at very low liquid velocities (G = 100 kg/m^2 s) which was attributed to the strongest effect of surface tension that maintains the bubble shape during elongation and coalescence leading to the formation of a thick liquid ring. On the other hand, the transition from slug to annular flow through the churn flow occurred at high liquid velocities (G = 500 kg/m^2 s) which was attributed to the high turbulence and agitation of the liquid-vapour interface. Additionally, they reported that churn flow was the dominant over most experimental conditions compared to the slug-annular regime.

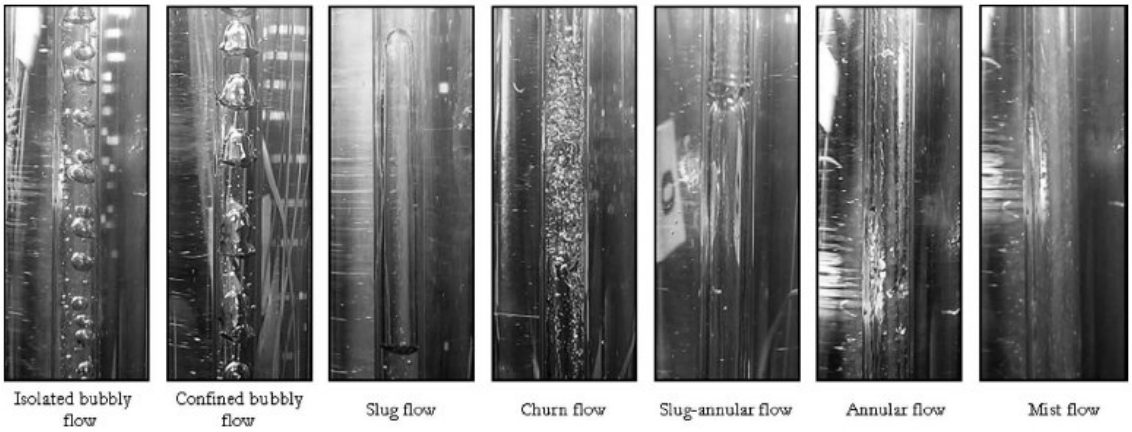

Figure 2.16 The flow patterns directly observed in a heated glass tube with D = 1.33 mm and R134a, Martin-Callizo et al. (2010).

2.3 Flow pattern maps

Flow maps are the most commonly used tool for predicting the two phase flow patterns. They are graphs with coordinates representing flow parameters that may be dimensional or dimensionless. These coordinates are not general and are more or less optional due to the lack of understanding the physics of two phase flow as reported by Taitel et al. (1980). Historically, Suo and Griffith (1964) proposed the first adiabatic flow map for mini tubes. In this map, the vertical axis was taken as the capillary number [$Ca = \mu_L U_B / \sigma$] to account for viscous and surface tension effects while the horizontal axis was selected to be the volumetric fraction of the liquid [$V_L /(V_L + V_g)$]. Recently, several flow maps were developed for small to micro diameter channels. This section presents some examples for the recently developed flow maps at microscale.

2.3.1 Validity of macroscale pattern transition models

Many researchers conducted flow visualization studies at microscale level and compared their results with the well known macroscale flow patterns transition models. Mishima and Hibiki (1996) developed flow maps using air-water flow in vertical tubes having inner diameters of 1.05, 2.05, 3.12 and 4.08 mm. Figure 2.17 shows the maps of the 2.05 and 4.05 mm tubes compared to the model of Mishima and Ishii (1984) (solid line), Barnea et al. (1983) for D = 4 mm (dashed line in Fig. 2.17b) and the transition boundaries of Kariyasaki et al. (1992) for D = 1 – 4.9 mm (chain lines). They concluded that, the model of Mishima and Ishii (1984) predicts the transition boundaries fairly well. Triplett et al. (1999) developed flow maps using air-water flow in circular tubes of diameters 1.1 and 1.45 mm and semi-triangular channels of 1.09 and 1.49 mm hydraulic diameter. They have compared their flow maps with the correlation of Suo and Griffith (1964) and the model of Taitel et al. (1980). It was found that the model of Taitel et al. satisfactorily predicted only the transition boundary between bubbly and slug while the correlation of Suo and Griffith demonstrated significant disagreement. However, the comparison with other similar experimental studies showed overall better agreement. Figure 2.18 depicts the map of the 1.097 mm tube including the comparison with other models. Coleman and Garimella (1999) developed flow maps using air-water flow in horizontal tubes of diameters ranging from 1.3 to 5.5 mm. The maps were compared with the model of Taitel and Dukler (1976) and with similar experimental data of Damianides and Westwater (1988). The model of Taitel and Dukler predicted the data poorly due to neglecting the surface tension effects. However, the comparison with the data of Damianides and Westwater, collected using similar diameter range of 1 – 5 mm, showed better agreement.

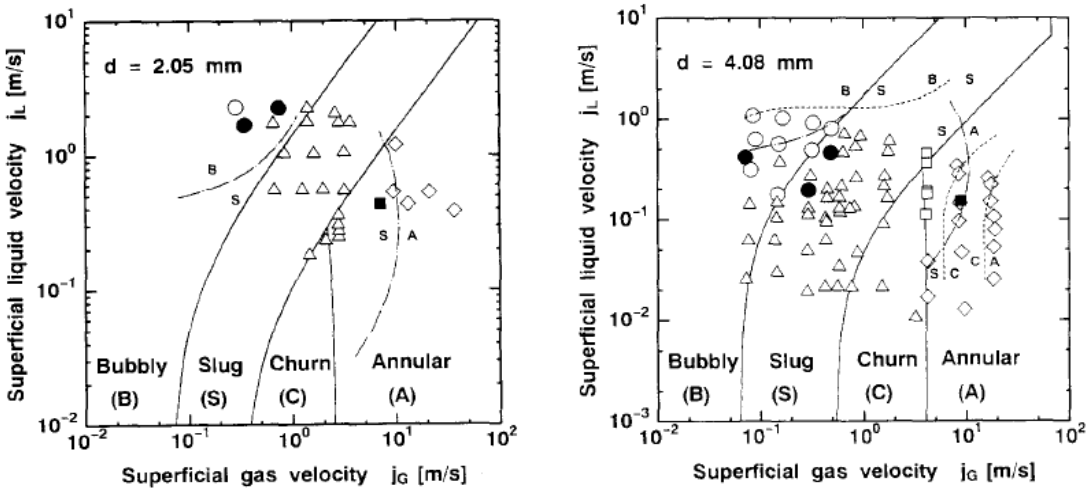

(a) (b)

Figure 2.17 The flow pattern maps of air-water flow in vertical small diameter tubes, Mishima and Hibiki (1996).

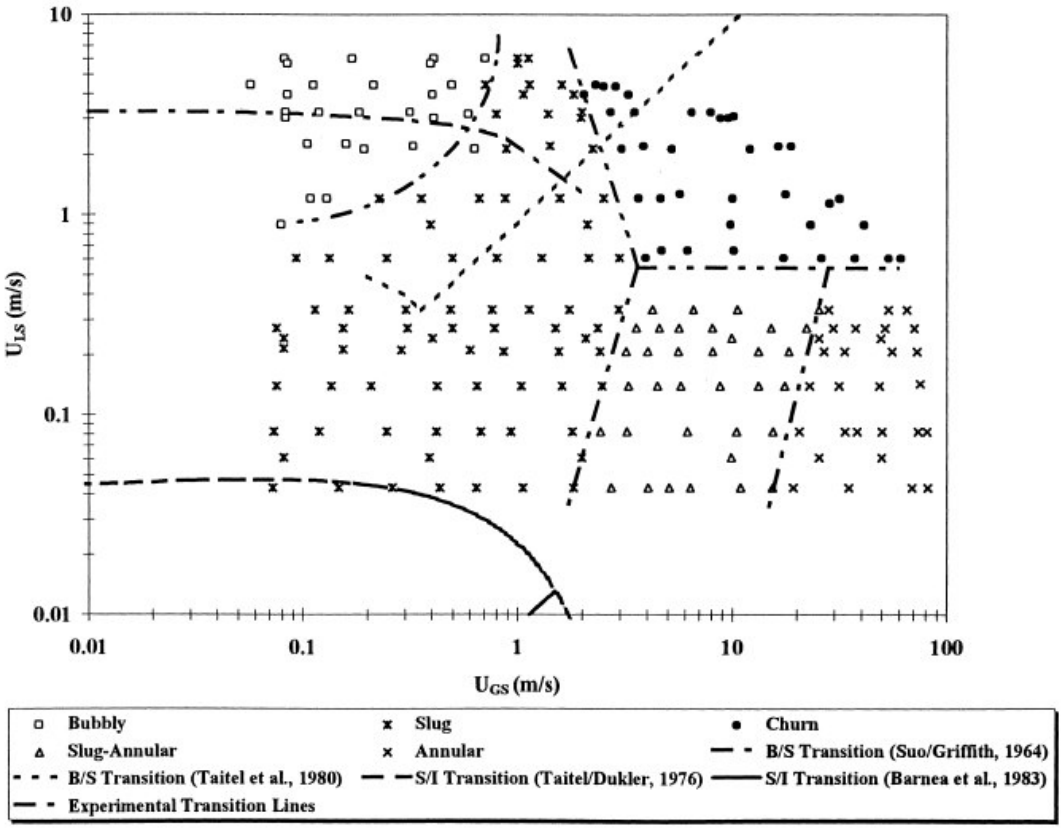

Figure 2.18 The flow map of air-water in a 1.097 mm circular tube, Triplett et al. (1999).

Zhao and Bi (2001) compared their flow maps with the model of Taitel et al. (1980) and the model of Mishima and Ishii (1984) and reported poor agreement. The maps were developed using air-water flow in vertical equilateral triangular channels of 2.886, 1.443 and 0.866 mm hydraulic diameters. The failure of the models was attributed to ignoring surface tension effects. In minichannels, there is a strong effect for the meniscus induced by the channel corners, which may affect the pattern transition mechanism. However, comparison with similar experimental studies for circular and rectangular channels with approximately similar hydraulic diameter demonstrated reasonable agreement. Chen et al. (2006) investigated flow boiling patterns of R134a in four vertical tubes of inner diameters 4.26, 2.88, 2.01 and 1.1 mm. They concluded that, the conventional models predicted poorly the experimental transition boundaries with the unified model of Taitel et al. (1990) reasonably predicting the dispersed bubbly/slug transition. The prediction was found to be worse when the diameter decreases.

2.3.2 Effect of channel diameter on transition boundaries

Coleman and Garimella (1999) reported that, channel diameter has a significant effect on the intermittent/bubbly, intermittent/dispersed and intermittent/annular transition boundaries. As channel diameter decreases, the transition from intermittent to dispersed or bubbly flow was found to occur at progressively higher superficial liquid velocities. This was attributed to the predominance of surface tension. The transition from intermittent to annular flow occurred at higher values of superficial gas velocities when the diameter was decreased from 5.5 to 1.75 mm while the effect was insignificant with further reduction in diameter as seen in Fig. 2.19. Xu et al. (1999) investigated the effect of reducing the gap size between two vertical walls, which form a rectangular channel, on the flow patterns transition boundaries. Reducing gap size was found to have a significant effect on the location of the transition boundaries. As gap size decreases, transition from bubbly to slug and from slug to churn occurred at lower gas velocities. They attributed this to the "squeeze and merge" of the smaller bubbles in case of bubbly/slug transition and the increased shear stress in rectangular channels in case of slug/churn transition. Chung and Kawaji (2004) reported similar results for the effect of diameter on slug/churn and slug/slug-annular transition boundaries where it occurred at lower gas velocities when the diameter decreases.

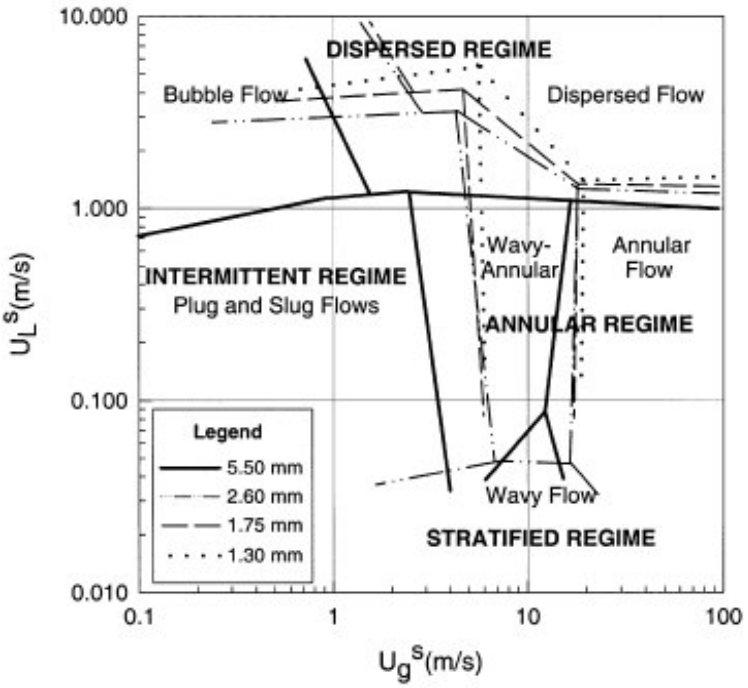

Figure 2.19 The effect of channel diameter on flow pattern transition boundaries, Coleman and Garimella (1999).

Zhao and Bi (2001) presented flow maps developed using air-water flow in vertical equilateral triangular channels of 2.886, 1.443 and 0.866 mm hydraulic diameters as seen in Fig. 2.20. Reducing the hydraulic diameter from 2.886 to 1.443 shifted the dispersed bubbly/slug transition boundary to occur at higher liquid superficial velocities. With further reduction in diameter to 0.886 mm, the dispersed bubbly pattern vanished and instead cap bubbly flow appeared at relatively lower liquid superficial velocities. It is clear from the figure that the churn flow region becomes much narrower when the diameter decreases which means that churn flow tends to vanish in very small diameter channels. In addition to that, the slug/churn and churn/annular transition boundaries were shifted to occur at higher superficial gas velocities when the diameter was decreased. This confirms the dominance of slug flow as the diameter decreases. They reported that the diameter effect in these triangular channels is opposite to the effect in large diameter circular channels in which the transition boundaries shift to the left when the diameter decreases.

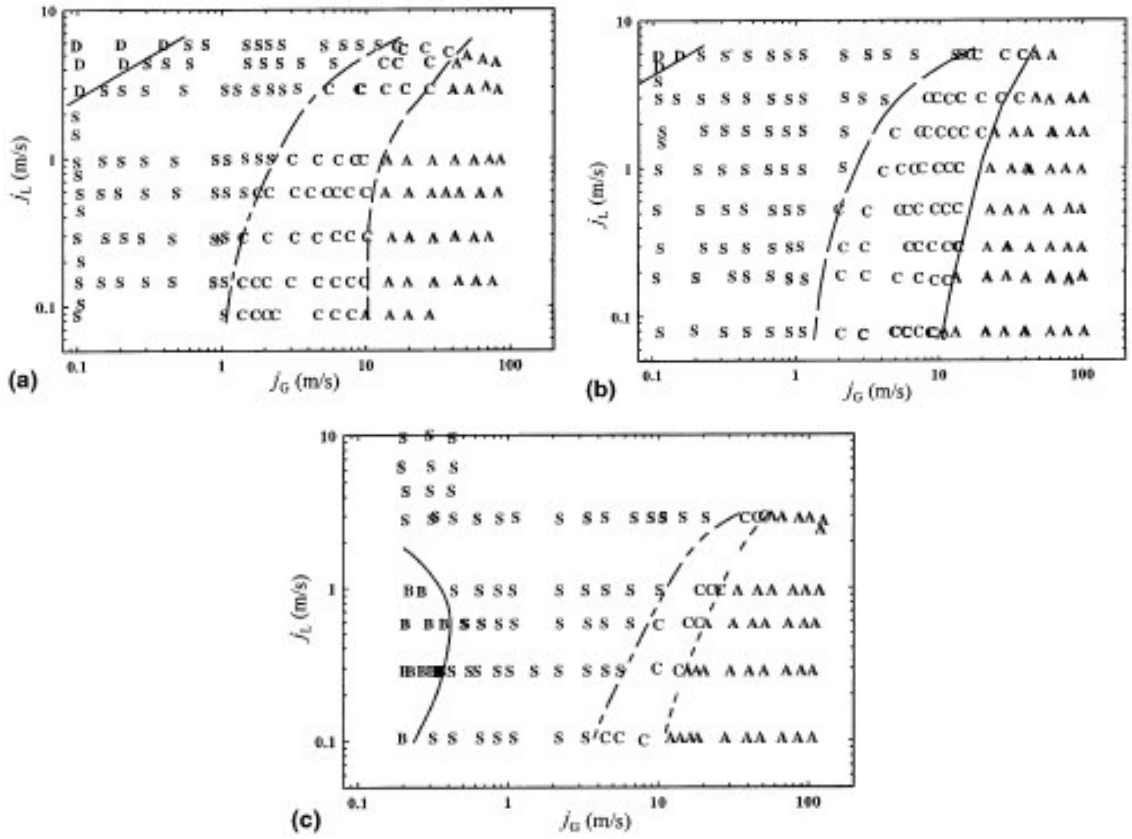

Figure 2.20 The flow pattern maps for upward flow in mini-triangular channels: (a) D_h = 2.886 mm, (b) D_h = 1.443 mm and (c) D_h = 0.886 mm, Zhao and Bi (2001).

Chen et al. (2006) investigated the effect of diameter on the flow boiling patterns of R134a in four vertical tubes of inner diameters 4.26, 2.88, 2.01 and 1.1 mm. Reducing diameter shifted the transition boundaries of slug/churn and churn/annular to occur at higher vapour velocities and the dispersed bubble/bubbly to occur at higher liquid velocities. The dispersed bubble/churn and bubbly/slug transition boundaries were not significantly influenced by tube diameter. Additionally, they developed flow maps using liquid and gas Weber numbers as coordinates instead of superficial velocities. Though the velocity maps showed some effect for tube diameter, using the Weber number maps the transition boundaries collapsed into one line. This led them to conclude that Weber number may be the right parameter for representing the effect of tube diameter on the transition boundaries. Figure 2.21 shows the effect of diameter plotted on velocity and Weber number planes.

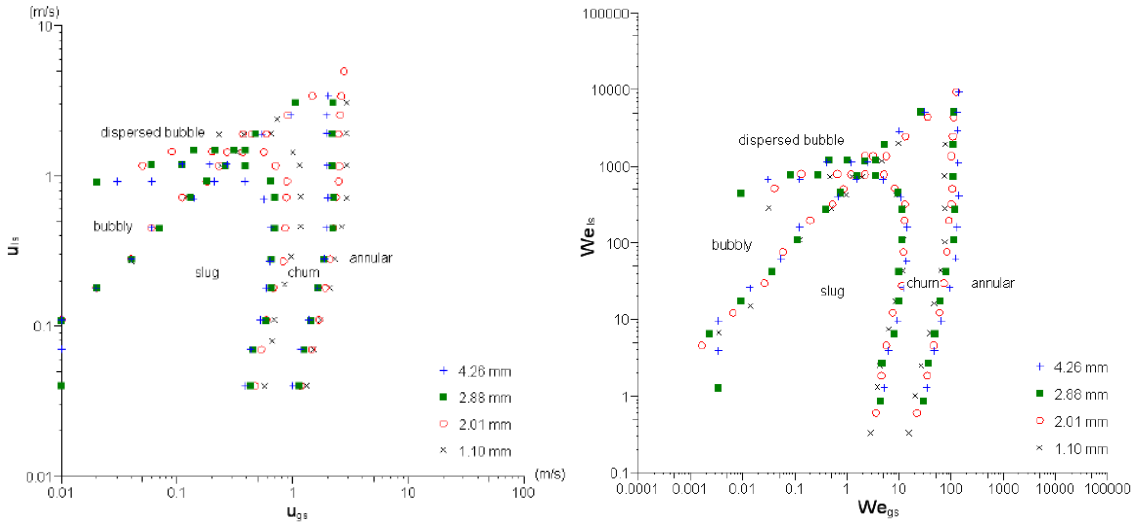

(a) (b)

Figure 2.21 The flow boiling patterns maps of R134a at p = 10 bar developed by Chen et al. (2005), (a) effect of diameter in velocities plane, (b) effect of diameter in Weber number plane.

Xiong and Chung (2007) investigated flow patterns of nitrogen-water mixture in three microchannels of 0.622, 0.412 and 0.209 mm hydraulic diameters. They presented the observed patterns on the Weber number map shown in Fig. 2.22. It is clear from the figure that the bubbly-slug region, which appeared in the two largest channels, is located in the left lowest corner corresponding to very small Weber number region. This means that this pattern is controlled by the dominance of surface tension force over inertia force. On the contrary, annular flow occupied the right area on the map corresponding to high Weber number, which reflects the dominance of inertia over surface tension force. Slug-ring flow and dispersed-churn flow almost occur at equal inertia and surface tension forces. However, slug-ring flow tends to be mostly controlled by surface tension while dispersed-churn was mostly controlled by liquid inertia required to break up the churn into dispersed fragments. In the smallest channel, slug-flow dominated at low Weber numbers while no bubbly-slug anymore, which was attributed to the dominance of surface tension over inertia at the same gas flow rate that prevents the break up of the liquid bridge between slugs into bubbles. Also, it was found that the transition lines tend to shift to the right at higher gas Weber numbers when the diameter decreases.

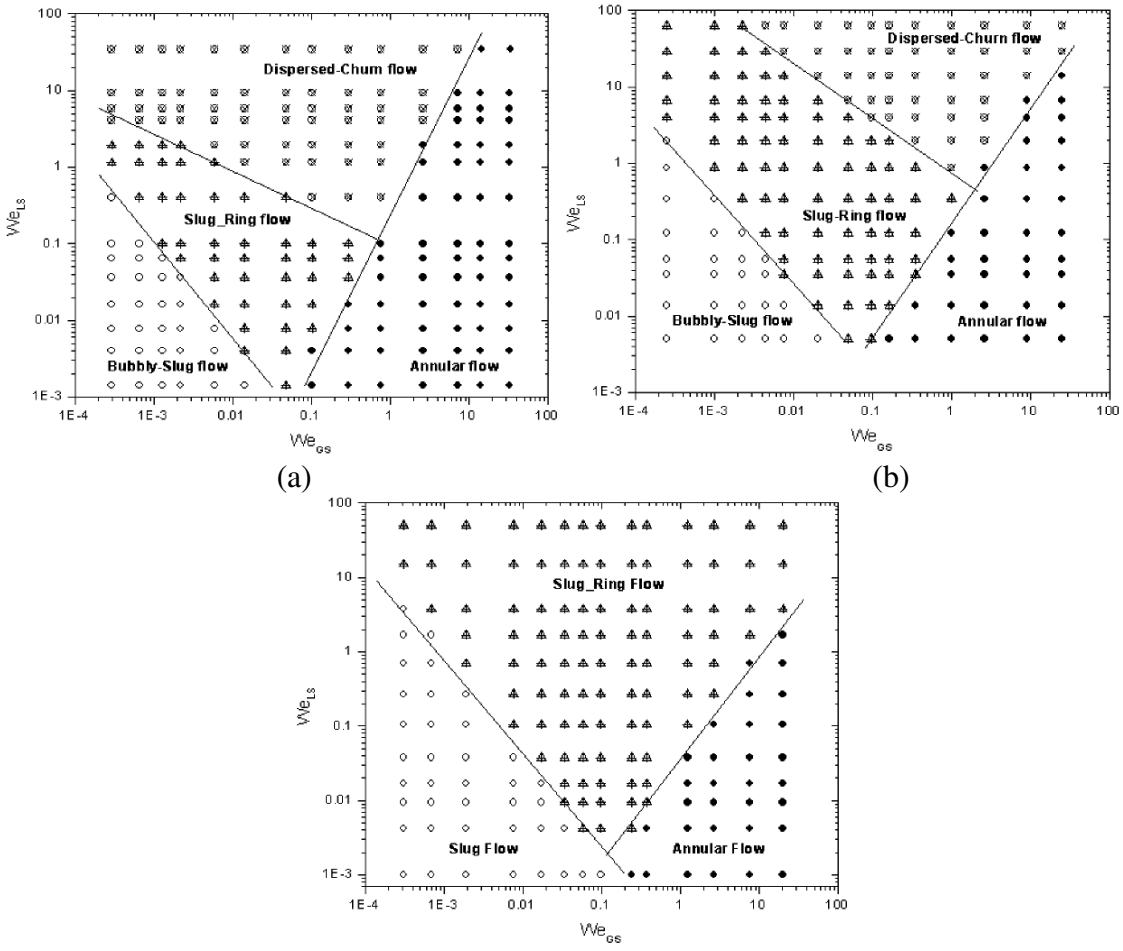

Figure 2.22 The flow maps of nitrogen-water flow in microchannels: (a) D_h = 0.622 mm, (b) D_h = 0.412 mm and (c) D_h = 0.209 mm; Xiong and Chung (2007).

Revellin and Thome (2007b) experimentally investigated two phase flow boiling characteristics of R134a and R245fa in two horizontal micro tubes having inner diameters of 0.51 and 0.79 mm. The developed maps were presented on the mass flux versus quality plane. To develop a more general flow map for micro tubes, they classified the observed flow patterns into isolated bubbles pattern that includes both bubbly and slug patterns, coalescing bubble and annular flow pattern. This map is shown in Fig. 2.23. Additionally, they proposed a correlation for transition from the isolated bubble regime to the coalescing bubble regime as a function of boiling number (q/Gh_{fg}), liquid only Reynolds number (GD/μ_L) and gas Weber number ($G^2D/\rho_g\sigma$) as given by Eq. (2.1). The transition from coalescing bubble regime to annular flow regime was correlated as a function of liquid Reynolds number and liquid Weber number ($G^2D/\rho_L\sigma$) as given by Eq. 2.2.

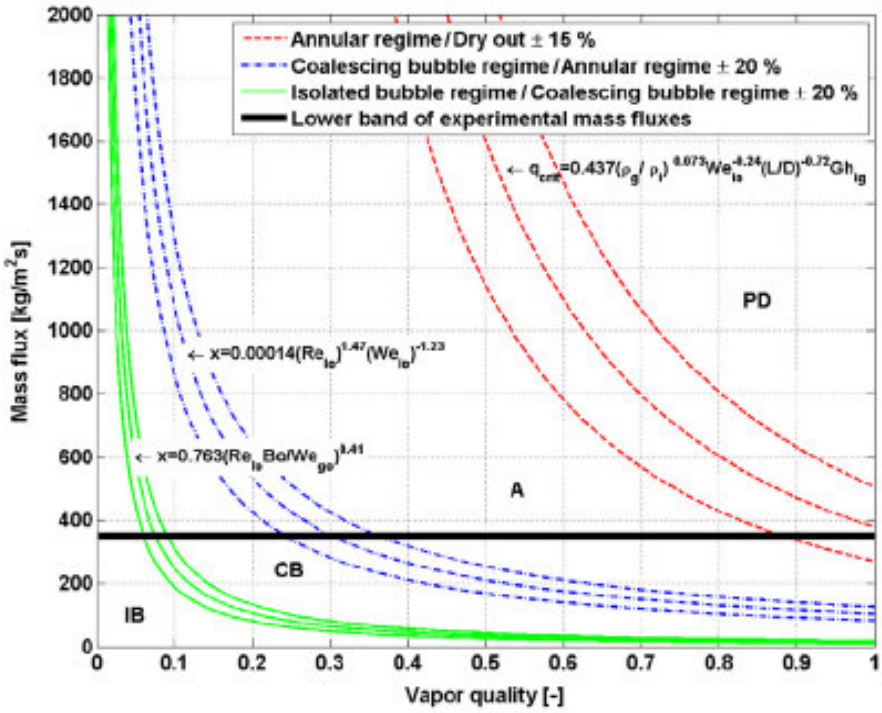

Figure 2.23 The new flow pattern map of R134a in a circular channel of 0.5 mm diameter. IB: isolated bubble pattern; CB: coalescing bubbles pattern; A: annular pattern; PD: post dryout pattern, Revellin and Thome (2007b).

$$x_{IB/CB} = 0.763\left(\frac{\mathrm{Re}_{lo}\, Bo}{We_{go}}\right)^{0.41} \tag{2.1}$$

$$x_{CB/A} = 0.00014\,\mathrm{Re}_{lo}^{1.47}\, We_{lo}^{-1.23} \tag{2.2}$$

Equation 2.1 indicates that, the transition from isolated bubbles into coalescence bubble regime is independent on tube diameter. On the other hand, Eq. (2.2) indicates some effect for tube diameter where the transition from coalescence bubble into annular regime occurs at lower qualities when the diameter decreases.

2.3.3 Effect of fluid properties on the transition boundaries

Few studies discussed the effect of liquid properties on the flow patterns transition boundaries. Yang and Shieh (2001) investigated flow boiling patterns of R134a and adiabatic patterns of air-water flow in three horizontal tubes of 1, 2 and 3 mm diameters. Comparing the flow maps of air-water with those of R134a confirmed that

fluid properties have a significant effect on the location of the transition boundaries. It is known that the surface tension of water is about 9.6 times that of R134a. Consequently, it was found that using fluids with smaller surface tension (R134a) resulted in a shift in the plug/slug and slug/annular transition boundaries to occur at lower superficial gas velocities. Also, the bubbly/intermittent transition was shifted up to occur at higher liquid superficial velocities for R134a (smaller surface tension). This behaviour was attributed to the effect of surface tension that keeps bubbles retaining circular shape and keeps liquid holdup between tube inner surfaces, which retard the transition from slug into annular. Figure 2.24 shows comparison between the maps of R134a and air-water.

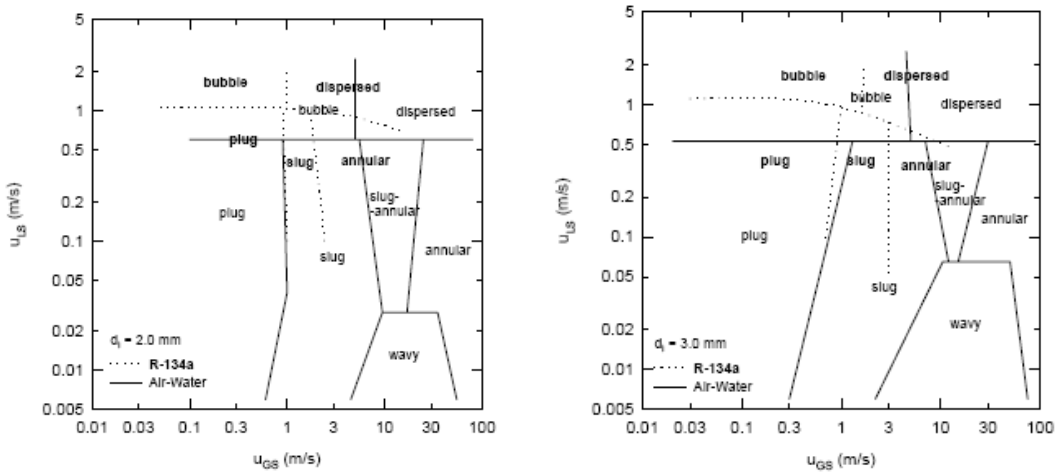

(a) (b)

Figure 24 Comparison of air-water and R134a flow boiling patterns maps for (a) 2 mm tube and (b) 3 mm tube, Yang and Shieh (2001).

Chen et al. (2006) investigated two flow boiling patterns of R134a at system pressures of 6, 10 and 14 bar. Due to the fact that system pressure influences surface tension, the transition boundaries may be influenced as well. The surface tension of R134a increased by about 88 % when the pressure decreased from 14 to 6 bar. The system pressure (hence fluid properties) was found to influence some of the transition boundaries. As the pressure increased (smaller surface tension), the slug/churn and churn/annular shifted slightly towards lower vapour velocities, which agrees with Yang and Shieh (2001), while dispersed bubble/bubbly shifted to lower liquid velocities. On the other hand, the bubble/churn and the bubbly/slug boundaries were found to be hardly

influenced by pressure. Figure 2.25 shows the effect of pressure on the transition boundaries.

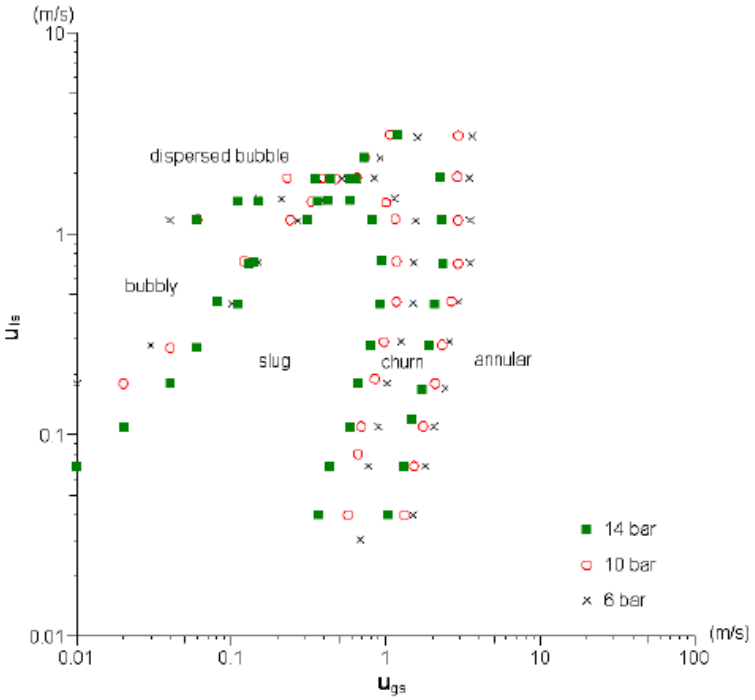

Figure 2.25 Effect of pressure on transition boundaries in the 1.1 mm diameter tube, Chen et al. (2006).

Recently, Martin-Callizo et al. (2010) conducted a visualization study for the flow boiling of R134a in a vertical glass tube (directly heated) of 1.33 mm inner diameter. They presented the flow patterns on the *G-x* and U_{LS}-U_{GS} maps. They investigated the effect of system pressure and inlet sub-cooling on the location of the transition boundaries. It was found that, increasing system pressure shifts all transition boundaries towards higher vapour qualities. This was attributed to the lower liquid to vapour density ratio at high pressure which results in bubbles with smaller size and consequently requires more energy for coalescence. Decreasing the inlet sub-cooling from 8 to 5 K did not show a significant effect on the positions of the transition boundaries. Further decreasing the sub-cooling from 5 to 3 K shifted the transition boundaries of isolated bubbly to confined bubbly, confined bubbly to slug and slug to slug-annular or churn to higher values of vapour qualities. However, they reported that the result of the inlet sub-cooling is not conclusive.

2.4 Two phase flow pressure drop

This section presents the effect of different parameters such as channel diameter, heat flux, mass flux and system pressure on pressure drop in microchannels. Two phase flow pressure drop depends to a great extent on flow patterns. Fukano and Kariyasaki (1993) found that, the Lockhart-Martinelli's model highly under-predicts the measured pressure drop data particularly in the intermittent flow regime. Accordingly, they believed that there is an additional mechanism other than wall friction that works during intermittent flow in capillary tubes. This mechanism is the sudden expansion occurring when the liquid trapped in the film flows into the liquid slug at the tail of the bubble. The contribution of pressure loss due to this mechanism was found to be more significant in horizontal capillary tubes than vertical ones. Kureta et al. (1998) measured the flow boiling pressure drop of water in a 2 mm diameter tube and plotted it versus heat flux. In the low heat flux region, the pressure drop increased with heat flux and peaked at certain value after which it dropped before it increases again almost linearly with heat flux. This peak was believed to be due to the growth of slug flow region, which was accompanied with high pressure fluctuation amplitude. Whereas the sudden drop after the peak was believed to arise from the shrinkage of slug region and the growth of churn-turbulent and annular regions. Revillin and Thome (2007c) measured the pressure drop of R134a and R245fa in two adiabatic glass micro tubes of 0.509 and 0.79 mm diameter. The vapour was created in a micro-evaporator located before the adiabatic glass section. It was found that the frictional pressure drop increases almost linearly with exit quality up to a quality value after which it slightly drops before it increases again, see Fig. 2.26. The conditions at which this drop occurs were found to be corresponding to the transition from wavy to smooth annular flow pattern. In addition to that, the pressure drop was found to increase with increasing mass flux, decreasing system pressure and decreasing tube diameter. The effect of system pressure was attributed to the reduction in vapour density when the pressure decreases, which results in higher vapour velocity and consequently higher pressure drop. Also, the type of fluid was found to have a strong effect on the two phase flow pressure drop where the pressure drop of the R245fa was found to be significantly higher than that of R134a. This was attributed to the high vapour density of R134a compared to that of R245fa, which is three times higher, leading to a much higher vapour velocity in case of R245fa and consequently higher pressure drop.

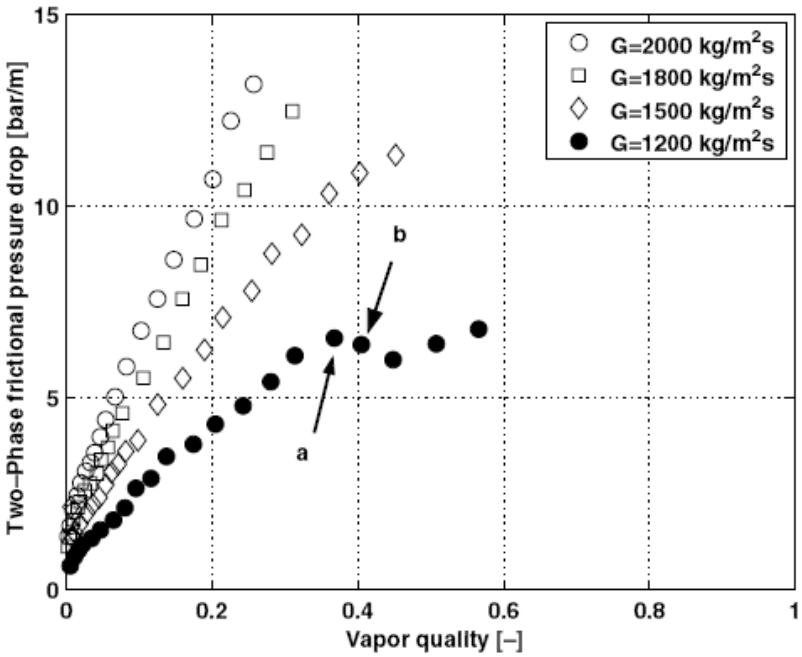

Figure 2.26 Two phase frictional pressure drop as a function of vapour quality for R134a, D = 0.509 mm, T_{sat} = 30, ΔT_{sub} = 3K, Revellin and Thome (2007c).

The pressure drop characteristics that are measured under adiabatic conditions may differ from that measured under boiling conditions. This may arise from the high local pressure fluctuations resulting from the bubble growth and expansion in boiling. For example, Wen and Kenning (2004) measured the local pressure fluctuations in flow boiling of water in a vertical minichannel (2 × 1 mm). Figure 2.27 shows the measured local pressure fluctuations at five axial locations. At all locations, the magnitude of fluctuations in the measured pressure is almost similar (5kPa) which is comparable to or greater than the time averaged pressure drop across the channel. Kaminaga et al. (2003) measured the adiabatic pressure drop of air-water flow in a 1.45 mm diameter tube and also measured the boiling pressure drop of water in the same tube. In both cases, the pressure drop was plotted versus gas superficial velocity at different mass fluxes and was found to increase linearly with increasing gas velocity. The difference between the two cases was that, there was no mass flux effect in case of boiling while the effect appeared under adiabatic conditions. They did not comment on this result. It is worth mentioning that, when the boiling pressure drop was plotted versus exit quality, the pressure drop increased exponentially not linearly.

Tong et al. (1997) investigated the effect of mass flux, tube diameter, fluid inlet temperature and exit pressure on the measured pressure drop of highly sub-cooled water flow boiling in four tubes of 1.05, 1.38, 1.8 and 2.44 mm diameters. They presented their results on the ΔP-q plane. It was found that, the pressure drop increases continuously with increasing heat flux and mass flux due to the enhancement in wall shear stress. When mass flux was increased by 80 %, the pressure drop increased by a

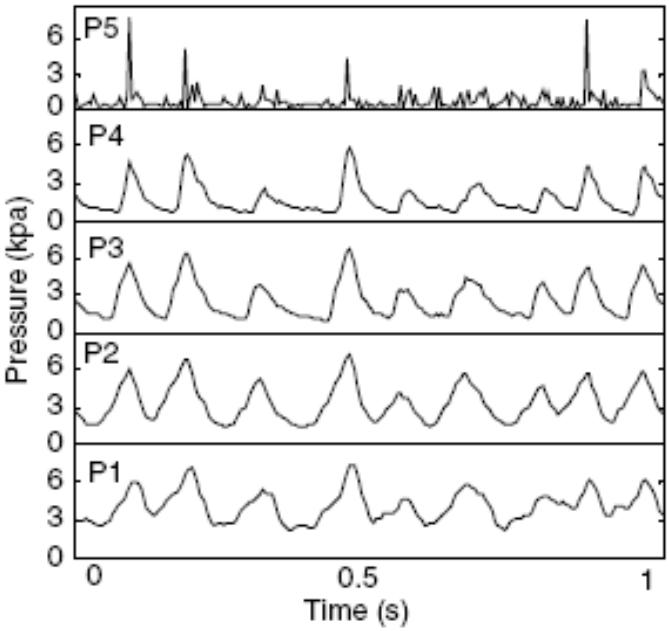

Figure 2.27 Pressure fluctuations at five axial positions (P1-P5) during flow boiling of water in a vertical channel (2 × 1 mm) at G = 134 kg/m2 s and q = 53 kW/m2, Wen and Kenning (2004).

factor of 3. Moreover, increasing exit pressure resulted in a decrease in pressure drop. The authors explained this effect in terms of the effect of exit pressure on flow patterns and temperature field. As the flow becomes two phase, higher exit pressure leads to higher sub-cooling at the exit that results in high bubble condensation. The condensation and disappearance of the bubbles in the core of the liquid reduces pressure drop. Regarding the effect of inlet temperature, it was found that, increasing inlet sub-cooling resulted in a decrease in pressure drop due to the stronger condensation in the channel core. Additionally, decreasing tube diameter was found to increase pressure drop. This was attributed to the fact that at a given mass flux the boundary layer becomes thinner as the diameter decrease, which results in higher velocity gradients leading to higher shear stress and in turn higher pressure drop. Peng et al. (1998a)

measured the flow boiling pressure drop of water and methanol in microchannels having V-shape cross section at different mass fluxes, heat fluxes and channel hydraulic diameters. The measured pressure drop was presented on the ΔP-q plane at different mass fluxes. At the onset of nucleate boiling, a sudden decrease in pressure drop was found, which seems peculiar. After boiling incipience, the pressure drop increased again almost linearly with increasing heat flux up to certain heat flux value at which the pressure drop suddenly jumps to a much higher value. They attributed the jump in pressure drop at high heat fluxes to the formation of a large number of bubbles in the inlet plenum, which in turn blocked channel inlet and thus the pressure drop suddenly increased. It is worth noting that, the measured pressure drop values were very small (about 16 Pa for channels of 0.2 to 0.6 mm hydraulic diameters). These very small values may be attributed to the fact that they did not observe any bubbles in their experiment where instead they reported "fictitious boiling". Moreover, the pressure drop was found to increase with decreasing channel diameter and increasing mass flux. Shuai et al. (2003) experimentally investigated flow boiling of water in two rectangular channels having dimensions of 2 × 4 mm and 0.5 × 2 mm at atmospheric pressure and found that the pressure drop of the smallest channel was much higher than that of the largest one. Also, the effect of inlet sub-cooling was found to be insignificant at low mass fluxes while clear effect was observed at high mass fluxes. Liu and Garimella (2007) and Lee and Garimella (2008) measured flow boiling pressure drop of water in microchannels with hydraulic diameters ranging from 162.5 to 588 μm. The measured pressure drop was found to decrease slightly with heat flux in the single phase region due to the decrease in viscosity while once boiling commences the pressure drop rapidly increases almost linearly owing to the increase in acceleration effect induced by vapour generation.

In the above studies, the pressure drop was measured using water as a test fluid. Now, the behaviour of the measured pressure drop for refrigerants is discussed. Yan and Lin (1998) investigated the effect of mass flux, heat flux and saturation pressure on the measured pressure drop of R134a in a 2 mm diameter tube. It was found that the pressure drop increased almost linearly with increasing vapour quality and mass flux. At low mass fluxes, the slope of the ΔP-q curve was very small, i.e. pressure drop increases slowly, while the slope of the curve significantly increased with increasing mass flux. Increasing saturation pressure resulted in a decrease in the measured pressure drop

especially for exit qualities greater than 0.65 while the effect was very small for qualities less than this value. Tran et al. (2000) measured flow boiling pressure drop for three refrigerants R134a, R12 and R113 using two circular test sections of 2.46 and 2.92 mm diameters and one rectangular channel of 2.4 mm hydraulic diameter. It was found that the measured two phase pressure drop increases with increasing exit quality, mass flux and decreasing system pressure. For R134a when the system pressure was decreased by about 47 %, the pressure drop has increased by about 60 % and also for R12 the pressure drop has increased by about 70 % when system pressure was decreased by about 37 %. Also, the pressure drop of R134a was found to be 31 – 44 % lower than that of R12 for the same heating rate. This arises from the fact that at the same heating rate and exit quality, R134a requires lower mass flow rate than R12 due to the higher latent heat of R134a. Lee and Mudawar (2005b) measured the two phase pressure drop of R134a in a multi-channel heat sink 231 × 713 μm. It was found that, pressure drop increases almost linearly with increasing heat flux up to a heat flux value after which the trend shows a plateau. This plateau was believed to occur due to the shrinkage of the two phase region and the growth of the single phase vapour region. Huo et al. (2007) and Karayiannis et al. (2008) investigated flow boiling pressure drop of R134a in five tubes of 4.26, 2.88, 2.01, 1.1 and 0.52 mm diameters. It was found that, the pressure drop increases almost linearly with heat flux and sometimes a decrease in pressure drop was observed at high heat flux values due to the occurrence of intermittent dryout. Also, it was found that increasing mass flux and decreasing system pressure resulted in an increase in the measured pressure drop. The effect of pressure was attributed to the reduction in liquid to vapour density ratio as the pressure increases. Decreasing tube diameter was found to increase pressure drop though the effect was less clear at high exit quality for the three larger tubes (4.26 – 2.01) as seen in Fig. 4.28. When the diameter was decreased from 2.01 to 1.1 mm, significant increase in pressure drop was found while the pressure drop of the 0.52 mm tube was much higher. The behaviour of the 0.52 mm tube was attributed to the very high single phase friction factor which was found to be more than twice the value predicted by laminar and Blasius equations. Analysing the inner surface of this tube showed that the cross section is not uniform along the tube, which may explain the very high two phase pressure drop in this tube. This size of tube was to be re-examined in the present study. Additionally, the contribution of the frictional pressure drop was the greatest while that of acceleration becomes important as the exit quality increases.

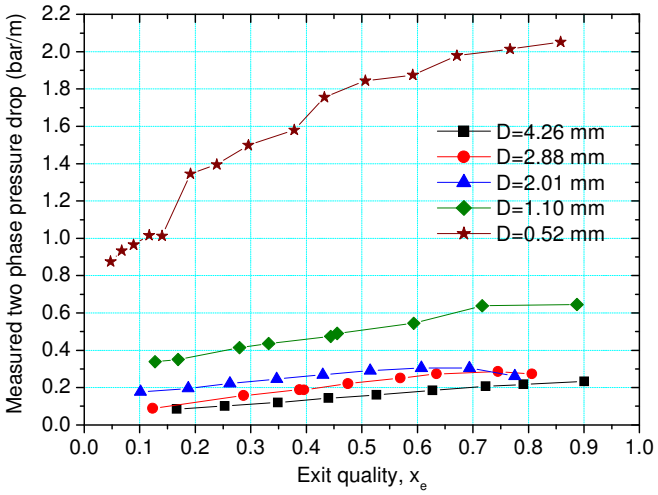

Figure 2.28 Effect of tube diameter on the two phase pressure drop as a function of exit quality at 8 bar system pressure for R134a, Karayiannis et al. (2008).

2.5 Prediction of two phase pressure drop

Generally, the two phase flow pressure drop can be estimated by applying the one dimensional steady momentum equation between channel inlet and outlet. On doing so, it can be deduced that the total two phase pressure gradient is composed of three components namely: frictional, gravitational and acceleration components as given by Eq. (2.3).

$$\left(\frac{dp}{dz}\right)_{tp} = \left(\frac{dp}{dz}\right)_{f} + \left(\frac{dp}{dz}\right)_{g} + \left(\frac{dp}{dz}\right)_{acc} \tag{2.3}$$

The three components of the right hand side can be estimated using either the homogeneous flow model (HFM) or the separated flow model (SFM). The details of these models can be found in Collier and Thome (1994). The final expressions of these components for a heated channel under constant heat flux boundary condition where the vapour quality varies linearly from 0 to x is given as:

Frictional pressure drop

$$\Delta p_f = \frac{2 f_{tp} L G^2 v_L}{D}\left[1 + \frac{x}{2}\frac{v_{Lv}}{v_L}\right] \qquad \text{(HFM)} \tag{2.4}$$

$$\Delta p_f = \frac{2 f_L L G^2 v_L}{D}\left[\frac{1}{x}\int_0^x \phi_L^2 dx\right] \qquad \text{(SFM)} \tag{2.5}$$

Gravitational pressure drop

$$\Delta p_g = \frac{Lg\sin\theta}{v_{Lv}x}\ln\left[1+x\frac{v_{Lv}}{v_L}\right] \qquad \text{(HFM)} \qquad (2.6)$$

$$\Delta p_g = \frac{Lg\sin\theta}{x}\int_0^x\left[\alpha\rho_g+(1-\alpha)\rho_L\right]dx \qquad \text{(SFM)} \qquad (2.7)$$

Acceleration pressure drop

$$\Delta p_{acc} = G^2 x v_{Lv} \qquad \text{(HFM)} \qquad (2.8)$$

$$\Delta p_{acc} = G^2 v_L\left[\frac{x^2}{\alpha}\frac{v_g}{v_L}+\frac{(1-x)^2}{1-\alpha}-1\right] \qquad \text{(SFM)} \qquad (2.9)$$

$$\alpha = \frac{1}{1+S\dfrac{1-x}{x}\dfrac{v_L}{v_g}} \qquad (2.10)$$

The acceleration and gravitational pressure drop components can be estimated if the void fraction α is known. Void fraction can be calculated from Eq. (2.10) by letting the slip ratio S = 1 in case of homogeneous model while in the separated flow model various empirical correlations can be used. Also, estimating the frictional pressure loss using the homogeneous model requires the two phase friction factor f_{tp} while using the separated flow model requires the two phase multiplier ϕ_L^2. Regarding the two phase friction factor, it is simply calculated in a way similar to the calculation of single phase friction factor but using mean mixture properties weighted by mass quality. The principle of the two phase multiplier was first proposed by Lockhart-Martinelli (1949). They ignored the interaction between the phases and plotted the two phase multiplier versus the Martinelli's parameter X defined by Eq. (2.11) for different flow patterns (laminar/turbulent).

$$\mathrm{X}^2 = \frac{(dp/dz)_{f,L}}{(dp/dz)_{f,g}} \qquad (2.11)$$

Chisholm (1967) has taken the interaction between the phases into account, which was incorporated in a constant C called Chisholm constant. Based on that, the two phase multiplier was given by Eq. (2.12) with the constant C takes values ranging from 5 – 20 based on whether each phase is laminar or turbulent.

$$\phi_L^2 = 1+\frac{C}{\mathrm{X}}+\frac{1}{\mathrm{X}^2} \qquad (2.12)$$

In addition to the homogeneous flow model and the separated flow model, the drift flux model (DFM) is also used. The drift-flux model was first introduced by Zuber-Findaly (1965) and is more appropriate for dispersion flow patterns to empirically correlate the experimental void fraction and the slip ratio. The details of the model can also be found in Collier and Thome (1994). Only, the final equations of the model will be given here.

$$\overline{V_b} = U_g / \alpha = C_0 \overline{J} + \overline{V_{gJ}} \tag{2.13}$$

In the above equation the hatches over the symbols denote that these quantities are coming from cross sectional area averaging. $\overline{V_b}$ is the bubble velocity, $\overline{J}$ is the total volumetric flux, which equals $(U_{GS} + U_{LS})$ where U_{GS} and U_{LS} are the superficial velocities of gas and liquid, respectively, C_0 is the distribution parameter defined by $\langle \alpha J \rangle = C_0 . \langle \alpha \rangle . \langle J \rangle$ and $\overline{V_{gJ}}$ is the drift velocity. Equation (2.13) can be written in a useful form by replacing $\overline{V_g}$ by U_{GS} / α where $U_{GS} = \beta J$ and β is called the volumetric void fraction and the resulting equation becomes:

$$\alpha = \frac{\beta}{C_0 + (\overline{V_{gJ}} / \overline{J})} \tag{2.14}$$

2.5.1 Empirical correlations

There is a large scatter in the open literature about the capability of macroscale models and correlations to predict pressure drop at microscale. Some researchers such as Tran et al. (2000), Zhang and Webb (2001), Kawahara et al. (2002), Qu and Mudawar (2003a), Wen and Kenning (2004), Cavallini et al. (2005), Karayiannis et al. (2008) and Choi et al. (2009) compared their experimental data with the conventional models and found poor predictions. Some other researchers such as Zhang and Webb (2001), Lee and Mudawar (2005b), Pehlivan et al. (2006), Qi et al. (2007a), Agostini et al. (2008b) and Kawahara et al. (2009) found that the homogeneous model predicts their data very well. The success of the homogeneous model in some studies and the failure in some others may be attributed to the difference in fluids tested in these studies. Fluid properties, particularly surface tension, may influence the boundaries of isolated

bubbles/slug flow regimes in which homogeneous model works better. For example, Qi et al. (2007a) attributed the success of the homogeneous model in predicting their flow boiling pressure drop data of liquid nitrogen to the effect of surface tension. Liquid nitrogen has a very small surface tension that allows for the dominance of discrete bubbles up to intermediate qualities and allow for the dominance of annular mist flow at high qualities.

In an attempt to develop new pressure drop correlations for microscale applications, most researchers such as Lazarek and Black (1982), Warrier et al. (2002), Mishima and Hibiki (1996), Holt et al. (1997), Yun and Kim (2004), Lee and Lee (2001), Lee and Mudawar (2005b), Lee and Garimella (2008), Chen et al. (2007), Choi et al. (2008) and Sun and Mishima (2009) modified the Chisholm's constant *(C)* in Eq. (2.12) to consider the microscale effects. Other researchers such as Tran et al. (1996), Yu et al. (2002) and Kaminaga et al. (2003) proposed correlations for the two phase multiplier in a functional form that is different from Eq. (2.12). In addition to that, Revellin and Thome (2007c) proposed a correlation for the two phase friction factor to be used with the homogeneous model. The details of these correlations will be discussed later in chapter 6 and the equations are summarized in appendix A.

2.5.2 Mechanistic models

The prediction of pressure drop in small to micro diameter channels using flow patterns-based models seems to be more accurate than using empirical correlations. There are a limited number of studies that discussed modelling issues in microchannels. Holt et al. (1999) presented a flow pattern based model for predicting the total two phase pressure drop in upward vertical flow in narrow passages. In this model, the slug/churn and slug/dispersed bubble transition criteria proposed by Brauner and Barnea (1986) and the churn/annular transition criterion given by McQuillan and Whalley (1985) were used. In bubbly flow, the void fraction correlation of Zuber and Findlay (1965) was used to estimate the gravitational component, the homogeneous model was used to estimate the acceleration component and the method suggested by Wallis (1969) was used to calculate the frictional component. In slug and churn flows, they used the model of De Cachard and Delhaye (1996) which was developed for predicting pressure drop in slug and churn flows in air-lift pumps. In annular flow, they used the annular flow model

proposed by Whalley (1987). The comparison of the model with pressure drop data collected using channels with hydraulic diameter ranging from 2.2 to 10 mm showed excellent predictions in bubbly, slug and annular flow. In churn flow, the model showed poor predictions but when the churn flow model was replaced with the annular flow model the predictions became much better. Also, in bubbly and slug flow the gravitational component contributed to 90 % of the total pressure drop. Garimella et al. (2002) developed a model for intermittent slug flow during condensation of R134a in horizontal microchannels of hydraulic diameters ranging from 0.5 to 4.91mm. They selected a control volume as a unit cell consisting of a cylindrical bubble surrounded by a uniform liquid film and followed by a moving liquid slug. In the liquid slug, the frictional pressure gradient was calculated using the Blasius's equation for friction factor and using slug velocity. In the bubble/film region, the bubble velocity was calculated using the drift flux model with zero drift velocity and $U_B / U_{LS} = 1.2$. Also, in the bubble/film region, the pressure gradient was calculated using the Blasius's equation and the relative velocity between the bubble and the interface. Interface velocity was obtained by solving the momentum equation in the film and the bubble iteratively. Additionally, they accounted for the pressure loss arising from liquid film flowing into the liquid slug, which was called transition pressure losses. These losses were calculated based on the relative velocity between the liquid slug and film interfacial velocity. Finally, the relative lengths of each zone in the cell were calculated using expressions that were given by Fukano et al. (1989). The required frequency was correlated as a function of liquid slug Reynolds number. This model was found to capture 88 % of the data within 25 % error bands with mean absolute error of 13.4 %. However, they reported that the slug frequency is a weak point that needs further modelling in order to correlate it with flow conditions, channel diameter and fluid properties. Furthermore, the contribution of each zone to the total pressure drop was found to be: 53 % was resulting from the liquid slug, 12 % from the bubble-film region and 35 % from the transition losses.

Based on the fact that, annular flow pattern dominates during water flow boiling in microchannels, Qu and Mudawar (2003b) developed an annular flow model including droplet entrainment. They assumed that the film is uniform and smooth with a thickness much less than channel diameter. In the model, the conservation equations were applied

in the film and gas core separately. They used the criterion of Taitel and Duckler (1976) for the onset of annular flow. The model predicted the data with a mean absolute error of 12.7 % that was similar to the comparison with Mishima and Ishii (1996). Chung and Kawaji (2004) extended the model of Garimella et al. (2002) to be applicable for channels of size down to 0.1 mm hydraulic diameter. They ignored the transition pressure losses that were taken into account in the model of Garimella et al. Also they developed their own correlations for void fraction and the relative lengths of each zone. The model predicted their measured pressure drop data very well. Shiferaw et al. (2009) developed a semi-mechanistic model for slug flow based on the 3-zone heat transfer model that was proposed by Thome et al. (2004) with the assumption of smooth liquid film. In this model the total pressure drop was calculated by time averaging the pressure drop for single phase liquid, elongated bubble with a thin liquid film and single phase vapour. The model predicted the flow boiling data of R134a in vertical tubes with diameters of 4.26, 2.88, 2.01, 1.1and 0.52 mm with mean errors 23, 20, 16.8, 16.3 and 22 %, respectively. Also, the effect of film waviness was assessed and showed significant effect on pressure drop and should be taken into considerations.

2.6 Bubble dynamics and void fraction

Void fraction is a key parameter in estimating the total two phase pressure drop. This section presents the experimental studies that measured void fraction, bubble rise velocity and liquid film thickness in small diameter channels. Many investigators such as Mishima and Hibiki (1996), Chen et al. (2002), Kawahara et al. (2002), Serizawa et al. (2002), Chung and Kawaji (2004), Xiong and Chung (2007), Hayashi et al. (2007) and Fu et al. (2008) ignored the drift velocity and correlated the measured void fraction using the drift flux model defined by Eq. (2.13) and Eq. (2.14). Mishima and Hibiki (1996) measured the void fraction of air-water flow in vertical tubes of 1.05 – 4.08 mm diameters and correlated the bubble rise velocity by Eq. (2.15) and the distribution parameter by Eq. (2.16).

$$U_B = 1.1J \tag{2.15}$$

$$C_0 = 1.2 + 0.51e^{-0.691D} \qquad (D \text{ in mm}) \tag{2.16}$$

Triplett et al. (1999) measured the void fraction for air-water flow in circular and semi-triangular mini-channels. They have found that the homogeneous flow model

satisfactorily predicts the void fraction in bubbly and slug flow but over-predicts it in churn and annular flow. Thus, they concluded that the slip ratio in mini-channels is lower than that in conventional ones. Kawahara et al. (2002) measured the time averaged void fraction of air-water flow in 0.1 mm diameter tube. The measured void fraction α was plotted versus the homogeneous void fraction $\beta = U_{GS}/(U_{GS}+U_{LS})$ and the trend was found to be nonlinear as seen in Fig. 2.29. The measured void fraction values remained very small for $\beta < 0.8$ but increased rapidly after $\beta = 0.8$. They have attributed the non-linearity to: (i) the appearance of single phase liquid flow most frequently at most conditions and (ii) the effect of wall shear stress and surface tension that make the liquid to bridge the channel cross section completely at low liquid flow rates. Eventually, they concluded that the slip ratio in microchannels could be an order of magnitude greater than that in channels of diameters greater than 1 mm. The new void fraction correlation that fitted their data was given by Eq. (2.17).

$$\alpha = \frac{0.03\beta^{0.5}}{1-0.97\beta^{0.5}} \tag{2.17}$$

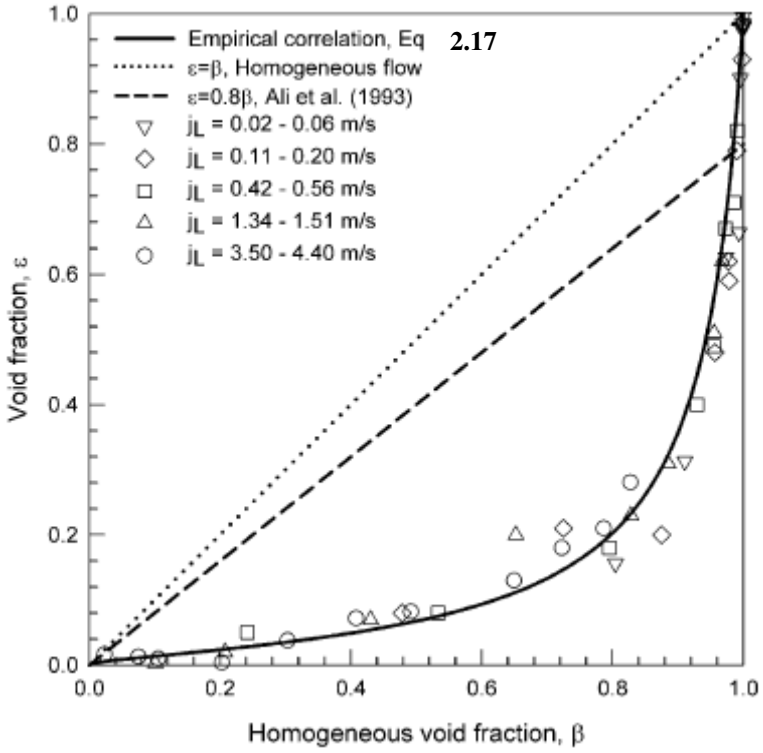

Figure 2.29 The measured void fraction compared to the homogeneous void fraction for air-water flow in a 0.1 mm diameter tube, Kawahara et al. (2002).

Chen et al. (2002) estimated the bubble rise velocity for air-water flow in tubes of 1 and 1.5 mm diameters and found that the relative velocity between the bubble and the mixture volumetric flux is a function of Capillary number and the liquid superficial velocity. They have correlated the bubble velocity in slug, bubble-train slug and churn flow patterns using the drift flux model. The calculations of the drift velocity showed that it is less than 3 % of the bubble rise velocity and thus it was reasonable to be neglected. Accordingly, a correlation for the bubble rise velocity in slug, bubble-train and churn flow was given by Eq. (2.18). In their flow patterns description churn flow was regarded as a slug with a cloud of tiny bubbles at the tail. Based on the correlated bubble rise velocity, the average void fraction was given by Eq. (2.19) with mean deviation of ± 20 %.

$$U_B = 0.932J^{1.11} \tag{2.18}$$

$$\alpha = \frac{U_{GS}}{0.932J^{1.11}} \tag{2.19}$$

However Kawahara et al. (2002) reported non-linear trend between the measured and homogeneous void fractions with large deviations, some investigators such as Serizawa et al. (2002), Hayashi et al. (2007) and Saisorn and Wongwises (2008) found a linear trend. Serizawa et al. (2002) measured the cross-sectional void fraction for bubbly and slug flow in 20 μm diameter tube and reported good agreement between the measured void fraction and the conventional Armand (1946) type correlation ($\alpha = 0.833\beta$), i.e. good linearity. Hayashi et al. (2007) reported also that Armand's correlation reasonably predicts the measured void fraction in a 0.6 mm diameter tube whereas it over-predicts the data of the 0.3 mm tube. Saisorn and Wongwises (2008) determined the cross sectional void fraction of air-water flow in a 0.53 mm tube and found that the homogeneous model predicts the data very well as seen in Fig. 2.30. Chung and Kawaji (2004) measured the void fraction in four tubes of 530, 250, 100 and 50 μm diameters. For the two largest tubes the measured void fraction agreed with the homogeneous void fraction and Armand type correlation. On the other hand, the trend in the channels with diameter 50 and 100 μm was similar to that found in Fig. 2.28 given by Kawahara et al. (2002). In this tube, the void fraction increased almost linearly with β up to $\beta = 0.8$ after which void fraction rapidly increased exponentially. Accordingly, they fitted the data of the two smallest tubes into a correlation given by Eq. (2.20).

$$\alpha = \frac{C_1 \beta^{0.5}}{1 - C_2 \beta^{0.5}} \tag{2.20}$$

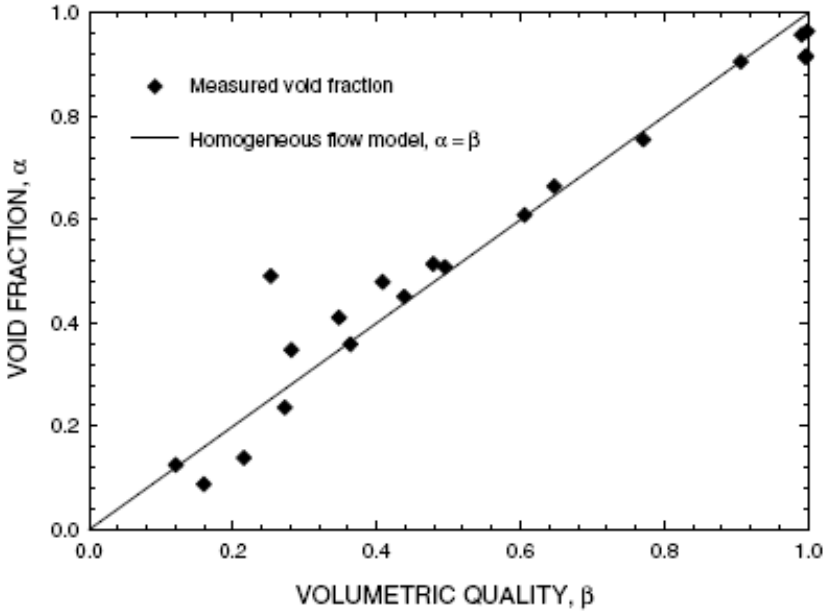

Figure 2.30 The measured void fraction versus the homogeneous void fraction for air-water flow in a 0.53 mm diameter tube, Saisorn and Wongwises (2008).

In the above equation C_1 and C_2 are experimental constants that equal to 0.03 and 0.97 for the 100 μm tube and equal 0.02 and 0.98 for the 50 μm tube. They have explained why the void fraction in microchannels was much less than in mini-channels for $\beta < 0.8$ as follows: for values below 0.8 the observed flow patterns were short gas slugs and long liquid slugs. The long liquid slugs resulted in high pressure gradient, which accelerated the gas slug and reduced its residence time and consequently reduced the measured void fraction. On the other hand, at values above 0.8 the gas slug becomes very long and the pressure gradient decreases. This makes the gas slug to move less rapidly with high residence time and high probability to be recorded or occur more frequently which makes the void fraction increases rapidly after β = 0.8 and approaches unity. Ide and Fukano (2005) measured the void fraction of air-water flow in tubes of 1.1 and 1.45 mm diameters and semi-triangular channels of 1.09 and 1.49 mm hydraulic diameters. It was found that, the homogenous model satisfactorily predicts the void fraction in bubbly and slug flow patterns whereas it over-predicts it with large margins in churn and annular flow patterns. Also, the examined macro-scale correlations over-predicted the data in annular flow pattern suggesting that the momentum transfer

phenomena at microscale may be different from that at macro-scale. Xiong and Chung (2007) measured the time averaged void fraction of nitrogen-water flow in rectangular microchannels of 0.209, 0.412 and 0.622 mm hydraulic diameters. It was found that, the trend of the measured void fraction against the homogenous one was not linear and the values depend on channel diameter. As a result, they proposed a correlation, given by Eq. (2.21), that incorporates the effect of channel size.

$$\alpha = \frac{c\beta^{0.5}}{1-(1-c)\beta^{0.5}} \tag{2.21}$$

where:

$$c = \frac{0.266}{1+13.8e^{-6.88D_h}}$$

Fu et al. (2008) experimentally determined the time averaged void fraction during flow boiling of liquid nitrogen in a 1.931 mm diameter tube. The comparison of the measured void fraction with the homogeneous one was similar to that of Kawahara et al. (2002), Xiong and Chung (2007) and Chung and Kawaji (2004). As a result, they have fitted their data into a correlation given by Eq.(2.22).

$$\alpha = \frac{0.06391\ \beta^{0.5}}{1 - 0.93609\ \beta^{0.5}} \tag{2.22}$$

This review demonstrates that some researchers found good agreement between the measured void fraction and the homogenous one whereas some others did not. This discrepancy could be attributed to the difference in the method used to determine the measured void fraction. Some researchers such as Kawahara et al. (2002) determined the time averaged void fraction through assigning a value of 0 when a liquid slug is passing or 1 when a vapour slug is passing. In this case, the residence times of each phase influences the calculated void fraction. This may explain the disagreement with the homogeneous model and the trend in Fig. 2.28 for $\beta < 0.8$ where the residence time of liquid phase was much higher than gas phase. On the other hand, researchers such as Serizawa et al. (2002) and Saisorn and Wongwises (2008) who measured the cross sectional void fraction reported reasonable agreement with the homogeneous model.

Revellin et al. (2006) used an optical measurement technique to measure the flow pattern characteristics in micro tubes such as bubble frequency, bubble velocity and bubble length. At low vapour qualities of about 0.1, the measured bubble velocity and

the cross sectional void fraction were found to be in a good agreement with their homogeneous counterparts. However, the time averaged centreline void fraction showed higher values than both the homogeneous and cross sectional void fractions. The centreline time averaged void fraction was calculated by letting α = 1 when vapour passes and α = 0 when liquid passes. Using the same technique, Agostini et al. (2008c) and Revellin et al. (2008a) experimentally and theoretically investigated the elongated bubble characteristics in micro tubes of 0.509 and 0.79 mm diameters. The measurements were carried out using image processing software, which was specifically developed for this purpose. It was found that, for short bubbles of length less than 30 mm the relative velocity ($U_B - U_H$) rapidly increases when bubble length increases while for longer bubbles of length greater than 30 mm the relative velocity remained almost constant. The value of the relative velocity of the bubble reached in some cases 0.7 m/s, which is large to be neglected. Other observations were that the bubble relative velocity increased with mass flux and channel diameter. Based on these findings, they developed a model for predicting the relation between bubble relative velocity and bubble length. The model started with applying mass, energy and momentum conservation on the bubble itself as a control volume. The details of the equations can be found in their paper. Moreover, they did not find any obvious relationship between the relative velocity and the length of the liquid slug; conventionally the wake behind the bubble was found to influence the velocity of bubble coming behind. The final expression of the bubble velocity as a function of bubble length was given as:

$$U_B = \frac{D \cdot \gamma}{1 - 0.58/Co} \frac{1 - \exp\left(-2 \cdot f_i \cdot L_g / D\right)}{2 \cdot f_i} + U_H \qquad (2.23)$$

In the above equation D is the tube diameter, $\gamma = 4q/D\rho_g h_{fg}$, Co is the confinement number, L_g is the bubble length, u_h is the homogeneous velocity, f_i is the interfacial Darcy friction factor calculated based on u_g as an approximation. Equation 2.23 is valid as long as $Co > 0.58$ because of the singularity point at this value. Revellin et al. (2008b) have carried out further analysis and measurements using laser beams instead of using image processing, which was believed to be relatively less accurate. They identified the flow patterns using two laser beams one located near from the inlet of the

observation section while the second was near from the exit. They have found that Eq. (2.23) is still valid and also found that the number of bubbles with a very short length observed near the channel inlet was much higher than that observed near the channel exit. This observation confirmed that there is an interaction between the bubbles due to collision and coalescence. Equation (2.23) indicates that the long bubbles travel faster than short bubbles that are moving a head and thus coalescence will occur. But, if all the bubbles have approximately constant length, the bubbles will travel with the same velocity and no collision or coalescence will occur.

Boye et al. (2007) developed an analytical model for the annular flow pattern using the separated flow model. This model neglected the body and capillary forces and assumed smooth interface. They applied the momentum equation for each phase and from a mass balance they obtained analytical expressions for the velocity of each phase. Consequently, they gave an expression for the slip ratio defined by Eq. (2.24).

$$S = 2 + \frac{\mu_L}{\mu_g} \frac{(r_{ph}/R)^2}{1-(r_{ph}/R)^2} \tag{2.24}$$

where r_{ph} is the radius of the liquid-vapour interface given by

$$\sqrt{\frac{\rho_L}{\rho_g}\frac{\mu_g}{\mu_L}\frac{x}{1-x}} = \frac{(r_{ph}/R)^2}{1-(r_{ph}/R)^2} \tag{2.25}$$

Fukano and Kariyasaki (1993) investigated the bubble rise velocity and film thickness in tubes of 1, 2.4 and 4.9 mm. First, they measured the drift velocity of the bubble due to buoyancy force in a stagnant water and found that this velocity tends to zero when the diameter becomes smaller than 5.6 mm. Physically, this reflects the strong effect of capillary force F_C on the shape of bubble nose, which determines the liquid flow rate flowing down around the bubble as a liquid film. The film thickness measurements showed that the thickness decreases with decreasing tube diameter and superficial gas velocity. This was attributed to the fact that the pressure difference between the inside and outside of the bubble becomes larger as the diameter decreases resulting in more rigid bubbles due to the strong effect of surface tension. Accordingly, this will make it difficult for the liquid to flow around the long bubble. Also, they have reported that the film thickness around the long bubble can be smoothly connected to the base film

thickness in annular flow when it develops. Kawahara et al. (2009) experimentally investigated the effect of liquid physical properties on bubble characteristics in a micro tube of 0.25 mm diameter. The bubble velocity and length were measured from the recorded high speed videos. It was found that, both bubble velocity and the distribution parameter increases with increasing liquid viscosity and/or decreasing surface tension. This was attributed to the decrease in liquid film thickness with the increase in liquid viscosity. Also, the bubble nose becomes sharpen with increasing liquid viscosity and/or decreasing surface tension. Finally, they incorporated the physical properties of the liquid and correlated the distribution parameter of the drift flux model as a function of Bond number, liquid Reynolds number and gas Weber number as given by Eq, (2.26).

$$C_0 = aBd^{0.19}\,\mathrm{Re}_L^{-0.01}\,We_g^{0.01} \tag{2.26}$$

In the above equation, a = 3 for flow without inlet contraction and a = 3.3 for flow with inlet contraction. At the same homogeneous void fraction, the bubble in case of flow with inlet contraction was longer than without contraction. This was arising from the effect of the T-junction that has a diameter larger than test section diameter. So, larger bubbles would be produced first in the T-junction then the bubble will stretch more when it flows into the main test section.

2.7 Film thickness in slug flow

The thickness of the liquid film surrounding the bubble in slug flow plays a significant role in the pressure drop and heat transfer calculations. This parameter is very important for developing mechanistic models. For example, the performance of the three zone heat transfer model proposed by Thome et al. (2004) depends strongly on the initial film thickness formed underneath the bubble. Few experimental studies measured the initial film thickness in slug flow and correlated it as a function of different experimental conditions. Moriyama and Inoue (1996) measured the thickness of the liquid film of R113 formed by a growing flattened bubble in a narrow gap between two horizontal glass plates of width ranging from 0.1 to 0.4 mm. A very thin layer (0.2 μm) of Indium-Tin Oxide was deposited on one side of the plates to act as a heater. The initial film thickness was deduced from the transient temperature distribution in the film. After triggering the bubble, the surface temperature rapidly falls to a minimum within few milliseconds then it increases again and asymptotically approach final value, which is

lower than the initial wall superheat. Consequently, the moment at which the thermocouple reading starts to decrease indicates the onset of film formation and evaporation, which continues until the thermocouple reading reaches the minimum value. Assuming that all the heat removed from the wall was totally consumed in evaporating the film, the thickness was obtained from an energy balance. Finally, they measured the bubble growth velocity by high speed photography and incorporated it into dimensionless groups such as Capillary number, Weber number and Bond number in order to correlate the initial film thickness. The developed correlation is given by Eq. (2.27). This equation shows that, the film thickness is either controlled by the viscous boundary layer or the Capillary number.

$$\frac{\delta_0}{D} = \begin{cases} 0.1\delta^{*0.84}, & Bd > 2 \\ 0.07Ca^{0.41}, & Bd \le 2 \end{cases} \tag{2.27}$$

where: $\delta^* = \frac{\sqrt{\nu t_g}}{D}$

and t_g is the time required for the bubble edge to reach the measuring point from bubble initiation.

Han et al. (2009) measured the liquid film thickness in slug flow using a laser focus displacement meter and micro tubes of 0.3, 0.5, 0.7, 1 and 1.3 mm diameters and air, ethanol, water and FC40 as working fluids. They have examined the uniformity of the film around the tube cross section by measuring at the top, bottom and side walls of the horizontal and vertical orientations. It was found that, the initial film thickness in the 1.3 mm measured at side locations in horizontal orientation was identical to that of vertical orientation but they are different from the one measured at top and bottom. On the other hand, the measured initial film thickness in the 0.3 mm tube was identical regardless of orientation and measuring position. In other words, the largest tube showed some stratification due to gravity while the 0.3 mm does not. Also, it was found that the liquid slug length has a weak effect on the initial film thickness. Whereas for Capillary numbers less than 0.01, the effect was weak for bubbles of length > 2D but the film was found to be thicker for bubble lengths less than 2D. At high capillary numbers the film became thick regardless of bubble length. Also, the thickness was found to increase

with increasing bubble velocity and tube diameter due to the dominance of viscous force that make the film thicker over surface tension force that make it thinner. After their extensive parametric study, they have proposed a correlation for the film thickness as a function of Capillary number, Reynolds number, Weber number and tube diameter as given by Eq. (2.28).

$$\frac{\delta_0}{D}=\begin{cases}\dfrac{0.67Ca^{2/3}}{1+3.13Ca^{2/3}+0.504Ca^{0.67}\,\mathrm{Re}^{0.589}-0.352We^{0.629}}, & \mathrm{Re}<2000\\ \dfrac{106\left(\dfrac{\mu^2}{\rho\sigma D}\right)^{2/3}}{1+497\left(\dfrac{\mu^2}{\rho\sigma D}\right)^{2/3}+7330\left(\dfrac{\mu^2}{\rho\sigma D}\right)^{0.67}-5000\left(\dfrac{\mu^2}{\rho\sigma D}\right)^{0.629}}, & \mathrm{Re}>2000\end{cases} \tag{2.28}$$

2.8 Heat transfer characteristics

2.8.1 Nucleation in microchannels

Nucleation in microchannels may be different compared to that occurring in macrochannels and pool boiling. Kenning and Yan (2001) found that nucleation characteristics during water flow boiling in a vertical channel of 2 × 1 mm cross section are different from those of pool boiling. They observed that small bubbles nucleate and grow to a visible size slowly compared to the rapid bubble growth in nucleate pool boiling. Also, Peng et al. (1998b) observed that nucleation in microchannels has different characteristics compared to nucleation in macrochannels. They did not see any bubbles during water flow boiling in multi microchannels although the wall superheat was large enough to trigger boiling. However, the boiling curves demonstrated fully developed nucleate boiling. Accordingly, they proposed the terms “minimum evaporating space” and “fictitious boiling” to explain this unique behaviour. In fictitious boiling, the flow was believed to contain numerous invisible micro-bubbles that explain the nucleate boiling on the boiling curve. To validate their premises, they applied the thermodynamic phase stability theory and proposed a threshold criterion, which includes the heat flux, for the onset of nucleation given by Eq. (2.29) and also deduced an expression for the required wall superheat at boiling incipience given by Eq. (2.30).

$$\frac{h_{fg} a_v}{c \pi v_{Lv} q D} \leq 1 \tag{2.29}$$

$$\Delta T_{\text{sup}} \geq \frac{1120 T_{sat} v_{Lv} \sigma}{h_{fg} D} \tag{2.30}$$

In the above equations, c is an empirical constant that was taken equal to 1 and a_v is the vapour thermal diffusivity. Equation (2.29) predicts the heat flux at which nucleate boiling starts and indicates the difficulty of boiling incipience when the diameter decreases. Also, it is obvious that fluid physical properties significantly influence the nucleation process. Fluids with greater liquid to vapour density ratio, higher latent heat and larger thermal diffusion coefficients require larger heat fluxes to trigger nucleate boiling. Peng et al. (2002) argued that, due to the highly superheated liquid in fictitious boiling, nuclei form randomly and pressure impulses propagate through the surrounding liquid. Based on that argument, they got an expression for the radius of the density wave/bubble embryo as a function of channel radius, liquid isothermal compressibility and pressure drop across the channel. This radius should be much smaller than channel radius to satisfy mechanical conditions required for nucleation. Furthermore, they found that bubble embryos generate and collapse continuously at a very high frequency in microchannels. The growing and collapsing process of the invisible micro-embryos absorbs a great amount of energy that explains the huge enhancements in heat transfer without normal nucleation. Also, their analysis showed that the formation of the nuclei depends strongly on the collisions between the clusters and channel walls.

Kandlikar et al. (1995) investigated the effects of different operating conditions on nucleation characteristics during water flow boiling in a narrow horizontal channel of 3 × 50 mm cross section. The upper face of the channel was covered with glass window for flow visualization while an aluminium rod heater of 10 mm diameter was vertically inserted into the lower face of the channel. Nucleation process was visualized by a microscope and a high speed camera. It was found that, increasing mass flow rate shifts the range of active cavities towards smaller radii, requires larger wall superheat to activate the cavities and deactivate the larger cavities. Also, increasing wall superheat activated the smaller cavities while decreasing inlet sub-cooling resulted in too rapid nucleation. Lee et al. (2003) investigated flow boiling of de-ionised water in rectangular silicon microchannels of 24 μm hydraulic diameter (14× 120 μm). Figure 2.31 depicts

one cycle for the bubble formation, growth and departure. They observed very few active nucleation sites due to the smoothness of the surface resulting from the micro-fabrication process. The active sites were almost at defects along the micro-channel top surface. The figure shows that, once the bubble forms, it grows in the flow direction until it fills the entire channel cross section then it stretches away in the flow direction while it still anchored to the nucleation site. When the forces on the bubble are sufficient, it leaves the nucleation site and the cycle repeats periodically. After departing from the site, they observed that the bubble disappeared immediately. However, using a regular speed camera located at channel exit, they observed a bubble with a diameter similar to that of the departing bubble from the nucleation site. Therefore, they suggested that these bubbles originated from dissolved gas inside the water and also because the water temperature was lower than saturation. Consequently, they concluded that the departing bubbles did not condense back into the liquid but rather reformed, i.e. coalesce into larger bubble, due to the impact with the micro-channel exit wall.

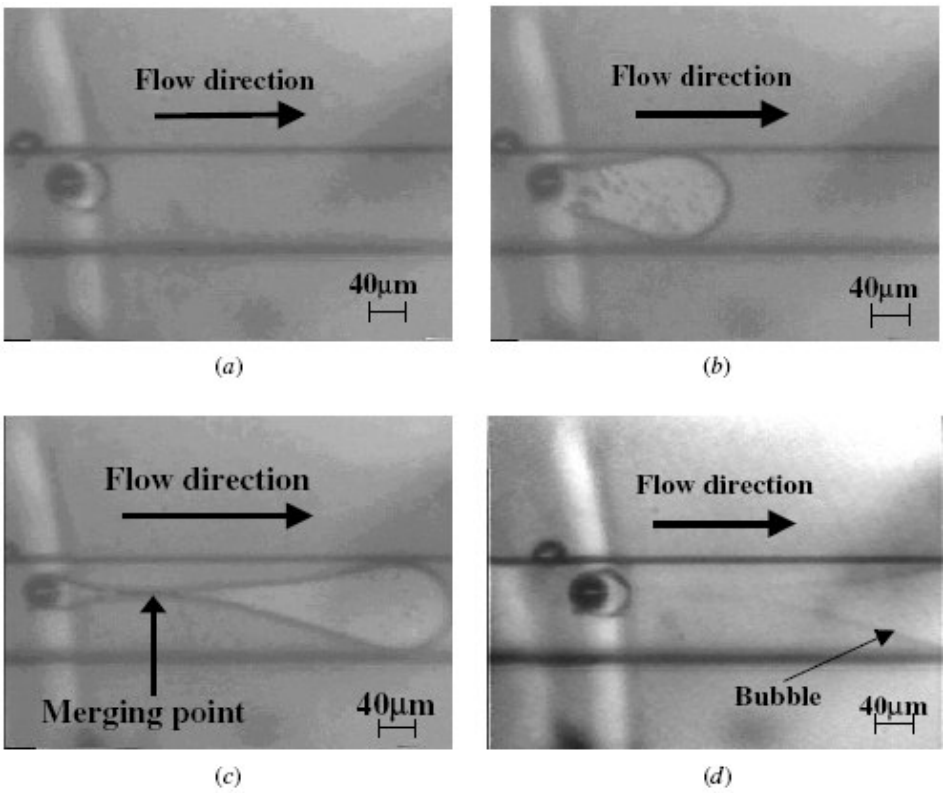

Figure 2.31 Bubble behaviour in an active nucleation site demonstrating (a) bubble formation, (b) bubble growth, (c) bubble on the verge of departure, (d) bubble after departure, Lee et al. (2003).

Wang and Cheng (2009) observed micro-bubbles in the liquid especially at very high inlet sub-cooling and called this case Micro Bubble Emission (MBE). They investigated the incipience of (MBE) during flow boiling of de-ionised water in a partially heated trapezoidal micro-channel of 155 µm hydraulic diameter. Boiling was triggered using a micro-heater having dimensions of 200 × 2000 µm that was fabricated by MEMS and inserted at a mid location on the lower plate of the channel. The nucleating bubble on the micro-heater was observed to undergo three stages namely: bubble growth, bubble size fluctuation and bubble collapse, see Fig. 2.32. Bubble size fluctuation was attributed to the non-equilibrium between condensation at the bubble top and evaporation from the micro-layer at the bubble base. After collapsing, the large bubble was observed to disintegrate into very fine bubbles of about 10 µm diameter and this is why they called it micro-bubble emission (MBE).

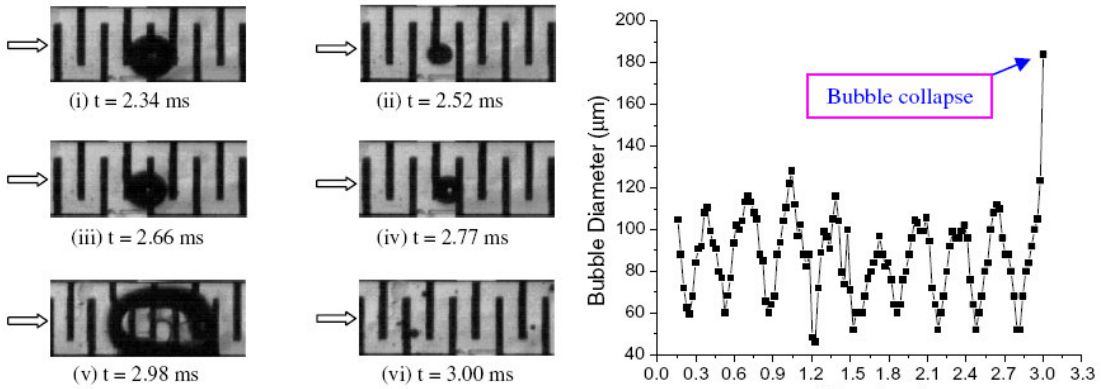

(a) Photos of bubble diameter fluctuation and collapse into microbubbles (taken at 44000 frame/s)

(b) Bubble size fluctuation with time

Figure 2.32 Photos and sketch of bubble behaviour at the onset of micro bubble emission at q = 3.31 MW/m^2, G = 294.6 kg/m^2 s, T_{in} = 20 ^{0}C, Wang and Cheng (2009).

2.8.2 Boiling incipience in microchannels

Boiling incipience may be detected from the *ΔP–G* plot at fixed heat flux or from the boiling curve or directly using a high-speed visualization. The fundamentals of flow boiling incipience are originally "borrowed" from the pool boiling fundamentals. The difference between pool boiling and flow boiling incipience may arise from the difference in the characteristics of the thermal sub-layer that is strongly influenced by the viscous and inertia forces in flow boiling. This section presents a review for the studies that investigated flow boiling incipience in microchannels.

Qu and Mudawar (2002) experimentally investigated boiling incipience of water flow in multi microchannels heat sink of 231 × 713 μm cross section. The inlet sub-cooling was varied from 15K to 75K. The channels were heated from the bottom side using 12 cartridge heaters and the boiling incipience was identified using a microscope. They observed that the boiling incipience in microchannels is completely different from that occurring in large channels for sub-cooled flow. In large channels, small bubbles nucleate, grow and collapse while still attached to or even sliding along the heated surface, see Collier and Thome (1994). On the contrary, in microchannels, Qu and Mudawar (2002) observed that: (i) bubbles nucleate and grow to a size comparable to the channel size before leaving the cavity then after departure they move downstream and collapse in the outlet plenum, (ii) boiling commences close to the exit of several channels and (iii) the majority of the first bubbles forms on the bottom wall while few bubbles were observed on the side walls (although their channels were heated only from the bottom), Based on these observations, they concluded that the macroscale criterion for boiling incipience may not work at microscale. Accordingly, they developed a model for boiling incipience in rectangular microchannels taking into account the nucleation on the sidewalls, the bottom wall and the channel corners. The model was based on applying the bubble departure criterion that combines both mechanical and thermal considerations, i.e. force balance on the bubble and solving the conjugate heat transfer problem for the temperature field. Their model predicts the bubble departure diameter, the temperature field around the bubble interface and the location of boiling incipience. They reported that, the model referred to some peculiarities for boiling incipience in microchannels. These peculiarities include, for example, the growth of the bubble to the channel size particularly at low flow velocities and the departure of the first bubble near, but not at, the hottest corner, which the authors attributed it to the complex combined effect of bubble size and temperature field on the bubble departure.

Liu et al. (2005) experimentally and theoretically investigated the boiling incipience for water flow in a copper micro-channel of 275 × 636 μm cross section. The onset of nucleate boiling was detected from flow visualization using a high speed camera and a microscope and also from the recorded pressure drop and wall temperature. It was observed that: (i) at boiling incipience, bubbles appeared near the channel exit in few channels while in several channels they appeared at an upstream location, (ii) bubbles

were observed to be created near the channel corners and (iii) the incipient heat flux was found to increase with increasing mass flux and inlet sub-cooling. In addition to the experimental measurements, they developed an analytical model for predicting the boiling incipience heat flux and wall superheat. They assumed that the bubble nucleus takes the shape of a truncated sphere, the nucleus does not affect the temperature profile in the surrounding liquid, the phases are in equilibrium under saturated conditions and the temperature profile in the thin layer next to the wall is linear. In their derivation, they argued that the commonly used classical superheat equation for bubble nucleus should be corrected such that the temperature in the right hand side of Eq. (2.31) should be the bubble temperature not the saturation temperature. This was believed to arise from the fact that, at nucleation the surrounding liquid should be superheated so it can not be represented on the vapour pressure equilibrium curve. Based on that, the derived criterion for the wall superheat at boiling incipience was given by Eq. (2.32) with C is a shape factor ($1 + cos\theta$) where θ is the contact angle.

$$T_B - T_{sat}(p_L) = T_B \frac{2\sigma}{r_B \rho_g h_{fg}} \tag{2.31}$$

$$T_w - T_{sat} = \frac{2\sigma C}{\rho_g h_{fg}} \frac{q}{k_L} + 2\sqrt{T_{sat}} \sqrt{\frac{2\sigma C}{\rho_g h_{fg}}} \frac{q}{k_L} \tag{2.32}$$

Lie and Lin (2006) investigated boiling incipience and bubble characteristics of R134a in a horizontal annular duct with gap sizes of 1 and 2 mm. The outer tube was made of Pyrex glass while the inner tube was made of copper with a surface which was polished by a fine sand paper. It was observed at boiling incipience that tiny bubbles nucleate and grow until they depart from the nucleation site. Also, it was observed that the first bubble did not appear at the same axial location on the upper and lower surface of the heater. Instead, boiling started first on the lower surface of the heater while it appeared later on the upper surface due to buoyancy effects. This was believed to arise from the higher temperature on the lower surface compared to that on the upper one. In addition to that, the motion of the nucleating bubbles on the upper surface of the heater was found to be completely different from the motion on the bottom surface. On the upper surface, bubbles were observed to lift off directly from the nucleation site or slide slowly for a short distance then accelerate with a speed higher than that of the

surrounding bulk liquid. While on the lower surface, the nucleating bubbles were observed to slide circumferentially along the heated surface. Additionally, it was found also that increasing mass flux and inlet sub-cooling results in a reduction in the bubble departure diameter and frequency while the gap size influenced the dynamics of the nucleating bubbles. Reducing the gap size resulted in: (i) increasing coalescence rate and forming larger bubbles that were observed to slide along the heating surface for a short distance before leaving the nucleation site, (ii) increasing bubble departure frequency due to the higher shear force and (iii) decreasing the required wall superheat for triggering boiling however some people reported an opposite effect. This was attributed to the lower mass flow rate in the smallest gap compared to that in the larger one at the same mass flux. Consequently, the axial temperature rise in fluid temperature becomes higher for smaller gaps at the same heat flux, pressure and inlet sub-cooling. Finally, they proposed a correlation for predicting the mean bubble departure diameter given by Eq. (2.33) and correlations for the bubble departure frequency and active nucleation site densities given by Eq. (2.34) and Eq. (2.35), respectively.

$$\frac{D_b}{\sqrt{\frac{\sigma}{g(\rho_L-\rho_g)}}}=\frac{315Co(\rho_L/\rho_g)^{0.333}}{\sqrt{\mathrm{Re}}\left[Ja+\frac{165(\rho_L/\rho_g)^{1.333}}{Bo^{0.5}\,\mathrm{Re}^{0.25}}\right]} \tag{2.33}$$

$$\frac{f_b D_b}{\mu_L/(\rho_L D)}=1642\,\mathrm{Re}^{0.887}\,Ja^{-0.05}Bo^{0.887}Co^{0.01} \tag{2.34}$$

$$N_{ans}=80352+8034\Delta T_{sat}^{1.67}Co^{0.51} \tag{2.35}$$

Though Lie and Lin (2006) found that the wall superheat at boiling incipience decreases when the annulus gap was decreased, several people reported an opposite effect. For example, Hapke et al. (2000) investigated boiling incipience of de-ionised water in a vertical tube of 1.5 mm inner diameter. Wall temperature was recorded by a thermographic technique. It was found that, wall superheat at boiling incipience reached about 40K at G = 500 kg/m^2 s and q = 150 kW/m^2, which is much higher than the value in large diameter channels. Furthermore, boiling incipience was found to be accompanied with high pressure and mass flow rate oscillations due to the growth of the nucleating bubble to a size comparable to channel diameter, which causes high pressure

drop that in turn influences bubble detachment and frequency. Ghiaasiaan and Chedester (2002) found that the macroscale models of predicting boiling incipience heat flux under-predict the data of water in micro tubes of diameters ranging from 0.1 to 1 mm. In other words, boiling commences in micro tubes at higher heat fluxes/wall superheat compared to large diameter tubes. This deviation led them to suggest that boiling incipience in microchannels occurs when the thermo-capillary force acting on a bubble is balanced by the aerodynamic force acting on the same bubble. As a result, they proposed a semi-empirical model for predicting boiling incipience in micro tubes. In their method, the correlation of Davis and Anderson (1966) was used but with different expression for the shape factor C that is equal to 1 for chopped spherical and hemispherical bubbles. The constant C was introduced as a function of a dimensionless parameter ζ defined by Eq. (2.36) below. This parameter is a ratio between the order of magnitude of thermo-capillary and aerodynamic forces.

$$\zeta = \frac{\sigma_L - \sigma_w}{\rho_L U^2 R^*} \tag{2.36}$$

where R^* is the critical cavity radius that satisfies nucleation conditions and was given as:

$$R^* = \left[\frac{2\sigma T_{sat} v_{Lv} k_L}{q_{ONB} h_{fg}} \right]^{1/2} \tag{2.37}$$

The value of C and consequently the boiling incipience heat flux was found to increase monotonically with increasing ζ. This implies that, the bubbles were strongly suppressed by the thermo-capillary force when ζ increases. Based on that, the dependence of C on ζ was fitted to $C = 22\zeta^{0.765}$. Yen et al. (2003) investigated flow boiling of R123 and FC72 in three stainless steel tubes of diameters 0.19, 0.3 and 0.51 mm. It was found that, the wall superheat required for triggering boiling increased when the diameter was decreased. The 0.19 mm diameter tube required 100K wall superheat while the 0.51 mm diameter tube required 45K. The boiling number at which boiling starts was found to be independent of tube diameter. Qi et al (2007) investigated the boiling incipience of nitrogen using cold drawn stainless steel tubes having diameters of 0.531, 0.834, 1.042 and 1.931 mm. These commercial tubes are used to fabricate the medical injection needles. The tubes were heated by a manganin wire that was tightly

coiled around the micro tube. It was observed that boiling started first near tube outlet then moved upstream with increasing heat flux and with superheat values that were as high as 16K. Also, they have found similar behaviour to that found by Hapke et al. (2000) where distinctive features for mass flux, pressure drop and wall temperature compared to large diameter tubes were observed. At boiling incipience, mass flux and wall temperature experienced a sudden drop while pressure drop increased. It is interesting to note that the drop in mass flux was not small where the mass flux decreased by 40 %. Martin-Callizo et al. (2007b) presented the flow boiling curve of R134a for a micro tube having inner diameter of 0.64 mm and heated length of 213 mm. The curve was plotted for three axial locations at different mass fluxes. It was found for the location which is in the entry region that, wall superheat of about 18K was required to activate nucleation especially at the highest mass flux though inlet sub-cooling was about 1K. But at the other axial locations, nucleation process was normal without requiring very high wall superheat. Although the extreme values of wall superheat and the instability of system parameters at boiling incipience that was reported above, some researchers observed normal nucleation process. Liu and Garimella (2007) investigated flow boiling of water in copper microchannels having dimensions of 275 × 636 and 406 × 1063 μm and found that boiling was normally triggered at low wall superheat of about 4K. Muwanga and Hassan (2007) investigated flow boiling of FC-72 in a single stainless steel tube of 1.067 mm inner diameter. They have found that, boiling incipience characteristics, i.e. drop in wall temperature and increase in pressure drop, disappeared at high mass flux (G = 2050 kg/m^2 s) while these characteristics were observed only at lower mass fluxes. Bertsch et al. (2008a) investigated flow boiling of R134a in multi-channels of 1.09 mm hydraulic diameter. On the contrary to the drop in wall temperature at boiling incipience that was reported by other people, insignificant temperature drop was observed where nucleate boiling developed smoothly at wall superheat of about 6K. The same authors extended the work in 2009 to include refrigerant R245fa and channel hydraulic diameter of 0.54 mm. Again they did not observe temperature drop for R134a at boiling incipience while a small drop was observed with R245fa. They attributed this to the different wetting behaviour of the two fluids. In case of R245fa stable flow patterns were visually observed with nucleate boiling in some of the channels while others still under single phase conditions. In contrast, for R134a once boiling initiates in any channel it rapidly establish in all channels. Su et al. (2005) investigated flow boiling incipience of water flow in an

annulus having narrow gaps of 1 and 1.5 mm. Boiling incipience was identified from plotting the wall temperature versus axial location at different heat fluxes and mass fluxes. The incipient heat flux was found to be dependent on mass flux, gap size and wall superheat. This dependence was incorporated into a correlation given by Eqn. 2.38.

$$q_{ONB} = 0.175 \mathrm{Re}^{0.92} \Delta T_{sat}^{0.11} \tag{2.38}$$

2.8.3 Boiling hysteresis in microchannels

Regarding the issue of boiling hysteresis in microchannels, there is a very few number of experimental studies that investigated this phenomenon. Lazarek and Black (1982) developed boiling curves for R113 in a 3.1 mm diameter tube including increasing and decreasing heat fluxes. Hysteresis was found to occur only in the region of boiling incipience due to the effect of local size distribution of active cavity sites and the surface wett-ability characteristics. Piasecka and Poniewski (2004) experimentally investigated flow boiling incipience and nucleation hysteresis of R123 in a vertical narrow rectangular channel of 1 mm depth by 40 mm width. The channel was heated by a heating foil that formed the channel base. The outer surface of the heating foil was covered with a glass layer leaving a gap between the heater and the glass, which was filled with liquid crystal for measuring the heater temperature using liquid crystal thermography (LCT). Plotting the boiling curves for increasing and decreasing heat fluxes indicated the occurrence of what they called “stepped course of nucleation hysteresis”. In this case, the boiling curve potted by increasing heat flux exhibited a stepped behaviour as seen in Fig. 2.33. The figure shows that, the wall superheat increased from point A to BI (boiling incipience), then it decreased from BI to B then it increased again from B to C. Decreasing the heat flux, the boiling curve followed the path CD, which shows that there is a hysteresis below heat flux value of about 55 kW/m^2. Chin and Thome (2009) examined the flow boiling hysteresis of R134a at mass flux of 300 kg/m^2 s in a horizontal stainless steel tube having inner diameter of 1.03 mm. They developed the boiling curves by gradually increasing the heat flux followed by decreasing at thermocouple location near from tube exit. It was found that, wall superheat reached about 21K before boiling incipience and dropped to about 4K after incipience. When the heat flux was decreased, no hysteresis on the wall superheat was observed except only at the onset of nucleate boiling. Consolini and Thome (2009)

obtained similar boiling curves for R134a, R236fa and R245fa in a 0.51 mm stainless steel horizontal tube. Wall superheat reached about 16 K for R134a and about 30 – 35 K for R245fa and R236fa without any hysteresis except the region of boiling incipience.

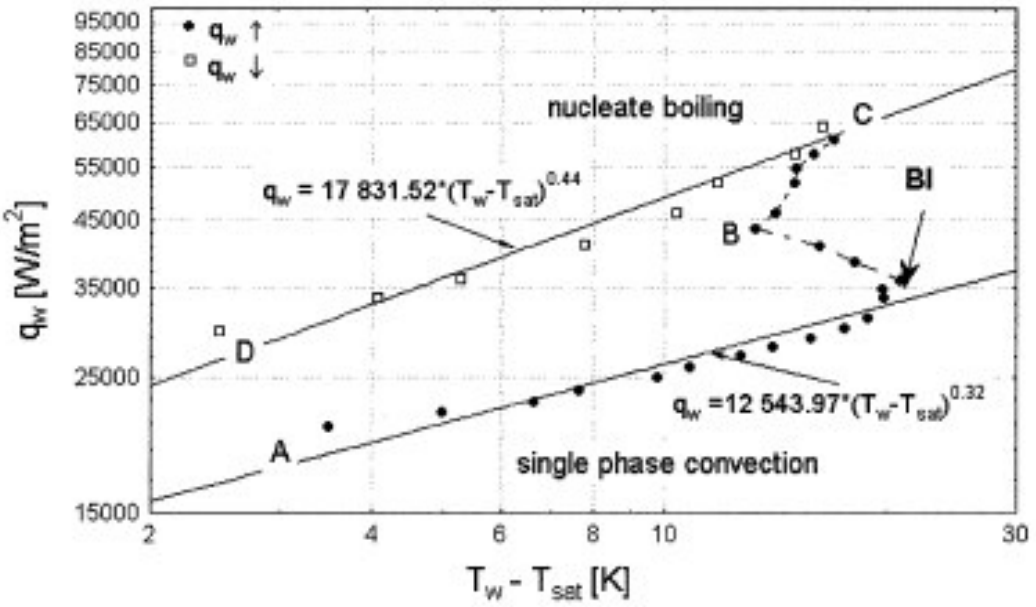

Figure 2.33 The boiling curve of R123 for increasing and decreasing heat flux that shows nucleation hysteresis for q < 55 kW/m^2, Piasecka and Poniewski (2004).

2.9 Flow boiling heat transfer coefficient

2.9.1 Effect of channel diameter

As presented above, the flow patterns observed in microchannels demonstrated different features compared to those observed in macrochannels. These features include the diminishing churn flow, the elongation of the vapour slug, the thinning of the liquid film and the stable liquid-vapour interface. As a result, the heat transfer rates may also be influenced by the reduction in channel size. Ribatski et al. (2006) carried out an extensive review about flow boiling heat transfer and pressure drop in microchannels and concluded that the flow boiling heat transfer coefficient increases with decreasing channel diameter. This section presents the effect of channel diameter on the flow boiling heat transfer coefficient.

Kew and Cornwell (1997) measured the local flow boiling heat transfer coefficient of R141b using three stainless steel tubes of diameters 3.69, 2.87 and 1.39 mm

corresponding to confinement number values of 0.33, 0.42 and 0.87, respectively. According to their criterion, only the 1.39 mm tube can be regarded as a small diameter tube. All tubes have 500 mm heated length. It was found that, the trend of the heat transfer coefficient of the two largest tubes was similar to that of conventional large diameter tubes whereas the trend of the smallest tube was different especially at high mass fluxes, see Fig.2.34. Inspecting Fig 2.34a and b at almost similar experimental conditions, it can be seen that the heat transfer coefficient of the 2.87 mm diameter tube is lower than that of 3.69 mm diameter tube especially in the high quality region but the effect is insignificant in the low quality region. Using the same experimental facility and fluid R141b, Lin et al. (2001a) examined flow boiling in four circular stainless steel tubes of diameters 1.1, 1.8, 2.8 and 3.6 mm and one square tube of 2 × 2 mm^2 cross section *(D_h = 2 mm)*. It was reported that the confinement, which appeared with reducing channel diameter, strongly influences the conditions at which dryout occurs. As the confinement increases (diameter decreases), the boundaries of heat flux, mass flux and vapour quality within which boiling occurs without dryout becomes more restricted. As the diameter was decreased, dryout was found to occur earlier at lower heat fluxes than larger diameter channels. Although the factors that influence the local heat transfer coefficient are complex, the authors found that the average heat transfer coefficient without considering dryout was independent of tube diameter. Figure 2.35 shows a map sketched by the authors that summarises the trends of heat transfer coefficient as a function of tube diameter, vapour quality and heat flux.

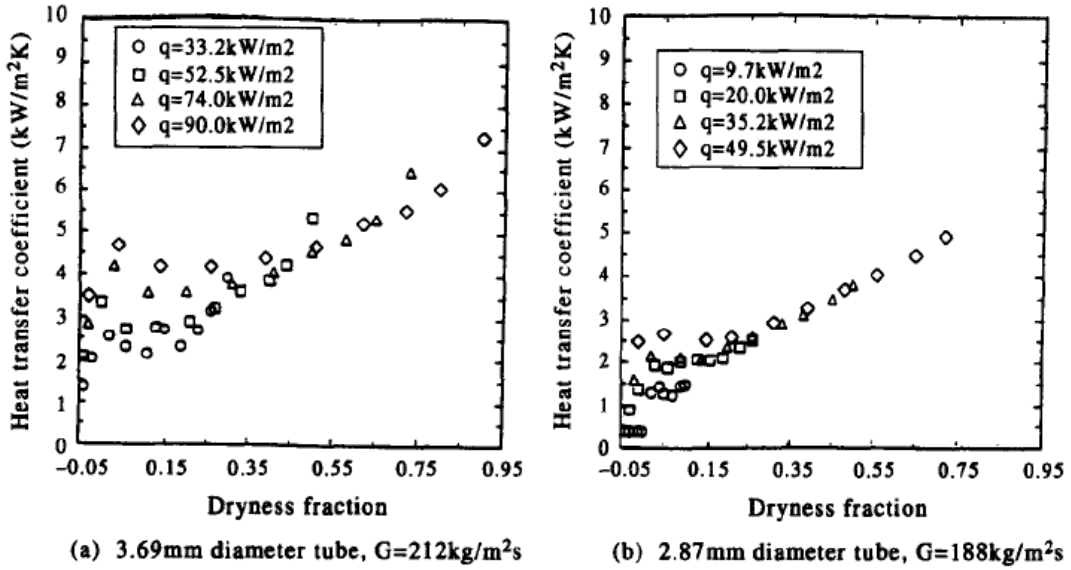

(a) 3.69mm diameter tube, G=212kg/m²s (b) 2.87mm diameter tube, G=188kg/m²s

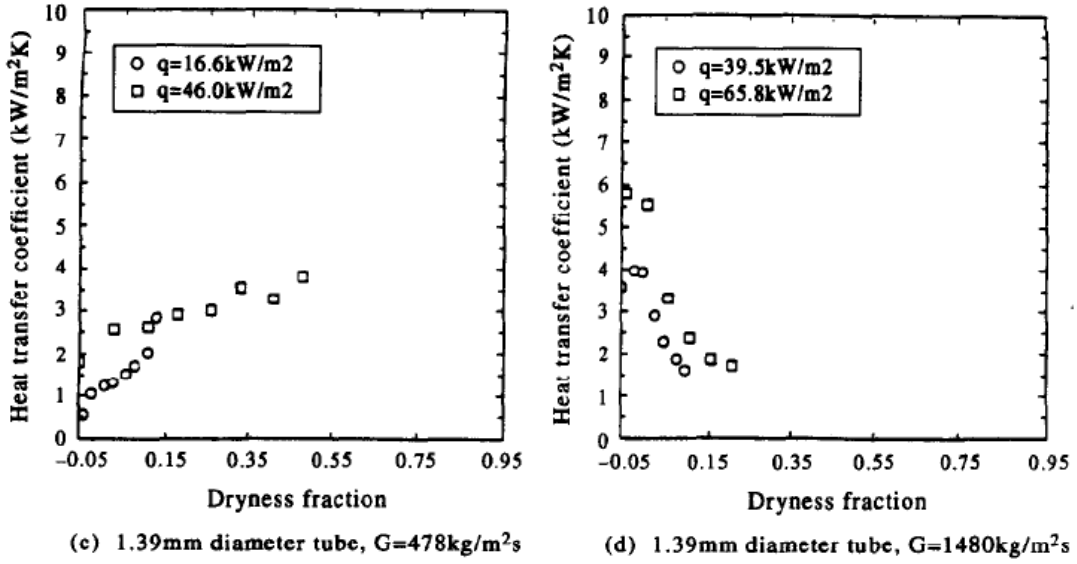

Figure 2.34 Effect of tube diameter on the local heat transfer coefficient, Kew and Cornwell (1997).

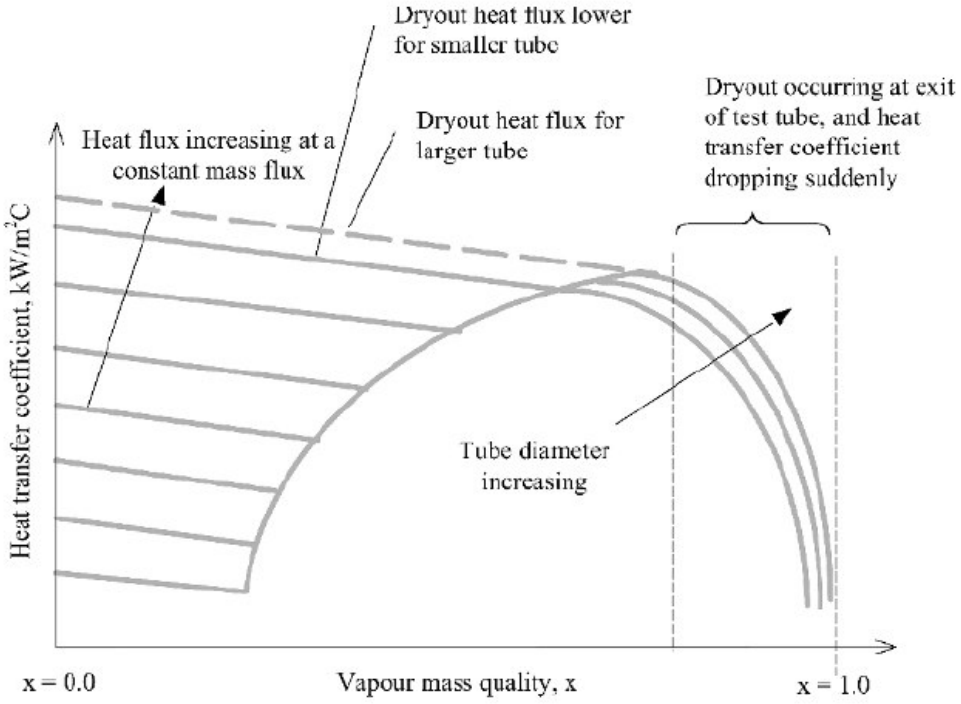

Figure 2.35 Sketch of h-x in small diameter tubes that shows the diameter effect, Lin et al. (2001).

Kureta et al (1998) measured the local flow boiling heat transfer coefficient of highly sub-cooled water using two metallic vertical tubes of diameters 2 and 6 mm and heated lengths of 100 and 360 mm, respectively. The results were presented in the form of

Nusselt number versus local quality up to exit quality of 0.6. It was found that Nu decreased by about 75 % (heat transfer coefficient decreased by 25%) when the diameter was decreased from 6 to 2 mm. This behaviour was attributed to the difference in flow regime upstream the heated section. In large diameter channels the prevailing flow regime at most operating conditions is turbulent whereas it is laminar in the small diameter channels. As a result, the higher heat transfer coefficient in the larger channel was attributed to the good mixing arising form the turbulence and bubble agitation which are suppressed in small diameter channels. Yen et al. (2003) investigated flow boiling of R123 and FC-72 in three stainless steel tubes of diameters 0.19, 0.3 and 0.51 mm and heated lengths of 280 mm. They excluded the results of the 0.3 mm diameter tube because of measurements instability problem. The heat transfer coefficient in the two tubes was found to decrease from its high value at x ~ 0 until x ~ 0.4 then it remains constant with quality until x = 1. However, the effect of diameter on the magnitudes of the heat transfer coefficient was not clear. Huo et al. (2004) measured the flow boiling heat transfer coefficient of R134a in two vertical stainless steel tubes of diameters 4.26 and 2.01 mm and heated lengths of 500 and 211 mm, respectively. Figure 2.36 presents the heat transfer coefficient of the two tubes on the *h-x* plane. This figure indicates that the effect of tube diameter on the magnitude of the heat transfer coefficient was insignificant up to intermediate heat fluxes but at high heat fluxes the coefficient increased with decreasing diameter. However the two tubes demonstrated similar trends, there is a remarked effect on the vapour quality at which dryout occurs. When the diameter was decreased, dryout occurred early at lower quality (0.4 – 0.5 for 4.26 mm and 0.2 – 0.3 for the 2.01 mm tubes). Using the same experimental facility, fluid and heating method Karayiannis et al. (2008) presented the experimental results of a wide range of tube diameters including 4.26, 2.88, 2.01, 1.1 and 0.52 mm tubes and heated lengths of 500, 300, 211, 150 and 100 mm, respectively. The average heat transfer coefficient was plotted against heat flux excluding the data after dryout as shown in Fig. 2.37. It was found that, there is no significant effect on the magnitude of the heat transfer coefficient when the diameter was decreased from 4.26 to 2.88 mm. However, 14 %, 17% and 73 % increase in the heat transfer coefficient was found when the diameter was decreased from 2.88 to 2.01 mm, 1.02 to 1.1 mm and 1.1 to 0.52 mm, respectively.

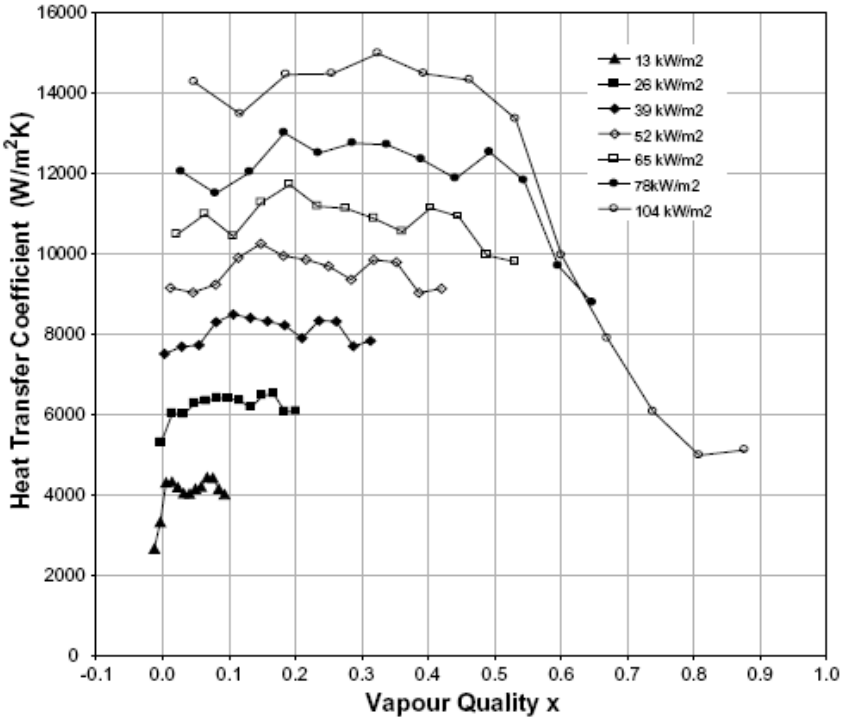

(a)

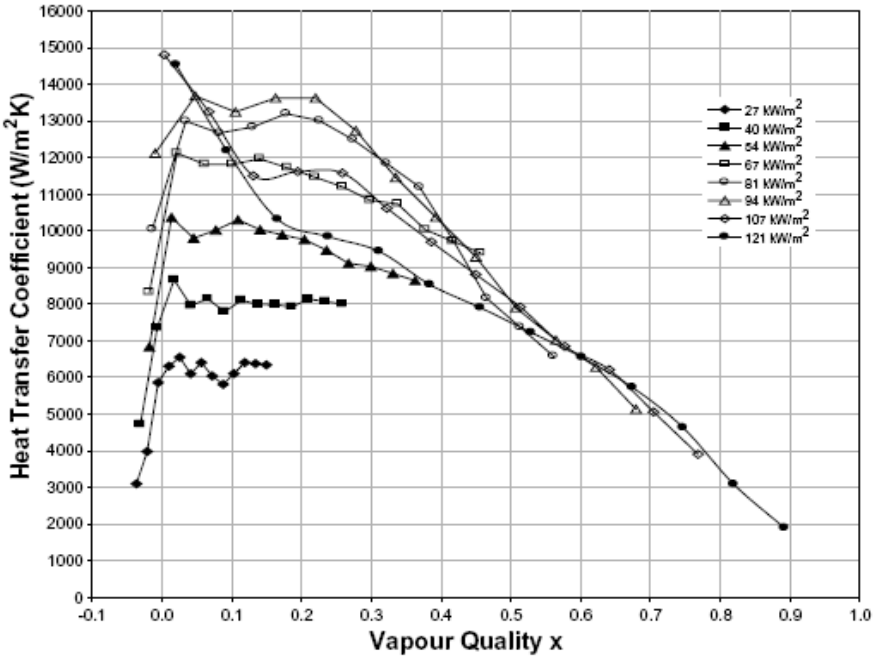

(b)

Figure 2.36 Local flow boiling heat transfer coefficient versus local quality for G = 300 and P = 8 bar for (a) D = 4.26 mm, (b) D = 2.01 mm, Huo et al. (2004).

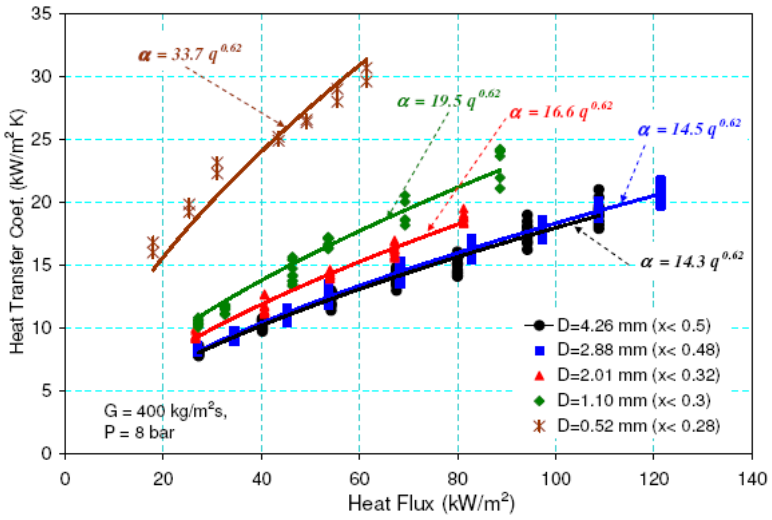

Figure 2.37 Effect of tube diameter on the average flow boiling heat transfer coefficient excluding the dryout region, Karayiannis et al. (2008).

Saitoh et al (2005) investigated the effect of tube diameter on flow boiling of R134a using three tubes of diameters 0.51, 1.12 and 3.1 mm and heated lengths of 550, 935 and 3325 mm, respectively. The inlet quality was varied from 0 to 0.2 by a throttling valve located upstream of the test section. It was found that, the heat transfer coefficient of the 0.51 mm tube was the highest especially before dryout or up to quality values of 0.5. The enhancement was about 27 % when the diameter decreased from 3.1 to 0.51 mm. The other effect was the shift of the vapour quality at which dryout occurs to a lower value when the diameter was decreased as shown in Fig. 2.38. Martín-Callizo et al. (2007a) measured the local heat transfer coefficient of R134a in three stainless steel tubes having diameters of 0.83, 1.2 and 1.7 mm and 220 mm heated length and reported that the heat transfer coefficient increases with decreasing diameter. Yun et al. (2005) experimentally tested flow boiling heat transfer of CO_2 in a 2 mm diameter stainless steel tube and heated length of 1200 mm. They compared their results with those published for a tube of 0.98 mm diameter and 400 heated lengths at similar experimental conditions. The comparison did not show any significant differences for these two diameters.

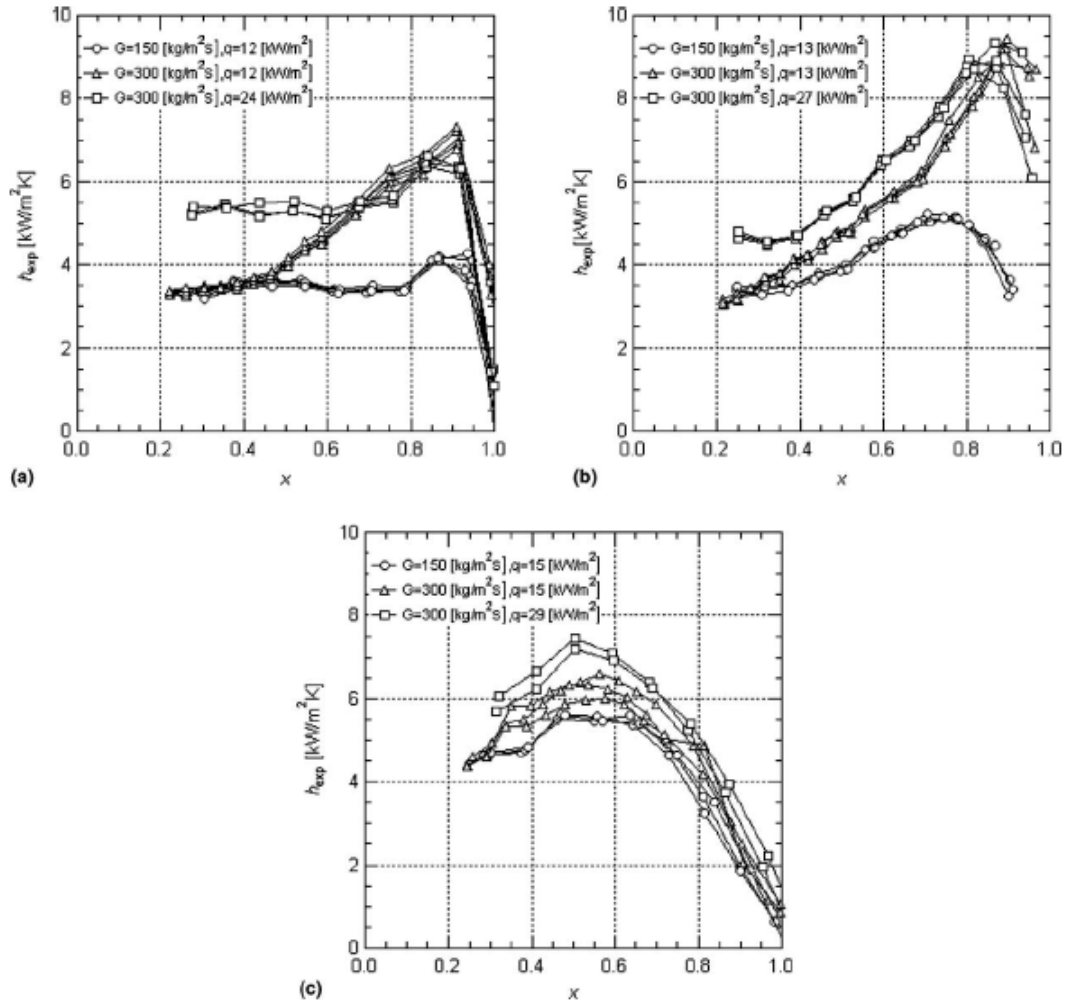

Figure 2.38 Effect of heat and mass fluxes on heat transfer coefficient for three tubes (a) 3.1 mm, (b) 1.12 mm, (c) 0.51 mm, Saitoh et al. (2005).

Qi et al. (2007b) investigated flow boiling of liquid nitrogen in stainless steel tubes having inner diameters of 1.931, 1.042, 0.834 and 0.531 mm and a fixed heated length of 250 mm. It was found that the local heat transfer coefficient of the largest tube behaved in a way similar to conventional large diameter tubes. But the other tubes showed similar behaviour, which was completely different from that of the largest tube. Accordingly, they concluded that D = 1.92 mm may be regarded as a threshold value between macro and minichannels for liquid nitrogen. The value of the confinement number corresponding to this diameter is 0.52 (it agrees with the Kew and Cornwell (1993) criterion). Jang et al. (2008) investigated flow boiling of FC-72 in two round tubes having inner diameters of 2 and 4 mm and both have heated length of 100 mm. The results showed that when the diameter was decreased from 4 to 2 mm, the heat transfer coefficient increased by a factor of 30.6 % on average due to the rapid increase

in convective boiling in smaller tubes. Choi et al. (2009) investigated flow boiling heat transfer of propane in two stainless steel tubes of diameters 1.5 and 3 mm and heated lengths of 1000 and 2000 mm, respectively. It was found that, the heat transfer coefficient of the 1.5 mm tube was about 23 % higher than that of the 3 mm tube in the low quality region (x ~ 0.25) while the effect becomes insignificant in the high quality region. The authors believed that, the reason is due to the more active nucleate boiling in the smaller tube and also due to the increase in heat transfer surface area. In addition to that, dryout was found to occur earlier at smaller quality when the diameter was decreased which was reasoned to the early transition to annular flow in the smallest tube. Consolini and Thome (2009) presented flow boiling results of R134a, R236fa and R245fa in two stainless steel tubes having inner diameters of 0.51 and 0.79 mm and same heated length of 75 mm. It was found that reducing channel diameter from 0.79 to 0.51 mm resulted in an enhancement in the heat transfer coefficient by about 15 % as seen in the Fig. 2.39. However, when the heat transfer coefficient of the 0.51 mm diameter tube was compared to that measured by Shiferaw et al. (2007) for 2.01 mm diameter tube at similar experimental conditions, the effect of diameter was remarked only at low heat fluxes. On the other hand, when the results of the 0.79 mm diameter tube were compared to the results of Shiferaw et al. (2007) for the 4.26 mm diameter tube, the diameter effect was unclear.

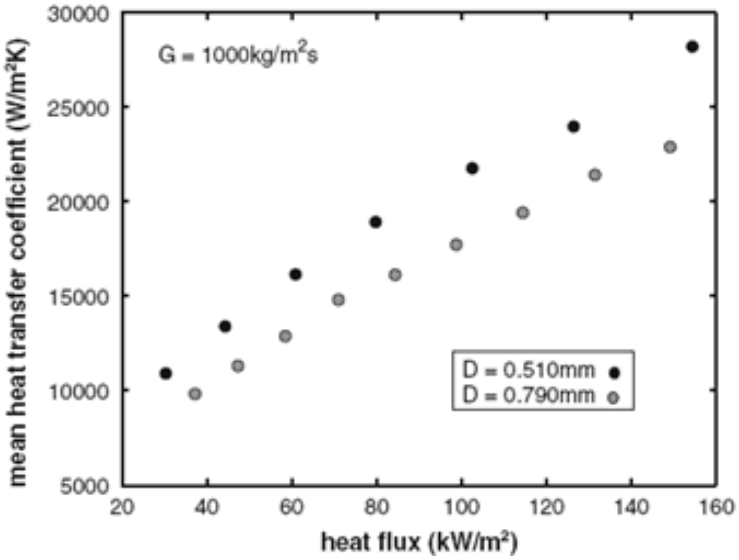

Figure 2.39 Effect of tube diameter on the average heat transfer coefficient for R134a at 8 bar and 1000 kg/m^2 s, Consolini and Thome (2009).

Harirchian and Garimella (2008) investigated the effect of channel size on the local flow boiling heat transfer of FC-77 in rectangular channels having constant depth of 400 μm and variable widths ranging from 100 to 5850 μm. The average heat transfer coefficient was plotted against the wall heat flux and the base heat flux as shown in Fig. 2.40. It is clear from this figure that when wall heat flux was used, the heat transfer coefficient was independent on channel width for channels with widths 400 μm and larger and even for smaller widths the dependence was week. At intermediate heat fluxes the channel with width of 100 μm showed relatively higher heat transfer coefficient. They attributed the high heat transfer coefficient of the smallest width to the higher exit quality, which leads to an early transition to annular flow at low heat fluxes compared to other widths. This means that the contribution of convective boiling increased when channel width was decreased resulting in higher heat transfer coefficient. Harirchian and Garimella (2009a) confirmed this explanation by flow visualization and observed that nucleation process was suppressed at relatively lower heat fluxes when channel width was reduced to 100 μm. On contrary, when the base heat flux was used rather than wall heat flux, the heat transfer coefficient was found to increase with increasing channel width for a given heat dissipation rate from the chip. Nevertheless, the maximum amount of heat dissipation from the chip increased when the micro-channel width was decreased (~ 640 kW/m^2 for the smallest width and 280 kW/m^2 for the largest one). Harirchian and Garimella (2009b) extended the work to

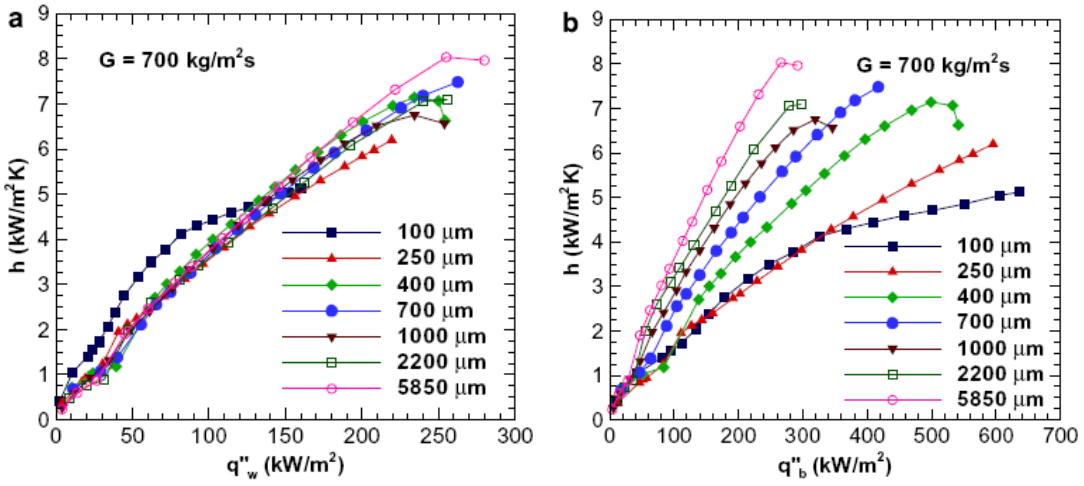

Figure 2.40 Effect of channel width on the average heat transfer coefficient as a function of (a) wall heat flux and (b) base heat flux, Harirchian et al (2008).

include the effect of varying channel depth as well. The heat transfer coefficient was plotted versus channel cross section area at different heat fluxes. It was found that, the heat transfer coefficient remained constant with decreasing cross section area up to a value of 0.089 mm^2 below which the heat transfer coefficient rapidly increased due to confinement and the contribution of thin liquid film evaporation. Since the heat transfer coefficient of the 100 × 100 μm channel was found to be higher than that of 400 × 400 μm, they emphasized that channel aspect ratio is not the determining geometric factor affecting boiling heat transfer but cross sectional area.

Peng et al. (1998a) investigated experimentally the geometrical effects on boiling heat transfer characteristics of water and methanol through V-shape stainless steel microchannels of 18 mm heated length. The channel geometry was varied by changing the groove angle, which changes the hydraulic diameter that was varied from 0.2 to 0.6 mm. It was found that, the heat transfer coefficient increased when the hydraulic diameter was increased. Their interpretation was that, when the channel hydraulic diameter becomes very small the liquid flowing to the channel becomes very restricted and heat transfer process deteriorates. However, they recommended further investigations for the upper limit of hydraulic diameter after which heat transfer deteriorates. Yun et al. (2006) investigated flow boiling of R-410 in two commercial heat exchangers produced for automobile and residential air conditioners. The first one consists of 8 rectangular channels having hydraulic diameter of 1.44 mm (1.79 × 1.2 mm) while the second one consists of 7 channels with hydraulic diameter of 1.36 mm (1.57 × 1.2 mm). It was found that, the heat transfer coefficient of the 1.36 mm hydraulic diameter channels was 25 % higher than that of the 1.44 mm hydraulic diameter channels at same experimental conditions. Since the tested exchangers had almost comparable hydraulic diameters, the observed enhancement in heat transfer with the smallest hydraulic diameter may not arise from the diameter effect. The authors believed that the enhancement was coming from the increase of the wetted perimeter, which contributed to the effective distribution of the heat load to each channel. It is worth mentioning that the perimeter only increased by 5.9 %, which seems small, while the cross section area was decreased by 12.3 %. As a result, the enhancement may be arising from the reduction in cross section area and the increase in perimeter.

2.9.2 Heat transfer mechanism(s)

In large diameter channels, it is known that heat transfer is dominated by the nucleation mechanism in the low quality region and forced convection mechanism in the high quality region. Conventionally, the criterion of identifying the controlling mechanism is the dependence of the local heat transfer coefficient on local vapour quality x, mass flux G and heat flux q. Nucleate boiling mechanism dominates when the heat transfer coefficient increases with increasing q but does not depend on x and G. On the other hand, convective boiling dominates when the heat transfer coefficient increases with increasing x and G but does not change with q. This section presents the effect of mass flux G and heat flux q on the local flow boiling heat transfer coefficient. The previous experimental studies are segregated into two groups: one group investigated single channel and second group investigated multi-channels. This arises from the fact that, heat transfer characteristics in multi-channels may be influenced by flow mal-distribution and instability problems.

Single channels: Many researchers investigated flow boiling heat transfer in single microchannels using refrigerants, hydrocarbons and water as test fluids. However, there is a wide scatter in the dominant heat transfer mechanism. One group of researchers such as Lazarek and Black (1982), Wambsganss et al. (1993), Bao et al. (2000) and Del Col et al. (2008) concluded nucleate boiling as a dominant mechanism even at high vapour qualities. Lazarek and Black (1982) measured the local flow boiling heat transfer coefficient of a highly sub-cooled R113 (ΔT_{sub} = 33K) in a stainless steel tube of 3.1 mm diameter. In their experiment, the liquid Reynolds number at channel inlet was varied from 791 to 4745, which covers laminar and early turbulent region. They have found that, the saturated boiling heat transfer coefficient strongly depends on heat flux and is not significantly dependent on local vapour quality as seen in Fig. 2.41. This indicates that nucleate boiling is the dominant heat transfer mechanism.

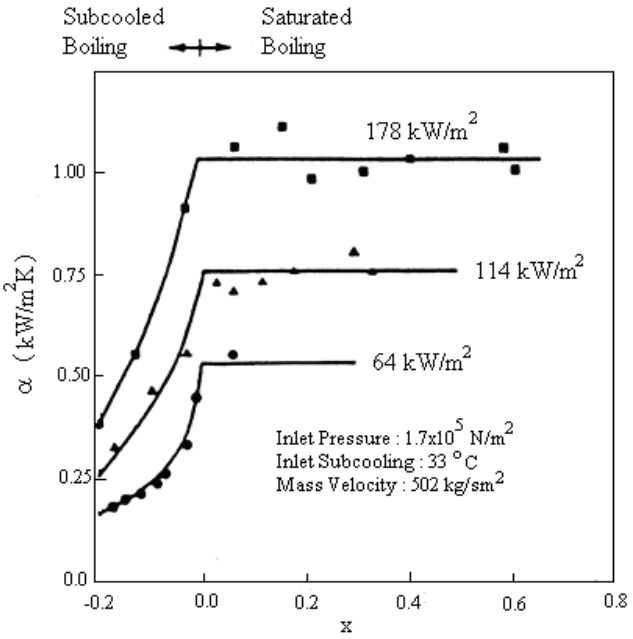

Figure 2.41 Local heat transfer coefficient versus local vapour quality at different heat flux values, Lazarek and Black (1982).

Wambsganss et al. (1993) experimentally determined the local heat transfer coefficient of R113 in a stainless steel horizontal tube of 2.92 mm diameter. The tube was heated by a DC current and the thermocouples were attached to the surface by using electrically insulating, thermally conducting epoxy. The exit quality ranged from 0 to 0.9 and the liquid inlet Reynolds number was varied from 298 to 1788. The local heat transfer coefficient was found to be dependent on heat flux but independent on quality and mass flux, which confirms the dominance of nucleate boiling. Additionally, they used the flow map of Damianides and Westwater (1988) that was developed for air-water adiabatic flow in 3 mm diameter tube to predict their flow boiling patterns. It was shown that, the majority of boiling data are located in slug and plug flows, which existed up to quality of 0.6 – 0.8. As a result, they reported that nucleate boiling dominates due to the thick liquid region of slug flow, which may support nucleate boiling better than the thin liquid film in annular flow. Figure 2.42 depicts the local heat transfer coefficient as a function of local vapour quality at different heat and mass fluxes and also the flow patterns transition boundaries are shown in the figure.

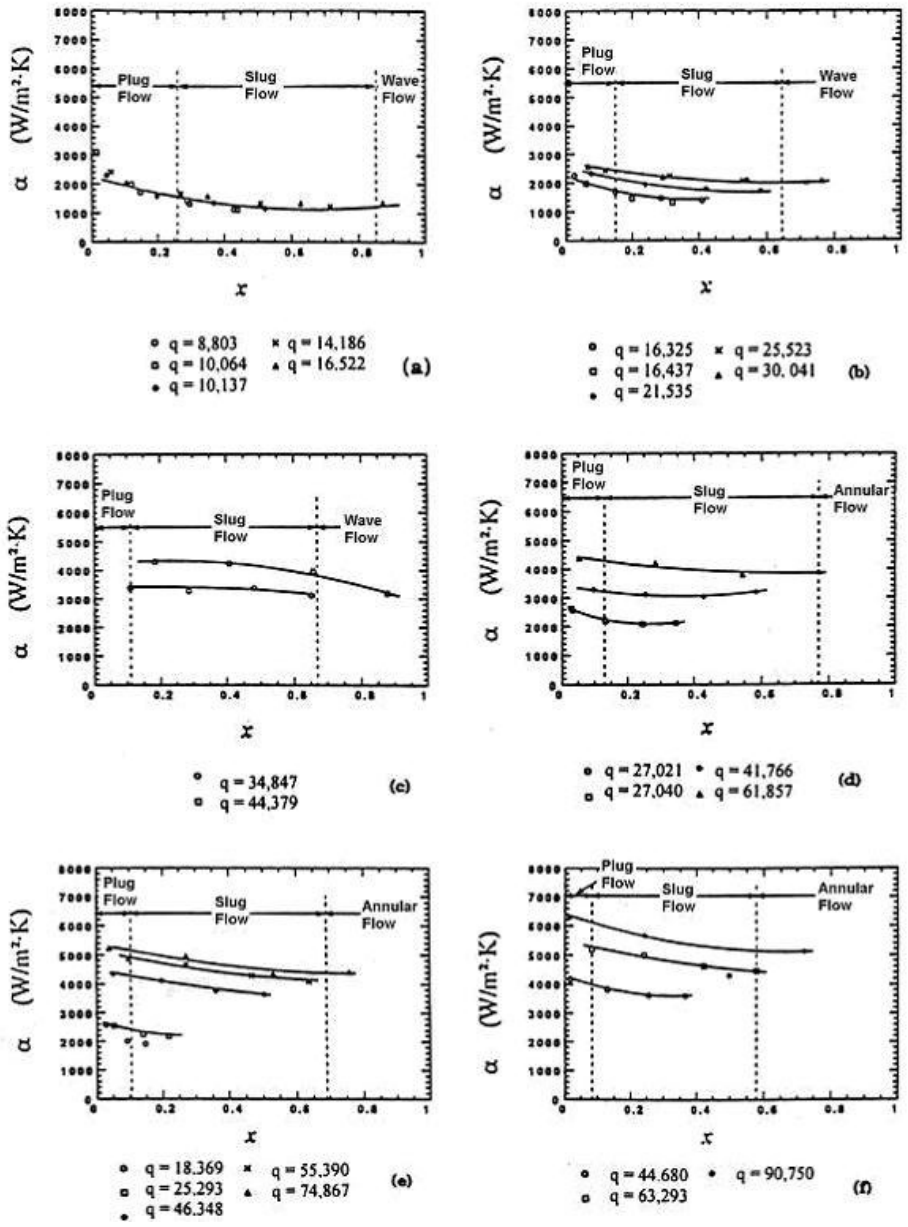

Figure 2.42 Heat transfer coefficients at constant mass flux of: (a) G = 50 kg/m²s, (b) G = 100 kg/m²s, (c) G = 150 kg/m²s, (d) G = 200 kg/m²s, (e) G = 242 kg/m²s, (f) G = 300 kg/m²s, Wambsganss et al. (1993).

Bao et al. (2000) measured the local heat transfer coefficient of R11 and R123 using a smooth horizontal copper tube of 1.95 mm diameter and 270 mm heated section. Liquid inlet Reynolds number ranged from 333 to 11976 or G = 50 – 1800 kg/m^2 s, heat flux from 5 to 200 kW/m^2 and exit quality from 0 to 0.9. The test section was surrounded by 10 pieces of cooper blocks, which were separately heated by a band heater. The copper blocks were soldered to the tube to improve the thermal contact with tube surface. The tube outer wall temperature was measured by inserting thermocouples through a narrow hole < 1 mm diameter drilled in the copper block and 2 mm away from the tube wall. It

is worth mentioning that, the applied heat flux was not perfectly constant across the heating sections due to the difference in the heat input and inter-block heat transfer. However, they reported that heat flux was constant within 10 %. It was found that, the heat transfer coefficient increases rapidly from single phase value and peaks at vapour quality of about zero then it remains constant with increasing quality, see Fig. 2.43. Also, the coefficient increases with increasing heat flux with insignificant mass flux effect. This led them to conclude that, nucleate boiling is the dominant mechanism. Del Col et al. (2008) investigated flow boiling of R134a in a thick wall copper tube having inner diameter of 0.96 mm. The tube was heated by circulating hot water in a way similar to counter current heat exchangers. They measured the heat transfer coefficient which strongly depended on heat flux with little dependence on mass flux and quality. Conventionally, this may be interpreted as nucleate boiling.

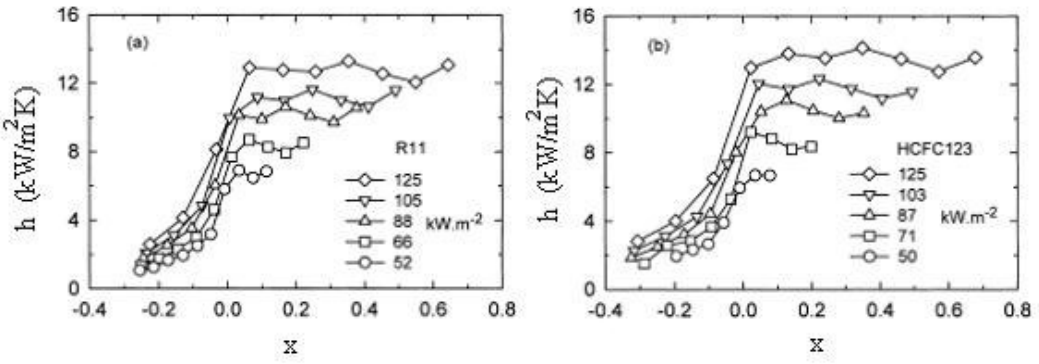

Figure 2.43 Heat transfer coefficient versus vapour quality at different heat fluxes, (a) P_{in} = 4.6 bar and G = 446 kg/m^{2}s; (b) P_{in} = 4.5 bar and G = 452 kg/m^{2}s. Bao et al. (2000).

A second group of researchers such as Kew and Cornwell (1997), Lin et al. (2001a), Sumith et al. (2003), Diaz et al. (2006) and Chin and Thome (2009) reported *nucleate-convective* boiling mechanism, i.e. nucleation at low qualities and convection at high qualities. Kew and Cornwell (1997) measured the local flow boiling heat transfer coefficient of R141b in three stainless steel tubes with diameters of 1.39, 2.87 and 3.69 mm. They have found that, the behaviour of the heat transfer coefficient in the 2.87 and 3.69 mm tubes was similar in trend to that observed in conventional channels, see Fig. 2.24. On the other hand, the 1.39 mm tube behaved in a different way where at high mass fluxes the heat transfer coefficient decreased rapidly with quality. This decreasing

trend was attributed to the local dryout occurred due to the removal of the liquid in the tube by a rapidly expanding bubble which ultimately fill the tube. Lin et al. (2001a) used the same experimental facility of Kew and Cornwell to investigate flow boiling heat transfer of R141b in small diameter tubes with diameters of 1.1, 1.8, 2.8 and 3.6 mm and heated lengths 500, 496, 498 and 454 mm, respectively. For all tubes, the heat transfer coefficient was found to be dependent on heat flux in the very small quality region up to x ~ 0.1 and increases with increasing heat flux. At a fixed heat flux, the heat transfer coefficient was found to decrease from its peak value at quality close to zero and at x > 0.1 it increases again with quality. They attributed the decrease in the heat transfer coefficient with quality, which was remarked only in the smaller tubes, to two possible reasons. The first reason was the high pressure gradient observed in small diameter tubes, which reduces the local pressure and consequently the nucleate boiling part as it is clear from Cooper's pool boiling correlation (1984). The second reason was the presence of confined bubbles which influenced the micro-layer thickness underneath the bubble. As the confined bubble expands the velocity of the bubble front increases and the liquid film becomes thicker which increases the conductive thermal resistance in the layer. Eventually, they concluded that nucleate boiling mechanism dominates in the low quality region while convective boiling mechanism dominates in the intermediate to high quality region. Additionally, they observed that the transition from nucleate boiling into convective boiling occurs at higher qualities in the smaller tubes and shifts to lower qualities as mass flux increases. Figure 2.44 depicts the local heat transfer coefficient versus local quality for the 2.88 mm tube. Also, the flow patterns transition boundaries predicted by a map developed by the same authors are shown on the figure.

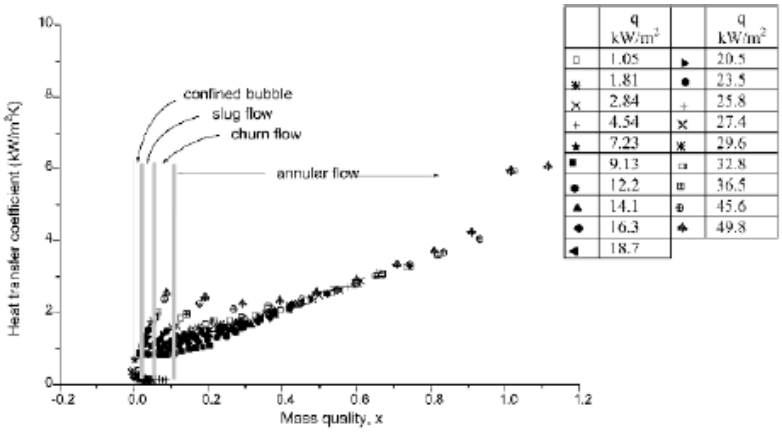

Figure 2.44 Local heat transfer coefficient versus local quality for R141b, D = 2.8 mm, G = 130 kg/m^2 s, Co = 0.434, Lin et al. (2001a).

Sumith et al. (2003) measured the local heat transfer coefficient of water in a vertical stainless steel tube having inner diameter of 1.45 mm. They used the flow pattern map of Triplett et al. (1999) developed for adiabatic air-water flow in a 1.45 mm tube to predict the transition boundaries. They presented the local heat transfer coefficient as a function of the local superficial vapour velocity rather than local quality. Three patterns were identified namely; slug flow, slug-annular and annular flow with slug-annular and annular flow was the dominant flow patterns. The results indicated that nucleate boiling mechanism dominates in the slug and initial slug-annular flow regimes. They attributed the occurrence of nucleate boiling to the existence of thick liquid film in slug-annular flow and even the film of wavy-annular flow. A threshold superficial vapour velocity value of 7 m/s (x = 0.05) was found between nucleate and convective boiling. For velocities less than this value (low quality), nucleate boiling dominates while convective boiling dominates at values greater than 7 m/s. At low mass fluxes, the coefficient decreased with mass flux while the effect was insignificant at high mass fluxes. Diaz et al. (2006) measured the heat transfer coefficient of pure water, pure hydrocarbons, and hydrocarbons mixture using an infrared camera and a circular channel of 1.5 mm diameter. For water and n-octane/n-hexane mixture, nucleate boiling was found to dominate in the low quality region while convective boiling dominated in the high quality region. Chin and Thome (2009) investigated flow boiling of R134a, R245fa and R236fa in a horizontal stainless tube of 1.03 mm diameter and 180 mm heated length. Figure 2.45 shows the effect of fluid type on the local heat transfer behaviour. For R134a, the figure shows that the heat transfer coefficient increases with heat flux with little variations with quality for $x < 0.35$ (isolated and coalesced bubble region) then it slightly decreases with quality in the annular flow regime. By contrast, the trends of R236fa and R245fa were different where both fluids showed heat transfer coefficient that remained almost constant with quality in the low quality region and increases with quality in the high quality region. The value of vapour quality at which the increasing trend appears was much lower in case of R245fa than R236fa. Additionally, the mass flux effect was also investigated. In the isolated and coalescence bubble regimes, no mass flux effect was detected for all fluids while in the annular flow regimes all fluids demonstrated mass flux effect including R134a. Accordingly, they concluded that, the mechanism in the isolated bubble and coalescence bubble regimes is not clear. However, if the conventional criterion was applied, nucleate boiling will be the controlling mechanism in this region. At high vapour quality in the annular regime,

all fluids showed convective boiling. The different behaviour of R134a compared to R236fa and R245fa was attributed to the effect of surface tension. The surface tension of R245fa is the highest followed by R236fa and R134a which improves the wet-ability and bubble confinement. Similar behaviour for the three fluids was also reported by Consolini and Thome (2009) using horizontal stainless steel tubes of 0.51 and 0.79 mm diameters and 75 mm heated length.

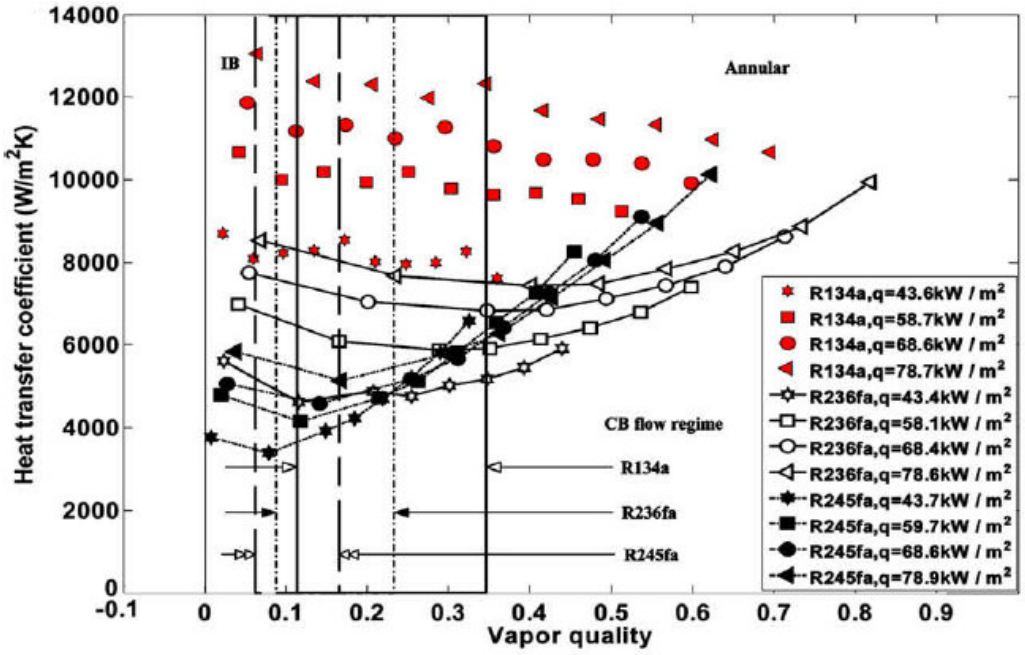

Figure 2.45 Local heat transfer coefficient versus quality for R134a, R236fa and R245fa at G = 400 kg/m^2 s, T_{sat} = 31 ^{0}C and ΔT_{sub} = 4K, Chin and Thome (2009).

Contrary to the *nucleate-convective* mechanism, Tran et al. (1996) reported *convective-nucleate* boiling mechanism, i.e. convection at low quality and nucleation at high quality. They measured the local flow boiling heat transfer coefficient of R12 in a horizontal brass tube with diameter of 2.46 mm and 870 mm heated length. The wall temperature was measured using resistance temperature devices RTDs. The Reynolds number varied from 775 to 10233. They have found that for qualities greater than 0.2 or wall superheat greater than 2.75 K, the local heat transfer coefficient increases with heat flux but is independent of mass flux and vapour quality as seen Fig. 2.46. When they extended the experiments to include wall superheat less than 2.75 K, the boiling curve showed mass flux dependence as seen in Fig. 2.47. Accordingly, they concluded that

nucleate boiling mechanism dominates for wall superheat greater than 2.75 K or x > 0.2 while convective boiling dominates below wall superheat 2.75 K.

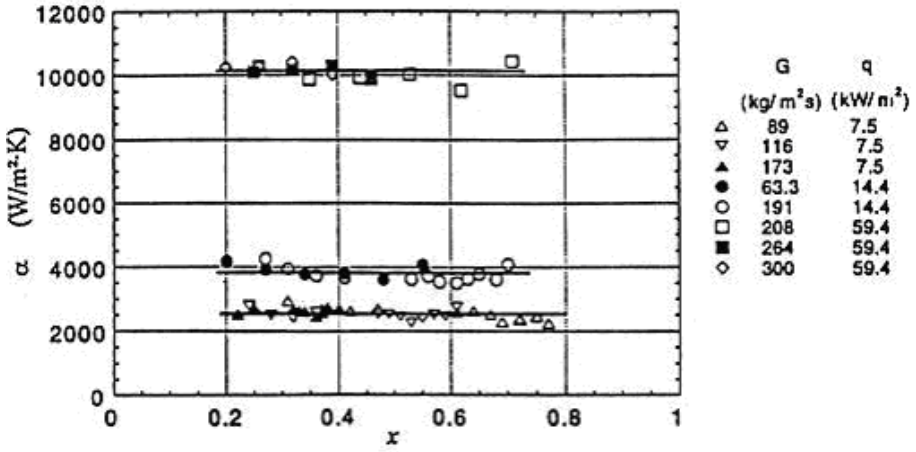

Figure 2.46 Effect of heat and mass flux on the local heat transfer coefficient of R12 at ΔT_{sup} > 2.75K and P = 825 kPa, Tran et al. (1996).

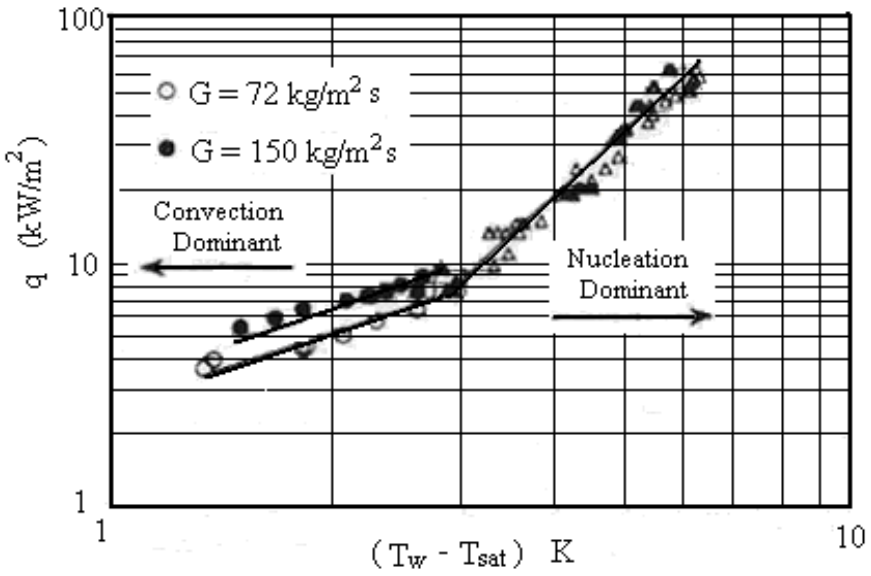

Figure 2.47 Mass flux effects on the boiling curve including data with ΔT_{sup} < 2.75K, Tran et al. (1996).

A third group of researchers such as Huo et al. (2004) and Martin Callizo (2007b) for R134a reported *nucleate-dryout*, i.e. nucleation up to intermediate heat fluxes and dryout at high heat fluxes. Huo et al. (2004) investigated flow boiling heat transfer of R134a in vertical stainless steel tubes having inner diameter of 4.26 and 2.01 mm. It was found that, the heat transfer coefficient increases with heat flux with little

dependence on quality for x less than 0.45 – 0.5 and 0.2 – 0.3 for the 4.26 and 2.01 mm tubes, respectively as seen in Fig. 2.36. For vapour qualities higher than this threshold value, the heat transfer coefficient rapidly decreased with quality with little dependence on heat flux. The sharp decrease of the heat transfer coefficient with quality at high heat fluxes was attributed to the high bubble generation frequency at high heat fluxes which results in too many bubbles that cover tube wall and suppress nucleate boiling. Moreover, the effect of mass flux on the heat transfer coefficient was insignificant as long as the local quality is less than 0.5. This means that, nucleate boiling dominates when the quality is less than 0.5 while the mechanism changes to partial dryout at high heat fluxes and qualities greater than 0.5. Marin-Callizo et al. (2007b) investigated flow boiling of R134a in a micro tube of 0.64 mm diameter. It was concluded from their results that nucleate boiling dominates up to quality values of 0.45 – 0.5. On the other hand, at higher quality and heat flux the heat transfer coefficient decreased with quality with insignificant effect for heat flux. This led them to conclude that intermittent partial dryout mechanism dominates at high quality and heat fluxes.

Saitoh et al. (2005) found *nucleate-convective-dryout* for R134a in three horizontal stainless steel tubes having inner diameters of 3.1, 1.12 and 0.51 mm with heated length of 3240, 935 and 550 mm, respectively. The inlet quality was varied from 0 to 0.2. Their results showed that, the heat transfer coefficient increased with heat flux with little dependence on mass flux in the low quality region ($x<0.6$) while the heat transfer coefficient increased with quality and mass flux with little dependence of heat flux in the high quality region, see Fig, 2.38. This suggests nucleate boiling in the low quality region while convective boiling occurs at high quality. Additionally, dryout was observed with the three tubes where the quality at which the heat transfer coefficient decreases was shifted to lower value when the diameter decreases, i.e. from 0.9 for 3.1, 0.8 – 0.9, for 1.12, and 0.5 for the 0.51 mm tube. Another different local heat transfer behaviour was reported by Lin et al. (2001b) for R141b in a 1 mm tube at G = 500 kg/m^2 as seen in Fig. 2.48. Heat flux was varied from 18 to 72 kW/m^2, inlet sub-cooling from 11 – 23K and exit pressure was kept atmospheric. As seen in the figure, for heat fluxes from 18 – 60 kW/m^2, the heat transfer coefficient rapidly increases from single phase value to a peak at quality around zero and then decreases with an increase in quality then increase again with further increase in quality. On the other hand, for heat

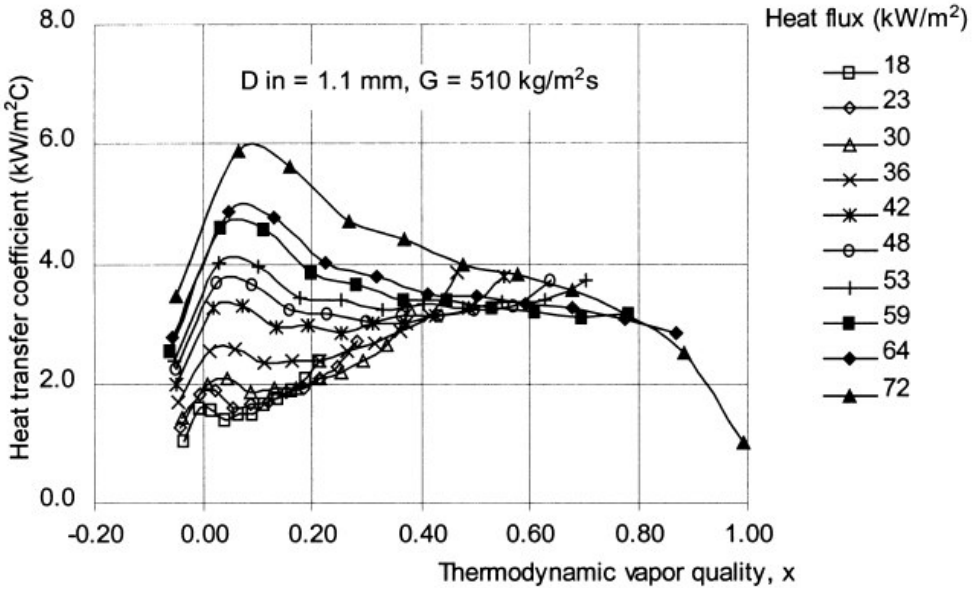

Fig. 2.48 Local heat transfer coefficient of R141b at G = 500 and D = 1.1 mm versus local quality, Lin et al. (2001b).

fluxes greater than 60 kW/m^2, the heat transfer coefficient monotonically decreases with quality. The reason for the reduction in heat transfer coefficient in the low quality region was attributed to the high pressure drop encountered in small diameter tubes. The pressure fluctuations with time showed that, significant portion of the measured pressure drop would occur at the onset of boiling with the generation of confined bubbles. Thus, the local pressure and saturation temperature in the low quality region may be somewhat lower than those predicted from linear assumption. Additionally, high pressure drop may influence the fluid properties between inlet and outlet.

Multi microchannels: Qu and Mudawar (2003c) investigated flow boiling of de-ionized water in a multi micro-channel heat sink of 0.35 mm hydraulic diameter. They plotted the heat transfer coefficient versus quality for the last thermocouple location. It was found that, the heat transfer coefficient increases with increasing mass flux at the same value of quality while decreases with quality at the same value of mass flux. Since the heat transfer coefficient decreased with quality, they deduced that it may decrease with increasing heat flux – the thing that is not supporting nucleate boiling mechanism. Since annular flow was found to be dominant at low to moderate heat fluxes, they reported that convective boiling is the dominant mechanism. They used the explanation proposed by Mukherjee and Mudawar (2003) to interpret the absence of nucleate

boiling in water compared to refrigerants. The reason was attributed to the smaller surface tension and contact angle of refrigerants that result in a smaller bubble departure diameter compared to water. Based on that, Qu and Mudawar (2003c) reported that refrigerants may sustain nucleate boiling over a significant portion of the channel even at high vapour quality values. The decrease of the heat transfer coefficient with quality in their study in the annular flow regime was believed to arise from a unique behaviour of annular flow in microchannels. This behaviour was that, large amount of liquid droplets entered the gas core at the onset of annular flow whose deposition upon the liquid film increases it's thickness in the stream-wise direction. This results in a decrease in heat transfer coefficient with increasing quality. Yun et al. (2006) investigated flow boiling of R410a in two commercial rectangular evaporators for automotive air conditioning having hydraulic diameters of 1.36 and 1.44 mm. They have found that, the effect of heat flux and mass flux on the heat transfer coefficient is very small up to qualities $x < 0.5$ or before dryout. After dryout, the heat transfer coefficient increased with heat flux and mass flux. They did not comment on the controlling mechanism which seems unclear. Kuo and Peles (2007) investigated flow boiling of de-ionized water in rectangular silicon multichannel heat sink having hydraulic diameter of 0.22. They designed the channels such that, the separating walls between the channels have an array of re-entrant cavities with a mouth of 7.5 μm connected to a hole of 25 μm diameter. Additionally, the flow was directed to each channel through a rectangular orifice to reduce flow instability. For all mass fluxes, the heat transfer coefficient dropped from its highest value at vapour quality of about $x = 0$ and reached asymptotic value after $x = 0.05$. The effect of mass flux was found to be insignificant in the very low quality region $x < 0.05$. So, they believed that nucleate boiling dominates only in the very small quality region up to $x = 0.05$. Though there is mass flux effect at $x > 0.05$, convective boiling mechanism was difficult to be ruled out due to the presence of nucleating bubbles departing from the re-entrant cavities even at high mass fluxes. Agostini et al. (2008d) observed three trends for the heat transfer coefficient of R236fa based on the value of heat flux. At low heat fluxes, vapour quality and mass flux, the heat transfer coefficient increases with quality but is independent of heat and mass flux. At intermediate heat fluxes, the heat transfer coefficient was almost independent of vapour quality and mass flux but increases with increasing heat flux. At very high heat fluxes, the heat transfer coefficient increased weakly with mass flux but decreased with increasing heat flux as a result of the intermittent dryout. Accordingly,

they concluded that convective boiling does not seem to exist in microchannels where nucleate boiling is the prevailing mechanism. Bertsch et al. (2009a) investigated flow boiling heat transfer of R134a and R245fa in a copper multi microchannels heat sink with channel hydraulic diameter of 1.09 and 0.54 mm. The heat transfer coefficient was found to peak at quality of about 0.1 then stay approximately constant up to quality of 0.4 – 0.5 then it rapidly decreases with quality as seen in Fig. 2.49. At high heat fluxes, the plateau disappears where the coefficient rapidly decreases with quality from its maximum value. Since the heat transfer coefficient showed strong dependence on heat flux while the mass flux effect was found to be small, nucleate boiling was concluded as a dominant mechanism. It is interesting to note that, the behaviour of R245fa is different from that reported by Chin and Thome (2009) where convective boiling was reported at high qualities. This could be due to the difference between single tube and mutli-channels configurations.

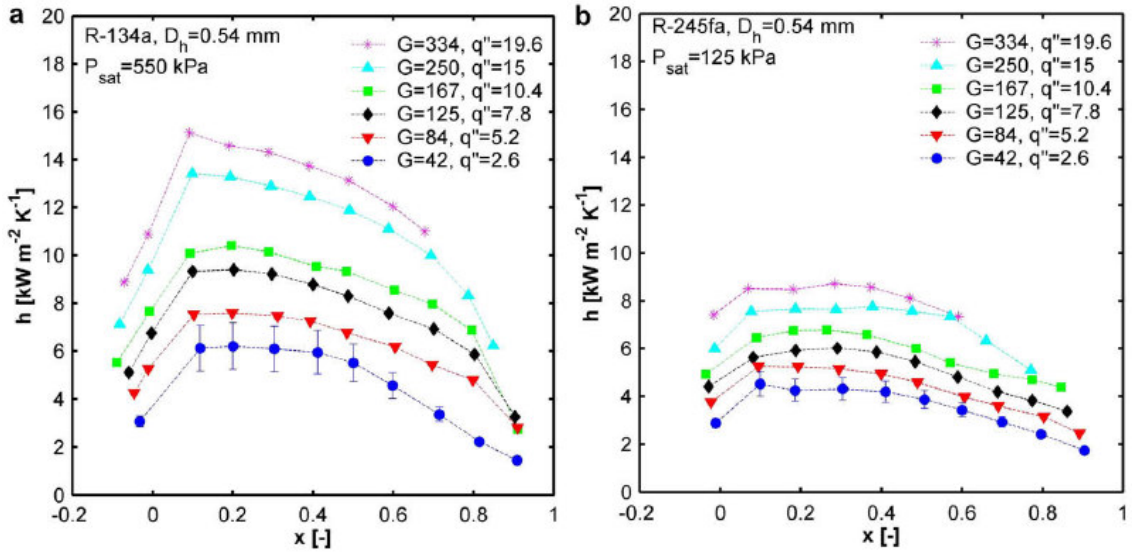

Figure 2.49 Effect of heat flux, mass flux and vapour quality on the heat transfer coefficient (a) R134a (b) R245fa, Bertsch et al. (2009a).

Thome (2004) and Thome et al. (2004) argued that the controlling heat transfer mechanism in micro tubes is the transient thin film evaporation in the elongated bubble regime rather than nucleate boiling. This point was the basis of the three zone evaporation model that was developed by them for slug flow in micro tubes. In fact, it is difficult to judge whether heat transfer occurs by film evaporation or nucleation is not fully understood. Some researchers such as Kasza et al. (1997) observed nucleating

bubbles in the liquid film around the vapour slug during water flow boiling in a narrow rectangular channel. Also, Haririchian and Garimella (2009a) observed small nucleating bubbles in the liquid film of the wispy-annular flow during flow boiling of FC-77 in rectangular microchannels. In conclusion, the heat transfer mechanism(s) at microscale is far from clear.

2.9.3 Effect of inlet sub-cooling

The effect of fluid inlet temperature, i.e. inlet sub-cooling, on the boiling heat transfer coefficient was considered in few studies. Yu et al. (2002) investigated flow boiling of water in a 2.98 mm diameter tube at 200 kPa system pressure (120 ^{0}C saturation temperature) and varied the water inlet temperature from ambient to 80 ^{0}C. They presented the results on the boiling curve at different inlet temperatures plotted for axial location near the channel exit. It was found that, the fluid inlet temperature does not affect the boiling curve in the nucleate boiling regime. In their experiment, the nucleate boiling regime occurred at wall superheat less than 8K. Liu and Garimella (2007) investigated flow boiling of water in microchannels with hydraulic diameter ranging from 0.38 to 0.58 mm and they varied the water inlet temperature from 67 to 95 ^{0}C. They presented their results on the boiling curve in a similar way to Yu et al. (2002). It was found that, after the onset of nucleate boiling, all boiling curves merged together irrespective of the fluid inlet temperature. In other word, the fluid inlet sub-cooling does not affect the nucleate boiling curve. Martín-Callizo et al (2007a) investigated sub-cooled flow boiling of R134a in three vertical tubes having inner diameter of 0.8, 1.22 and 1.7 mm. The liquid inlet sub-cooling was varied from 5 to 15K. They found that, the liquid inlet sub-cooling does not affect the maximum wall superheat at the onset of nucleate boiling. After the onset of nucleate boiling, all boiling curves collapsed into one curve indicating insignificant effect for the liquid inlet sub-cooling. Agostini et al (2008d) investigated flow boiling of R245fa in a rectangular multi microchannels heat sink of 0.336 mm hydraulic diameter. The liquid inlet sub-cooling was varied from 0 to 19K. They also included their previous data for R236fa. The heat transfer coefficient was plotted versus vapour quality for different values of inlet sub-cooling at a fixed value of heat and mass flux. They reported that there is no much effect of the liquid inlet sub-cooling on the saturated boiling heat transfer coefficient. For the sub-cooled boiling region, they found that the heat transfer coefficient decreases as the liquid inlet sub-

cooling increases. On the contrary, in the sub-cooled boiling, Martin-Callizo et al. (2007a) found that the heat transfer coefficient increases with increasing the inlet sub-cooling. This was attributed to the higher heat flux required to attain the same quality when the inlet sub-cooling increases. As a result, the wall temperature becomes higher and thus the surface becomes more active for nucleation.

2.9.4 Effect of system pressure

System pressure influences the fluid properties such as liquid to vapour density ratio and surface tension. As the pressure increases, surface tension decreases and consequently the bubble departure diameter. Some researchers investigated the effect of system pressure on the heat transfer coefficient with some discrepancy. One group of researchers such as Bao et al. (2000), Owhaib et al. (2004), Martin-Callizo et al. (2007b), Qi et al. (2007b), Choi et al. (2009) and Shiferaw et al. (2009) found that, the heat transfer coefficient increases with increasing system pressure. The increase in heat transfer with increasing pressure was attributed to: (a) reduction in the wall superheat required for bubble nucleation when the pressure increases as suggested by Qi et al. (2007b), (b) reduction in surface tension as proposed by Choi et al. (2009) and (c) reduction in bubble departure diameter and the increase in frequency of bubble generation as proposed by Shiferaw et al. (2009). On the other hand, another group of researchers such as Agostini and Bontemps (2005), Bang et al. (2007), Jang et al. (2008) and In and Jeong (2009) reported that system pressure has insignificant or very small effect. Agostini et al. (2008d) found that the effect of pressure depends on the type of fluid. In their study, the heat transfer coefficient increased with increasing system pressure for R236fa while the effect was not clear in case of R2345fa. On contrary, Kaew-On and Wongwises (2009) reported that the heat transfer coefficient decreases with increasing system pressure. They attributed this behaviour to the reduction in the vapour velocity at the vapour-liquid interface, which results in lower vapour shear at high saturation pressure. They also believed that it could be related to the reduction in the liquid thermal conductivity at high temperature, which reduces the heat transfer in the liquid film during annular flow.

2.10 Prediction of heat transfer coefficient (HTC)

2.10.1 Empirical correlations

This section presents the empirical correlations that were developed to predict flow boiling heat transfer coefficient in small to micro diameter channels. The details of these correlations will be presented later in chapter 5 and the equations are summarized in appendix B. Here, the principles based on which the correlations were developed are presented briefly. Conventionally, nucleate boiling and forced convective boiling mechanisms contribute to flow boiling heat transfer. Based on that, the correlations of heat transfer were developed by adopting approaches that consider the contribution of the two mechanisms. The first approach was proposed by Chen (1966) in which nucleate boiling and convective boiling contributions were simply added together. The second approach was adopting the asymptotic model in which the heat transfer coefficient approaches either the nucleate boiling or the convective boiling components, i.e. selecting the component which is the largest. Unfortunately, these macro-scale correlations poorly predicted the heat transfer coefficient at microscale as found for example by Bao et al. (2000), Warrier et al. (2002), Yun et al. (2006), Martin-Callizo et al. (2007b) and Shiferaw et al. (2007). Accordingly, several correlations were developed using large experimental database collected at microscale level. Lazarek and Black (1982) correlated their 728 local saturated boiling heat transfer data points by fitting the data using the least square method. The data were collected for boiling flow of R113 in a 3.1 mm diameter tube with upward and downward flow directions. In addition, the data covered the entire range of qualities until dryout with nucleate boiling being the dominant mechanism. Since the experimental trend showed independence of the local quality, the correlation was introduced as a function of the all liquid Reynolds number and Boiling number and successfully predicted the data within ± 15 % (9 % r.m.s error). In addition to the developed correlation, they assessed the conventional correlations of Chen (1966) and Shah (1976). At low heat and mass fluxes, the two correlations over-predicted the HTC while at high mass and heat fluxes the correlation of Chen under-predicted the data. From this comparison, they recommended modifying the correlation of Shah since it was reasonably consistent with their data and their new correlation. Tran et al. (1996) compared their experimental data with three of the conventional correlations namely: Kandlikar (1991), Jung and Radermacher (1991) and Liu and Winterton (1991) and all of them significantly under-predicted the data. Accordingly,

they developed a correlation for the nucleate boiling dominant pattern using refrigerants R12 and R113 and channels of diameters 2.4 and 2.46 mm. Since nucleate boiling was dominating and the mass flux effect was minimal, they modified the correlation of Lazarek and Black (1982) by replacing the liquid Reynolds number with the Weber number and accounting for the variation of fluid properties. This correlation predicted most of the data within ± 15 %. However, the new correlation was found to be less accurate when it was compared against flow boiling data of R-134a. As a result, Tran et al. (1997) proposed a new correlation based on the nucleate boiling model of Rohsenow (1952) and the confinement number proposed by Kew and Cornwell (1997). Kew and Cornwell (1997) proposed a modified version of Lazarek and Black by multiplying their equation by $(1 - x)^{-0.143}$ to account for the increasing trend of HTC with quality arising from the confinement effect. Lee and Lee (2001) investigated flow boiling heat transfer of R113 in a horizontal rectangular channel of mini gaps raging from 0.2 to 2 mm. They compared their data with four conventional correlations and all of them predicted less than 70 % of the data within ± 20 %. Since the dominant mechanism in their experiment was convective boiling, they correlated their data based on the fact that the film evaporation model of Hewitt and Hall-Taylor (1970) can be applied for narrow passages at very small flow rates provided that the local pressure gradient is known. So, the applicability of the Chen (1966) correlation was extended to include laminar film flow after dropping the nucleate boiling part from the original Chen correlation and introducing the enhancement factor as a function of channel aspect ratio and the liquid two phase multiplier. The new correlation captured the trend and values within an uncertainty of ± 20 %. Yu et al. (2002) investigated flow boiling of water in a horizontal tube of 2.98 mm inner diameter. Since the Chen correlation predicted poorly their data and their experimental results were similar in trend to those of Tran et al. (1996), they correlated their experimental data in a form similar to that of Tran's correlation. Warrier et al. (2002) investigated flow boiling heat transfer of FC-84 in aluminium multi-channels with hydraulic diameter of 0.75 mm. They compared their data with two conventional correlations: Kandlikar (1990) and Liu and Winterton (1991) and two microscale correlations: Lazarek and Black (1982) and Tran (1997). All the examined correlations significantly over-predicted the experimental data but captured the experimental trend of the local HTC, which was independent of local quality. The only exception in their comparison was the correlation of Tran that predicted incorrect trend where it showed decreasing trend with increasing quality. It is worth mentioning that,

the behaviour of the Tran correlation was not consistent with the experimental results of Tran which does not show any dependency on local quality. The incorrect trend of Tran's correlation was resulting from the fact that the authors multiplied the confinement number by (1 – x), which did not exist in the Tran original correlation. It looks as if they were confused between the Tran pressure drop and heat transfer correlations. Eventually, they correlated the normalized two phase heat transfer coefficient by the single phase laminar heat transfer coefficient as a function of boiling number and vapour quality. Kandlikar and Balasubramanian (2004) extended the correlation of Kandlikar (1990), which was developed for large diameter channels, to include transition and laminar patterns in microchannels. In the original correlation, the two phase heat transfer coefficient was selected to be the largest of nucleate and convective boiling components. These components were introduced as a function of the single phase liquid heat transfer coefficient, convective number (proposed by the authors), boiling number and local quality. Zhang et al. (2004) assessed six well known macro-scale correlations using data collected from 13 different laboratories covering four fluids namely: water, R11, R12 and R113 and diameters ranging from 0.78 to 6 mm. The assessed correlations were: Chen (1966), Shah (1976), Gungor and Winterton (1986), Liu and Winterton (1991), Kandlikar (1990) and Steiner-Taborek (1992). All correlations except those of Gungor-Winterton (1986) and Steiner-Taborek (1992) gave reasonable predictions with the Chen correlation being the best. Based on that, a new correlation of the Chen type was developed to incorporate flow with low Reynolds number in small diameter channels. For the nucleate boiling part, they used the Forster and Zuber (1955) correlation for pool boiling. The convective part was correlated based on the annular flow model of Hewitt and Hall-Taylor (1970) using the two phase friction multiplier. However, this correlation predicted the data of the 13 studies with mean error comparable to that of the Chen correlation, which was in the order of 21 %. Lee and Mudawar (2005a) investigated flow boiling heat transfer of R134a in a micro-channel heat sink and compared their data with three conventional correlations and five correlations developed for small diameter channels. All the examined correlations predicted poorly the data where the macro-scale correlations generally over-predicted the data in the high quality region while under-predicted the data in the low quality region. Surprisingly, the correlation of Yu et al. (2002) that was developed for microscale highly over-predicted the data with mean absolute error of 1032.3%. Accordingly, they developed new correlation for water and R134a based on the

Marinelli parameter, Boiling number and liquid Weber number accounting for the microchannels effects that were not considered in the previous correlations. They divided the quality domain into three ranges; 0.0 – 0.05, 0.05 – 0.55 and 0.55 – 1. In the first and last ranges, the heat transfer coefficient was influenced by the Martinelli parameter while in the second range it was sensitive to the Boiling number and the liquid Weber number in addition to the Martinelli's parameter. The new correlation predicted most of the data within ± 30 % and mean error of 12.26 %. Yun et al. (2006) investigated flow boiling of R410 in rectangular channels of 1.36 and 1.44 mm hydraulic diameters. It was found that, the heat transfer coefficient was poorly predicted by macro and microscale correlations with a mean absolute error greater than 50 %. Since their data showed strong dependency on the boiling number, the liquid Weber number and the liquid Reynolds number, they correlated their data as a function of these dimensionless parameters and predicted their data with mean error of 18 %. Saitoh et al. (2007) proposed a correlation of the Chen type taking into account the effect of channel diameter. The correlation was based on a 2224 data points collected for R134a in horizontal tubes of diameters ranging from 0.51 to 11 mm. The effect of diameter was taken into consideration using the gas phase Weber number where the convective boiling enhancement factor in the original Chen correlation was introduced as a function of Weber number and Martinelli's parameter. Also, they interrelated the nucleate boiling suppression factor with the modified enhancement factor or in other words as a function of Weber number. For the nucleate boiling part, they suggested using the nucleate pool boiling correlation of Stephan-Abdelsalam (1980) that was developed for refrigerants. The new correlation gave a mean deviation of 13.6 % with 93.6 % of the data within ± 30 % compared to corresponding values of 19.7 % (80.7 %) and 20.5 % (77.5 %) predicted using the correlations of Kandlikar (1990) and Gungor-Winterton (1987), respectively. Bertsch et al. (2009b) proposed a correlation for predicting saturated flow boiling heat transfer coefficient in mini and microchannels. This correlation was developed based on a large experimental data base consisting of 3899 data points which were collected from 14 different experimental studies and included 12 different fluids including refrigerants and diameters ranging from 0.16 to 2.92 mm. The correlation was developed in the same form of the Chen correlation. Cooper correlation (1984) was recommended for the nucleate boiling heat transfer coefficient while the convective heat transfer coefficient was calculated as the average of the single phase liquid heat transfer coefficient and single phase vapour heat transfer coefficient. The

correlation took into account the effect of confinement by incorporating the confinement number in the enhancement factor while the suppression factor was only introduced as a function of vapour quality. This correlation predicted the data with a mean error of 28 % with more than 60 % of the data located within 30 % error bands.

Although the above correlations were developed specifically for saturated flow boiling in small to micro diameter channels, it was found that theses correlations are not general. Betesh et al. (2008b) performed an extensive review and comparative analysis of saturated flow boiling in microchannels. They have assessed 25 correlations using 1847 data points collected from 10 different Laboratories of which 19 correlations were developed for small to micro diameter channels. They have concluded that, the best prediction was achieved with mean error of 40 % with less than 50 % of the data within 30 % error bands. This led them to conclude that, microscale correlations did not add any improvements over the conventional macro-scale ones. Also, correlations that were developed based on fitting the experimental data failed to be extrapolated for predicting other data points while nucleate pool boiling correlations were the best indicating the dominance of nucleate boiling in microchannels. Finally, they confirmed the need for physics-based models for predicting flow boiling heat transfer coefficient in microchannels.

Mikielewicz (2010) proposed a model based on a theoretical basis that considers energy dissipation in the flow where boiling occurs. The model shares the analogy between momentum transfer and energy transfer. In this approach, the energy dissipation under steady state conditions in two phase flow was approximated by the viscous energy dissipation in the boundary layer. As a result, the two phase heat transfer coefficient was introduced in the form of the asymptotic model with exponent n = 2, which was obtained based on the theoretical analysis. The model was reported to be used for conventional and microchannels. Since the model over-predicted the data for channels of less than 1 mm diameter, they proposed to drop the nucleate boiling part from their equation where slug and annular flow dominates.

2.10.2 Mechanistic models

Since the developed macro or microscale correlations are not general and can not be extrapolated outside their applicability ranges, the physics-based models seem to be more accurate. Unfortunately, there is a very limited number of mechanistic models in the open literature – the thing that reflects the lack of knowledge and physics at the microscale level. Jacobi and Thome (2002) proposed a heat transfer model based on the premise that thin-film evaporation into elongated bubble is the most important mechanism in microchannels. At a fixed location, a pair composed of an elongated bubble and liquid slug was assumed to pass with a velocity equal to the homogeneous velocity. Principally, this model is based on the idea that during elongated bubble flow a thin liquid film of uniform thickness forms around the bubble and the film becomes thinner as evaporation starts until the arrival of the next liquid slug. This model requires the knowledge of the critical nucleation radius or effective wall superheat in order to estimate the frequency of the pairs and also requires the knowledge of the initial film thickness. When the model was compared with experimental data assuming initial film thickness in the order of 10 – 20 μm, the model managed to predict the data which confirmed that thin-film evaporation is the dominant mechanism in microchannels. Thome et al. (2004) extended this model to include the passage of a vapour slug when dryout occurs and called it "three-zone model". In this version, a cyclic passage of liquid slug, elongated bubble and vapour slug was considered. The model assumptions were: (i) homogeneous flow, uniform and constant heat flux, (ii) all energy entering the fluid was consumed in vaporizing the liquid, (iii) thermal inertia of channel wall is neglected, (v) the film remains smooth and attached to the wall. Based on the work of Moriyama and Inoue (1996) and applying the asymptotic approach they got a continuous relation for the initial film thickness. Dupont et al. (2004) confronted the model against large experimental database and optimised the pair generation frequency, the final film thickness and the adjustable constant in the initial film thickness correlation. The model successfully predicted 70 % of the data within ± 30 % and the effects of various parameters such as heat flux, mass flux, system pressure and vapour quality. Qu and Mudawar (2003b) developed a mechanistic heat transfer model for annular flow pattern in microchannels. The model has taken into account the liquid droplets entrainments to the vapour core. The model assumed: (1) steady two phase flow with uniform pressure across the channel cross section, (2) vapour quality in

annular flow was the thermodynamic equilibrium quality and the vapour core was considered as a homogeneous mixture of vapour and liquid droplets that are in thermal equilibrium at saturation temperature, (3) evaporation occurs only at the interface between the film and the vapour core with negligible droplet evaporation, (4) the film has a uniform thickness at the circumference of the channel and is smooth, (5) the flow is laminar in the liquid film and vapour core and (6) there is a continuous and uniform droplet deposition from the core to the liquid along the stream-wise direction. Using these assumptions and a proposed correlation for the deposition mass transfer coefficient, they applied the one dimensional mass and momentum conservation equations and obtained local parameters such as pressure gradient, film thickness, interfacial shear stress and flow rate in the liquid film. Based on that, the two phase heat transfer coefficient was calculated by dividing the liquid thermal conductivity by the determined film thickness. This model predicted all their experimental data for water with an uncertainty of ± 40 % and average error of 13.3 %. Boye et al. (2007) presented a one dimensional, steady state and incompressible flow model with constant properties for annular flow in microchannels. They applied the momentum equation for liquid and vapour phases and got an analytical expression for the variation of the vapour core radius (film thickness) as a function of quality. The local heat transfer coefficient was then lated from the local film thickness $h(z) = k_l / \delta(z)$.

Consolini and Thome (2010) developed a heat transfer thin film evaporation model for the coalescence bubble pattern in microchannels. The model is valid in the quality range from the transitional quality from isolated bubbles to coalescing bubble and the transition quality from coalescing to annular flow. This was to account for the redistribution of the liquid in flow structure resulting from the breakup of liquid slugs during coalescence. The assumptions adopted in the model were: (1) the two phases are in thermodynamic equilibrium, (2) bubbles nucleated periodically only at the inlet of the heated section, (3) bubbles depart axially instead of radial, (4) the liquid film is laminar and driven only by interfacial shear, (5) the interface of the liquid film varies linearly in the axial direction, (6) heat transfer to the liquid slug and dry patches is negligible, (7) pressure drop is negligible and the film thickness is small compared to channel diameter. They selected a control volume such that it has a stationary boundary at the channel inlet where all liquid flow enters the channel and a moving boundary with a velocity equal to bubble nose velocity. Inside the control volume there is a series of

vapour slugs. Applying mass and energy conservations on this control volume, they obtained an expression for the axial position of bubble nose as a function of time. Selecting another control volume inside the evaporating liquid film and applying conservation equations, they obtained an analytical expression for the variation of the film thickness as a function of interfacial shear stress and time. The passage frequency was introduced in a function form depending on the quality where when the quality equals the transition quality to annular flow frequency becomes zero while when the quality equals transition from isolated bubbles to coalescing bubble the frequency becomes maximum. Finally, after performing integration, an analytical expression for the average heat transfer coefficient was given. Comparing the model against 980 experimental data points indicated that 83 % of the data were predicted with the ± 30 % error band.

2.11 Critical heat flux (CHF)

Critical heat flux is a commonly used term in boiling systems that represents the upper limit of safe operation. Conventionally, this phenomenon may be triggered by one of the following mechanisms, Whalley (1987): (i) formation of hot spots underneath a growing bubble when the liquid micro-layer evaporates before the bubble leaves the cavity, (ii) near-wall bubble crowding that results in the formation of a vapour blanket on the surface, (iii) dryout of the thin liquid film in slug flow and (iv) depletion of liquid film in annular flow. In microchannels, Bergles and Kandlikar (2003) addressed some of the significant issues that may influence CHF. These issues include the conjugate heat transfer, flow mal-distribution and instability. In this section, the effect of different experimental parameters on CHF and the proposed triggering mechanisms and correlations are presented.

Lazarek and Black (1982) measured the critical heat flux of R-113 in a 3.1 mm diameter tube having 123 and 246 mm heated lengths. It was found that, at all experimental conditions, the dryout always commences near the tube exit and depends on inlet sub-cooling. Once dryout occurred, wall temperature experienced large oscillations due to the intermittent rewetting of the wall. Since the macro-scale correlations under-predicted the measured values, they proposed a new correlation for the critical quality at which dryout occurs as a function of *L/D*, *G* and inlet sub-cooling as given by Eq.

(2.39). On the contrary, Bowers and Mudawar (1994) did not find any effect for the inlet sub-cooling on the critical heat flux of R-113. They examined a multi mini-channel heat sink of 2.54 mm diameter and multi microchannels heat sink of 0.51 mm diameter, both of 10 mm heated length. Based on the observed characteristics of the critical heat flux, they have addressed some unique features for miniature channels heat sinks. Firstly, the vapour quality corresponding to the measured critical heat flux was found to exceed unity. Secondly, the small size of channels increases the frequency and effectiveness of droplet impact with channel wall at high vapour quality; the thing that may enhance critical heat flux in microchannels compared to droplet flow pattern in large diameter channels. Thirdly, the small overall size of the heat sink delayed the critical heat flux due to the conduction of heat away from the downstream region undergoing dryout. Additionally, it was observed that critical heat flux was triggered first at an upstream location then moved downstream towards the channel exit.

$$x_{crit} = 1 - 6.075 \times 10^{-3} G D^{0.25} \left(\frac{D}{L} \right)^{0.59} \left[1 + 3.11 \left(\frac{\Delta h_i}{h_{fg}} \right) \right] \qquad (2.39)$$

Sturgis and Mudawar (1999a) investigated flow boiling of FC72 in a single rectangular channel of 5 × 2.5 mm cross section and 101.6 mm heated length. The channel was heated from one side and flow visualization was conducted to characterize the liquid film at dryout. From the captured photographs, the wavy film characteristics were measured including vapour patch length (λ_{mea}), maximum vapour patch height (δ_{mea}), location of the upstream edge (d_{up}) and the length of liquid contacting the surface between the adjacent vapour patches (l_{mea}) as shown in Fig. 2.50. It was found from these measurements that vapour patch length increases in the streamwise direction until it reaches an asymptotic value. It was also found that, increasing the mass flux and inlet sub-cooling resulted in an increase in CHF and a decrease in the vapour patch length and height. This was believed to arise from the bulk condensation of a portion of the vapour patch. The visual observations also demonstrated that, the most commonly observed shape of the film was wave-like shape with vapour patches that grow by the newly generated vapour and the coalescence of the adjacent vapour patches. In addition to that, this wave-like shape remains attached to the wall surface. Another shape called

"overhanging" was also observed only at high inlet sub-cooling as a result of the momentum of the newly generated vapour.

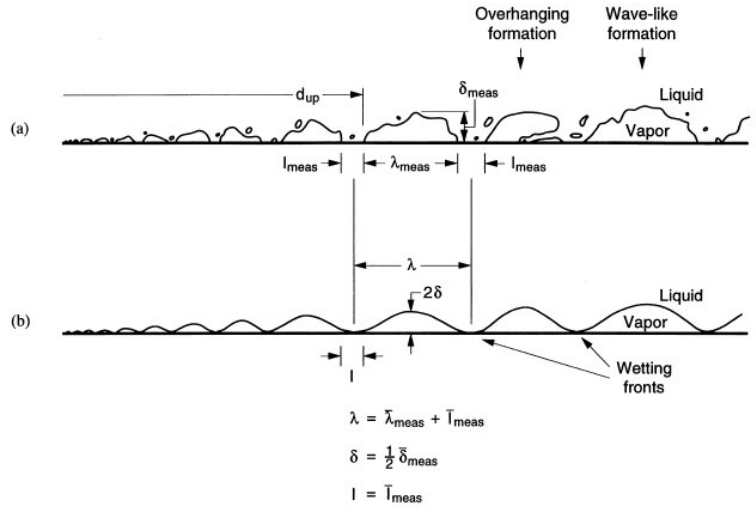

Figure 2.50 Definitions of vapour and liquid dimensions at critical heat flux: (a) real shape from flow visualization and (b) idealized shape for wavy vapour layer for modelling purpose, Sturgis and Mudawar (1999a).

Based on these experimental measurements and observations, Sturgis and Mudawar (1999b) developed a theoretical model for the predicting critical heat flux in rectangular channels. The wavy liquid vapour interface observed immediately before critical heat flux was simplified to a periodic wave-like distribution along the surface as shown in Fig. 2.49b. It was assumed that, heat transfer occurs only at the wetting fronts while the portion of channel surface underneath the vapour patch was considered adiabatic. In this model, the critical heat flux was assumed to be triggered when the momentum of vapour generated at a wetting front overcomes the pressure force holding the interface in contact with the wall surface. When this happens, the interface detaches from the surface and eliminates the wetting fronts. Accordingly, their model incorporated separated flow model principles, instability analysis, energy balance and lift-off criterion. Their assumptions were as follows: vapour layer has steady and uniform thickness at any location, vapour layer starts at the leading edge of the heated channel, vapour remains at saturation temperature, constant heat flux, phase change occurs only at channel surface and constant inlet sub-cooling. The model gave very good predictions for near saturated conditions, i.e. low inlet sub-cooling; with mean error of 10 % while

for highly sub-cooled conditions the model did not work. This was arising from the condensation effect, which was not considered in the model.

Qu and Mudawar (2004) measured the critical heat flux for de-ionized water flow in a micro-channel heat sink consisting of 21 parallel 215 × 821 μm channels. The mass flux ranged from 86 to 368 kg/m^2 s and inlet temperatures of 30 and 60 ^{0}C. It was found that, fluid inlet temperature has no effect on the critical heat flux. Increasing mass flux resulted in an increase in critical heat flux and a decrease in the exit quality at which dryout occurs. The insignificant effect of inlet temperature was reported to be unique for mini/micro-channel heat sinks compared to single mini/micro-channel. This was attributed to the observed instability prior to the critical heat flux in the multi-channels such as flow reversal into the upstream plenum. This kind of instability has resulted in a strong mixing between the vapour and the incoming fresh liquid and consequently the temperature of the fresh liquid has increased and become close to saturation. The comparison with macro-scale correlations for circular and rectangular channels showed that the correlation of Sudo et al. (1985) predicted all the data within ± 40 % and MAE of 19.8 %. Since this correlation did not include the effect of any geometrical parameters, they proposed a new correlation for water flow in multi-channels heat sinks and R113 flow in single mini/microchannels. The new correlation was based on the conventional correlation of Katto and Ohno (1984) and is given by Eq. (2.40). The MAE of this correlation was 4 % with all the data within ± 20 %. Sumith et al. (2003) investigated flow boiling of water in a vertical stainless tube of 1.45 mm diameter and 100 mm heated length and found dryout was to start first at channel exit. However the poor prediction reported above using conventional correlations, the correlation of Katto (1980) was found to consistently predict the experimental trend with slightly over-prediction by 20 %.

$$\frac{q''_{CHF}}{Gh_{fg}} = 33.43\left(\frac{\rho_g}{\rho_L}\right)^{1.11} We^{-0.21}\left(\frac{L}{D}\right)^{-0.36} \tag{2.40}$$

Owhaib et al. (2006) conducted flow boiling experiments using a quartz tube of 1.33 mm diameter and R134a as the working fluid. The tube was coated with a transparent heater in order to directly visualize the flow patterns and conduct heat transfer measurements simultaneously. They have focused on flow visualization at dryout

conditions. It was found that, dryout always occurs first at the end of the channel as seen in Fig. 2.51 that also shows how the oscillations in wall temperature looks like at dryout conditions. Additionally, CHF was found to increase with increasing mass flux and decreasing system pressure. The observed flow pattern at dryout conditions was found to be annular flow with liquid entrainments as well as the deposition of some liquid drops on tube surface. At low mass fluxes, the wavy liquid front was observed to undergo high fluctuations with a thin liquid film in between the waves. But at the location of dryout, which was found to occur at local quality of 0.58, the surface was observed to be temporarily dry and temporarily flushed by a passing liquid wave. After this location, small droplets were observed on the surface due to the evaporation of the wave front. On the other hand, the wavy liquid front was less fluctuating at high mass fluxes and the liquid film was observed to break up into small size liquid droplets before its full evaporation.

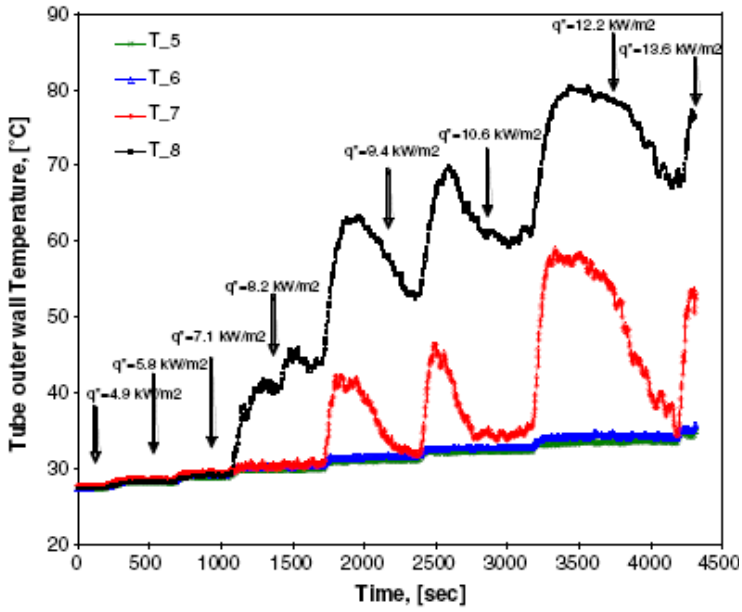

Figure 2.51 Wall temperature behaviour as a function of heat flux at G = 47.7 and p = 6.425 bar that shows dryout occurs first close from the exit at T_8, Owhaib et al. (2006).

Wojtan et al. (2006) measured the saturated critical heat flux for R134a and R245fa in micro tubes of 0.5 and 0.8 mm diameters at different mass fluxes, heated lengths, inlet

sub-cooling and saturation temperature. The critical heat flux was found to increase with increasing mass flux, increasing tube diameter and decreasing heated length. When the heated length was increased by a factor of 2.5, CHF was decreased by 67 %. Additionally, the effect of inlet sub-cooling was found to be insignificant. The comparison with the conventional correlation of Katto-Ohno (1984) gave a mean error of 32.8 % with 41.2 % of the data within 15 % while the comparison with Qu and Mudawar (2004) highly over-predicted the data but correctly captured the trend. Accordingly, they have correlated their data in a form exactly similar to the Katto-Ohno (1984) correlation but with different constants which is given by Eq. (2.41). This correlation predicted their data with mean error of 7.6 % and 82.4 % of the data located within 15%.

$$q_{CHF} = 0.437\left(\frac{\rho_g}{\rho_L}\right)^{0.073} We^{-0.24}\left(\frac{L}{D}\right)^{-0.72} Gh_{fg} \tag{2.41}$$

Zhang et al. (2006) assessed the existing CHF correlations for water flow boiling in small diameter tubes against a large database. This database was consisting of 3837 data points including sub-cooled and saturated boiling conditions, pressures ranging from 0.101 to 19 MPa, mass fluxes ranging from 5.33 to 1.34 × 10^5 kg/m^2 s, length to diameter ratio ranging from 1 to 975 and hydraulic diameters ranging from 0.33 to 6.22 mm. It was found for saturated boiling that, the correlation of Shah (1987) gave the lowest mean deviation of 20.6 % while the correlation of Hall and Mudawar (1999) was recommended to be used for sub-cooled flow boiling with a mean error of 19.2 %. In addition to the evaluation of the existing correlations, they proposed a new correlation for predicting the saturated boiling CHF. The proposed correlation was a function of four dimensionless parameters namely: L/D_h, We_L, ρ_g/ρ_L and x_{in} as given by Eq. (2.42).

$$\begin{aligned} Bo = 0.0352\left[We_L + 0.0119(L/D_h)^{2.31}(\rho_g/\rho_L)^{0.361}\right]^{-0.295} \\ \times (L/D_h)^{-0.311}\left[2.05(\rho_g/\rho_L)^{0.17} - x_{in}\right] \end{aligned} \tag{2.42}$$

Qi et al. (2007b) measured the critical heat flux of liquid nitrogen using four stainless steel tubes of 0.531, 0.834, 1.042 and 1.931 mm diameter and 250 mm heated length. The critical heat flux was detected from the reading of the last thermocouple location when the wall temperature increases rapidly. It was found that, increasing mass flux and

tube diameter resulted in an increase in the measured critical heat flux values. Also, the critical quality at which dryout occurs was found to shift to higher values when the diameter decreases. It was shifted to lower values when mass flux was increased since the high mass flux may tear the liquid film away from the wall and increase the possibility of having dryout. A comparison with the Katto correlation (1978) and the Zhang et al. correlation (2006) for mini-channels showed under-prediction for the experimental data. Accordingly, they modified the correlation of Katto as given by Eq. (2.43).

$$\frac{q_{CHF}}{Gh_{fg}} = \left(0.214 + 0.14Co\right)\left(\frac{\rho_g}{\rho_L}\right)^{0.133}\left(\frac{1}{We}\right)^{0.333}\frac{1}{1+0.03L/D} \qquad (2.43)$$

Kosar and Peles (2007) experimentally investigated critical heat flux of R123 in silicon-based microchannels of 200 × 264 μm cross section. Mass flux was varied from 291 to 1118 kg/m^2 s and pressure from 227 to 520 kPa. The channel was heated from the bottom side. It was found that, increasing the mass flux and system pressure resulted in increasing CHF. The effect of mass flux was believed to arise from the reduction in exit quality for a given heat flux when the mass flux increases. The effect of pressure seems complex since it affects many parameters such as latent heat, density ratio, surface tension and inlet sub-cooling (for same fluid inlet temperature). Increasing system pressure results in a reduction in latent heat, liquid-vapour density ratio and surface tension and also results in increasing inlet sub-cooling. Decreasing density ratio and increasing inlet sub-cooling tends to reduce the CHF. Also, decreasing surface tension and latent heat tend again to reduce the CHF. The visualization revealed that, the mechanism of CHF is dryout of the liquid film in annular flow.

Revellin and Thome (2008c) developed a theoretical model for the prediction of the critical heat flux in heated circular microchannels. This model assumed that dryout occurs in microchannels during annular flow according to two possible mechanisms. The first one is the normal depletion of the liquid film during evaporation without interfacial waves, i.e. when the film thickness becomes zero at quality x = 1. Usually, this occurs at low mass fluxes. The second mechanism was the overcoming of shear forces over surface tension forces which tears the film away from the wall and this

occurs at qualities approaching to 1 when the film is wavy. The model ignored the axial and radial conduction in the wall and it was a one dimensional model accounting for the height of the interfacial waves through applying mass, momentum and energy conservation. The model neglected the liquid entrainments into the vapour core and the effect of surface tension was incorporated using the Young-Laplace equation. Thus, they got a system of non-linear differential equations that were solved using the Runge-Kutta method according to the following boundary conditions. At the channel inlet, the minimum radius of the vapour core was set to a value of 0.1 of the tube radius, the velocity of liquid and vapour was assumed to be equal and their value was G/ρ_L, vapour pressure was taken as the saturation pressure while the liquid pressure was taken as $p_{sat} - \sigma/r_{min}$. From the solution of these equations the velocities and pressures of each phase as well as the film thickness were determined. In their program, critical heat flux was assumed to occur when the calculated liquid film thickness becomes equal to the interfacial wave height. This height was predicted assuming that it depends on (u_v/u_L) and using the Kelvin-Helmholtz critical wave length. On doing so, they got an expression for the film thickness at which dryout occurs and was given by Eq. (2.44).

$$\delta_{dryout} = 0.15R\left(\frac{u_g}{u_L}\right)^{-3/7}\left(\frac{\left(\rho_L-\rho_g\right)gR^2}{\sigma}\right)^{-1/7} \tag{2.44}$$

The comparison of the model with data fro R245fa , R134a and R113 including three different diameters and wide range of inlet sub-cooling from 2 to 77 showed very good agreement with the model at MAE of 8% and 96 % of the data within error band of 20 %. Using the developed model, Revellin and Thome (2009a) performed a parametric study to investigate the effect of fluid, saturation temperature, mass flux, inlet sub-cooling, diameter and heated length on CHF. The assessed fluids were R134a, R245fa, R236fa, FC-72 and water. Of the examined fluids, water was found to have the highest CHF with an order of magnitude followed by R245fa. This parametric study demonstrated that CHF can be enhanced by decreasing channel length, decreasing saturation temperature, increasing mass flux, increasing inlet sub-cooling and increasing channel diameter. Revellin et al. (2009) have assessed six macro and microscale correlations and also the model of Revellin and Thome (2008c) for predicting the critical heat flux. The comparison was conducted against a large data base consisting of

2996 data point and a wide range of fluids. The model predicted the data of all examined fluids except those of water with 86 % of the data with error band 30 %. The data of water were predicted well by the correlation of Zhang et al. (2006) with 83 % of the data with the same error band.

Agostini et al. (2008b) experimentally investigated the CHF of R236fa saturated flow boiling in multi-channels with hydraulic diameter of 0.336 mm. It was shown that the CHF increases with increasing mass flux where if the mass flux is doubled the CHF increases by 70 %. The effect of inlet sub-cooling on the CHF was found to be insignificant. Also, it was shown that at constant mass flux and inlet sub-cooling the CHF increased only by 15 % when the saturation temperature increased by around 69 % which is thought to be minor effects as the inlet sub-cooling. Comparing the experimental CHF data with the macro and microscale models and correlations it was depicted that the correlation of Wojtan et al. (2006) and the Revillin and Thome model (2009) predicted the data very well with 100 % of the data within ± 20 % and 10.1 mean deviation. The model of Revillin and Thome captured the trend of mass flux against critical quality, see Eq. (2.45) below, after which dryout will occur very well within ± 20 %.

$$x_{crit} = \frac{q_{CHF}}{G(h_{fg} + h_{sub})} \frac{4L}{D} \tag{2.45}$$

Kosar (2009) developed a model for predicting the critical heat flux in mini and microchannels. In this model, critical heat flux was assumed to be triggered by the dryout of the liquid film occurring at high heat fluxes. This was based on the observation at high heat fluxes where three flow patterns were found to appear along the channel namely: bubbly flow that occupied the entry region, slug flow that developed down stream the bubbly region and spray-annular flow that developed near the channel exit. With increasing heat flux, the liquid film became thinner until a permanent dry spot has formed, which trigger the critical heat flux. They applied mass conservation at a section in annular flow including both deposition and entrainment rates and then the set of equations were solved iteratively. They have compared their model against 151 data point collected from literature for mini and microchannels and fluids water, R123, R113, R134a and R245fa with a mean absolute error of 25.8 %.

Park and Thome (2010) measured the saturated critical heat flux in two different multi-micro-channel copper heat sinks using refrigerants R134a, R236fa and R245fa. One of the tested heat sinks has 20 parallel rectangular channels 467 µm wide by 4052 µm deep while the second heat sink is composed of 29 channels 199 µm wide by 756 µm deep. The length of the tested heat sinks was 30 mm of which 20 mm is heated. Each channel has an orifice at the inlet to suppress back flow and induce some flashing to overcome the high temperature overshoot required to trigger boiling. For each fluid, parameters such as saturation temperature, mass flux and inlet sub-cooling were varied. They have carried out the test by applying heat flux which is slightly lower than the expected critical value at a certain mass flux and then increased heat flux in small steps until the wall temperature increased by a certain value. They have found three different types of boiling curves. For R236fa at G = 250, T_{ast} = 35, DT_{sub} = 10 and channel depth 4052 the wall temperature steadily increased with heat flux until a sudden temperature jump from 60 to 110 occurred. On the other hand, for the same channel depth at G = 150, T_{sat} = 15, DT_{sub} = 15, R134a showed smaller temperature jump while at high G = 3000, Tsat = 25 and DT_{sub} = 3 no sudden spike of wall temperature was observed. Also, at the moment of dryout the heat flux was found to decrease as well where they mentioned that the local heat flux can vary depending on the local heat transfer coefficient, fin efficiency at that location and the heater resistance. The parametric study showed that the CHF increases with mass flux and the rate of increase decrease at high mass fluxes while also the CHF moderately increases with increasing the inlet sub-cooling. Amongst the test refrigerants R134a showed better performance from the CHF point of view as a coolant. The effect of system pressure was as follows: in the largest channel at lower mass flux the CHF increased with saturation temperature while the effect was reversed in the smallest channel at high mass fluxes. They attributed this to the adverse effects of other key parameters related to system pressure. Increasing system pressure reduces the liquid to vapour density ratio which enhances CHF while other parameters such as surface tension and latent heat decrease CHF.

2.12 Flow boiling instability

Hydrodynamics and thermal instabilities represent an important issue that should be taken into consideration during the design of micro evaporators. It has a dramatic effect on the overall system performance where in some cases system failure may occur. Once

the flow becomes unstable, all system parameters such as mass flow rate, pressures and temperatures oscillate with large amplitudes. These amplitudes reached up to about 36 ^{0}C for wall temperature as found by Wang et al. (2007) and reached 992.4 kg/m^2 s and 60 kPa for mass flux and pressure drop, respectively as found by Fu et al. (2008). Thus, the local time averaged heat transfer coefficient may be strongly influenced by these local fluctuations. Aligoodarz et al. (1998) investigated flow boiling of water at atmospheric pressure in two vertical rectangular channels of 2 × 2 mm and 2 × 1 mm cross sections. The channels were heated uniformly from three sides using a ripple free DC current while the fourth side was covered with glass for flow visualization using a colour video camera of 200 Hz speed. Local pressures were only recorded for the channel of 2 × 1 mm cross section at five axial locations on the glass side while wall temperature was measured by liquid crystal thermography (LCT). The wall temperature and flow visualization were recorded simultaneously. For the channel of 2 × 2 mm cross section at very low inlet sub-cooling and inlet Reynolds number of 720, the behaviour of wall temperature fluctuations was found to be dependent on heat flux. At low heat flux values, the local wall temperature was found to increase by 10 K since the confined bubble was observed to remain stationary for a very short time period with small axial oscillations or slow creeping. Accordingly, the evaporation of the thin liquid layer underneath the bubble during this period results in the formation of a dry patch, which is responsible for the instantaneous jump in wall temperature. When the bubble moved away from the nucleation site, fresh liquid wetted the surface and the wall temperature dropped again to a value slightly above saturation temperature. With increasing heat flux, the frequency of temperature oscillation was increased but with lower amplitudes. Furthermore, local pressure measurements demonstrated significant fluctuations that were equivalent to local variation in saturation temperature of ± 2 K. This value was comparable to the local wall superheat that in turn influences the local heat transfer coefficient. As a result of that, the authors recommended including these fluctuations in physical-based heat transfer models. Using the same facility and camera with a higher recording speed of 500 frames/s, Yan and Kenning (1998) measured local pressure fluctuations in the 2 × 1 mm cross section channel at five axial locations. Wall temperatures were recorded locally at locations opposite to those of the local pressure transducers using thin foil thermocouples instead of using LCT. Both pressure and temperature fluctuations were synchronized. Local pressure measurements indicated that bubble growth was significantly influenced by the inlet compressibility. For high

inlet compressibility, the confined bubble was found to grow axially in the upward and downward directions simultaneously until it reached channel inlet. While at low inlet compressibility, the lower end of the growing bubble was found to remain almost stationary and in the mean time other confined bubbles were created during the growth period of the previous bubble. Eventually, they indicated that the fluctuations in local pressure are thermally induced – the thing which is contrary to pressure fluctuations observed in adiabatic gas-liquid flows, which was related to specific flow patterns.

Lin and Kew (2001) investigated the relationship between pressure fluctuations and air-water flow patterns in a 1 mm diameter vertical tube. Local pressure was recorded at the same location of the high speed camera. They observed high frequency pressure fluctuation superimposed on a low frequency wave in the confined bubble pattern. These high frequency fluctuations were believed to be resulting from the passage of liquid slugs and bubbles. However, the pressure signal showed negative pulse when the liquid slug was passing that is not consistent with the passage of liquid slug. This observation led them to conclude that not only flow patterns influence local pressure fluctuations but also other factors such as the transient total flow rate may cause these fluctuations. The same behaviour was also observed in slug flow. While in churn flow, the high frequency fluctuations were dominated and the low frequency fluctuations became flat compared to confined bubble and slug flows. In annular flow dominant, the low frequency fluctuations diminished while the high frequency fluctuations were the major. Eventually, they concluded that the variation of the low frequency fluctuation with flow patterns may be taken as an indicator for identifying flow patterns but it still requires more investigations.

Brutin et al. (2003) investigated flow boiling instabilities of n-pentane in single vertical upward rectangular channels having dimensions of $0.5 \times 4 \times 50$ mm^3 and $0.5 \times 4 \times 200$ mm^3. The channels were heated from the back side and a buffer tank was installed before the channel in order to reduce the fluctuations in the mass flow rate. The measurements did not include synchronization between the measured pressure and flow visualization. At certain heat flux, a cyclic oscillatory pattern was observed with large fluctuations in the inlet and outlet pressures and temperatures. Beyond this heat flux, the oscillating phenomenon was found to disappear and the flow stabilizes again when the annular flow pattern develops. These cyclic oscillations were observed only during the

formation of the confined bubbles. During one cycle, the flow changes from single phase liquid into tiny nucleating bubbles that move downstream where they coalesce to a big bubble that span the whole channel cross section. At that moment, the bubble seems stationary and expands in upstream and downstream directions until the entire channel becomes full of vapour. When the inlet pressure becomes sufficient to overcome vapour resistance, fresh liquid enters the channel and the cycle repeats again. In other words, the cyclic nature of outlet pressure signal was arising from the cyclic nature of evacuating and refilling the channels. In addition to that, the average pressure drop under unsteady conditions was found to be much higher than the one measured under steady conditions. During this unstable boiling pattern, the inlet pressure was found to fluctuate regularly with an amplitude of 8 kPa while the outlet pressure was found to fluctuate by less than 2 kPa.

Hetsroni et al. (2004) conducted flow visualization during boiling flow of water in triangular horizontal multi channels of hydraulic diameters ranging from 0.129 to 0.161 mm. They have observed that, vapour was generated in some of the channels while some other channels remained under single phase. Focusing on a region near from the inlet plenum, unsteady flow behaviour was observed. In that region at high heat fluxes, clusters of vapour appeared as a jet penetrating the bulk flow and moving in the downstream direction resulting in an unstable annular flow which disappears after a short time interval. Accordingly, they concluded that blocking in microchannels does not take place as was expected. Wang et al (2007) investigated flow boiling instability of water flowing in a single rectangular channel and parallel multi-channels of 186 μm hydraulic diameters heated by a film heater. They observed during stable flow pattern that bubbles nucleate, grow and elongate then moves downstream towards channel exit. While during unstable boiling, bubbles were found to nucleate, grow and expand axially in both directions before the incoming fluid inertia push them towards channel exit. They attributed these instabilities to two reasons (1) the periodic growth and elongation of vapour bubbles in the upstream and downstream directions (2) flow pattern transition from bubbly to annular flow. Additionally, the oscillations in the inlet pressure was believed to occur due to the collapse of the expanding bubbles in the inlet plenum while wall temperature fluctuations was attributed to reduction in mass flux, which influences the amount of heat removed from the channel.

Qi et al (2007a) investigated flow boiling of liquid nitrogen in four cold drawn stainless steel tubes having diameters of 0.531, 0.834, 1.042 and 1.931 mm. The test sections were connected between two mixing chambers (tubes of diameters larger than test section diameter) and the flow rate was controlled by a valve located after the test section outlet. They have observed severe oscillations in temperatures, pressures, pressure drop and mass fluxes which were induced by the onset of nucleate boiling. For example, pressure drop and mass flux fluctuated with amplitude of 30 KPa and 2250 kg/m^2.s, respectively which is extremely high. The wall temperature fluctuated with amplitude of 2.9 – 9.4 K and it was in phase with pressure drop but out of phase with mass flux as seen in Fig. 2.52. The authors interpreted this behaviour as follows: after boiling incipience, small bubbles enter the mixing chamber at tube outlet where their velocity decreases due to sudden area enlargement and more bubbles accumulate inside the chamber until a large vapour patch forms. This vapour patch blocks the outlet restriction leading to a sharp decrease in mass flux which in turn increases the wall temperature and vapour quality. The sudden jump in quality due to reduction in mass flow rate results in a sudden peak in pressure drop. Once the vapour patch passes through the outlet restriction, fresh liquid enters the tube and the mass flux starts to increase again improving the heat transfer process and reducing wall temperature.

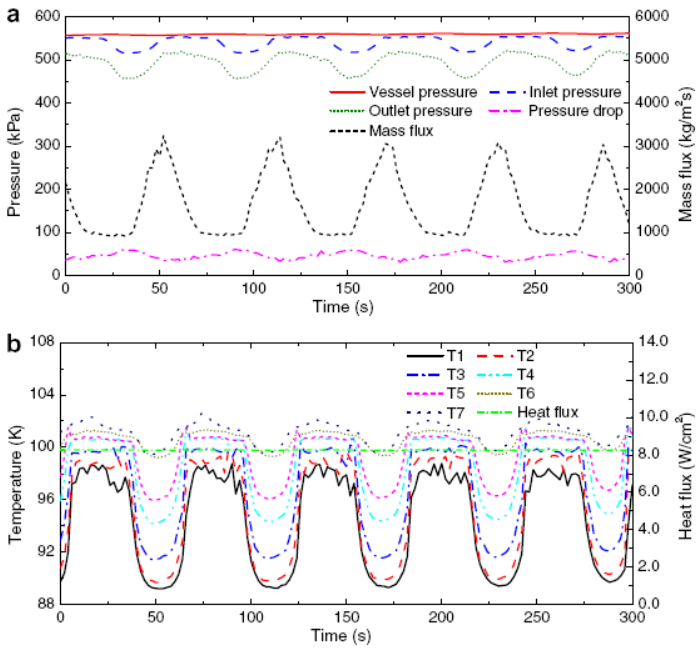

Figure 2.52 Onset of nucleate boiling induced instability during flow boiling of liquid nitrogen in vertical upward small to micro diameter tubes; (a) pressure and mass flux fluctuations, (b) temperature and heat flux fluctuations, Qi et al. (2007a)

Fu et al. (2008) used the same experimental facility and testing fluid of Qi et al. (2007a) and observed flow reversal in a vertical tube of 1.931 mm diameter. They removed the outlet restriction and added an exit calming section of similar diameter to the test section. Thus, this configuration avoided the influence of sudden area enlargement after the test section exit. Surprisingly, they observed a Taylor bubble while it was moving downward in the adiabatic visualization section as seen in Fig. 2.53. At that moment severe fluctuations in the inlet pressure were recorded and the pressure drop values became negative. Also, the observed flow patterns in one period at different heat and mass fluxes were not stable and showed alternating nature with three types. In the first type, the flow pattern changed from single phase liquid to bubbly, slug, annular, churn, slug, bubbly and again single phase liquid with annular flow as the prevailing pattern. In this type, the fluctuations amplitude of mass flux, pressure drop, wall temperature and inlet temperature were 202.8 kg/m^2 s, 5.6 kPa, 0.5 K and 0.6 K, respectively. In the second type, single phase liquid does not appear and the period started with bubbly, slug, churn and annular then the flow became bubbly again with bubbly and annular flow dominating. The oscillation amplitude during this period were found to be 650.6 kg/m^2 s, 11.9 kPa, 17.9 K and 0.2 K for mass flux, pressure drop, wall temperature, and fluid inlet temperature, respectively. In the third period, liquid and annular flows were observed alternately while bubbly, slug and churn were not. In that case, the oscillation amplitude in mass flux, pressure drop, wall temperature and fluid inlet temperature were 992.4 kg/m^2 s, 60 kPa, 6K and 1K, respectively.

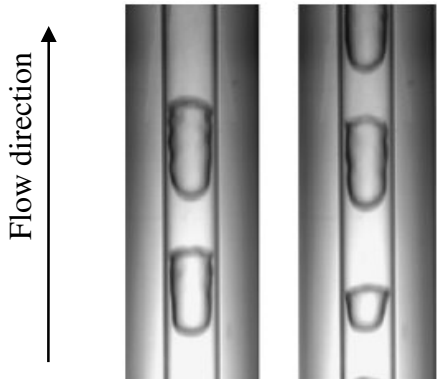

Figure 2.53 Observed flow reversal corresponding to negative pressure drop in a vertical tube of 1.931 mm diameter during flow boiling of liquid nitrogen, Fu et al. (2008)

On the contrary, Chang and Pan (2007) investigated flow boiling instabilities of water in silicon multi microchannels of 86.3 μm hydraulic diameter and observed very stable boiling at the heat flux corresponding to the onset of nucleate boiling. Beyond this heat flux flow reversal was observed with significant pressure fluctuations. Under stable boiling, the bubble length was found to increase exponentially while bubble length variations were observed under unstable conditions due to their alternating growing and shrinking. Muwanga and Hassan (2007) investigated flow boiling of FC-72 in a 1.067 mm diameter tube using liquid crystal thermography for wall temperature measurements. The recorded signal of wall temperature at low heat flux was semi-periodic with fluctuating amplitude of 1 – 5 K, which was found to increase more at high heat fluxes. It is worth mentioning that, they observed insignificant fluctuations in mass flux, fluid temperatures and pressure drop. This indicates that the fluctuation in wall temperature is not resulting from pressure drop or density instabilities. Instead, it was due to thermal oscillations where there is a thin liquid film that oscillates due to bubbles being purged at the interface. Consolini and Thome (2009) investigated flow boiling of R134a, R236fa and R245fa in micro tubes of 0.509 and 0.79 mm diameters. They presented unstable boiling case in which the wall temperature oscillated periodically by about ± 2 K and at frequency of about 4 Hz. They attributed this periodic nature to (1) local changes in fluid temperature associated with pressure fluctuations arising from bubble growth and expansion and (2) cyclic variations in the heat transfer mechanism. In this unstable case, the local heat transfer coefficient of R-134a versus vapour quality was found to be uninfluenced by wall temperature instability as shown in Fig. 2.54. On the other hand, fluctuations in wall temperature resulted in a reduction in the dependence of the heat transfer coefficient on local quality for R236fa and R245fa.

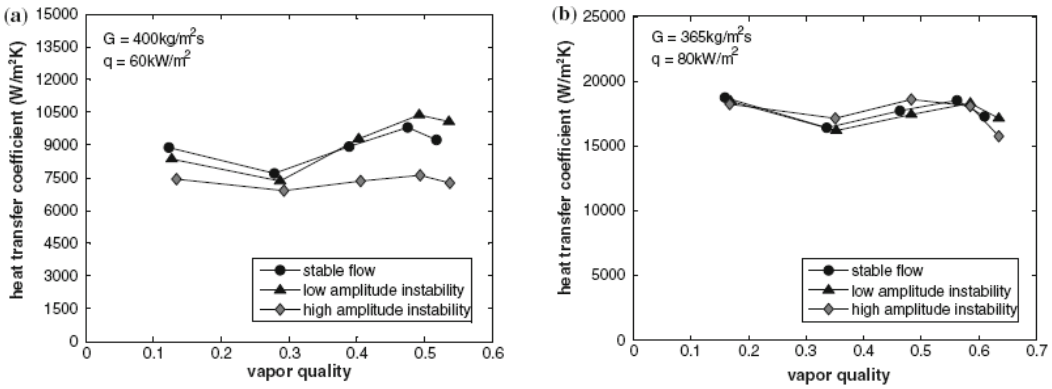

Figure 2.54 Stable and unstable behaviour of the local flow boiling heat transfer coefficient of (a) R236fa and (b) R134a; Consolini and Thome (2009).

Similar trends were reported by Ohta et al. (2009). They investigated the effect of fluctuations in flow rate on the measured flow boiling heat transfer coefficient of FC-72 in a horizontal stainless steel tube of 0.51 mm diameter. The inlet fluctuations were varied by inserting an auxiliary tank after the pump that was open to the atmosphere. When the tank was isolated from the loop, they called this condition "strictly inlet flow regulation Mode S" in which flow rate fluctuated by ± 4 % while when the tank was connected they called it "weak inlet flow rate regulation Mode W" in which the flow rate fluctuated by ± 20 %. It was found that, for the stable case, the heat transfer coefficient showed an increasing trend with increasing vapour quality, i.e. convective boiling, until dryout occurs at very high vapour quality as shown in Fig. 2.55. On the contrary, when the flow rate was unstable, the heat transfer coefficient did not show any dependence on quality before dryout where the trend remained constant with quality. Additionally, the fluctuations in wall temperature were higher in case of unstable flow rate where it reached 0.8K at the location of boiling incipience and about 2K at location close to the channel exit.

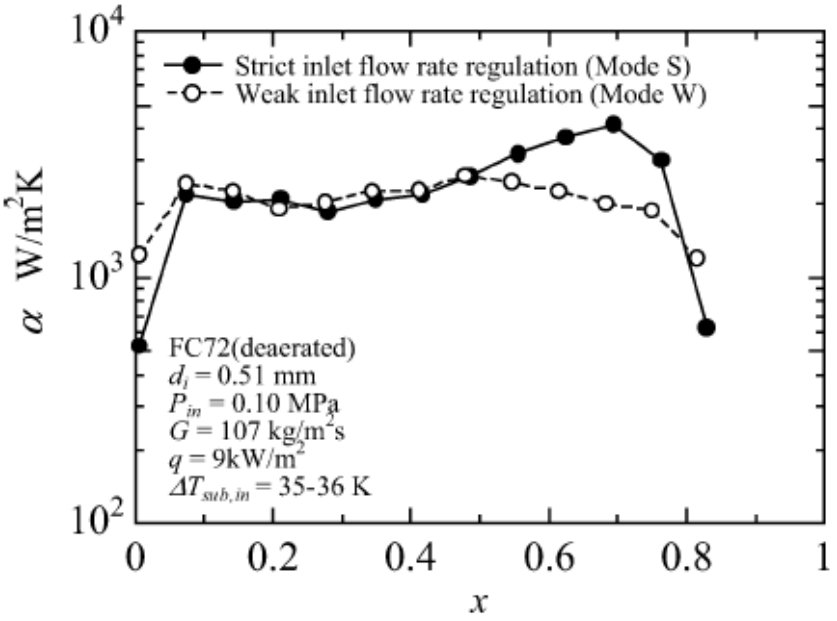

Figure 2.55 Effect of stability in flow rate on the local heat transfer coefficient of FC-72 in a 0.52 mm diameter tube, Ohta et al. (2009)

To reduce flow reversal encountered in multi microchannels, Kosar et al (2006) used rectangular orifice with a fixed width of 20 μm and variable length at each channel inlet to suppress flow instability. Their principle was to increase the ratio of pressure loss in the inlet restrictor to the major pressure loss across the channel and they called this ratio *M*. They have found that, as *M* increases, i.e. longer orifice, the heat flux at which the flow becomes unstable increases asymptotically. This means that, the longer the inlet restrictor, the wider the stability region. Kuan and Kandlikar (2007) showed experimentally that heat transfer and flow stability were enhanced for channels with inlet restrictions. In their testing module, each channel was connected to the inlet manifold through 0.127 mm diameter hole which represents 6.1 % of the channel cross section area. Lu and Pan (2008) designed their channels with a variable cross section where the channels were diverging to mitigate flow reversal. However, mild flow reversal, but not to the inlet manifolds, was still observed in some of the channels at stable flow conditions. This reversal was attributed to the high wall superheat at boiling incipience that result in rapid bubble growth.

2.13 Summary and conclusions

A detailed review about the two phase flow boiling studies in small to micro diameter channels was presented. The review covered several issues such as the flow patterns and

maps, the effect of different experimental parameters on pressure drop and heat transfer, boiling incipience, nucleation, boiling hysteresis, critical heat flux and dryout, flow instability and the prediction of heat transfer and pressure drop. The main conclusions which can be drawn from the above review are summarized below.

Flow patterns and maps

The different flow patterns observed in the above experimental studies are summarized here in Table 2.1. The bold text in the table highlights the new features/patterns that were reported as a result of the channel size reduction. The various conclusions about flow patterns and maps include the following:

1. The diminish of stratified flow in horizontal channels, Triplett et al. (1999), Coleman and Garimella (1999), Kawahara et al. (2002), Serizawa et al. (2002), Chung and Kawaji (2004), Hayashi et al. (2007), Xiong and Chung (2007), Yeom et al. (2007), Saisorn and Wongwises (2008 and 2009) and Weinmueller et al. (2009).
2. The dominance of surface tension over the gravity and buoyancy forces resulting in an insignificant effect for the channel orientation, Fukano and Karaiyasaki (1993), Suo and Griffith (1964), Chen et al. (2002) and Akbar et al. (2003).
3. The churn flow is the difficult flow regime to be characterized and there is a subjectivity problem about this regime, see for example the studies of Mishima and Hibiki (1996) and Wang and Bao (2009). Another example is the study of Chung and Kawaji (2004). They considered the "serpentine-like gas core" regime observed in the two largest tubes as a churn flow, see Table 2.1. On the contrary, for the two smallest tubes, they observed the same regime and did not call it churn flow.
4. The new flow patterns which appeared in small to micro diameter channels and considered as unique flow patterns for microchannels include the following.
    a. The "bubble-train slug flow" observed by Chen et al. (2002).
    b. The "gas core with a ring shaped liquid film" and the "serpentine-like gas core with a deformed liquid film" observed by Kawahara et al. (2002).

c. The “liquid ring flow”, the “liquid lump flow” and the “skewed flow” observed by Serizawa et al. (2002). The “liquid-ring flow” was also observed by Shiferaw (2008).
d. The “confined bubble flow” observed by Kew and Cornwell (1997) and Chen et al. (2006).
e. The “cap bubbly”, the “slug-droplet” and the annular-droplet flow regimes observed by Xu et al. (1999) in non circular channels.
f. The “elongated bubble regime” reported by Shiferaw (2008).
g. In addition to the above new flow regimes, new features were reported such as the thinning of the liquid film, the elongation of the gas slug and the diminishing of bubbly and churn flows.

5. The surface wet-ability significantly influences the morphology of the flow patterns as reported by Serizawa et al. (2002).
6. The inlet conditions in adiabatic studies may influence the features of bubbly flow as reported by Hayashi et al. (2007). Some researchers such as Mishima and Hibiki (1996) injected the gas coaxially into the tube whilst some others such as Fukano and Karaiyasaki (1993) injected the gas through three holes distributed at 120 degree intervals on the circumference. A third group such as Coleman and Garimella (1999), Triplett et al. (1999), Kawahara et al. (2002) and Serizawa et al. (2002) used a mixing chamber before the tube inlet. This might influence the transition boundary between bubbly flow and the other regimes.
7. The conventional flow patterns transition models failed to predict all the transition boundaries, Coleman and Garimella (1999), Triplett et al. (1999), Zhao and Bi (2001), Chen et al. (2005), Chen et al. (2006) and Revellin and Thome (2007a) and Revellin and Thome (2007b).
8. The effect of channel diameter on the transition boundaries may be summarized as follows:
    a. As the diameter decreases, the following transition boundaries: intermittent/bubbly, intermittent/dispersed bubble and dispersed/bubbly shifts to higher liquid superficial velocities, Coleman and Garimella (1999), Zhao and Bi (2001) and Chen et al. (2005 and 2006).
    b. There is a discrepancy about the diameter effect on the following transition boundaries: bubbly/slug, slug/churn and churn/annular. Most researchers reported that these transition boundaries shift to higher

superficial gas velocity when the diameter decreases, Coleman and Garimella (1999), Zhao and Bi (2001), Chen et al. (2005) and Chen et al. (2006) and Xiong and Chung (2007). On the contrary, Xu et al. (1999) reported an opposite effect.

9. The fluid properties, particularly surface tension, influence the location of the transition boundaries, Yang and Shieh (2001). They found that, using fluids with smaller surface tension shifts the plug/slug and the slug/annular transition boundaries to occur at lower gas superficial velocities and the bubbly/intermittent transition boundaries to occur at higher liquid superficial velocities.

Table 2.1 The observed flow patterns in small to micro diameter channels reported in past experimental studies

Flow patterns in circular microchannels		
Reference	Channel diameter and fluid	Flow patterns and comments
Mishima and Hibiki (1996)	1 – 4.08 Air – water	Bubbly, slug, churn, annular, annular mist flow • **New features were observed in the 1.05 mm tube for the bubbly and slug flow (bubbles aligned at the tube centreline and the slug became too long).**
Kew and Cornwell (1997)	1.39 – 3.69 R141b	Isolated bubble, **confined bubble**, annular-slug
Triplett et al. (1999)	1.1, 1.45 Air – water	Bubbly, slug, churn, slug-annular, annular flow • The confined bubbles were observed and considered as slug. • The churn flow included unstable elongated bubbles. • The liquid film at the bottom was slightly thicker than at the top. • **No stratified flow**
Coleman and Garimella (1999)	1.3 – 5.5 Air – water	Bubbly, dispersed bubble, stratified smooth, stratified wavy, plug, slug, wavy annular, smooth annular. • **No stratified flow for D < 5.5 mm.**
Yang and Shieh (2001)	1 – 3 Air – water R134a	Bubble, slug, plug, stratified wavy, dispersed, annular • **No stratified flow in the 1 mm tube.** • The transition boundaries were very sharp and clear for R134a compared to air-water.
Chen et al. (2002)	1, 1.5 Nitrogen – water	Bubbly, slug, **bubble-train slug flow**, churn, annular • **The bubble train-slug flow is unique for microchannels.**
Kawahara et al., (2002)	0.1 Nitrogen – water	**Liquid alone, gas core with: (a) a smooth thin liquid film, (b) a smooth thick liquid film, (c) a ring-shaped liquid film, (d) a deformed liquid film** • **Bubbly, churn and stratified flows are absent** • **The gas core with a ring-shaped liquid film and a deformed liquid film are unique for microchannels**.
Serizawa et al. (2002)	0.02 – 0.1 Air – water 0.05 Steam – water	Dispersed bubbly flow, slug flow, **liquid ring flow and liquid lump flow** (for air-water and steam-water). • In case of steam-water: (a) liquid droplets were observed sticking on the wall in the slug flow regime and (b) the liquid film in the liquid ring flow was thinner and distributed uniformly at the tube wall. • The enhancement in surface wet-ability resulted in: (a) a reduction in the bubble size in bubbly flow without bubbles coalescence, i.e. more discrete bubbles, (b) the appearance of a new pattern called "skew flow" (several bubbles connected in series) and (c) the appearance of wispy annular flow, i.e. tiny

		bubbles in the liquid film.
Chung and Kawaji (2004)	0.05 – 0.53 Nitrogen – water	For D = 0.25 – 0.53 mm: Bubbly, slug, churn, slug-annular and annular flow. • The churn flow definition included the gas core with a smooth thin liquid film and a wavy liquid film, serpentine-like gas core and streaked pattern. For D = 0.05 – 0.1 mm **Liquid alone and gas slugs with: (a) a thin-smooth liquid film, (b) a ring-shaped liquid film and (c) serpentine like gas core** • **The bubbly, churn, slug-annular and annular flows were not observed.**
Saitoh et al. (2005)	0.51 – 3.1 R134a	Plug, slug, annular flow
Chen et al. (2006)	1.1 – 4.26 1.2 R134a	Dispersed bubble, bubbly, **confined bubble**, slug, churn, annular and mist flow • The mist flow was observed only in the 4.26 mm tube • The confined bubble flow appeared first in the 2.01 mm tube at some conditions and appeared at all conditions in the 1.1 mm tube. • The 2.01 mm size was considered as a threshold between small and conventional channels.
Revellin and Thome (2007)	0.5 and 0.8 R134a and R245fa	Bubbly, bubbly-slug, slug, slug-semi-annular, semi-annular and annular flow. • The bubbly-slug and slug-semi-annular were considered as transition regimes
Fu et al. (2008)	1.931 Liquid nitrogen	Bubbly, slug, churn and annular flow • **In bubbly flow, they observed a regime called "wall-peaking bubbly flow" (tiny bubbles with a neck-like shape attached to the wall).**
Shiferaw et al. (2008)	0.52 R134a	Bubbly flow, **elongated bubble, liquid-ring**, wavy annular and annular flow.
Wang and Bao (2009)	1.6 Nitrogen – aqueous CuO Nitrogen – pure water	Bubbly, slug, churn, annular • The churn flow had features similar to the wavy film flow.
Martin-Callizo et al. (2010)	1.33 R134a Circular	Isolated bubbly flow, confined bubbly flow, slug flow, churn flow, slug-annular flow, annular flow and mist flow. • The slug-annular flow appeared at low mass flux (G = 100 kg/m^2 s) • The churn flow dominated over the slug-annular flow at most operating conditions.
Flow patterns in non circular channels		

Reference	Channel hydraulic diameter and fluid	Flow patterns and comments
Xu et al. (1999)	0.58 – 1.85 Air – water Vertical mini-gaps	For D_h = 1.14 and 1.85 mm Bubbly, slug, churn and annular flow For D_h = 0.58 mm **Cap-bubbly, slug-droplet**, churn and **annular-droplet** flow. • Bubbly flow was never observed • Slug-droplet and annular-droplet flow regimes are new regimes that appeared in this channel with dimensions 0.3 × 12 mm.
Triplett et al. (1999)	1.09 and 1.49 Air-water Semi-triangular	Bubbly, slug, churn, slug-annular and annular flow • **No stratified flow**
Zhao and Bi (2001)	0.866 – 2.886 Air-water Triangular	Dispersed bubble, slug, churn and annular flow • **The dispersed bubble flow disappeared in the channel with D_h = 0.866 mm and a new regime called "capillary bubbly flow" appeared.**
Chen et al. (2006)	0.389 FC-77 Rectangular	Bubbly, slug and alternating regime between churn and wispy annular.
Sobierska et al. (2007)	0.48 Water Rectangular	Bubbly, slug and annular
Harirchian and Garimella (2009)	0.16 – 0.749 FC-77 Rectangular	Bubbly, slug, churn, wispy-annular, annular and inverted annular flow. • **For channels with D_h < 0.4 mm, bubbly flow did not appear and slug flow established immediately after boiling incipience.**

Pressure drop

The following notes may be concluded from the past studies about the two phase pressure drop in small to micro diameter channels:

1. All experimental studies agreed on the effect of heat and mass flux, system pressure and channel diameter. The pressure drop increases with increasing heat flux (exit quality), increasing mass flux, decreasing system pressure and decreasing channel diameter. See for example the experimental studies of Tong et al. (1997), Peng et al. (1998), Yan and Lin (1998), Tran et al. (2000), Huo et al. (2007), Revellin and Thome (2007c) and Karayiannis et al. (2008).
2. The local pressure fluctuations, induced by bubble growth in boiling experiments are very significant, Wen and Kenning, (2004). They measured the local pressure fluctuations in minichannels and found that the oscillation amplitude reached about 5 kPa, which was comparable to the measured pressure drop across the channel.
3. The contribution of the transition pressure losses in the slug flow, i.e. pressure losses occurring when the liquid trapped in the film flows into the liquid slug, to the total pressure drop is more significant in horizontal flow compared to vertical flow, Fukano and Karaiyasaki (1993).
4. The homogeneous flow model performed better than the separated flow model-based correlations. This was found by Zhang and Webb (2001), Agostini et al. (2005), Lee and Mudawar (2005b), Pehlivan et al. (2006), Qi et al. (2007a), Agostini et al. (2008) and Kawahara et al. (2009).

Void fraction and film thickness

The void fraction studies were included in this review in order to contribute in explaining why most of the separated flow model-base correlations predicted the pressure drop poorly compared to the homogeneous flow model. The experimental studies included in this review measured the void fraction and compared it with the homogeneous one. The following conclusions may be drawn:

1. The measured cross sectional area-averaged void fraction agreed reasonably with the homogeneous void fraction, Mishima and Hibiki (1996), Chen et al. (2002), Serizawa et al. (2002), Chung and Kawaji (2004) and Hayashi et al.

(2007). These researchers reported also that the drift velocity at microscale is very small and can be neglected.

2. Based on the above conclusion, the slip ratio (u_g / u_L) in microchannels seems to be close to one compared to the large diameter channels. This point may explain the success of the homogeneous flow model in predicting the two phase pressure drop, which was reported in some studies.
3. On the contrary, the measured time-averaged void fraction disagreed with the homogeneous void fraction, Kawahara et al. (2002), Xiong and Chung (2007) and Fu et al. (2008). In the time-averaged void fraction estimation, the void fraction was considered zero for liquid and one for vapour. Accordingly, if the liquid was observed most frequently, the overall time averaged void fraction will be very small.
4. The bubble velocity relative to the mixture homogeneous velocity depends on the bubble length, Revellin et al. (2008a). The longer the bubbles, the higher the bubble velocity.
5. The film thickness measurements demonstrated that, the initial film thickness is controlled by the viscous force, the surface tension force and the inertia force. Accordingly, it was correlated as a function of the capillary number, the Weber number, the Bond number and the Reynolds number. As the capillary number increases (low surface tension, high viscous forces) and also as the bubble velocity increases, the initial film thickness increases. Also, the measurements indicated that there are some stratification effects in a 1.3 mm tube whilst no stratification in a 0.3 mm tube, Han et al. (2009).

Heat transfer characteristics

Nucleation in microchannels

1. Nucleation in microchannels differ from pool boiling in that, the bubbles nucleate and grow slowly compared to the rapid bubble growth in pool boiling, Kenning and Yan (2001).
2. Some researchers such as Peng et al. (1998b) and Peng et al. (2002) reported different nucleation characteristics in microchannels compared to the conventional large diameter channels. According to their view point, a “minimum evaporating space” is required for the bubbles to nucleate and grow.

When the channel size is below the required space, invisible micro-bubbles may form and the boiling process was called in that case “fictitious boiling”.

3. The mass flux, wall superheat and liquid inlet sub-cooling significantly influence the nucleation process, Kandlikar et al. (1995). As the mass flux and wall superheat increase, the range of active nucleation cavities shifts towards smaller radii, i.e. activates more nucleation sites. Decreasing the liquid inlet sub-cooling results in a too rapid nucleation. Increasing mass flux and inlet sub-cooling results in a reduction in the bubble departure diameter and frequency, Lie and Lin (2006).
4. The smoother the channel surface, the more difficult nucleation process, Lee et al. (2003). They observed few active nucleation sites in a silicon microchannel. The sites were observed only at some defects in the top cover of the channel (glass side) whilst no nucleating bubbles were observed on the other walls of the channel.

Boiling incipience in microchannels

1. The features of boiling incipience in microchannels are different compared to large diameter channels, Qu and Mudawar (2002). These features include the following:
    a. Bubbles nucleate and grow to the channel size before leaving the cavity.
    b. In sub-cooled boiling, the bubble was observed to move downstream after departing the nucleation site and collapse (condense) in the outlet plenum. This is completely different compared to the conventional channels where the bubbles nucleate, grow and condense before leaving the cavity.
    c. Some nucleating bubbles were observed on the side walls of the rectangular channels although they were heated only from the bottom side.
2. Some researchers such as Hapke et al. (2000), Ghiaasiaan and Chedester (2002), Yan et al. (2003), Qi et al. (2007a) and Martin-Callizo et al. (2007b) reported very high wall superheat at boiling incipience. Ghiaasiaan and Chedester (2002) attributed this to the large effect of the thermo-capillary force compared to the inertia force.

3. The incipience of boiling in microchannels was found to be accompanied with large fluctuations in pressure and mass flux, Hapke et al. (2000) and Qi et al. (2007a).

Boiling hysteresis in microchannels

Few studies investigated flow boiling hysteresis in small to micro diameter channels. These studies demonstrated that hysteresis exists only at very low heat fluxes in the region of boiling incipience, Lazarek and black (1981), Piasecka and Peniewski (2004), Chin and Thome (2009) and Consolini and Thome (2009).

Flow boiling heat transfer coefficient

Effect of channel diameter

The effect of channel diameter on the flow boiling heat transfer coefficient is summarized in Table 2.2 as follows:

Table 2.2 The effect of diameter on the flow boiling heat transfer coefficient (HTC).

Reference	Fluid	Diameter range, mm	Diameter effect
Kew and Cornwell (1997)	R141b	1.39, 2.87, 3.69	Unclear diameter effect
Lin et al. (2001a)	R141b	1.1, 1.8, 2.8, 3.6	• The HTC does not depend on tube diameter. • Dryout occurs at lower heat fluxes when the diameter decreases.
Kureta et al. (1998)	Water	2, 6	The HTC decreases when the diameter decreases
Yen et al. (2003)	R123, FC-72	0.19, 0.3, 0.51	Unclear diameter effect
Huo et al. (2004)	R134a	2.01, 4.26	• The HTC increases with decreasing diameter for intermediate to high heat flux values before dryout. • Dryout occurs at lower quality as the diameter decreases.
Saitoh et al. (2005)	R134a	0.51, 1.12,	• The HTC increases with

		3.1	decreasing diameter. • Dryout occurs at lower quality as the diameter decreases.
Martin-Callizo et al. (2007a)	R134a	0.83, 1.2, 1.7	The HTC increases as the diameter decreases
Karayiannis et al. (2008)	R134a	0.52, 1.1, 2.01, 2.88, 4.26	• Reducing the diameter from 4.26 – 2.88 mm does not show significant effect. • The HTC increased significantly when the diameter decreased from 2.88 – 0.52 mm. • Dryout occurs at lower quality as the diameter decreases.
Jang et al. (2008)	FC-72	2, 4	The HTC increases as the diameter decreases
Choi et al. (2009)	Propane	1.5, 3	• The HTC increases as the diameter decreases only for $x < 0.25$ whilst the effect is insignificant for $x > 0.25$. • Dryout occurs at lower quality as the diameter decreases.
Consolini and Thome (2009)	R134a, R236fa, R245fa	0.51, 0.79	The HTC increases as the diameter decreases.
Harirchian and Garimella (2008) and Harirchian and Garimella (2009b)	FC-77	0.16 – 0.75 Rectangular channels	• The HTC does not depend on the channel hydraulic diameter when the HTC was plotted versus the wall heat flux. • The HTC increases with increasing the hydraulic diameter when the HTC was plotted versus the channel base heat flux. • The maximum heat dissipation rate increases when the hydraulic diameter decreases. • There is a critical value for the channel cross section area (0.089 mm^2) below which the HTC increases with decreasing the area and above which the HTC does not change.
Peng et al. (1998)	Water Methanol	0.2 – 0.6 V-shape channels	The HTC increases with increasing the channel hydraulic diameter.

Table 4.2 indicates that, there is an agreement on the effect of diameter on the vapour quality at which dryout occurs. As the diameter decreases dryout occurs at smaller qualities. Also, most studies in the above table reported that the heat transfer coefficient increases with decreasing diameter. Few studies reported the increase of the heat transfer coefficient with increasing diameter.

Effect of mass and heat flux

The effect of mass and heat flux on the flow boiling heat transfer coefficient is summarized in Table 2.3. The table also summarizes the dominant heat transfer mechanism(s).

Table 2.3 The effect of mass and heat flux on the flow boiling heat transfer coefficient (HTC) including the dominant mechanism(s) with ↑ means increase, ↓ means decrease and ↕ means does not depend on.

Reference	Fluid	Diameter (mm)	Effect of G and q [the dominant mechanism(s)]
Lazarek and Black (1982)	R113	3.1	• HTC ↑ as q ↑ • HTC ↕ x [nucleate boiling]
Wambsganss et al. (1993)	R113	2.92	• HTC ↑ as q ↑ • HTC ↕ x and G [nucleate boiling]
Bao et al. (2000)	R11 R123	1.95	• HTC ↑ as q ↑ • HTC ↕ x and G [nucleate boiling]
Del Col et al. (2008)	R134a	0.96	• HTC ↑ as q ↑ • HTC ↕ x and G [nucleate boiling]
Lin et al. (2001a)	R141b	1.1 – 3.6	• HTC ↑ as q ↑ for $x < 0.1$ • HTC ↕ q for $x > 0.1$and ↑ as x ↑ [nucleate – convective boiling]

Sumith et al. (2003)	Water	1.45	• HTC ↑ as q ↑ for U_{gs} < 7 m/s or x < 0.05. • HTC ↕ q for x > 0.05 and ↑ as x ↑ [nucleate – convective boiling]
Diaz et al. (2005)	Water Hydrocarbons	1.5	• HTC ↑ as q ↑ in the low quality region. • HTC ↕ q and ↑ with x in the high quality region. [nucleate – convective boiling]
Chin and Thome (2009)	R134a R236fa R245fa	1.03	For R134a: • HTC ↑ as q ↑ for all x values • HTC ↑ as G ↑ except the very low quality region where the HTC ↕ G. [unclear mechanism] For R236fa and R245fa: • HTC ↑ as q ↑ in the low x region. • HTC ↕ q and ↑ as x ↑ in the high x region. • HTC ↑ as G ↑ except the very low quality region where the HTC ↕ G. [unclear mechanism in the very low x region] [convective boiling after the low x region]
Tran et al. (1996)	R12	2.46	• HTC ↑ as q ↑ for x > 0.2 and the HTC ↕ G and x. • HTC ↑ as G ↑ for x < 0.2. [convective – nucleate boiling]
Huo et al. (2004)	R134a	4.26 2.01	• HTC ↑ as q ↑ in the low to intermediate x region. • HTC ↕ q and ↓ as x ↑ in the high x region. • HTC ↕ G. [nucleate boiling] up to intermediate x Dryout occurred at high x
Martin-Callizo et al. (2007)	R134a	0.64	• HTC ↑ as q ↑ for x < 0.45 – 0.5 and the HTC ↕ x and G. • HTC ↕ q and ↓ as x ↑ in the high x

			region. [nucleate boiling] up to intermediate x Dryout occurred at high x
Saitoh et al. (2005)	R134a	0.51– 3.1	• HTC ↑ as q ↑ for x < 0.6 and the HTC ↕ x and G. • HTC ↕ q and ↑ as x ↑ for x ≈ 0.6 – 0.8. • HTC ↕ q and ↓ as x ↑ for x > 0.8. [nucleate – convective] Dryout occurred at very high x
Qu and Mudawar (2003)	Water	0.35	• HTC ↑ as G ↑ for same x. • HTC ↓ as x ↑ for same G. [convective boiling]
Yun et al. (2006)	R410	1.36, 1.44	• HTC ↕ q and G for x < 0.5. [They did not comment] Dryout occurred at very high x

Table 2.3 indicates that there are various conclusions about the dominant heat transfer mechanism. One group of researchers such as Lazarek and Black (1982), Wambsganss et al. (1993), Bao et al. (2000) and Del Col et al. (2008) reported nucleate boiling as a dominant mechanism. A second group such as Lin et al. (2001a), Sumith et al. (2003) and Diaz et al. (2005) reported *nucleate-convective* boiling mechanism. A third group such as Huo et al. (2004), Yun et al. (2005), and Martin Callizo (2007b) found nucleate boiling at low to intermediate quality values and dryout at high qualities.

Effect of system pressure and inlet sub-cooling

1. Most experimental studies presented in this review confirmed the increase of heat transfer coefficient with increasing system pressure. On the contrary, Kaew-On and Wongwises (2009) found an opposite effect for system pressure where the heat transfer coefficient decreases with increasing system pressure. Some researchers such as Agostini et al. (2008), Bang et al. (2007), Jang et al. (2008) and In and Jeong (2009) found insignificant effect for system pressure.

2. In saturated flow boiling, the liquid inlet sub-cooling does not affect significantly the heat transfer coefficient as found by Yu et al. (2002), Liu and Garimella (2007), Martin-Callizo et al. (2007a) and Agostini et al. (2008).

Critical heat flux

1. Critical heat flux mechanisms in microchannels differ from those in macrochannels as reported by Bowers and Mudawar (1994). This can be deduced from the fail of the conventional correlations in predicting CHF at microscale as found by Lazarek and Black (1982), Qu and Mudawar (2004), Wojtan et al. (2006), Zhang et al. (2006) and Qi et al. (2007b).
2. There is no agreement on the location of the onset of dryout. Some researchers reported the appearance of dryout first near the channel exit such as Lazarek and Black (1982), Sumith et al. (2003) and Owhaib et al. (2006) while Bowers and Mudawar (1994) reported that dryout appears first at an upstream location that moves downstream towards channel exit.
3. There is a common agreement on the triggering mechanism which was the detachment of the wetting fronts of the wavy liquid film in annular flow. This was believed to occur when the momentum force of the generated vapour oriented in the transverse direction becomes high enough to tear the wetting fronts away from the wall.
4. Critical heat flux is influenced by inlet sub-cooling, mass flux, system pressure, channel diameter and heated length. There is a common agreement on the mass flux effect where the CHF was found to increase with increasing mass flux. While the effect of inlet sub-cooling showed some discrepancy where some researchers reported enhancements in the CHF with increasing inlet sub-cooling such as Lazarek and Black (1982), Sturgis and Mudawar (1999a) and Revellin and Thome (2009b). On the other hand, insignificant effect for the inlet sub-cooling was found by Bowers and Mudawars, Qu and Mudawar (2004) and Wojtan et al. (2006). There is an agreement of the effect of channel diameter and heated length where increasing diameter and decreasing heated length results in an increase in the CHF. The effect of system pressure on CHF looks unclear where Park and Thome (2010) found the effect of pressure depends on mass flux and channel size, Agostini et al. (2008) and Kosar and Peles (2007) reported an

increase in CHF with increasing pressure while Owhaib et al. (2006) and Revellin and Thome (2009b) reported an opposite effect.

Flow boiling instability

1. Hydrodynamics and thermal instabilities with very high oscillation amplitudes were encountered during flow boiling in microchannels. Wall temperature oscillation amplitude as high as 36 K was measured by Wang et al. (2007) and mass flux oscillation amplitudes as high as 942 and 2250 kg/m^2 s was measured by Fu et al. (2008) and Qi et al. (2007a), respectively.
2. Local variations in saturation temperature induced by local pressure fluctuations was addressed by Aligoodarz et al. (1998) to be significant and should be taken into consideration. They measured local pressure fluctuations corresponding to ± 2 K oscillation in the local saturation temperature that is comparable to the wall superheat.
3. Most people attributed the instability to the cyclic growth of the confined bubble that was found strongly influenced by inlet compressibility, Yan and Kenning (1998). With low inlet compressibility, the bubble grew in the downstream side while flow reversal occurred with high inlet compressibility. Additionally, they reported that local pressure fluctuations mechanism under flow boiling is different from that under adiabatic conditions.
4. Stability may influence the local heat transfer behaviour. Some researchers such as Consolini and Thome (2009) and Ohta et al. (2009) found that under stable boiling conditions the local heat transfer coefficient increased with quality towards the channel exit before the occurrence of dryout while under unstable boiling the coefficient experienced little dependency on quality.
5. Flow boiling instabilities may be mitigated by designing channels with inlet restrictions or using channels with convergent cross section as proposed by Kosar et al. (2002) Kuan and Kandlikar (2007) and Lu and Pan (2008).

Chapter 3

Experimental Facility and Methodology

3.1 Introduction

As presented in the preceding chapters, several issues still need to be investigated in order to safely design micro heat exchangers for cooling high heat flux systems. These issues include: (i) the threshold diameter between macro/mini/micro-heat exchangers; (ii) the dominant heat transfer mechanism(s); (iii) the pressure drop and heat transfer prediction methods; (iv) the lack of flow boiling fundamentals. This chapter presents a detailed description for the experimental facility, the test sections, the measurement and uncertainty analysis, single phase validation and data reduction. The chapter is organised as follows: section 3.2 provides a description for the experimental facility whereas section 3.3 gives the details of the tests sections investigated in the current experimental study. Section 3.4 presents the experimental uncertainty analysis. Section 3.5 presents the data reduction and all single phase validations are given in section 3.6. Section 3.7 summarizes the chapter.

3.2 Experimental facility

The current experimental study is a part of a long term experimental program that aims at investigating flow boiling heat transfer of R134a in vertical small to micro diameter stainless steel tubes. The experimental facility was designed and constructed by X. Huo (2005) who investigated flow boiling heat transfer and pressure drop in two stainless

steel tubes having inner diameters of 4.26 mm and 2.01 mm. Using the same experimental facility and fluid, Chen (2006) conducted a detailed flow visualization study to investigate the flow boiling patterns and to develop flow maps using four stainless steel tubes having inner diameters of 4.26, 2.88, 2.01 and 1.1 mm. Shiferaw (2008) investigated flow boiling heat transfer and pressure drop in three stainless steel tubes of inner diameters 2.88, 1.1 and 0.52 mm. The experimental facility consists of two systems. The first is the R134a main system while the second is the auxiliary R22 cooling system.

3.2.1 R134a main system

Figure 3.1 and Fig. 3.2 show a schematic diagram and a photograph for the R134a main system, respectively. As indicated in Fig. 3.1, the system consists of the following components: (a) R134a tank; (b) R134a gear pump; (c) filter dryers; (d) sight glass; (e) flow meters; (f) sub-cooler; (g) pre-heater; (h) test section; (i) liquid separator; (j) R134a condenser. The tank contains most of the liquid in the system and has a total volume of 40L. Inside the tank, there is a 1 kW heater whose power is controlled by a variac and also there is a small cooling coil with a cooling capacity of 500 W. The tank is equipped with a safety valve, two sight glasses, a pressure gauge and a thermocouple. The safety valve protects the tank from excessive pressure and the sight glasses allow observing the liquid level inside the tank. The thermocouple is used to detect the vapour temperature inside the tank and thus send a signal to the PID controller to switch off the heater automatically when the temperature exceeds a certain preset value. The system pressure is controlled by the tank heater through the PID controller and the pressure stabilizes when the applied heating load to the tank heater balances with the cooling load of the cooling coil. The cooling coil inside the tank works also as a small condenser particularly when the heating load at the test section is low (in case of the smallest diameter tubes). This is to avoid the instability in system pressure that occurs when the main condenser is used. The gear pump model is 1010/028 and manufactured by Tuthill Pump Group with a flow rate of 6 L/min and 5 bar pressure head. At the exit of the pump, a bypass line with a needle valve and a filter dryer were fitted to return the extra fluid back to the tank and to avoid any over pressure that may result when micro tubes are used due to the increased flow resistance. The pump sucks the liquid from the tank and circulates it inside a closed loop. After leaving the pump, the liquid passes

through a filter dryer to remove any fine particles and moisture from the system then it passes through a sight glass, flow meters, sub-cooler, pre-heater, test section, liquid separator and condenser. The sight glass before the flow meters is to make sure that there are no bubbles or compressibility in the upstream side of the test section and the flow meters. Two models of Coriolis flow meters supplied by Micro Motion Ltd. are used to measure the flow rates. The first model is CFM010 with a range of 0 – 25 kg/h and the second model is CFM025 with a range of 0 – 500 kg/h. A three way valve was fitted before the flow meters in order to switch between the flow meters, i.e. isolate one of the meters from the flow loop while use the other for measurements. After the sight glass and before the flow meters, a thermocouple and a pressure transducer are inserted to confirm that the state of the fluid before the flow meters is single phase liquid. The flow rate is precisely controlled by a needle valve located after each flow meter. The sub-cooler located after the flow meters is a tube-in-tube heat exchanger with a maximum cooling capacity of 3.1 kW in which the R134a liquid is cooled by R22 supplied from the cooling system. The fluid temperature at the test section inlet (inlet sub-cooling) is controlled by a pre-heater located after the sub-cooler with its heating power controlled by a variac. The test section consists of an adiabatic calming section, a heated section and an observation section. Pressure and temperature at the test section inlet and outlet, pressure drop across the heated section and wall temperature are measured. In the test section, the liquid is heated up to boiling then the two phase mixture passes through a liquid separator located before the condenser in order to reduce the pressure drop in the condenser. The separated liquid returns back to the R134a tank while the vapour is sent to the condenser where it condenses and returns to the tank. The main R134a condenser is a tube-in-tube heat exchanger with a design capacity of 11.6 kW and is cooled by the R22 supplied from the cooling system. All pipes in the system are made of stainless steel that has a high corrosion resistant.

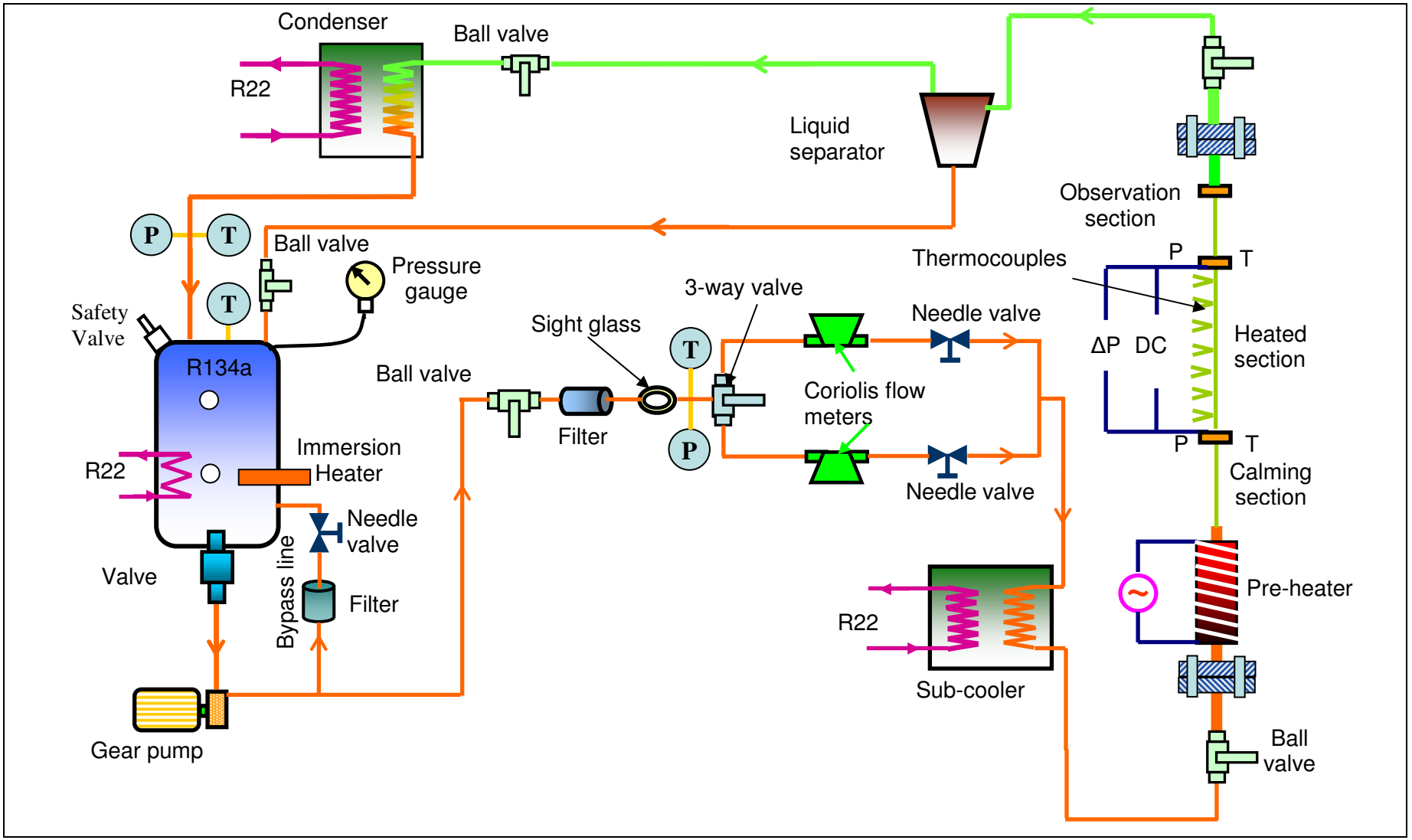

Figure 3.1 Schematic diagram of the R134a system

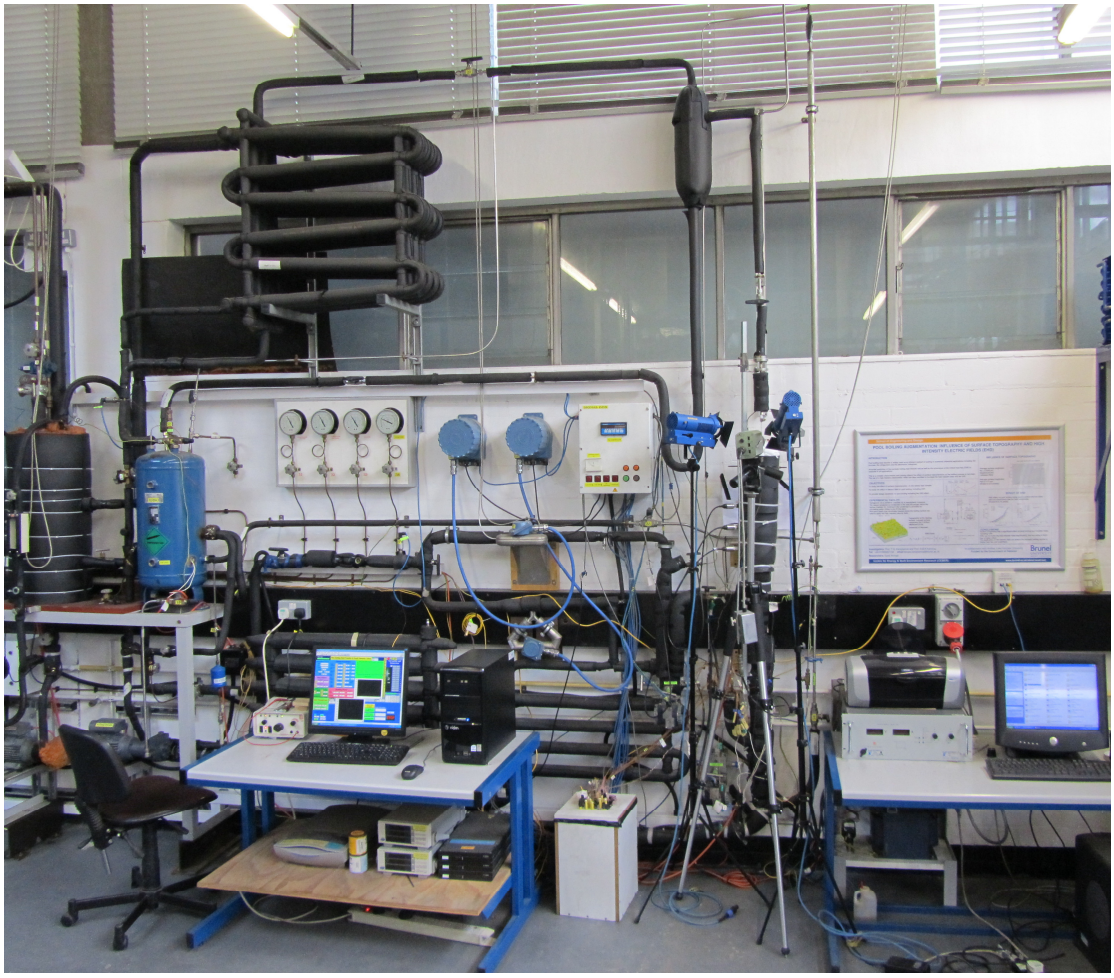

Figure 3.2 A photograph for the R134a main system

3.2.2 R22 cooling system

A schematic diagram and a photograph for the R22 cooling system are shown in Figs. 3.3 and 3.4, respectively. This cooling system supplies the cooling duties required for the R134a main system. The system is composed of the following components: (a) R22 tank which works also as an evaporator; (b) R22 gear pump which is similar to the R134a pump with a bypass line fitted at the pump exit; (c) R134a sub-cooler; (d) the R134a cooling coil inside the R134a tank; (e) R134a condenser; (f) compressor manufactured by BITZER; (g) oil separator; (h) air-cooled condenser; (i) R22 liquid

receiver; (j) filter dryer and sight glass; (h) thermostatic liquid level controller (TLLC); (k) hot gas bypass regulator.

A high pressure hot gas leaves the compressor to the oil separator in which most of the oil separates from the gas and returns back to the compressor crankcase. After leaving the oil separator, the hot gas flows to the R22 air-cooled condenser where it condenses and returns back to the R22 tank through a liquid receiver, filter dryer, sight glass, solenoid valve and a thermostatic liquid level controller. The thermostatic liquid level controller reduces the temperature of the liquid coming from the condenser down to about – 40 ^{0}C using the expansion valve which also reduces the pressure to the evaporator pressure (tank pressure). The liquid level is controlled by inserting the bulb of the expansion valve at the required position in the tank. When the level becomes lower than the position of the bulb, the temperature of the bulb increases and the gas inside the bulb expands and pushes the valve to open further and allow for more R22 liquid to flow into the tank. When the liquid covers the bulb, the temperature of the bulb decreases and the gas shrinks resulting in closing the valve and the extra liquid is stored in the liquid receiver located after the condenser. A hot gas bypass line was fitted on the compressor discharge line after the oil separator to return the hot gases into the R22 tank through a solenoid valve and a pressure regulator. The hot gas bypass line allows for the compressor to work continuously all the time regardless of the variation in the load. The regulator is set at a pressure slightly above atmospheric pressure where a value of about 2 bar was selected at which the saturation temperature inside the tank is – 25 ^{0}C. Accordingly, when the temperature inside the tank decreases to a value below – 25 ^{0}C, the pressure in the tank decreases and thus the pressure difference between the pressure in the tank and the preset pressure in the regulator pushes the hot gas valve to open and allow for more hot gas to flow into the tank. When the temperature reaches the set value, the hot gas valve closes. All solenoid valves in the system and the liquid level controller operate automatically when the compressor is switched on.

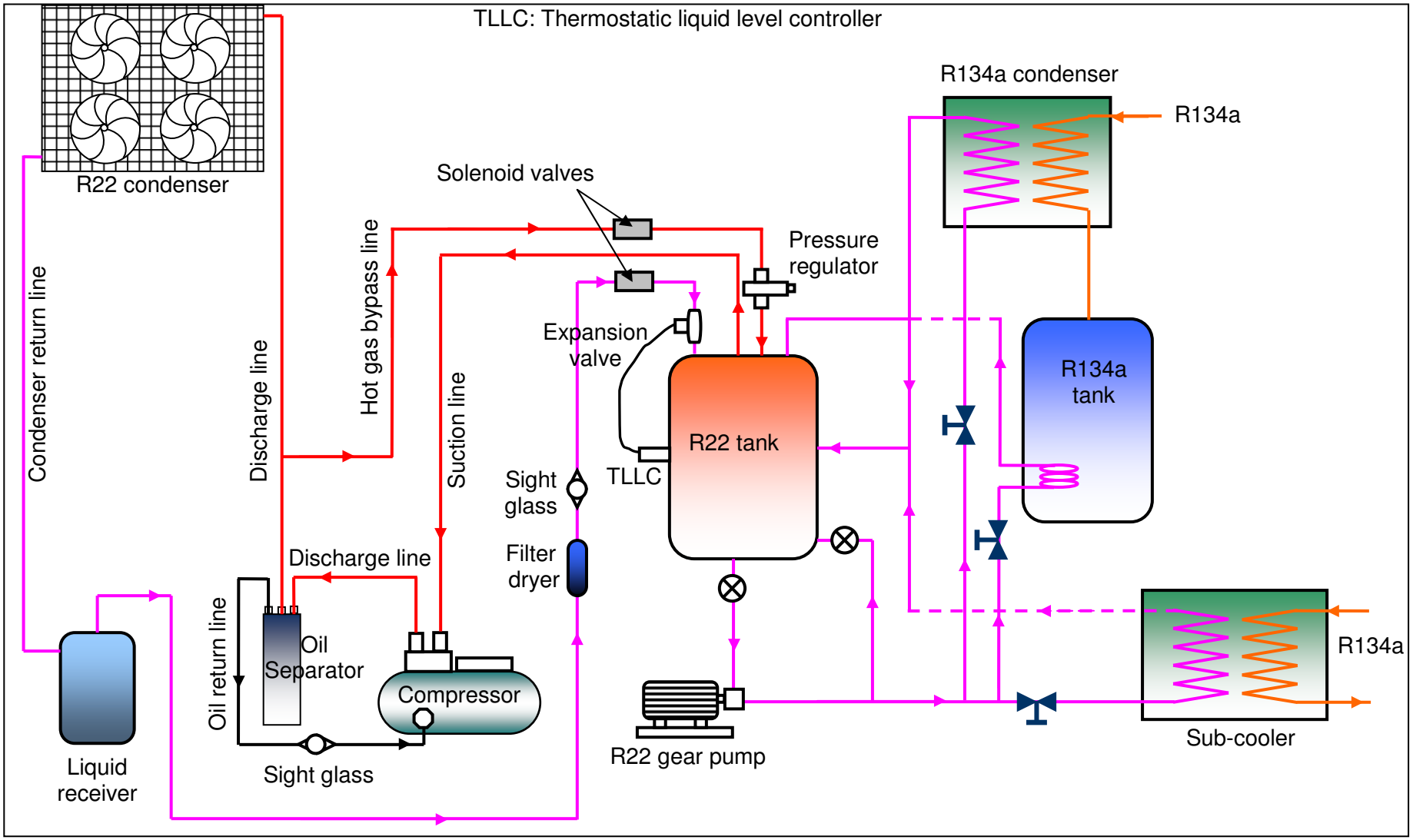

Figure 3.3 Schematic diagram of the R22 cooling system

Figure 3.4 A photograph for the R22 cooling system

The R22 gear pump sucks the cold liquid from the tank and pumps it to the R134a condenser, R134a sub-cooler and the cooling coil in the R134a tank. The flow rate of R22 supplied to these units is controlled by needle valves. Due to the fact that the efficiency of the oil separator is less than 100 % and the compressor operates continuously, most of the compressor oil settles down in the R22 tank. Therefore, an oil return system was designed to return the oil back from the R22 tank to the compressor crankcase. In this system, a mixture of R22 liquid and oil is pumped by the R22 gear pump or by a separate oil pump to a small tank where the mixture is heated and the R22 vapour goes back to the compressor suction whereas the oil settles down and returns back to the compressor crankcase through a certain valve. The oil return system is not shown in Fig. 3.3.

3.2.3 Upgrading the experimental facility

In the current experimental setup, the main R134a system was upgraded. The upgrade included the data acquisition system, the test section heating method and the method of attaching thermocouples to the test section wall. The old logging system was consisting of two models of Solartron Instruments data loggers namely SI3535F and SI35951E. All test section thermocouples were connected to the data logger SI35951E whereas all pressure transducers, differential pressure transducers, flow meters, power meters and the other thermocouples in the main system were connected to the data logger SI3535F. Also, all experimental parameters were monitored using a visual basic program developed by X. Huo (2005) and L. Chen (2006). The logging speed of this system was one data per six seconds (logging frequency of 0.167 Hz), which is relatively slow. Due to the low logging speed, only 20 data points were collected and averaged to be used in the calculations. In the current study, the old data logger SI3535F was replaced with two new data loggers from the same manufacturer (Model SI35951C) while the other data logger SI35951E was kept unchanged. Additionally, the monitoring program was changed from visual basic to Labview program. On doing so, the logging speed has been improved to 1Hz, which is six times the old logging system. Thus, the new system was programmed to collect 90 data points per 90 sec and the values used in the calculations was the average of 90 data points. Collecting more data points at a faster rate is very important in boiling experiments.

The other modification is the replacement of the AC heating system with a DC heating system. In the old heating system, AC current was supplied by a high current transformer to the test section and was controlled by a variac. The AC heating system was selected at that stage due to its lowest cost. Whereas in the current experimental system, the test section is heated using a direct current supplied by a 6 kW DC power supply. This was to avoid the possible fluctuations in wall temperature due to AC heating. The magnitude of temperature oscillations due to AC heating depends on parameters such as frequency, tube material and wall thickness. To estimate the effect of these parameters on wall temperature oscillation, a theoretical analysis was conducted in this section following the same approach of Jeglic (1962). In this analysis, the transient heat conduction equation with internal heat generation for a sinusoidally heated flat plate was solved analytically. The solution gives the transient temperature

profile at any location in the wall or the temperature profile at a given time as given by Eq. (3.1). The details of this analysis are presented in Appendix C.

$$T^*(x^*,\tau^*) = 2\sum \frac{\sin\lambda_n \cos\lambda_n x^*}{\lambda_n^2\left(\frac{1}{2}\sin 2\lambda_n + \lambda_n\right)}\left[\left(1 - e^{\frac{-\lambda_n^2\tau^*}{\omega^*}}\right) - \left(\frac{\lambda_n^4}{\lambda_n^4 + 4\omega^{*2}}\right)\left(\cos 2\tau^* + \frac{2\omega^*}{\lambda_n^2}\sin 2\tau^* - e^{-\frac{\lambda_n^2\tau^*}{\omega^*}}\right)\right] \tag{3.1}$$

The symbols in the above equation with asterisks are dimensionless parameters defined as:

$$T^* = \frac{k(T_w - T_\infty)}{qs}, \quad x^* = x/s, \quad \tau^* = \omega\tau, \quad \omega^* = \frac{\rho c_p \omega s^2}{k}, \quad h^* = hs/k \tag{3.2}$$

Where q is the heat flux defined using the effective value of the AC current ($I_{eff}^2 R/A$). The effective value of an AC current is the value that produces the same heating effect as DC current. T_w is the wall temperature, T_∞ is the fluid temperature away from the wall, s is the wall thickness, k is the thermal conductivity of the wall, x is any position in the direction of the thickness as seen in Fig. 3.5, ω is the angular frequency, ρ and c_p are the density and specific heat of the wall material, respectively, h is the convection heat transfer coefficient, τ is time and λ_n gives the eigenvalues of the characteristic equation:

$$\lambda \tan l\lambda = h^* \tag{3.3}$$

When the time parameter τ^* in Eq. (3.1) approaches infinity, the exponential terms (transient part) vanishes and the equation reduces to the steady state oscillatory part. The mina and maxima of the resulting steady state wave can be obtained by differentiating the reduced equation. Thus the magnitude of the uniform temperature

oscillations resulting from AC heating can be obtained from the difference between the maximum and minimum temperature parameters. Jeglic (1962) defined this difference as:

$$\Delta T^* = T^*_{\max} - T^*_{\min} = \frac{(T_{\max} - T_{\min})k}{qs} \tag{3.4}$$

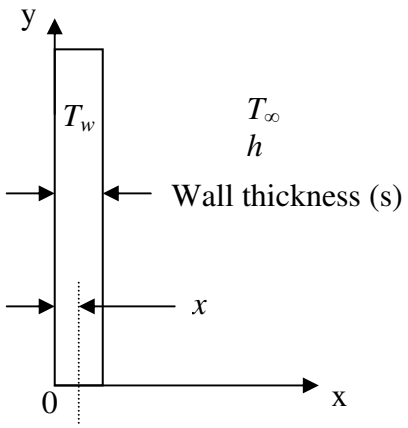

Figure 3.5 A schematic drawing for the tube wall (considered as a flat plate) used for the solution of the one dimensional transient energy equation.

Figure 3.6 presents the dimensionless uniform temperature oscillation ΔT^* as a function of the dimensionless angular frequency parameter ω^* at various Biot number h^*. The figure shows that after a certain frequency value for each Biot number, the magnitude of oscillation decreases when the frequency increases whereas it remains constant below this frequency. Additionally, the magnitude of oscillations increases with decreasing Biot number (decreasing wall thickness) at low frequency values. The aim of the analysis conducted in this section is to estimate the effect of AC heating on the wall temperature oscillations in the five tubes previously tested in this long term project. The details of the previously investigated tubes are summarized in Table 3.1. The two arrows on Fig. 3.5 refer to the frequency corresponding to wall thickness of 0.15 mm and 0.245 mm. The calculations were conducted for the stainless steel tubes with thickness of 0.15 and 0.245 mm at a frequency value of 50 Hz, heat transfer coefficient of about 19000 W/m^2 K, which was measured for R134a, and heat flux value of 120 kW/m^2. From the calculations, the magnitude of the uniform temperature oscillation $(T_{\max} - T_{\min})$ in the tube with 0.245 mm thickness is 0.05 K while that in the tube with

0.15 mm is 0.058 K. These magnitudes affect insignificantly the local wall superheat and thus the local heat transfer coefficient in flow boiling experiments. It is worth noting that when the calculations are carried for water at approximately the same heat transfer coefficient, the magnitude of temperature oscillation is much higher. For example, at heat flux value of 3 MW/m^2, the oscillation magnitude is 1.31K for the 0.245 mm thickness and 1.45K for the 0.15 mm thickness which is a big value that affects significantly the local heat transfer coefficient. This is due to the fact that, in water flow boiling experiments, much higher heat flux (heating power) is required to reach exit quality x ≈ 1 and Eq. (3.4) indicates that the oscillation magnitude increase with increasing heat flux. It can be concluded from this analysis that, AC heating has an insignificant effect on the wall temperature fluctuations in the previously investigated test sections. This is due to the fact that, the AC frequency was high enough to give low temperature oscillations as indicated in Fig. 3.6 where the dimensionless frequency value ranged from 2 to 5. The dimensionless frequency was calculated based on main source frequency of 50Hz, tube wall thickness and material properties as given by Eq. (3.2).

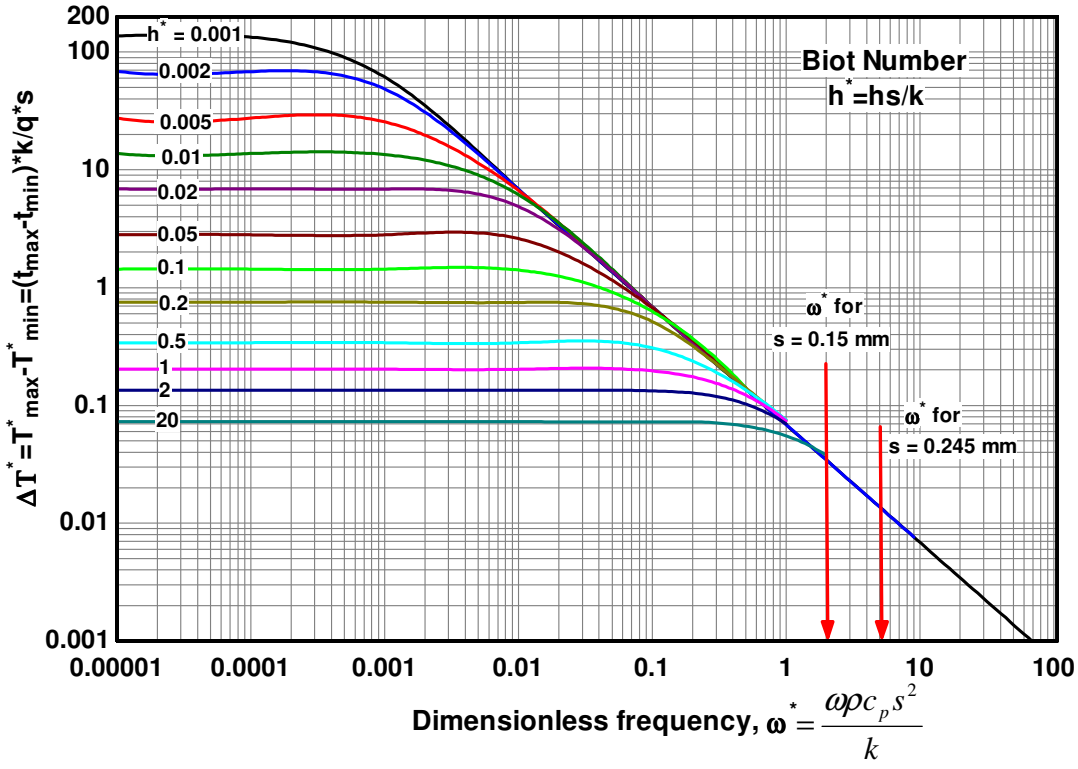

Figure 3.6 The magnitude of uniform temperature oscillation due to sinusoidal AC heating as a function of the dimensionless frequency and Biot number.

Table 3.1 The diameters and wall thickness of the previously investigated tubes

Tube No.	1	2	3	4	5
Inner diameter	4.26	2.88	2.01	1.1	0.52
Wall thickness	0.245	0.15	0.19	0.247	0.15

3.2.4 Experimental methodology

All measurements in the current study were recorded after the experimental facility reaches steady state conditions. It takes about 2 hours as a warming up period for the facility to stabilize and all signals exhibit low fluctuations. The stability issue in the current study is discussed later in the next chapter with the heat transfer results. Once it stabilizes, the mass flux and system pressure are adjusted at the required values with keeping inlet sub-cooling high enough to conduct one single phase run before the boiling experiment. The single phase experiment is used to estimate the thermal loss coefficient that is required for estimating the heat loss during the boiling tests. Since the inlet sub-cooling is high, the power of the pre-heater is increased until the sub-cooling degree reaches value of about 5K. After that, the high speed camera is adjusted and switched on and small amount of heat is supplied to the test section using the DC power supply. After applying the heat, the system is given enough time until the readings of the test section wall thermocouples reaches steady state then 90 data points are collected over 90 seconds (1Hz frequency). If boiling commences at that heat flux, the video is recorded simultaneously with the heat transfer data. After saving the data at that heat flux, a new value of heat flux is applied and the process is repeated until the exit quality reaches about 0.9 or if dryout occurs. After finalizing the last step of heat flux, the experiments are repeated through decreasing the heating power gradually at the same steps of heat flux. On doing so, the experiment at that pressure and mass flux is finished. In the next experiment, the next mass flux was adjusted at the same pressure and all the above procedures are repeated. After finishing all mass fluxes at that pressure, another system pressure value was set and all experiments are repeated in a similar way to the first pressure. In conclusion, the experiments are conducted by varying the heat flux at fixed mass flux and system pressure. The collected data are processed using an EES programs for calculating the local heat transfer coefficient.

3.3 Test sections details

In the current study, five stainless steel test sections are investigated. They include one tube of 0.52 mm inner diameter and four tubes of 1.1 mm diameters. As will be presented later in Chapter 4, the flow patterns and heat transfer results in the 0.52 mm diameter tube are different compared to those in the 1.1 mm diameter tubes. Accordingly, in the current study, the 0.52 mm size will be considered roughly as "micro" whilst the 1.1 mm size will be considered roughly as "mini". All tubes are seamless cold drawn except one minitube, which is a welded tube. The welded tube was selected to investigate the effect of inner surface characteristics on flow boiling heat transfer characteristics. The other three minitubes were designed to investigate the effect of varying the heated length on the local heat transfer behaviour. The details of the investigated test sections are summarized in Table 3.2. All test sections have similar design which is shown schematically in Fig. 3.7 and the photograph in Fig. 3.8.

Table 3.2 The test sections investigated in the current study

Inner Diameter, mm	0.52	1.16	1.1	1.1	1.1
Manufacturing process	Seamless	Welded	Seamless	Seamless	Seamless
Wall thickness, mm	0.15	0.16	0.247	0.247	0.247
Heated length, mm	100	150	150	300	450
Entry length, mm (Eq. 3.5)	52	110	110	110	110
Calming section length, mm	150	150	150	150	150

As seen in Fig. 3.7, each test section is installed vertically between two flanges and consists of a pre-heating section, an entry calming section, a heated section, an observation section and another exit calming section. In the pre-heating section, a rope heater is wrapped around a 6 mm diameter stainless steel tube and the supplied power is controlled by a variac. The entry calming section is made of the same piece of tube as

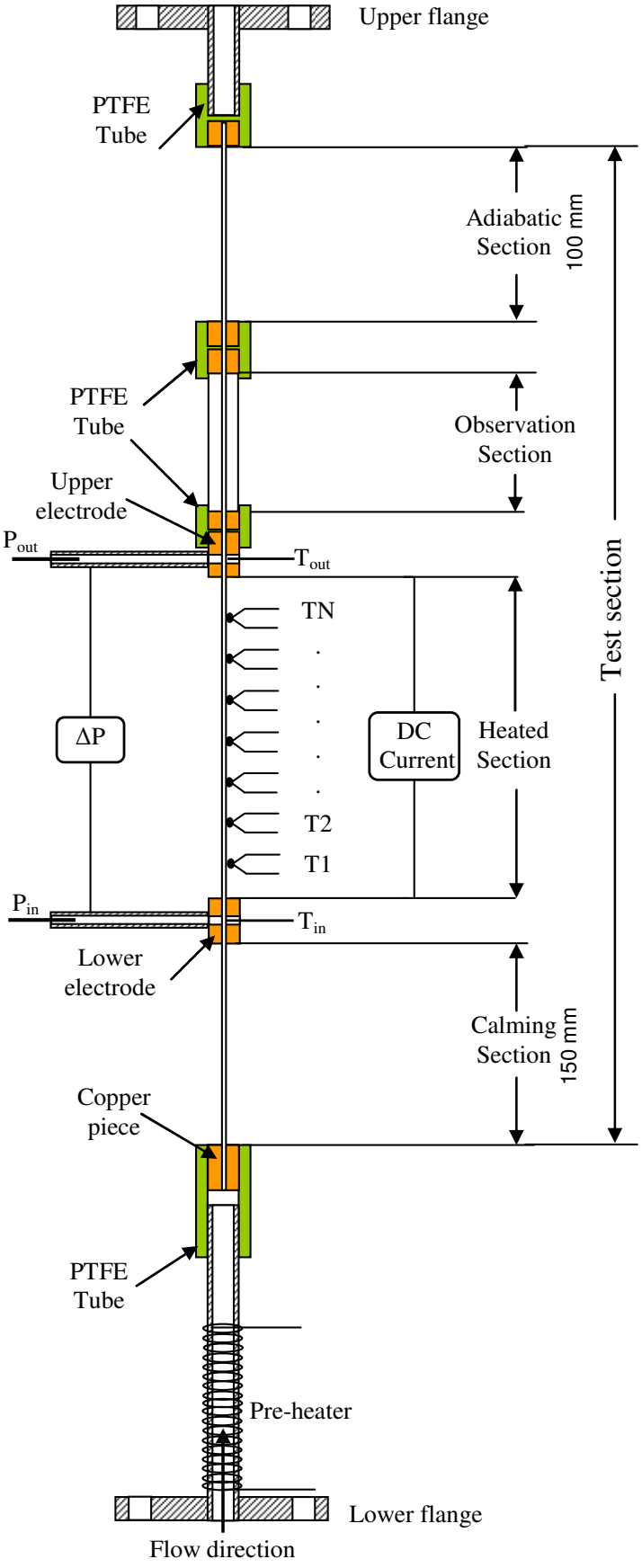

Figure 3.7 the schematic diagram of the test section

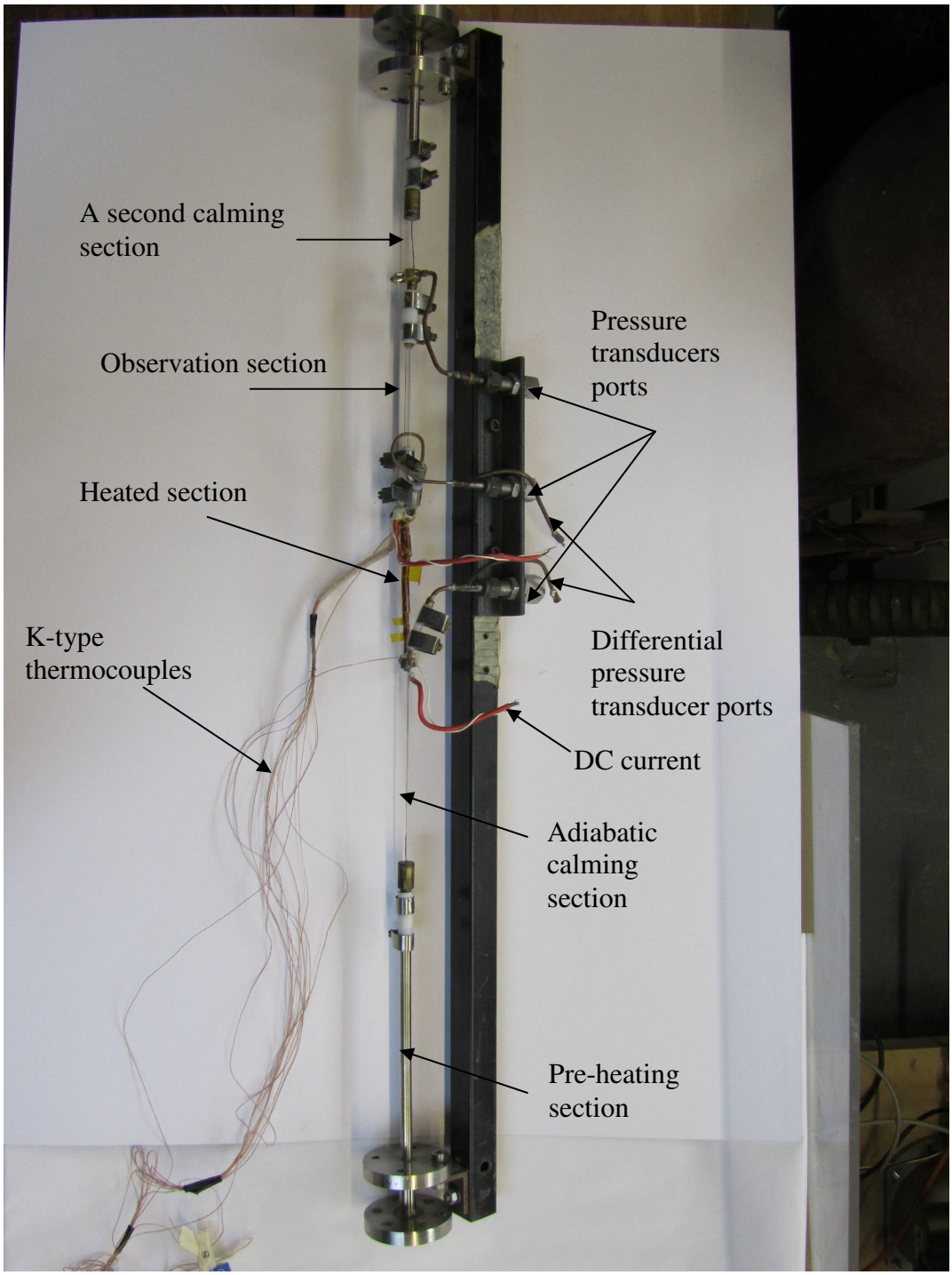

Figure 3.8 Photograph of the test section

the heated section and works as a hydrodynamic developing length before the heated section. Since the turbulent entry length is much shorter than the laminar one, the length of the entry calming section was calculated at the extreme case of Re = 2000. There are many equations for calculating the entry length in the literature. In this study, the equation cited in Incropera (2007) which is given by Eq. (3.5) was used. The difference between most of the equations was the value of the constant in the right hand side of Eq. (3.5). To avoid the uncertainty about this constant, the length of the calming section was selected to be greater than the calculated value summarized in Table 3.2.

$$\frac{L_{h,fd}}{D} = 0.05\,\mathrm{Re} \tag{3.5}$$

The heated section was directly heated by the passage of a DC electric current along the tube. The direct current was supplied by a 6 kW DC power supply *DELTA ELEKTRONIKA BV*, Model SM30-200 (0 – 30V and 0 – 200A) which is supplied by TELONIC INSTRUMENTS LTD. The two terminals from the power supply were soldered to copper pieces (electrodes) at the two ends of the heated section using soft soldering technique. The test section was electrically insulated from the other parts of the facility by PTFE connections at the two ends of the test section. The outer wall temperature was measured using K-type thermocouples and was attached at equal distances. Table 3.3 summarizes the details of all test sections wall thermocouples. For all test sections, the first and last thermocouples were attached away from the electrodes by enough spacing to avoid any possible heat losses at the electrodes. All thermocouples were attached to the wall using an electrically insulating but thermally conducting epoxy supplied by Omega. Before attaching the thermocouples, the outer surface of the tubes was covered with a thin layer of electrically insulating varnish. The pressure at the inlet and outlet of the heated section was measured using Druck pressure transducers PDCR4010 and PDCR910-0826, respectively. Also, the fluid temperature at the inlet and outlet of the heated section was measured using T-type mini hypodermic needle temperature probes supplied by Omega. Additionally, the differential pressure was measured between the two ends of the heated section using a differential pressure transducer supplied by Omega, Model PX771A-025DI.

Table 3.3 The details of the wall temperature thermocouples locations

Diameter of the test tubes, mm	0.52	1.16	1.1	1.1	1.1
Heated length, mm	100	150	150	300	450
Number of thermocouples	10	14	13	14	14
Spacing between thermocouples, mm	10	10	10	20	30
Spacing from the lower electrode, mm	5	10	15	15	30
Spacing from the upper electrode, mm	5	10	15	25	30

At the exit of the heated section, a borosilicate glass visualization section with an inner diameter similar to that of the heated section was installed for flow visualization. At this visualization section, a digital high speed camera (Photo-Sonics, Model Phantom V4 B/W, 1000 frames/s and 512 × 512 pixels) was used to record the movies of the observed flow patterns. The recorded movies are converted into pictures using the camera software to be used for further analysis in explaining the heat transfer and pressure drop results. The speed of the camera can reach up to 32000 frames/s if the lowest resolution (128 × 32 pixels) was selected. At the exit of the visualization section, an additional exit calming section made of the same tube as the heated section was installed. This was to avoid the possible effects of sudden area enlargement on the hydrodynamics of the flow patterns. The sudden area enlargement results in a sudden reduction in the flow velocity and consequently bubble velocity which might cause a propagated effect in the upstream side towards the heated section. So, the entry and exit calming sections eliminate the effects of inlet and outlet restrictions. As previously mentioned, one of the objectives of the current study is investigating the effect of inner surface characteristics using welded and seamless tubes. Therefore, a SEM analysis was conducted at Brunel University in the Experimental Techniques Centre (ETC) for a sample of the welded and seamless cold drawn tubes. Each tube sample was carefully chopped into two halves by a grinding technique without touching the inner surface. Figure 3.9 shows an example for a chopped tube sample of the welded tube prepared for the SEM examination. The results of the SEM analysis for the welded tube and the seamless cold drawn tube are shown in Fig. 3.10. In this figure, picture (a) shows for the welded tube that the surface is very smooth with the presence of fragments or debris.

On the other hand, picture (b) shows for the seamless cold drawn tube that the inner surface characteristics are completely different from those of the welded tube. The surface shows several longitudinal and uniform scratches which may play a significant role in flow boiling heat transfer characteristics compared to the welded tube. Accordingly, it was interesting to reduce the scale of the SEM into 2 μm to see whether these scratches form cavities or not. The result of this examination is depicted in Fig. 3.11 which shows one cavity (marked by a circle in the figure). The difference between the inner surface characteristics of the welded and seamless cold drawn tubes could be attributed to the effect of the manufacturing process. The fabrication of seamless cold drawn tubes starts with hot extrusion process to form the hollow shape of the tube. Since the mandrels used in the hot extrusion process have standard sizes, cold drawn process is used for further size reduction. Therefore, the longitudinal scratches on the surface of the cold drawn tube may be arising from the tensile stresses resulting from the drawing process. On the other hand, the fabrication of the welded tubes starts with rolling a strip of metal with the required thickness and joining the edges together using advanced welding techniques such as laser welding. Accordingly, if the initial metal strip is smooth, the final inner tube surface will be smooth. This may explain why the inner surface of the welded tube looks very smooth. The fragments observed on the surface may be due to the quality of welding technique, e.g. if the laser beam leaked to the inner surface for any reason, the surface may be damaged locally.

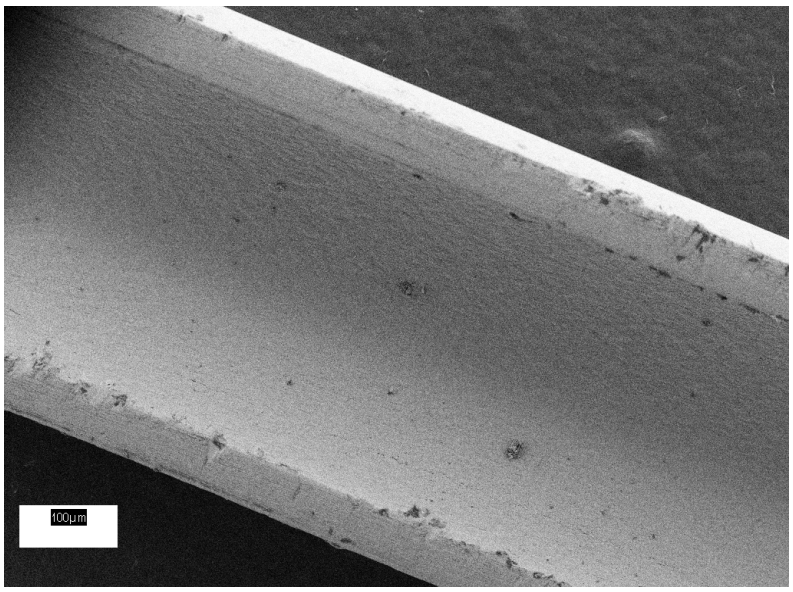

Figure 3.9 A sample of the welded tube prepared for the SEM examination by a grinding technique.

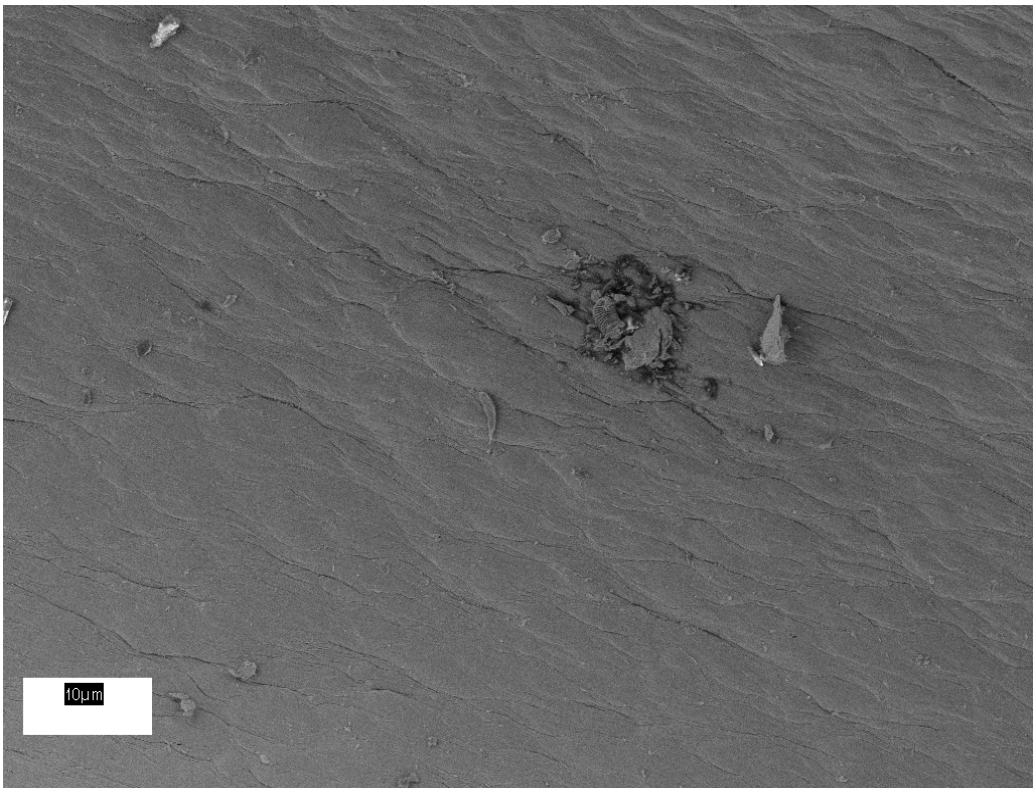

(a) The welded tube

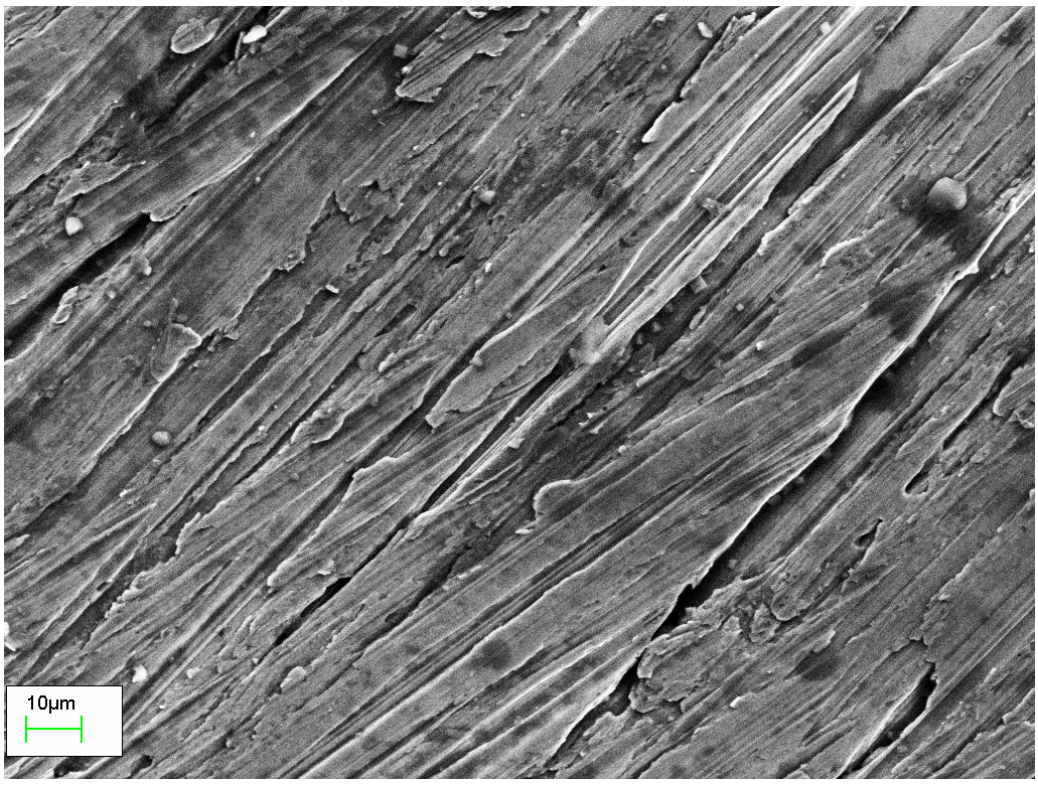

(b) The seamless cold drawn tube

Figure 3.10 SEM analyses for the inner surface of the 1.16 mm diameter welded tube and the 1.1 mm diameter seamless cold drawn tube.

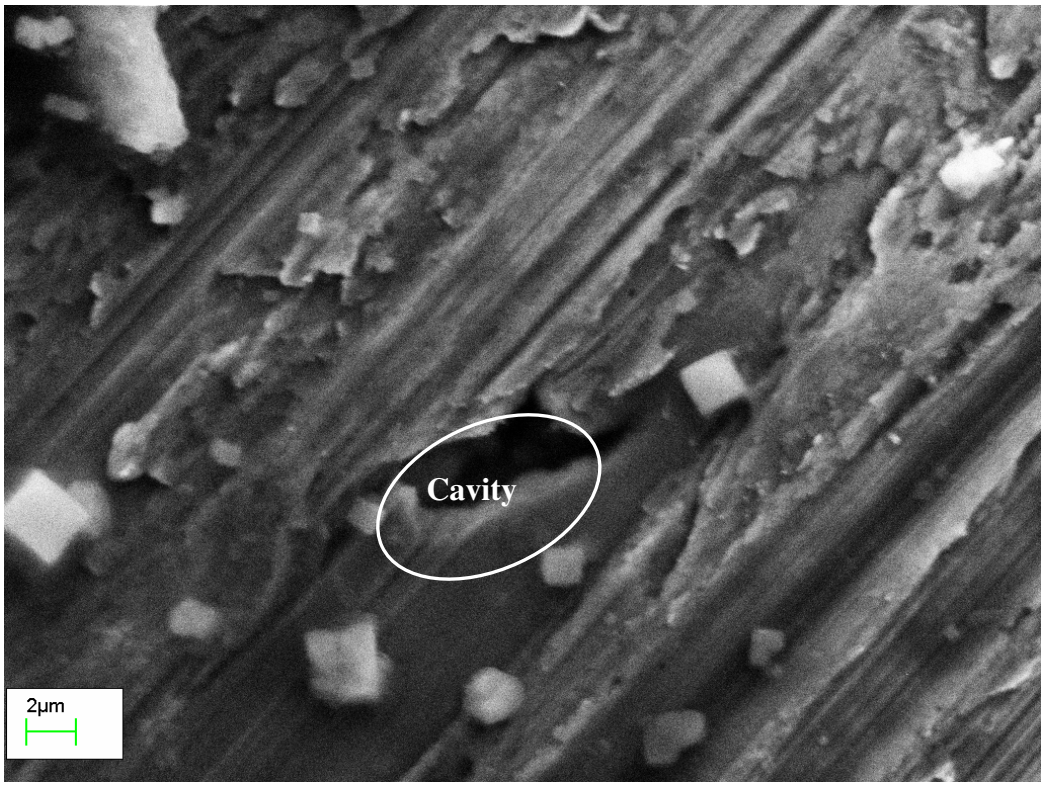

Figure 3.11 SEM analyses for the inner surface of the seamless cold drawn tube of 1.1 mm diameter that shows one cavity.

3.4 Data reduction

The whole experimental measurements in the current study aim at determining the local flow boiling heat transfer coefficient and the two phase frictional pressure drop. Since these two parameters can not be directly measured, a data reduction method should be applied to estimate these parameters. This section presents the detailed equations used to reduce the experimental data for single phase and flow boiling parameters. Single phase parameters include the friction factor and heat transfer coefficient and are used for validating the overall experimental system. All the measured parameters that are used in these calculations are the time average of 90 data points collected over 90 seconds.

Single phase friction factor

As the flow is hydro-dynamically developed in the calming section and there are no inlet or outlet restrictions, the classical equation of fully developed flow can directly be applied to calculate the single phase fanning friction factor as:

$$f = \frac{\pi^2}{32}\frac{\rho_L \Delta P_m D_i^5}{\dot{m}^2 L} \tag{3.6}$$

where f is the fanning friction factor, ρ_L is the single phase liquid density, ΔP_m is the measured single phase pressure drop, D_i is the tube inner diameter, $\dot{m}$ is the mass flow rate and L is the pressure drop length.

Heat flux

The calculation of the applied heat flux requires determining the heat loss (Q_{loss}), which is estimated from single phase experiments, measuring the DC current (I) and voltage (V) across the heated section. Thus, the heat flux is calculated from:

$$q = \frac{VI - Q_{Loss}}{\pi D_i L_h} \tag{3.7}$$

where, L_h is the heated length. The method of calculating the heat loss is given later in section 3.4.3.

Single phase heat transfer coefficient

$$h_{sp}(z) = \frac{q}{T_{wi}(z) - T_{fb}(z)} \tag{3.8}$$

The local inner surface temperature of the tube wall $T_{wi}(z)$ can be calculated by solving the steady one dimensional heat conduction equation with internal heat generation and is given by Eq. (3.9). From an energy balance, the local fluid bulk temperature $T_{fb}(z)$ can be calculated from Eq. (3.10)

$$T_{wi}(z) = T_{wo}(z) + \left(\frac{Q_v D_o^2}{16 k_w}\right)\left[1 - \left(\frac{D_i}{D_o}\right)^2 + \ln\left(\frac{D_i}{D_o}\right)^2\right] \tag{3.9}$$

$$T_{fb}(z) = T_{in} + \frac{q\pi D_i}{GAc_p} z \tag{3.10}$$

where $T_{wo}(z)$ is the local measured outer wall temperature, Q_v is the volumetric heat generation, D_o is the outer diameter, D_i is the inner diameter, k_w is the thermal conductivity of stainless steel, z is the axial distance, T_{in} is the fluid inlet temperature, A is the cross section area, G is the mass flux given by Eq. (3.11) and C_p is the liquid specific heat. For the comparison with the single phase heat transfer correlations, the local single phase heat transfer coefficient $h_{sp}(z)$ is introduced in the dimensionless form of Nusselt number *Nu(z)* given by Eq. (3.12).

$$G = \frac{4\dot{m}}{\pi D_i^2} \tag{3.11}$$

$$Nu(z) = \frac{h_{sp}(z) D_i}{k_L} \tag{3.12}$$

where k_L is the liquid thermal conductivity. Equation (3.12) was integrated with distance to obtain the average Nu number, i.e.

$$\overline{Nu} = \frac{1}{L_T} \int_0^{L_T} Nu(z)\, dz \tag{3.13}$$

where L_T is the span between the first and last thermocouples.

Two phase heat transfer coefficient

The local time averaged flow boiling heat transfer coefficient is calculated from the following equation:

$$h_{tp}(z) = \frac{q}{T_{wi}(z) - T_{sat}(z)} \tag{3.14}$$

The local saturation temperature $T_{sat}(z)$ is calculated from the local pressure $P(z)$ with the assumption that the two phase pressure drop along the tube is linear. Since the flow enters the test section under sub-cooled conditions, the length of the sub-cooled section should be taken into consideration. From an energy balance, the sub-cooled length z_{sub} can be found by iterations using Eqs. (3.15) – (3.17)

$$z_{sub} = \frac{GAc_p\left(T_{sat}(z_{sub}) - T_{in}\right)}{q\pi D_i} \tag{3.15}$$

$$\Delta P_{sp} = \frac{G^2}{\rho_L}\frac{2f}{D_i} z_{sub} \tag{3.16}$$

$$P(z_{sub}) = P_{in} - \Delta P_{sp} \tag{3.17}$$

$$\Delta P_{tp} = \Delta P_m - \Delta P_{sp} \tag{3.18}$$

$$P(z) = P(z_{sub}) - \frac{z - z_{sub}}{L_h - z_{sub}} \Delta P_{tp} \tag{3.19}$$

where $T_{sat}(z_{sub})$ and $P(z_{sub})$ are the saturation temperature and pressure at the location of zero quality, ΔP_{sp} is the single phase pressure drop, P_{in} is the inlet pressure and ΔP_{tp} is the two phase pressure drop. The average two phase heat transfer coefficient is calculated from:

$$\overline{h_{tp}} = \frac{1}{L_T}\int_0^{L_T} h_{tp}(z)\, dz \tag{3.20}$$

Local vapour quality

$$x(z) = \frac{h(z) - h_f(z)}{h_{fg}(z)} \tag{3.21}$$

The local enthalpy of saturated liquid $h_f(z)$ and the local latent heat $h_{fg}(z)$ are calculated based on the local pressure given by Eq. (3.19). The local enthalpy $h(z)$ at position z can be calculated from an energy balance up to this position as:

$$h(z) = h_{in} + \frac{q\pi D_i z}{GA} \tag{3.22}$$

where h_{in} is the inlet enthalpy that is estimated using the measured inlet pressure and temperature.

Two phase frictional pressure drop

The two phase experimental frictional pressure drop is calculated from the following equation:

$$\Delta P_{tp,f} = \Delta P_m - \Delta P_{sp} - \Delta P_g - \Delta P_{acc} \tag{3.23}$$

The single phase pressure drop component is calculated using Eq. (3.16). For the acceleration component ΔP_{acc} and the gravitation component ΔP_g, a correlation for void fraction is required. In the current study, for comparison purpose, the void fraction correlation that was used in the model with which the data are compared was used. In other words, each model was taken as a package that includes its own void fraction correlation. For example, the homogenous void fraction given by Eq. (3.24) is used when the experimental data are compared with the homogenous model. Thus, the acceleration and gravitation components estimated from the homogeneous model are given by Eqs. (3.25) and (3.26), respectively.

$$\alpha_H = \frac{1}{1 + \frac{1-x}{x}\frac{\nu_L}{\nu_g}} \tag{3.24}$$

$$\Delta p_{acc} = G^2 x v_{fg} \tag{3.25}$$

$$\Delta p_g = \frac{Lg\sin\theta}{v_{Lv}x}\ln\left[1 + x\frac{v_{Lv}}{v_L}\right] \tag{3.26}$$

On the other hand, when the experimental data are compared with the separated flow model, the acceleration and gravitation components are given by:

$$\Delta p_{acc} = G^2 v_L \left[\frac{x^2}{\alpha} \frac{v_g}{v_L} + \frac{(1-x)^2}{1-\alpha} - 1 \right] \tag{3.27}$$

$$\Delta p_g = \frac{Lg \sin\theta}{x} \int_0^x [\alpha \rho_g + (1-\alpha)\rho_L] dx \tag{3.28}$$

In Eqs. (3.27) and (3.28) several void fraction correlations can be used for α depending on the model. For example, the Lockhart-Martinelli void fraction correlation given by Eq. (3.29) is used with the Lockhart-Martinelli model whereas Chisholm's void fraction correlation given by Eq. (3.30) is used with the Chisholm model. For more details about the void fraction correlations, see Woldesemayat and Ghajar (2007) who presented and assessed 68 different void fraction correlations for different flow patterns and tube orientations.

$$\alpha_{LM} = \frac{1}{1 + X_{LM}} \tag{3.29}$$

where:

$$X_{LM} = 0.28 \left(\frac{1-x}{x} \right)^{0.64} \left(\frac{\rho_g}{\rho_L} \right)^{0.36} \left(\frac{\mu_L}{\mu_g} \right)^{0.07}$$

and

$$\alpha_{CH} = \frac{1}{1 + X_{CH}} \tag{3.30}$$

where:

$$X_{CH} = \left(\frac{1-x}{x} \right) \left(\frac{\rho_g}{\rho_L} \right) \sqrt{1 - x \left(1 - \frac{\rho_L}{\rho_g} \right)}$$

3.5 Propagated uncertainty analysis

The total error in a measured quantity is the sum of systematic errors (bias) and random errors (precision). The systematic errors are those fixed errors (repeatable) that result from a fault in the measuring instruments and can be reduced by calibration. The random errors are not repeatable, result from unknown influences and can be reduced by increasing the sample size (multiple readings). These random errors are usually estimated using statistical analysis assuming that a sample of *N* measurements follows normal or Gaussian distribution with a certain confidence level. Coleman and Steele

(1999) proposed 95 % confidence level to calculate the random uncertainty of a measured variable X as follows:

$$u_{random} = t_{95\%} S_X \tag{3.31}$$

$$S_X = \sqrt{\frac{1}{N-1}\sum_{i=1}^{N}(X_i - \overline{X})^2} \tag{3.32}$$

$$\overline{X} = \frac{1}{N}\sum_{i=1}^{N} X_i \tag{3.33}$$

where $t_{95\%}$ is the value from the *t* distribution that achieves 95 % confidence level, S_X is the standard deviation of the sample population and $\overline{X}$ is the mean value. On the other hand, the systematic uncertainty of the measured variable X is calculated as a root sum square RSS given by Eq. (3.34).

$$B_X = \sqrt{\sum_{k=1}^{M}(B_X)_k^2} \tag{3.34}$$

where $(B_X)_k$ is the bias resulting from the element k, i.e. calibration, data acquisition, etc…, and can be estimated from the specifications given by the manufacturer. According to the ISO guide (1993) cited in Coleman and Steele (1999), the overall uncertainty (U) of a measured variable is given as:

$$U = t_{95\%} u_c \tag{3.35}$$

where u_c is the combined uncertainty (systematic and random uncertainties) given by Eq. (3.34).

$$u_c = \sqrt{S_{BX}^2 + S_X^2} \tag{3.36}$$

where S_{BX} is the standard deviation of the systematic uncertainty given as:

$$S_{BX} = B_X / 2 \tag{3.37}$$

For a variable r defined by Eq. (3.38) which is a function of j measured variable X, the error propagation can be calculated using Eq. (3.39).

$$r = r(X_1, X_2, \ldots\ldots\ldots X_j) \tag{3.38}$$

$$U_r^2 = \left(\frac{\partial r}{\partial X_1}\right)^2 U_{X_1}^2 + \left(\frac{\partial r}{\partial X_2}\right)^2 U_{X_2}^2 + \ldots\ldots\ldots\ldots + \left(\frac{\partial r}{\partial X_j}\right)^2 U_{X_j}^2 \tag{3.39}$$

Equation (3.39) gives the absolute uncertainty and can also be written in a dimensionless form given by Eq. (3.40) to give the relative uncertainty.

$$\frac{U_r^2}{r^2} = \left(\frac{X_1}{r}\frac{\partial r}{\partial X_1}\right)^2 \left(\frac{U_{X_1}}{X_1}\right)^2 + \left(\frac{X_2}{r}\frac{\partial r}{\partial X_2}\right)^2 \left(\frac{U_{X_2}}{X_2}\right)^2 + \ldots\ldots + \left(\frac{X_j}{r}\frac{\partial r}{\partial X_j}\right)^2 \left(\frac{U_{X_j}}{X_j}\right)^2 \tag{3.40}$$

Following the above approach given by Coleman and Steele (1999), the propagated uncertainty analysis for all parameters was carried out and presented below. The ranges of experimental parameters covered in this study are summarized in Table. 3.4. The uncertainty in each measured quantity is summarized in Table 3.5.

Table 3.4 The ranges of experimental parameters

Parameter	Range
Inner diameter, [mm]	0.52, 1.16, 1.1 mm
Heated length, [mm]	100, 150, 300, 450 mm
System pressure, [bar]	6, 8, 10
Mass flux, [kg/m^2 s]	100 – 500
Heat flux, [kW/m^2]	1.8 – 159
Exit quality, [-]	0 – 0.95
Inlet sub-cooling, [K]	5

Table 3.5 The uncertainty value in each measured parameter

Parameter	Measuring instrument	Uncertainty
Outer diameter	Micrometer	± 0.01 mm
Heated length	Vernier calliper	± 0.1 mm
	Tape meter	± 1 mm
DC voltage	Yokogawa power meter WT110	± 0.2 % (manufacturer)
DC current		
Mass flow rate	Coriolis flow meters (CMF010 and CMF025)	± 0.044 % (manufacturer)
Test section inlet pressure	DRUCK PDCR4010	± 0.42 % (calibration)
Test section outlet pressure	DRUCK PDCR910-826	± 0.26 % (calibration)
Observation section outlet pressure	DRUCK PDCR910-826	± 0.26 % (calibration)
Fluid temperature	T-type thermocouples	± 0.08K (calibration)
Wall temperature	K-type thermocouples	± 0.22K (calibration)
Differential pressure transducer	PX771A-025DI	± 0.07 % (calibration)

3.5.1 Tube inner diameter and heated length

The inner diameter of the investigated tubes D_i was estimated using the same method reported in Chen (2006). It was calculated through measuring the outer diameter D_o, length L and mass M of a sample of each tube. The length and diameter were measured using a Vernier Caliper with an uncertainty of ± 0.01mm while the mass was measured using a digital balance scale with a resolution of five decimal digits or uncertainty of ± 0.00001g. The inner diameter was calculated as follows:

$$\frac{\pi}{4}\left(D_o^2 - D_i^2\right)L = \frac{M}{\rho} \tag{3.41}$$

$$D_i = \sqrt{D_o^2 - \frac{4M}{\pi \rho L}} \tag{3.42}$$

Assuming there is no uncertainty in the material density ρ, the absolute uncertainty in the inner diameter can be calculated according to Eq. (3.39) as:

$$U_{D_i} = \left(D_o^2 - \frac{4M}{\pi\rho L} \right)^{-1/2} \cdot \sqrt{\left(D_o U_{D_o}\right)^2 + \left(\frac{-2}{\pi\rho L} U_M \right)^2 + \left(\frac{2M}{\pi\rho L^2} U_L \right)^2} \tag{3.43}$$

The uncertainties in the inner diameter of the investigated tubes are summarized in Table 3.6. The lengths of the samples were measured using Vernier calliper with the uncertainty of ± 0.01 mm. The heated length of the shortest tube (0.52 mm) was measured using the Vernier calliper while a metric tape measure with an uncertainty of ± 1 mm was used for measuring the heated lengths of the long test sections.

Table 3.6 The uncertainties in the inner diameters of the investigated test sections

Calculated inner diameter, mm	Uncertainty, %
0.52, seamless cold drawn	± 3.017
1.1 (seamless cold drawn)	± 1.28
1.16 (welded)	± 1.1

In the current study, the same borosilicate glass visualization tubes that were used by Shiferaw (2008) were also used. The diameters of these tubes were measured using the same method as the stainless steel test sections and also using an optical microscope. The uncertainties in the 0.52 and 1.1 mm glass tubes were 0.19 and 0.36 %, respectively.

3.5.2 Mass flux

The mass flux is calculated from Eq. (3.11) which is a function of the measured mass flow rate and tube inner diameter. Hence, the propagated uncertainty can be calculated using Eq. (3.44). Table 3.7 presents the mass flux ranges covered in the current experiment with the uncertainty values.

$$U_G = \sqrt{\left(\frac{4}{\pi D_i^2} U_{\dot{m}}\right)^2 + \left(-\frac{8\dot{m}}{\pi D_i^3} U_{D_i}\right)^2} \tag{3.44}$$

Or

$$\frac{U_G}{G} = \sqrt{\left(\frac{U_{\dot{m}}}{\dot{m}}\right)^2 + \left(2\frac{U_{D_i}}{D_i}\right)^2}$$

Table 3.7 Uncertainty values in mass flux

Test section diameter, mm	Mass flux range	Uncertainty %
0.52	300 – 700	6.03
1.16, welded	200 – 500	2.56
1.1, seamless cold drawn	100 – 500	2.2

3.5.3 Heat flux

The uncertainty in the heat flux is due to the uncertainty in the measured voltage (V), current (I), heat loss (Q_{loss}), inner diameter (D_i) and heated length (L) as given by Eq. (3.7). But, the uncertainty in the heat loss is not known and it should be estimated first. The heat loss was estimated following the same approach of Huo (2005), Chen (2006) and Shiferaw (2008) as follows:

$$Q_{loss} = C_L \overline{\Delta T} \tag{3.45}$$

$$\overline{\Delta T} = \frac{1}{N}\sum_{J=1}^{N} T_{w,J} - T_{ins,o} \tag{3.46}$$

where $\overline{\Delta T}$ is the average temperature difference between the inner and outer surface of the insulation, $T_{w,J}$ is the local measured tube wall temperature, $T_{ins,o}$ is the insulation outer surface temperature measured using a K-type thermocouple and C_L is a thermal loss coefficient estimated from the single phase experiments as:

$$C_L = \frac{VI - \dot{m}c_p(T_{out} - T_{in})}{\overline{\Delta T}} = \frac{VI - \dot{m}c_p \Delta T_L}{\overline{\Delta T}} \tag{3.47}$$

According to Eq. (4.45), the uncertainty in the thermal heat loss is given by Eq. (3.48) which is due to the uncertainty in the calculated loss coefficient and the uncertainty in the average temperature difference $\overline{\Delta T}$.

$$U_{Q_{loss}} = \sqrt{\left(\overline{\Delta T} U_{C_L}\right)^2 + \left(C_L U_{\overline{\Delta T}}\right)^2} \tag{3.48}$$

The uncertainty in the average temperature difference $\overline{\Delta T}$ is given as:

$$U_{\Delta T_1} = \sqrt{\frac{1}{N}\sum_{J=1}^{N}\left(U_{T_{w,J}}\right)^2 + \left(-U_{T_{ins}}\right)^2} \tag{4.49}$$

Using the uncertainty value of ± 0.22 K for the wall temperature and ± 0.16 K for the insulation outer surface temperature, the uncertainty in the average temperature according to Eq. (4.49) is 0.27 K. The remaining unknown is the uncertainty in the loss coefficient, which can be calculated according to Eq. (3.47) as:

$$U_{C_L} = \sqrt{\left(\frac{I}{\overline{\Delta T}} U_V\right)^2 + \left(\frac{V}{\overline{\Delta T}} U_I\right)^2 + \left(-\frac{c_p \Delta T_L}{\overline{\Delta T}} U_{\dot{m}}\right)^2 + \left(-\frac{\dot{m}c_p}{\overline{\Delta T}} U_{\Delta T_L}\right)^2 + \left(-\frac{\dot{m}c_p \Delta T_L}{\overline{\Delta T}^2} U_{\overline{\Delta T}}\right)^2} \tag{3.50}$$

The above equation gives an uncertainty value of ± 0.014 W/K for the loss coefficient. Using Eq. (3.48) and the uncertainty value in C_L and $\overline{\Delta T}$, the uncertainty in the heat loss is ± 0.12 W. Based on the above equations, the uncertainty in the applied heat flux is given by Eq. (3.51) and the values are summarized in Table 3.8 for all test sections.

$$U_q = \sqrt{\left(\frac{I}{\pi D_i L} U_V\right)^2 + \left(\frac{V}{\pi D_i L} U_I\right)^2 + \left(-\frac{1}{\pi D_i L} U_{Q_{loss}}\right)^2 + \left(-\frac{q}{D_i} U_{D_i}\right)^2 + \left(-\frac{q}{L} U_L\right)^2} \quad (3.51)$$

Table 3.8 The uncertainty values in heat flux for all test sections

Test section diameter, mm	Heat flux range, kW/m^2	Uncertainty %
0.52	2.6 – 126.8	1.95
1.16, welded	2.4 – 110.7	0.94
1.1, seamless (L = 150 mm)	3.4 – 158.7	0.97
1.1, seamless (L = 300 mm)	0.9 – 86.2	0.96
1.1, seamless (L = 450 mm)	1.8 – 49.4	0.95

3.5.4 Heat transfer coefficient

The uncertainty in the heat transfer coefficient defined by Eq. (3.14) can be given as:

$$U_h = \sqrt{\left(\frac{U_q}{\Delta T}\right)^2 + \left(-\frac{\alpha}{\Delta T} U_{\Delta T}\right)^2} \quad (3.51)$$

Where the temperature difference ΔT for single phase heat transfer coefficient is defined as $T_{W_i} - T_f$ while it is defined as $T_{W_i} - T_{sat}$ for boiling heat transfer coefficient. Table 3.9 summarizes the uncertainty values in the measured flow boiling heat transfer coefficient.

Table 3.9 The uncertainty values in the measured flow boiling heat transfer coefficient

Test section diameter, mm	Uncertainty %
0.52	7.9 – 13.5
1.16, welded	4.6 – 12.1
1.1, seamless cold drawn, L = 150	5.8 – 10.25
1.1, seamless cold drawn, L = 300	3.6 – 8.6
1.1, seamless cold drawn, L = 450	4.88 – 13.7

3.5.5 Local vapour quality

Combining Eqs. (3.21) and (3.22), the local vapour quality can be calculated from the following equation:

$$x(z) = \frac{h_{in} - h_f}{h_{fg}} + \frac{q\pi D_i z}{\dot{m} h_{fg}} \tag{3.52}$$

With the assumption of the uncertainty in fluid properties (enthalpies) being negligible, the uncertainty in the local vapour quality can be given as:

$$U_x = \sqrt{\left(\frac{\pi D_i z}{\dot{m} h_{fg}} U_q\right)^2 + \left(\frac{q\pi z}{\dot{m} h_{fg}} U_{D_i}\right)^2 + \left(\frac{q\pi D_i}{\dot{m} h_{fg}} U_z\right)^2 + \left(-\frac{q\pi D_i z}{\dot{m}^2 h_{fg}} U_{\dot{m}}\right)^2} \tag{3.53}$$

Using the above equation, the uncertainty in the calculated vapour quality ranged from 1.7 – 2.6 %.

3.5.6 Single phase fanning friction factor

According to Eq. (3.6), the uncertainty in the fanning friction factor is due to the uncertainty in the measured pressure drop, inner diameter, mass flow rate and length. Thus, the propagated uncertainty can be calculated from the following equation:

$$U_f = \sqrt{\left(\frac{\pi^2 \rho_L D_i^5}{32\dot{m}^2 L} U_{\Delta P_m}\right)^2 + \left(\frac{5\pi^2 \rho_L D_i^4 \Delta P_m}{32\dot{m}^2 L} U_{D_i}\right)^2 + \left(-\frac{\pi^2 \rho_L D_i^5 \Delta P_m}{16\dot{m}^3 L} U_{\dot{m}}\right)^2 + \left(-\frac{\pi^2 \rho_L D_i^5 \Delta P_m}{32\dot{m}^2 L^2} U_L\right)^2} \tag{3.54}$$

The uncertainty value in the friction factor according to the above equation is 13 %. This value is an average value since the uncertainty varies with the experimental conditions according to Eq. (3.54).

3.6 Single phase validation

In addition to the experimental uncertainty analysis, the overall experimental system and measuring instruments are further validated by conducting single phase flow and heat transfer experiments. In the current study, the single phase experiments were conducted for each test section before conducting boiling experiments and the results were compared with the conventional single phase correlations and also with some of the micro-scale correlations. The single phase correlations included in the comparison are summarized as follows:

Fanning friction factor correlations

Laminar flow theory: $$f = \frac{16}{\mathrm{Re}} \tag{3.55}$$

Blasius (1913): $$f = 0.079\,\mathrm{Re}^{-0.25} \tag{3.56}$$

Choi et al. (1991): $$f = 0.035\,\mathrm{Re}^{-0.182} \qquad 4000 < \mathrm{Re} < 18000 \tag{3.57}$$

The correlation of Choi et al. (1991) was proposed for the flow of nitrogen gas in micro-tubes having inner diameter ranging from 3 to 81 μm.

Heat transfer correlations

For fully developed laminar flow under constant heat flux boundary condition:

$$Nu = 4.36 \tag{3.58}$$

In the current experimental study, the single phase liquid flow was assumed to be hydrodynamically developed in the calming section that is located directly ahead of the heated section. Therefore, the correlation of Shah and London (1978) for hydrodynamically developed but thermally developing laminar flow given by Eq. (3.59) was included in the comparison.

$$Nu = \begin{cases} 1.953 Gz^{1/3} & Gz \le 33.3 \\ 4.364 + 0.0722 Gz & Gz > 33.3 \end{cases} \tag{3.59}$$

Where, Gz is the Graetz number defined as:

$$Gz = \frac{\mathrm{Re}\,\mathrm{Pr}}{L/D} \tag{3.60}$$

Choi et al. (1991) ignored the entry length because it was too short for the examined diameter ranges and proposed correlations for fully developed laminar and turbulent flows given by Eq. (3.61).

$$Nu = \begin{cases} 0.000972\,\mathrm{Re}^{1.17}\,\mathrm{Pr}^{1/3} & \mathrm{Re} < 2000 \\ 3.82\times10^{-6}\,\mathrm{Re}^{1.96}\,\mathrm{Pr}^{1/3} & 2500 < \mathrm{Re} < 20000 \end{cases} \tag{3.61}$$

For turbulent flow, the correlations due to Dittus and Boelter (1930), Petukhov (1970), Gnielinski (1976) and Adams et al. (1998) given by Eqs. (3.62 – 3.65) are used for the comparison purpose.

Dittus-Boelter (1930): $$Nu_{DB} = 0.023\,\mathrm{Re}^{0.8}\,\mathrm{Pr}^{0.4} \tag{3.62}$$

Petukhov (1970): $$Nu_P = \frac{(f_P/8)\,\mathrm{Re}\,\mathrm{Pr}}{1.07+12.7(f/8)^{1/2}(\mathrm{Pr}^{2/3}-1)}\left(\frac{\mu_{bulk}}{\mu_{wall}}\right)^{0.14} \tag{3.63}$$

Gnielinski (1976): $$Nu_G = \frac{(f_P/8)(\mathrm{Re}-1000)\,\mathrm{Pr}}{1+12.7(f/8)^{1/2}(\mathrm{Pr}^{2/3}-1)}\left(\frac{\mu_{bulk}}{\mu_{wall}}\right)^{0.14} \tag{3.64}$$

where $$f_P = \left[1.82\log\mathrm{Re}-1.64\right]^{-2}$$

Adams et al. (1998): $$Nu_{Ad} = Nu_G\left(1+F_{Ad}\right) \tag{3.65}$$

where: $$F_{Ad} = 7.6\times10^{-6}\,\mathrm{Re}\left[1-\left(\frac{D}{1.164}\right)^2\right]$$

Figures 3.12 and 3.13 depict the measured single phase friction factor and heat transfer coefficient for the investigated tubes compared to some of the conventional and micro scale correlations. For the 0.52 mm diameter tube (Fig. 3.12a), the single phase pressure drop experiments were conducted first by decreasing the mass flow rate and the

transition jump from laminar to turbulent flow was not very clear, i.e. smooth transition from laminar to turbulent. Accordingly, the experiments were conducted once again by increasing the mass flow rate. On the other hand, for the other tubes, the experiments were conducted only in the direction of increasing mass flow rate. Figure 3.12 demonstrates that, the measured friction factor is in a reasonable agreement with the classical laminar flow theory in the laminar region and the Blasius and Choi et al. equations in the turbulent region. Additionally, the figure indicates that the transition from laminar to turbulent occurs between Re = 2000 and 3000, which is in a good agreement with the conventional theory. In other words, the early transition from laminar to turbulent flow that was reported by some researchers such as Mala and Li (1999) and Liu et al. (2007) for water flow in micro tubes was not observed in the current study. Mala and Li investigated tubes with diameters ranging from 50 – 254 μm whilst Liu et al. investigated tube with diameter of 168 and 399 μm. Moreover, in the turbulent region, the friction factor was slightly lower than that predicted by Blasius's equation but keeping similar trend. Hegab et al. (2001) reported the same behaviour in the turbulent region for R134a in a single rectangular channel with hydraulic diameters ranging from 0.112 to 0.21 mm. They attributed the reduction in friction factor in the turbulent region to a small bias in the instrumentation. However, as demonstrated in the present experiments, this reduction may have been based on physical reasons.

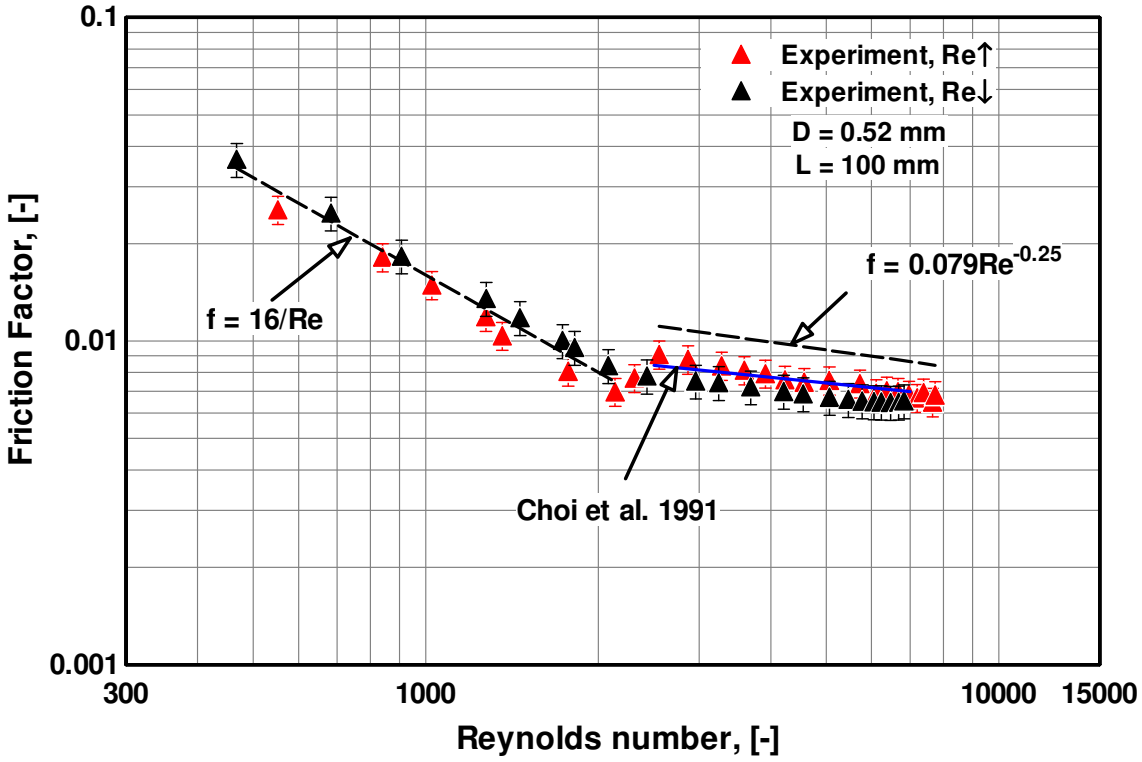

(a) D = 0.52 mm

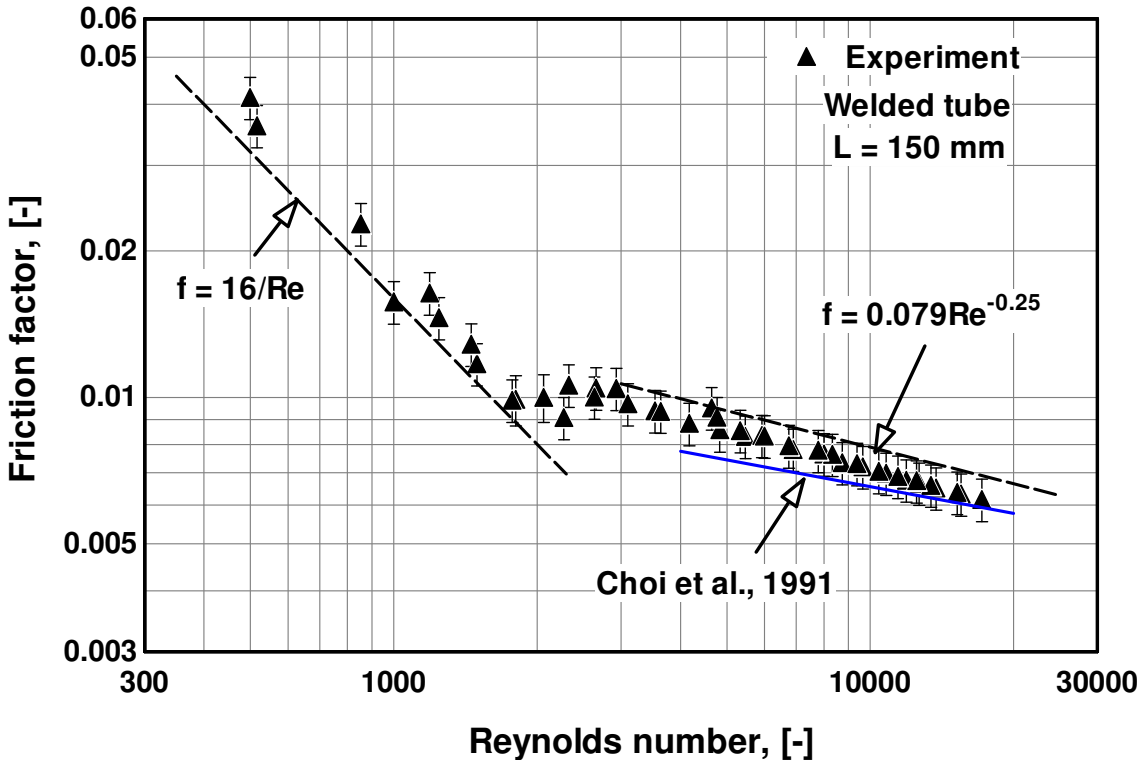

(b) D = 1.16 mm

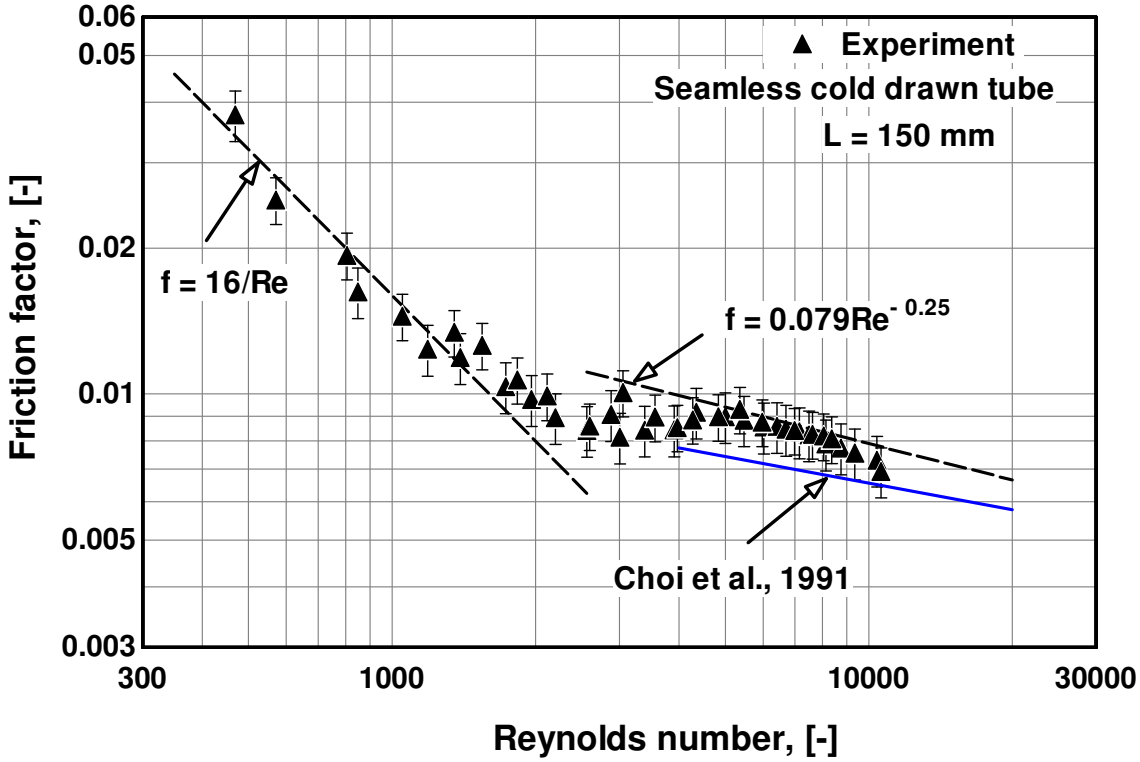

(c) D = 1.1 mm, L = 150 mm

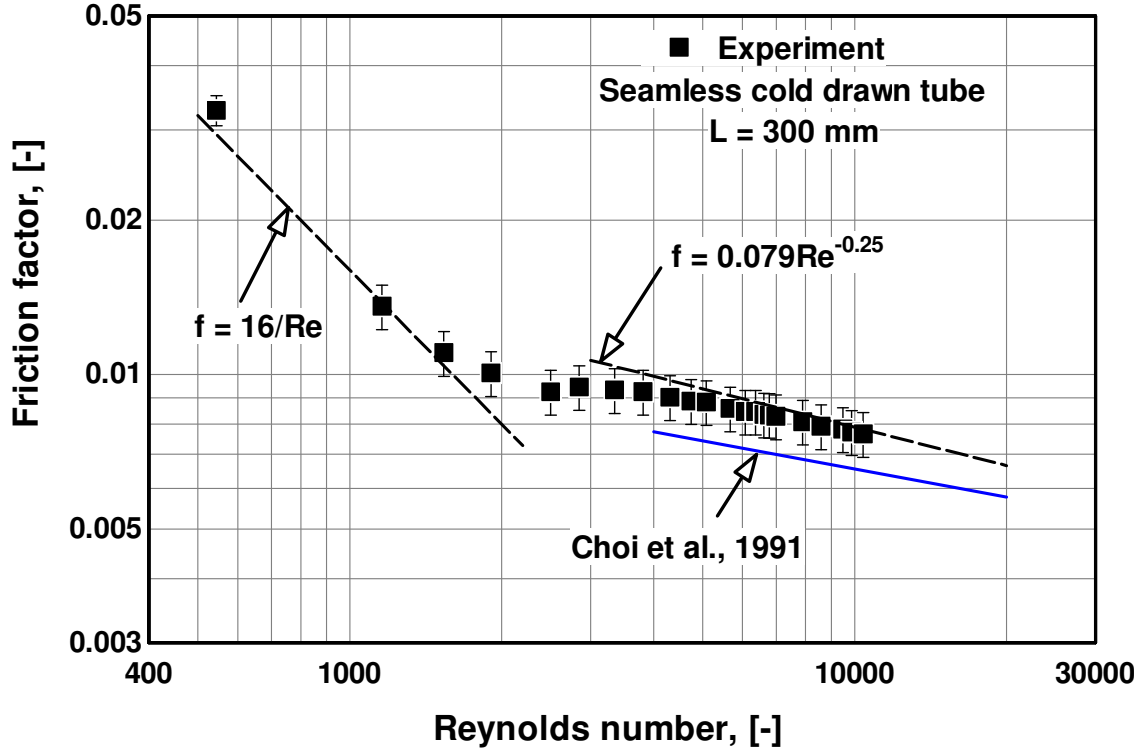

(d) D = 1.1 mm, L = 300 mm

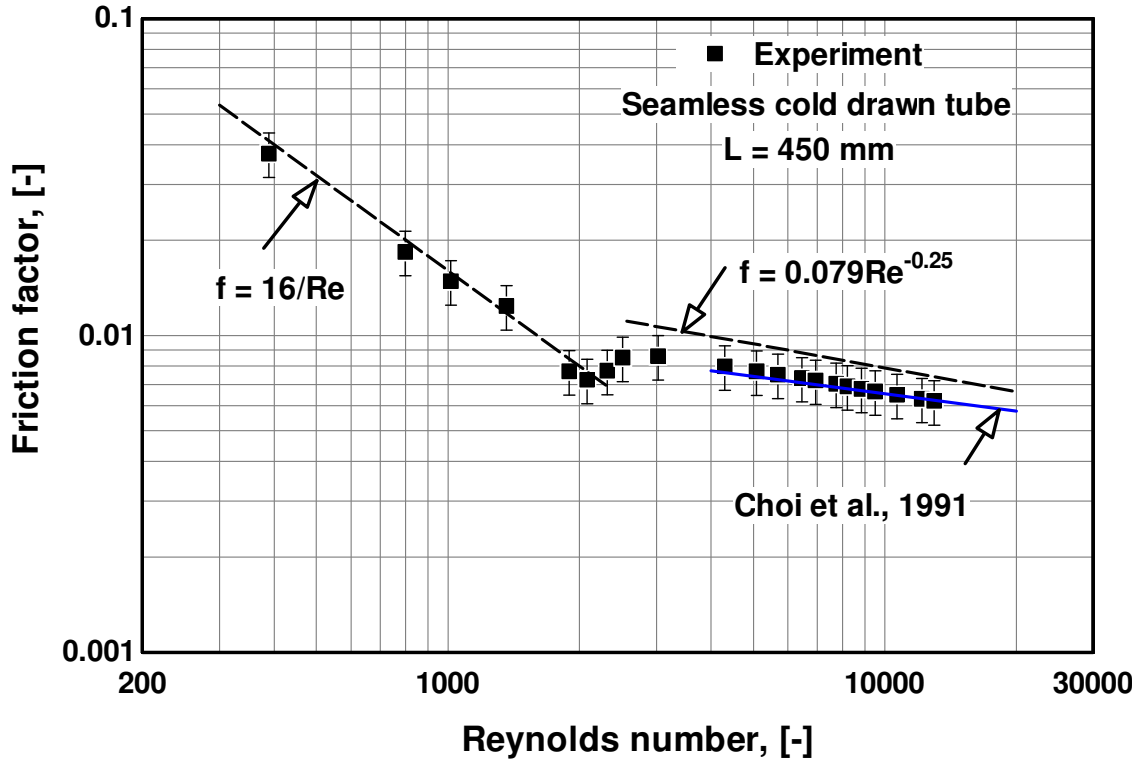

(e) D = 1.1, L = 450 mm

Figure 3.12 Single phase friction factor compared to the laminar flow theory and turbulent flow correlations.

Another observation in Fig. 3.12a is the transition jump, which is usually observed in large diameter tubes. In large diameter tubes, the transition from laminar to turbulent flow depends on the surface roughness and the degree of turbulence, which might be different in micro-tubes. As seen in the figure, the transition jump appeared when the experiments of the 0.52 mm tube were conducted in the direction of increasing Reynolds number (increasing turbulence) but not in case of decreasing Reynolds number.

Figure 3.13 demonstrates in the laminar region that the experimental Nusselt number increase with increasing Reynolds number, which is consistent with the trend in the thermal entry region of large diameter tubes. Conventionally, at very small values of Reynolds number (negligible entry length), the Nusselt number should be close to the asymptotic value of 4.36 and becomes greater than this value as Reynolds number increases (the entry length becomes larger). This conventional behaviour is clear from the trend of the Shah and London (1978) correlation. The measured values showed a similar trend to that of Shah and London's correlation with reasonable agreement for all

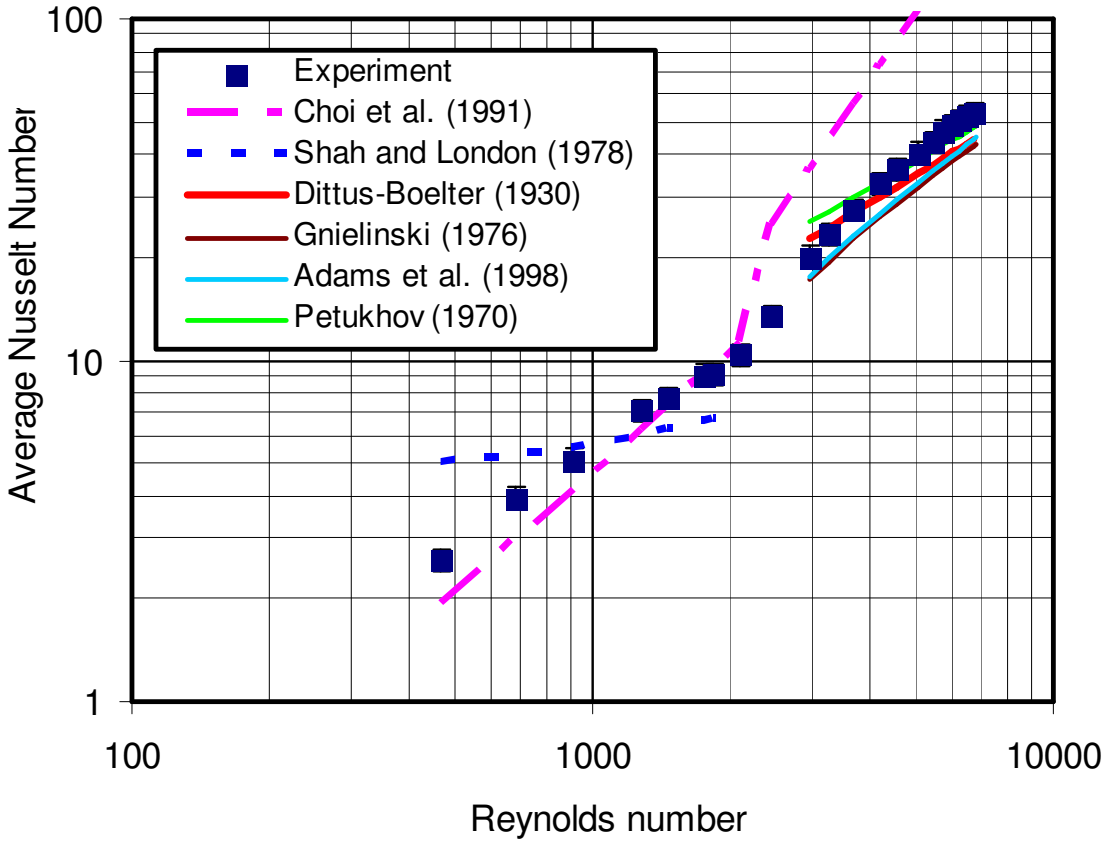

(a) D = 0.52 mm

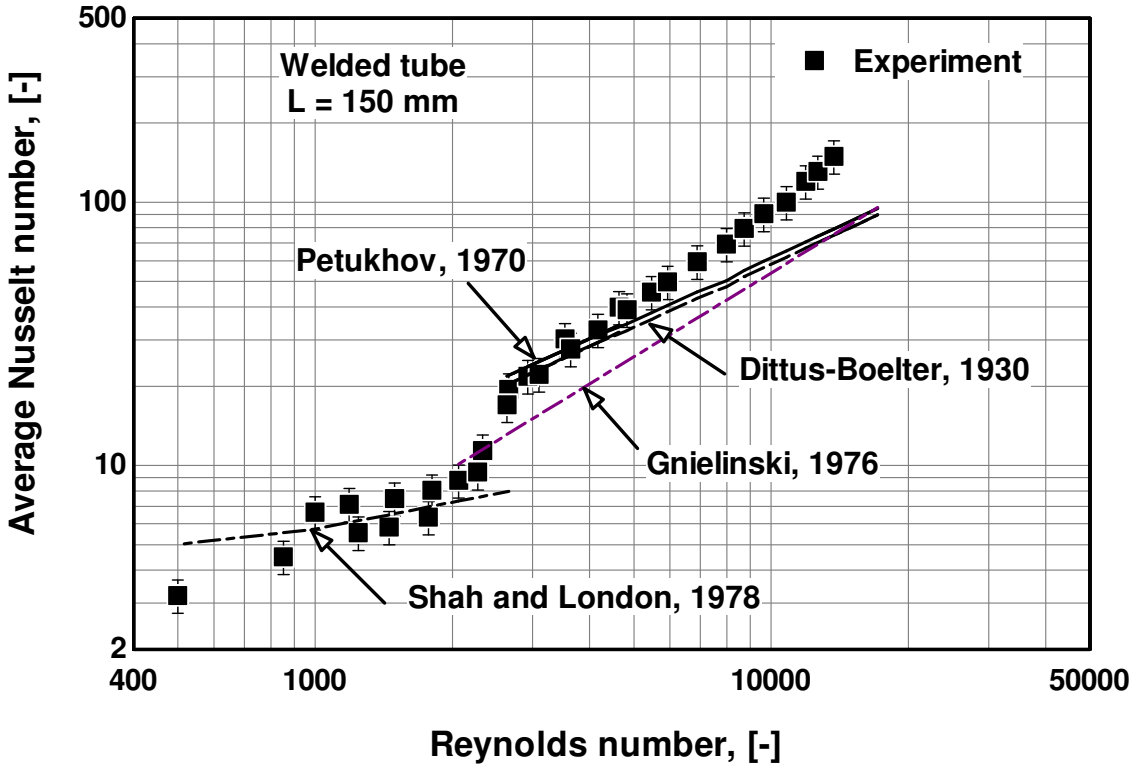

(b) D = 1.16 mm

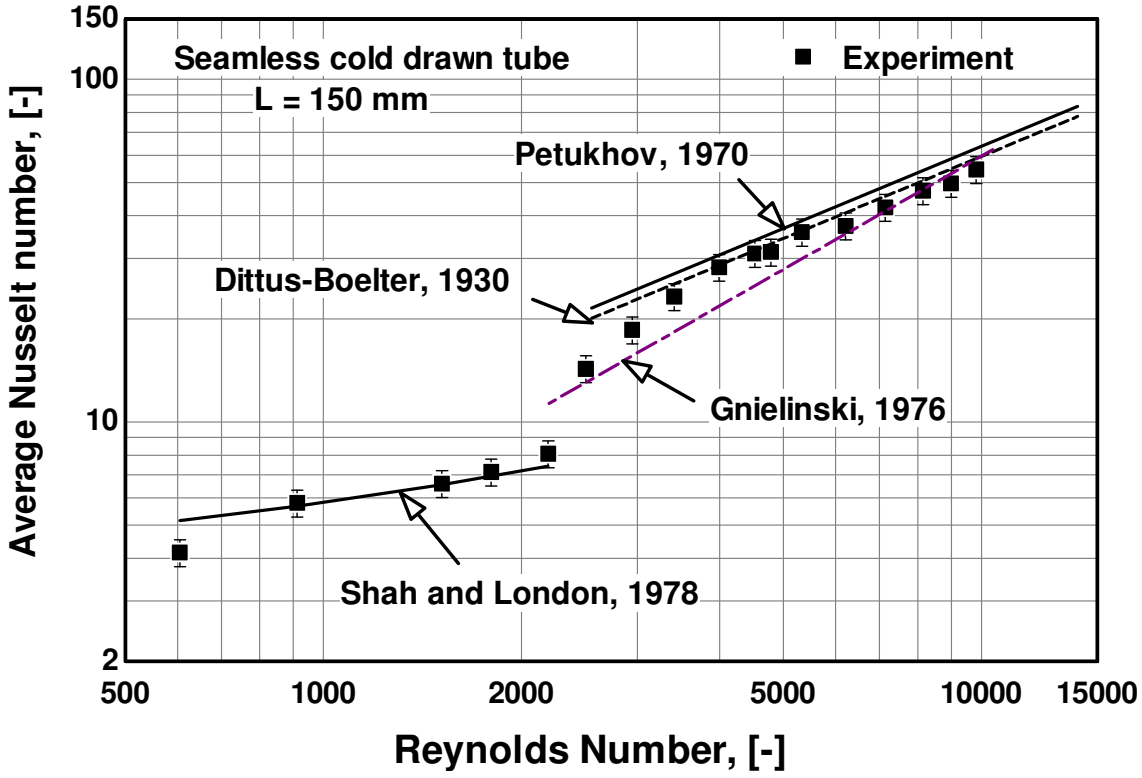

(c) D = 1.1 mm, L = 150 mm

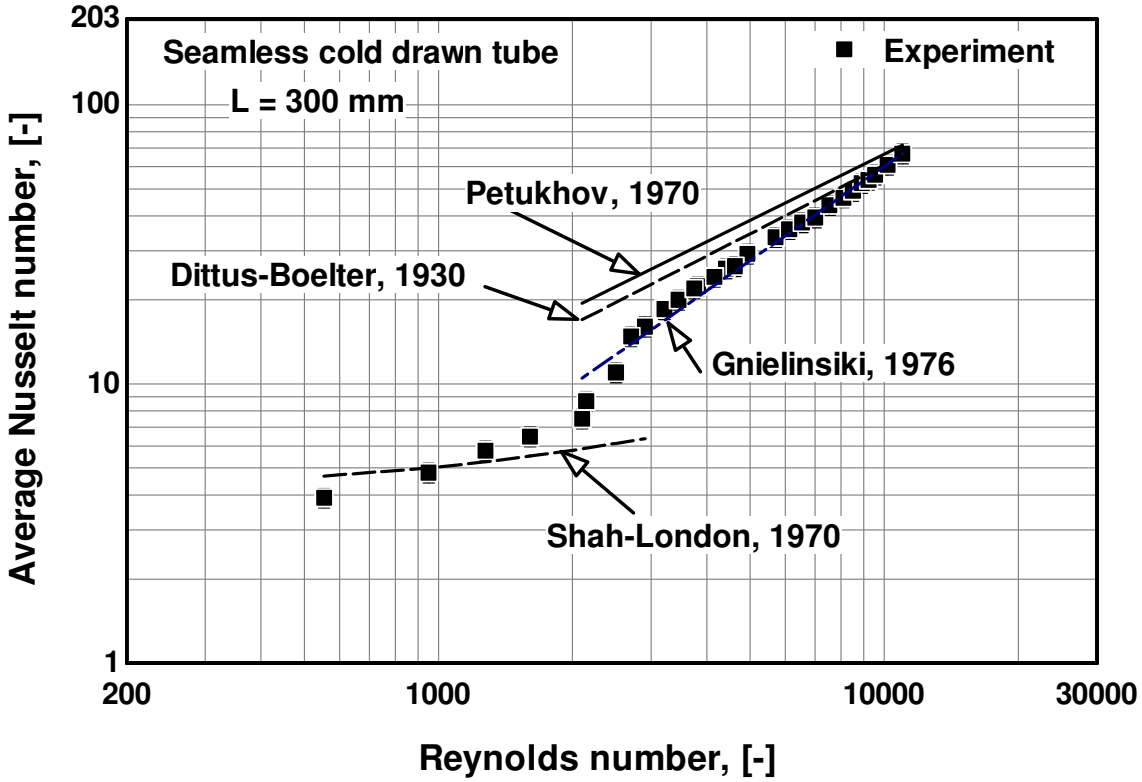

(d) D = 1.1 mm, L = 300 mm

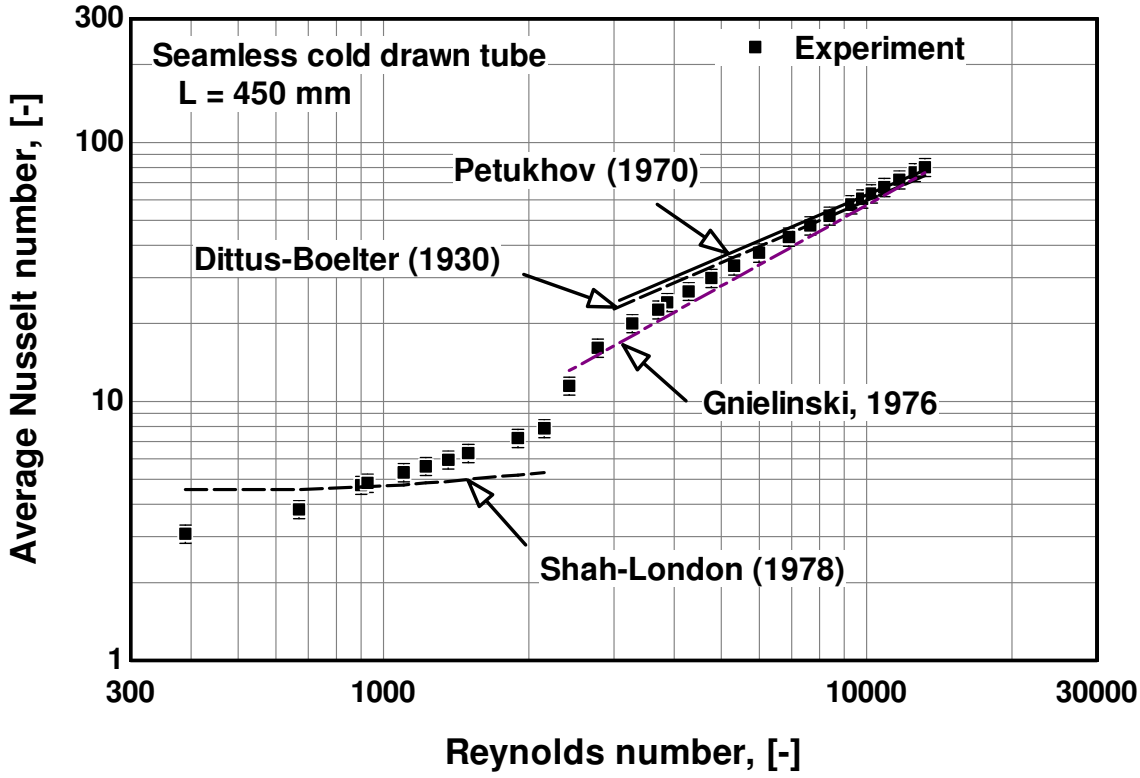

(e) D = 1.1 mm, L = 450 mm

Figure 3.13 Single phase heat transfer coefficient compared to conventional and micro-scale correlations.

tubes except the 0.52 mm diameter tube. The only exception is that, at very low Reynolds numbers, the measured values highly deviated from those predicted by Shah and London's correlation. This deviation could be attributed to the possible effects of axial heat conduction that is more significant at small mass flow rates. For the 0.52 mm tube, the measured values poorly predicted by the Shah and London correlation but were reasonably predicted using the Choi et al. correlation. The lower values at small Re number and the same trend was also observed by Celata et al. (2006) in the laminar region for a tube with diameter of 0.528 mm (thermally developing flow) who attributed this behaviour to the axial heat conduction. The dependence of Nusselt number on Reynolds number in the laminar region was also reported by some other researchers such as Lee et al. (2005) even for fully developed flow.

In the turbulent region, the measured Nusselt number agreed reasonably with the conventional correlations for all tubes except the 1.16 mm diameter welded tube. In Fig. 3.13a, the experimental results were in rough agreement with the Petukhov (1970)

correlation while the Gnielinski (1976) correlation under-predicted the data. The micro scale correlations could not predict the experimental values; Adams et al. (1998) under-predict, while Choi et al. (1991) greatly over-predict the data. This result was previously concluded by Owhaib and Palm (2004). In Figs. 3.13c and 3.13e, the measured values can be roughly predicted by the correlations of Dittus-Boelter (1930) and Gnielinski (1976) while the Gnielinski correlation predicted perfectly the data of Fig. 3.13d. Additionally, when the Reynolds number approaches a value of about 10 000, all correlations tend to merge and predict the data very well. Thus, the Gnielinski correlation may be recommended to be used for Re < 10000 where it can capture the transition region better than the other correlations. Regarding the measured trend for the welded tube in Fig. 3.13b, the data can be predicted well using the correlation of Petukhov (1970) and Dittus-Boelter (1930) only up to $Re \approx 6000$. The correlation of Gnielinski (1976) highly under-predicts the measured values. Above $Re = 6000$, increasing Reynolds number results in a large increase in the measured Nu with large deviations from all the correlations. Figure 3.14 shows a direct comparison between the welded and seamless cold drawn tube. This figure indicates that there is a good agreement between the welded and seamless cold drawn tube up to a Reynolds number value of about 6000. After this value, the average Nusselt number in the welded tube deviated highly from that in the seamless cold drawn tube. The different heat transfer behaviour in the welded tube compared to the other seamless cold drawn tubes may be attributed to the difference in the inner surface characteristics as previously discussed in section 3.3. For further explanation, Fig. 3.15 shows a comparison between the local Nusselt number for the welded and seamless cold drawn tubes as a function of axial distance at approximately similar Reynolds number. The arrows on the figure refer to the local higher values that make the average Nusselt number much bigger. These local jumps are corresponding to the measured local drops in wall temperature. This behaviour may be due to the effect of additional local turbulence resulting from the local debris in the surface of the welded tube as previously presented and discussed. This local heat transfer behaviour indicates also that this debris is not uniformly distributed along the surface. On the other hand, due to the uniformly distributed longitudinal scratches along the seamless cold drawn tube, the local heat transfer behaviour seams to be uniform as seen in Fig. 3.15. Finally, it can be concluded from these single phase experiments that the overall experimental system is valid and accurate for conducting flow boiling experiments.

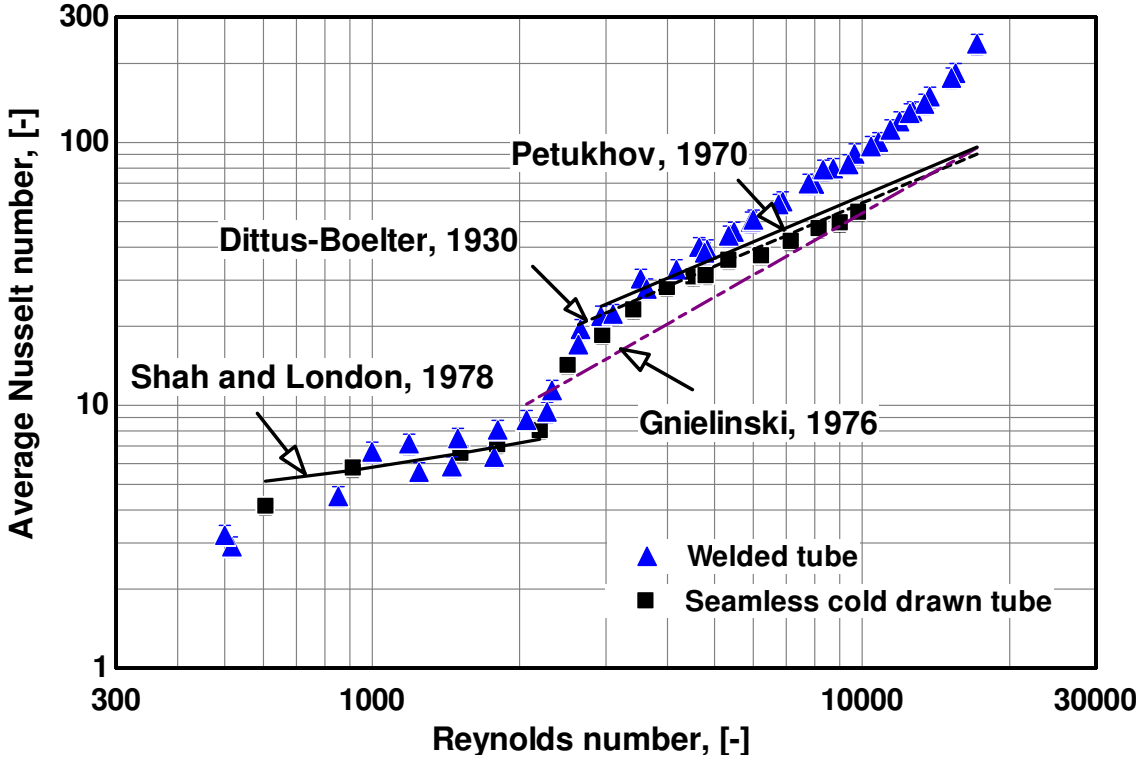

Figure 3.14 A direct comparison between the average Nusselt number in the welded tube (D = 1.16 mm, L = 150 mm) and the seamless cold drawn tube (D = 1.1 mm, L = 150 mm).

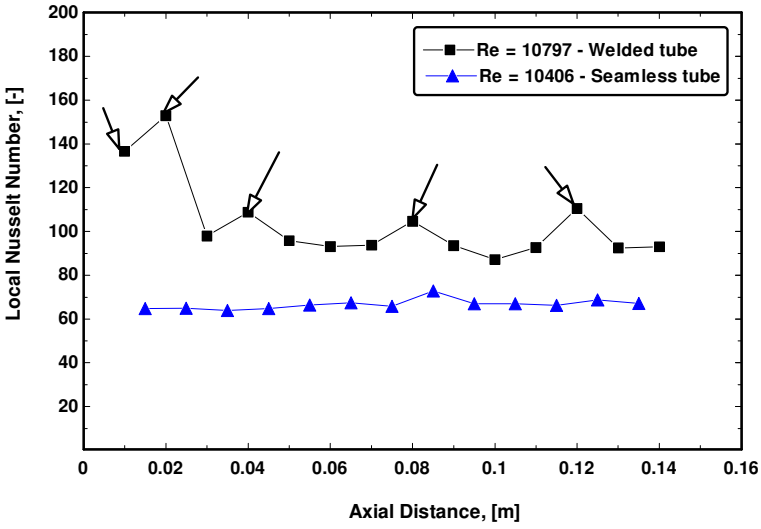

Figure 3.15 The local Nusselt number versus axial distance for the welded and seamless cold drawn tubes in the turbulent region at approximately similar Reynolds numbers and same length of 150 mm.

3.7 Summary

The experimental facility designed first by Huo (2005) and Chen (2006) to investigate flow boiling patterns, heat transfer and pressure drop in small to micro-diameter stainless steel tubes has been described. The facility was designed such that the test sections were directly heated by AC current and the data were collected at a logging speed of 0.17 Hz through a visual basic program. In the current study, the heating system was modified to DC heating and the data were collected at a logging speed of 1 Hz through a new Labview monitoring program. Five test sections were selected to be investigated in the current study including one micro-tube with diameter of 0.52 mm and four mini tubes with diameter of 1.1 mm. The four mini tubes are classified as follows: three seamless cold drawn tubes with three different heated lengths and one welded tube to investigate the effect of heated length. The welded tube was included to investigate the effect of the variation in inner surface characteristics resulting from the manufacturing process, e.g. cold drawn versus welded. Flow visualization is conducted using a high speed camera and the movies were recorded simultaneously with the heat transfer data. All measuring instruments were carefully calibrated and the propagated uncertainty analysis was conducted according to the standards with reasonable experimental error values. The overall system and all investigated tubes were also validated using single phase experiments. The single phase results (pressure drop and heat transfer) were compared with the laminar theory and the existing single phase correlations with a very good agreement.

Chapter 4

Flow Patterns and Heat Transfer Results and Discussion

4.1 Introduction

This chapter presents and discusses the experimental results of flow boiling patterns and heat transfer characteristics in the five investigated test sections. These test sections include: (i) one seamless cold drawn micro-tube with a diameter of 0.52 mm and 100 mm heated length; (ii) one welded mini-tube with a diameter of 1.16 mm and heated length of 150 mm; (iii) three seamless cold drawn mini-tubes with a diameter of 1.1 mm and heated lengths of 150, 300 and 450 mm. In addition, the previous flow patterns results of Shiferaw (2008) for the micro-tube with D = 0.52 mm are also presented here in this chapter for the purpose of comparison. The typically observed flow patterns are described and discussed first before presenting the heat transfer results. It is worth mentioning that, developing flow maps is not the scope of the current study. It requires investigating a wide range of mass and heat fluxes to cover all expected transition boundaries. The aim of the current study is mainly investigating heat transfer characteristics whereas the flow patterns are simultaneously recorded to assist in explaining the heat transfer and pressure drop results. The heat transfer results are presented in the form of: (i) local heat transfer coefficient versus local vapour quality, (ii) local heat transfer coefficient versus axial distance, (iii) local heat transfer coefficient versus heat flux and (v) classical boiling curves (heat flux versus wall superheat). This chapter is organised as follows: section 4.2 presents and discusses the characteristics of the observed flow patterns as well as comparison with some of the existing flow maps; section 4.3 presents the characteristics of the experimentally

determined heat transfer coefficient; section 4.4 presents the reproducibility of the heat transfer data; section 4.5 provides a summary for the chapter.

4.2 Flow patterns results

It is beneficial to start first with discussing the flow patterns observed at the exit of the heated section of each tube. This is for the sake of interpreting the heat transfer results presented later in the next section. In the current experimental study, all flow patterns were recorded using a high speed video camera at a speed of 1017 frames per second and resolution of 512 × 512 pixels. The experimental conditions include mass flux range of 100 – 500 kg/m^2 s and system pressure range of 6 – 10 bar. Since all the heat transfer results, which will be discussed later, are presented for 6 bar system pressure and 300 kg/m^2 s mass flux as an example, the features of the observed flow patterns in all tubes are also presented at the same conditions. The flow patterns in the 0.52 mm tube are also presented at 8 bar system pressure and 400 kg/m^2 s for the aim of comparison with those presented by Shiferaw (2008) at the same conditions.

4.2.1 Flow patterns in the 0.52 mm tube

As previously mentioned in Chapter one, the micro-tube with D = 0.52 mm was first investigated by Shiferaw (2008). This tube exhibited a different heat transfer behaviour compared to the larger tubes investigated in his study (D = 1.1 and 2.88 mm) and the tubes of D = 4.26 and 2.01 mm investigated by Huo (2005). As a result, this tube size was recommended for further investigations. Accordingly, a new test section (identical to that of Shiferaw) was designed and investigated in the current study. The new test section was cut from the piece of tube of which the Shiferaw test section was made. From now on, the Shiferaw test section will be called “the old test section” whilst the current one will be called “the new test section”. Figure 4.1 shows the typically observed flow patterns in the old test section. As seen in Fig, 4.1, five flow regimes were identified by Shiferaw namely bubbly, elongated bubble (slug), liquid-ring, wavy annular and annular flow regimes. The bubbly flow regime appeared at low exit quality (low heat flux) as seen in the first picture from the left in Fig. 4.1. With further increase in heat flux, the bubble grew in length and became elongated as seen in the second and third picture from the left in Fig. 4.1. The liquid-ring flow (no liquid bridge anymore) was believed to occur due to the bubbles coalescence when the heat flux increases

further. This regime is shown in the fourth, fifth and sixth picture from the left in Fig. 4.1. Shiferaw reported that when the bubble "pushes" up the liquid slug during the coalescence process, a wavy liquid film forms and consequently the wavy annular flow establishes as shown in the seventh and eighth picture in Fig. 4.1. With further increase in heat flux, the amplitude of the wave in the wavy-annular flow decreased and annular flow developed as seen in the last two pictures in Fig. 4.1.

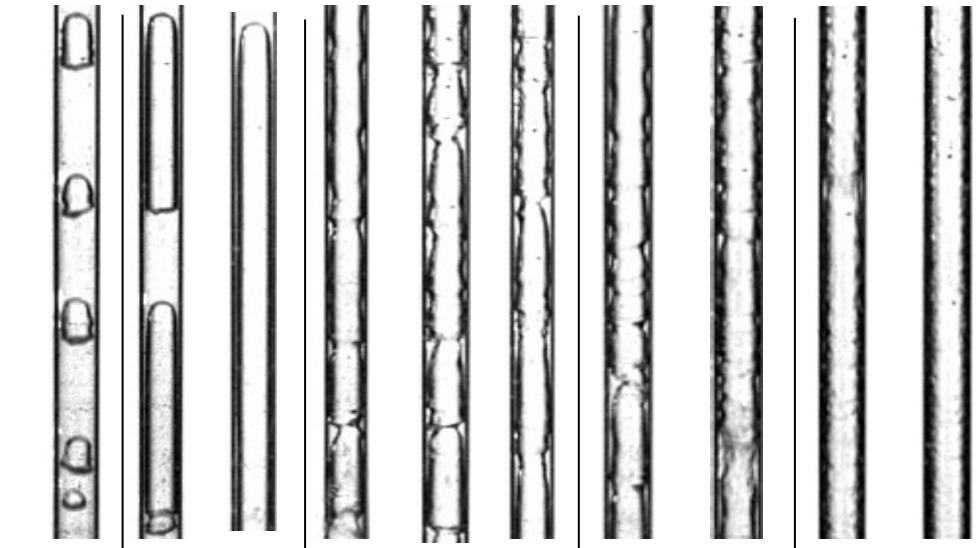

Figure 4.1 Flow patterns in the old test section as a function of the exit vapour quality and heat flux for D = 0.52 mm, G = 400 kg/m^{2}s and P = 8 bar, Shiferaw (2008).

Figure 4.2 shows the observed flow patterns in the new test section at approximately similar experimental conditions to those presented in Fig. 4.1. It is worth mentioning here that, the mass flux value in Figs. 4.1 and 4.2 is only a nominal value whilst the actual value is about 30 kg/m^2 s above/below the nominal value. This explains why the values of the exit quality at approximately similar heat flux values in Figs. 4.1 and 4.2 are not exactly the same. Figure 4.2 demonstrates that four flow regimes are observed in the new test section namely bubbly, elongated bubble (slug), transition to annular and annular flow. These flow regimes are similar to those observed by Shiferaw in the old one with little differences. The differences include the appearance of bubbly flow at much lower exit quality as seen in the first two pictures in Fig. 4.2. A second difference is the absence of the large amplitude waves during the transition from the elongated

bubble (slug) flow regime to the annular flow regime. A third difference is that the annular flow in Fig. 4.1, for the old test section, appears as if there were some liquid droplets entrainment into the vapour core as a result of the disruption of the liquid film. This droplets entrainment is not observed in the results of the new test section as seen in Fig. 4.2. Due to the fact that the flow regimes observed in the new test section between the slug and annular flow regimes do not show the conventional features of churn flow, i.e. highly unstable liquid/vapour interface, these regimes were called here "transition to annular". The transition to annular regime in this study includes the liquid-ring flow and the wavy-annular flow defined by Shiferaw as summarized in Table 4.1.

Table 4.1 The flow patterns observed in the old and new test sections

The names used by Shiferaw (2008)	The names used in the current study
Bubbly	Bubbly
Elongated bubble (slug)	Elongated bubble (slug)
Liquid-ring flow	Transition to annular
Wavy annular flow	
Annular	Annular

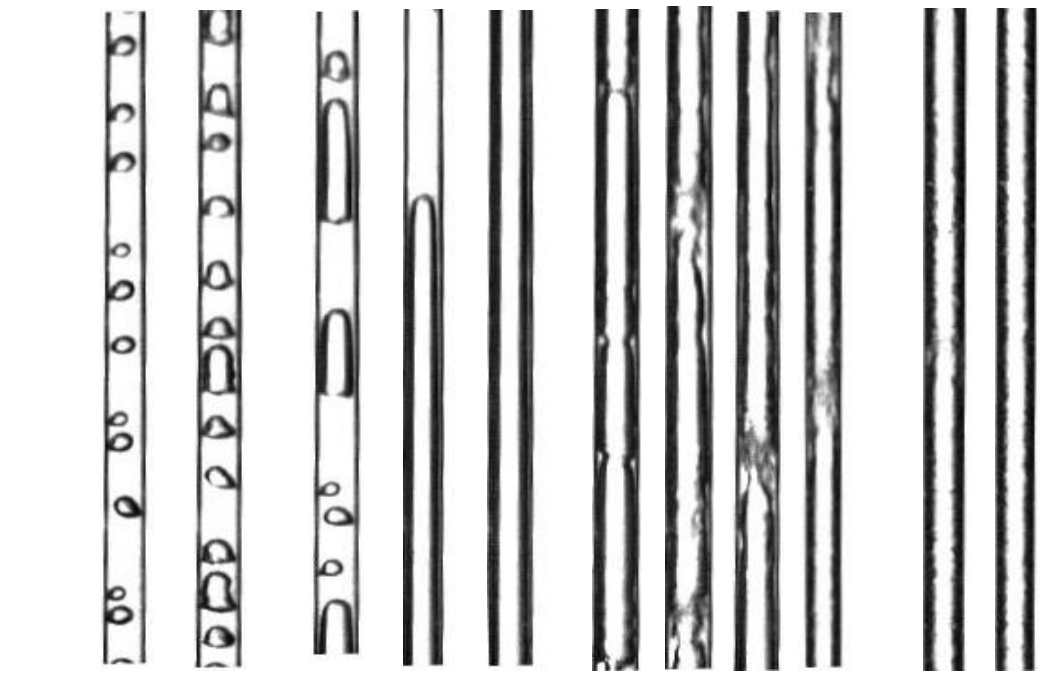

Figure 4.2 Flow patterns in the new test section as a function of the exit vapour quality and heat flux for D = 0.52 mm, G = 400 kg/m^2 s and P = 8 bar.

From now on, all the flow patterns results presented in the coming paragraphs are only for the new test section. The results are presented at experimental conditions similar to those of the heat results presented later. Figure 4.3 shows the flow patterns observed at a mass flux value of 280 kg/m^2 s (Re = 818) and a system pressure of 6 bar. The observed flow patterns are similar to those observed in Fig. 4.2 at 8 bar system pressure. These patterns include bubbly, elongated bubble (slug), transition to annular and annular flow. Bubbly flow was observed at very low exit vapour quality and was characterized as small bubbles with diameter less than tube diameter as seen in pictures No. 1 and No. 2 in Fig. 4.3. In these two pictures, there are some tiny bubbles attached to the wall with a tip similar to the shape of the bubble when it is about to leave the nucleation site. Fu et al. (2008) observed a similar kind of bubbles in the flow boiling of liquid nitrogen in a 1.931 mm diameter vertical tube; see Fig. 2.14. They called it "wall-peaking bubbly flow" and attributed the occurrence of this regime to the possibility of bubble nucleation, growth and departure from the same nucleation site before flowing into the adiabatic observation section. Additionally, the lower part and the mid-upper part of picture No. 1 shows one confined bubble with a hemi-spherical head and tail. This confined bubble seems to be formed as a result of the coalescence of the tiny bubbles after departing from the nucleation site. In other words, the nucleating bubble grows and departs from the nucleation site with sizes smaller than or equal to tube diameter then they coalesce to form bubbles with hemi-spherical nose and tail (confined bubble). The size of these small bubbles is measured using the camera software and it was found to be about 0.28 mm, which is approximately equal to the radius of the tube. The software gives the distance in pixels between any two points in the picture. Accordingly, it can measure the inner diameter of the glass tube in pixels. Since the inner diameter of the glass tube is already known (0.5 mm), the diameter of any bubble can be measured and calculated relative to the inner diameter of the glass tube as follows:

$$D_b = \frac{tube\ diameter\ in\ mm \times bubble\ diameter\ in\ pixels}{tube\ diameter\ in\ pixels} \tag{4.1}$$

It can be deduced from pictures No. 1 and No. 2 that, when the bubble departs from the nucleation site with sizes smaller than tube diameter, the tip-like shape remains as it is as long as the bubble does not coalesce with other bubbles. On the other hand, when the bubble departs with size approximately equal to tube diameter, the bubble takes the

shape of a hemi-spherical cap, which may be arising from the effects of surface tension and inertia forces. It is interesting to note that, the tip of the small bubbles is not normal to the tube wall but it is about 25^0 inclined with the horizontal axis which may reflect the significance of inertia force as shown in the schematic drawing of Fig. 4.4 This is consistent with the value of the liquid Weber number which is much greater than unity (inertia is greater than surface tension)–the Weber number value equals 9.25 at G = 280 kg/m^2 s. Figure 4.4 also shows the forces acting on a bubble attached to the wall. These forces include the lift force (F_L) due to shear, the buoyancy force (F_b), the surface tension force (F_s), the fluid inertia force (F_i) and the drag force due to the motion of the interface (F_D). It is also worthy noting that, at exit quality value of 0.025, bubbly and slug (elongated bubble) regimes have been observed with the presence of bubble coalescence; see pictures No. 1–8.

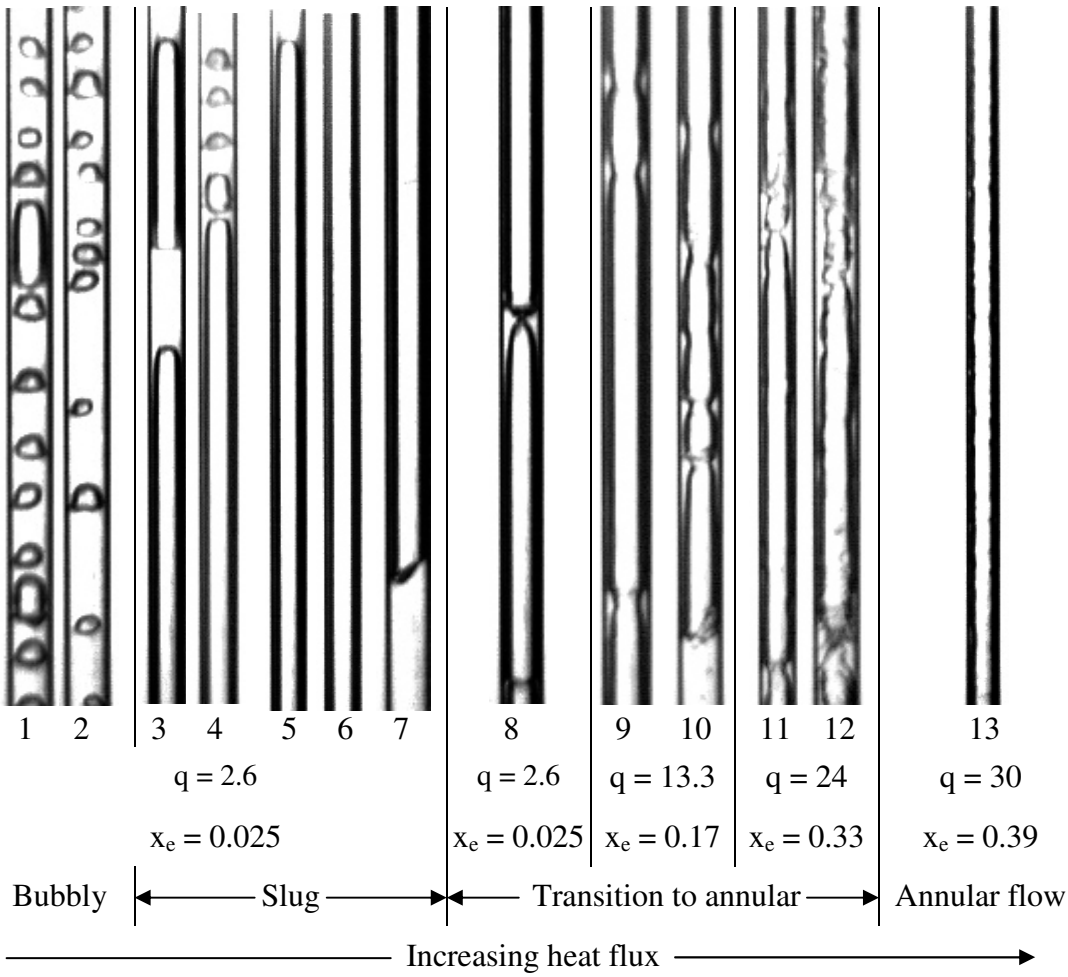

Fig. 4.3 Flow patterns observed at the exit of the 0.52 mm diameter tube at G = 280 kg/m^2.s and P = 6 bar as a function of exit vapour quality and heat flux *(q)* in kW/m^2.

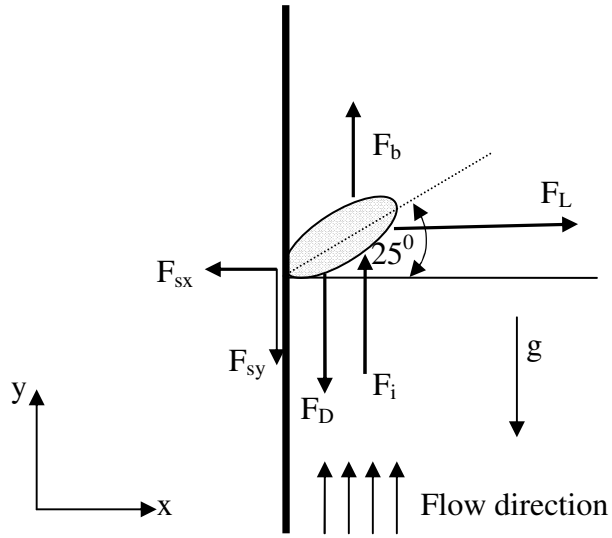

Figure 4.4 The inclination of the bubble on the tube wall with the forces acting on the bubble interface.

The elongated bubble regime appeared in some frames as if it was annular flow as seen in picture No. 6. In this picture, the bubble filled all the view length without observing any liquid slugs in the picture. However, pictures No. 5 and 7 show the head and tail of this elongated slug observed in picture No. 6. The tail of this elongated bubble appeared after 20.6 ms without any disturbance at the liquid/vapour interface. Moreover, the analysis of the 1017 pictures indicated that the lengths of the liquid and vapour slugs are not uniform. Therefore, the velocity of the moving slugs is expected to vary as reported by Agostini et al. (2008c); see Eq. (2.23). This equation indicates that, the velocity of the long bubbles is higher than the velocity of the short ones at the same heat flux and also it increases with increasing heat flux. Accordingly, with further increase in heat flux, the coalescence rate increases resulting in a kind of transition regime shown in pictures No. 9 – 12. This transition regime starts with the coalescence of two consecutive elongated bubbles as seen in picture No. 8. The coalescence process is expected to occur when the velocity and the pressure inside the bubble becomes sufficient to overcome the liquid bridge between the two coalescing bubbles. At the merging zone, a neck-like shape (ring) forms without any disturbance in the liquid film particularly at low heat fluxes as seen in picture No. 9. At high heat fluxes, the slug was observed with distortion at the tail. Kawahara et al. (2002) investigated nitrogen-water flow in a 0.1 mm tube and observed one regime similar to that shown in picture No. 9 and called it “gas core with ring-shaped liquid film”; see Fig. 2.6. Saisorn et al. (2010)

also investigated flow boiling of R134a in a 1.75 mm diameter tube and observed a similar regime and called it “throat-annular flow”. It is worth mentioning that, the liquid slugs still exist during this transition regime as seen in picture No. 10. When the heat flux was further increased, more disturbances were observed at the merging zone resulting in a narrow churning zone (pictures No. 11 and 12), the liquid slugs disappeared and the gas flowed continuously in the core. At locations far away from the churning zones, the liquid film was almost undisturbed. Dispersed bubbly flow was not observed in this tube possibly due to the experimental conditions. It is known that, dispersed bubbles are expected to appear at very high liquid superficial velocities and very low gas superficial velocities due to the high turbulence that disintegrates or disperses the large bubbles into fine bubbles. Additionally, the conventional churn flow pattern observed in large diameter tubes with high chaotic nature was not observed in this 0.52 mm tube due to the elongation of the vapour slugs with a highly squeezed liquid film and also due to the laminar nature of the flow (Re = 818). In micro-tubes, one bubble fills the whole channel cross section, and then becomes elongated and thus a smooth transition to annular flow occurs without the chaotic nature of the classical churn flow. The appearance or disappearance of wavy annular flow pattern depends on the length of the coalesced slugs and flow patterns instability. If there is a train of short vapour slugs, wavy annular flow may appear as a result of the increased number of necks at the merging point.

It is worthy noting from Fig. 4.3 that more than one flow pattern appeared at the same heat flux particularly at low heat flux values, which was also reported by Shiferaw (2008). This behaviour may be attributed to the possible nucleation instabilities especially occurring in micro-tubes at very low heat fluxes. When most nucleation sites are not active, few numbers of tiny bubbles appear for a while in some pictures as bubbly flow due to the low probability of bubble coalescence. Once the non-active sites become active, the number of bubbles increases. Consequently, the chance of bubble coalescence increases resulting in the appearance of slug and elongated bubbles as well as some small bubbles. Therefore, it was difficult to specify the flow pattern corresponding to a certain heat flux or exit quality, particularly at very low heat flux values. Accordingly, the 1017 pictures were analysed and the number of pictures associated with each flow pattern was determined. On doing so, a chart similar to the one shown in Fig. 4.5 was developed. In this figure, the vertical axis represents the time

fraction of each flow pattern while the horizontal axis represents the exit vapour quality. The time fraction of the flow pattern is defined as the number of pictures associated with that pattern divided by the total number of pictures (1017 pictures). In order to develop Fig. 4.5, the following criteria were followed; (i) when the picture shows small bubbles similar to those presented in pictures No. 1 and No. 2 of Fig. 4.3, the flow pattern was called bubbly flow; (ii) when both vapour and liquid slugs or a train of slugs appear in the picture with a configuration similar to that shown in picture No. 3, the flow pattern was called slug flow; (iii) when the picture shows similar features to those in pictures No. 5, 6 and 7, the pattern was considered as elongated bubble and (iv) when a neck-like shape or narrow churning zones appear without observing any liquid slugs in the picture, the flow pattern was called transition to annular.

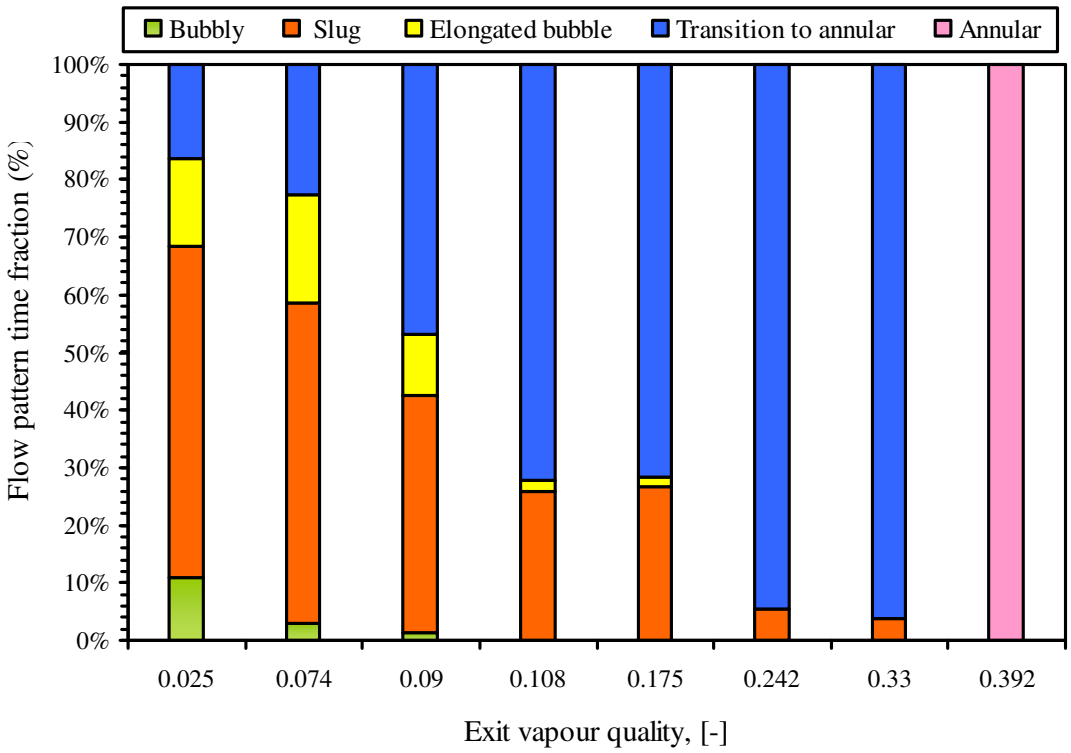

Figure 4.5 The time fraction of each flow pattern as a function of exit vapour quality at G = 280 kg/m^2 s and P = 6 bar for D = 0.52 mm tube.

Figure 4.5 indicates that, at x = 0.025, bubbly flow appears only in 11%, of the total number of pictures, slug flow appears in 57 %, elongated bubbles appear in 16 % and the transition to annular regime appears in 16 %. In other words, slug flow (short and elongated bubbles) dominates at low quality values and not bubbly flow which was

expected to be observed at very low exit qualities. Harirchian and Garimella (2009) found that slug flow was formed immediately after boiling incipience in channels with hydraulic diameter smaller than 0.4 mm and the bubbly flow regime was not observed. It is also observed that, the transitional regime (neck-like shape) appeared at low exit quality because it develops from the coalescence of the elongated bubbles. With increasing exit quality, the transition regime begins to dominate until annular flow becomes fully established. It can be concluded from Fig. 4.5 that, only three regimes are dominating in the 0.52 mm tube namely:

- Slug flow (including elongated bubbles).
- Transition to annular regime (resulting from long bubbles coalescence).
- Annular flow regime.

It is interesting to note that, at x = 0.025, some pictures showed that there are tiny bubbles trapped in the liquid film and protruded into the vapour slug as seen in Fig. 4.6. The size of these small bubbles was found to be about 0.26 mm, which is similar to the size of the bubble with a tip-like shape. After 10 ms, these bubbles disappeared due to coalesce with the main elongated slug.

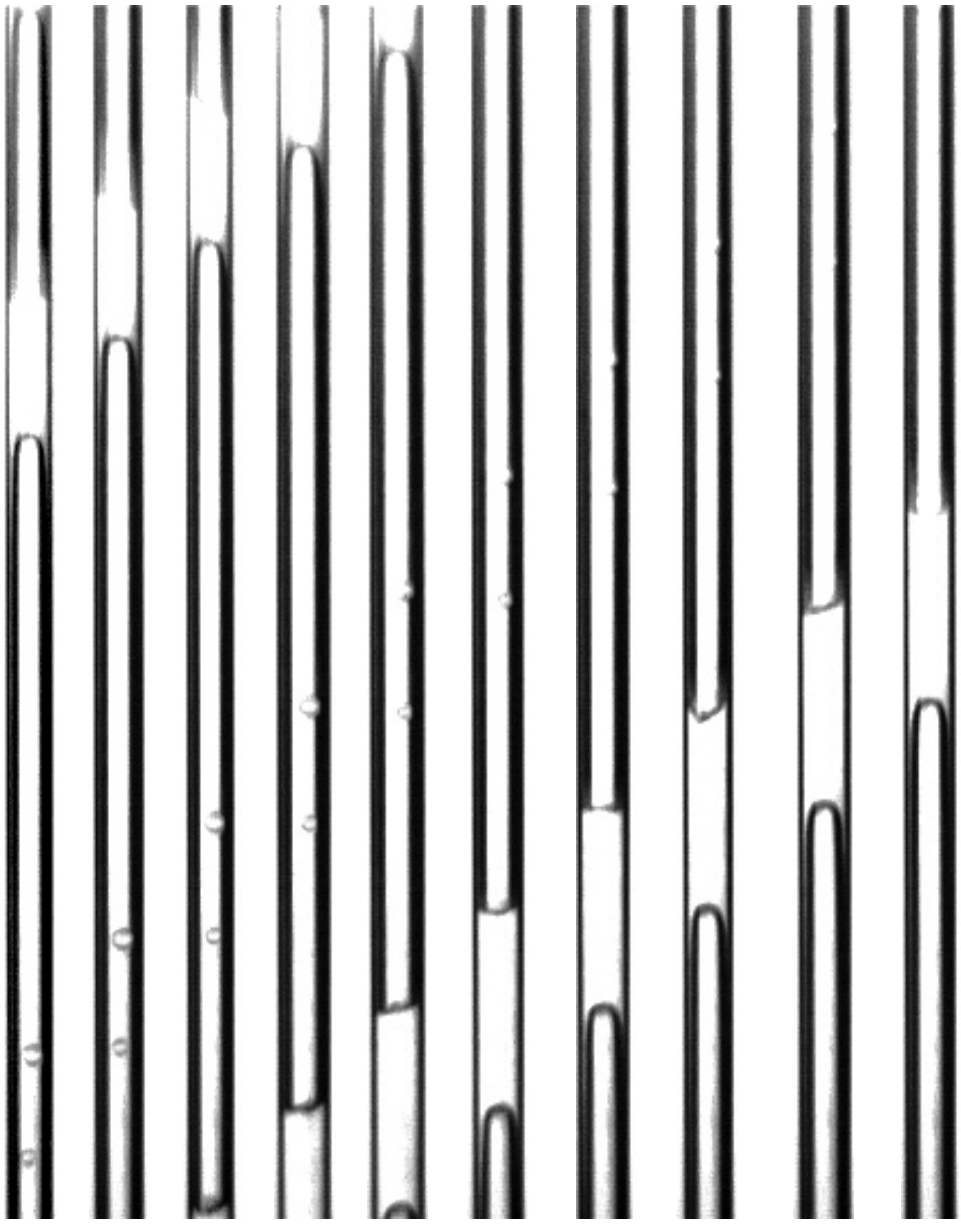

Figure 4.6 The sequence of pictures that shows the coalescence of the tiny bubbles trapped in the liquid film with the main vapour slug at $x_e = 0.025$, $q = 2.6$ kW/m^2. G = 280 kg/m^2 s and D = 0.52 mm.

Since the coalescence process occurred over a wide range of vapour qualities, its mechanism needs more explanation. Figure 4.7 shows an example for the coalescence process in the 0.52 mm diameter tube. As seen in Fig. 4.7a, the coalescence process occurs between a trailing bubble (relatively longer) and a train of leading small bubbles without forming a neck-like shape. In that case, the small bubble merges completely with the trailing bubble. However, when coalescence occurred between two relatively long bubbles whose tail and head are hemispheres, the neck-like shape appeared and

remained after coalescence until annular flow establishes as seen in Fig. 4.7b. This could be explained as follows: when the leading bubble or slug is small in size with a large curvature or flat tail, the pressure inside the leading bubble is expected to be less than that inside the trailing one ($\Delta P = 2\sigma / r$) and also the component of the surface tension force in the axial direction. This may facilitate the penetration of the trailing bubble into the leading one. On the other hand, when the difference in curvature at the tail and nose of the two coalescing slugs is small, the axial components of the surface tension force may equalize after the coalescence process and thus may leave part of the curvature. In conclusion, Fig. 4.7a explains how the elongated bubble forms with a nice spherical nose and without any disturbance at the liquid/vapour interface whilst Fig. 4.7b explains how the transition to annular flow regime develops from the coalescence of elongated bubbles with the formation of the neck-like shape that remains after the coalescence process.

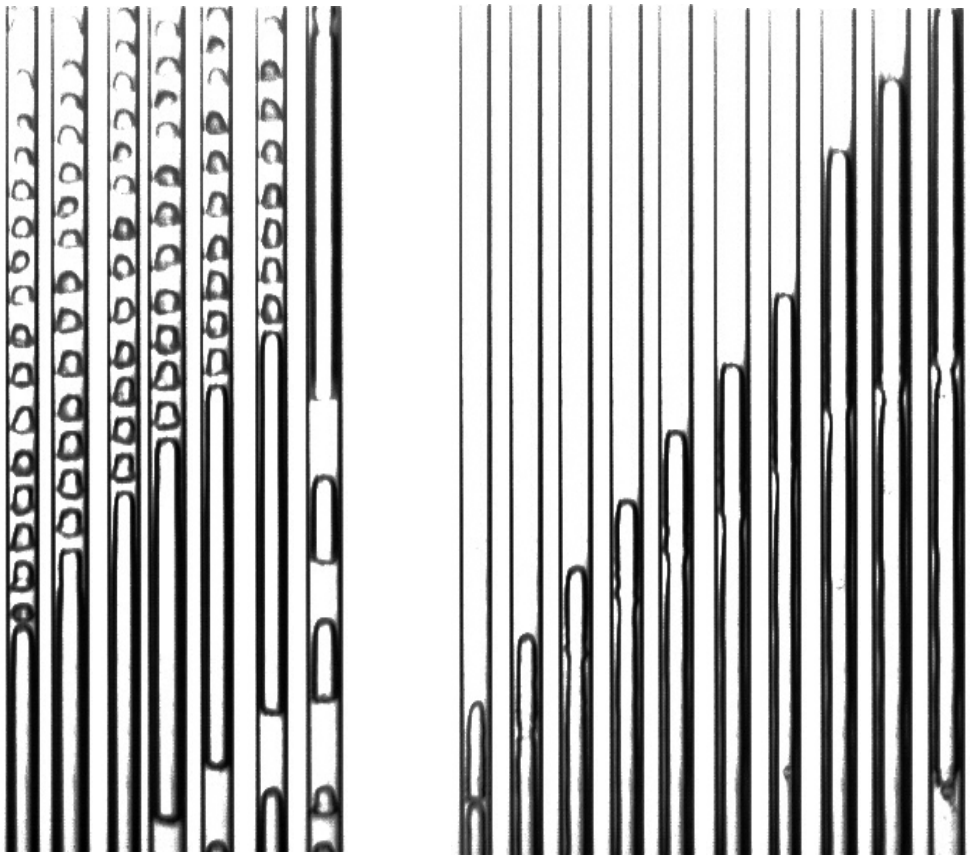

(a) coalescence without forming a neck-like shape, $x_e = 0.074$, $q = 6$ kW/m^2

(b) coalescence with the formation of a neck-like shape, $x_e = 0.09$, $q = 7.2$ kW/m^2

Figure 4.7 Sequence of frames showing bubbles coalescence in the 0.52 mm tube at G = 280 kg/m^2 s and P = 6 bar.

4.2.2 Flow patterns in the 1.1 mm tubes

Four tubes with inner diameter of 1.1 mm were used to investigate the effects of inner surface characteristics and heated length on heat transfer and pressure drop. The typically observed flow patterns in these tubes are presented herein this section. The results are presented at experimental conditions similar to those presented in the previous section for 0.52 mm diameter tube for the sake of comparison.

Effect of inner surface characteristics

Tube inner surface characteristics significantly influence the nucleation process in boiling and consequently it may influence the flow patterns, particularly at low heat fluxes. This parameter seems to be important in micro-tubes due to the expected few number of nucleation sites per unit length. The effect of inner surface characteristics was examined in the current study using two tubes having similar dimensions but manufactured by two different methods. The first tube was manufactured by a cold drawn process while the second tube was manufactured by welding technique and both have a 150 mm heated length. The surface characteristics of these tubes were presented and discussed previously in Chapter 3; see Fig. 3.10. Figures 4.8 and 4.9 show the typically observed flow patterns in the seamless cold drawn tube and the welded tube at G = 300 kg/m^2 s (Re = 1875) and P = 6 bar. For the seamless cold drawn tube, Fig. 4.8 shows that the observed flow regimes are bubbly, slug, churn and annular with slug, churn and annular dominating as seen in Fig. 4.10. In slug flow, small bubbles with a tip-like shape attached to the wall were observed in the liquid slug between the consecutive bubbles and also tiny bubbles were observed trapped in the liquid film as seen in the fourth picture from the left in Fig. 4.8. The elongated bubble regime was observed in few number of pictures as also seen in Fig. 4.10 at x = 0.018. As the heat flux increased, the slug length increased and the elongated slugs merged and resulted in a wide churning zone with the appearance of liquid slugs in some pictures. With further increase in heat flux, the liquid slugs disappeared and churn flow with a high chaotic liquid/vapour interface has developed. At x = 0.44, the features of annular flow appeared with a rough liquid/vapour interface as seen in the last picture in Fig. 4.8. Also, the picture shows that there is liquid droplets entrainment into the vapour core due to the breakup of the liquid film.

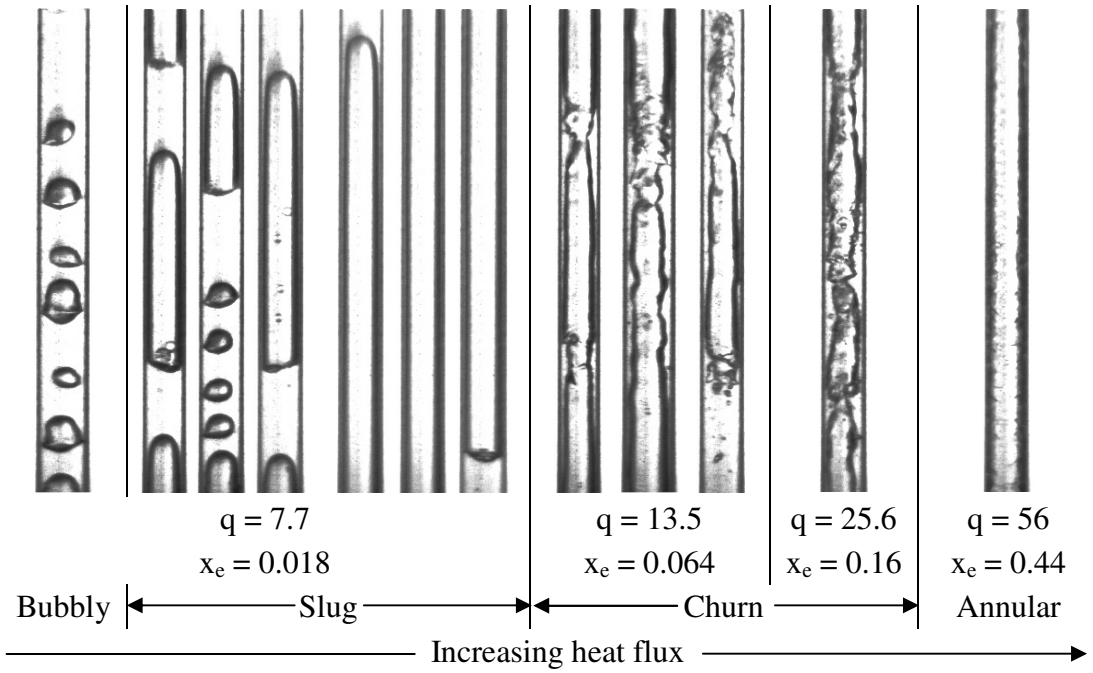

Fig. 4.8 Flow patterns observed at the exit of the 1.1 mm diameter seamless cold drawn tube, L = 150 mm at G = 300 kg/m^2.s, P = 6 bar as a function of exit quality and heat flux in kW/m^2.

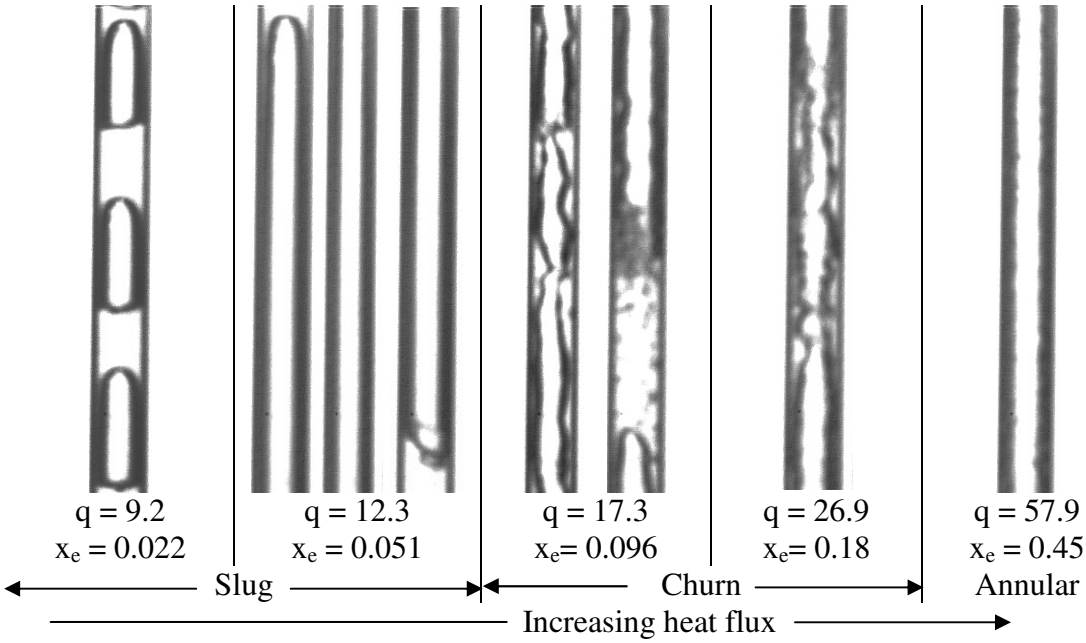

Fig. 4.9 Flow patterns observed at the exit of the 1.16 mm diameter welded tube, L = 150 mm at G = 300 kg/m^2.s, P = 6 bar as a function of exit quality and heat flux in kW/m^2.

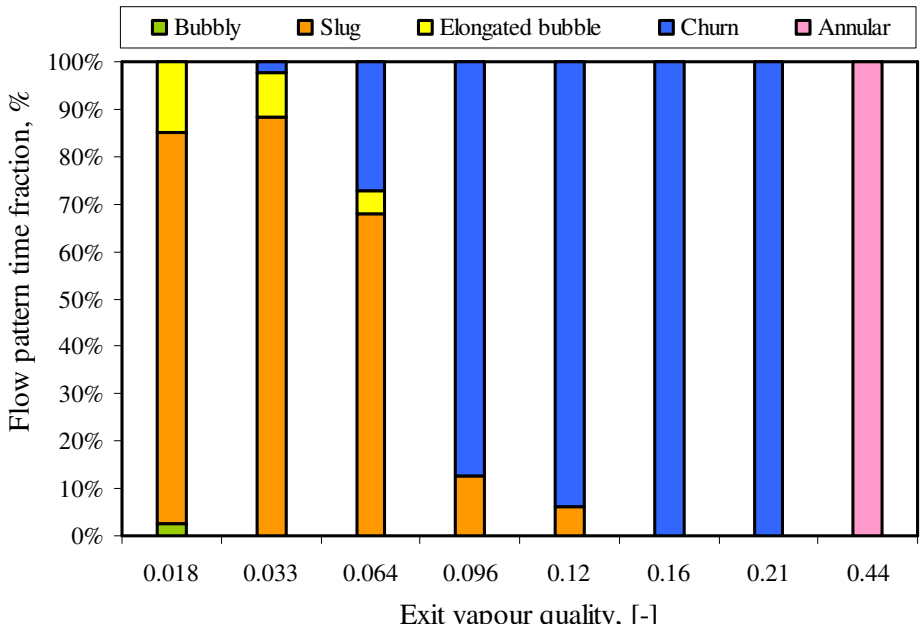

Figure 4.10 The time fraction of each flow pattern as a function of exit vapour quality at G = 280 kg/m^2 s and P = 6 bar for D = 1.1 mm diameter seamless cold drawn tube, L = 150 mm.

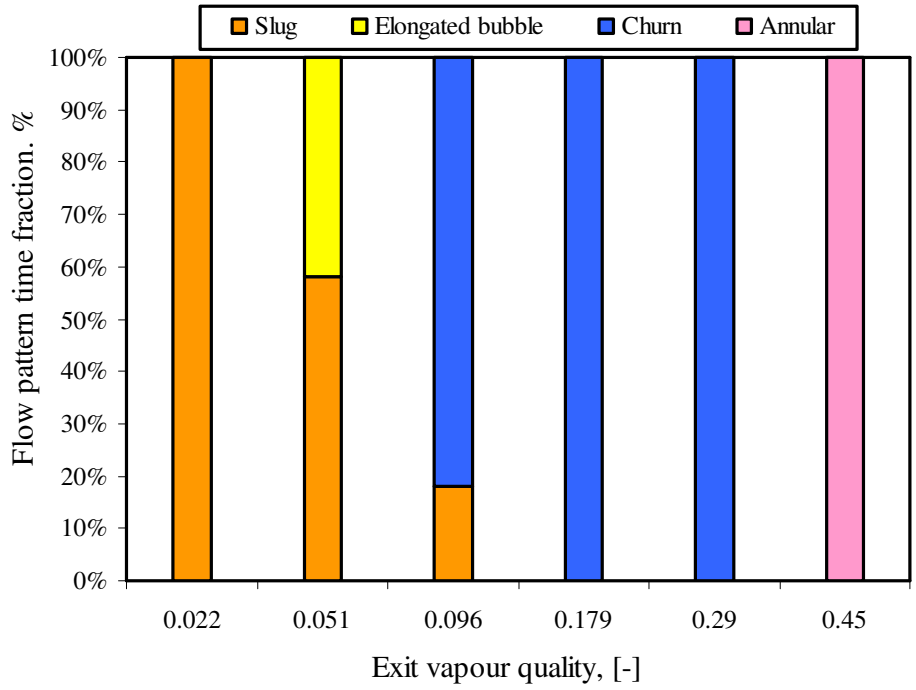

Figure 4.11 The time fraction of each flow pattern as a function of exit vapour quality at G = 300 kg/m^2 s and P = 6 bar for D = 1.16 mm diameter welded tube, L = 150 mm.

Figure 4.9 indicates that the observed flow regimes in the welded tube are slug, churn and annular flows. It is obvious from Figs. 4.8 and 4.9 that the difference between the flow patterns in the two tubes occurs only at low heat flux or low exit quality. In the welded tube, bubbly flow was not observed in any picture as seen in Fig. 4.11 whereas bubbly flow was observed in some pictures in the cold drawn tube. Once boiling started, a train of short vapour slugs with almost uniform length has appeared in the welded tube as seen in Fig. 4.9 at x = 0.022. Moreover, no tiny bubbles were observed in the liquid slugs between the consecutive bubbles. The absence of these kinds of bubbles in the welded tube at the lowest heat flux could be attributed to the effect of the tube inner surface characteristics. As previously discussed in Chapter 3, the SEM analysis of the welded tube indicated that the surface is very smooth with the existence of some local debris on the surface. This debris is defects resulting from the manufacturing process and they are not uniformly distributed along the length of the tube. In addition to that, the geometrical shape of the debris is not uniform and thus they may work as a nucleation cavity or may not. As a result, nucleation in the welded tube may commence only at some limited locations far away from the exit of the heated section (inlet of visualization section), i.e. in the first half of the tube. Accordingly, the nucleating bubble may then have a good chance to coalesce and form the well-ordered bubble train slug flow inside the heated section before it goes to the visualization section especially if they have formed near the entry of the heated test section. The resulting vapour slug may also prevent nucleation further away the entry section of the tube. The appearance of the well-ordered bubble train slug flow in the visualization section at almost uniform frequency may confirm that only very few sites are active and stable. On the contrary, the SEM analysis of the seamless cold drawn tube demonstrated that, the inner surface is uniformly scratched along the tube length which could be resulting from the stresses induced by the cold drawn manufacturing process. Therefore, more nucleation sites may exist along the length of the tube and there is a possibility for nucleation to occur at locations all along the heated section. As a result, bubbly flow and the tiny bubbles with a tip-like shape appeared with the seamless cold drawn tube. As the heat flux increased (x = 0.051), some of the well-ordered slug flow converted into elongated slugs which appeared in a considerable number of pictures compared to the seamless cold drawn tube as seen in Fig. 4.11. With further increase in heat flux, the features of the flow regimes in the welded and the seamless clod drawn tube were almost similar until the development of annular flow.

Effect of heated length

The flow patterns due to boiling in metallic tubes are observed in a glass section located immediately after the heated section. Nevertheless, there is debate that must be presented on whether the observed flow patterns may or may not be representing the actual flow patterns inside the heated section. This concern may occur at low to intermediate heat fluxes when the coalescence rate is too high. This point can be investigated experimentally either by fixing the length of the heated section and observing the flow regimes at different locations or varying the length of the heated section and fixing the observation location. Increasing the length of the heated section may give the flow patterns the chance to keep developing while they are moving towards the exit of the heated section. However, Revellin et al. (2007) varied the heated length from 30 to 70 mm for a 0.5 mm diameter tube and R134a refrigerant and did not find significant effect on the location of the transition boundaries. The investigated range of heated lengths by Revellin et al. may not be enough to see clearly whether there is an effect or not. Therefore, the current experimental study investigates the effect of varying the heated length on flow patterns and heat transfer. The length was varied from 150 to 450 mm for the 1.1 mm diameter seamless cold drawn tube. Figure 4.12 shows the typically observed flow patterns for the three test sections with heated lengths of 150, 300 and 450 mm at 6 bar system pressure and 300 kg/m^2 s mass flux whilst Fig. 4.13 shows the time fraction charts. Figures 4.12 and 4.13 demonstrate that, three regimes dominate for the different heated lengths namely slug, churn and annular flow regimes. Figures 4.12a and 4.13a were discussed before in the previous section (see Figs. 4.8 and 4.10) and they were included here for comparison only. It is interesting to note that, in Fig. 4.12b for the 300 mm length, no slug flow was observed as was the case in Figs. 4.12a and 4.12c for the other heated lengths. The reason is not the effect of the heated length but is the difficulty of boiling incipience which sometimes encountered in some experimental runs. In this tube at inlet sub-cooling value of 5.2K, boiling started at heat flux value of 7.5 kW/m^2 (x = 0.1) and the wall superheat reached more than 14K before boiling incipience. So, at heat flux values below 7.5 kW/m^2, the flow remains single phase liquid as seen in the first picture in Fig. 4.12b. When boiling started normally in the same tube (L = 300 mm) as seen in Fig. 4.14 for P = 8 bar and G = 300 kg/m^2 s as an example, bubbly and slug flow appeared in a considerable number of pictures.

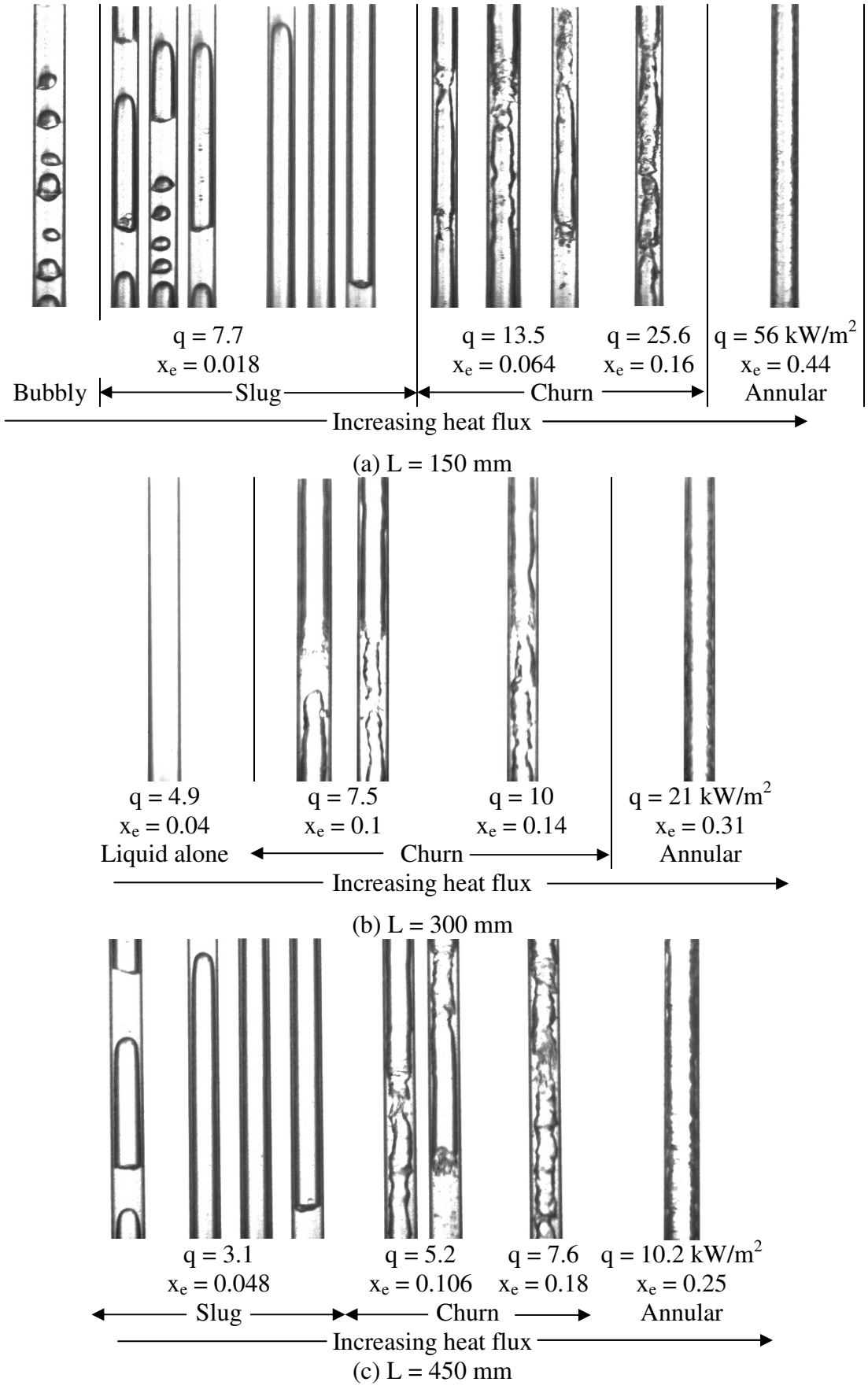

Fig. 4.12 Flow patterns observed at the exit of the 1.1 mm diameter seamless cold drawn tube for different heated lengths at G = 300 kg/m^2.s and P = 6 bar

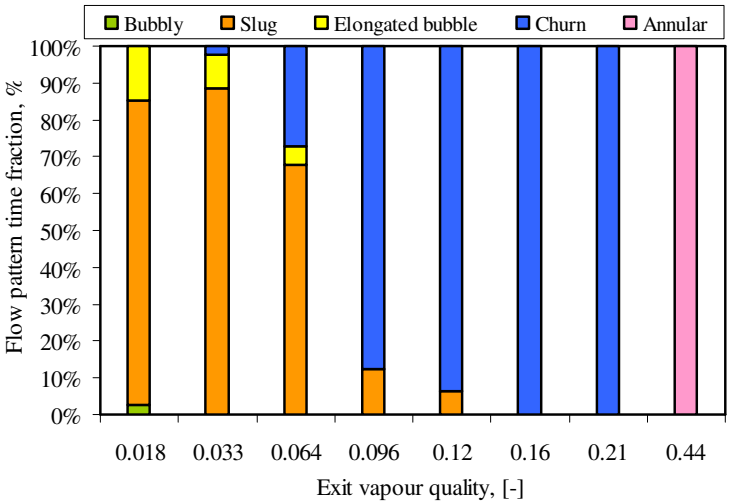

(a) L = 150 mm

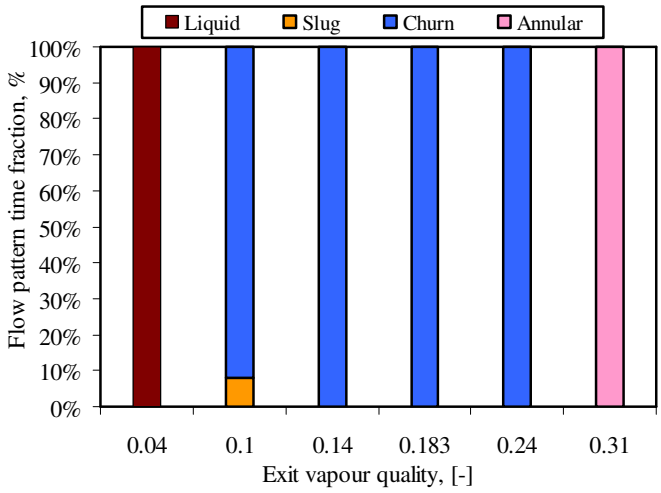

(a) L = 300 mm

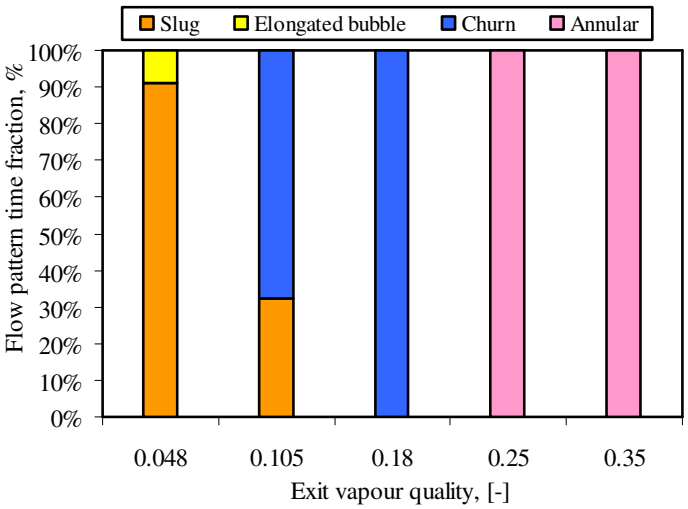

(b) L = 450 mm

Figure 4.13 The time fraction of each flow pattern as a function of exit vapour quality at G = 300 kg/m^2 s and P = 6 bar for D = 1.1mm for different heated lengths in the seamless cold drawn tube.

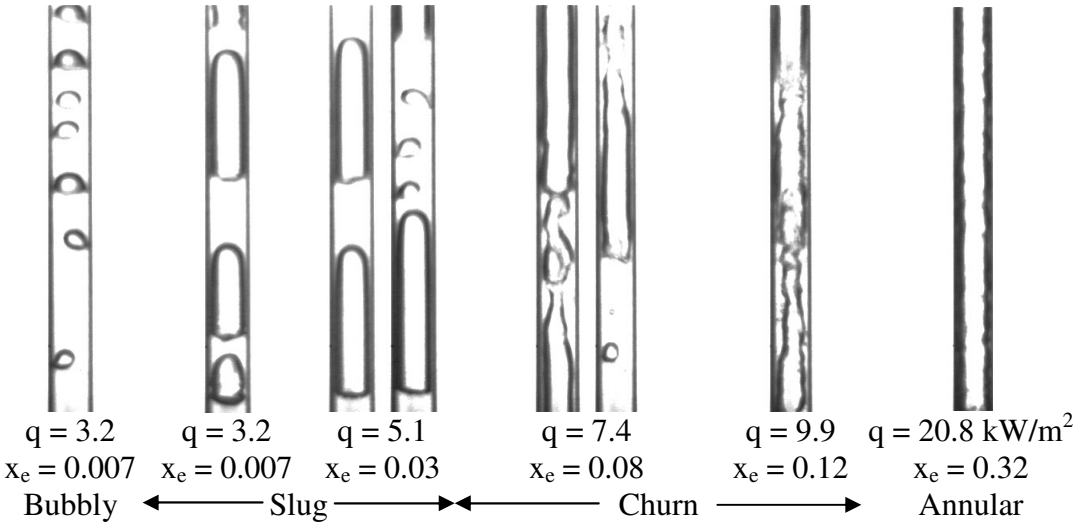

(a) Typically observed pictures

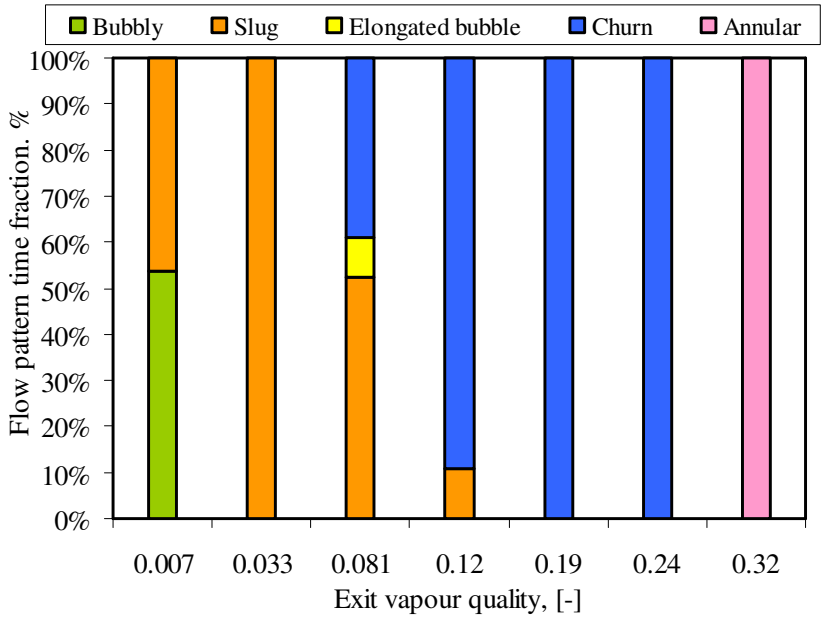

(b) Time fraction plot

Fig. 4.14 Flow patterns observed at the exit of the 1.1 mm diameter for the seamless cold drawn tube, L = 300 mm at G = 300 kg/m^2.s, P = 8 bar.

It is obvious from the above figures that, annular flow appears early at lower vapour quality for the longer heated section. The other flow patterns seem to be insignificantly influenced by the heated length. It is important to note that, the heated length will significantly affect the flow patterns if the comparison was conducted at same heat flux. The comparison at fixed heat flux means that the exit vapour quality of the longest section will be much greater than the exit vapour quality of the shortest one. Consequently, the flow patterns are expected to be different.

The above figures demonstrate that the features of the observed flow regimes in the 1.1 mm tubes are different compared to those observed in the 0.52 mm tube. The differences include the following: (i) the appearance of more than one flow pattern at the same heat flux that was observed in the 0.52 mm tube was found to be less frequent in the 1.1 mm tube. This could be due to the existence of relatively large number of active and stable nucleation sites in the 1.1 mm tubes compared to the 0.52 mm diameter tube; (ii) The length of vapour slugs was approximately uniform in most pictures in the 1.1 mm tubes compared to large variations in slug lengths in the 0.52 mm tube; (iii) The transitional regime with a neck-like shape that was observed in the 0.52 mm tube was not observed in the 1.1 mm tubes. This could be due to the difference in the liquid Reynolds number in the two tubes at the same mass flux and system pressure. In the 0.52 mm tube, the flow was laminar (Re = 818) whereas in the 1.1 mm tube the flow was at higher Reynolds number, Re = 1875. Inspecting the flow patterns observed in the 1.1 mm cold drawn tube (L = 150 mm) at a mass flux of 100 kg/m^2 s (Re =780) and 6 bar system pressure did not show any transition regime with a neck-like shape, which means that there is a mechanism other than flow conditions, i.e. laminar or turbulent. Figure 4.15 shows how the neck-like shape forms and disappears after coalescence in the 1.1 mm tube whereas they stay after coalescence in the 0.52 mm tube as seen in Fig. 4.7. Figure 4.15 shows that, after the liquid bridge between the two coalescing bubbles disappears, the liquid/vapour interface is disturbed with a wave that appears first at the tail of the leading bubble. After about 5 ms (picture 5 in Fig. 4.15), the disturbance disappeared and the neck-like shape formed with a smooth liquid/vapour interface up and down the neck. The two bubbles after coalescence seem moving with a very low velocity and after 30 ms (picture 30 in Fig. 4.15) from the onset of coalescence the neck released into the liquid slug following the bubble. The video indicated that the neck propagates in the upstream side and releases at the trailing liquid slug. In the 0.52 mm tube, due to the small curvature compared to the one in the 1.1 mm tube, the pressure inside the bubble creates a uniform radial force that squeezes the thin liquid film and damps the wave resulting from the coalescence process. On the other hand, the thick liquid film and the relatively low pressure inside the bubble in the 1.1 mm tube may allow the neck to propagate into the upstream side. It is interesting to note that, the tail of the long bubble after coalescence is moving with a velocity of 1.76 m/s whereas the head of the short bubble in Fig. 4.15 is moving with a velocity of 1.5 m/s

which agrees with Agostini et al. (2008c) who reported that long bubbles move faster than the shorter ones.

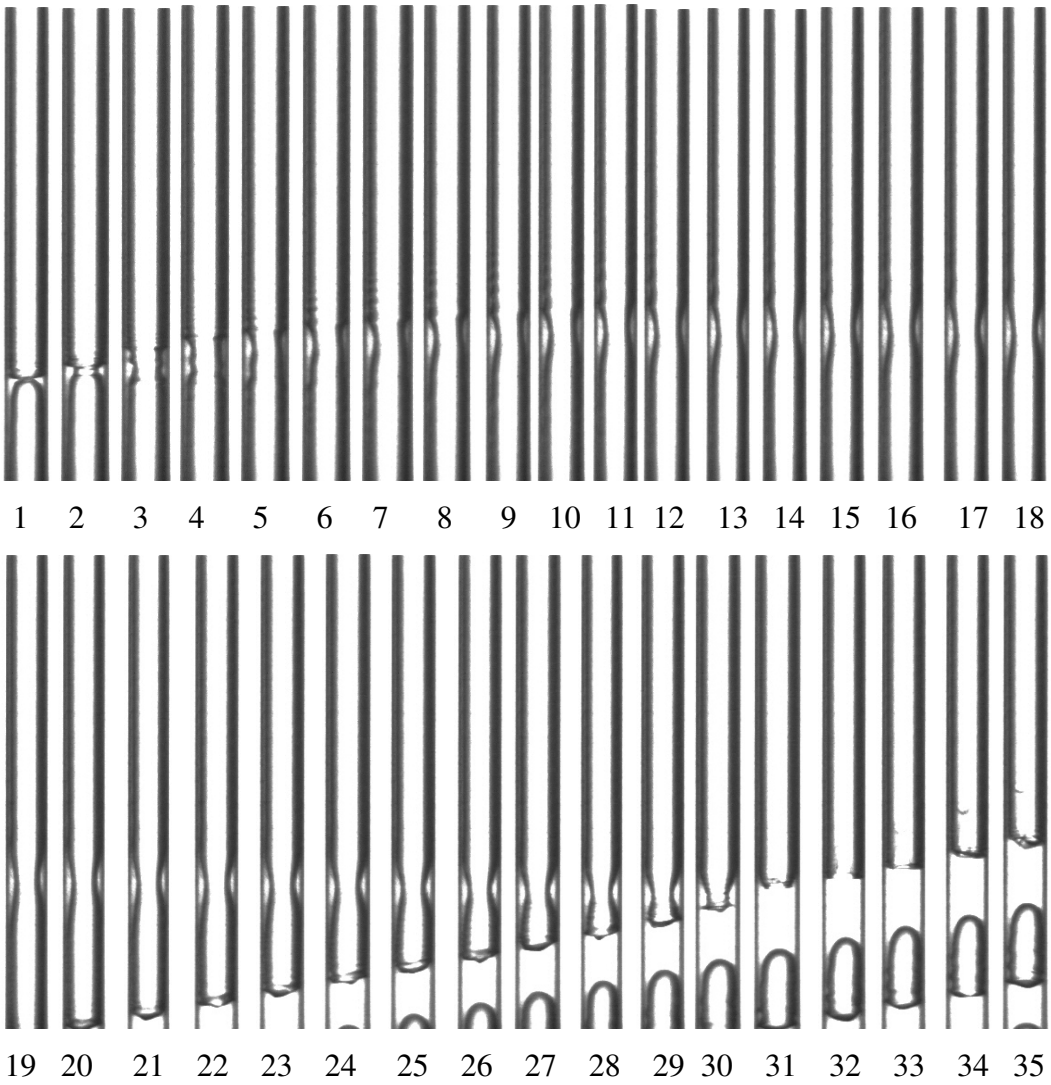

Figure 4.15 The sequence of pictures that shows how the neck-like shape forms and disappear in the 1.1 mm cold drawn tube (L = 150 mm) at G = 100 kg/m^2 s and P = 6 bar, the numbers underneath each picture refer to the time step in ms.

4.2.3 Comparison with flow maps

There are many flow maps in the open literature developed for small diameter tubes. Nevertheless, most of these maps were developed for adiabatic air-water mixture and the high surface tension of water compared to refrigerants may influence some of the transition boundaries. Therefore, the flow patterns results of the current study were compared with two maps developed using similar refrigerant and tube diameters as the

current study. The first map is the one developed by Chen (2006) for R134a and 1.1 mm diameter tube at 6 bar system pressure. He investigated a wide range of tube diameters (4.26 – 1.1 mm) and system pressure (6 – 14 bar). The second map is the one developed by Revellin and Thome (2007c) using two refrigerants (R134a and R245fa) and two tubes with diameters 0.509 and 0.79 mm. They proposed a new diabatic flow pattern map based on observing the flow regimes in two horizontal glass tubes located after a stainless steel micro-evaporator. The map was plotted as mass flux versus vapour quality map. Firstly, they classified the observed flow patterns in a classical way into bubbly flow, bubbly/slug transition regime, slug flow, slug/semi-annular transition regime, semi-annular flow and annular flow. Secondly, they re-classified these regimes again into isolated bubbles, coalescing bubbles and annular flow regimes based on the rates of bubble generation and bubble coalescence. The isolated bubbles regime (IB) included both bubbly and/or slug flow since the bubble coalescence rate was much lower than the bubble generation rate. Their flow map includes three transition boundaries namely: the isolated bubbles regime to coalescing bubble regime transition, the coalescing bubble regime to annular flow regime transition and the annular flow regime to post dry out transition. The post dry out transition boundary is not shown in the figures presented later. They correlated the isolated bubble regime to coalescing bubble regime transition boundary as a function of heat flux, liquid Reynolds number and gas Weber number whilst transition from coalescing to annular was given only as a function of liquid Reynolds and Weber numbers. According to their equations, as the heat flux increases, the transition line IB/CB shifts to the right, i.e. the isolated bubble region becomes wider. This effect of heat flux on the IB/CB transition boundary seems contradicting to the fact that increasing heat flux results in an increase in the bubble generation frequency and evaporation rate. Therefore, the small nucleating bubbles are expected to coalesce and elongate rapidly as the heat flux increases during their moving towards the exit of the heated section. Accordingly, it is hardly observing isolated bubbles or slugs at high heat fluxes. In the current study, the experimental transition boundary from isolated bubbles to coalescing bubbles was found to occur at about 10 kW/m^2 heat flux. Therefore, the map of Revellin and Thome was plotted at q = 10 kW/m^2 for the aim of comparison with the experimental values. For the sake of comparison with the Revellin and Thome map, the same classification of flow patterns has been followed. Bubbly and slug flow (including elongated bubble), which were observed in the current study, was considered as isolated bubbles and the transition to

annular regime was considered as a coalescing regime. Table 4.2 summarizes the flow patterns classification that was followed in the current study to match the same names proposed by Revellin and Thome for the purpose of comparison with their map. Similarly, the classification that was followed for the comparison with Chen (2006) is summarized in Table 4.3 especially for the 0.52 mm tube. For the 1.1 mm diameter tube, there is an agreement between the current study and that of Chen (2006) on the names of the flow patterns. Accordingly, the flow patterns were directly compared with that of Chen (2006) for the 1.1 mm tube.

Table 4.2 Flow patterns classification used for the comparison with the Revellin and Thome map.

The current study	Revellin and Thome (2007c) map
D = 0.52 mm	
Bubbly	Isolated bubbles
Slug	
Transition to annular	Coalescence bubble
Annular	Annular
D = 1.1 mm	
Bubbly	Isolated bubbles
Slug	
Churn	Coalescence bubble
Annular	Annular

Table 4.3 Flow patterns classification used for the comparison with the Chen (2006) map for the 0.52 mm tube*.

The current study	Chen (2006) map
Bubbly	Bubbly
Slug	Slug
Transition to annular	Churn
Annular	Annular

* For the 1.1 mm tubes, bubbly, slug, churn and annular were observed in the current study, which are exactly the same as those observed by Chen (2006)

Figure 4.16 shows the experimental results compared to the map of Revellin and Thome (2007c) for all investigated tubes. The figure indicates that all experimental transition boundaries shift to occur at lower vapour quality as the mass flux increases. It is also obvious that there is a rough agreement on the transition from isolated bubbles (IB) to the coalescing bubble (CB) for all investigated tubes. The small deviations at that boundary may be arising from the rough value of heat flux that was selected to plot this transition boundary. Additionally, this transition boundary seems to be independent of diameter and heated length. On the other hand, the transition from coalescence bubble (CB) to annular flow regime (A) exhibited different behaviour. For the 0.52 mm diameter tube, the experimental results agreed very well with the CB/A transition boundary. For the 1.1 mm diameter tubes, the experimental results indicate that the transition boundary CB/A shifts to occur at lower vapour quality compared to that given by Revellin and Thome. Figure 4.17 shows the effect of heated length on the IB/CB and CB/A transition boundaries. It is clear that there is no significant effect on the IB/CB transition boundary whilst there is a small effect on the CB/A transition. It tends to occur at lower quality as the length increases.

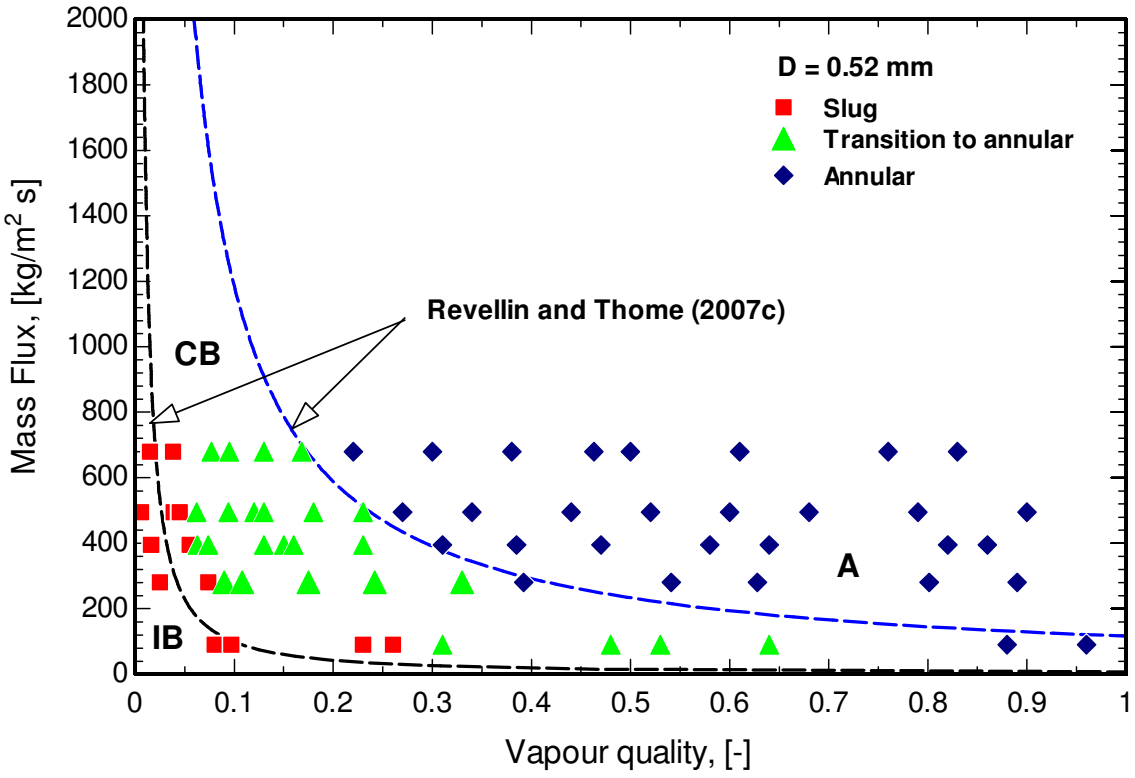

(a) D = 0.52 mm, L = 100 mm, seamless cold drawn

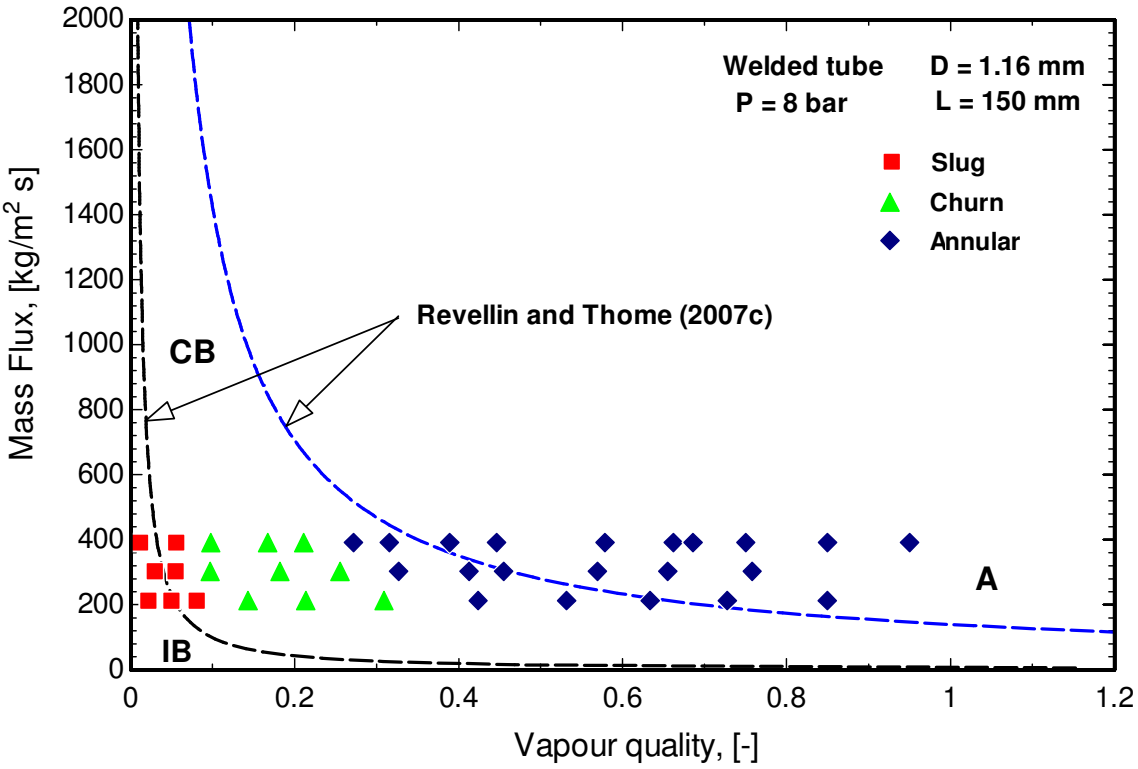

(b) D = 1.16 mm, L = 150 mm, welded tube

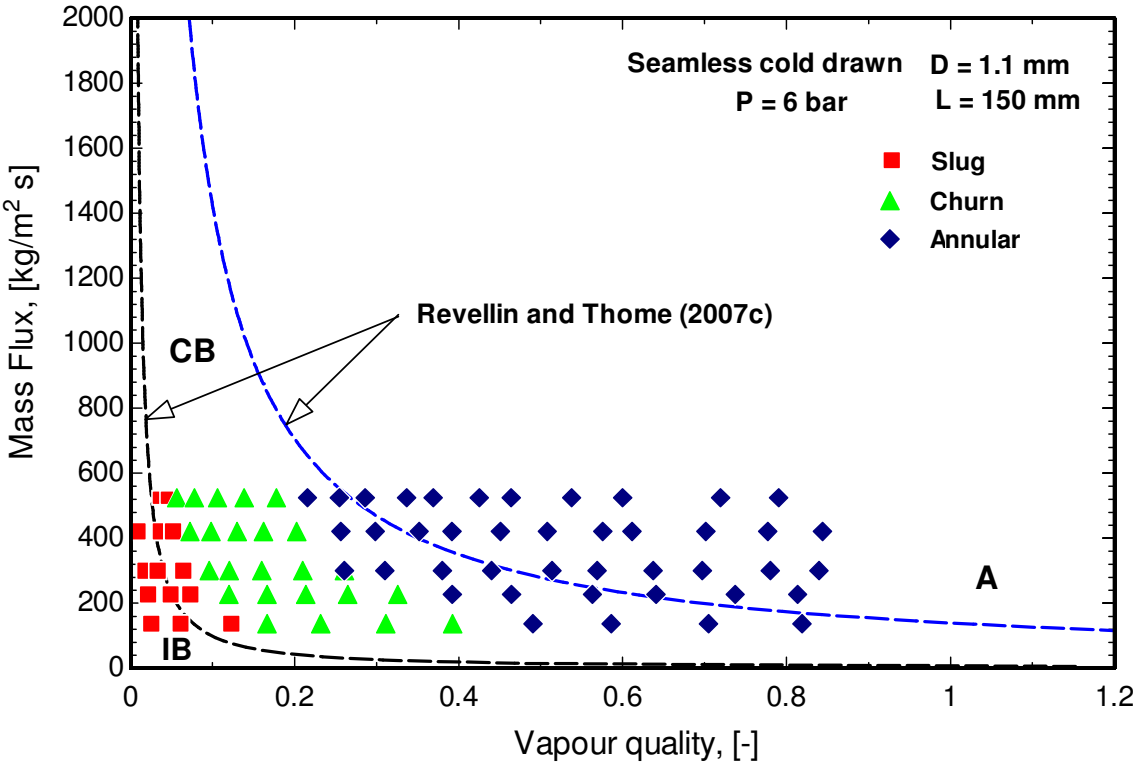

(c) D = 1.1 mm, L = 150 mm, seamless cold drawn tube

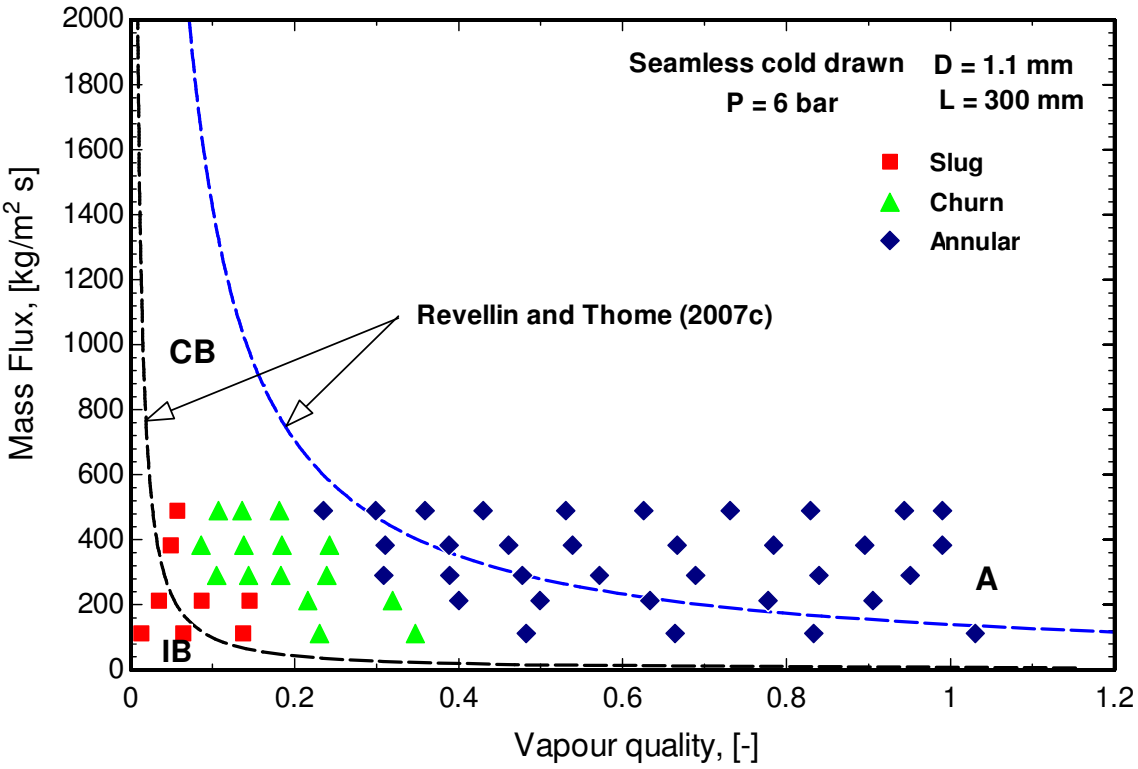

(d) D = 1.1 mm, L = 300 mm, seamless cold drawn tube

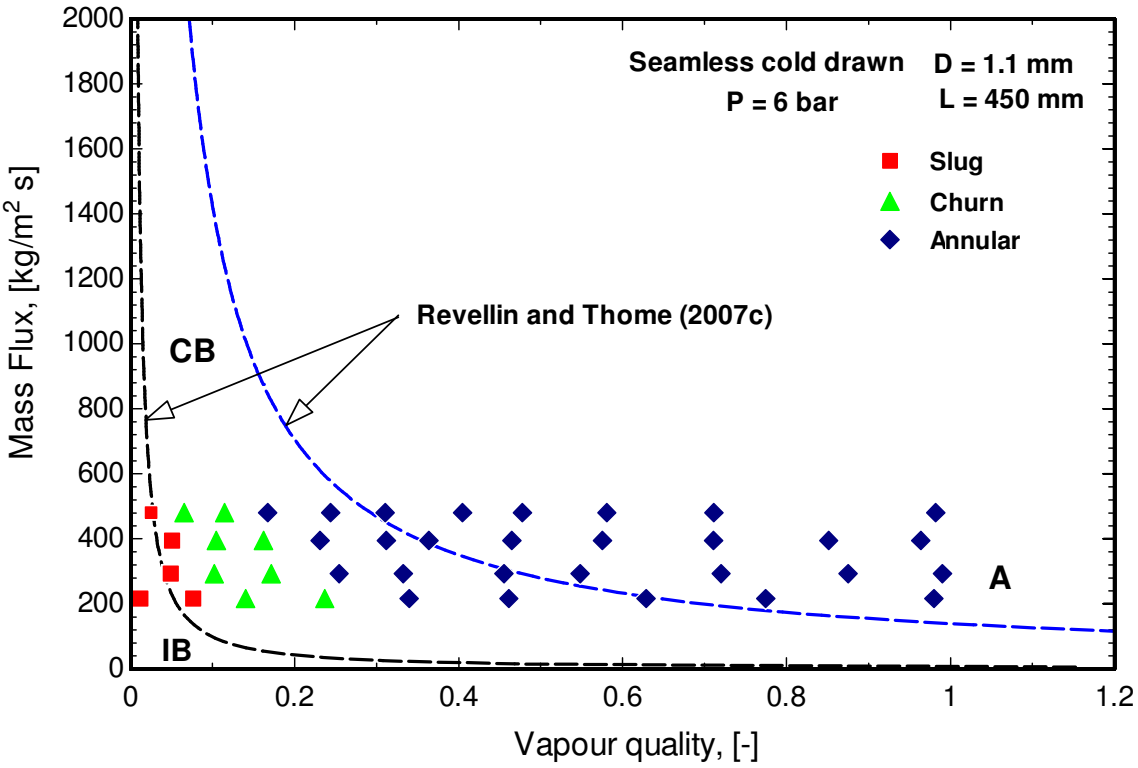

(e) D = 1.1 mm, L = 450 mm, seamless cold drawn tube

Figure 4.16 The experimental results compared to the flow map of Revellin and Thome (2007c) plotted at q = 10 kW/m^2 and 6 bar system pressure.

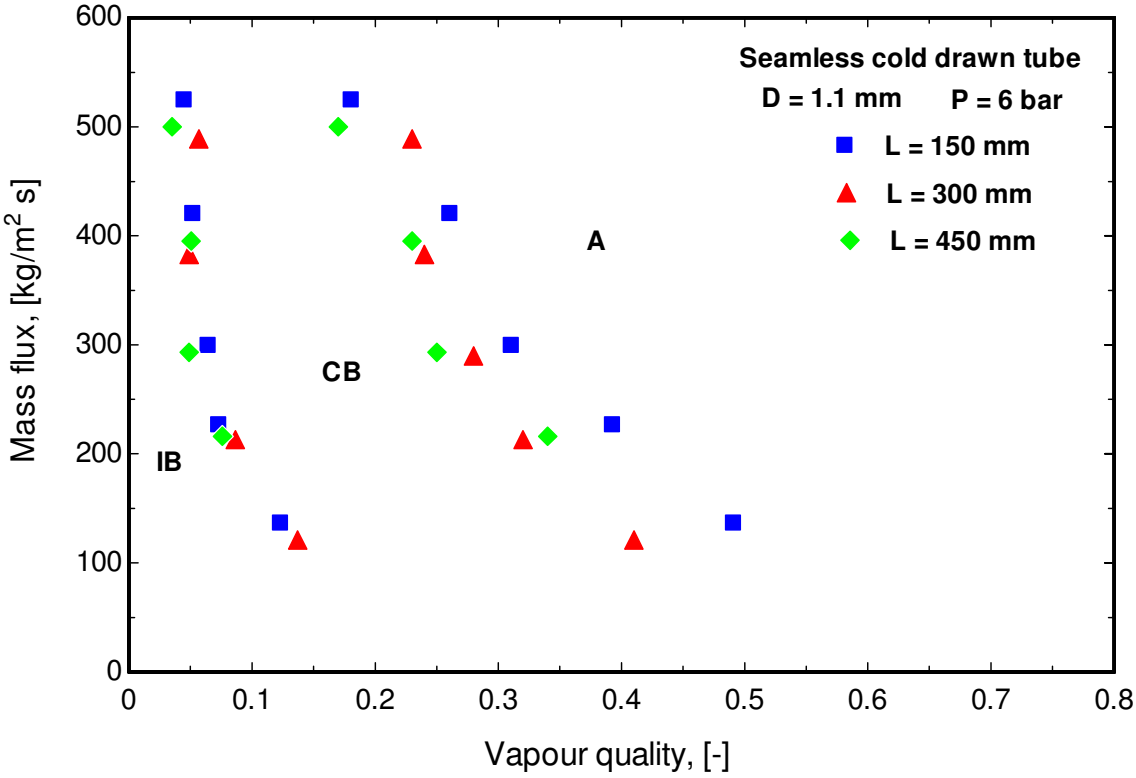

Figure 4.17 The effect of heated length on the flow patterns transition boundaries plotted on the mass flux versus exit quality map.

Figure 4.18 depicts the experimental results compared to the map of Chen (2006). The map was plotted as superficial liquid velocity versus superficial vapour velocity based on observing six flow regimes: bubbly, confined bubble, dispersed bubble, slug, churn and annular flow regimes. For the sake of comparison, the transitional regime between slug and annular observed in the current study was considered as a churn flow. The figure shows that, the experimental transition boundary between churn and annular flow was slightly shifted to the right compared to the Chen (2006) transition boundary but it keeps the same dependence on the gas superficial velocity. On the other hand, the experimental transition boundary between slug and churn flow showed little dependence on the gas superficial velocity. Figure 4.19 depicts the effect of system pressure on the flow patterns transition boundaries. It is obvious from the figure that, there is no clear effect for the system pressure (range 6 – 8 bar) on all transition boundaries though Fig. 4.19b shows that there is a tendency for the transition boundaries to be shifted to the left as the pressure increases. Chen et al. (2006) reported similar effect for pressure on slug-churn and churn-annular transition boundaries.

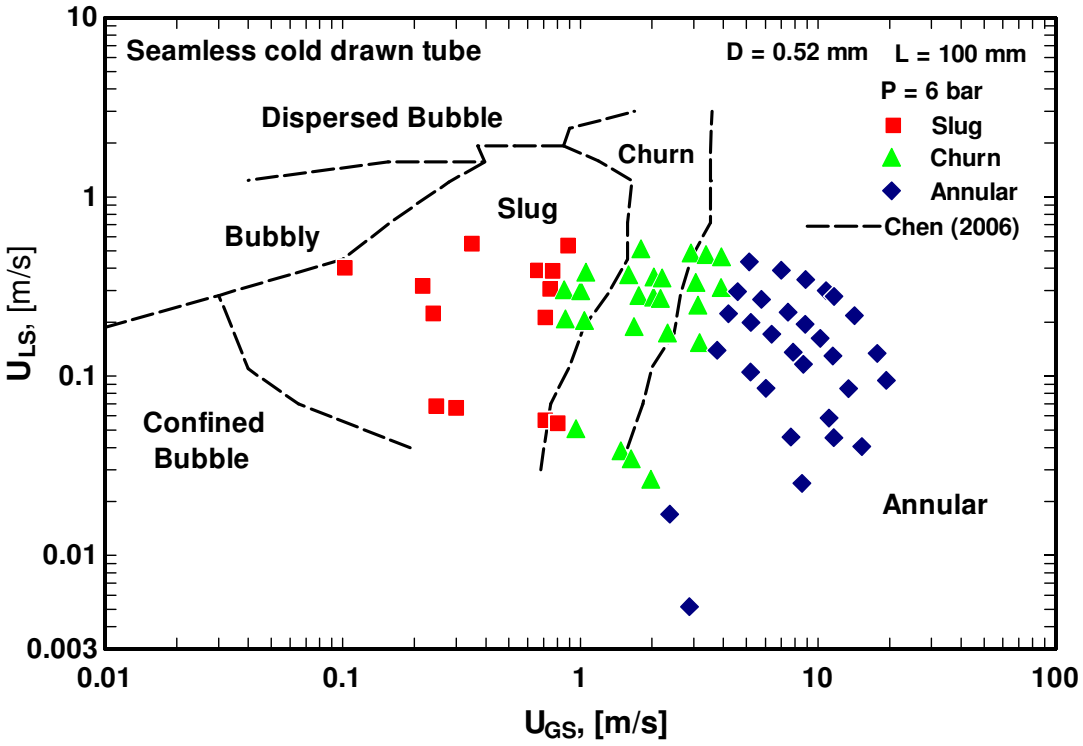

(a) D = 0.52 mm, L = 100 mm, seamless cold drawn

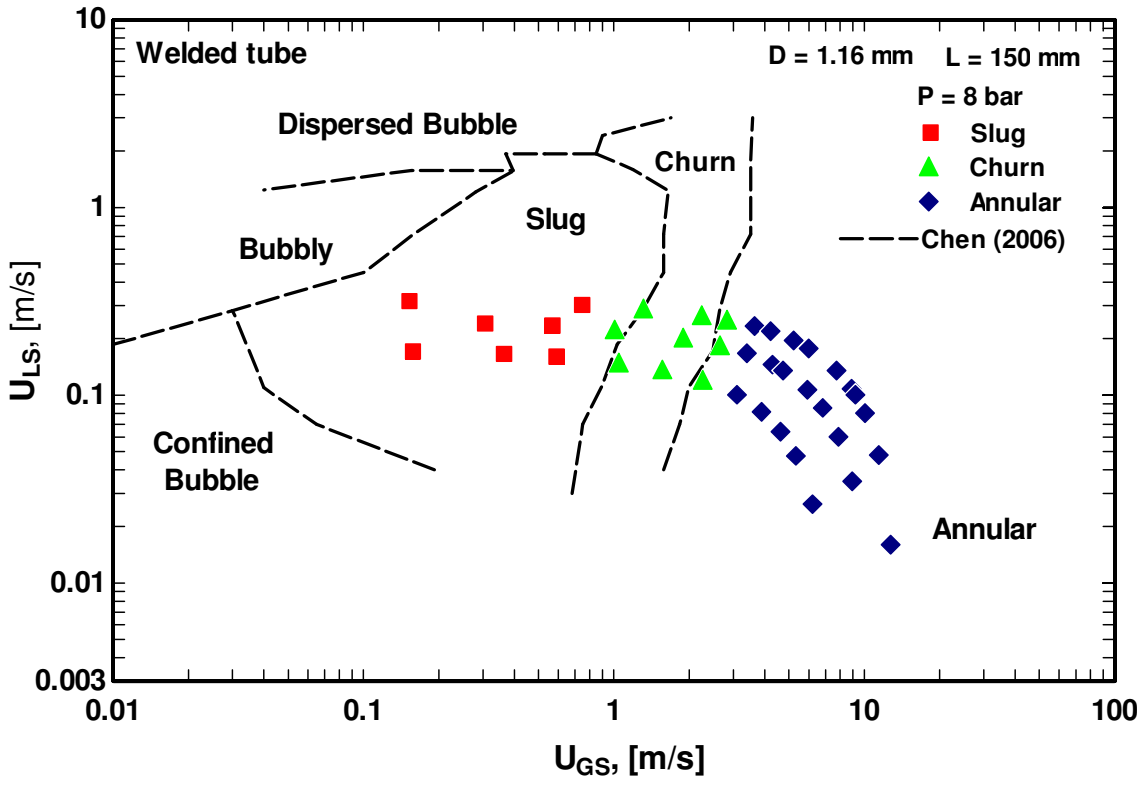

(b) D = 1.16 mm, L = 150 mm, welded tube

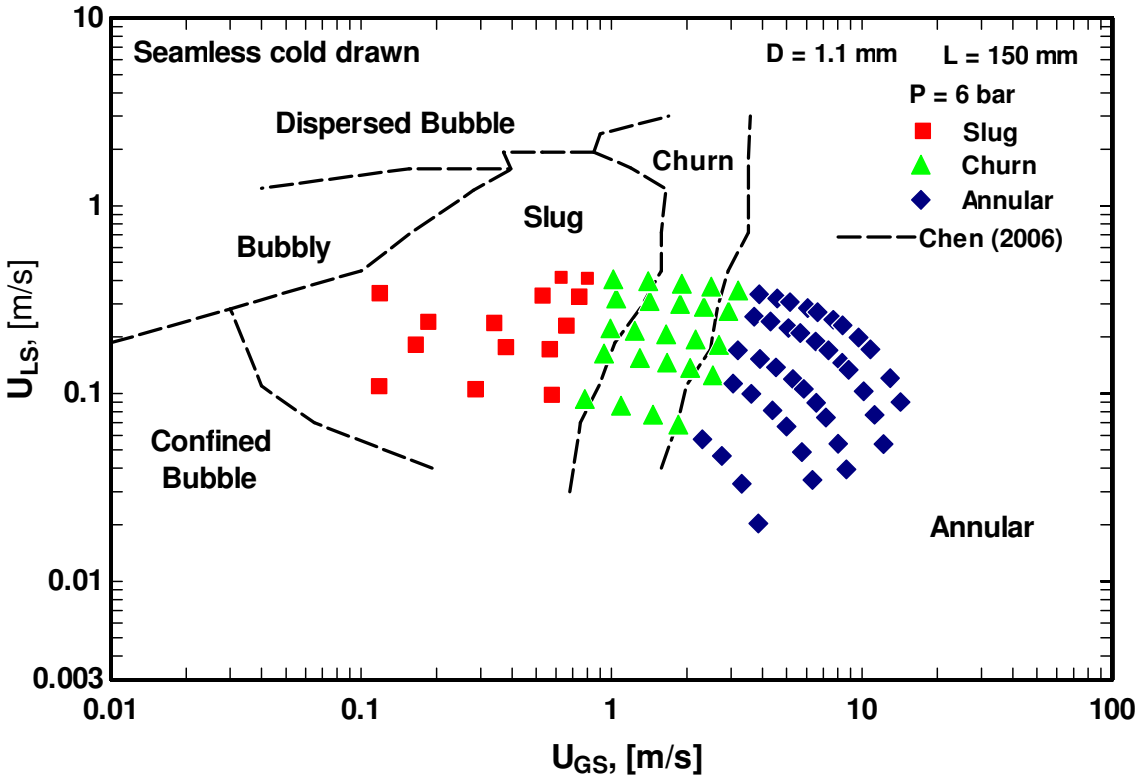

(c) D = 1.1 mm, L = 150 mm, seamless cold drawn tube

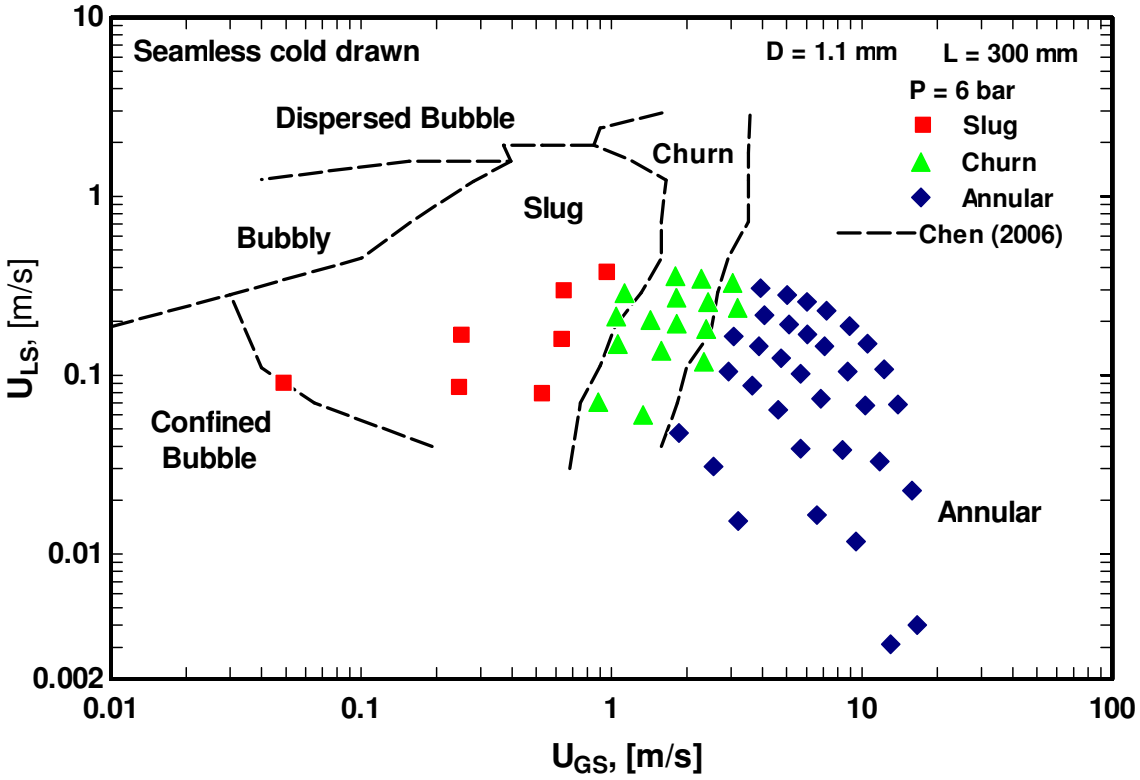

(d) D = 1.1 mm, L = 300 mm, seamless cold drawn

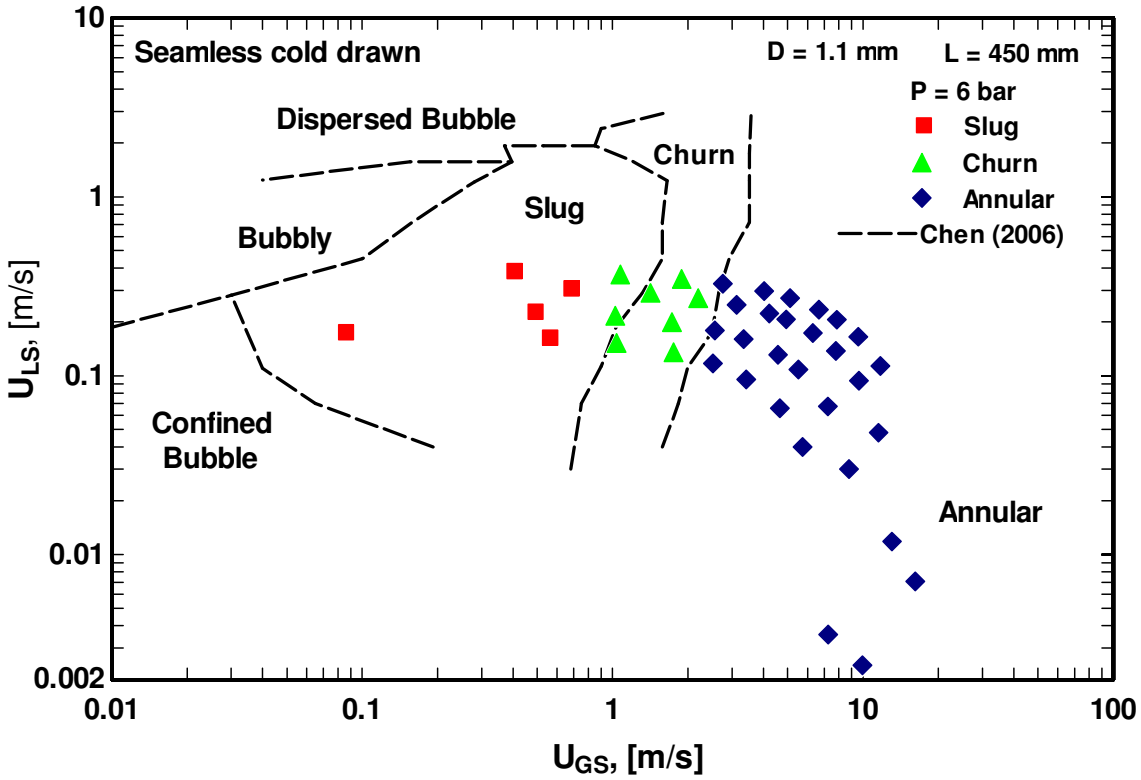

(e) D = 1.1 mm, L = 450 mm, seamless cold drawn

Figure 4.18 The experimental results compared to the flow map of Chen (2006) that were developed for 1.1 mm diameter tube at 6 bar system pressure.

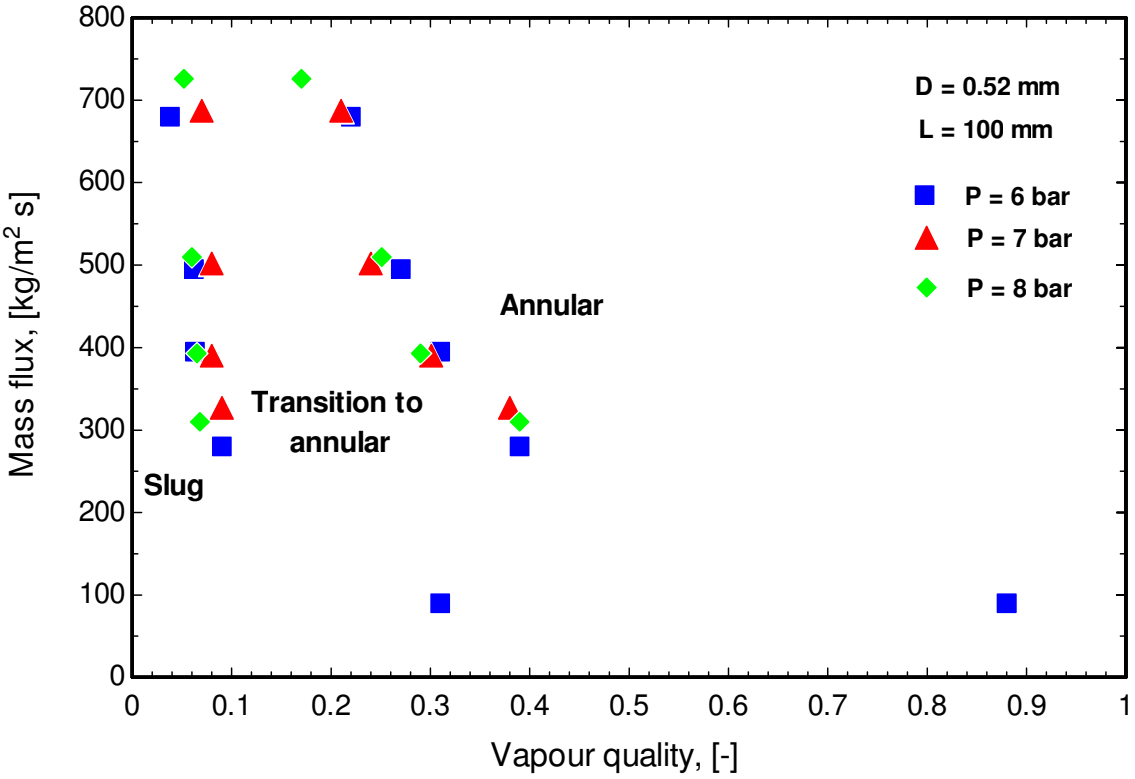

(a) Mass flux versus vapour quality plot

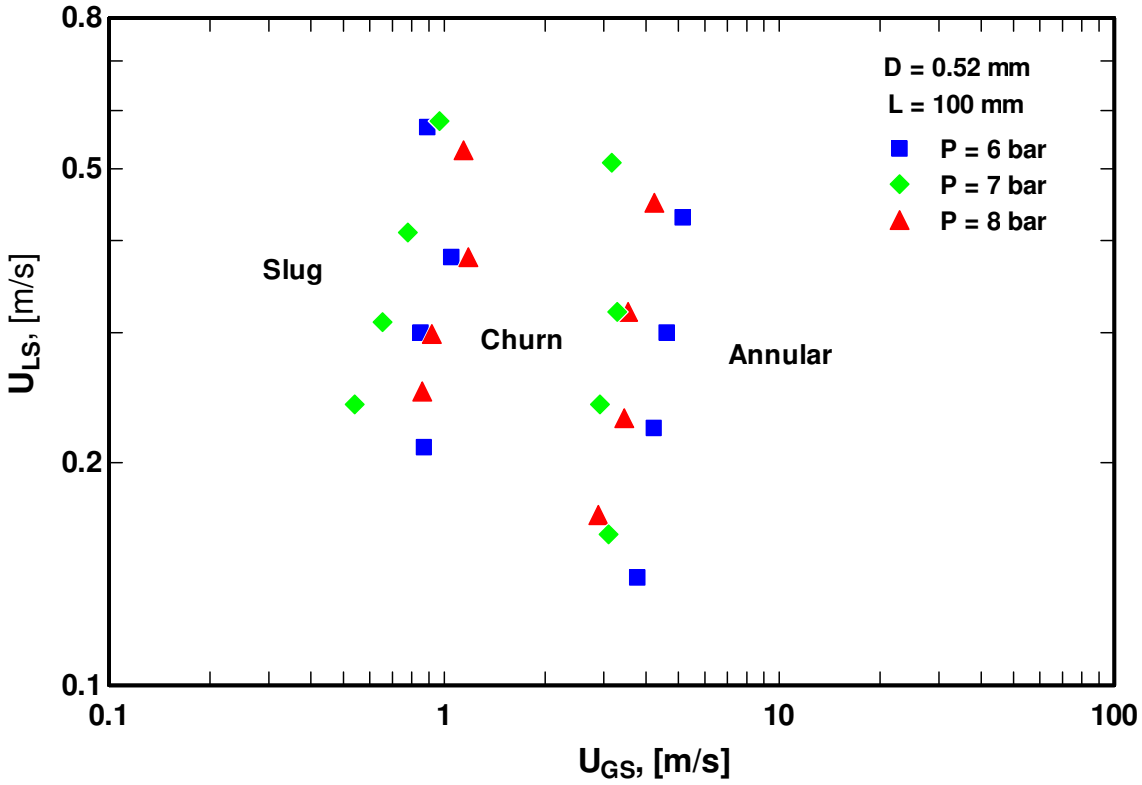

(b) Superficial velocities plot

Figure 4.19 Effect of system pressure on the transition boundaries for the 0.52 mm diameter tube.

4.3 Heat transfer results

This section presents the effect of heat flux, mass flux and system pressure on the local time averaged heat transfer coefficient. All measurements were recorded after the system reached steady state conditions, i.e. minimum oscillations in mass flow rate, pressures and temperature. Once the system stabilizes, the mass flux and system pressure were adjusted at the required values then heat flux was varied by gradually increasing the applied heating power. Figures 4.20 to 4.23 illustrate the oscillations in different parameters over a 90 sec period as a function of heat flux. These figures represent only one example for D = 1.1 mm, L = 150 mm at 6 bar system pressure and 300 kg/m^2 s nominal mass flux. For other experimental conditions and test sections, similar plots can be obtained. The figures indicate that, at zero heat flux, the oscillations in all parameters are very small, which confirms that the facility has reached its steady state. The oscillations in the outlet pressure shown in Fig. 4.22b at zero heat flux are

relatively high compared to the oscillations in the inlet pressure but both of them are very small. This could be due to the fact that the pressure transducers installed at the test section inlet and outlet are not similar. The one installed at the inlet has a range of 0 – 20 bar while the other one at the outlet has a range of 0 – 10 bar. Within the heat flux range from 0 to 96 kW/m^2, the fluctuations in mass flux were less than ± 6 % of the nominal value (300 kg/m^2 s) even when partial dryout occurred. On the other hand, at high heat fluxes, all parameters recorded relatively high oscillations due to the occurrence of partial dryout which causes some kind of system instability. Some researchers such as Wang et al. (2007) reported large oscillation in wall temperature with an amplitude of 36 K and also Fu et al. (2008) reported 992.4 kg/m^2 s and 60 kPa as oscillation amplitudes in mass flux and pressure drop, respectively which are very high compared to the current study. Table 4.4 summarizes the standard deviation of each parameter, which confirms the occurrence of steady state and stable boiling. The last column in the table is calculated by dividing the standard deviation over the mean value. The table shows that, at zero heat flux, the highest deviation was 4.29 % for the mass flux, which is too small whereas, at the highest heat flux (partial dryout), the highest deviation was 27.7 % for pressure drop due to the changes in the flow patterns between single phase vapour and two phase mixture at dryout conditions. Accordingly, all flow boiling heat transfer results presented in this chapter are representing stable boiling.

Table 4.4 The standard deviation of each parameter for a 90 data point sample

q, [kW/m^2]	Parameter	Mean value	Standard deviation	% deviation
0	Mass flow rate, [kg/hr]	1.12	0.044464	3.97
	Mass flux, [kg/m^2 s]	295.44	12.677	4.29
	Inlet temperature, [^{0}C]	14.023	0.0411	0.29
	Outlet temperature, [^{0}C]	14.237	0.0452	0.32
	Inlet pressure, [bar]	5.999	0.0009	0.015
	Outlet pressure, [bar]	5.992	0.021333	0.36
	Pressure drop, [bar]	0.00273	0.0000414	1.52
	Wall temperature, [^{0}C]	14.097	0.0489	0.35
97 (dryout)	Mass flow rate, [kg/hr]	1.1077	0.0611	5.5
	Mass flux, [kg/m^2 s]	291.04	16.054	5.52
	Inlet temperature, [^{0}C]	19.278	0.2173	1.13
	Outlet temperature, [^{0}C]	21.391	0.1169	0.55
	Inlet pressure, [bar]	6.0934	0.04668	0.77
	Outlet pressure, [bar]	6.0048	0.034	0.57
	Pressure drop, [bar]	0.06942	0.01922	27.7
	Wall temperature, [^{0}C]	31.2224	0.1976	0.63

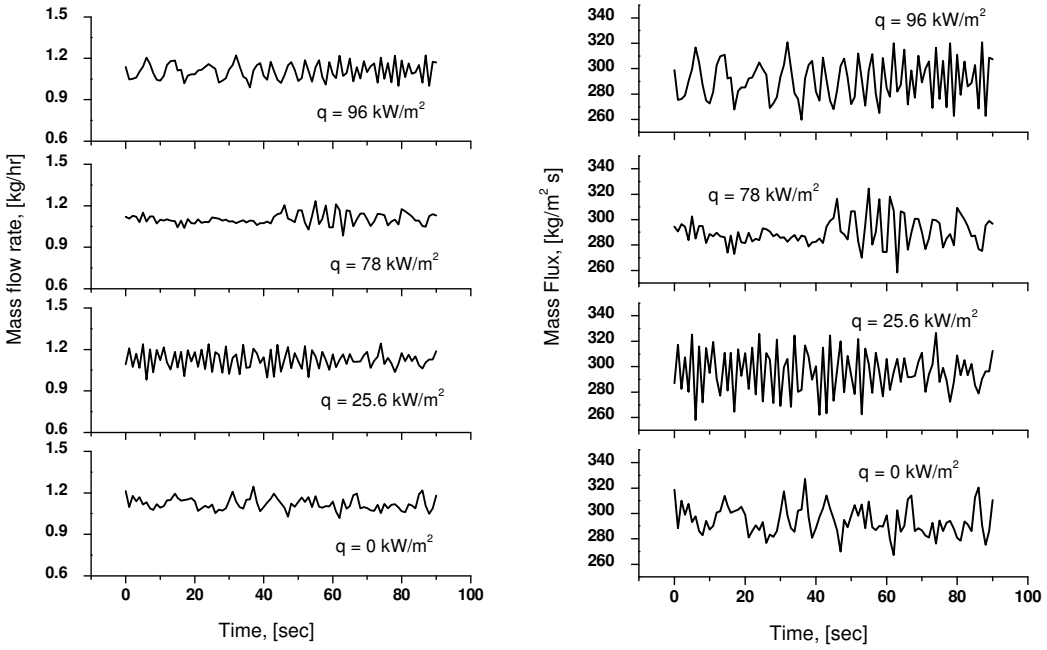

(a) mass flow rate (b) mass flux

Figure 4.20 The oscillations in mass flow rate and mass flux at some heat flux values for D = 1.1 mm and L = 150 mm at P = 6 bar and G = 300 kg/m^2 s.

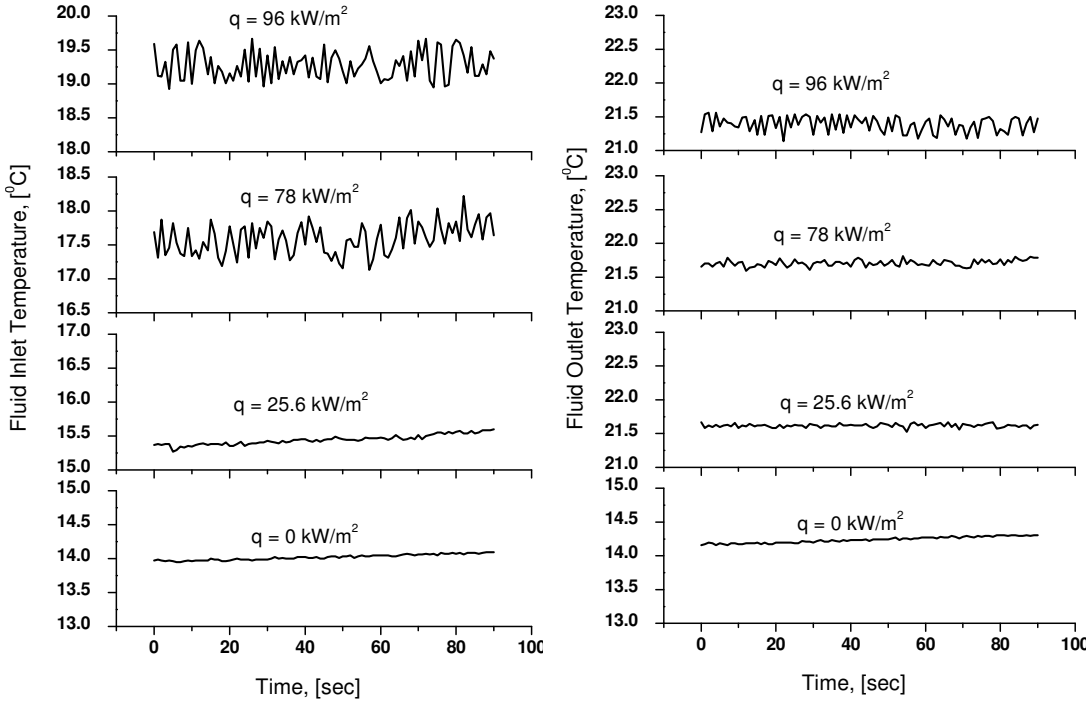

(a) fluid inlet temperature (b) fluid outlet temperature

Figure 4.21 The oscillations in fluid inlet and outlet temperatures as a function of heat for D = 1.1 mm and L = 150 mm at P = 6 bar and G = 300 kg/m^2 s.

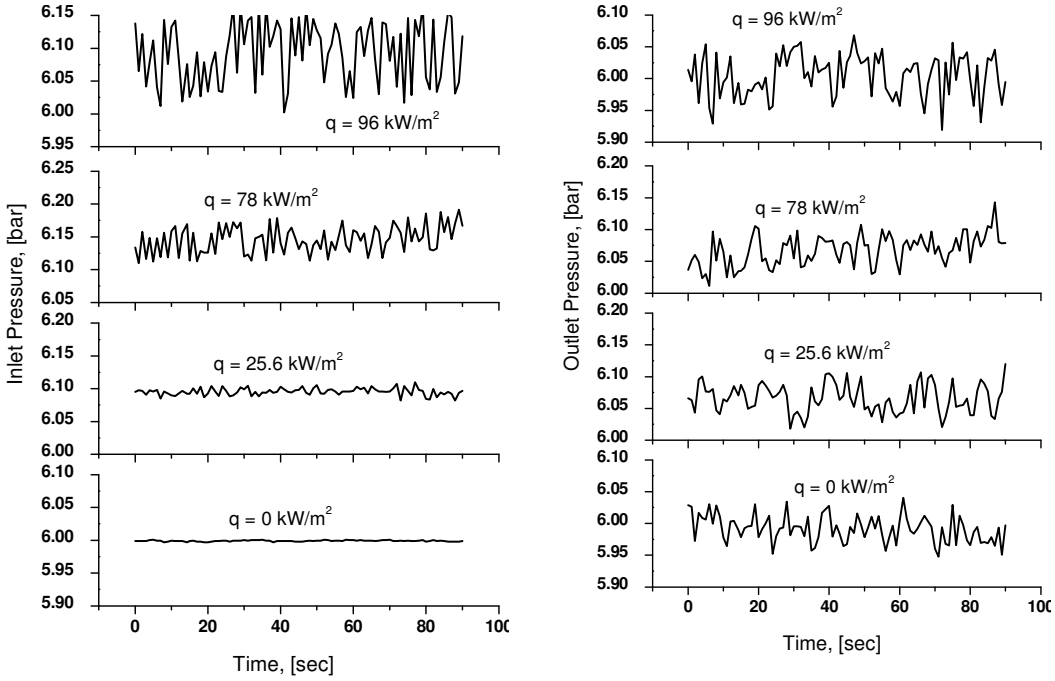

(a) test section inlet pressure (b) test section outlet pressure

Figure 4.22 The oscillations in the inlet and outlet pressures as a function of heat flux for D = 1.1 mm and L = 150 mm at P = 6 bar and G = 300 kg/m^2 s.

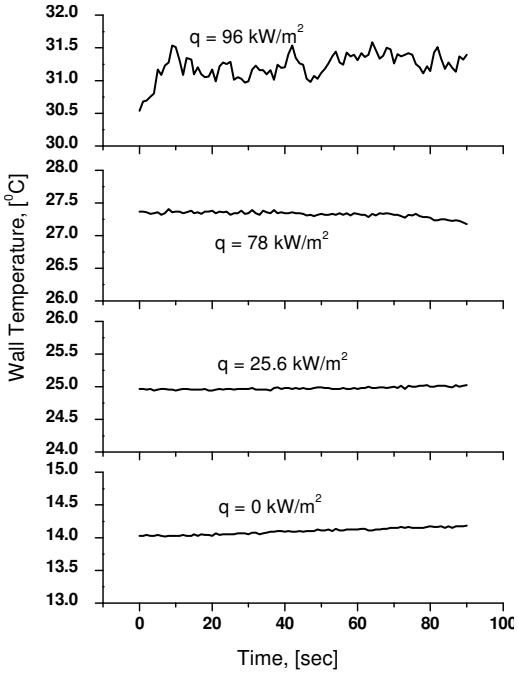

(a) wall temperature

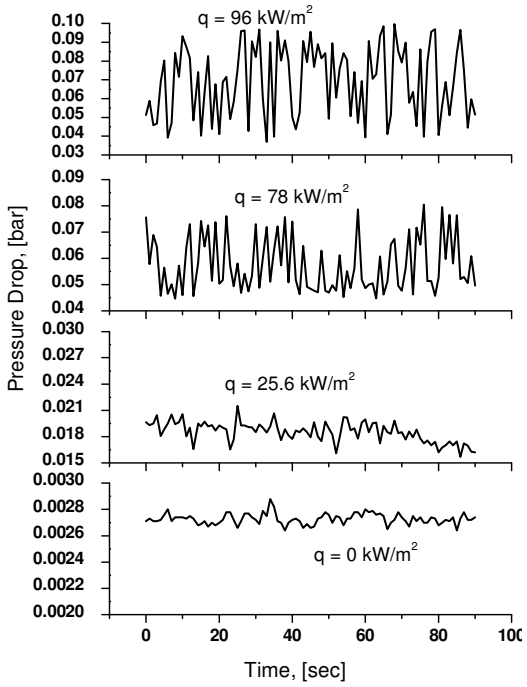

(b) pressure drop

Figure 4.23 The oscillations in wall temperature and pressure drop at the last thermocouple location as a function of heat flux D = 1.1 mm and L = 150 mm at P = 6 bar and G = 300 kg/m^2 s.

4.3.1 Heat transfer characteristics in the 0.52 mm tube

Effect of heat flux

Figure 4.24 shows the heat flux effect on the local time averaged heat transfer coefficient as a function of the local vapour quality (Fig. 4.24a) and axial distance (Fig. 4.24b) at G = 280 kg/m^2 s and P = 6 bar. The flow pattern transition boundaries predicted by the correlations of Revellin and Thome (2007c) that are given by Eqs. (2.1) and (2.2) are also shown on Fig. 4.24a. These boundaries divide the figure into three regions, isolated bubbles region (IB), coalescing bubble region (CB) and the annular flow region (A). Figure 4.24a depicts that, for most heat fluxes, the heat transfer coefficient decreases from its maximum value at the first thermocouple position or near zero quality values and then remains almost constant with quality up to thermocouple position number 5 after which it increases with quality up to the tube exit. Moreover, it is observed that in the low quality region (up to x ~ 0.4) the heat transfer coefficient increases with heat flux while for x > 0.4 there is no obvious dependence on heat flux. From the flow patterns presented above in section 4.2.1, this value of quality

corresponds to the onset of annular flow pattern. This trend is consistent with the trend observed by Chin and Thome et al. (2009) for R245fa and R236fa using a stainless steel horizontal tube with diameter of 1.04 mm. Their experimental study also included R134a but its trend does not show the increasing behaviour with quality towards the exit. Their explanation was based on the fact that the surface tension of R134a is lower than that of R245fa, which improves wet-ability and bubble confinement. The explanation of the current results is the same as proposed by Chin and Thome where the reduction in tube diameter adds more confinement and leads to early transition into annular flow. On the contrary, the heat transfer coefficient was found to increase with heat flux at all axial locations along the tube for most heat fluxes when the heat transfer coefficient was plotted versus axial distance rather than vapour quality as seen in Fig. 4.29b. The axial distance plot shows also that, the heat transfer coefficient depends on axial distance towards tube exit even at low heat fluxes, i.e. the flow pattern is not annular. The dependence of the local flow boiling heat transfer coefficient on axial position is different from the behaviour of the local single phase heat transfer coefficient, which does not depend on axial distance.

It is worth noting that, when the flow regime is isolated bubbles (IB), the heat transfer coefficient rapidly drops from its peak value at $x \cong 0$. This peak was not observed before in large diameter tubes and it may be attributed to the onset of nucleate boiling at which the heat transfer coefficient is too high. Lin et al. (2001b) obtained similar behaviour at $x \cong 0$ for R141b and D = 1 mm. As will be discussed later in section 4.3.3, they attributed the occurrence of this peak to the over-estimation of the heat transfer coefficient at boiling incipience resulting from assuming linear pressure drop variation along the tube. Another possible reason could be the very high wall superheat required in micro-tubes at boiling incipience compared to large diameter tubes. Principally, as the diameter decreases, the single phase heat transfer coefficient increases resulting in a thinner thermal boundary layer with a steep temperature gradient ($\delta_{tb} = k_L / h_{sp}$). Thus, high wall superheat is required to achieve the thermal equilibrium required for bubble growth and departure. Owing to the high energy added to attain the required wall superheat, the liquid becomes highly superheated before boiling commences. It was observed in some experimental runs that the fluid exit temperature demonstrated superheating conditions of about 8 K before the onset of nucleate boiling. Accordingly,

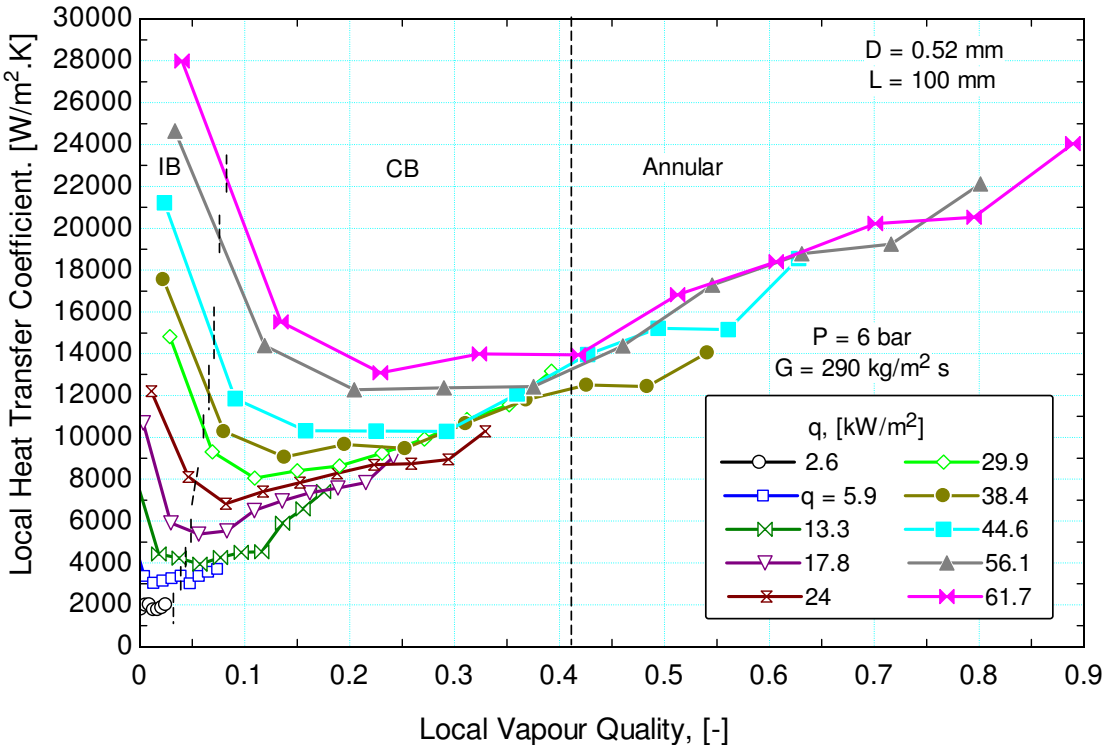

(a)

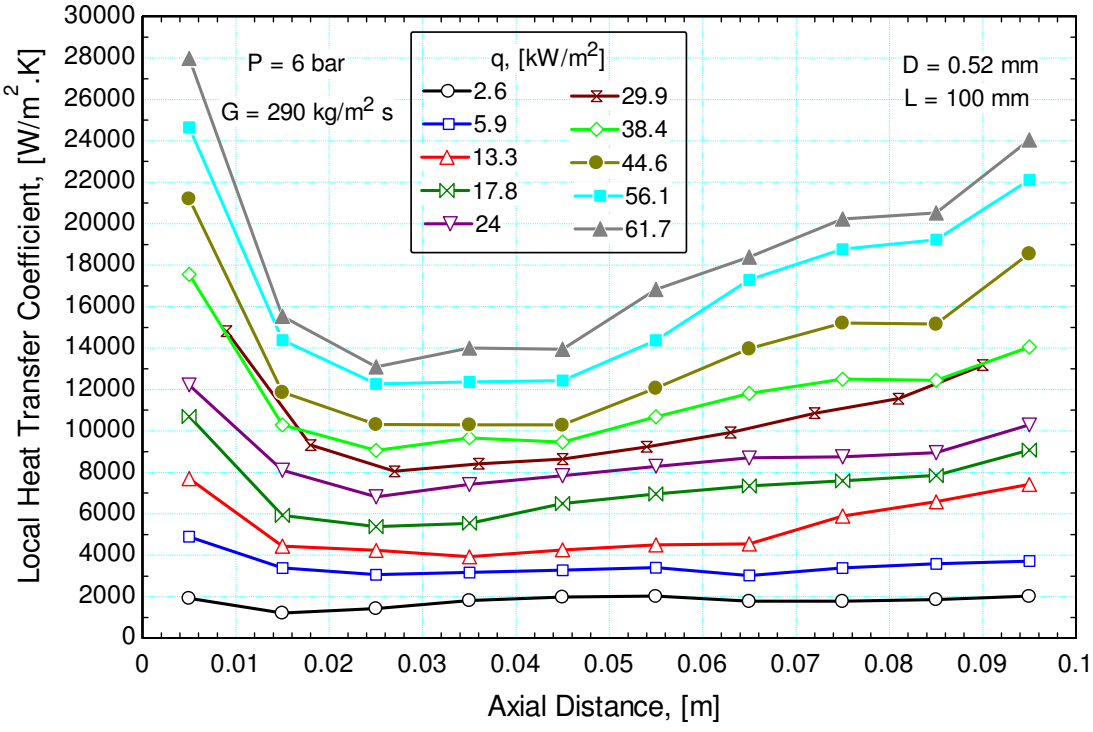

(b)

Figure 4.24 Effect of heat flux on the local time averaged heat transfer coefficient as a function of (a) local vapour quality and (b) axial distance for the 0.52 mm diameter tube at G = 300 kg/m^2 s, ΔT_{sub} = 2K and P = 6 bar.

the temperature undershoot (the drop in wall temperature after boiling incipience) in micro-tubes is expected to be much higher than in large diameter tube, i.e. very low wall superheat resulting in very high heat transfer coefficient.

For further analysis to clarify the heat flux effect, Fig. 4.25 shows the heat transfer coefficient versus heat flux plotted at three axial positions. The three positions were selected to represent the entry section (isolated bubble regime), the middle section (coalescing bubble regime) and the exit section (annular regime). Also, the Cooper (1984) correlation of pool boiling was plotted on the figure for the sake of comparison and understanding the controlling mechanism. The figure shows that, for all locations the heat transfer coefficient increases with heat flux even at the exit region although the α-x plot does not show any heat flux effect. It is interesting to note that, the experimental trends are similar to the trend of Cooper's pool boiling correlation but with higher magnitudes in the entry and exit regions.

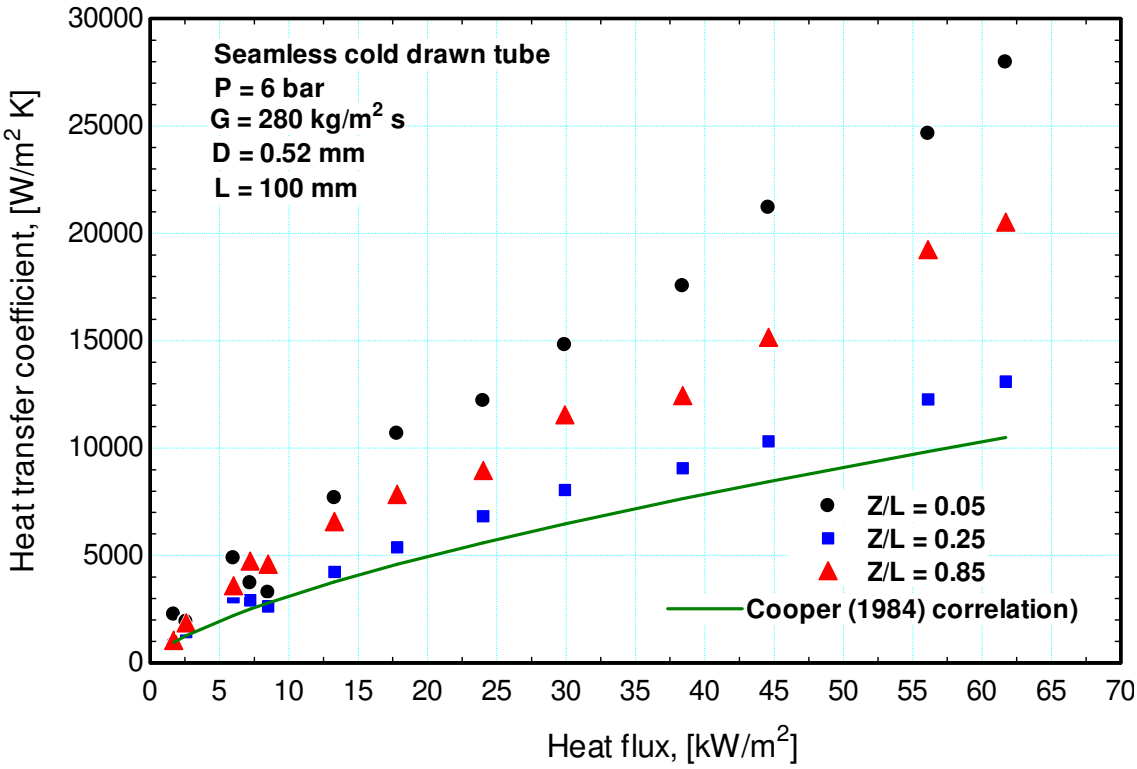

Figure 4.25 The effect of heat flux on the heat transfer coefficient at three axial locations for D = 0.52 mm, G = 280 kg/m^2 s and P = 6 bar.

Effect of mass flux

Figure 4.26 shows the effect of mass flux on heat transfer coefficient at almost the same heat flux value. It can be seen from the figure that the three mass flux curves almost merged into one curve in the region of $x < 0.4$ showing little dependence on mass flux. In the high quality region $x > 0.4$ the three curves separated and the heat transfer coefficient increased with mass flux. Conventionally, based on the heat flux effect in Fig. 4.24 and mass flux effect in Fig. 4.26a this trend is interpreted as a progression from nucleate boiling mechanism to convective boiling mechanism. However, when Fig. 4.26a was re-plotted in the form of heat transfer coefficient versus axial distance as seen in Fig. 4.26b all the three curves almost collapsed into one curve along the entire tube length showing little dependence on mass flux. The insignificant effect of mass flux on the heat transfer coefficient on the *h-z* plot and the agreement on the trend with the Cooper correlation in Fig. 4.25 even at locations close to the tube exit increases the doubt about whether convective boiling dominates or not. As previously presented, small bubbles were observed in the liquid film around the elongated bubble. It was not clear whether these bubbles formed by nucleation during the passage of the vapour slug or it were only trapped bubbles inside the liquid film. Nevertheless, the sequence of pictures indicated that these bubbles merged with the main vapour slug after 10 ms. Some investigators such as Kasza et al. (1997) observed nucleating bubbles in the liquid film around the vapour slug during water flow boiling in a narrow rectangular channel. Also, Haririchian and Garimella (2009a) observed small nucleating bubbles in the liquid film of the wispy-annular flow during flow boiling of FC77 in rectangular microchannels. This result opens one question about the criterion of the flow boiling controlling mechanism: which parameter should be used to predict or infer the mechanism? Is it local quality or axial position?

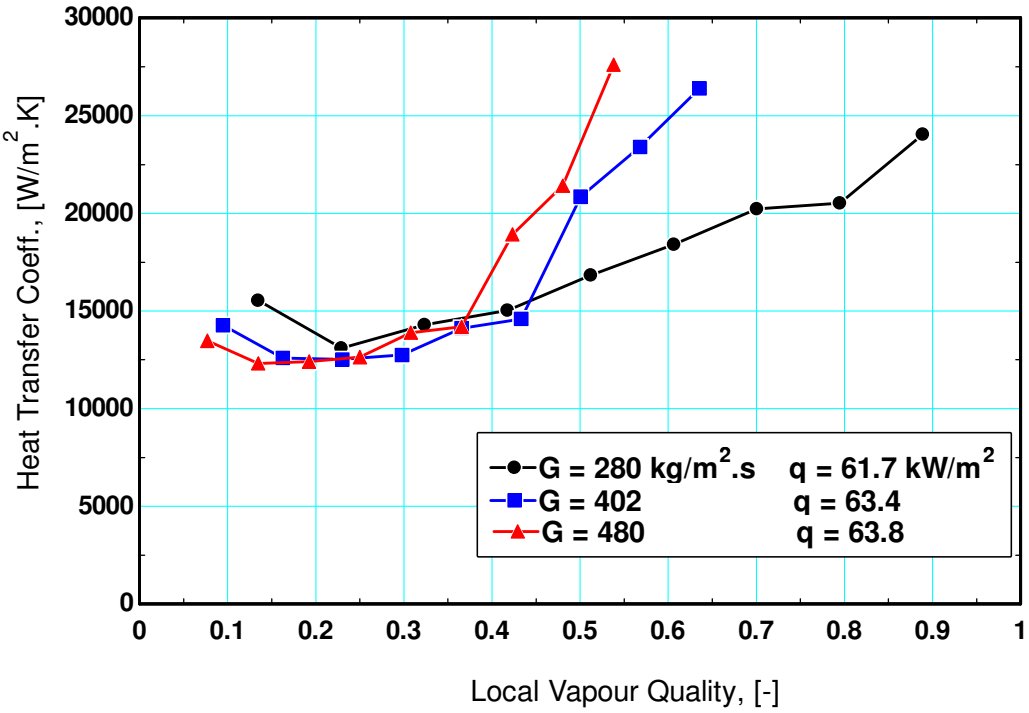

(a) heat transfer coefficient versus vapour quality

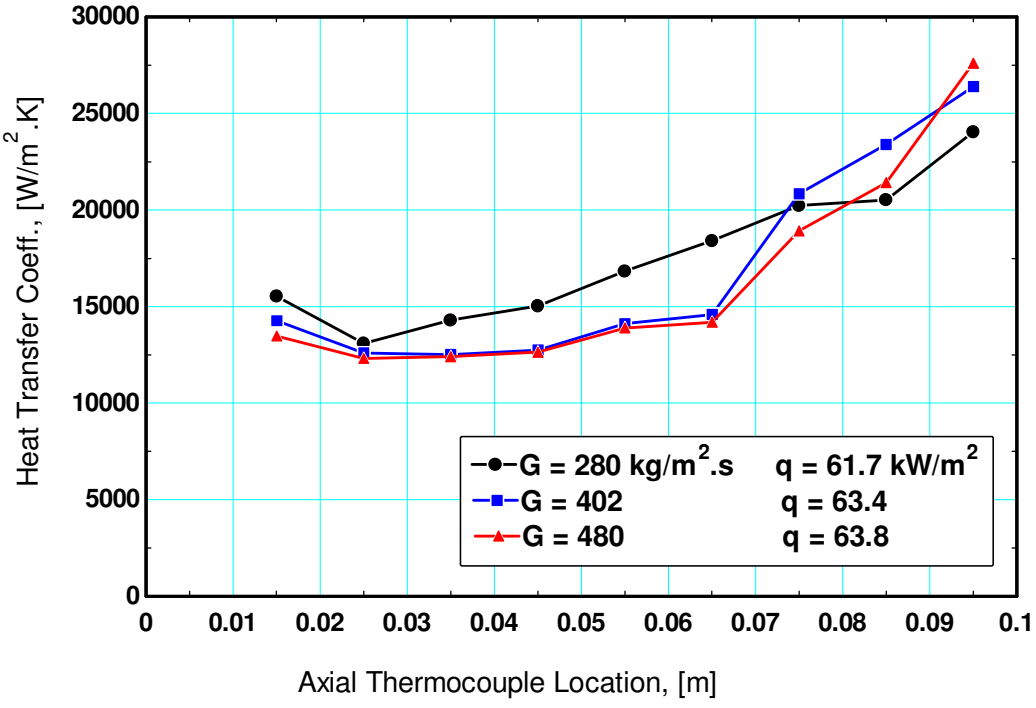

(b) heat transfer coefficient versus axial distance

Figure 4.26 The local heat transfer coefficient versus local vapour quality at almost same heat flux and 6 bar system pressure.

Figure 4.27 shows the effect of mass flux on the boiling curves plotted at two axial locations and developed by gradually increasing heat flux. The first location represents the region where nucleate boiling is believed to dominate whilst the second location represents the region where convective boiling is believed to dominate. As seen in the figure, the boiling curve at the first location shows similar behaviour to the classical pool boiling curve without any significant effect for mass flux. At the second location, the boiling curve showed a different behaviour after a heat flux value greater than about 30 kW/m^2 where the wall superheat slightly dropped as if it was a second step for boiling incipience. Also, the mass flux effect at the second location is not significant. The insignificant effect of mass flux on the boiling curve even near the exit is also contradicting to the classical criteria used to infer the boiling mechanism. Another important plot that may be used to infer the mechanism is the effect of system pressure on heat transfer coefficient shown in Fig. 4.28. It is obvious from the figure that, the heat transfer coefficient increases with increasing system pressure. This result agrees with the effect of pressure on the pool boiling heat transfer coefficient in Cooper's correlation.

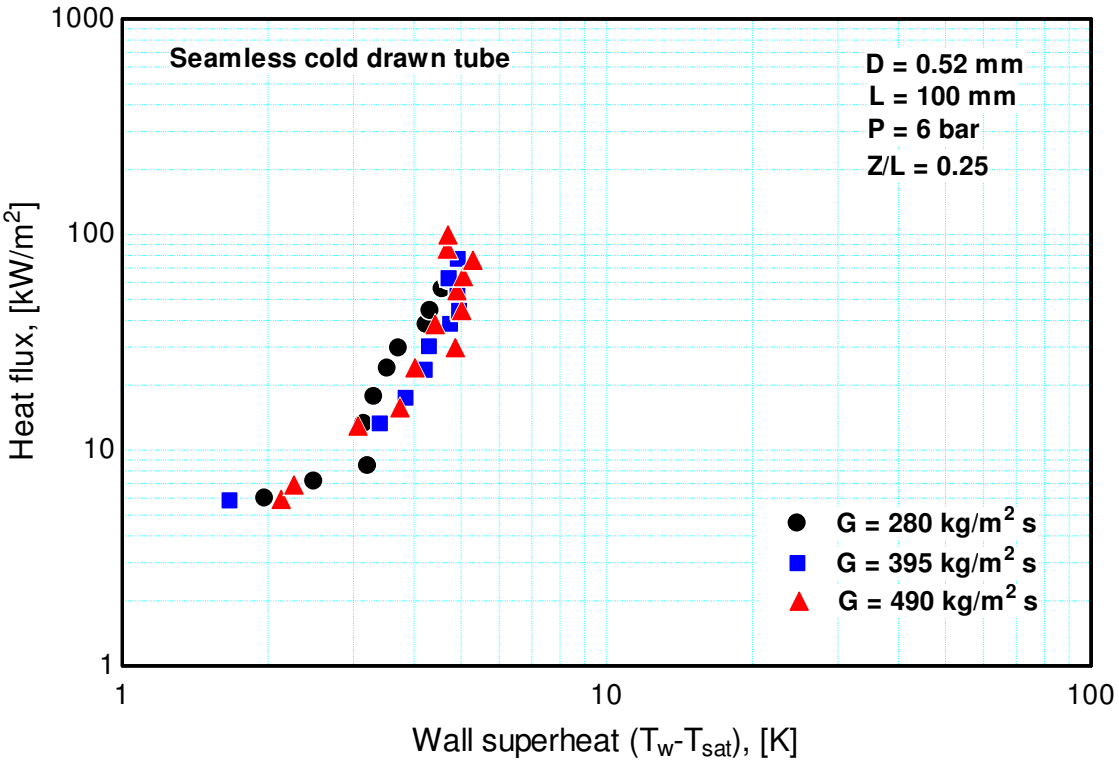

(a) Z/L = 0.25

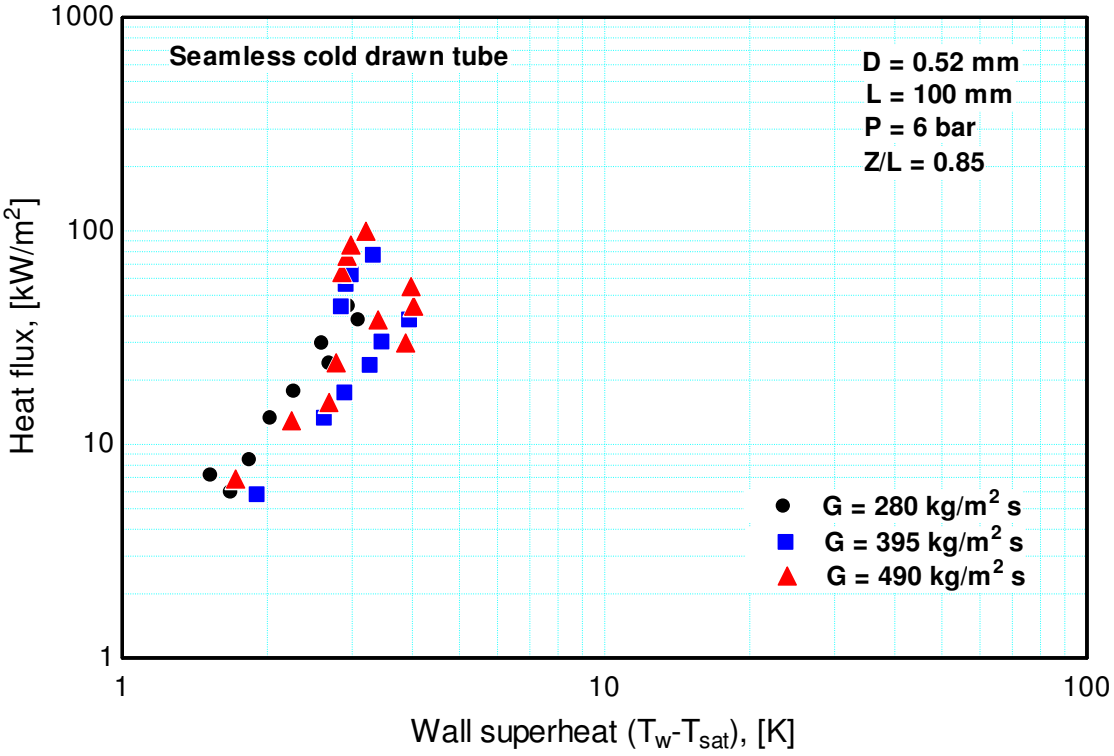

(b) Z/L = 0.85

Figure 4.27 The effect of mass flux on the boiling curve at 6 bar system pressure and axial position.

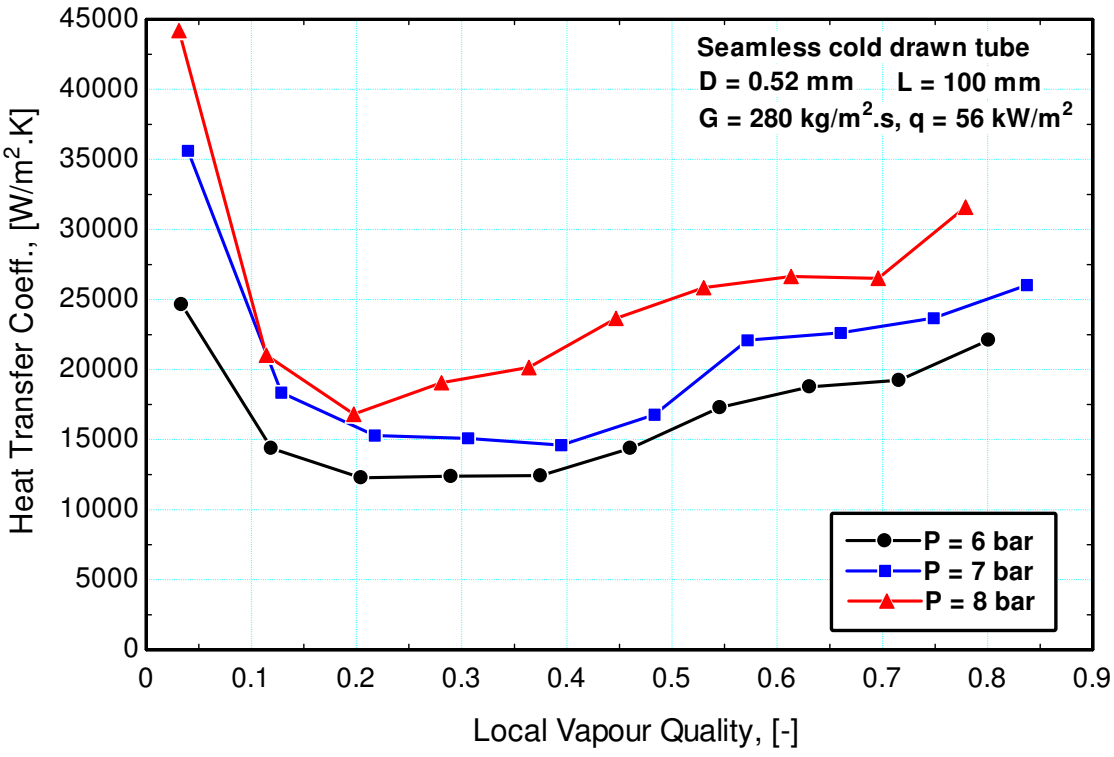

Figure 4.28 The effect of system pressure on the local heat transfer coefficient for D = 0.52 mm and G = 280 kg/m^2 s at q = 56 kW/m^2.

Hysteresis in the 0.52 mm tube

As the surface area in micro-tubes is relatively small, it is believed that flow boiling hysteresis may exist. Accordingly, in this study hysteresis was investigated by carrying out the experiment in both directions of increasing and decreasing heat fluxes. The results are depicted in Fig. 4.29 for two thermocouple locations. The first location is at Z/L = 0.25 to represent the region where nucleate boiling may occur, while the second location is at Z/L = 0.85 in the region where convective boiling is believed to occur. It is seen from the figure that, at Z/L = 0.25 there is boiling hysteresis only at heat fluxes below almost 18 kW/m^2 while no boiling hysteresis was observed for Z/L = 0.85. Nucleation sites which are not activated at low heat fluxes become active at high heat fluxes and remain active even when the heat flux was decreased to very small values.

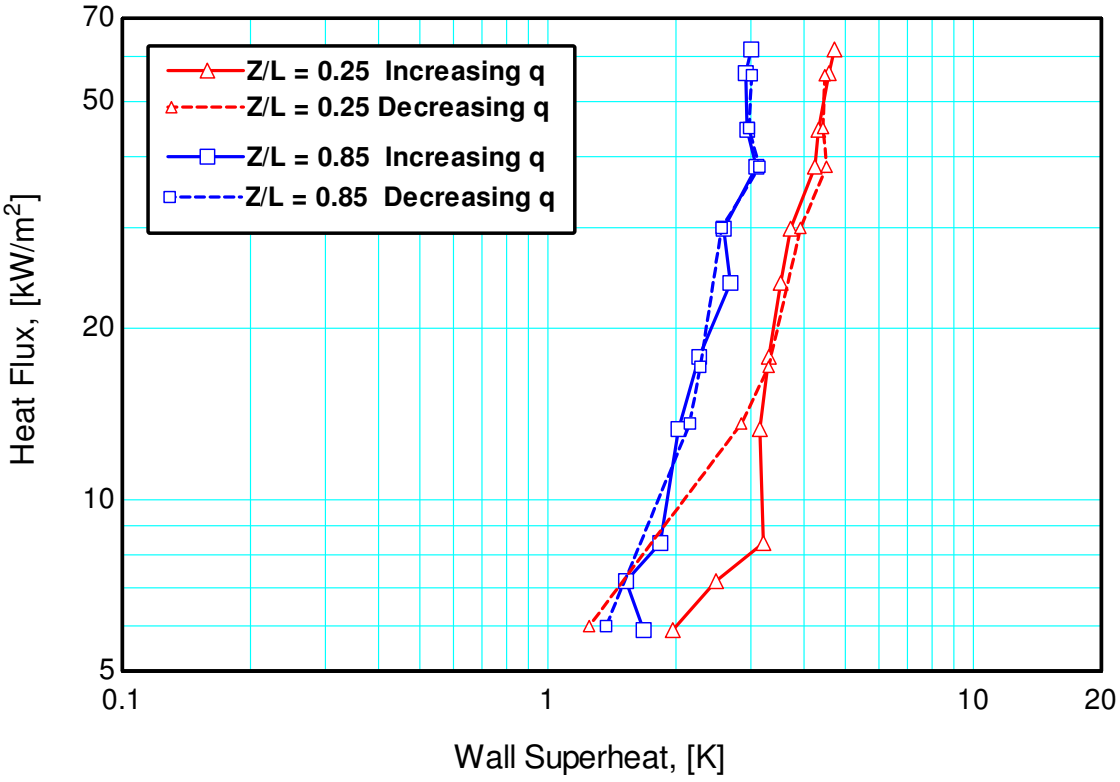

Figure 4.29 The boiling curve plotted for increasing and decreasing heat flux at 6 bar system pressure and 280 kg/m^2 s mass flux.

4.3.2 Heat transfer characteristics in the 1.1 mm tubes

This section presents and discusses the heat transfer results for two mini-diameter tubes having similar diameter of 1.1 mm and heated length of 150 mm. The first tube is a seamless cold drawn tube whilst the second is a welded tube, i.e. manufactured by welding process. The effect of heat and mass flux on the local flow boiling heat transfer coefficient are presented and discussed below.

Effect of heat flux

Figure 4.30 depicts the effect of heat flux on the local flow boiling heat transfer coefficient for the welded tube as a function of local vapour quality (Fig. 4.30a) and axial distance (Fig. 4.30b). The experimental flow patterns transition boundaries are also shown on the figure. It is clear from this figure that, the heat transfer coefficient shows a peculiar behaviour that was not observed before in the experiments of this research group or anybody else. The *h-x* plot (Fig. 4.30a), shows for most heat fluxes that after thermocouple location No. 4 (Z/L = 0.27) the heat transfer coefficient decreases rapidly to a minimum value at thermocouple location No. 8 (Z/L = 0.53) with approximately similar slope. After this minimum, the heat transfer coefficient rapidly increases with quality before it decreases again at the last thermocouple location. In the entry region, the heat transfer coefficient jumped from the single phase value and peaked at a value of quality near zero due to the onset of boiling. It is worth noting that, the observed drop at the last thermocouple location seems to be due to factors other than normal dry out because this behaviour was observed even at the lowest heat fluxes. Additionally, the effect of heat flux is not clear from the *h-x* plot where at some quality values (intermediate qualities) the heat transfer coefficient decreases with increasing heat flux while at very low qualities ($x \approx 0$) it increases with heat flux. In other words, the heat flux effect seems difficult to be detected in this plot. However, re-plotting the heat transfer coefficient versus the axial thermocouple location (Fig. 4.30b) instead of vapour quality demonstrated some minimal effect of heat flux but for some regions all the lines approximately merged together ($z = 0.04 – 0.06$ m and $z > 0.12$ m).

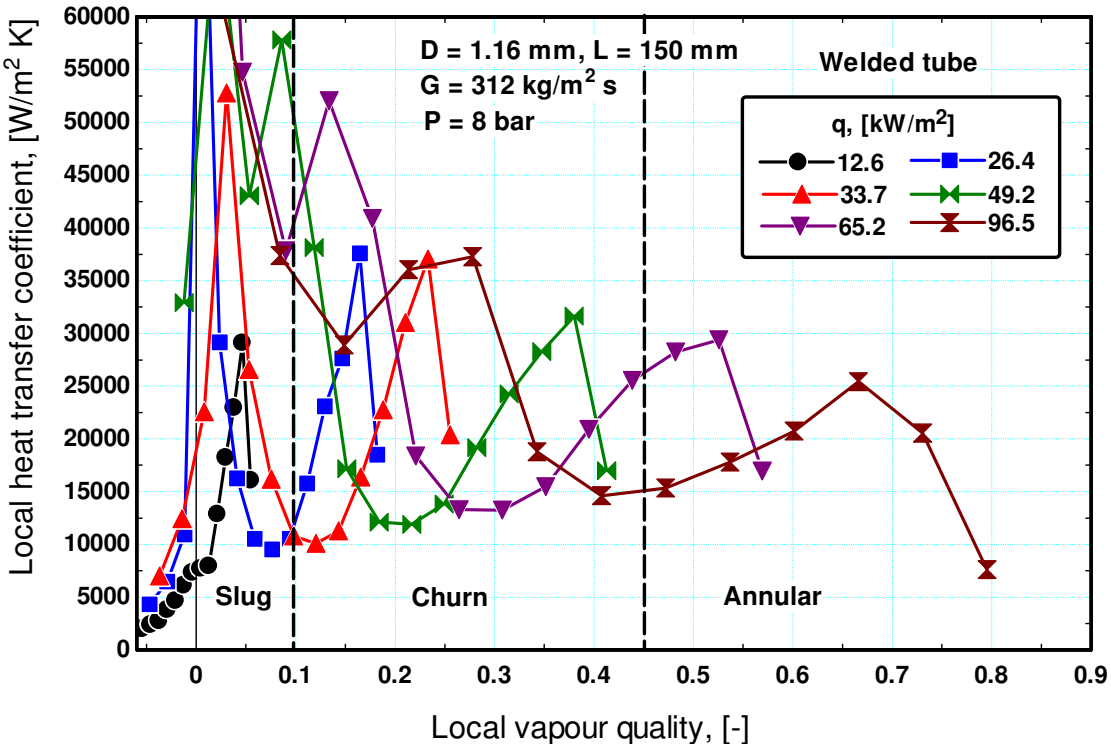

(a) heat transfer coefficient versus vapour quality

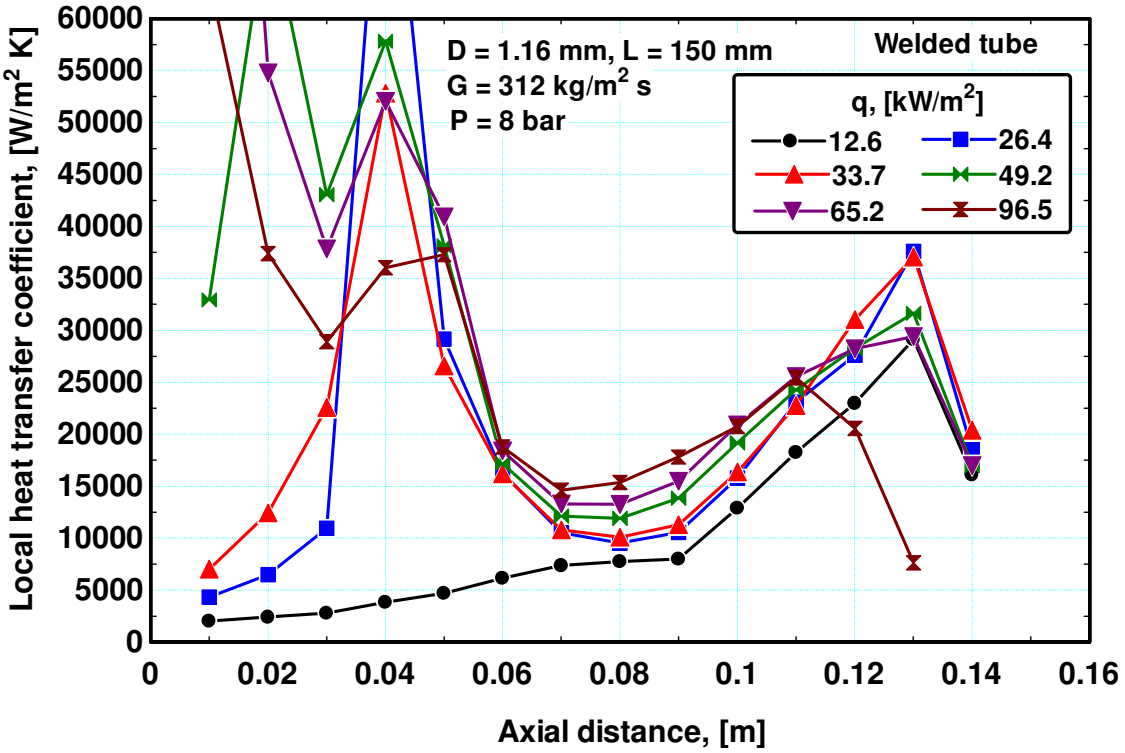

(b) heat transfer coefficient versus axial distance

Figure 4.30 The effect of heat flux on the local heat transfer coefficient as a function of local vapour quality and distance at P = 8 bar and G ≈ 300 kg/m^2 for the welded tube.

Figure 4.31 shows the effect of heat flux on the local heat transfer coefficient in the seamless cold drawn tube with the experimental flow patterns transition boundaries. It is seen from this figure that the behaviour of the heat transfer coefficient is completely different compared to that obtained using the welded tube. It is seen from Fig. 4.31a that, the heat transfer coefficient jumps from its single phase value and peaks at quality values very close to zero then it remains approximately constant with local quality. Contrary to Fig. 4.30, the effect of heat flux is very clear from both the *h-x* and *h-z* plots where the heat transfer coefficient increases with increasing heat flux. Since the heat flux effect is not clear in Fig. 4.30 for the welded tube, the heat transfer coefficient was re-plotted versus heat flux at three axial locations in Fig. 4.32a and the same thing was done in Fig. 4.32b for the seamless tube for the sake of comparison. Figure 4.32a shows that, the effect of heat flux depends on axial location for the welded tube. At the entry region, the heat transfer coefficient increased with heat flux up to q = 49.2 kW/m^2 after which it constantly decreased with heat flux. At the exit, the heat transfer coefficient increased with heat flux up to q = 26.4 kW/m^2 then it continuously decreased with increasing heat flux. At the middle of the tube, the heat transfer coefficient increased linearly with heat flux. On the contrary, Fig. 4.32b shows that the heat flux effect is almost similar at all locations in the seamless tube where it increases with heat flux.

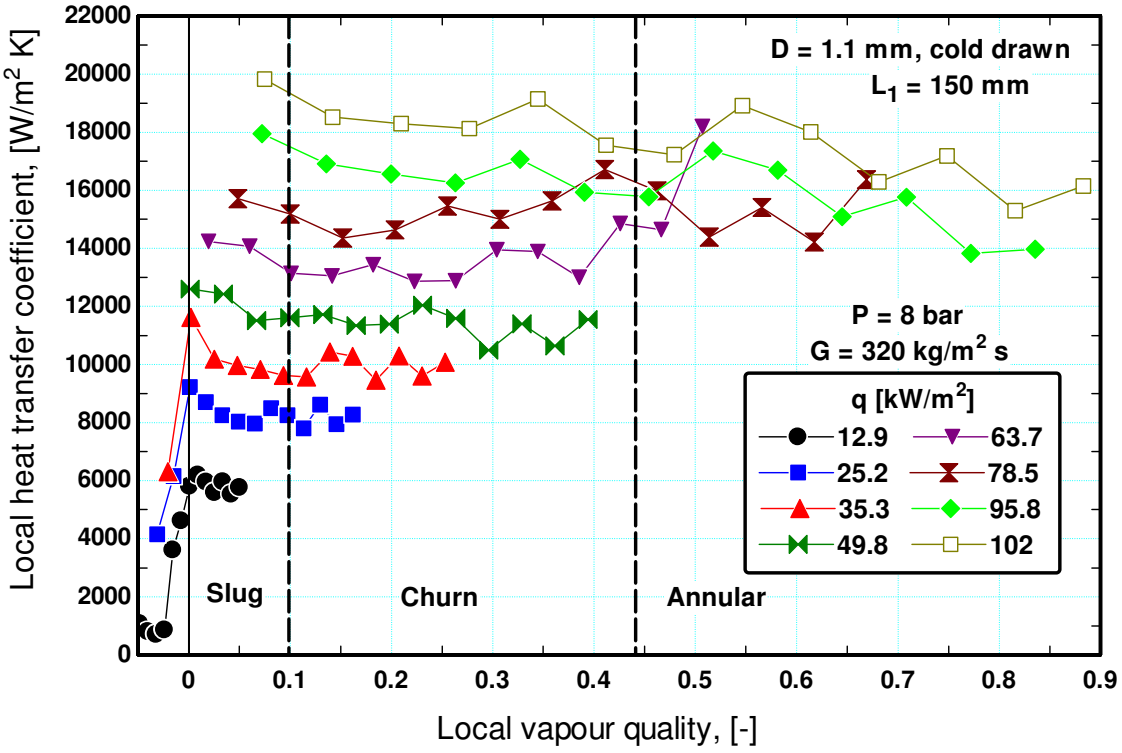

(a) heat transfer coefficient versus vapour quality

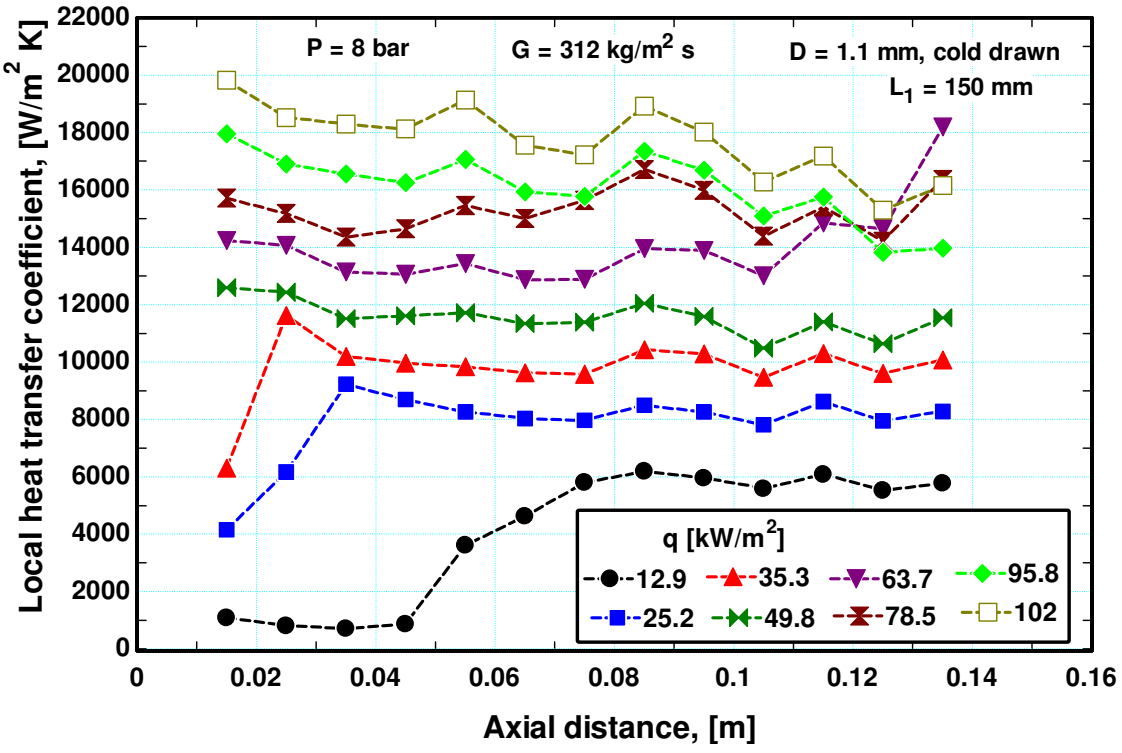

(b) heat transfer coefficient versus axial distance

Figure 4.31 The effect of heat flux on the local heat transfer coefficient as a function of local vapour quality and axial distance at P = 8 bar and G ≈ 300 kg/m^2 s for the seamless tube.

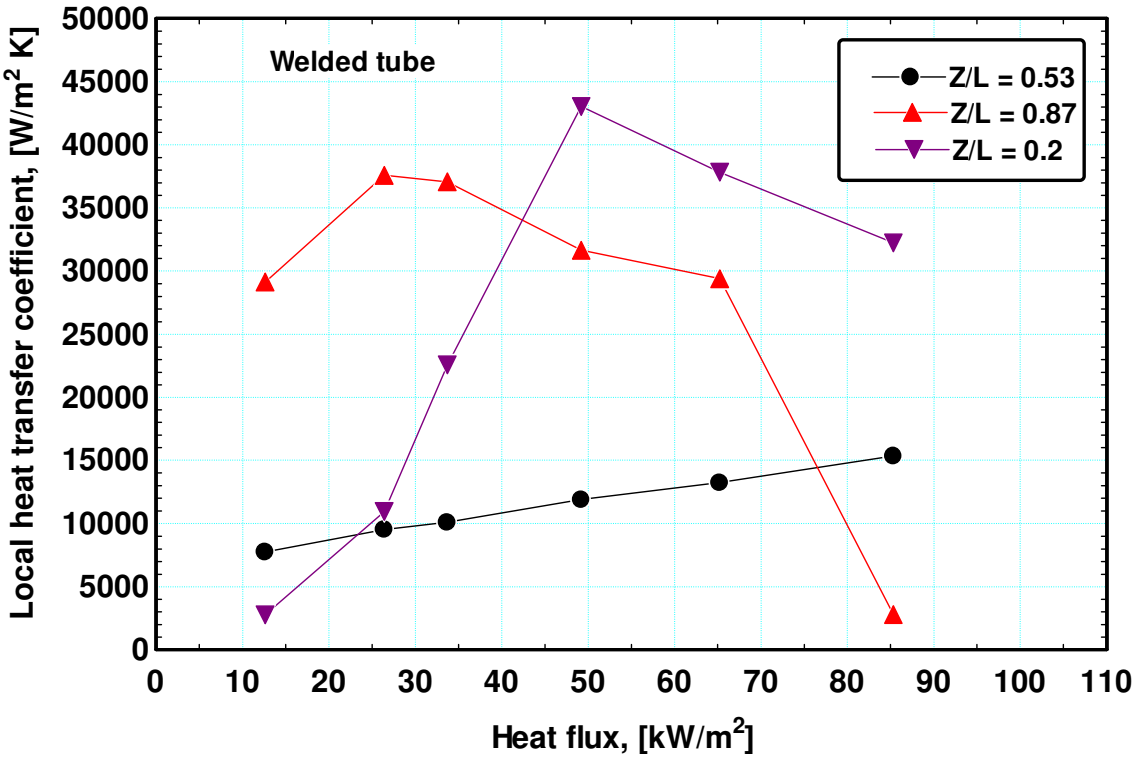

(a) Heat transfer coefficient versus heat flux for the welded tube

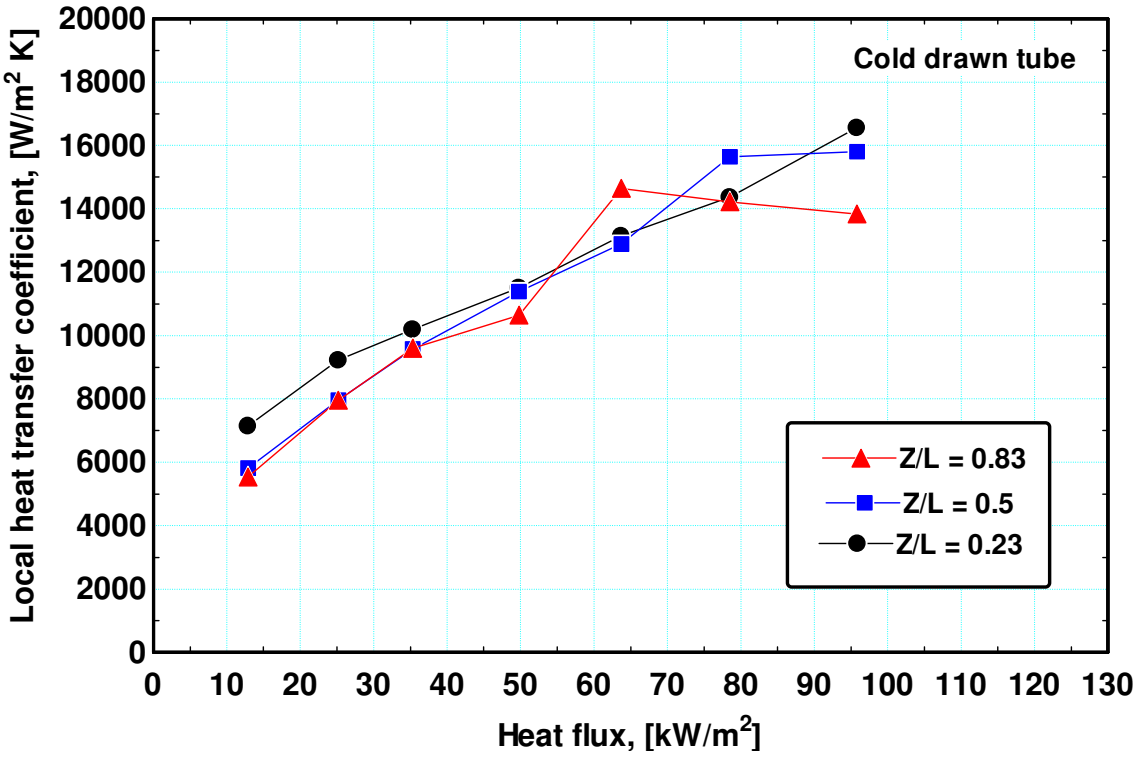

(b) Heat transfer coefficient versus heat flux for the seamless cold drawn tube

Figure 4.32 The heat transfer coefficient at three axial locations as a function of heat flux for: (a) the welded tube and (b) the seamless cold drawn tube.

Effect of mass flux

Figure 4.33 illustrates the effect of mass flux on the local heat transfer coefficient at q = 41 kW/m^2 for the welded tube (Fig. 4.33a) and for the seamless tube (Fig. 4.33b). Inspecting Fig. 4.33a, again the mass flux effect seems complex and difficult to deduce from the *h-x* plot, while the *h-z* plot shows a rather insignificant effect. The *h-x* and *h-z* plots of the seamless tube do not show any mass flux effect and all the lines merge into a single line. Figure 4.34 shows the local heat transfer coefficient plotted against mass flux at three axial locations for both tubes. Figure 4.34a indicates for the welded tube that, the heat transfer coefficient increases significantly with increasing mass flux at location near the tube exit (z/L = 0.87). At location near the entry region (z/L = 0.2), the heat transfer coefficient increased slightly with increasing mass flux. At a mid location (z/L = 0.53), the heat transfer coefficient was fluctuating with mass flux. On the contrary, Fig. 4.34b shows for the seamless cold drawn tube that the effect of mass flux is insignificant at all locations along the tube. Applying the conventional criterion for the controlling mechanism (the heat transfer coefficient depends on *q* but independent of *x* and *G*), it can be concluded from Fig. 4.31a, Fig. 4.32b, Fig. 4.33b and Fig. 4.34b that heat transfer is dominated by the nucleate boiling mechanism in the seamless cold drawn tube where the heat transfer coefficient does not show any dependence on local vapour quality and mass flux while it increases with heat flux. On the other hand, the controlling mechanism in the welded tube is not clear. Examination of Fig. 4.30a, Fig. 4.32a, Fig. 4.33a and Fig. 4.34a shows some features of nucleate boiling in the first half of the welded tube while in the second have it demonstrates some features of convective boiling.

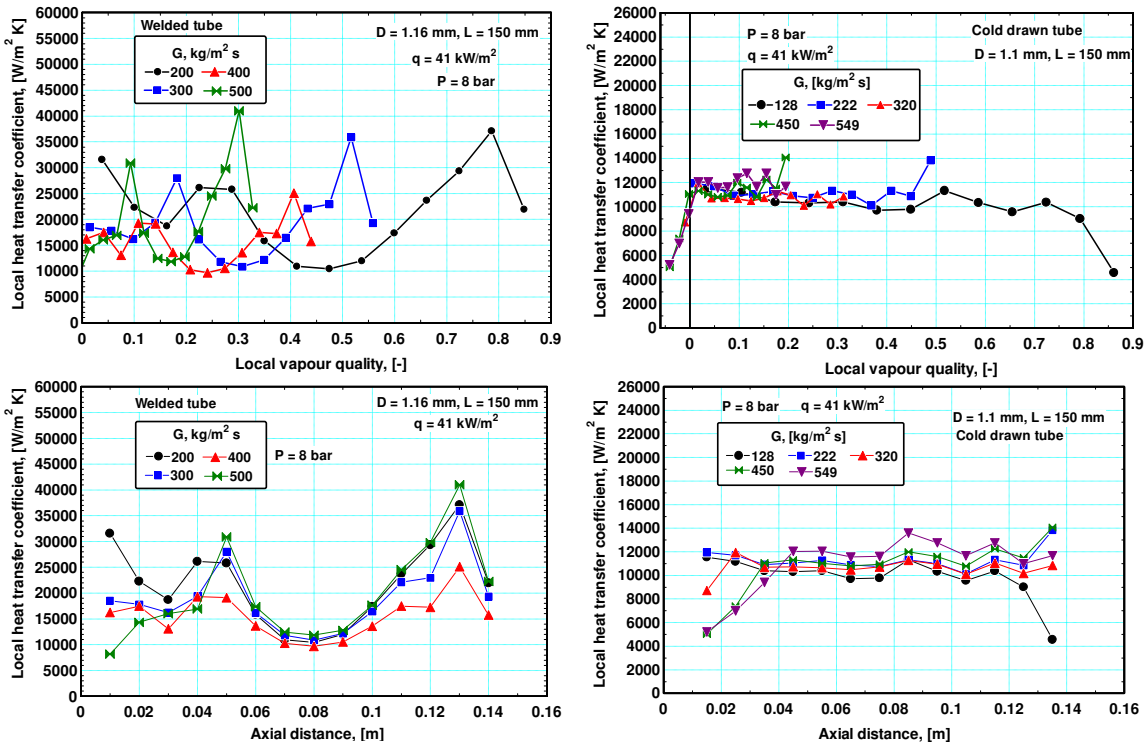

(a) (b)

Figure 4.33 The effect of mass flux on the local heat transfer coefficient at q ≈ 41 kW/m^2 for (a) the welded tube and (b) the seamless tube.

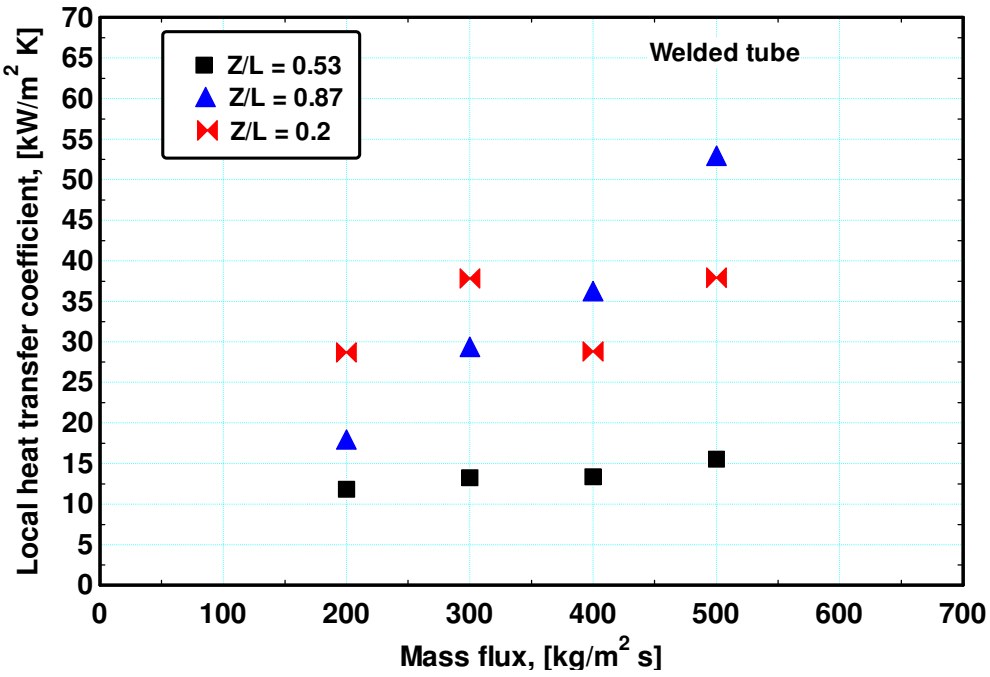

(a) Welded tube

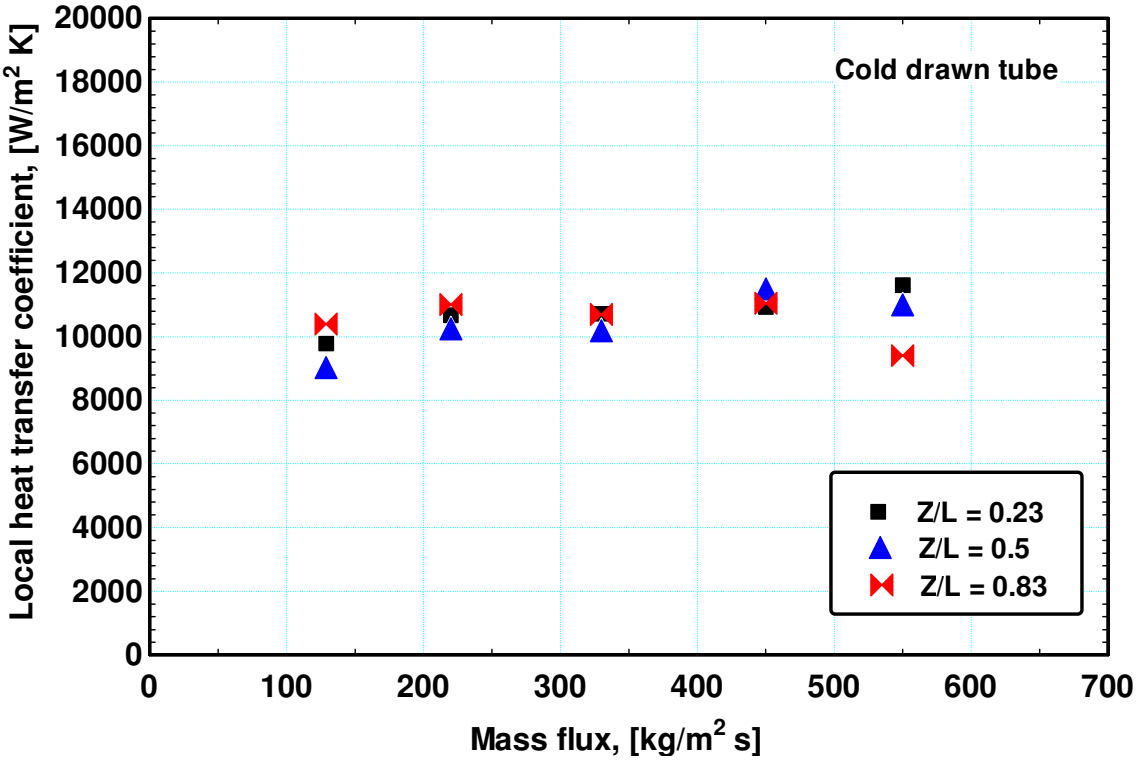

(b) Seamless cold drawn tube

Figure 4.34 Effect of mass flux on the heat transfer coefficient at three axial locations for (a) the welded tube, (b) the seamless cold drawn tube.

Boiling curves

Figure 4.35 compares the boiling curves of the welded and seamless tubes plotted at three axial locations with increasing heat flux in small increments. The first location represents the entry region while the second and third locations represent the middle and exit regions, respectively. In the entry region (Fig. 4.35a), the results of the two tubes agreed on the high wall superheat required for the onset of nucleate boiling, i.e. it reached 14.2K in the welded tube and 18K in the seamless tube. Also, the onset of nucleate boiling in the welded tube occurred at relatively lower heat flux value of 9.4 kW/m^2 compared to 12.9 kW/m^2 in the seamless tube. It is interesting to note that, after boiling incipience the two curves merged together into one single line with the wall superheat decreasing with heat flux up to q ≈ 25 kW/m^2. After this heat flux value, the two curves separate and behave in a different way. At q = 25 kW/m^2, the curve of the seamless cold drawn tube shows fully developed nucleate boiling and wall superheat increased by 2.85K when q was increased from 25 to 101 kW/m^2. In the welded tube,

the fully developed nucleate boiling established at q = 41 kW/m^2 and wall superheat increased by 2.3K when q was increased from 41 to 98 kW/m^2. At the mid location (Fig. 4.35b), the welded tube required 17.4K wall superheat for the onset of nucleate boiling which started normally in the seamless tube at a wall superheat of 3.7K. In this mid location, after the onset of nucleate boiling, the two curves merged into one single curve with some small difference appearing after q = 70 kW/m^2. At the location close to the exit (Fig. 4.35c), the required wall superheat for the onset of nucleate boiling remained high at 17.4K for the welded tube while it reached only 3.2K for the seamless tube. Additionally, at boiling incipience wall superheat dropped from 3.2K to 1.89K in the seamless tube while it dropped from 17.4K to 0.44K in the welded tube. This drop in wall superheat at boiling incipience may explain the very high values of the heat transfer coefficient in the welded tube at x ≈ 0 compared to the seamless cold drawn tube. After boiling incipience, the two curves showed fully developed nucleate boiling with the wall superheat in the welded tube much lower than that in the seamless tube for a given heat flux. It may be concluded from these figures that, triggering fully developed nucleate boiling in the seamless tube required high wall superheat only in the entry region while the welded tube required high wall superheat at all locations along the tube. It is worth noting that, Fig. 4.35d shows the flow patterns observed at boiling incipience in the two tubes. Pictures No. 1 and 3 illustrates the first bubbles that appeared in the observation section immediately after transition from single phase liquid flow to two phase boiling flow for the seamless and welded tubes, respectively. In the seamless tube, the first bubbles appeared at heat flux value of 5.3 kW/m^2 as a mixture consisting of short vapour slugs and small bubbles that are smaller than the tube diameter with a neck similar to the nucleating bubble on the cavity mouth before departure. This behaviour in the seamless tube suggests the activation of a few nucleation sites close to the tube exit, which is also clear from the boiling curve at q = 5.3 kW/m^2 in Fig. 4.35c. By contrast, the first bubbles appeared in the welded tube at relatively higher heat flux compared to the seamless tube (q = 9.4 kW/m^2) as a well-defined confined bubble/slug flow directly. It is worth noting that, these first bubbles appeared in both tubes while the wall temperature was still showing single phase trend. Pictures No. 2 and 4 show the flow patterns when fully developed nucleate boiling started, i.e. when the wall temperature changed from the single phase-similar trend into boiling. The flow patterns at that condition were very similar in the two tubes, where

long vapour slugs appeared with the presence of some tiny bubbles in the liquid slug between the consecutive vapour slugs.

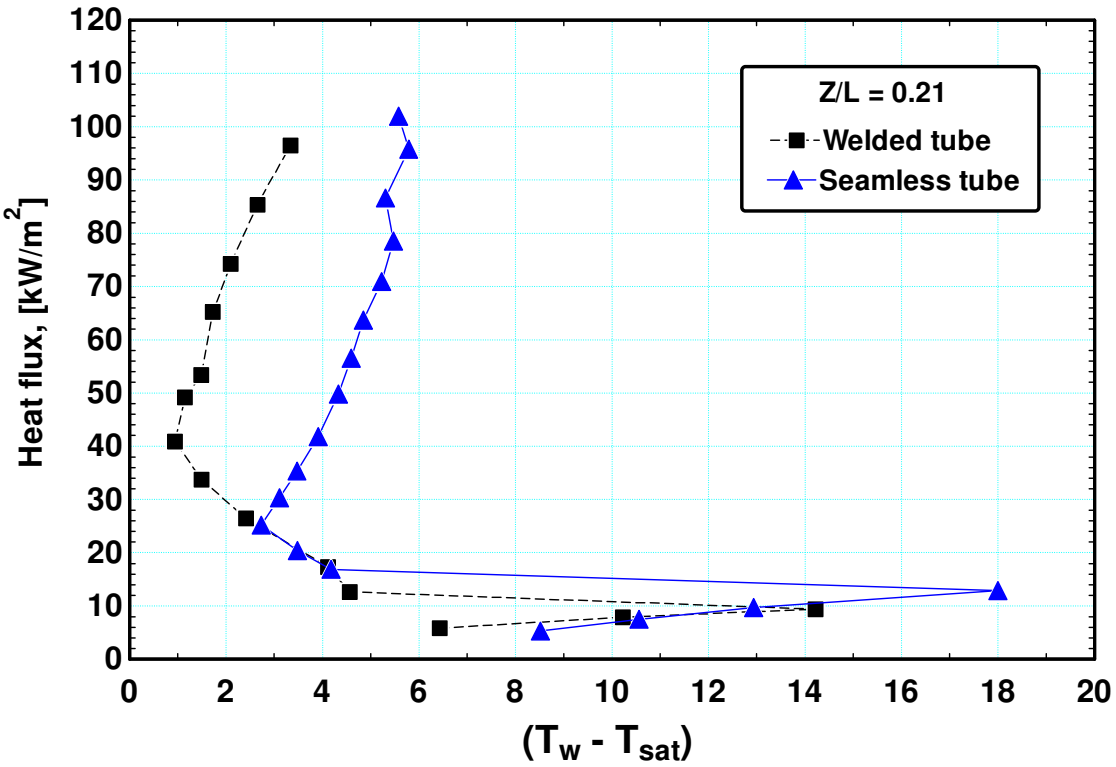

(a)

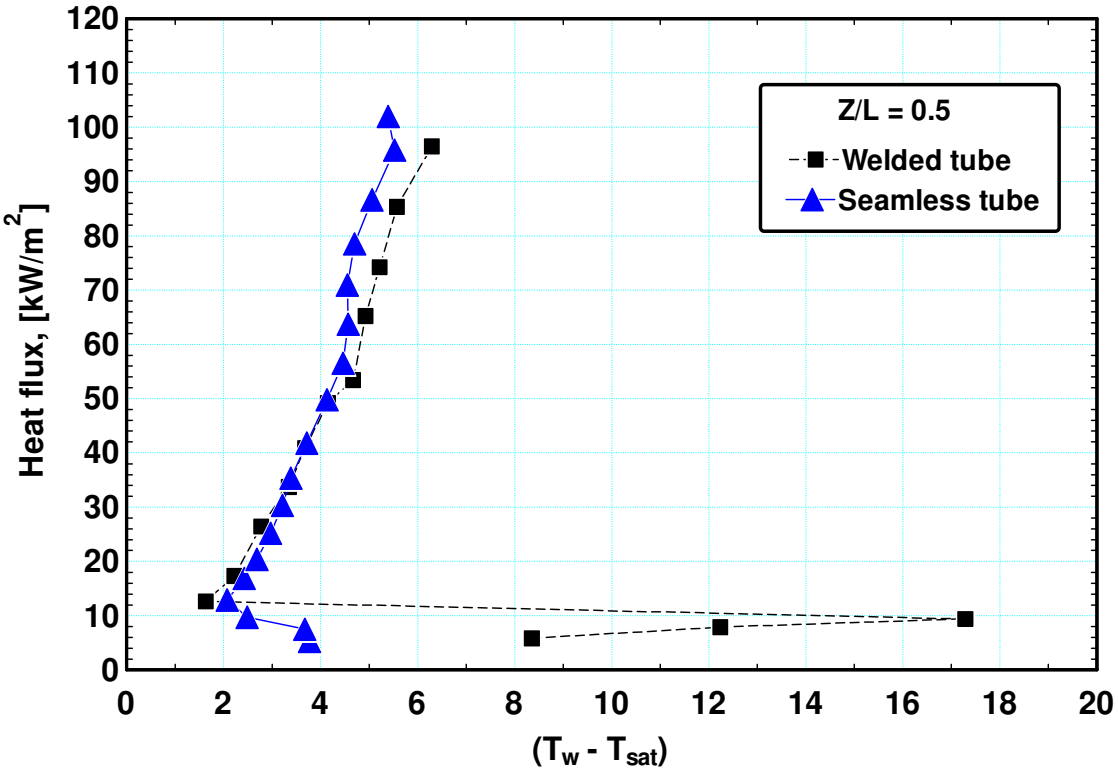

(b)

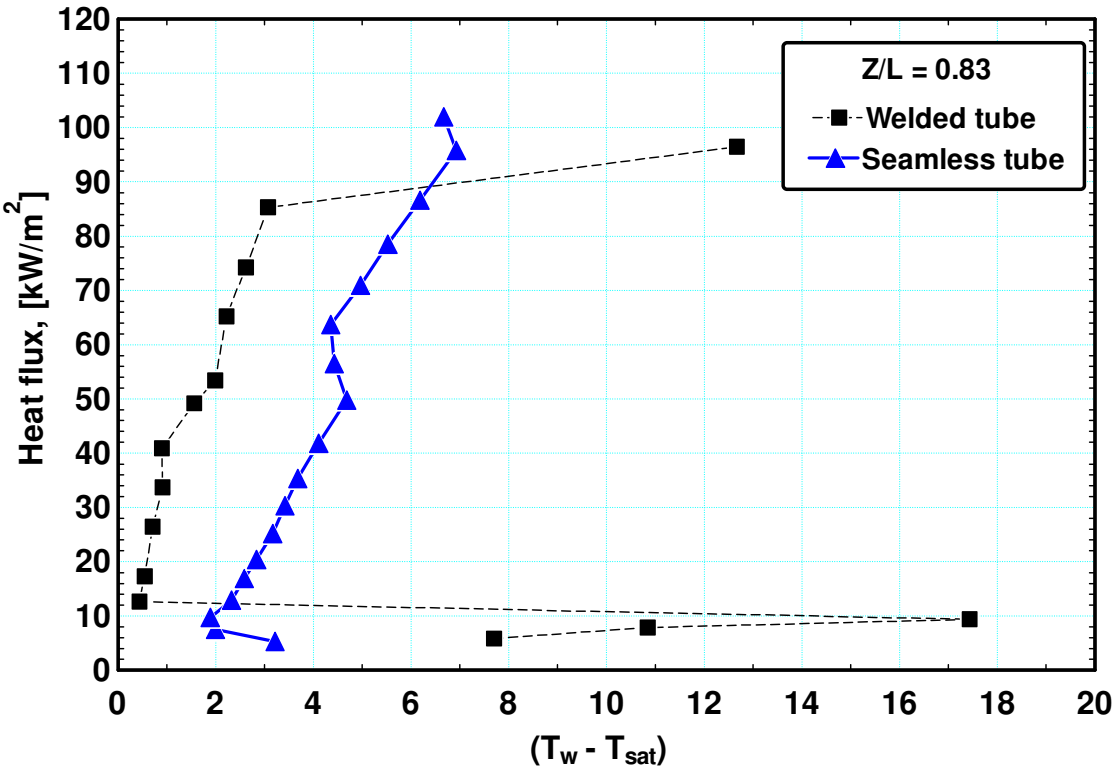

(c)

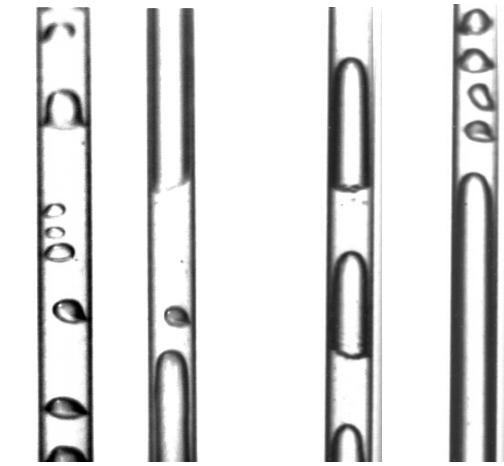

(d)

Figure 4.35 The boiling curves plotted through increasing heat flux at thee axial locations for the welded and seamless tubes: (a) at location near from entry region, (b) at middle location, (c) at location near from exit, (d) pictures 1 and 3 show the first bubbles observed and pictures 2 and 4 show the pattern at the onset of nucleate boiling

The above results show a clear difference in heat transfer behaviour between the seamless cold drawn tube and welded tube. Since the two investigated tubes are similar in dimensions, design and instrumentation, the difference in heat transfer results is believed to be caused by the difference in the inner surface characteristics as a result of the manufacturing process. The problem in flow boiling experimental studies in micro-tubes is that the investigated tubes are usually ordered from suppliers without taking the manufacturing process into consideration. Until now, there is no documentation of the effect of manufacturing process on the inner surface of the tube, particularly when the size becomes very small. This may be due to the fact that most people validate their test sections only by single phase flow, which is not enough to extend for flow boiling studies. This study confirms this point as presented previously in chapter 3 where the measured single phase friction factor in the welded tube agreed well with the conventional theory while peculiar behaviour was observed in flow boiling. For this reason, a sample of each tube (cut from the length from which the test sections were designed) was chopped into two halves and the inner surface was inspected using the scanning electron microscope (SEM) depicted in Figs. 3.10. As it is seen in the figure, the inner surface of the welded tube looks smooth with the existence of some fragments or debris on the surface. The smoothness of this surface may explain the high wall superheat that is required for the onset of nucleate boiling at all axial locations along the tube as presented above in Fig. 4.35. Also, it may explain the small effect of heat flux on the local flow boiling heat transfer coefficient along a major section of the heated tube as presented in Fig. 4.30. Moreover, the shape of the observed fragments is not regular and the nucleation process will depend on whether the debris forms a cavity-like shape or not. In other words, the heat transfer behaviour will depend on the shape and number of debris and also their local distribution along the heated section of the tube. By contrast, the SEM analysis showed a completely different texture for the inner surface of the seamless cold drawn tube, which looks like as if it has random scratches or channels that seem uniformly distributed along the tube. It is interesting to note that the inner structure of the seamless cold drawn tube is consistent with the manufacturing process. It is known that welded tubes are usually manufactured by rolling a strip of stainless steel into the required diameter and applying a welding process on the same rolling machine. Accordingly, if the original metal sheet is already smooth, the inner surface of the formed tube may be similar to the one formed in Fig.3.10. On the other hand, seamless tubes are usually manufactured by hot extrusion to form the hollow tube

first followed by a number of cold drawn processes to reduce the diameter to the required size. In the production of thin seamless tubes, an inner support (floating plug) is usually used during the drawing process, which may create the longitudinal random scratches on the inner surface shown in Fig. 3.10. Additionally, these random scratches together seem to form the sort of cavities that are required for the nucleation process.

In addition to the SEM analysis, Fig. 4.36 presents the trend of the measured wall temperature versus axial distance under single phase and boiling conditions which confirms the difference of the inner surface in the two tubes. Figure 4.36a shows, at very low Reynolds number and similar conditions, that the trend of the wall temperature in the two tubes is similar. With increasing Reynolds number, a sudden local drop in the wall temperature was observed in the two tubes but at two different locations ($z = 0.1$ for the welded tube and $z = 0.065$ for the seamless tube) see Fig. 4.36b. After this drop, the wall temperature increased linearly with axial distance. It is worth noting that the location of the temperature drop moved upstream when the Reynolds number increased further until it disappeared in the fully developed turbulent flow regime. This behaviour might arise from the existence of local turbulence induced by the local debris in the welded tube and the local scratches in the seamless tube. Accordingly, possible local heat transfer enhancement at these locations results in this local temperature drop. Additionally, Fig. 4.36c depicts the wall temperature at similar heat flux for the two tubes under boiling conditions. This figure shows that the wall temperature of the seamless cold drawn tube varies insignificantly with the axial distance which is not the case for the welded tube.

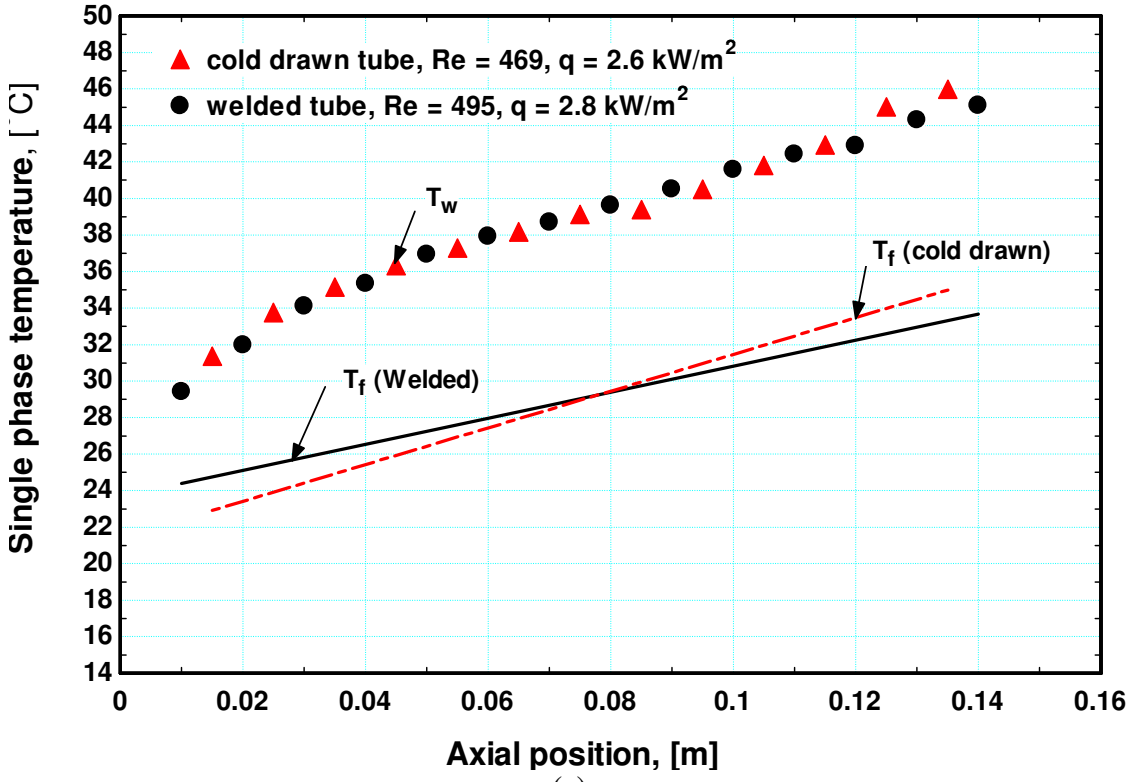
cold drawn tube, Re = 469, q = 2.6 kW/m2
welded tube, Re = 495, q = 2.8 kW/m2
Tw
Tf (cold drawn)
Tf (Welded)
Single phase temperature, [°C]
Axial position, [m]

(a)

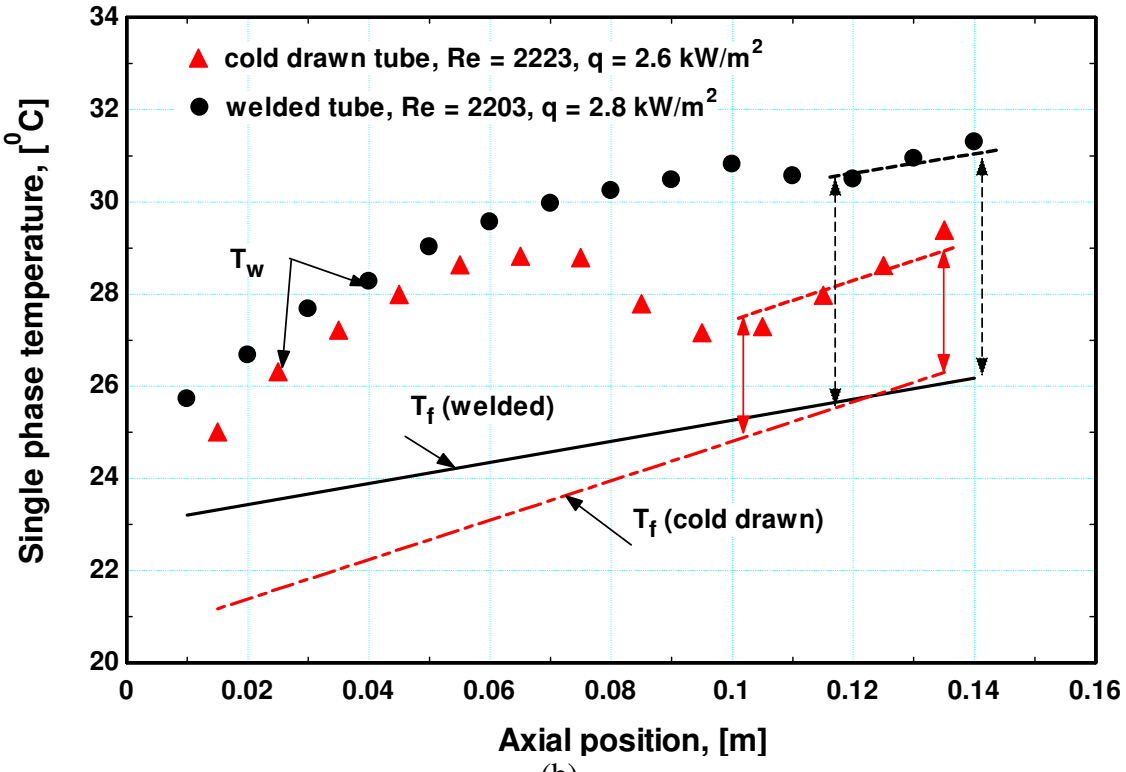
cold drawn tube, Re = 2223, q = 2.6 kW/m2
welded tube, Re = 2203, q = 2.8 kW/m2
Tw
Tf (welded)
Tf (cold drawn)
Single phase temperature, [°C]
Axial position, [m]

(b)

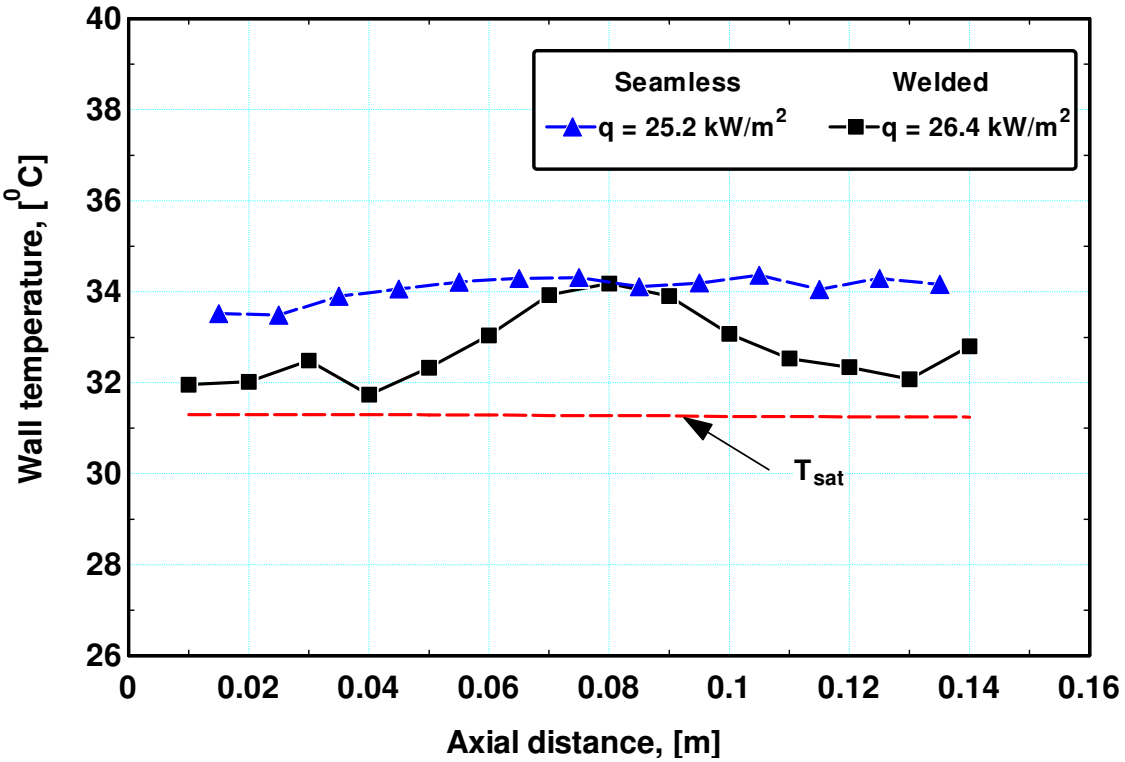

(c)

Figure 4.36 The wall temperature trends versus axial distance for (a) single phase at low Reynolds number, (b) single phase flow in the transition region, (c) boiling flow.

Hysteresis in the 1.1 mm diameter tubes

Figures 4.37 and 4.38 present the boiling curves for the welded and seamless tubes plotted through increasing and decreasing heat flux at three axial locations. The three locations represent the entry, the mid and the exit regions. For the welded tube at all locations, Fig. 4.37 indicates that there is hysteresis only for $q < 13$ kW/m^2, i.e. the region of boiling incipience. For the seamless cold drawn tube (Fig. 4.38), there is hysteresis only at the location which is near the entry for $q < 15$ kW/m^2. This may be due to the effect of the effect of the liquid inlet sub-cooling on the stability of the nucleation sites at low heat fluxes. The other locations (mid and near the exit) did not show any hysteresis. In both kinds of tubes, once nucleate boiling becomes fully established, the increasing and decreasing curves coincide with each other without any hysteresis.

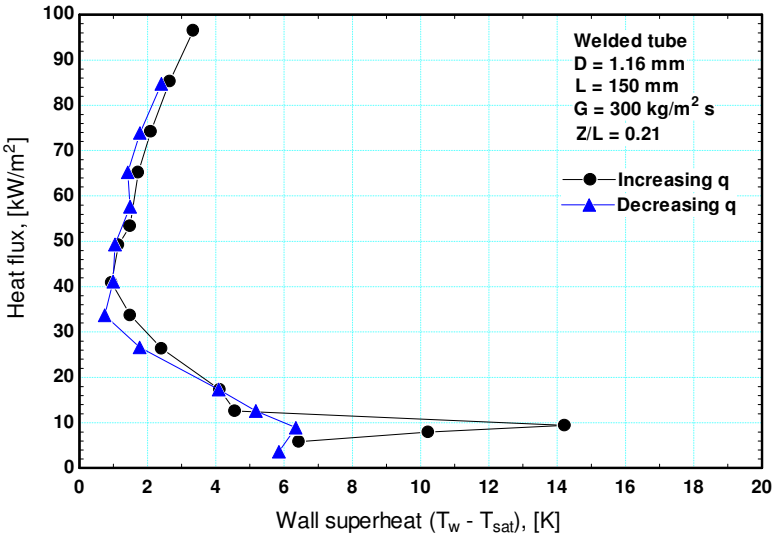

(a) Z/L = 0.21

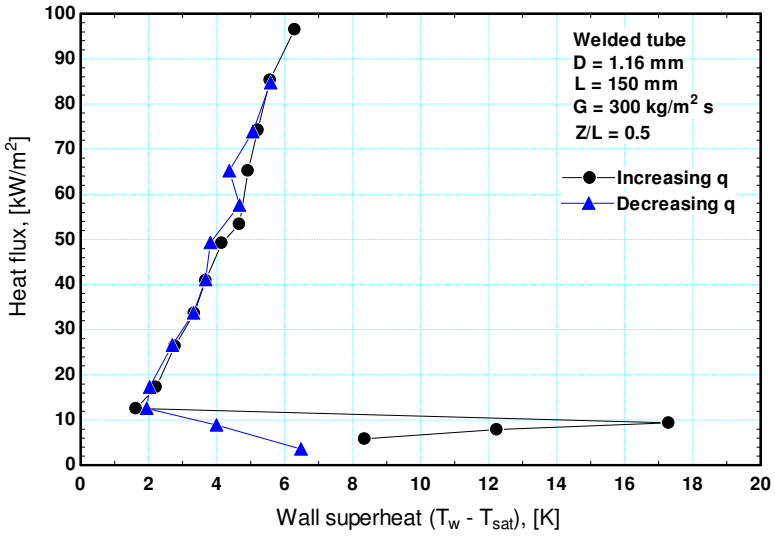

(b) Z/L = 0.5

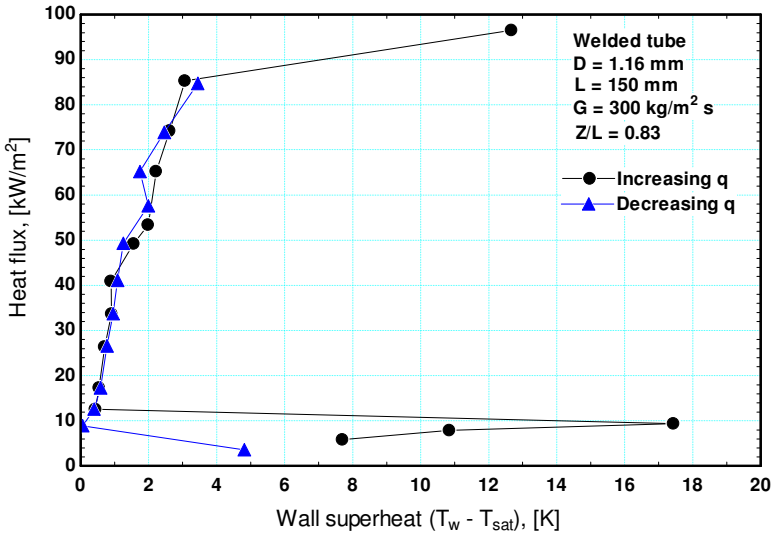

(c) Z/L = 0.83

Figure 4.37 The boiling curve plotted for increasing and decreasing heat flux at 6 bar system pressure and 280 kg/m^2 s mass flux for the welded tube.

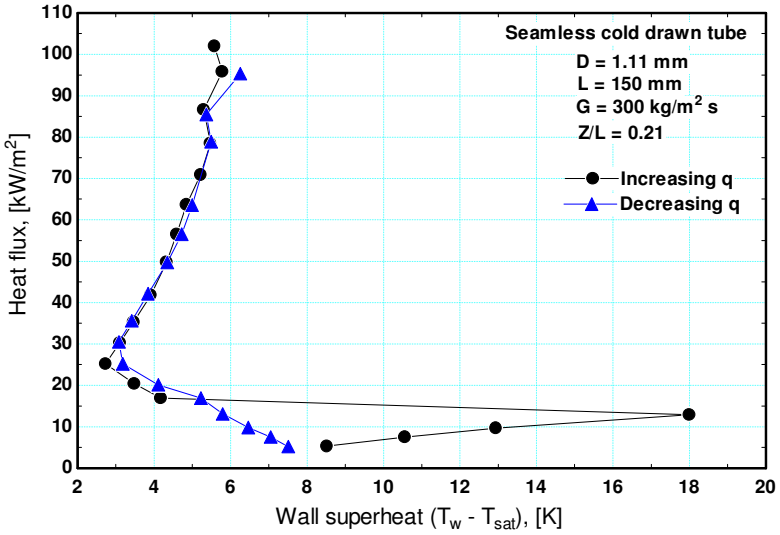

(a) Z/L = 0.21

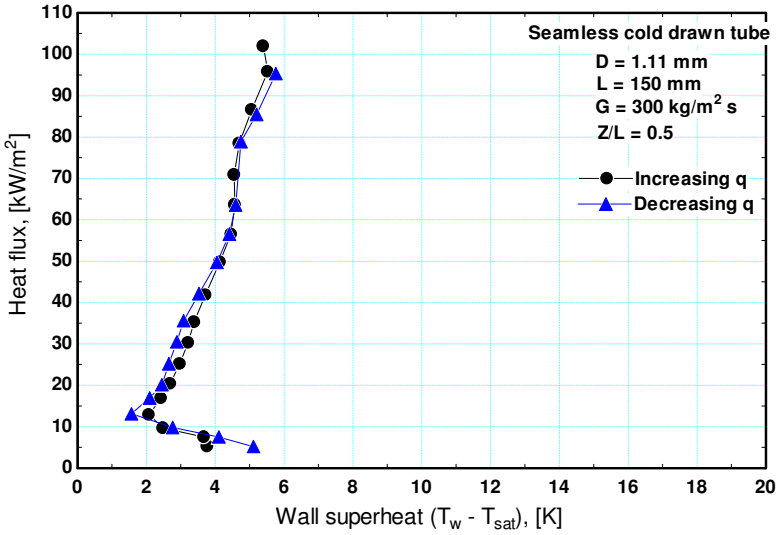

(b) Z/L = 0.5

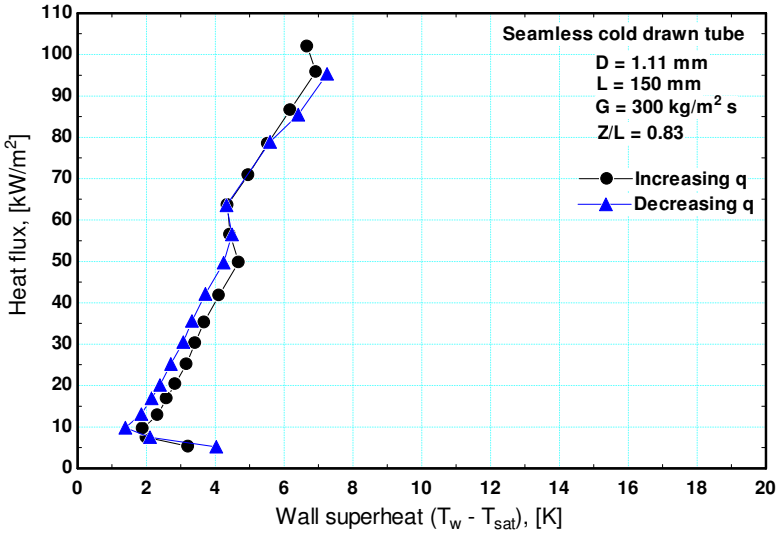

(c) Z/L = 0.83

Figure 4.38 The boiling curve plotted for increasing and decreasing heat flux at 6 bar system pressure and 280 kg/m^2 s mass flux for the seamless cold drawn tube.

Figure 4.39 depicts a direct comparison between the boiling curves of the 0.52 mm diameter tube (increasing and decreasing curves) and those of the 1.1 mm diameter tube. Both tubes are seamless cold drawn and the comparison is conducted at approximately similar axial distance. The curves of the 0.52 mm diameter tube are plotted for z/L = 0.25 whilst those of the 1.1 mm tube are plotted for z/L = 0.3. It is obvious that the boiling curve of the 0.52 mm tube (increasing heat flux) is very different from that of the 1.1 mm tube. The differences include the following: (i) The onset of nucleate boiling (ONB) in the 0.52 mm tube occurred at wall superheat value of 3.2 K compared to 15 K for the 1.1 mm tube. It is worth mentioning here that, in some experimental runs, the wall superheat exceeded 15 K in the 0.52 mm tube. For both sizes of tubes (0.52 and 1.1 mm), the value of the wall superheat at the ONB was varying randomly with the experimental conditions, i.e. sometimes boiling commences smoothly at low wall superheat and sometimes it requires very high wall superheat. In other words, the difference in wall superheat at the ONB in both tubes is not due to the effect of tube diameter. (ii) After the ONB, there is no temperature under-shoot for the 0.52 mm tube where the wall superheat did not change significantly between q = 8.4 – 13.3 kW/m^2. Additionally, the boiling curve after the ONB is very steep and the wall superheat increased only from 3.2 to 4.7 K when q was increased from 13.3 to 62 kW/m^2. On the contrary, the temperature under-shoot in the 1.1 mm tube is very clear where the wall superheat dropped from 15 K at q = 9.8 kW/m^2 to 1.9 K at q = 17.3 kW/m^2. After the ONB, the wall superheat increased slowly from 1.9 to 6.7 K compared to the 0.52 mm tube. Conducting the experiments in the direction of decreasing heat flux indicted that the boiling hysteresis in the 0.52 mm tube commences at a relatively higher heat flux value (q < 18 kW/m^2) compared to the 1.1 mm tube (q < 10 kW/m^2).

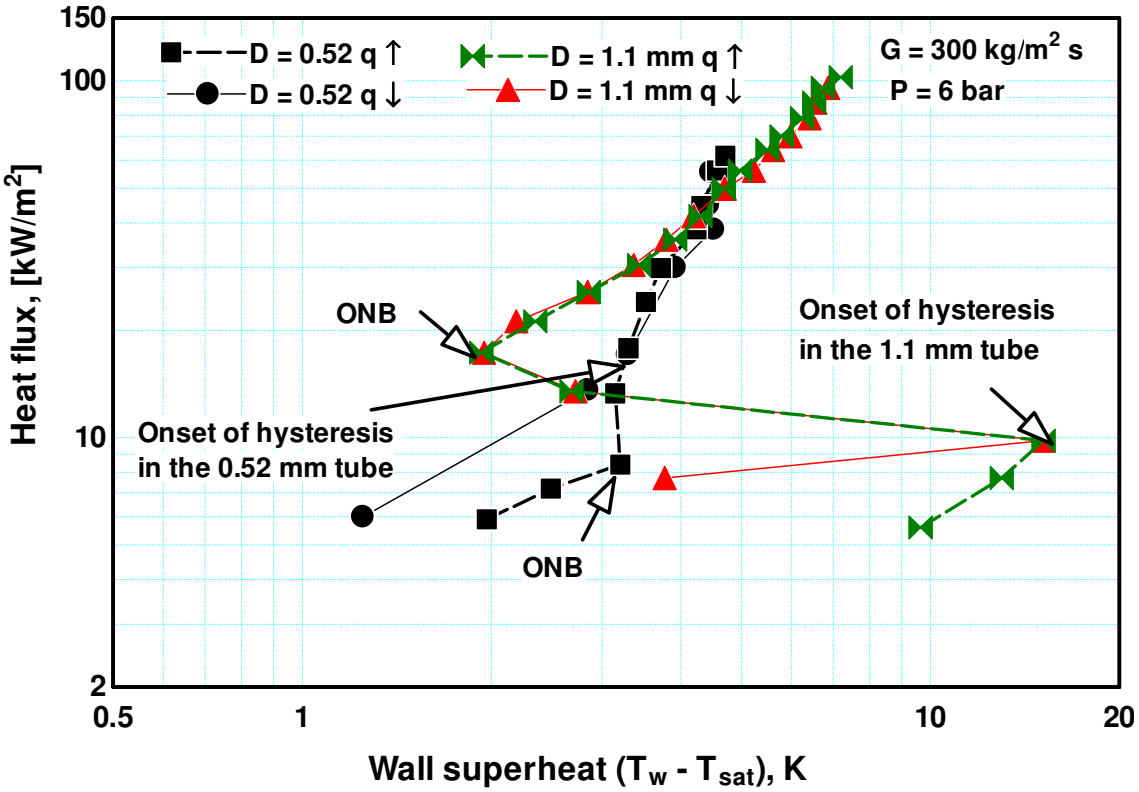

Figure 4.39 Comparison between the boiling curves of the 0.52 mm tube and those of the 1.1 mm seamless cold drawn tube at Z/L = 0.25 for the 0.52 mm and 0.3 for the 1.1 mm tube.

4.3.3 Effect of heated length

As reviewed in Chapter 2, there is a wide disagreement in the published heat transfer results about the trend of the local heat transfer coefficient versus local vapour quality. As a result, various conclusions about the dominant heat transfer mechanism(s) were reported. Unfortunately, the reasons behind this scatter are not yet understood. Possible reasons could be the effect of inner surface characteristics as presented and discussed in the previous section and/or the variation of the investigated heated lengths from one study to another. The effect of heated length on the local flow boiling heat transfer characteristics was not considered by most researchers. Accordingly, three heated lengths (L = 150, 300, 450 mm) were investigated herein this study for the same kind of tubes (seamless cold drawn) and same inner diameter of 1.1 mm. The results are presented here at the same mass flux (G = 300 kg/m^2 s) and same system pressure (P = 6 bar) for the sake of comparison between the three investigated lengths. The experimental flow patterns transition boundaries are also shown on the figures. The effect of heat flux on the heat transfer coefficient for the three heated lengths is

presented in Fig. 4.40 as a function of local vapour quality and Fig. 4.41 as a function of axial distance. The trend of the heat transfer coefficient in Fig. 4.40a is similar to the one presented and discussed previously in Fig. 4.31 at 8 bar system pressure. It is obvious from Fig. 4.40a that, the heat transfer coefficient increases with heat flux with little dependence on local vapour quality. At low heat fluxes where a considerable length of the tube is under single phase conditions, the heat transfer coefficient jumps at vapour quality values close to zero then it drops before it remains approximately constant with quality. Also, it is obvious that, the heat transfer coefficient tends to increase with quality at locations near the tube exit which is clear at heat flux values of 64.1 and 78.6 kW/m^2. For q $\geq$ 95.7 kW/m^2, the effect of heat flux was insignificant and dryout occurred at x $\approx$ 0.52. Figure 4.41a shows that, after boiling incipience, the heat transfer coefficient increases with heat flux with little dependence on axial distance. The only exception is q = 64.1 and 78.6 kW/m^2 where the heat transfer coefficient increased with axial distance towards the exit.

Figure 4.40b demonstrates for L = 300 mm that the trend of the local heat transfer coefficient changes with heat flux. At low heat flux values (q = 7.5 and 13.7 kW/m^2), the trend was similar to N-shape starting from the single phase region. The coefficient jumped from its single phase value and peaked at local quality values near to zero then suddenly dropped to a minimum value before it rapidly increases with vapour quality. At intermediate heat flux values, (q = 25.4 – 35.4 kW/m^2), the minima that appeared at lower heat fluxes have diminished and the trend changed. At theses conditions, after the heat transfer coefficient increased from its single phase value to its maximum value, it showed little dependence on vapour quality up to x = 0.25. After this quality value, the heat transfer coefficient increased with vapour quality and the curves collapsed into one single line. Another change in the trend was observed at high heat flux values (q = 41 – 55.8 kW/m^2). The heat transfer coefficient decreased from its maximum value at x $\approx$ 0.01 up to a vapour quality value of about x = 0.13 then it remained approximately constant with quality until dry out occurred at x $\approx$ 0.6. Additionally, it is obvious from the figure that the heat transfer coefficient increases with heat flux up to x $\approx$ 0.3 especially at low to intermediate heat flux values. At the three highest heat fluxes, the heat flux effect was insignificant. Figure 4.41b presents the local heat transfer coefficient as a function of heat flux and axial distance. For all heat fluxes, the heat

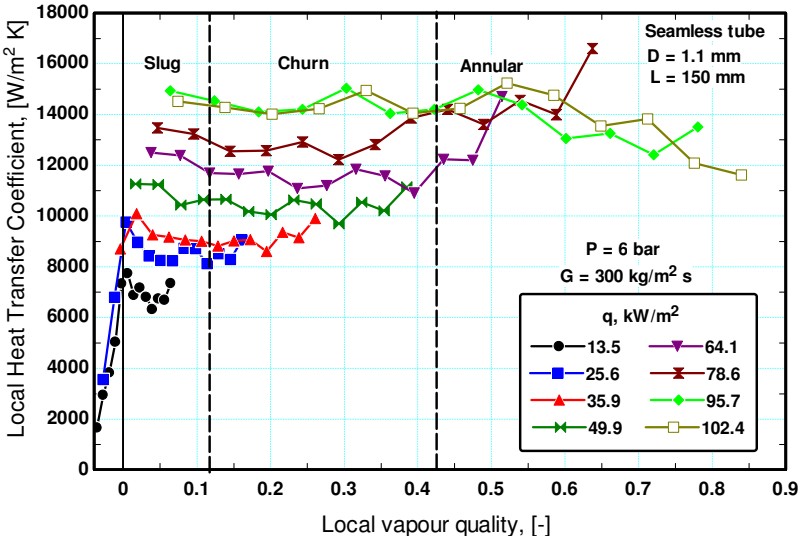

(a) L = 150 mm

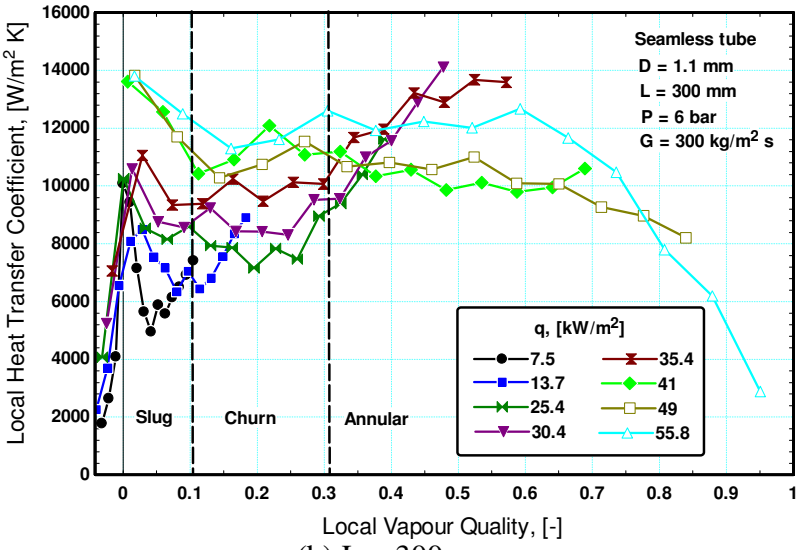

(b) L = 300 mm

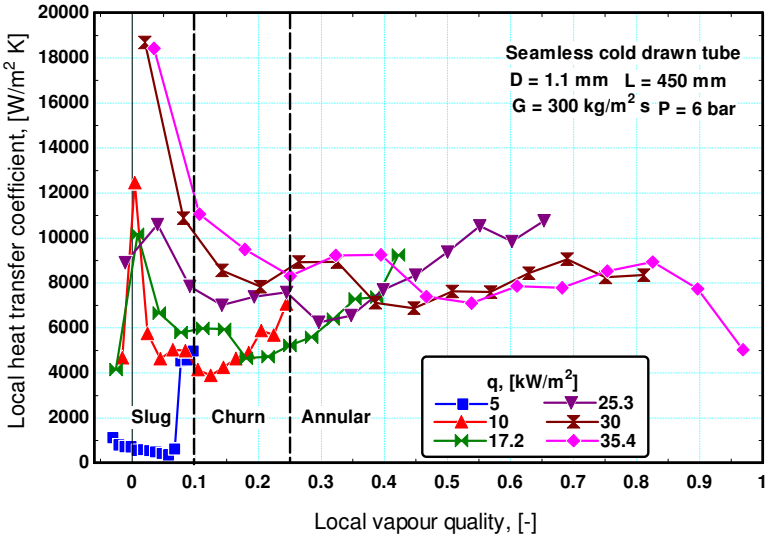

(c) L = 450 mm

Figure 4.40 The effect of heat flux on the local heat transfer coefficient as a function of local vapour quality at P = 6 bar, G = 300 kg/m^2 s, D = 1.1 mm.

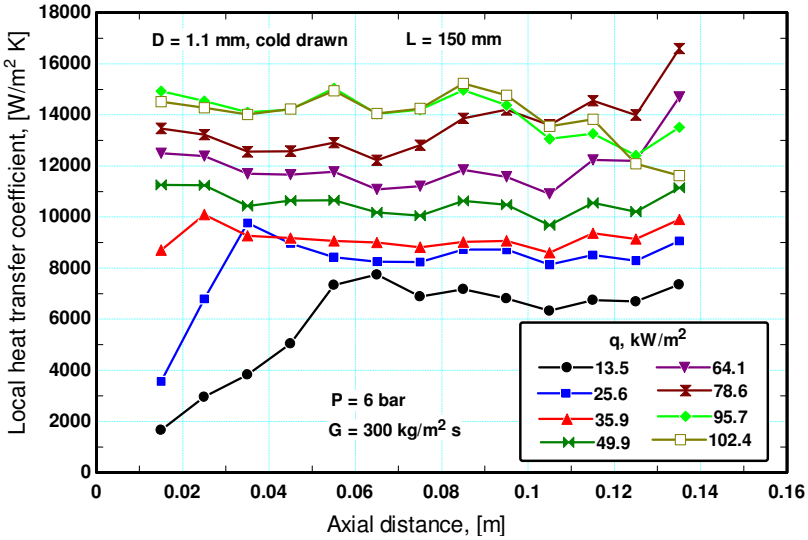

(a) L = 150 mm

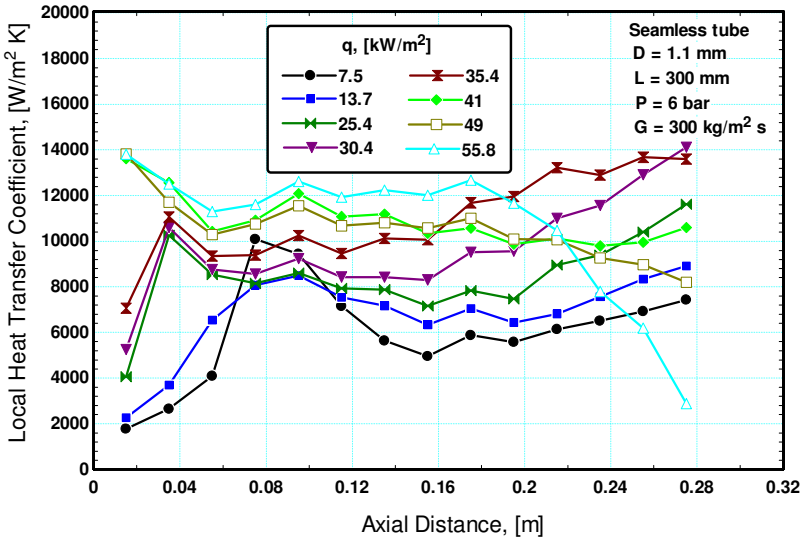

(b) L = 300 mm

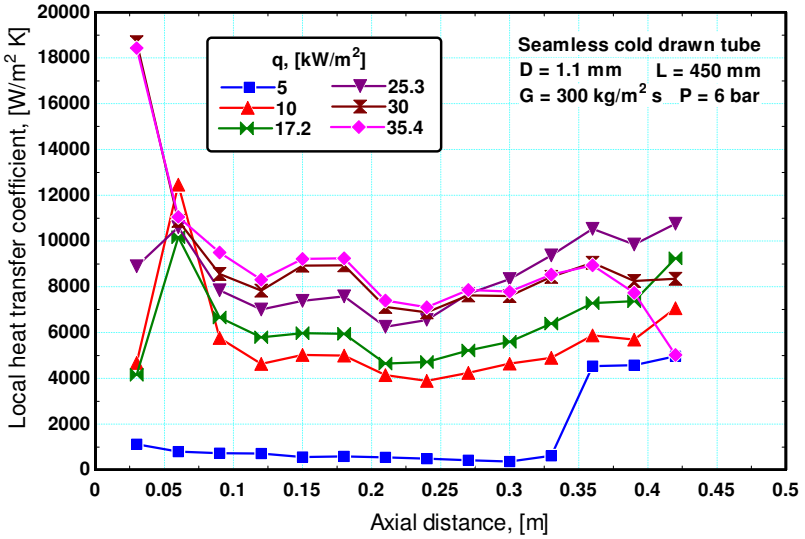

(c) L = 450 mm

Figure 4.41 The effect of heat flux on the local heat transfer coefficient as a function of axial distance at P = 6 bar, G = 300 kg/m^2 s, D = 1.1 mm.

transfer coefficient decreases with axial distance immediately after boiling incipience. After axial distance of about Z/L = 0.52, the heat transfer coefficient increases with distance and heat flux up to q = 35.4 kW/m^2. It is clear also from Fig. 4.41b that, the effect of heat flux is small in the first half of the tube compared to the second half towards the exit.

Figure 4.40c depicts the results for the longest tube and demonstrates that, for the lowest heat flux (q = 5 kW/m^2), the heat transfer coefficient remained very small up to thermocouple location No. 12 (Z/L = 0.8) at which boiling commenced and the heat transfer coefficient jumped from about 600 W/m^2 K to 4600 W/m^2 K. For intermediate heat flux values (q = 10 – 25.3 kW/m^2), the heat transfer coefficient drops from its maximum value at vapour quality close to zero then it remains approximately constant with vapour quality up to thermocouple location No. 6 (Z/L = 0.4). After this location, the heat transfer coefficient slightly drops up to location No. 7 (Z/L = 0.47) then it increases constantly with vapour quality. For the two highest heat fluxes (q = 30 – 35.4 kW/m^2), the trend is similar to the intermediate heat flux up to local vapour quality of 0.3. At vapour qualities greater than this value, the two lines merged together with little dependency on vapour quality and heat flux up to x = 0.82 after which dryout occurred. The figure indicates also that there is a clear heat flux effect for vapour qualities less than about 0.3. Figure 4.41c demonstrates that there is unclear heat flux effect on the heat transfer coefficient at locations Z/L < 0.2, which are near from the location of boiling incipience. After this location, the lines were separated indicating a clear heat flux effect with little dependence on axial distance for Z/L = 0.2 – 0.47. After Z/L = 0.47, the heat transfer coefficient increased rapidly with axial distance for heat fluxes up to 25.3 kW/m^2 whilst the increasing rate decreased with the two highest heat fluxes before dry out.

Figures 4.40 and 4.41 indicate that the heated length influences the behaviour and magnitudes of the heat transfer coefficient. All figures agreed on that, the heat transfer coefficient decreases with increasing vapour quality immediately after boiling incipience in the very small quality region. The magnitude of the drop of the heat transfer coefficient from its maximum value at quality close to zero increased with increasing the heated length. For L = 150 mm, the heat transfer coefficient dropped by 11.6 % at q = 13.5 kW/m^2 whilst for L = 300 mm and L = 450 mm it dropped by 50.8 %

and 59.6 %, respectively for q = 7.5 kW/m^2 and q = 10 kW/m^2, respectively. Lin et al. (2001b) obtained similar features during the flow boiling of R141b in a 1 mm diameter tube with a 500 mm heated length; see Fig. 2.47. It is worthy noting that, their figure was developed at much higher inlet sub-cooling conditions (12 – 23.6 K) compared to the current study (5K). They attributed the drop in heat transfer coefficient after boiling incipience to the inappropriate assumption of linear variation of pressure drop along the tube. They have supported their point using the model of Cornwell and Kew (1992) according to which a significant part of the pressure drop occurs at boiling incipience due to the bubble confinement associated with high local pressure fluctuations. The fluctuations in the local pressure during flow boiling in narrow channels were experimentally measured by Aligoodarz et al. (1998) and Yan and Kenning (1998). It was found that, the fluctuations in the local pressure attained values that are equivalent to about 2K fluctuations in the wall superheat. Based on that, Li et al. (2001b) believed that the local saturation temperature and pressure in the region of boiling incipience may be lower than the one estimated based on the linear assumption. Figure 4.42 shows a schematic drawing for the local variations in saturation pressure and temperature, which clarifies the point. When the local pressure varies linearly along the tube, the local wall superheat is ΔT_1. On the other hand, when the local pressure peaks at the onset of boiling due to the bubble formation and confinement, the local wall superheat is ΔT_2. Since, ΔT_1 is smaller than ΔT_2, the calculated heat transfer coefficient based on the linear assumption will be higher at boiling incipience which would not be the case if the pressure fluctuations at boiling incipience were taken into consideration. Thus, the linear assumption results in an over-estimation for the local heat transfer coefficient at vapour qualities near from zero. The behaviour of the heat transfer coefficient at boiling incipience in the current study may be explained in a similar way. Since the measured pressure drop in the shortest tube is the lowest compared to the other longer lengths, the variation in the local saturation temperature at boiling incipience may be small as well. Additionally, the heat flux required to attain the same exit quality is higher for the shortest heated section–the thing that may activate more nucleation sites at locations away from the extreme entry region. Accordingly, the magnitudes of the heat transfer coefficient in the shortest tube after boiling incipience are approximately close to the peak values.

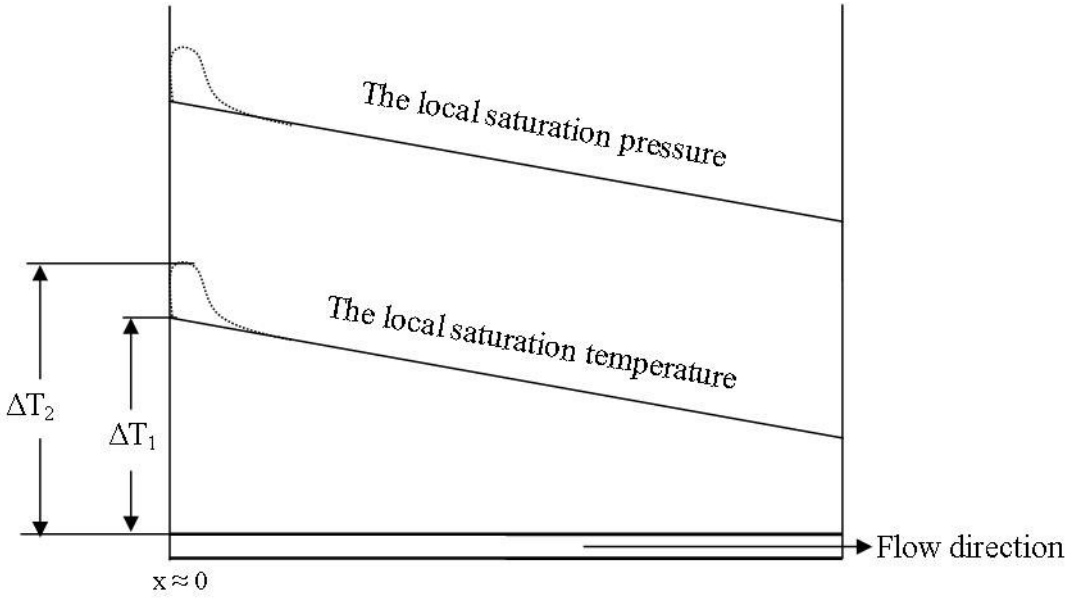

Figure 4.42 A schematic drawing for the variations in the local saturation pressure and temperature based on the linear assumption and when the pressure peaks at $x \approx 0$.

Also, Figs. 4.40 and 4.41 indicate that the heat flux effect was very clear in the shortest tube (L = 150 mm) where separate lines were observed with little dependence on local vapour quality and axial distance over the tube length. Nevertheless, Fig. 4.40a demonstrates that there was a tendency for the trend to change at q = 64.1 kW/m^2. As the heated length was increased, the change of the trend of the heat transfer coefficient versus vapour quality has become more obvious as seen in Figs. 4.40b and 4.40c. The heat transfer coefficient increased with increasing vapour quality over a considerable length of the tube which does not occur in the shortest tube. It is clear from Figs. 4.40b and 4.40c that the heat transfer coefficient increased with vapour quality even at the lowest heat fluxes where the flow pattern was slug and churn. In other words, this behaviour does not occur due to film evaporation that is expected to dominate in annular flow. Possible reasons could be the increase in pressure drop with the increase of the heated length which influences the local saturation temperature. However, the saturation temperature decreased by 0.2 %, 0.48 % and 1.2 % for L = 150, 300 and 450 mm respectively which seems to be small to cause this effect. Another possible reason could be the value of heat flux corresponding to the same exit quality where for $x \approx 0.9$ the heat flux was 102.4, 55.8 and 35.4 kW/m^2 for L = 150, 300 and 450 mm respectively. The very high values of heat fluxes in the shortest tube may be sufficient

to activate more nucleation sites over a considerable length of the tube. This is clear from Fig. 4.43 that depicts the effect of the heated length on the magnitudes of the heat transfer coefficient. When the comparison is conducted at same exit quality (Fig. 4.43a), the heat transfer coefficient in the shortest tube was the highest. On the other hand, when the comparison is conducted at same heat flux, the magnitudes were approximately similar in the low quality region. Thus, the low heat flux values in the longer tubes may be sufficient only to activate few numbers of nucleation sites. It is clear from Figs. 4.40 and 4.41 that after a certain heat flux value ($q > 35.4$ kW/m^2 for L = 300 mm and $q = 25.3$ kW/m^2 for L = 450 mm), the increasing trend with vapour quality disappears and the heat transfer coefficient remains approximately unchanged with quality even at very high vapour qualities. This turn in trend may be attributed to the features of annular flow observed in the 1.1 mm diameter tube as previously described in the flow patterns section. The pictures indicated that there is some liquid entrainment to the vapour core. In that case, for the heat transfer coefficient to increase or remain constant depends on the rate of liquid droplet deposition and entrainment. If the two rates are approximately equal, the heat transfer coefficient is expected to increase with local quality. On the other hand, if the deposition rate is higher than the entrainment rate the film thickness may build up and the heat transfer coefficient is expected to decrease with quality or remains approximately constant.

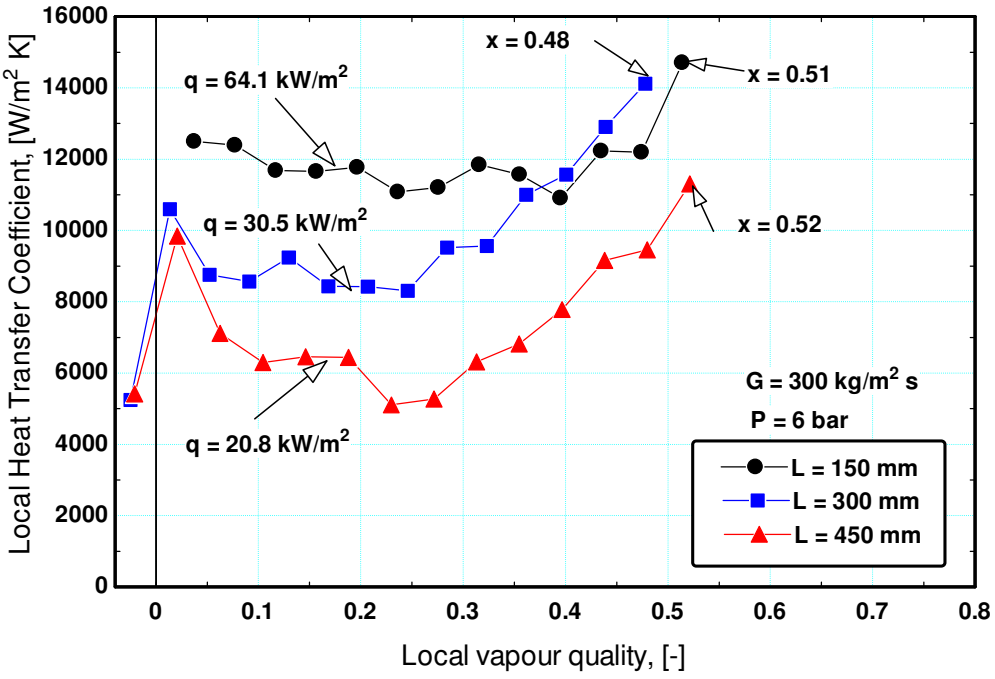

(a) Comparison at same exit quality

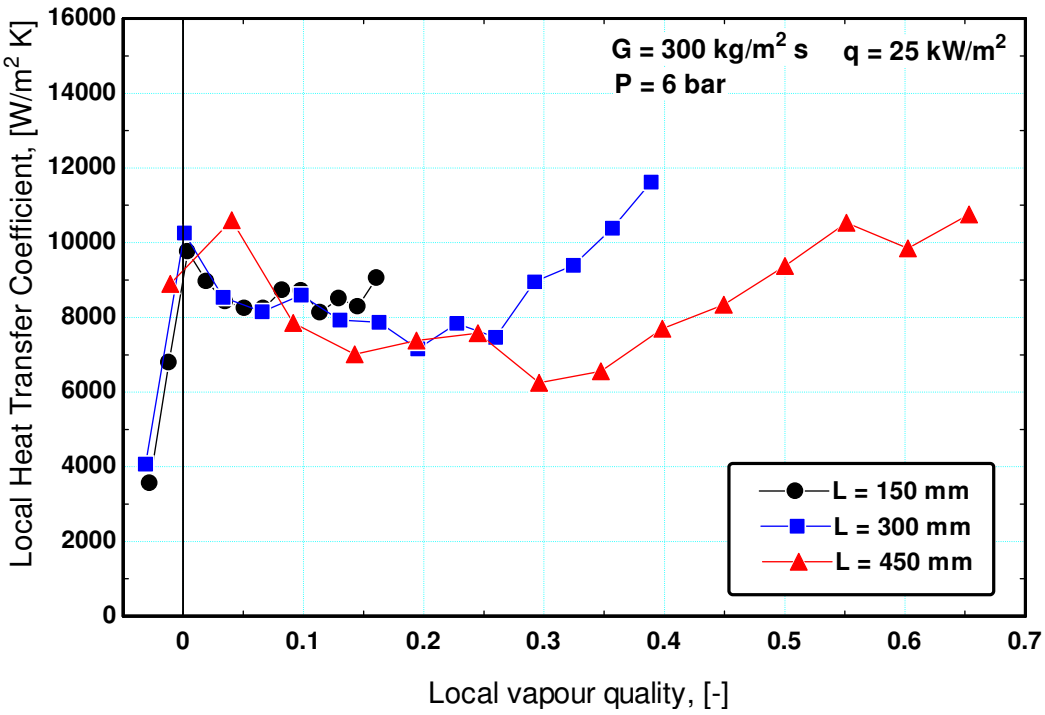

(b) Comparison at same heat flux

Figure 4.43 The effect of the heated length on the magnitude of the heat transfer coefficient.

Figure 4.44 illustrates the wall temperature versus axial distance as a function of heat flux just before boiling incipience at G = 300 kg/m^2 s (Re = 1941), P = 6 bar and inlet sub-cooling value of about 5K. For L = 150 and 300 mm, boiling commenced at an upstream location very near the inlet at heat flux values of 13.5 and 7.5 kW/m^2, respectively. On the other hand, boiling commenced in the longest tube (L = 450 mm) at downstream location very near the exit at q = 5 kW/m^2 and with further increase in heat flux, the location of boiling incipience moves upstream towards the inlet. The occurrence of boiling at lower heat flux values as the heated length increases is understood from the energy balance. At the same heat and mass flux values, the fluid outlet temperature increases with increasing heated length. Consequently, the fluid becomes superheated at lower heat flux values in the longer test sections compared to the shorter ones. It is also interesting to note that, the wall temperature before the onset of nucleate boiling (single phase temperature) is not linear for the three heated lengths. Some local drops in wall temperature were observed for all the investigated lengths. For L = 150 mm, the wall temperature increases with location according to a parabolic curve up to thermocouple location No. 7 after which a linear drop in temperature occurred up to location No. 9 then the temperature increased linearly with distance. For

L = 300 mm, the parabolic part appeared up to location No. 5 then the temperature increased up to location No. 8 followed by a decrease in temperature up to location No. 11 after which the temperature increased again almost linearly. For L = 450 mm, the temperature slightly dropped after location No. 5 then increased almost linearly up to the outlet of the tube. The local drops in wall temperature with axial distance were found to be dependent on Reynolds number. Figure 4.45 presents one example for the single phase wall temperature versus axial distance in the laminar region at low values of Reynolds number. It is clear from the figure that the wall temperature behaves according to a perfect linear relationship with axial distance. The locations at which the drop in wall temperature occurs in Fig. 4.44 are also appearing in Fig. 4.45 but with insignificant magnitudes. When Reynolds number increases, the magnitude of the drop becomes significant and clear. This means that, these local drops in temperature, i.e. the non linearity, is due to local turbulence resulting from the inner surface characteristics.

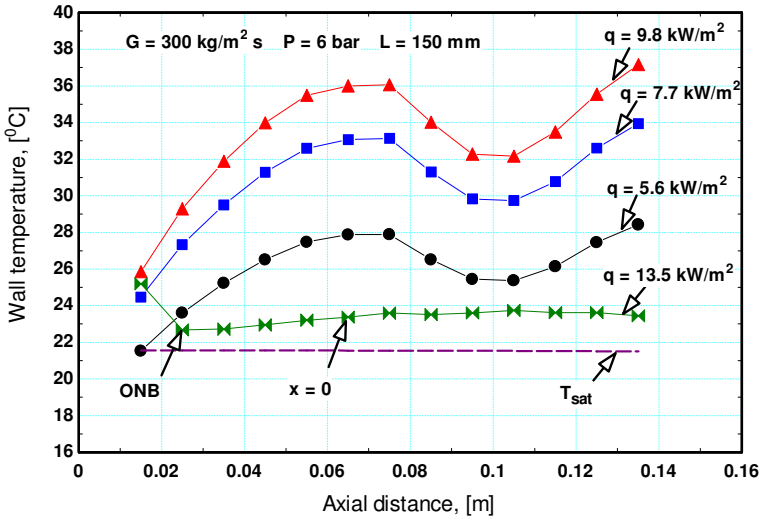

(a) L = 150 mm

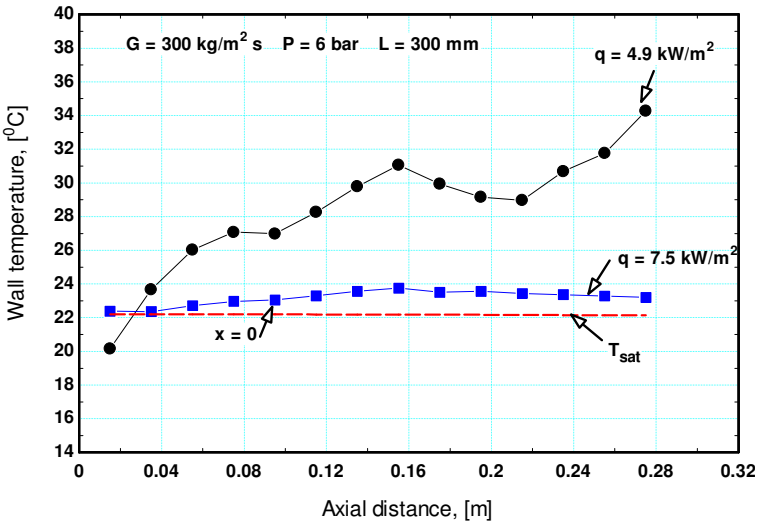

(b) L = 300 mm

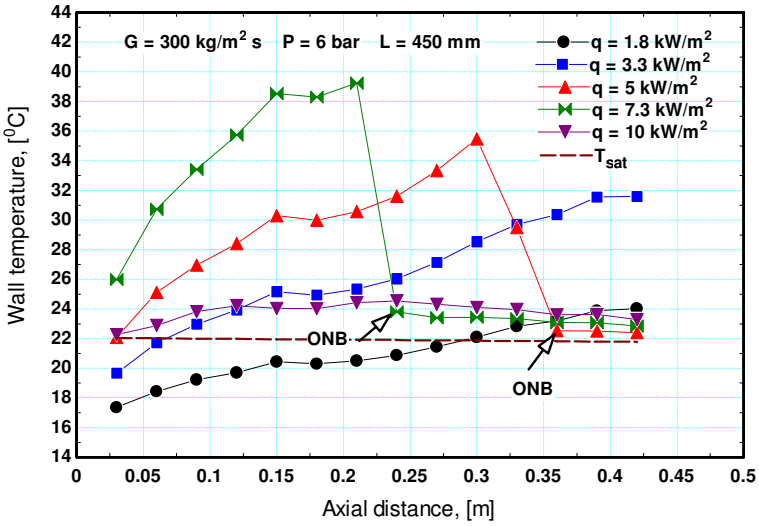

(c) L = 450 mm

Figure 4.44 The wall temperature versus axial distance just before boiling incipience at G = 300 kg/m^2 s (Re = 1941) and P = 6 bar.

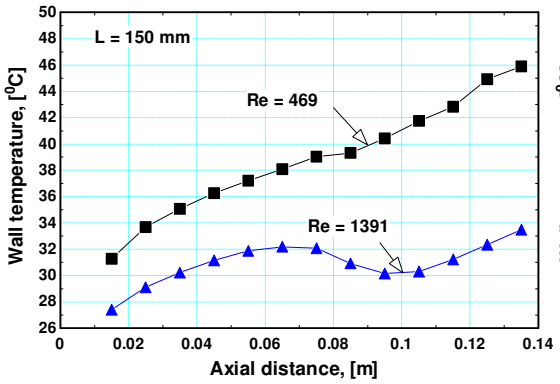

(a) L = 150 mm

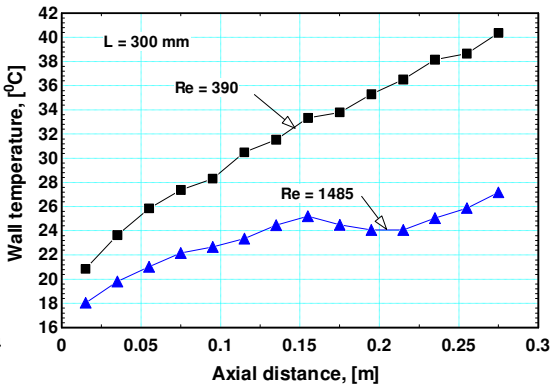

(b) L = 300 mm

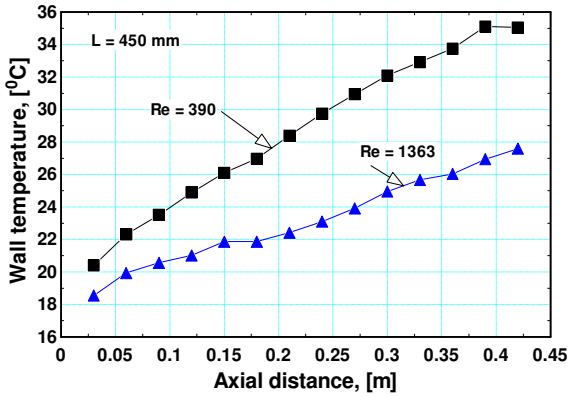

(c) L = 450 mm

Figure 4.45 Single phase wall temperature versus axial distance in the deep laminar region.

To further clarify the effect of heat flux on the heat transfer coefficient, the coefficient was plotted versus heat flux at three axial locations as seen in Fig. 4.46 for the three heated lengths. Figure 4.46a shows for the shortest tube that the heat transfer coefficient increases almost linearly with heat flux with insignificant effect for the axial distance. On the other hand, Figs. 4.46b and 4.47c show that the heat transfer coefficient depends on the axial location where it was higher at locations near from the exit for heat flux values below 35 kW/m^2. Also, it is obvious that the slope of the line at the three axial locations is less than that of the shortest tube indicating that the effect of heat flux becomes less as the length increases. This may be an indication for the progression from nucleate to convective boiling over a considerable portion of the tube as the heated length increases. At high heat fluxes and locations near the exit, the heat transfer coefficient either decreased with heat flux due to dryout or exhibited little changes with heat flux. The small heat flux effect at locations towards the exit may confirm the presence of convective boiling.

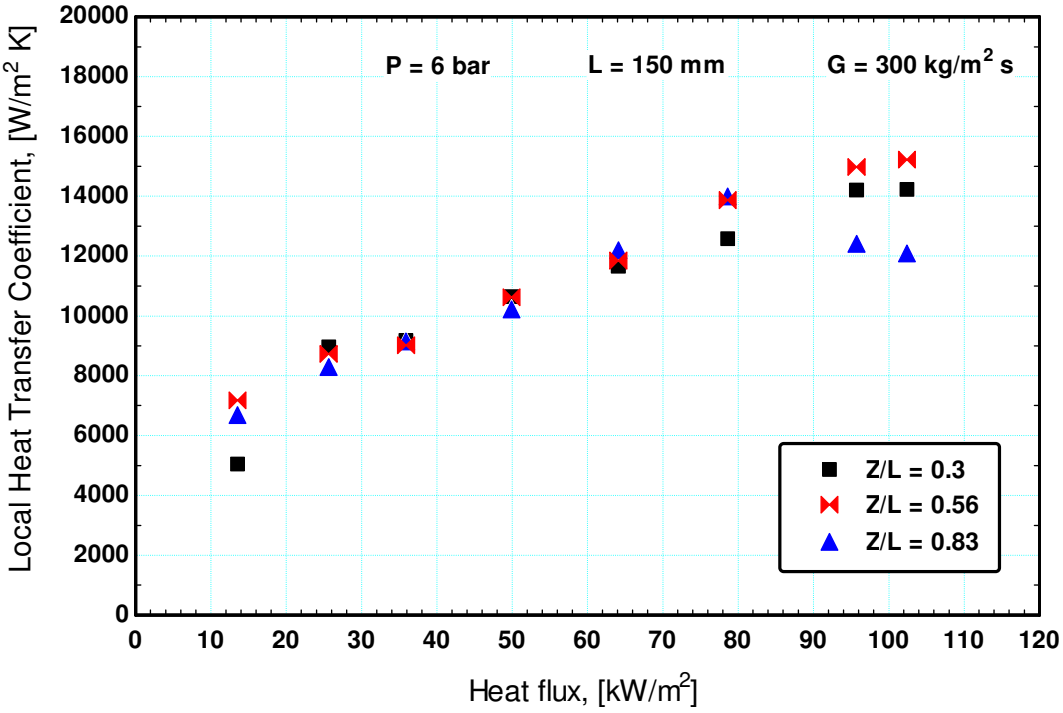

(a) L = 150 mm

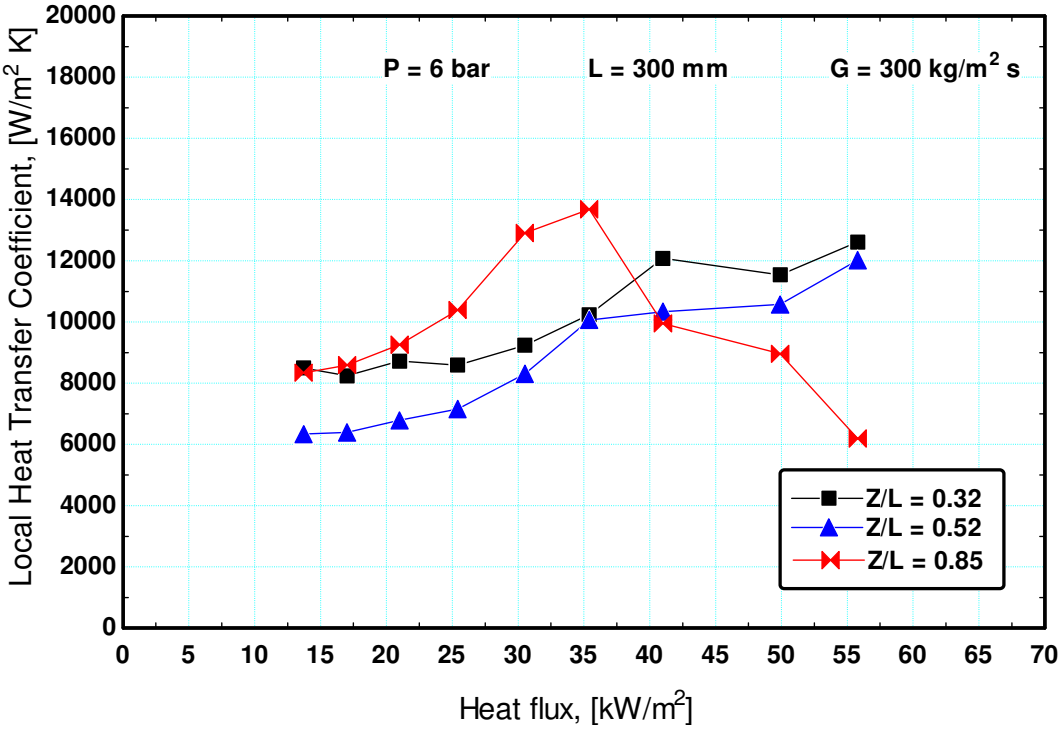

(a) L = 300 mm

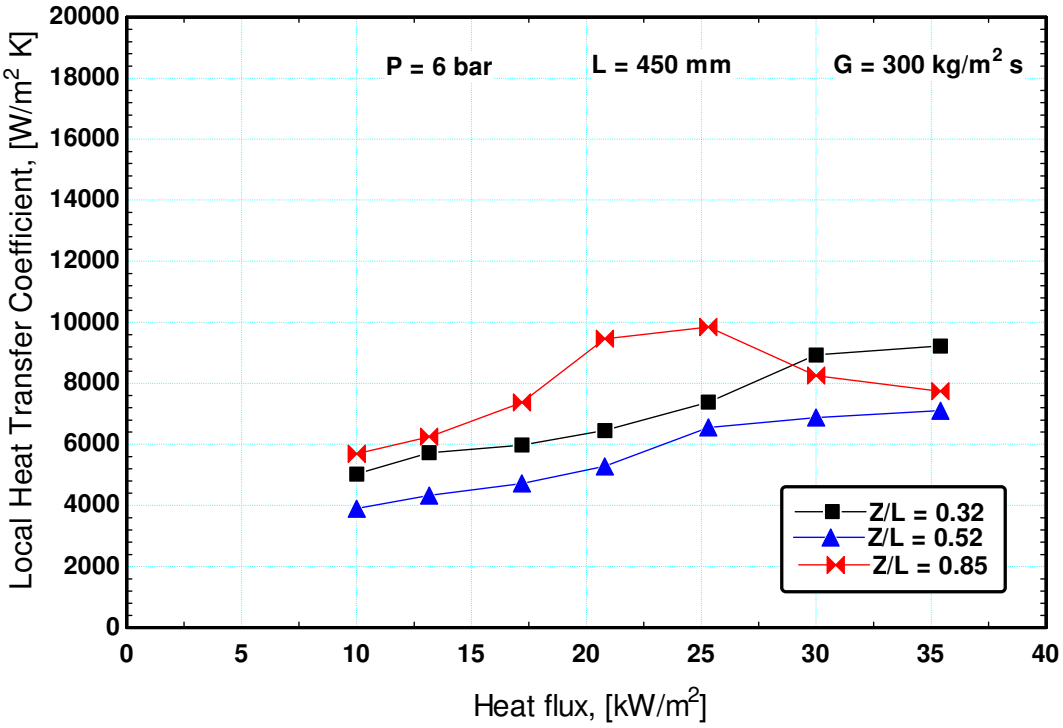

(c) L = 450 mm

Figure 4.46 The heat transfer coefficient as a function of heat flux for the three heated lengths at P = 6 bar and G = 300 kg/m^2 s.

Figures 4.47 and 4.48 illustrate the effect of mass flux on the local heat transfer coefficient for the three heated lengths at heat flux value of 35.5 kW/m^2 and 6 bar system pressure. Figure 4.47 presents the mass flux effect as a function of local vapour quality whilst Fig. 4.48 presents the effect plotted as a function of axial distance. Figure 4.47a shows that the effect of mass flux on the local heat transfer coefficient is not significant in the shortest tube (L = 150 mm). On the other hand, Figs. 4.47b and 4.47c demonstrate that there is insignificant mass flux effect up to quality values of 0.2 – 0.25. After this value the mass flux effect is clear where the heat transfer coefficient increases with increasing mass flux. On the contrary, the plots with axial distance in Fig. 4.48 do not show clear mass flux effect. It can be concluded from Figs. 4.40 and 4.47 that, nucleate boiling dominates in the shortest tube even at high vapour quality. In the longer tubes, nucleate boiling dominates in the low quality region while convective boiling seems to dominate in the intermediate to high quality region. As mentioned above, the dominance of nucleate boiling in the shortest tube could be attributed to the operation at much higher heat fluxes compared to the longer tubes.

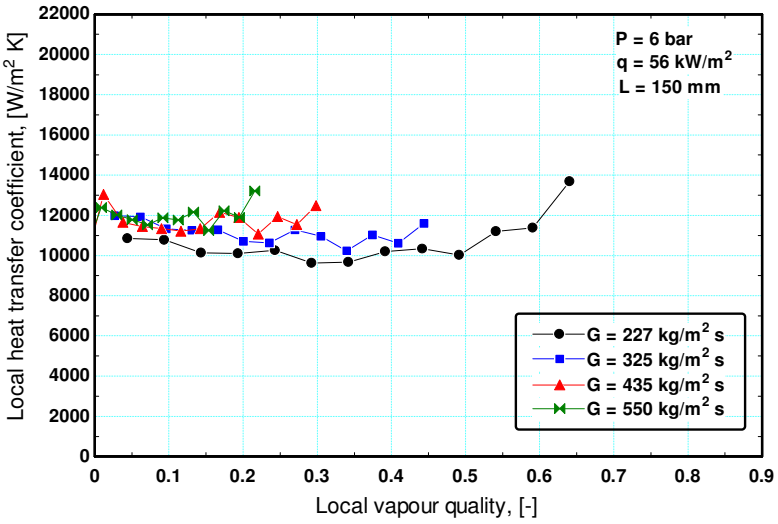

(b) L = 150 mm

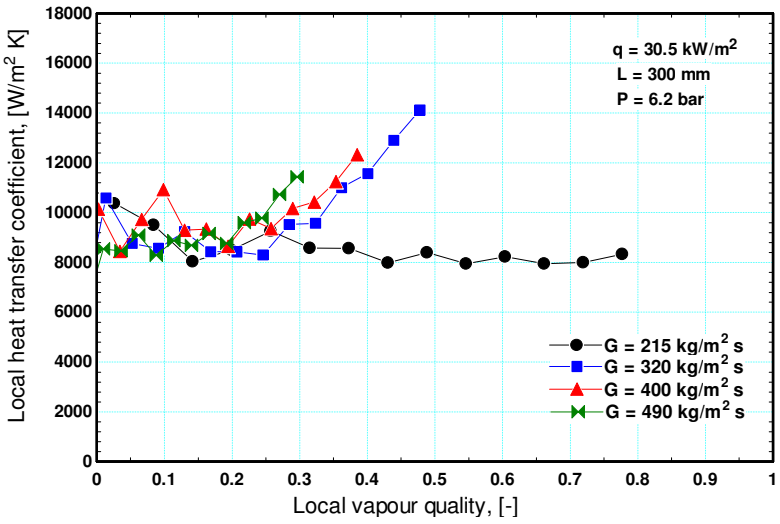

(c) L = 300 mm

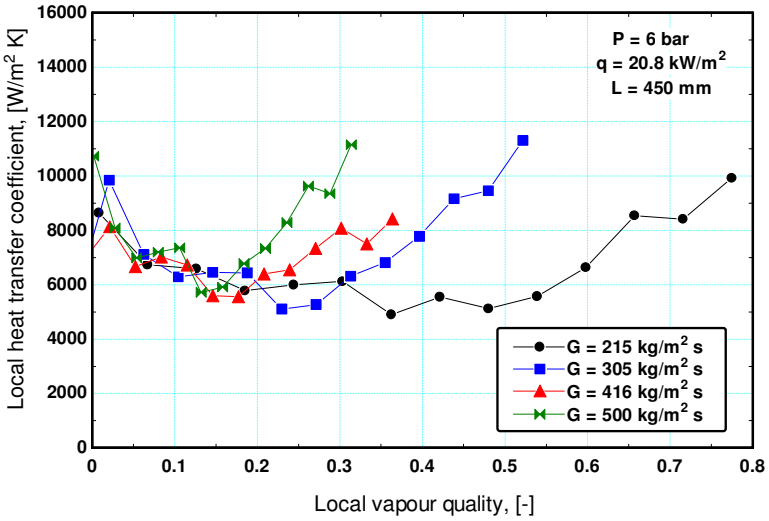

Figure 4.47 The mass flux effect at q = 35.5 kW/m^2 and P = 6 bar for the three heated lengths as a function of local vapour quality.

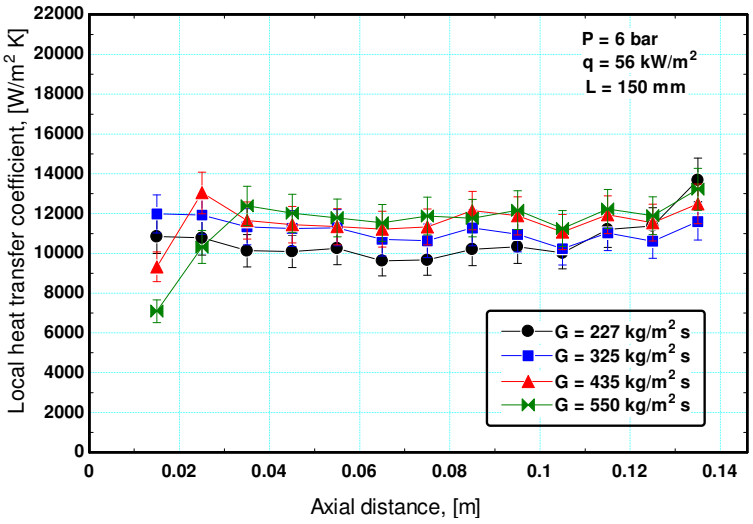

(a) L = 150 mm

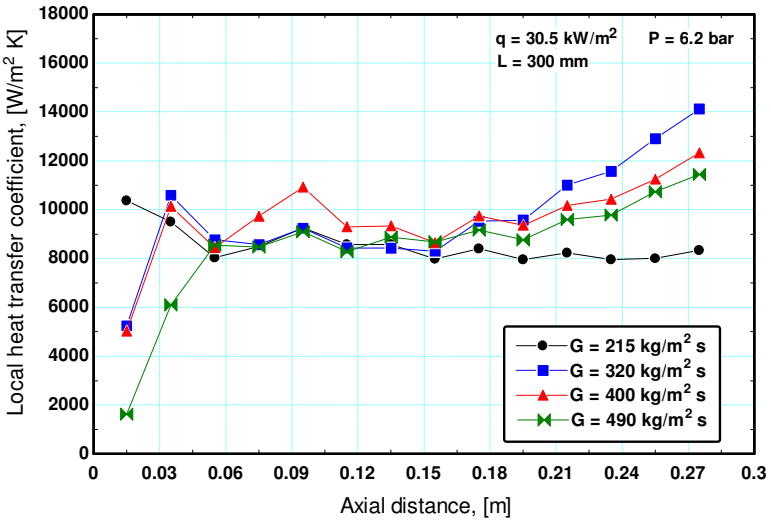

(b) L = 300 mm

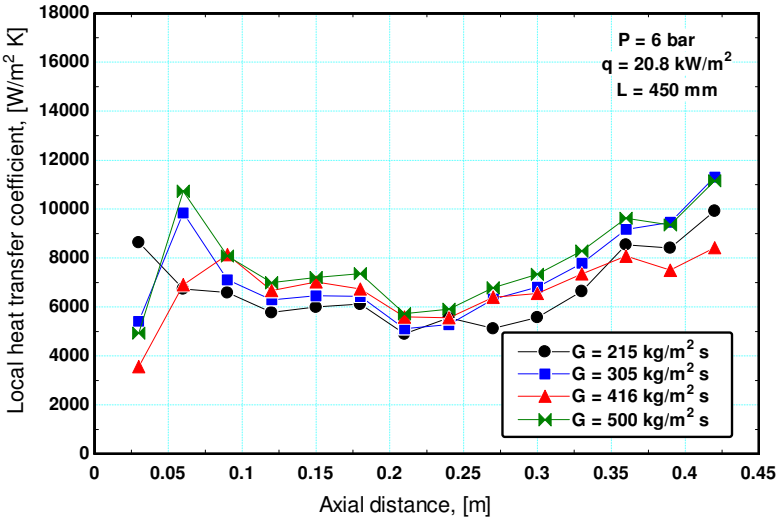

(c) L = 450 mm

Figure 4.48 The mass flux effect at q = 35.5 kW/m^2 and P = 6 bar for the three heated lengths as a function of the axial distance.

Figure 4.49 shows the boiling curves at two axial locations for all heated lengths. The curves were plotted through increasing and decreasing heat fluxes gradually in small steps to investigate whether there is hysteresis or not. It is obvious from the figure for all heated lengths that there is no boiling hysteresis after boiling incipience for all axial locations. The hysteresis occurred only at the very low heat fluxes near the onset of boiling. The curves indicate that, high wall superheat is required to trigger nucleate boiling which ranged from about 7.5 to 17K. It is also clear that the boiling curves at all locations are similar to the classical pool boiling curve even at locations near the exit.

Figure 4.50 presents the effect of system pressure on the local heat transfer coefficient at similar heat flux value for the three heated lengths. Figures 4.50a and 4.50b show that the heat transfer coefficient increases with increasing system pressure for L = 150 and 300 mm. On the other hand, Fig. 4.50c shows for L = 450 mm that the heat transfer coefficient increases with system pressure up x = 0.3 after which the effect becomes insignificant. The increase of the heat transfer coefficient with increasing system pressure arises from the effect of pressure on surface tension. As the pressure increases from 6 to 10 bar, the surface tension of R134a decreases by about 29 %. The reduction in surface tension value results in a reduction in the bubble departure diameter and thus increases the contribution of nucleate boiling. Figure 4.50b shows some local peaks in the heat transfer coefficients at thermocouple locations No. 2 and No. 5. It is interesting to note that the magnitude of the peak at these locations increases with increasing system pressure. In other words, these locations seem to be representing nucleation sites and the peak value increases with pressure due to the increase in the bubble generation frequency when the pressure increases.

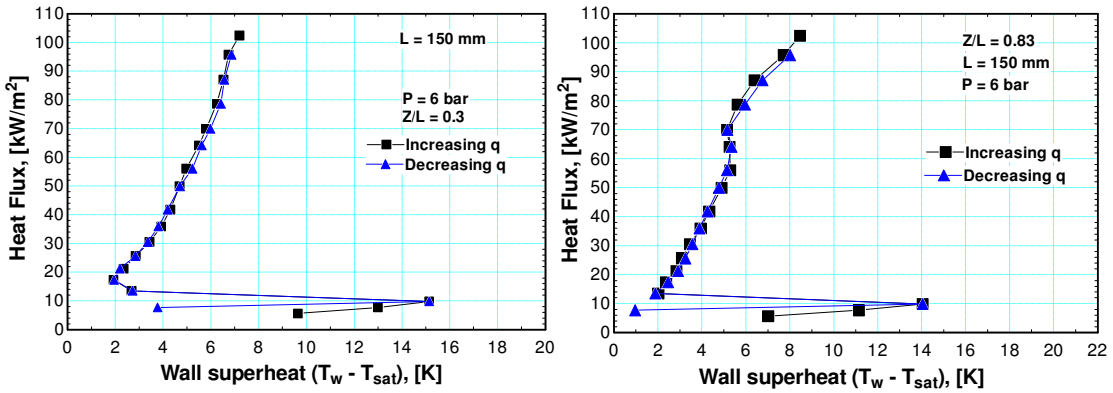

Z/L = 0.3 Z/L = 0.83

(a) L = 150 mm

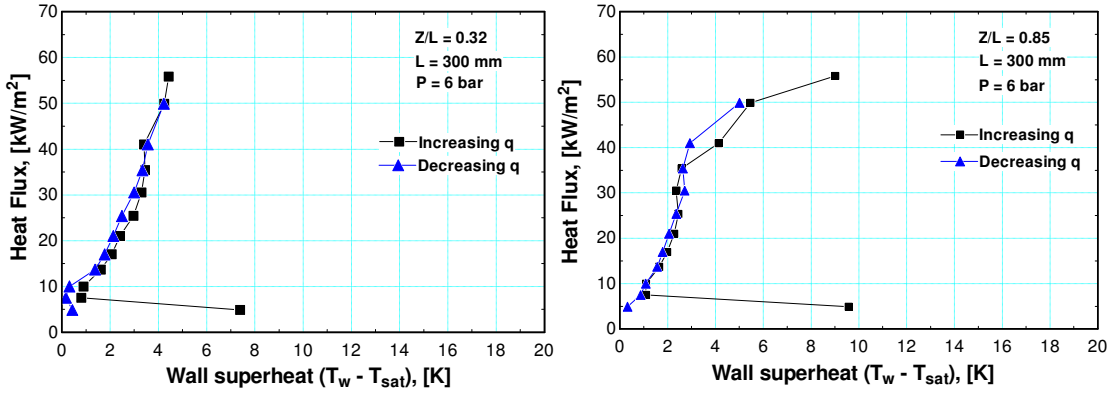

Z/L = 0.32 Z/L = 0.85

(b) L = 300 mm

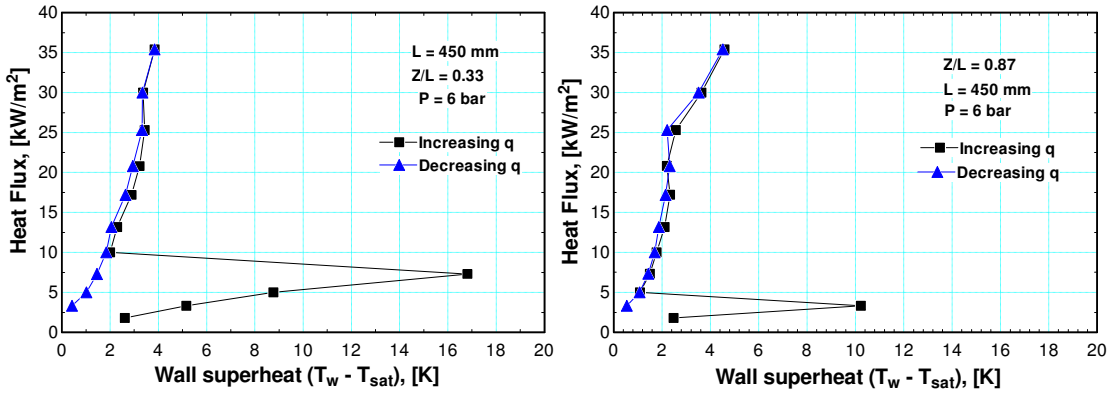

Z/L = 0.33 Z/L = 0.87

(c) L = 450 mm

Figure 4.49 The boiling curves developed through increasing and decreasing heat fluxes for the 1.1 mm tube at G = 300 kg/m^2 s and P = 6 bar.

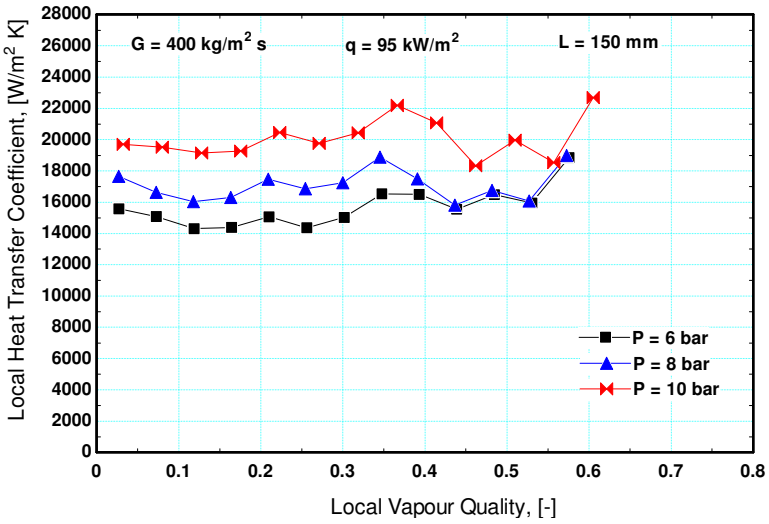

(a) L = 150 mm

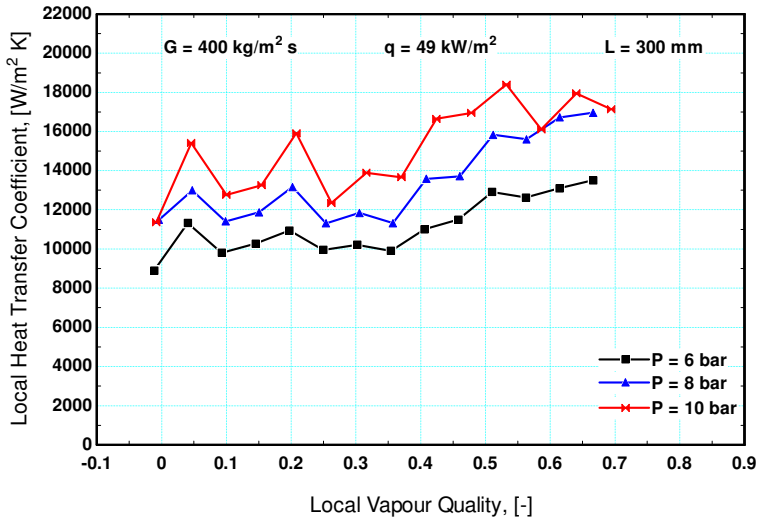

(b) L = 300 mm

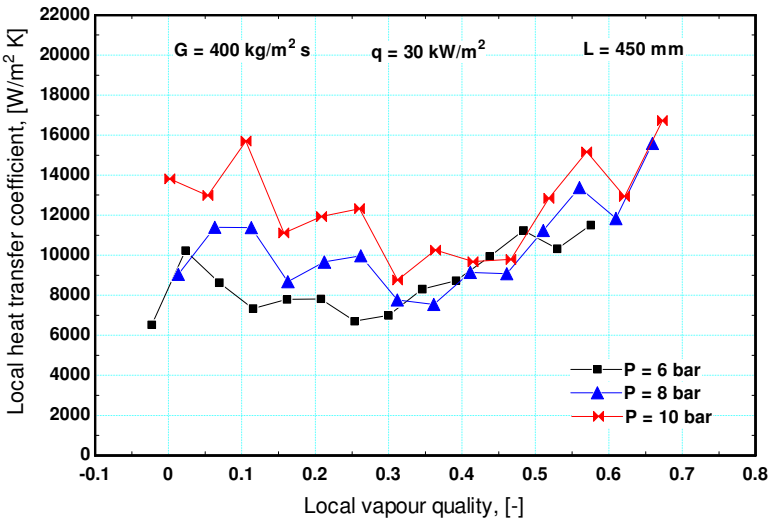

(c) L = 450 mm

Figure 4.50 Effect of system pressure on the heat transfer coefficient for the three heated lengths.

4.4 Effect of tube diameter

The effect of tube inner diameter on the heat transfer coefficient was first presented by Shiferaw (2008) for D = 4.26 – 0.52 mm at P = 8 bar and G = 400 kg/m^2 s, see Fig. 2.37. It was found that the heat transfer coefficient in the 4.26 mm tube is similar to that in the 2.88 mm tube. Reducing the diameter from 2.88 to 2.01 mm resulted in an average increase of 14 % in the heat transfer coefficient. Further reduction in tube diameter from 2.01 to 1.1 mm resulted in a 17 % further increase in the heat transfer coefficient. As the diameter was decreased from 1.1 to 0.52 mm, a very large increase in the heat transfer coefficient was obtained, i.e. the coefficient increased by about 70 %. It is worth mentioning that, the heat transfer results of the 0.52 mm tube (Shiferaw tube) exhibited a peculiar behaviour compared to the larger tubes. The examination of the inner surface of this tube indicated that the surface has some twisting and the diameter seems non uniform along the tube. Additionally, the single phase friction factor in this tube was much higher compared to the conventional laminar flow theory. Accordingly, the figure produced by Shiferaw that shows the effect of tube diameter was re-plotted again in this thesis as shown in Fig. 4.51. In this figure, the same data sets used by Shiferaw were also used except the 0.52 mm data, which was replaced with the new data of the current study. The vapour quality ranges shown in Fig. 4.51 for D = 4.26 – 1.1 mm refer to the quality at which dryout occurs in each tube. For the 0.52 mm tube, the quality range in the figure refers to the region where nucleate boiling is dominating. In the new figure (Fig. 4.51), reducing the tube diameter from 1.1 mm to 0.52 mm resulted in 42.6 % an average increase in the heat transfer coefficient. Shiferaw (2008) attributed the increase in the heat transfer coefficient when the diameter decreased from 2.88 to 2.01 then to 1.1 mm to the appearance of the confined bubble regime, which was observed by Chen (2006) and the large increase in the heat transfer coefficient in the 0.52 mm tube to the significant difference in the flow patterns characteristics.

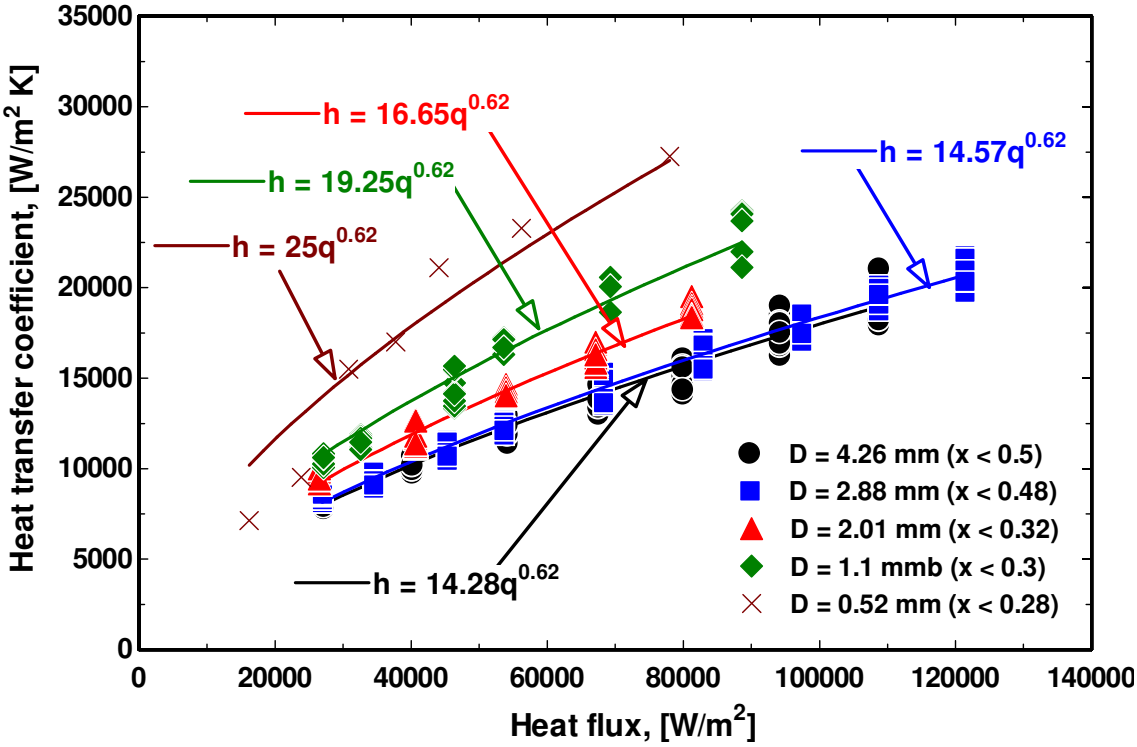

Figure 4.51 The effect of tube diameter on the heat transfer coefficient at G = 400 kg/m^2 s and P = 8 bar, Shiferaw (2008) updated using the new 0.52 mm tube results.

4.5 Reproducibility of the data

The repeatability of the experimental results is one of the issues that may be raised in flow boiling studies particularly when the diameter becomes very small. As the tube diameter decreases, the number of nucleation sites per unit length is expected to decrease and their stability may or may not affect the overall characteristics of this tube significantly. Thus, it is very important to know whether there is any disparity in the measured local heat transfer coefficient from day to day or not. This point should be taken into consideration during the design stage of micro-evaporators otherwise the performance of the evaporator might get worse with time. It is not the scope of the current study to investigate the aging of the investigated tubes. The experiments were repeated at one selected experimental condition for all investigated tubes over a time period from two weeks to one month. Figure 4.52 depicts the repeatability of the experiments at low, intermediate and high heat flux values. Figure 4.52a shows the repeatability of the 0.52 mm diameter tube results at 6 bar system pressure and 300

kg/m^2 s. It is clear that, the data, which were taken about one month apart, are repeatable within the experimental uncertainty for intermediate and high heat flux values. At low heat flux values, the magnitudes of the heat transfer coefficient are not repeatable whereas the trend is the same for day 1 and day 2. The lack of repeatability of the data at low heat fluxes could be arising from the instability of the nucleation sites. It is worth mentioning that, the behaviour of the local heat transfer coefficient at low heat fluxes depends on the conditions of boiling incipience, i.e. the wall superheat. In other words, when boiling starts normally at small wall superheat, the behaviour of the heat transfer coefficient may differ from the case if boiling started after very high wall superheat. For the 0.52 mm diameter tube, the wall superheat at boiling incipience was not repeatable which may cause this unrepeatability at the low heat flux conditions. For higher heat flux values on the contrary, Figs. 4.52b – d demonstrate that the repeatability of the 1.1 mm diameter seamless cold drawn tube is very good for all heated length at all heat fluxes. Figure 4.52e indicates that, the trend of the heat transfer coefficient is also repeatable for the welded tube with only some of the magnitudes were unrepeatable, particularly at few thermocouple locations near from the exit.

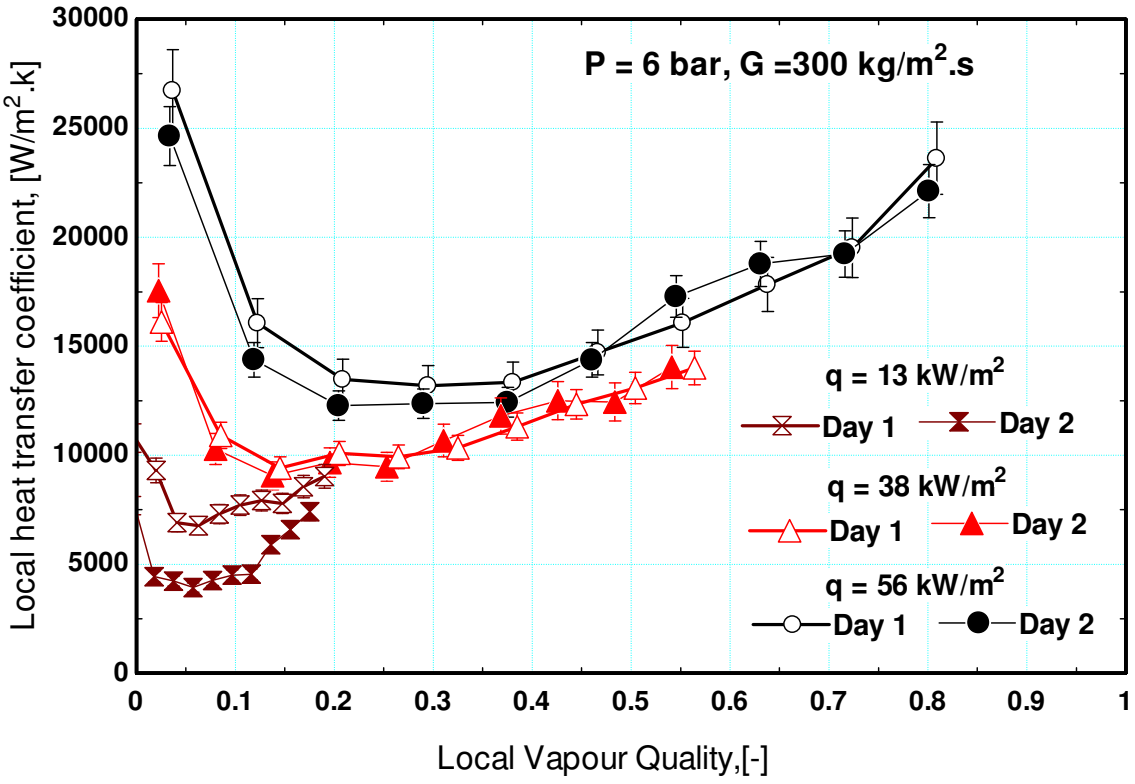

(a) D = 0.52 mm

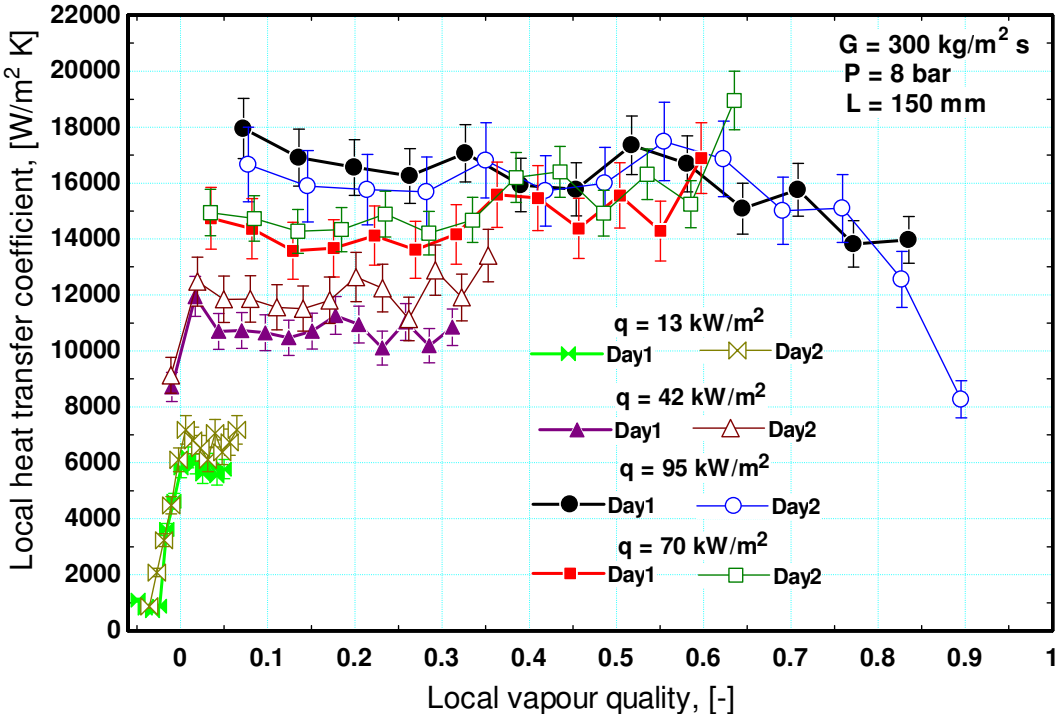

(b) L = 150 mm

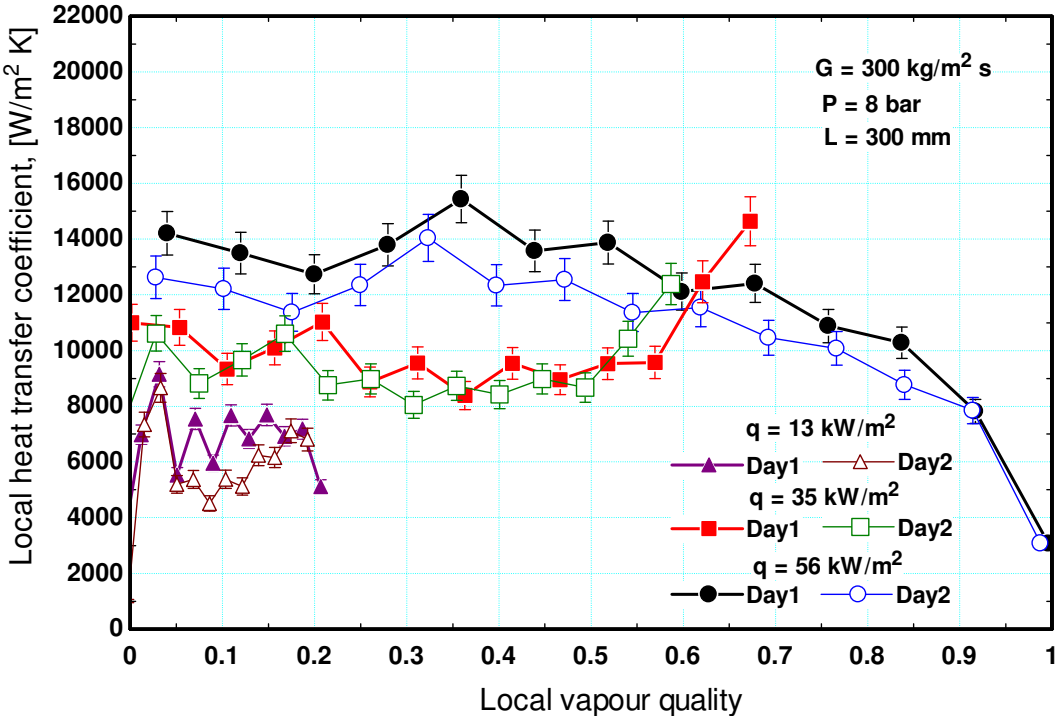

(c) L = 300 mm

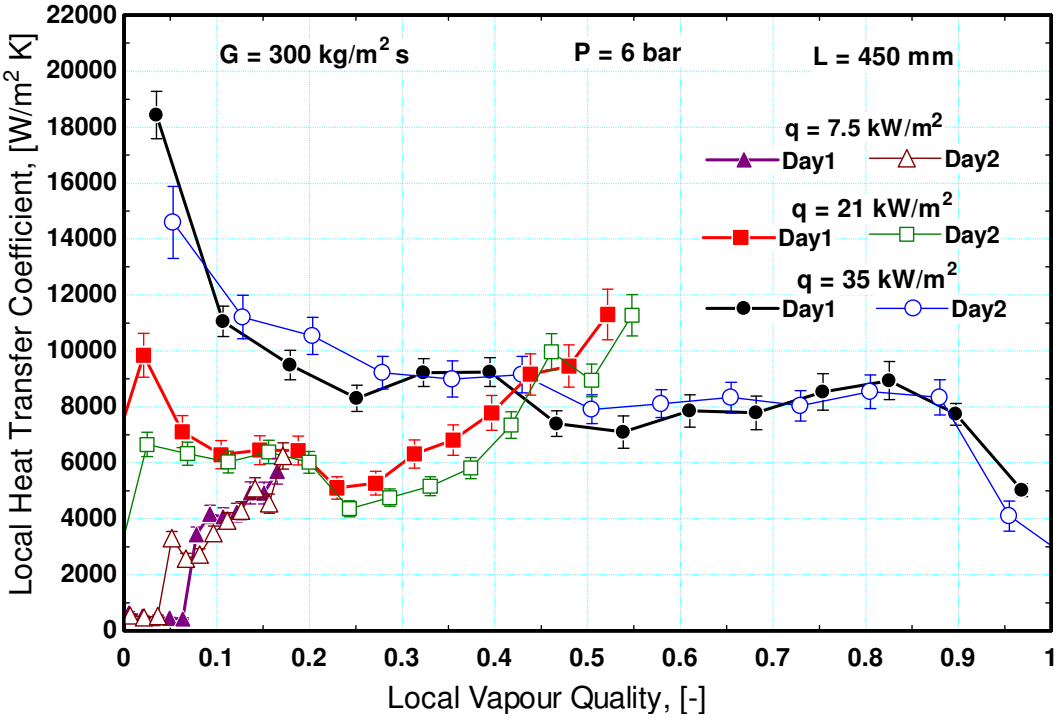

(d) L = 450 mm

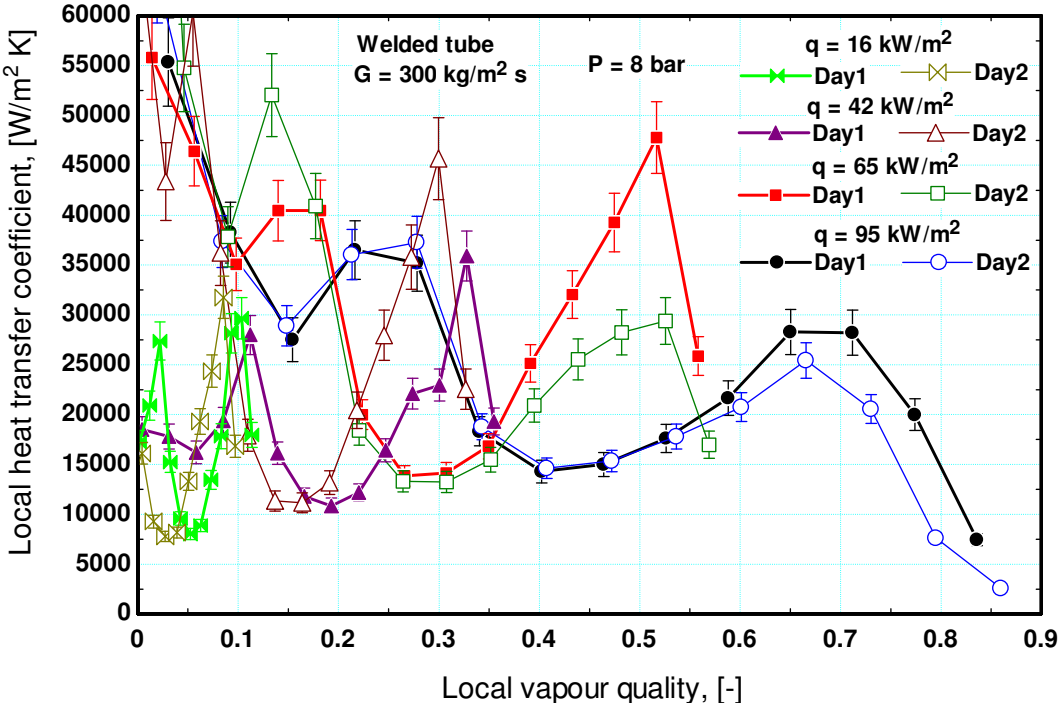

(e) Welded tube L = 150 mm and D = 1.1 mm

Figure 4.52 The repeatability of the experimental data for the five investigated test sections

4.5 Summary

This chapter presented and discussed the experimental heat transfer results and the simultaneously recorded flow patterns for five investigated test sections. The test sections included one seamless cold drawn micro-tube with diameter of 0.52 mm and heated length of 100 mm, one welded tube with diameter of 1.16 mm and heated length of 150 mm, three seamless cold drawn tubes with diameter of 1.1 mm and heated lengths of 150, 300 and 450 mm. The results were presented for stable boiling conditions at mass flux value of 300 kg/m^2 s and 6 bar system pressure for the sake of comparison. The flow patterns were observed in a glass section located immediately after the heated section. The following points may be given as a summary:

The most frequently observed flow patterns in the 0.52 mm diameter tube at the covered experimental conditions are slug (elongated bubble), transition to annular and annular flow. Bubbly flow was only observed in few numbers of pictures at low heat flux values. Also, at very low exit qualities, the flow patterns were observed to fluctuate between bubbly and slug (elongated bubble) flow regimes. This may reflect the instability of the nucleation sites in this micro-tube and may explain the lack of repeatability of the heat transfer data at low heat flux values (low exit quality).

On the other hand, the frequently observed flow patterns in the 1.1 mm tubes were slug, churn and annular regimes without any flow patterns fluctuations at low exit quality as was the case in the 0.52 mm tube. Additionally, bubble coalescence appeared in a significant number of pictures in the 0.52 mm tube compared to the 1.1 mm diameter tube. This could be due to the variation in slug lengths in the 0.52 mm tube while the length of slugs in the 1.1 mm diameter tube was approximately uniform. Slug length influences the velocity and dynamics of the moving bubble and consequently the coalescence rate.

The observed flow patterns in the 0.52 mm diameter tube agreed very well with the map of Revellin and Thome (2007c) and roughly agreed with the map of Chen (2006). The flow patterns in the 1.1 mm diameter tubes agreed well with the map of Chen (2006) developed for 1.1 mm diameter tube and R134a. Whereas, the map of Revellin and Thome (2007c) over-estimated the transition boundary from coalescence bubble to

annular regime which also seem to be dependent on the length of the heated section particularly at low mass fluxes.

The heat transfer coefficient in the 0.52 mm diameter tube increases with increasing heat flux and exhibits little dependence on vapour quality in the low to intermediate quality region. In the high quality region, the heat transfer coefficient increases with increasing vapour quality with insignificant heat flux effect. Additionally, the mass flux effect was insignificant in the low to intermediate quality region whilst the heat transfer coefficient increases with increasing mass flux in the high quality region. Conventionally, this heat transfer behaviour indicates that there is a progression from nucleate boiling at low to intermediate quality values to convective boiling at high quality values. However, the plot of the local heat transfer coefficient versus axial distance demonstrated that there is a heat flux effect along the total length of the tube and the heat transfer coefficient increased with distance towards the exit for some heat flux values. Also, the heat transfer coefficient increased almost linearly with heat flux in a way similar to the Cooper pool boiling correlation for three axial locations representing the entry, the mid and the exit sections. Additionally, the coefficient increased with increasing system pressure. The effect of system pressure, the boiling curves and the agreement with the Cooper pool boiling correlation mean that nucleate boiling seems to be prevailing over convective boiling which contradicts the conventional criterion used to infer the dominant heat transfer mechanism. Plotting the boiling curves in both direction (increasing and decreasing heat fluxes) indicated that there is hysteresis only at heat flux values less than 18 kW/m^2.

The experiments indicated that, the inner surface characteristics of the investigated tubes strongly influence the local heat transfer behaviour. This is clear from the comparison between the heat transfer results of the seamless cold drawn tube and the welded tube. The effect of different parameters as mass flux, heat flux and system pressure is not clear in the welded tube whereas there is clear effect in the seamless cold drawn tube. The SEM analysis demonstrated that the inner surface characteristics are completely different which explains the unique heat transfer behaviour found in the welded tube. Most researchers did not consider this parameter in their studies and they did not report any information about the manufacturing process of the investigated tubes. This parameter can contribute in explaining the various conclusions reported in

the open literature on the local heat transfer trends and the dominant heat transfer mechanism.

Another important parameter that was not considered by researchers in the open literature is the effect of the heated length. This parameter was investigated in the current study and it was found to have a significant effect on the local heat transfer behaviour and the dominant heat transfer mechanism. In the shortest mini-tube (L = 150 mm), the heat transfer coefficient increases with heat flux and system pressure but it does not depend on mass flux and vapour quality over all vapour quality values. The axial distance plots for this tube are consistent with the local quality plots where there is a heat flux effect at all locations whilst no mass flux effect. Applying the conventional criteria, the dominant heat transfer mechanism in this tube is nucleate boiling. As the heated length increases, the trend of the local heat transfer coefficient versus local quality changes and becomes dependent on heat flux. Instead of the constant trend with quality that appeared in the shortest tube, the coefficient exhibited increasing trend towards the exit at low to intermediate heat flux values when the heated length was increased. After this intermediate heat flux value, the increasing trend with vapour quality disappeared and the dependence on vapour quality became small. Additionally, as the heated length increased, the heat transfer coefficient increased with mass flux in the high quality region which was not the case in the shortest tube. Accordingly, it may be concluded that, nucleate boiling dominates in short tubes while both nucleate and convective boiling are contributing in long tubes due to the difference in the heat flux values. In short tubes, high heat flux values are required to attain exit quality of about 0.95 while these values decreases as the heated length increases. The boiling curves for the three investigated heated lengths indicated that there is no boiling hysteresis except at boiling incipience.

Chapter 5

Heat Transfer Correlations and Models

5.1 Introduction

There are many correlations in the open literature developed for the prediction of the flow boiling heat transfer coefficient in large diameter tubes (macroscale correlations). These correlations did not take into account the microscale effects such as bubble confinement and the dominance of surface tension and laminar flow. They also highly under-predict or over-predict the heat transfer coefficient at microscale level. Thus, if these correlations are directly used for the design of micro-evaporators, the heat transfer surface area is expected to be highly over-estimated or under-estimated. This has a direct effect on the cost and thermal performance of the micro-evaporator and hence the overall system. As presented in Chapter 2, the number of flow boiling experimental studies at microscale level is dramatically increasing. These studies evaluated several macroscale correlations and reported large deviations between the measured and predicted values. As a result, some researchers proposed new correlations to predict the flow boiling heat transfer coefficient in small to micro-diameter tubes, which are called here "microscale correlations". This chapter presents a detailed evaluation for six widely used macroscale correlations, eleven microscale correlations and two mechanistic models. Additionally, Cooper pool boiling correlation was included in the comparison just to be a base case for pure nucleate boiling. The comparison will be conducted globally in a statistical basis and locally as local heat transfer coefficient versus local vapour quality. The local comparison provides the performance of the correlation compared to the experimental trend whilst the global comparison provides the validity of the correlation over a wide range of experimental conditions. The widely

used parameters for global comparison are the mean absolute error (MAE) defined by Eq. (5.1) and the percentage of data *(β)* within ± 30 % error bands. *N* in Eq. (5.1) is the number of experimental data points.

$$MAE = \frac{1}{N}\sum_{i=1}^{N}\frac{\left|h_{\Pr ed,i} - h_{Exp,i}\right|}{h_{Exp,i}} \times 100 \qquad (5.1)$$

The global comparison includes the data of a micro-tube (D = 0.52 mm) and three mini-tubes (D = 1.1 mm) at mass flux range of 100 – 500 kg/m^2 s and system pressure range of 6 – 10 bar. **The data after dryout were excluded** from the comparison because most correlations did not consider post dryout heat transfer. Table 5.1 summarizes the vapour quality range at which dryout occurred for each tube. The lower limit of the vapour quality range in Table 5.1 is corresponding to G > 200 kg/m^2 s (the flow is turbulent flow or in the transition region) whilst the upper limit is corresponding to G ≤ 200 kg/m^2 s (laminar flow). The data of the welded tube were excluded from the comparison because of the few data points collected with this tube and the unique heat transfer behaviour observed in this tube as presented and discussed in Chapter 4.

Table 5.1 The vapour quality range at which dryout occurred for each tube.

Test section	Dryout quality range
D = 0.52 mm	No dryout up to x ≈ 0.9
D = 1.1 mm, L = 150 mm	0.55 – 0.85
D = 1.1 mm, L = 300 mm	0.65 – 0.88
D = 1.1 mm, L = 450 mm	0.85 – 0.9

5.2 Evaluation of macroscale correlations

This section presents a comparison between the experimental heat transfer coefficient and six widely used macroscale correlations developed for large diameter tubes. The examined correlations include those of Chen (1966), Shah (1982), Gungor and Winterton (1986), Kandlikar (1990), Liu and Winterton (1991) and Stiener and Taborek (1992). The details of the equations are summarized in Appendix B.1. Figure 5.1 presents the local comparison between the macroscale correlations and the experimental

results at mass flux value of 300 kg/m^2 s, system pressure of 6 bar and a selected value of heat flux. Since all correlations superimpose the contributions of nucleate and convective boiling mechanisms, the heat flux value was selected such that the corresponding exit quality is about 0.7 – 0.8 to cover nucleate and convective boiling regions if they exist. The ± 30 % error band is also shown in Fig. 5.1. It is obvious from Fig. 5.1a, for the 0.52 mm tube, that all correlations failed to predict the correct experimental trend except the correlation of Shah (1982). It shows similar trend to the experiment but with values much lower than the experimental values. Both Shah (1982) and Kandlikar (1990) correlations show a change in trend at x ≈ 0.1 and x ≈ 0.4, respectively while other correlations do not show this change. Stiener and Taborek (1992) correlation highly over-predicts the experimental data and gives heat transfer coefficient almost constant with local vapour quality. Gungor and Winterton (1986) correlation gives constant heat transfer coefficient that slightly decreases with increasing vapour quality. It is clear also that, there is no significant difference between Chen (1966) and Liu and Winterton (1991) correlations. Additionally, the difference between all correlations, except those of Gungor and Winterton (1986) and Stiener and Taborek (1992), becomes small as the vapour quality increases. The values predicted by the Kandlikar (1990) correlation are the closest to the experimental values over a narrow quality range x ≈ 0.1 – 0.3. Figure 5.1b shows for D = 1.1 mm and L = 150 mm that, the Kandlikar (1990) correlation gives excellent agreement with the experimental trend and magnitudes of the heat transfer coefficient. Contrary to the 0.52 mm diameter tube, the Stiener and Taborek (1992) correlation now under-predicts the experimental values and gives heat transfer coefficient that increases with increasing vapour quality like the behaviour of the Liu and Winterton (1991) correlation. This reflects the sensitivity of this correlation to tube diameter as will be discussed later in the next sections. The performance of the other correlations in this tube was similar to that in the 0.52 mm tube. As the heated length increased to 300 and 450 mm for D = 1.1 mm, the behaviour of all correlations does not change with the Kandlikar (1990) correlation predicting the trend and magnitudes in the case of L = 450 mm very well and slightly under-predicts the magnitudes in the case of L = 300 mm. Figure 5.1 contributes to explaining the overall performance of these correlations when they are globally compared with the experimental data. Each correlation is discussed in some detail and globally compared with the experimental data in the coming sections.

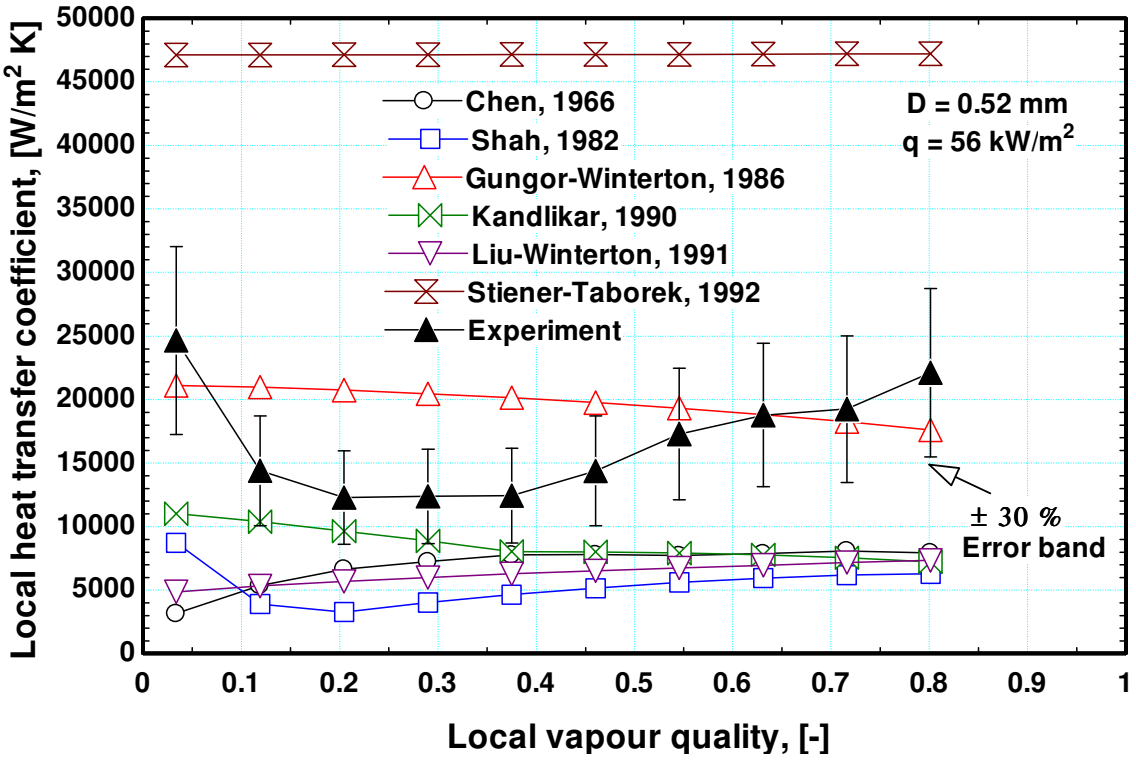
Local heat transfer coefficient, [W/m^2 K]
Local vapour quality, [-]
Chen, 1966
Shah, 1982
Gungor-Winterton, 1986
Kandlikar, 1990
Liu-Winterton, 1991
Stiener-Taborek, 1992
Experiment
D = 0.52 mm
q = 56 kW/m^2
± 30 %
Error band

(a)

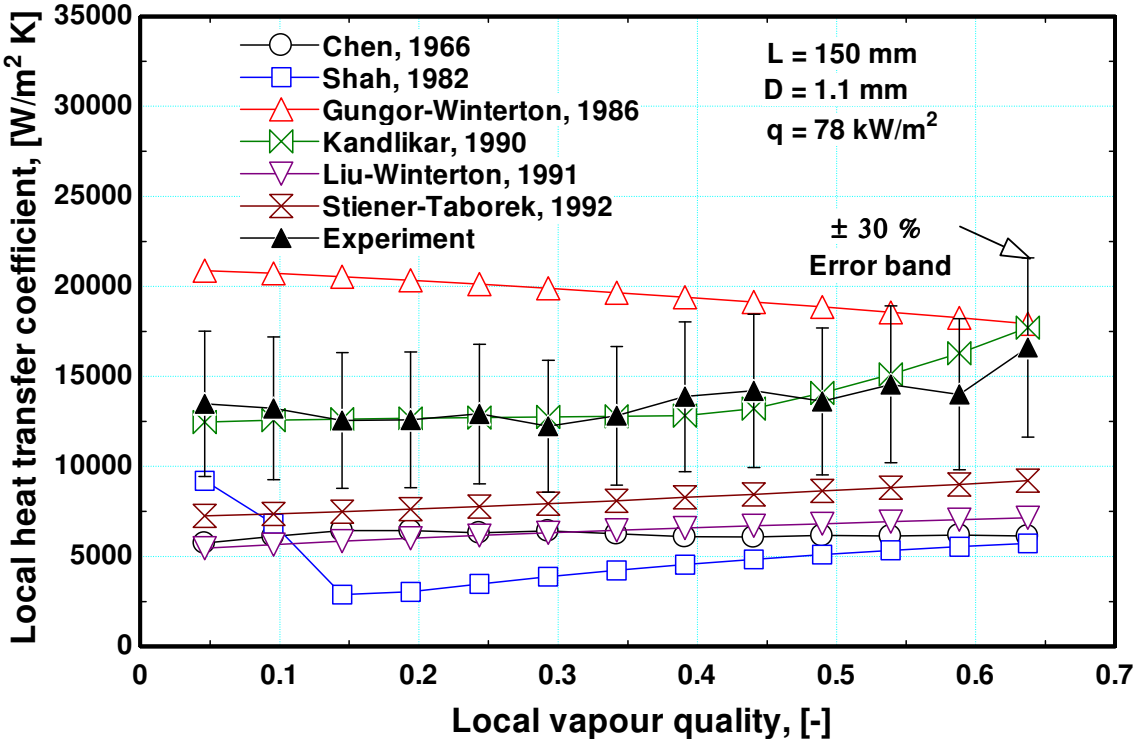
Local heat transfer coefficient, [W/m^2 K]
Local vapour quality, [-]
Chen, 1966
Shah, 1982
Gungor-Winterton, 1986
Kandlikar, 1990
Liu-Winterton, 1991
Stiener-Taborek, 1992
Experiment
L = 150 mm
D = 1.1 mm
q = 78 kW/m^2
± 30 %
Error band

(b)

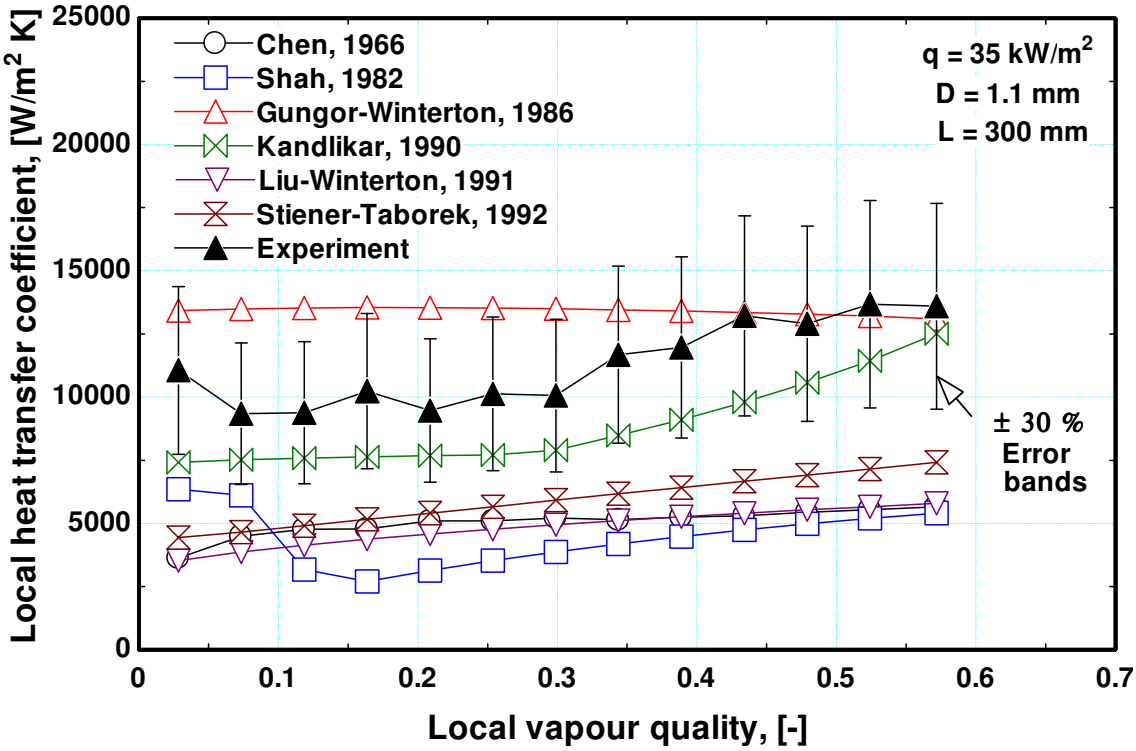

(c)

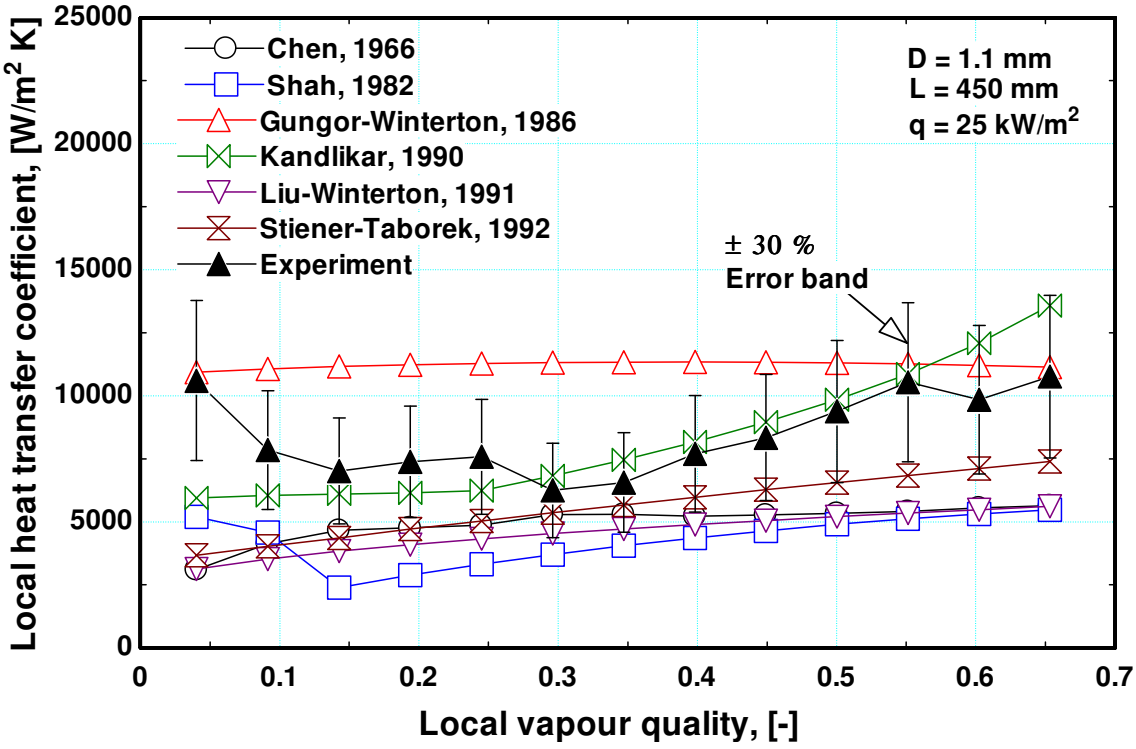

(d)

Figure 5.1 Comparison with macroscale correlations at G = 300 kg/m2 s, P = 6 bar and a selected value of heat flux for (a) D = 0.52 mm, L = 100 mm, (b) D = 1.1 mm, L = 150 mm, (c) D = 1.1 mm, L = 300 mm and (e) D = 1.1 mm, L = 450 mm.

The Chen (1966) correlation

Chen (1966) postulated that there are two basic mechanisms that contribute to the heat transfer process in forced convective boiling. The first is the micro-convective mechanism associated with bubble nucleation and growth whereas the second is the conventional macro-convective mechanism due to the flow velocity. These two mechanisms were assumed to be additive in their contribution to the heat transfer process as given by Eq. (5.2). Two adjustable parameters were used in the correlation namely the nucleate boiling suppression factor (*S)* and the convective boiling enhancement factor (*F)*. The suppression factor principle was introduced to account for the reduction in the effective liquid superheat encountered in flow boiling as the thermal boundary layer gets thinner. This factor was correlated as a function of the two phase Reynolds number such that its magnitude diminishes as Reynolds number increases whereas its value approaches unity at low Reynolds number values. The enhancement factor *(F)* was found to be dependent only on Martinelli parameter (X) such that its value is greater than or equal to one. In Eq. (5.2), the single phase liquid heat transfer coefficient was calculated from the Dittus-Boelter (1930) equation whilst the Forster-Zuber (1955) correlation was used for the nucleate pool boiling heat transfer coefficient.

$$h_{tp} = Sh_{pool} + Fh_L \qquad (5.2)$$

Figure 5.2 depicts the global comparison with the Chen (1966) correlation. It is clear from the figure that, the correlation highly under-predicts the experimental data for all tubes. For the micro-tube (Fig. 5.2a), the MAE value is 69.8 and only 27.2 % of the data are located within the ± 30 % error bands. For the mini-tubes (Fig. 5.2a – 5.2d), the MAE/β values are 66.1/0.2, 102.6/10.6 and 70.7/21 % respectively for L = 150, 300 and 450 mm. Additionally, the correlation is not sensitive to the variation in system pressure. It is worth noting that, the value of the MAE for all tubes is approximately the same except for the tube with L = 300 mm where the value is about 30 % higher. This high deviation is attributed to the very small values of the measured heat transfer coefficient at the lowest heat flux values. In some experimental runs, the onset of nucleate boiling has delayed to occur at very high wall superheat. In theses cases, heat balance calculations indicated that the thermodynamic quality was greater than zero. Therefore, the values of the calculated two phase heat transfer coefficient becomes close

to the values of the single phase heat transfer coefficient. Accordingly, the deviation between the measured and predicted values at these low heat flux values exceeded 1000 %, which makes the overall MAE value high. Excluding these few data points from the comparison, the MAE value reduced to 55 % without affecting the percentage of data within the error bands (10.6 %). Figure 5.1 indicates that the Chen correlation gives heat transfer coefficient that moderately increases with increasing vapour quality in the very low quality region then it shows a plateau as the quality increases. The behaviour of the correlation at very low vapour quality values is opposite to the experimental behaviour where the heat transfer coefficient drops from its maximum value at $x \cong 0$. Accordingly, the maximum deviation between the predicted and measured values is expected to occur at very low vapour quality values and also at high vapour quality values when the experimental heat transfer coefficient exhibits increasing trend with vapour quality. The overall high deviation between the correlation and the experimental values may be attributed to the fact that the correlation was developed using data for water and hydrocarbons only. These fluids have a much higher surface tension compared to R134a refrigerant, which significantly influences the bubble departure diameter and the characteristics of the flow patterns. Another reason could be the accuracy of the nucleate pool boiling correlation of Forster and Zuber which gives much lower values than the Cooper (1984) correlation which takes into account the effect of fluid, surface roughness, heat flux and reduced pressure.

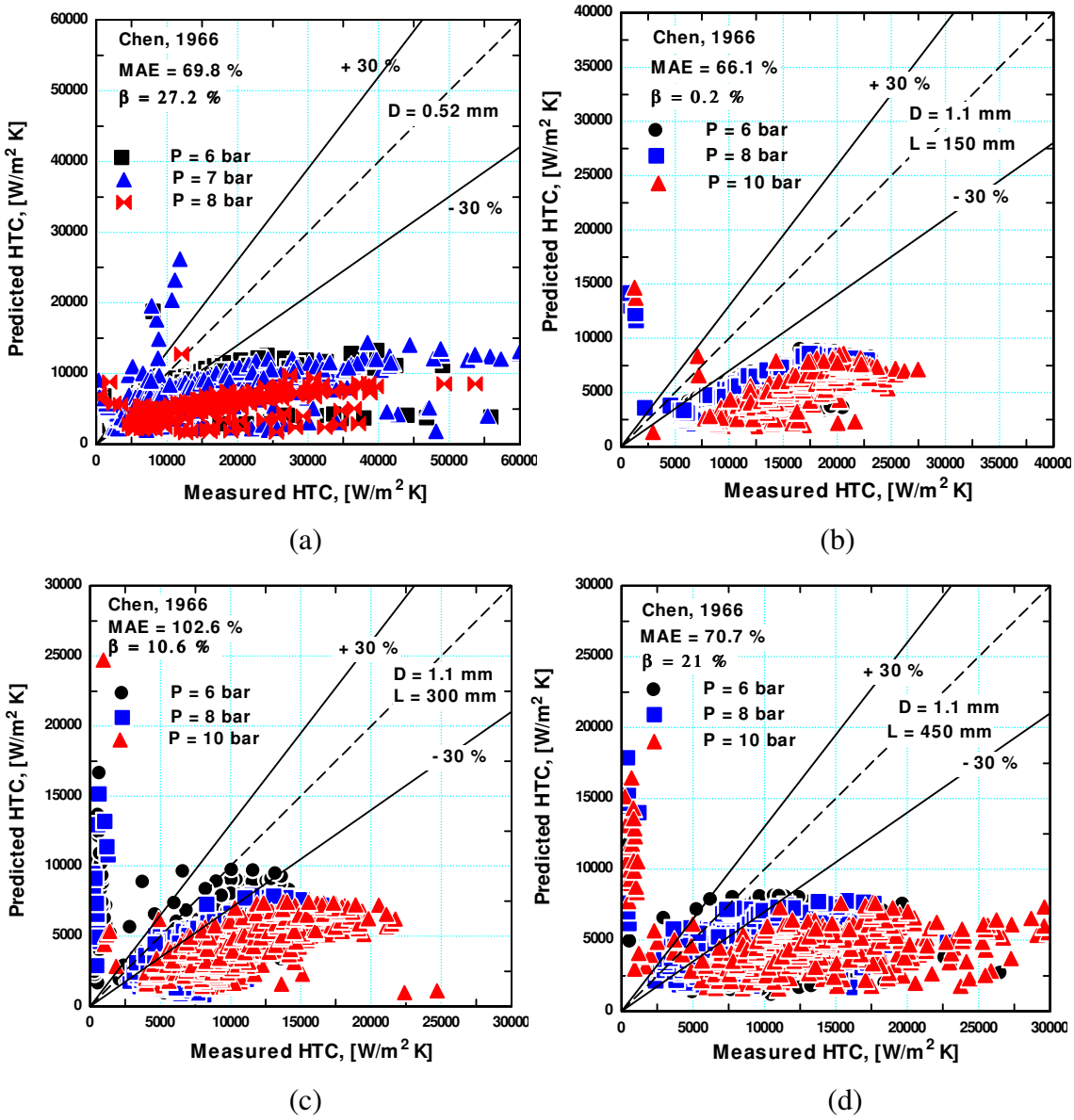

Figure 5.2 Comparison with the Chen (1966) correlation for (a) D = 0.52 mm, L = 100 mm, (b) D = 1.1 mm, L = 150 mm, (c) D = 1.1 mm, L = 300 mm and (e) D = 1.1 mm, L = 450 mm.

The Shah (1982) correlation

After the work of Chen (1966), several correlations have been developed but with different ideas for combining the contribution of the nucleate and convective boiling terms. Shah (1982) proposed selecting the larger of the nucleate and convective boiling terms for the total two phase heat transfer coefficient rather than the simple addition. He found that the convective boiling term depends only on the convection number N_{Co} defined by Eq. (5.3) rather than the Martinelli parameter (X) as proposed

originally by Chen (1966). However, the new convection number is similar to the turbulent-turbulent Martinelli's parameter after ignoring the viscosity ration. On the other hand, the nucleate boiling term was expressed only as a function of the boiling number *Bo*.

$$N_{Co} = \left(\frac{1-x}{x}\right)^{0.8} \left(\frac{\rho_L}{\rho_g}\right)^{0.5} \tag{5.3}$$

Figure 5.3 compares the experimental results with the Shah (1982) correlation. It is obvious that the correlation is highly under-predicting the experimental data in all tubes. The MAE value in the micro-tube is 60.1 % with 11.8 % of the data with the error bands. For the mini-tubes, the MAE/β values are 56.8/15, 47.3/12.5 and 60.4/10.4 respectively for L = 150, 300 and 450 mm. As presented in Fig. 5.1, the heat transfer coefficient predicted by Shah correlation drops from a high value at very low vapour qualities then it increases constantly with increasing vapour quality. This trend was similar to the experimental trend in the micro-tube and the mini-tube with heated lengths of 300 and 450 mm. Figure 5.3 indicates that there is a tendency for the correlation to work better in the very low quality region, at high system pressure, and at very high vapour quality. The higher the system pressure, the lower the latent heat and consequently the higher the Boiling number. As mentioned above, the nucleate boiling term was introduced as a function of the Boiling number only. Therefore, increasing heat flux at high system pressure (increasing Boiling number) results in high magnitudes of the predicted heat transfer coefficient in the very low quality region (nucleate boiling) and becomes close to the experimental values. Additionally, as the vapour quality increases to high values, the magnitude of the convection number becomes very small and consequently the convective heat transfer coefficient becomes too large; see Eq. (5.4). It approaches infinity as x approaches 1. Therefore, few numbers of data points matched the experimental values at these conditions (high pressure, very low quality and very high quality). The overall tendency of the correlation to highly under-predict the experimental values could be due to the use of Boiling number only to correlate the nucleate boiling term in the correlation. This means that other parameters that significantly influence the nucleate boiling heat transfer were not taken into consideration. Theses parameters include surface roughness,

fluid properties and reduced pressure. Boiling number includes only the latent heat as a fluid property, which may not be enough.

$$h_{cv} = \frac{1.8 h_L}{N_{Co}^{0.8}} \tag{5.4}$$

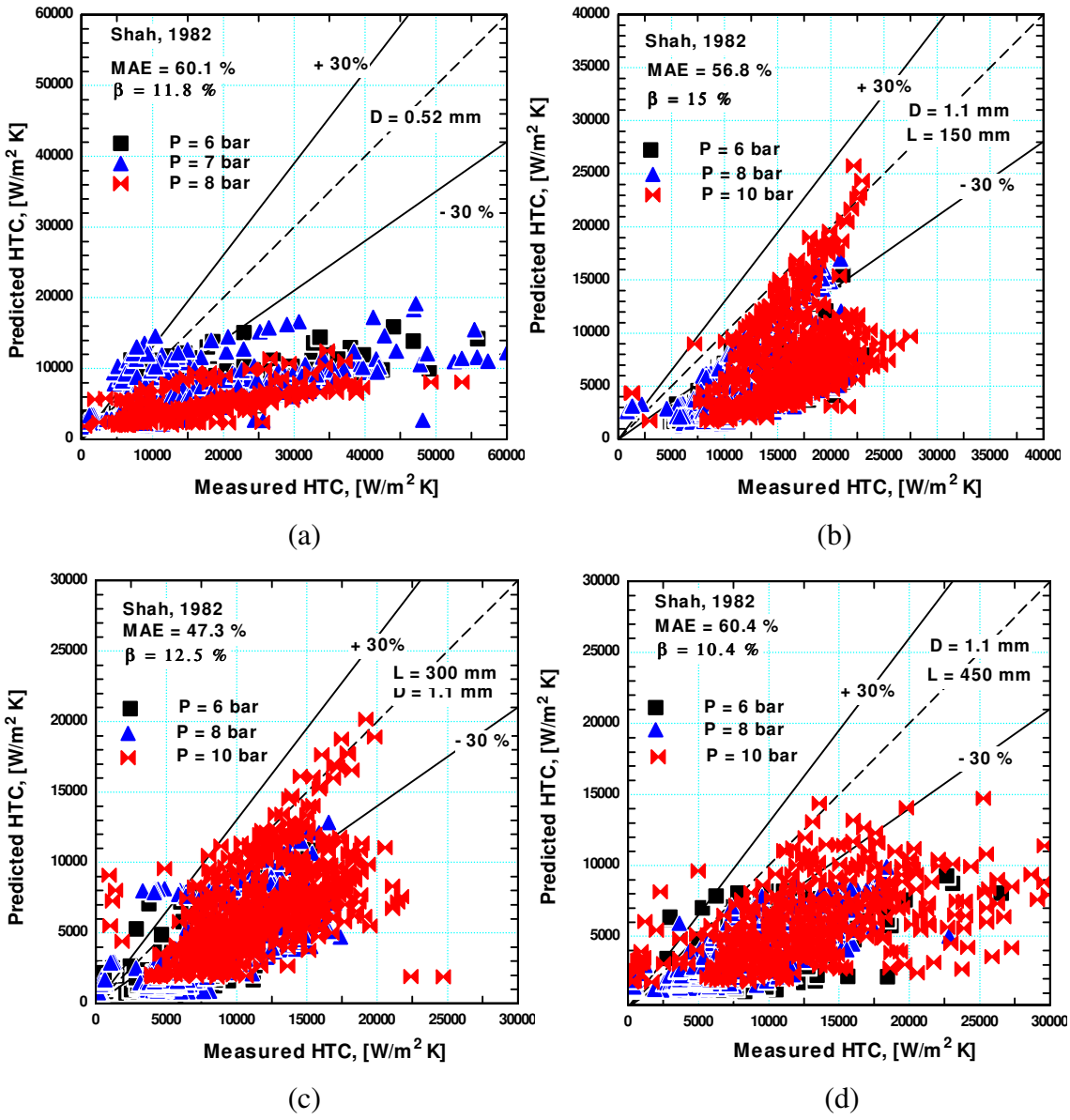

Figure 5.3 Comparison with the Shah (1982) correlation for (a) D = 0.52 mm, L = 100 mm, (b) D = 1.1 mm, L = 150 mm, (c) D = 1.1 mm, L = 300 mm and (e) D = 1.1 mm, L = 450 mm.

The Gungor-Winterton (1986) correlation

Gungor and winterton (1986) followed the superposition approach of Chen (1966) and proposed a correlation based on 3700 data points for water, refrigerants and ethylene glycol. They modified the convective boiling enhancement factor *(F)* in the Chen correlation to be a function of the Boiling number (*Bo*) and the Martinelli parameter (X). The incorporation of the Boiling number into the enhancement factor was to account for the additional enhancements in convective boiling due to vapour generation that creates additional disturbance to the boundary layer next to the wall. Also, they suggested using Cooper pool boiling correlation instead of the Forster and Zuber correlation for the nucleate boiling term.

Figure 5.4 depicts the comparison with the Gungor and Winterton's correlation. It is clear that the correlation performs much better than the Chen and shah correlations. The correlation predicts 36.7 % of the micro-tube data within the ± 30 % error bands with a MAE value of 62.8 %. On the other hand, the prediction gets better in the mini-tubes particularly in the tube with the shortest heated length where the correlation predicted 50.2 % of the data within the ± 30 % error bands with a MAE value of 33.4 %. The performance of the correlation in all tubes can be explained using Fig. 5.1. This figure shows that, the correlation gives a heat transfer coefficient that is almost independent on vapour quality in the low quality region whereas it slightly decreases with quality in the high quality region. This trend is consistent with the experimental trend in the tube with heated length of 150 mm. However, the correlation over-predicts the experimental values at high heat flux values. In other words, the correlation works reasonably at low to intermediate heat flux values. The over-estimation of the heat transfer coefficient at high heat fluxes could be attributed to the inclusion of the Boiling number in the convective boiling enhancement factor *(F)*. This means that, the heat flux effect was considered in the convective boiling term as well as the nucleate boiling term. The exponent of q was 0.67 in the nucleate boiling term whilst it was 1.16 in the convective boiling term. As a result, increasing the heat flux with small values will result in very high increments of the heat transfer coefficients that exceed the experimental values. As the heated length increased, the experimental heat transfer coefficient exhibited some dependency on vapour quality after $x = 0.3 – 0.4$ where the coefficient increased with

vapour quality. This quality effect was not predicted by the correlation and this resulted in higher mean absolute error compared to the 150 mm heated length.

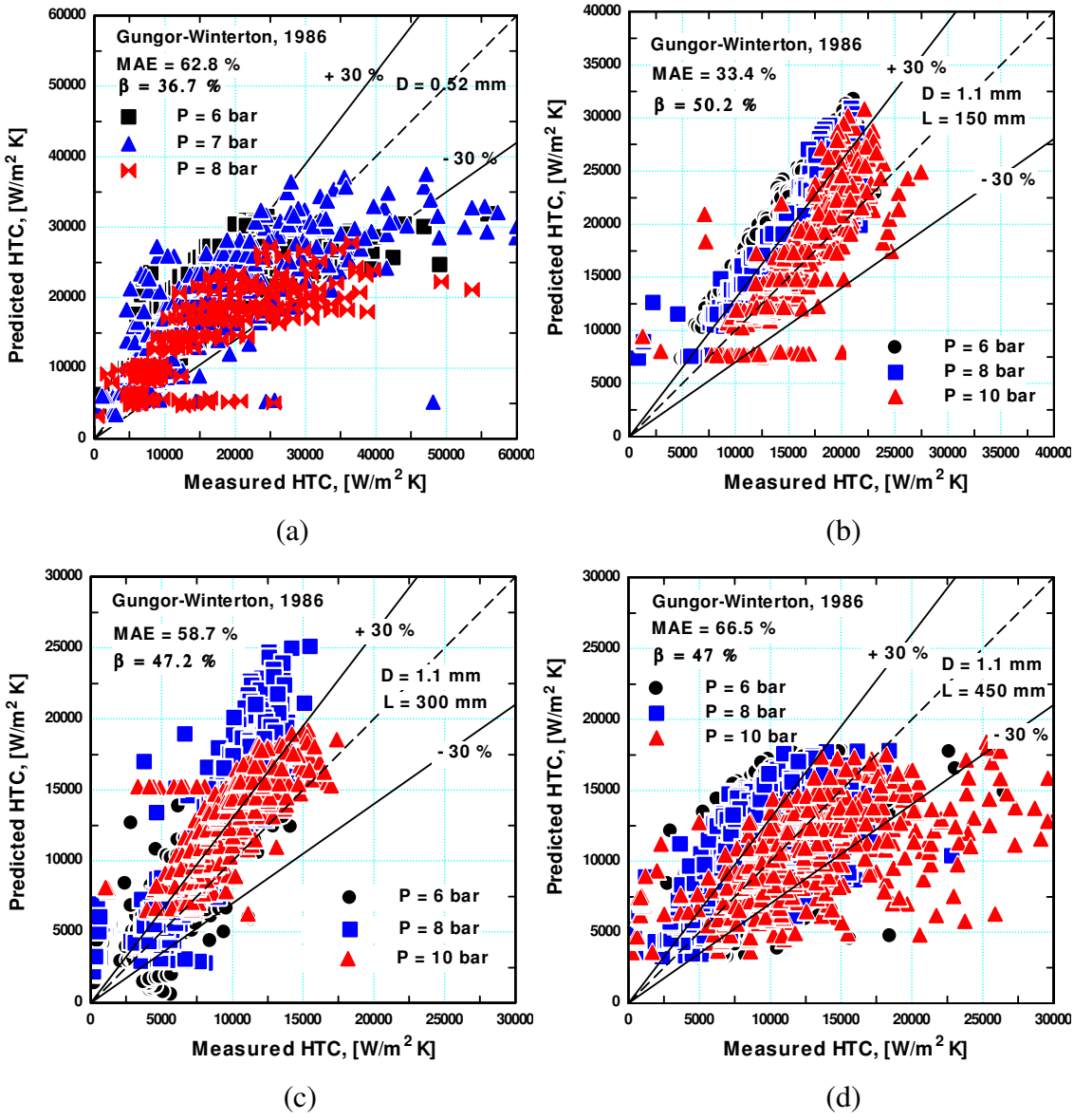

Figure 5.4 Comparison with the Gungor and Winterton (1986) correlation for (a) D = 0.52 mm, L = 100 mm, (b) D = 1.1 mm, L = 150 mm, (c) D = 1.1 mm, L = 300 mm and (e) D = 1.1 mm, L = 450 mm.

The Kandlikar (1990) correlation

Kandlikar (1990) followed the same approach as Shah (1982) and proposed a general correlation for saturated flow boiling heat transfer in horizontal and vertical plain tubes. The correlation was developed based on a database consisting of 5264 data points

including water and refrigerants, D = 4.6 – 32 mm and vapour qualities up to 0.98. Kandlikar assumed that the contribution of nucleate and convective boiling mechanisms is additive for each region, i.e. the nucleate boiling dominant region and the convective boiling dominant region. Similar to Shah, the total two phase heat transfer coefficient was selected as the larger of the heat transfer coefficient in the nucleate boiling dominant region and the convective boiling dominant region. Kandlikar used the same dimensionless numbers as Shah namely the convection number and the boiling number to correlate the convective and nucleate boiling terms, respectively. The effect of fluid type was incorporated using a fluid dependent parameter (F_{fl}) in the nucleate boiling term. This parameter works as a correction factor that accounts for all other parameters influencing nucleate boiling.

Figure 5.5 compares the experimental data with the Kandlikar (1990) correlation. The correlation under-predicts the data of the micro-tube with a MAE value of 40.1 % and 45.2 % of the data within the ± 30 % error band. For the mini-tube with heated length of 150 mm, the correlation gives very good predictions compared to the other correlations. It predicted 68 % of the data within the ± 30 % error bands with a mean absolute error value of 32.3 %. On the other hand, for the mini-tube with heated lengths of 300 and 450 mm, the performance of the correlation was the same with a MAE value of about 50 % and about 45 % of the data within the ± 30 % error bands. Figure 5.1 explains the performance of the correlation in the global comparison. Figure 5.1a indicates for the micro-tube that there is a partial agreement between the predicted and experimental values over a narrow range of vapour quality (x ≈ 0.1 – 0.3) with magnitudes less than the experiment. This is clear from Fig. 5.5a where the correlation under-predicts most of the data in this tube. On the contrary, the correlation captured the correct experimental trend and magnitudes in the shortest mini-tube up to x = 0.7. The over-prediction appeared in Fig. 5.5 for the mini-tubes was found to occur at vapour qualities greater than 0.7. According to the correlation, as the quality approaches unity the convection number approaches zero and thus the heat transfer coefficient approaches infinity. This creates a very high over-estimation for the heat transfer coefficient at very high vapour quality values. So, it can be concluded that the Kandlikar correlation tends to under-predict the experimental values up to intermediate vapour quality values whereas it over-predicts the values at high vapour qualities.

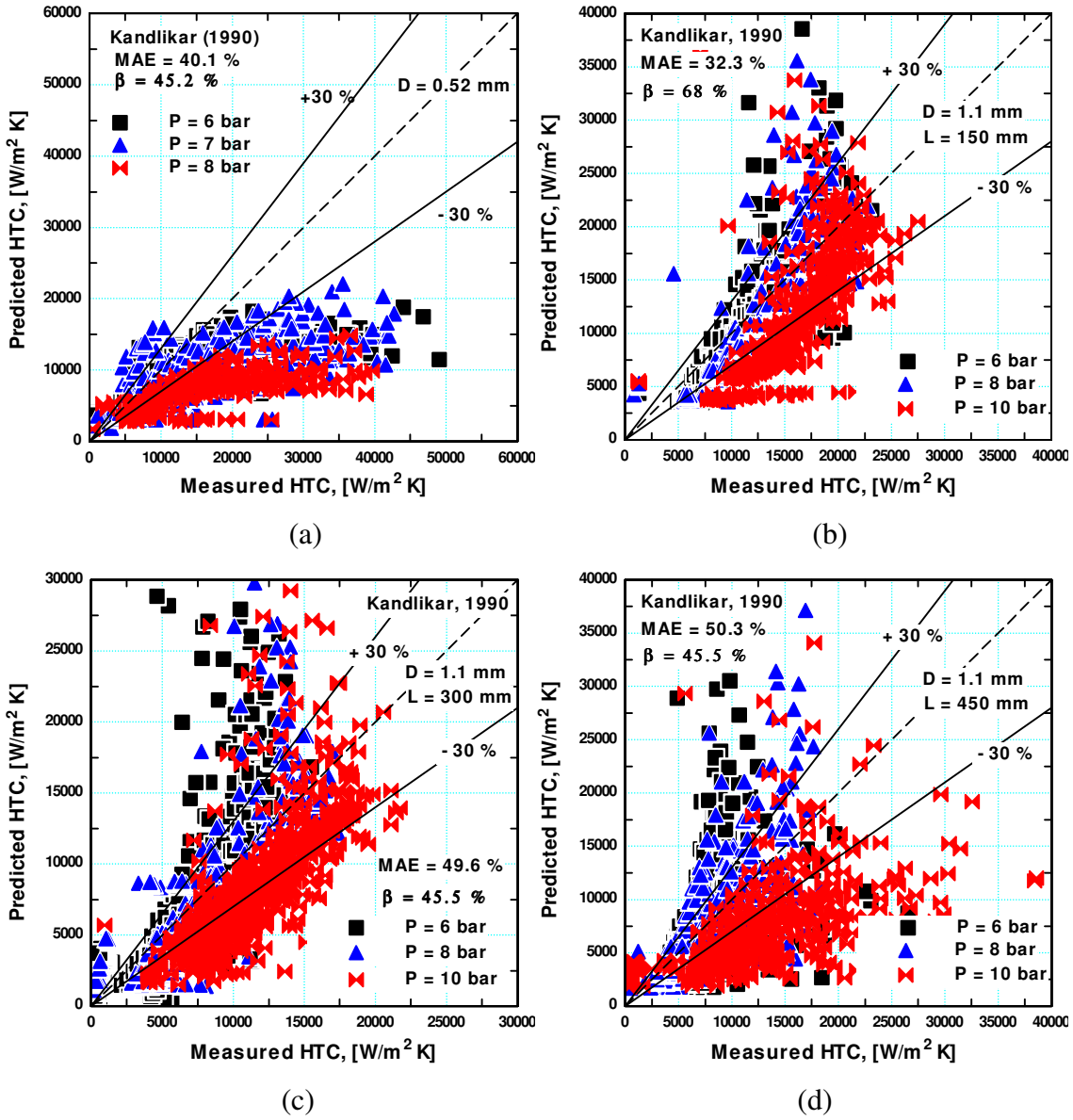

Figure 5.5 Comparison with th Kandlikar (1990) correlation for (a) D = 0.52 mm, L = 100 mm, (b) D = 1.1 mm, L = 150 mm, (c) D = 1.1 mm, L = 300 mm and (e) D = 1.1 mm, L = 450 mm.

The Liu and Winterton (1991) correlation

Liu and Winterton (1991) reported that saturated boiling correlations with explicit nucleate boiling term can be extended easily to sub-cooled boiling. Based on that, they did not recommend using the boiling number to correlate the nucleate boiling term. Instead, Cooper pool boiling correlation was recommended for the nucleate boiling

term. In their model, they followed the power law model with n = 2 to combine the nucleate and convective boiling contributions as given by Eq. (5.5). The enhancement factor *(F)* was found to be dependent on the liquid to vapour density ratio and the liquid Prandtl number. The suppression factor was correlated in a similar functional form as Gungor and Winterton (1991). The correlation was based on more than 4200 data points for saturated boiling and more than 990 data points for sub-cooled boiling.

$$h_{tp} = \left[\left(Sh_{pool} \right)^n + \left(Fh_L \right)^n \right]^{1/n} \tag{5.4}$$

Figure 5.6 depicts the comparison with the Liu and Winterton (1991) correlation. As mentioned above, the correlation uses Cooper's pool boiling correlation for the nucleate boiling part and it gives much higher values than the Forster-Zuber correlation. However, the Liu and Winterton correlation highly under-predicts the experimental data in all tubes. The correlation predicted only 18.7 % of the micro-tube data whilst it predicted 0.3, 4 and 15.6 % of the mini-tube data with lengths of 150, 300 and 450 mm respectively. This correlation is similar in performance to the Chen correlation though the method of combining the contribution of the nucleate and convective boiling is different. The differences between the Liu-Winterton correlation and the others are that for the single phase liquid heat transfer coefficient they used Reynolds number based on all flow as liquid, i.e. using G not (1-x)G. Also, the suppression factor was correlated in a similar way to Chen and Gungor-Winterton, i.e. as a function of the enhancement factor and Reynolds number but with much smaller exponents. This means that the suppression factor decreases very slowly with increasing Reynolds number.

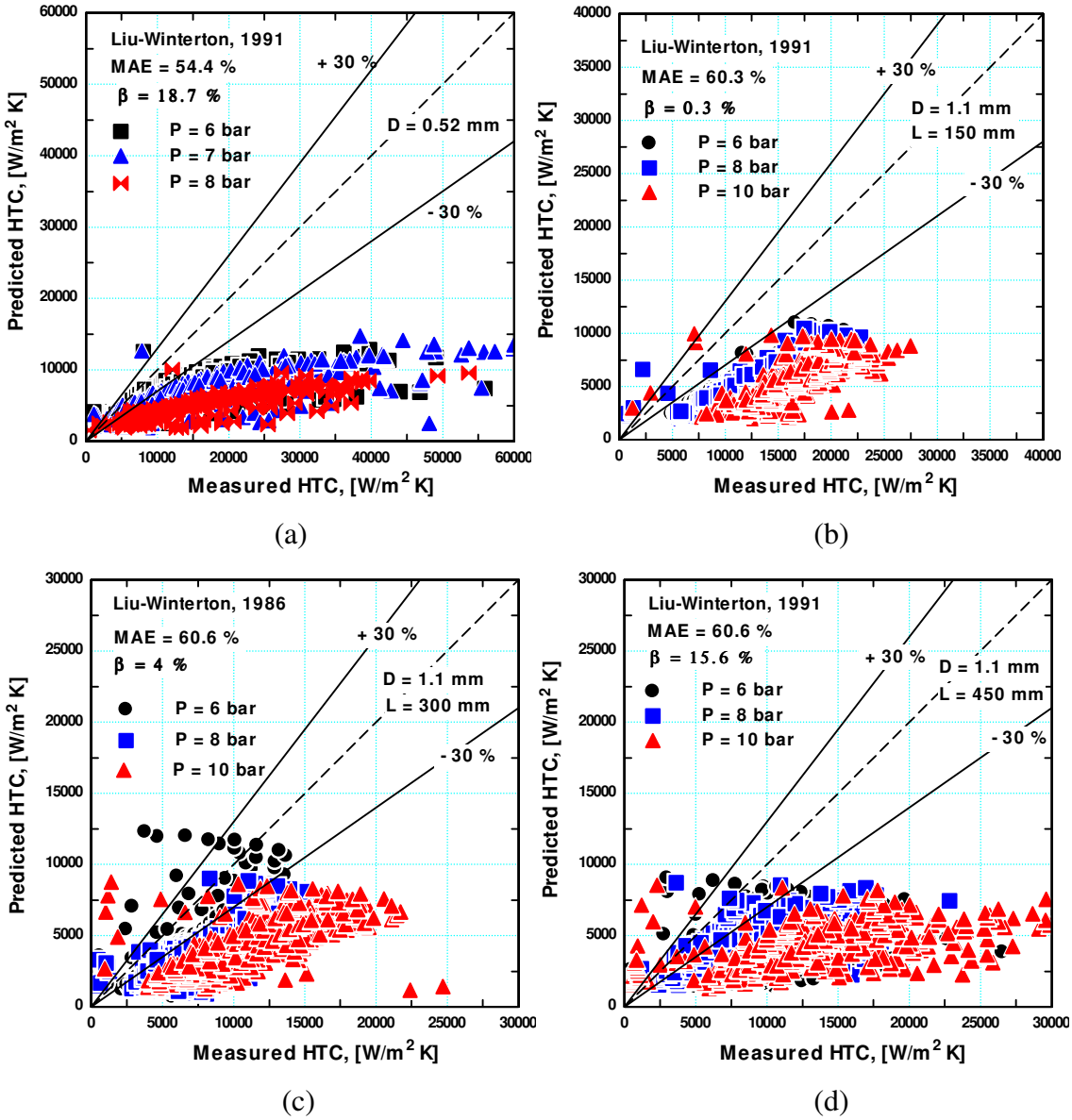

Figure 5.6 Comparison with the Liu and Winterton (1991) correlations for (a) D = 0.52 mm, L = 100 mm, (b) D = 1.1 mm, L = 150 mm, (c) D = 1.1 mm, L = 300 mm and (e) D = 1.1 mm, L = 450 mm.

The Steiner and Taborek (1992) correlation

Steiner and Taborek (1992) proposed an asymptotic model with n = 3 for predicting the heat transfer coefficient in vertical tubes which was considered the most accurate one. The model assumes that for $q < q_{ONB}$ only pure convective boiling exists and the coefficient approaches the single phase values at x = 0 and x = 1. On the other hand, when $q > q_{ONB}$ and the quality is less than the critical value (no dry out) nucleate boiling becomes important and the contribution of nucleate and convective boiling are

superimposed. The nucleate boiling correction factor was given as a function of heat flux, tube diameter, reduced pressure, surface roughness and fluid molecular weight. Figure 5.7 shows the comparison with the Steiner and Taborek asymptotic model. The correlation very highly over-predicts the experimental data in the micro-tube with MAE of 237 % and only 1.1 % of the data within the error bands. On the other hand, the correlation predicted 4.3, 15.8 and 27 % of the data in the mini-tube with lengths 150, 300 and 450 mm, respectively. The mean absolute error in the mini tubes was much smaller than that in the micro-tube where its values were 48.4, 52.8 and 54.4 % for L = 150, 300 and 450 mm respectively. It is very clear that, the correlation takes into consideration the effect of tube diameter in the nucleate boiling factor as given by Eq. (5.5).

$$F_{nb} = F_{pf}\left(\frac{q}{q_0}\right)^{nf}\left(\frac{D}{D_0}\right)^{-0.4}\left(\frac{R_p}{R_{p,0}}\right)^{0.133} f(MW) \qquad (5.5)$$

As the diameter decreases, Eq. (5.5) increases and consequently the heat transfer coefficient. Increasing the diameter from 0.52 to 1.1 mm resulted in a decrease in the normalized diameter term by 26 %. It is interesting to note that, if the MAE value of the micro-tube (237%) is multiplied by this value (0.26), the mean error will be 61.6 %, which is similar to the error values in the mini-tubes.

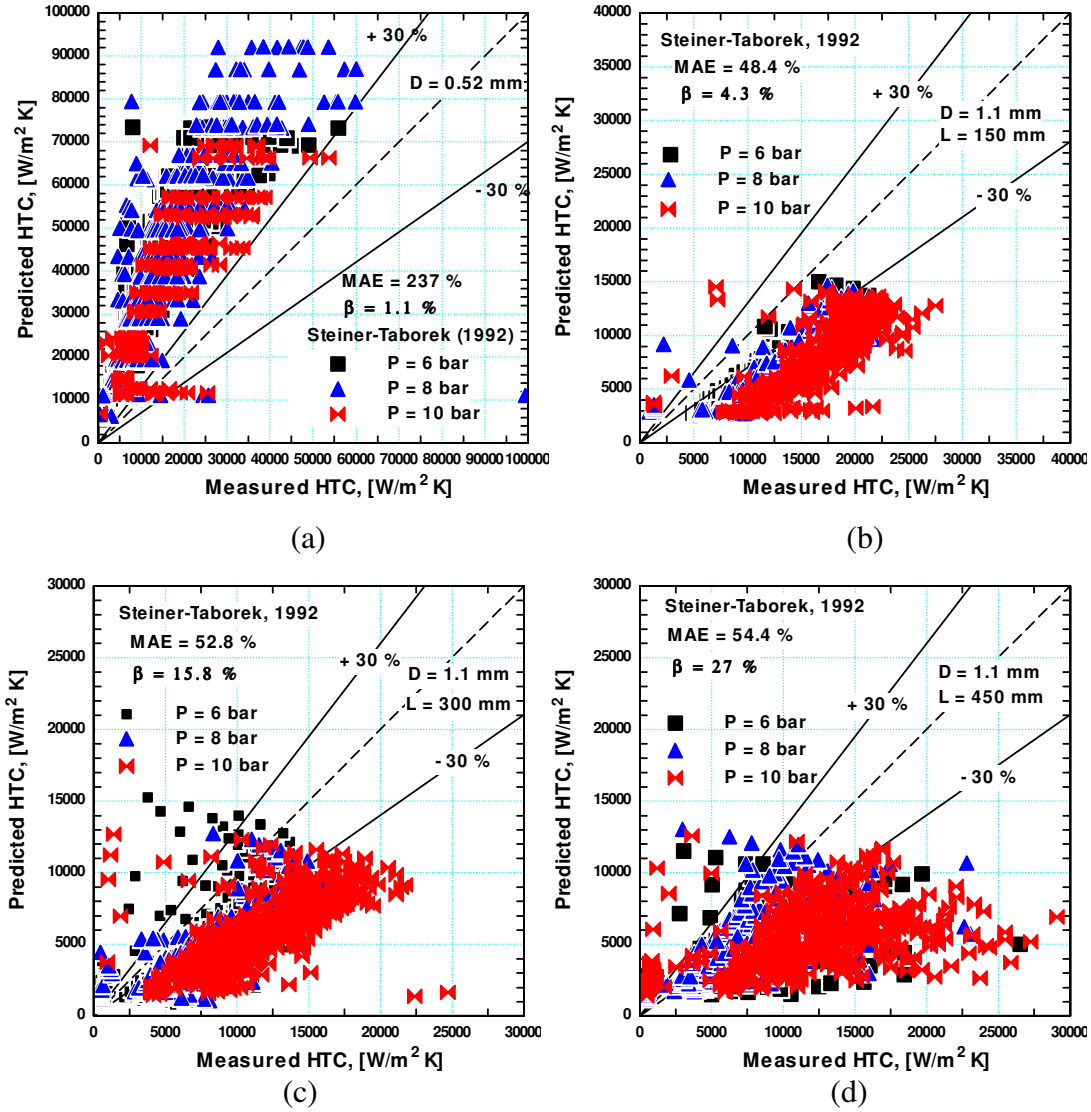

Figure 5.7 Comparison with the Steiner and Taborek (1992) correlations for (a) D = 0.52 mm, L = 100 mm, (b) D = 1.1 mm, L = 150 mm, (c) D = 1.1 mm, L = 300 mm and (e) D = 1.1 mm, L = 450 mm.

5.3 Evaluation of microscale correlations

As discussed above, the widely used macroscale correlations poorly predicted the heat transfer data of the current study. These correlations should be modified in order to capture the microscale new features such as bubble confinement, bubble elongation, thinning of the liquid film, scarcity and instability of nucleation sites and the difficulty of triggering boiling. Accordingly, several correlations have been proposed by many authors for predicting the heat transfer coefficient in small to micro-diameter tubes. This section presents a detailed comparison with some of the existing microscale correlations. Eleven correlations were selected for the comparison with the current

experimental data. These correlations include those of Lazarek and Black (1982), Tran et al. (1996), Kew and Cornwell (1997), Warrier et al. (2002), Kandlikar and Balasubramanian (2004), Zhang et al. (2004), Lee and Mudawar (2005), Saitoh et al. (2007), Bertsch et al. (2009b), Mikielewicz (2010) and Li and Wu (2010a). In addition to these correlations, the Cooper pool boiling correlation was included in the comparison since many researchers reported the dominance of nucleate boiling in micro-channels. The details of these correlations and their applicability ranges are summarized in Appendix B.2. The correlations of Warrier et al. and Lee and Mudawar were developed for multi-channels and are included here to examine whether they can be extended for circular channels or not.

Figure 5.8 depicts the local comparison between the microscale correlations and the experimental data at 6 bar system pressure and 300 kg/m^2 s mass flux. For the micro tube, Fig. 5.8a indicates that all correlations failed to capture the experimental trend except the correlation of Bertsch et al. (2009) that shows similar trend if the first data point in the low quality region was excluded. Kew and Cornwell (1997), Saitoh et al. (2007) and Mikielewicz (2010) correlations give heat transfer coefficient that increases almost linearly with vapour quality. The Warrier et al. (2002) correlation predicts heat transfer coefficients that are much lower than the experimental values and remain almost constant with quality. The Kandlikar and Balasubramanian (2004) correlation predicts heat transfer coefficients that slightly decrease with quality up to a certain quality value after which the coefficient remains approximately constant. The Zhang et al. (2004) correlation behaves in a similar way to the Chen (1966) correlation where the coefficient increases with quality in the very low quality region whereas the effect of quality diminishes in the high quality region. The heat transfer coefficient predicted by the correlation of Lee and Mudawar (2005) shows an N-shape trend where it increases with quality to a peak value at $x \approx 0.1$ then it rapidly decreases with quality up to $x \approx 0.55$ after which it jumps again to another peak value. The Li and Wu (2010) correlation predicts heat transfer coefficient that shows little dependency on vapour quality in the very small quality region and rapid decrease with vapour quality in the high quality region. It can be concluded from Fig. 5.8a that, there is a rough agreement between the experimental values and all correlations over the quality range from 0.1 to 0.3 except the correlations of Warrier et al. (2002), Kandlikar nd Balasubramanian (2004) and Zhang et al. (2004).

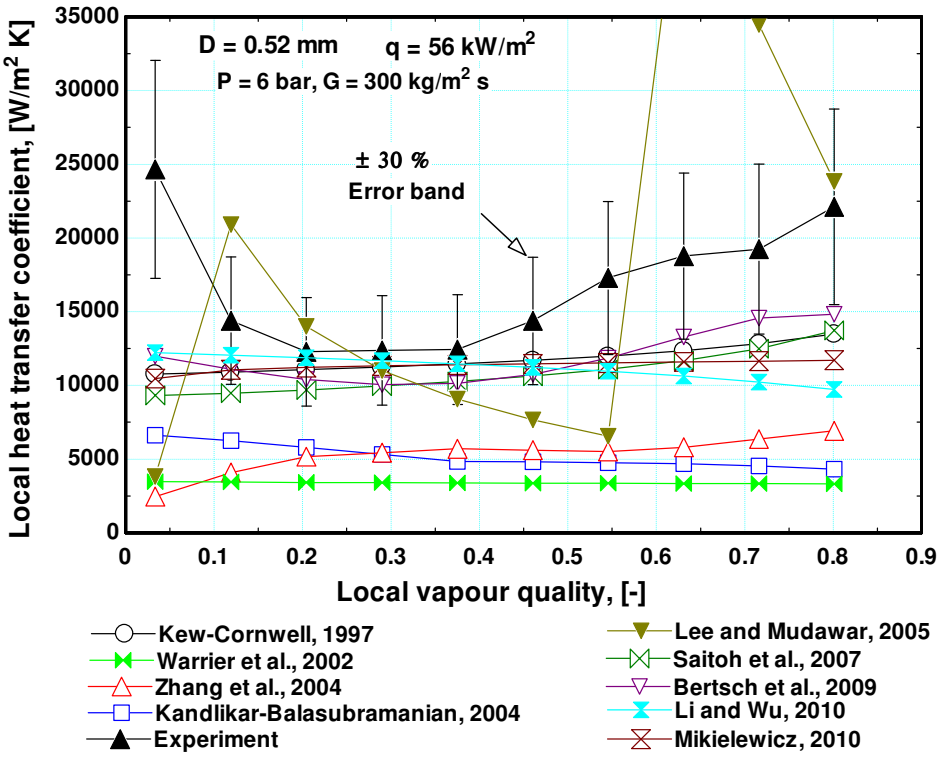
D = 0.52 mm
q = 56 kW/m2
P = 6 bar, G = 300 kg/m2 s
± 30 %
Error band
Local heat transfer coefficient, [W/m2 K]
Local vapour quality, [-]
Kew-Cornwell, 1997
Warrier et al., 2002
Zhang et al., 2004
Kandlikar-Balasubramanian, 2004
Experiment
Lee and Mudawar, 2005
Saitoh et al., 2007
Bertsch et al., 2009
Li and Wu, 2010
Mikielewicz, 2010

(a)

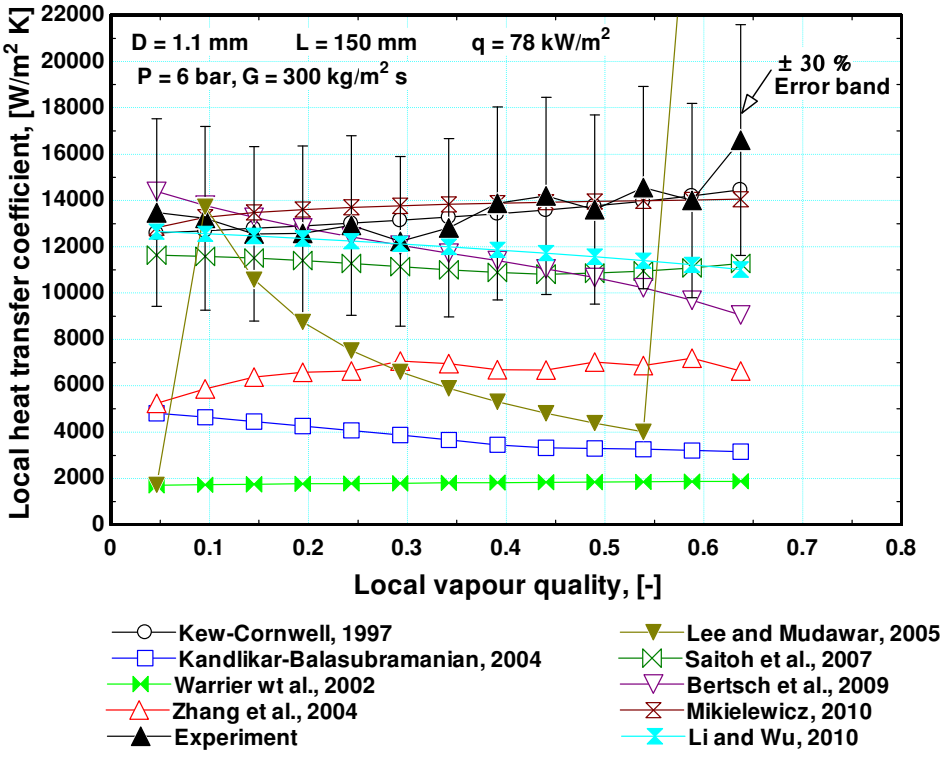
D = 1.1 mm
L = 150 mm
q = 78 kW/m2
P = 6 bar, G = 300 kg/m2 s
± 30 %
Error band
Local heat transfer coefficient, [W/m2 K]
Local vapour quality, [-]
Kew-Cornwell, 1997
Kandlikar-Balasubramanian, 2004
Warrier wt al., 2002
Zhang et al., 2004
Experiment
Lee and Mudawar, 2005
Saitoh et al., 2007
Bertsch et al., 2009
Mikielewicz, 2010
Li and Wu, 2010

(b)

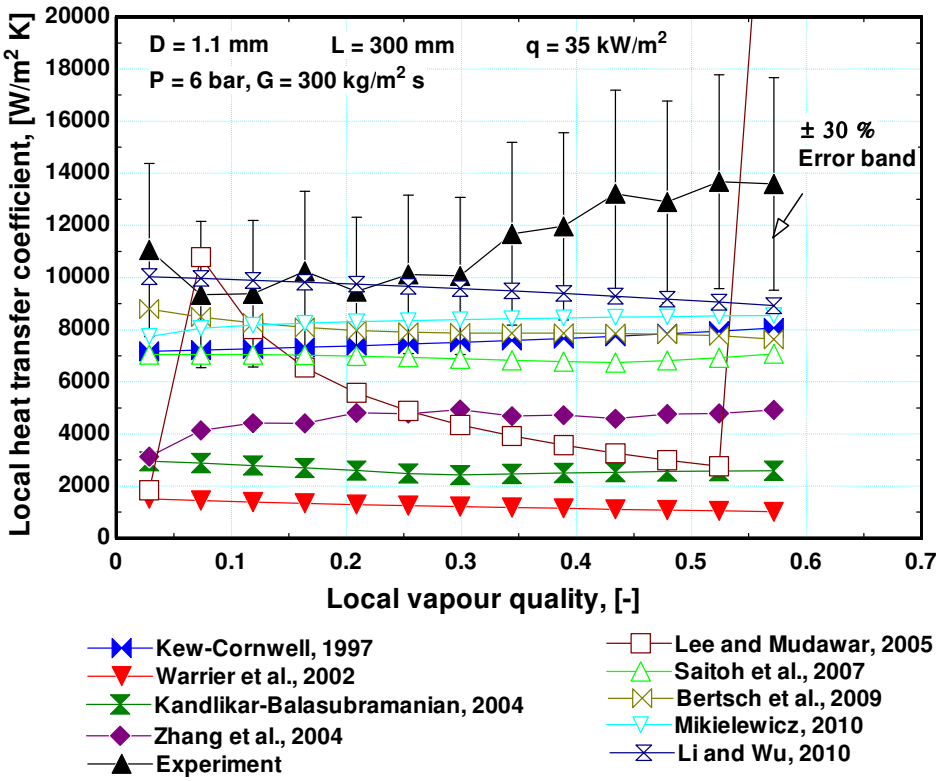

(c)

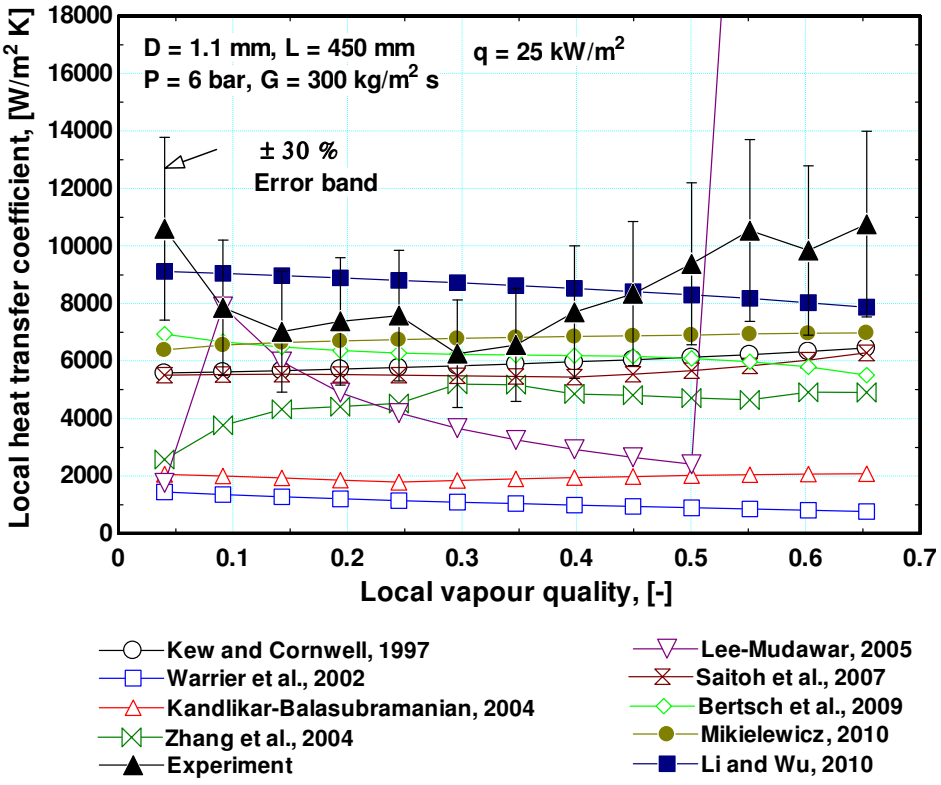

(d)

Figure 5.8 Comparison with microscale correlations at G = 300 kg/m2 s, P = 6 bar and a selected value of heat flux for (a) D = 0.52 mm, L = 100 mm, (b) D = 1.1 mm, L = 150 mm, (c) D = 1.1 mm, L = 300 mm and (e) D = 1.1 mm, L = 450 mm.

Figure 5.8b indicates for the mini-tube with L = 150 mm that only the correlations of Kew and Cornwell (1997) and Mikielewicz (2010) agree with the experimental values. The correlations of Saitoh et al. (2007), Bertsch et al. (2009) and Li and Wu (2010) reasonably agree with the experimental values in the low quality region (up to x ≈ 0.3). All other correlations highly deviate from the experimental values. Figure 5.8c indicates for L = 300 mm that all correlations disagree with the experimental values except the correlation of Li and Wu (2010) which agreed very well up to x ≈ 0.3. In Fig. 5.8d for L = 450 mm, only the correlation of Mikielewicz (2010) agreed very well with the data over the quality range 0.1 – 0.4. It is obvious that the performance of some correlations varies with the variation of the heated length.

The Lazarek and Black (1982) correlation

Lazarek and Black (1982) investigated flow boiling heat transfer of R113 in a stainless steel tube with diameter of 3.1 mm and heated length of 126 mm. The measured heat transfer coefficient was independent of mass flux and vapour quality but increases with increasing heat flux. Thus, they correlated 728 data points using the least square method in the functional form given by Eqn. 5.6. The exponent of Reynolds number in the equation is very similar to the one in the single phase Dittus-Boelter's equation. Whereas the exponent of the boiling number (Bo) is similar to the exponent of heat flux in nucleate pool boiling which reflects the strong heat flux effect. In other words, the correlation confirms the dominance of nucleate boiling and also takes into consideration the effect of diameter. Also, it is clear from the correlation that the mass flux effect is insignificant where the exponent of the mass flux is 0.143.

$$\begin{aligned} h_{tp} &= 30\,\mathrm{Re}^{0.857}\, Bo^{0.714}\, \frac{k_L}{D} \\ &= 30 G^{0.143} D^{-0.143} q^{0.714} \mu_L^{-0.857} h_{fg}^{-0.714} k_L \end{aligned} \tag{5.6}$$

This correlation is valid for R113, q = 14 – 380 kW/m^2, G = 125 – 750 kg/m2 s, P = 1.3 – 4 bar, Re = 860 – 5500 and Bo = 0.00023 – 0.0076. The current experimental data locate within this range except system pressure which is higher (6 – 10 bar), tube diameter which is less and fluid (R134a). Figure 5.9 depicts the global comparison with

the Lazarek and Black (1982) correlation. For the micro-tube (Fig. 5.9a), the correlation predicted only 43.7 % of the data within the error bands with a mean absolute error value of 51.6 %. The performance of the correlation is consistent with the behaviour of the measured heat transfer coefficient in this tube. The measured coefficient drops from maximum value at $x \approx 0$ then it remains approximately constant over $x \approx 0.1 – 0.4$ then it continuously increases with quality. Since the correlation predicts that the heat transfer coefficient remain constant with quality, it is expected that the correlation highly under-predicts the experimental values at $x < 0.1$ and $x > 0.4$. On the other hand, the correlation performed much better in the shortest mini-tube with MAE of 32.15 % and 65.8 % of the data within the error bands whilst the prediction gets worse as the heated length was increased. The success of the correlation in predicting most of the data in the shortest tube is attributed to the dominance of nucleate boiling over all quality values. As the heated length of the mini tube was increased, nucleate boiling prevailed in the low to intermediate quality region whilst convective boiling prevailed in the high quality region. Since the correlation was developed based on the fact that nucleate boiling is the only dominant mechanism, the prediction gets worse as the heated length increases due to contribution of nucleate and convective boiling.

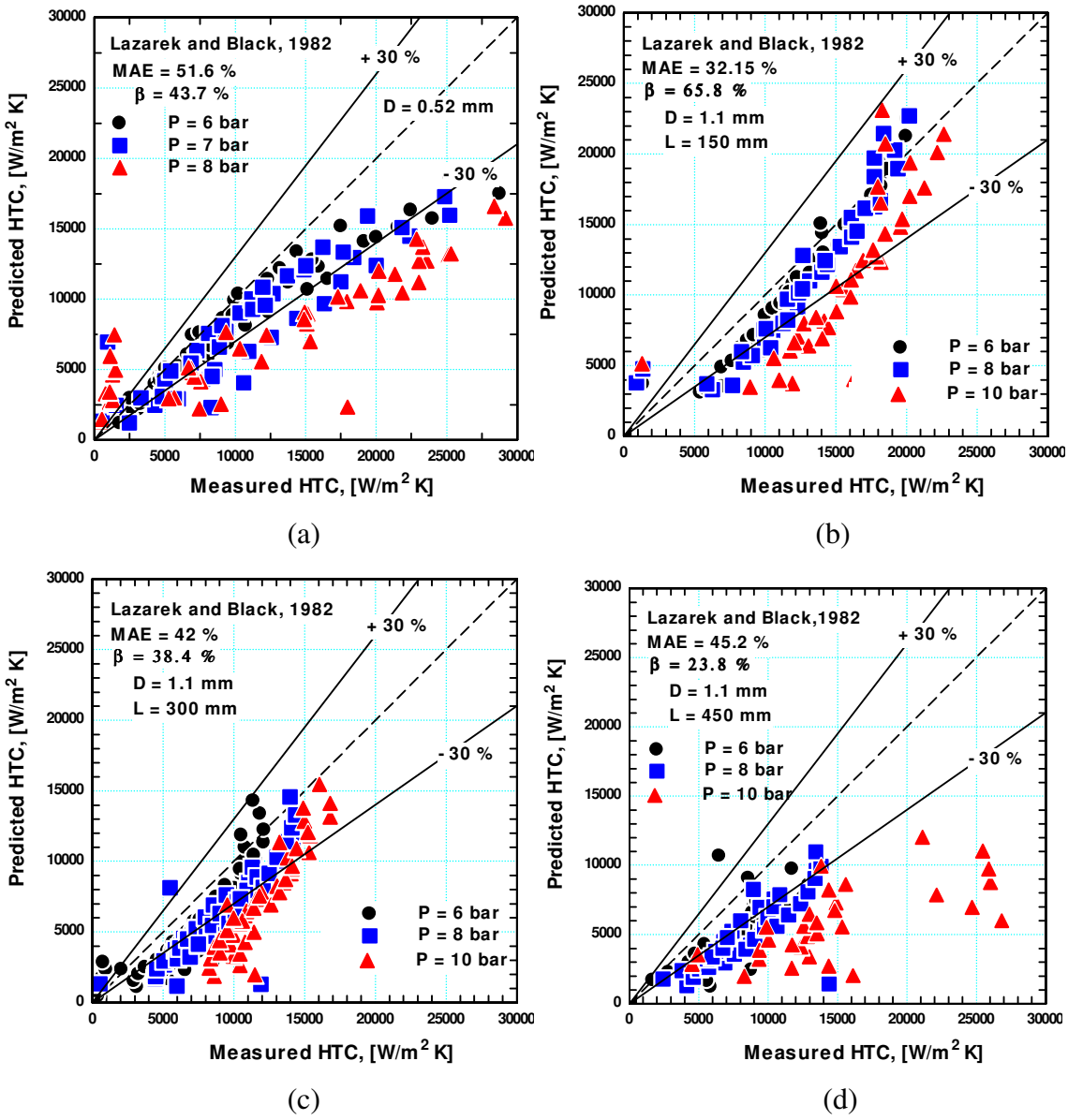

Figure 5.9 Comparison with the Lazarek and Black (1982) correlation for (a) D = 0.52 mm, L = 100 mm, (b) D = 1.1 mm, L = 150 mm, (c) D = 1.1 mm, L = 300 mm and (d) D = 1.1 mm, L = 450 mm.

The Tran et al. (1996) correlation

Tran et al. (1996) investigated flow boiling heat transfer of R12 in a circular channel with diameter of 2.46 mm and a rectangular channel with hydraulic diameter of 2.4 mm. All channels are made of brass with heated length of 870 mm. They found that, nucleate boiling is the dominant mechanism and the mass flux effect was insignificant. Accordingly, they modified the correlation of Lazarek and Black (1982) by replacing the Reynolds number with the Weber number and considering the variations in fluid

properties as given by Eq. (5.7). The Weber number was used to eliminate the viscous effects in favour of surface tension. The correlation indicates that there is no mass flux effect where the exponent of mass flux is zero and the diameter effect is small which is clear from the exponent of the Weber number. It is worth mentioning that the liquid Weber number is defined based on the total mass flux (G) and the correlation does not show any dependency on vapour quality. The correlation was based on 222 data points for R12 and 27 data points for R113.

$$\begin{aligned} h_{tp} &= (8.4\times10^{-5}) We_L^{0.3} Bo^{0.6} \left(\frac{\rho_L}{\rho_g}\right)^{-0.4} \\ &= (8.4\times10^{-5}) G^{0.6} D^{0.3} \rho_L^{-0.3} \sigma^{-0.3} q^{0.6} G^{-0.6} h_{fg}^{-0.6} \rho_L^{-0.4} \rho_g^{0.4} \\ &= (8.4\times10^{-5}) D^{0.3} q^{0.6} h_{fg}^{-0.6} \sigma^{-0.3} \rho_L^{-0.7} \rho_g^{0.4} \end{aligned} \qquad (5.7)$$

The above correlation is valid for D = 2.4 – 2.92 mm, G = 44 – 832 kg/m^2 s, q = 7.5 – 129 kW/m^2 and reduced pressure from 0.045 – 0.2. Figure 5.10 shows the global comparison with the Tran et al. (1996) correlation. It is obvious that the correlation poorly under-predicts the experimental values, i.e. less than 5 % of the data are within the error bands. The experimental results of the shortest mini-tube (L = 150 mm), the correlations of Tran et al. and Lazarek and Black all agree on the dominance of nucleate boiling mechanism. However, there is a big difference in the performance of these two correlations compared to the experimental data of this tube. Since the study of Tran et al. and Lazarek and Black were conducted using the same fluid and almost similar tube diameter, the difference in performance may be attributed to the following reasons. First reason could be the difference in tube material; where Tran et al. investigated a brass tube whilst Lazarek and Black investigated a stainless steel tube. Since brass is more ductile than stainless steel, the inner surface characteristics are expected to be different and consequently nucleation characteristics and heat transfer coefficient. This effect can be deduced from the exponent of the boiling number in Eqs. (5.6 and 5.7). The Tran et al. correlation indicates that the heat flux effect is less compared to th Lazarek and Black correlation. Second reason could be the difference in the investigated heated lengths where Lazarek and Black used tube with a heated length of 124 mm whilst Tran et al. used a heated length of 870 mm. As presented and discussed in Chapter 4, increasing the heated length results in a reduction in the heat transfer coefficient for the

same exit quality. This factor explains why the Tran et al. correlation highly under-predicts the experimental data. Third reason could be the method of considering the effect of tube diameter. In the Lazarek and Black correlation, the decrease in tube diameter results in an increase in the heat transfer coefficient which is clear from Eq. (5.6). On the other hand, the heat transfer coefficient predicted by Tran et al. correlation decreases with decreasing tube diameter, which is clear from Eq. (5.7).

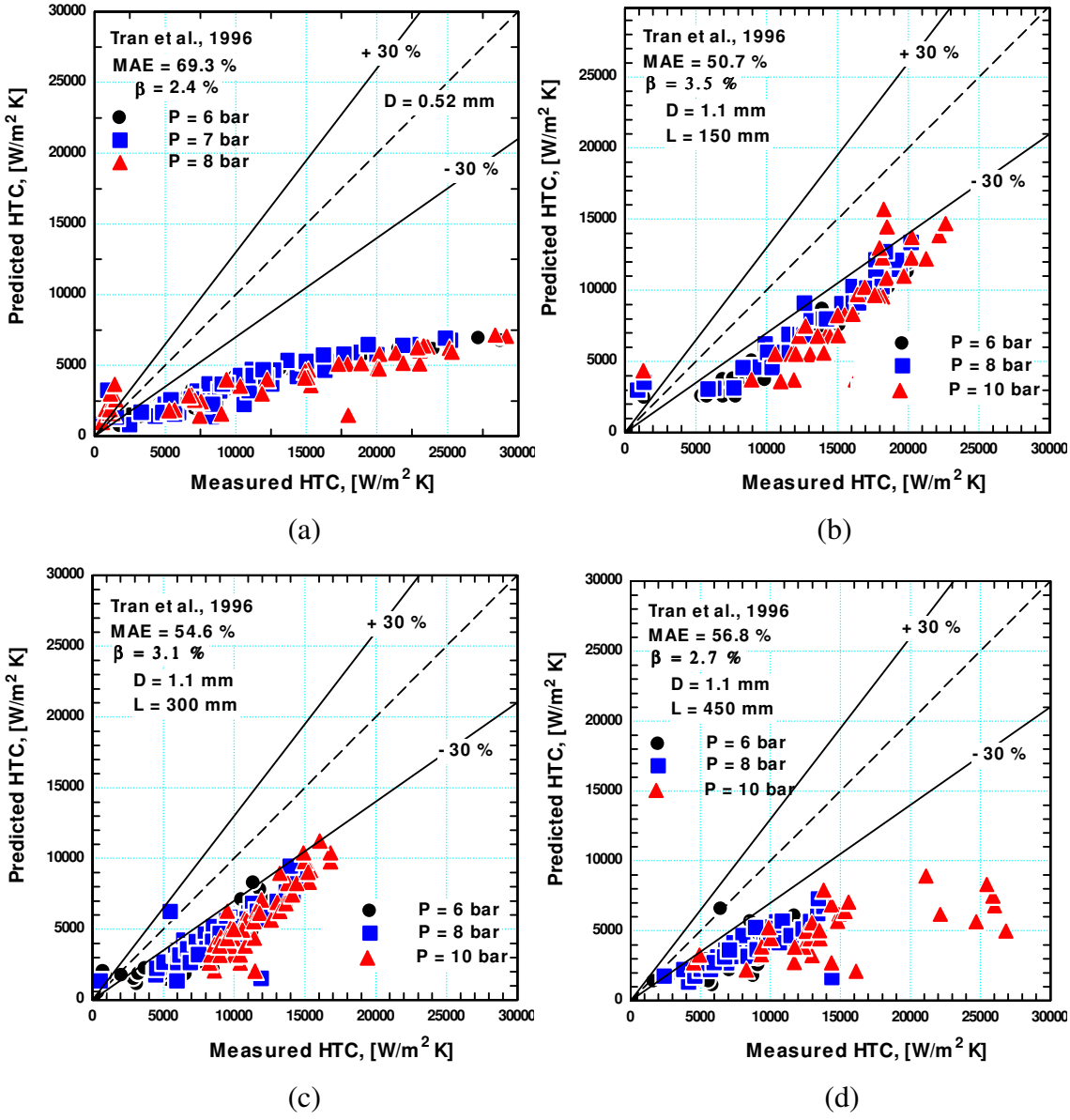

Figure 5.10 Comparison with the Tran et al. (1996) correlation for (a) D = 0.52 mm, L = 100 mm, (b) D = 1.1 mm, L = 150 mm, (c) D = 1.1 mm, L = 300 mm and (d) D = 1.1 mm, L = 450 mm.

The Kew and Cornwell (1997) correlation

Kew and Cornwell (1997) investigated flow boiling heat transfer of R141b in stainless steel tubes with diameters of 1.39 – 3.69 mm and heated length of 500 mm. The measured heat transfer coefficient in their experiment increased with increasing vapour quality towards the exit over a wide range of vapour quality. Accordingly, they modified the Lazarek and Black correlation by the term $(1 - x)^{-0.143}$ to account for the increasing trend of the heat transfer coefficient with quality as given by Eq. (5.8).

$$\begin{aligned} h_{tp} &= 30\,\mathrm{Re}^{0.857}\, Bo^{0.714}\, \frac{k_L}{D}(1-x)^{-0.143} \\ &= 30 G^{0.143} D^{-0.143} q^{0.714} \mu_L^{-0.857} h_{fg}^{-0.714} k_L (1-x)^{-0.143} \end{aligned} \tag{5.8}$$

Figure 5.11 shows the global comparison with the Kew and Cornwell (1997) correlation. Since the correlation is originally a modified version of Lazarek and Black correlation, the difference in performance is not that big. For the micro-tube (Fig. 5.11a), the Kew and Cornwell correlation performed better than the Lazarek and Black correlation where the MAE/β values are 32.5/52.7 compared to 51.6/43.7. For the shortest mini-tube (L = 150 mm), the performance was very similar to the Lazarek and Black correlation, i.e. MAE/β values of 25.7/69.1 compared to 32.15/65.8. As the heated length was increased (Fig. 5.11c and Fig. 5.11d), the performance of the correlation got worse but it was slightly better than that of Lazarek and Black. The performance of the Kew and Cornwell correlation can be explained using Fig. 5.8. The correlation predicts that the heat transfer coefficient increases very slowly with quality in the very low quality region and increases with a relatively faster rate in the high quality region. However, the slope of the *h-x* curve predicted by the correlation is much smaller than the slope of the experimental curve particularly after $x \approx 0.3 – 0.4$ for all tubes. Accordingly, the correlation highly deviates from the experimental values at $x > 0.4$ and at the first data point for all tubes except the shortest mini-tube. In this tube, the experimental slope of the h-x curve was very small, i.e. the coefficient was independent of vapour quality, which is close to the predicted slope by the correlation. This may explain why the correlation succeeded to predict 69.1 % of the data in this tube with a small error value of 25.7 %.

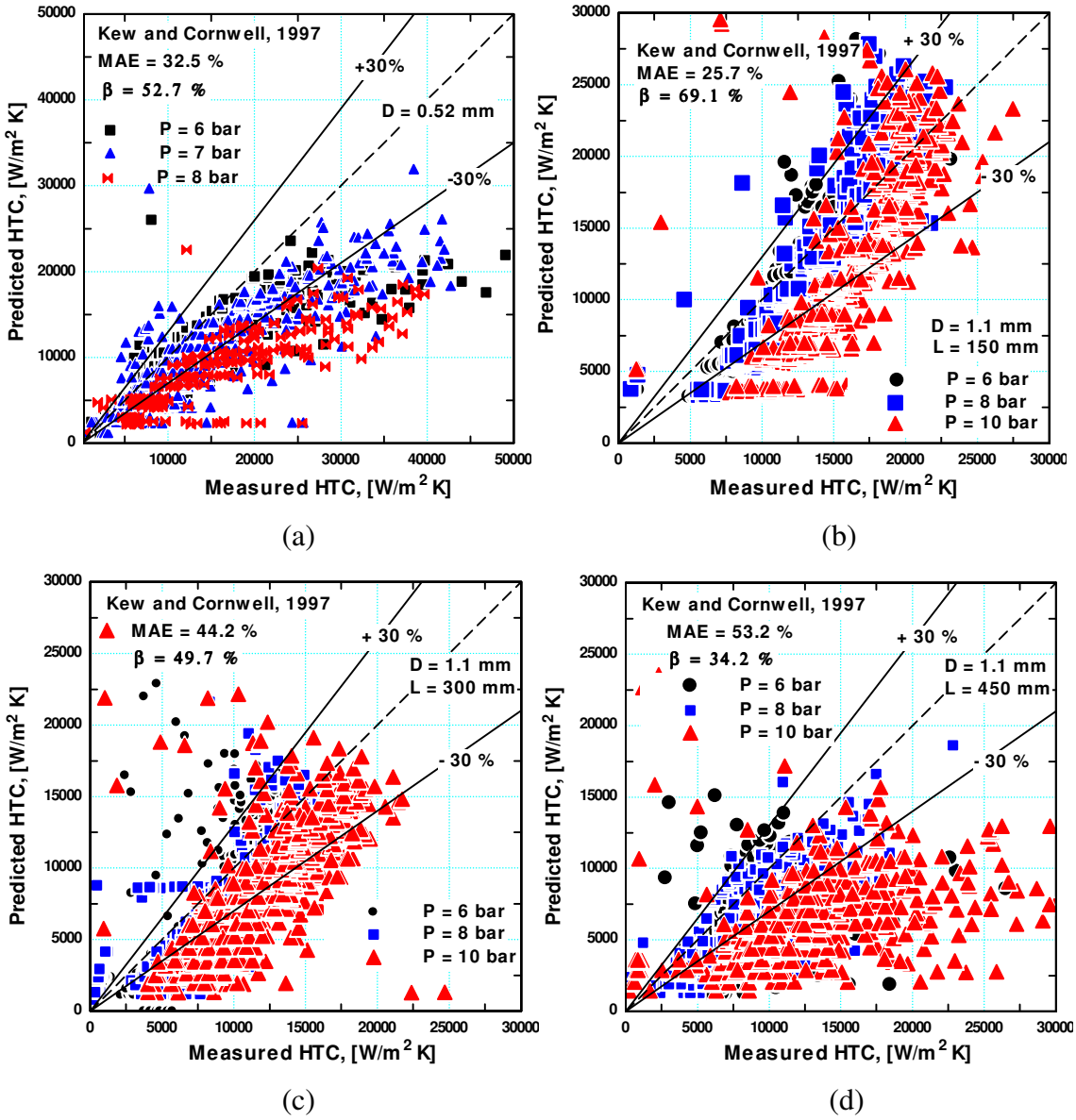

Figure 5.11 Comparison with the Kew and Cornwell (1996) correlation for (a) D = 0.52 mm, L = 100 mm, (b) D = 1.1 mm, L = 150 mm, (c) D = 1.1 mm, L = 300 mm and (d) D = 1.1 mm, L = 450 mm.

The Warrier et al. (2002) correlation

Warrier et al (2002) investigated flow boiling heat transfer of FC-84 in aluminium multi-channels with hydraulic diameter of 0.75 mm. They proposed a correlation for saturated flow boiling in the functional form given by Eqn. 5.9 which is valid for x = 0.01 – 0.55. The two phase heat transfer coefficient was normalised by the fully developed single phase laminar heat transfer coefficient.

$$\frac{h_{tp}}{h_{sp,lam}} = 1 + 6Bo^{1/16} - 5.3x^{0.65}\left(1 - 855Bo\right) \qquad (5.9)$$

The above correlation was compared with the current experimental data and the result is shown in Fig. 5.12. It is obvious that, the correlation highly under-predicts the current experimental data with a large error and very few data located within the error bands. The high deviation could be attributed to the following reasons. First reason could be the type of fluid. There is a big difference between the properties of R134a refrigerant and FC84 dielectric fluid particularly surface tension, latent heat and molecular weight. Compared to R134a, the surface tension value of FC84 is about 150 % higher, the latent heat is about 50 % less and the molecular weight is 380 % higher. These three properties play a significant role in nucleate pool boiling heat transfer. The smaller the surface tension, the smaller the bubble departure diameter and consequently the higher the heat transfer coefficient. This surface tension effect was deduced from the correlation of Stephan and Abdelsalam (1980) for bubble departure diameter in nucleate pool boiling. Additionally, Cooper's nucleate pool boiling correlation indicates that the fluid molecular weight significantly affects the heat transfer coefficient where the heat transfer coefficient decreases for fluids with high molecular weight. Accordingly, the heat transfer coefficient of FC84 is expected to be much smaller than that of R134a–the thing that may explain the tendency of the correlation to highly under-predict the experimental values. Second reason could be the multi-microchannels arrangements compared to single tubes as well as the channels material. Multi-microchannels configuration has the problems of uneven flow distribution to each channel and instability, which may influence the heat transfer characteristics.

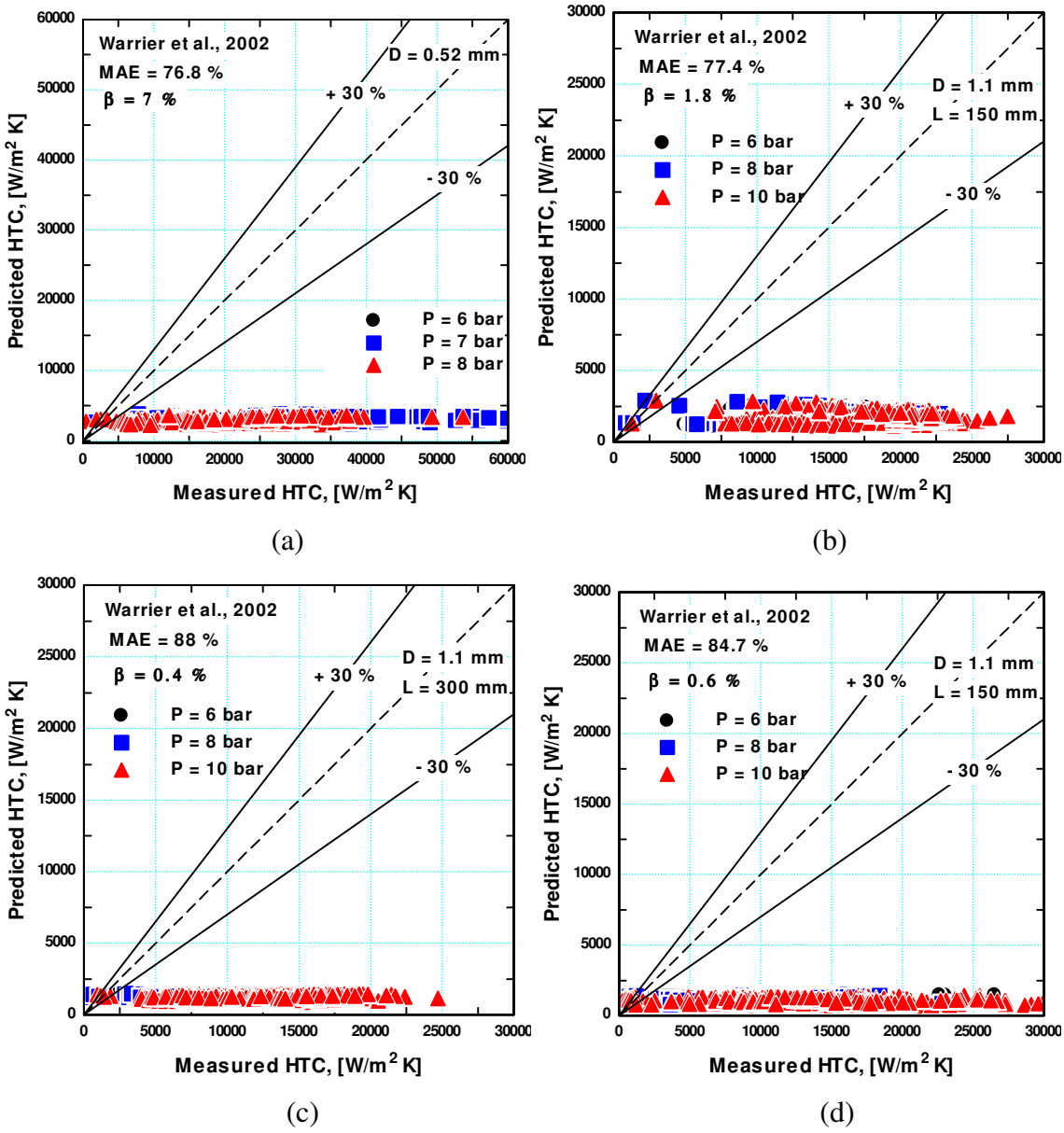

Figure 5.12 Comparison with the Warrier et al. (2002) correlation for (a) D = 0.52 mm, L = 100 mm, (b) D = 1.1 mm, L = 150 mm, (c) D = 1.1 mm, L = 300 mm and (d) D = 1.1 mm, L = 450 mm.

The Kandlikar and Balasubramanian (2004) correlation

The correlation of Kandlikar (1990) presented in section 5.2.4 was originally developed for large diameter tubes where all data was in the turbulent region. Kandlikar and Balasubramanian (2004) extended the applicability of this correlation to micro-channels and mini-channels by accounting for the low Reynolds number values. The modifications included only dropping the Froude number from the equations since channel orientation is insignificant in mini/micro-channels and modifying the single

phase heat transfer coefficient based on flow conditions, i.e. laminar, turbulent, and transition. Figure 5.13 illustrates the global comparison with the correlation of Kandlikar and Balasubramanian (2004). Surprisingly, the performance of the correlation was very poor compared to the original Kandlikar (1990) correlation; see Fig. 5.5. For all tubes, the correlation highly under-predicts the experimental data with an error value ranging from 62.3 to 69 % and very few percentages of data locates within the error bands. On the contrary, the old version of the correlation predicted all tubes data with an error values ranging from 32.2 to 50.3 % and the percentages of data within the error bands ranged from 45.2 to 68 %. The difference in performance between the new and old versions of this correlation needs some comment. Visiting the two original papers of these authors, one can simply explain why they are performing in a different way. Kandlikar and Balasubramanian (2004) presented the old version of the correlation with small difference compared to the original form in Kandlikar (1990) though they referred to the original paper (Kandlikar (1990)). The difference was that, all equations were multiplied by the term $(1-x)^{0.8}$ which was not included in the original form. They did not comment on this term and it was unclear whether it was included as a new modification or it was included to the equations by mistake. At vapour quality values very close to zero, the magnitude of this term approaches unity and the effect on the predicted values is expected to be small. By contrast, as the quality increases, the magnitude of these terms becomes much smaller than unity and consequently the magnitudes of the predicted heat transfer coefficient are expected to be much smaller than the values predicted by the original correlation.

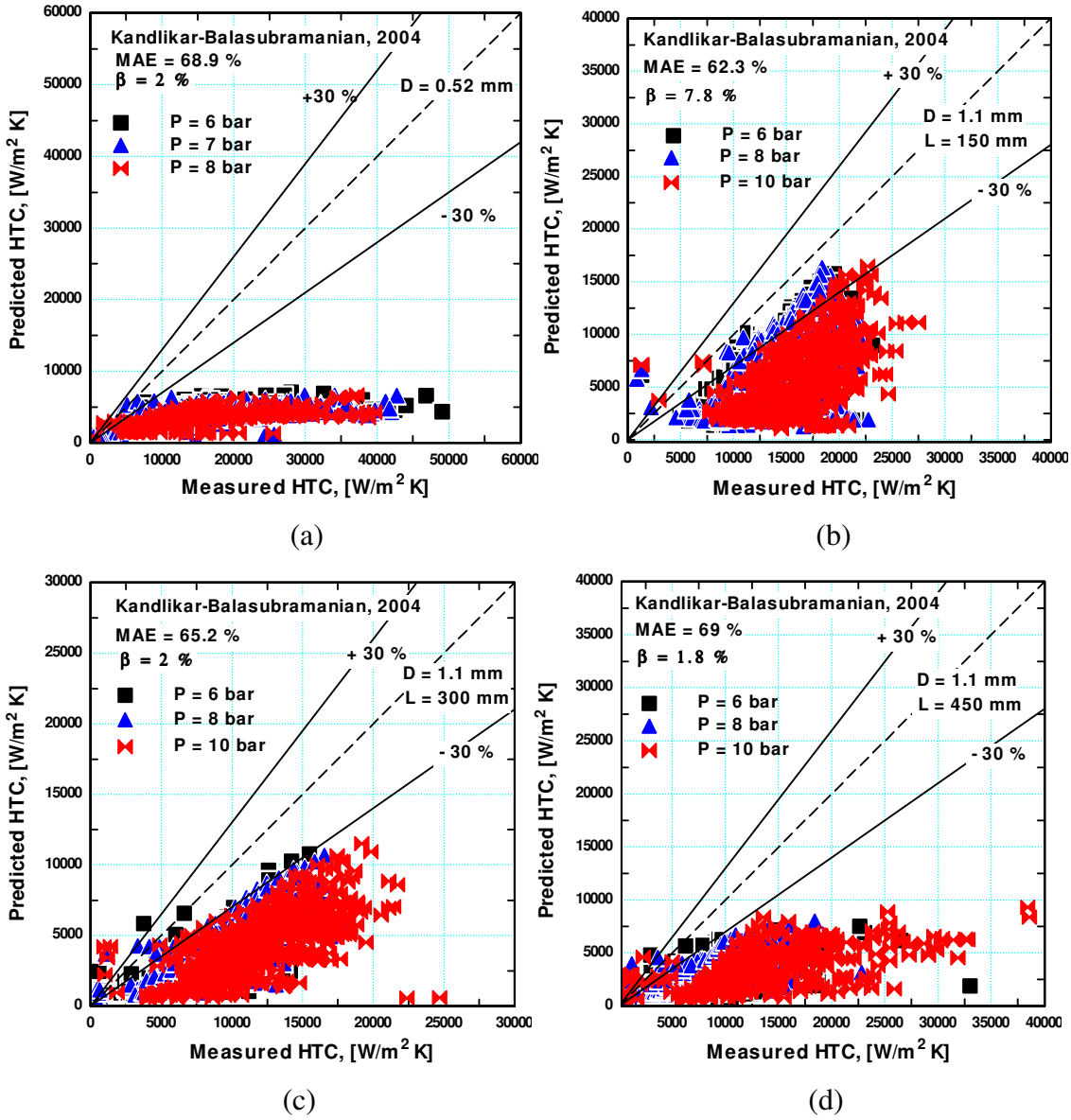

Figure 5.13 Comparison with the Kandlikar and Balasubramanian (2004) correlation for (a) D = 0.52 mm, L = 100 mm, (b) D = 1.1 mm, L = 150 mm, (c) D = 1.1 mm, L = 300 mm and (d) D = 1.1 mm, L = 450 mm.

The Zhang et al. (2004) correlation

Zhang et al. (2004) proposed a correlation for saturated flow boiling in mini-channels based on a database consisting of 1203 data points for four fluids (water, R11, R12 and R113), diameters ranging from 0.78 to 6 mm, system pressure from 0.101 to 1.21 MPa, mass flux from 23.4 to 2939 kg/m^2 s and heat fluxes from 2.95 to 2511 kW/m^2. Most of the data located in the laminar liquid-turbulent gas flow condition. The proposed correlation is of the Chen type given by Eq. (5.2). They modified the enhancement factor F in Eq. (5.2) to be a function of the two phase frictional multiplier which

depends on the flow conditions (laminar/turbulent). In the original correlation, this factor was given as a function of the turbulent-turbulent Martinelli parameter. Also, the single phase heat transfer coefficient was modified based on flow conditions instead of using Dittus-Boelter correlation. All other terms in the Chen correlation were kept without changes except the suppression factor *S* where the two phase Reynolds number was replaced with the liquid Reynolds number. Figure 5.14 depicts the global comparison with the correlation of Zhang et al. (2004). Although the correlation is a modified version of Chen (1966) correlation, it is clear from the figure that the correlation does not add any improvements in predictability. Figure 5.8 indicates that, the behaviour of the predicted local heat transfer coefficient using Zhang et al. (2004) correlation is similar to that predicted by Chen (1966) correlation. Both correlations predict heat transfer coefficient that rapidly increases with quality in the very low quality region and increases very slowly with quality in the high quality region, which is different from the experimental trend.

Figure 5.15 shows the comparison between the experimental data and the Zhang et al. (2004) correlation modified by the Cooper pool boiling correlation instead of using the Forster-Zuber correlation. It is obvious from the figure that the performance of the modified correlation improved significantly compared to the original correlation. For the 0.52 mm tube (Fig. 5.15a), the modified correlation predicted 66.1% of the data within the ± 30 % error bands compared to the 11.4 % predicted by the original correlation. Also, the MAE value decreased from 79.7 % to 33.7 %. For the shortest mini tube (Fig. 5.15b), the modified correlation predicted 77 % of the data within the ± 30 % error bands at MAE value of 24.8 % compared to 1.5 % at a MAE value of 64.2 % for the original correlation. For the 1.1 mm tube with L = 300 mm (Fig. 5.15c), the β/MAE values are 72.6/46.2 % compared to the 15/122.6 % predicted by the original correlation. For the longest 1.1 mm tube (Fig. 5.15d), the performance of the modified correlation decreased but still much better than the performance of the original correlation. It predicted 57 % of the data within the ± 30 % error bands at a MAE value of 55.6 % compared to the prediction of only 21 % of data at a MAE value of 133.6 % using the original correlation.

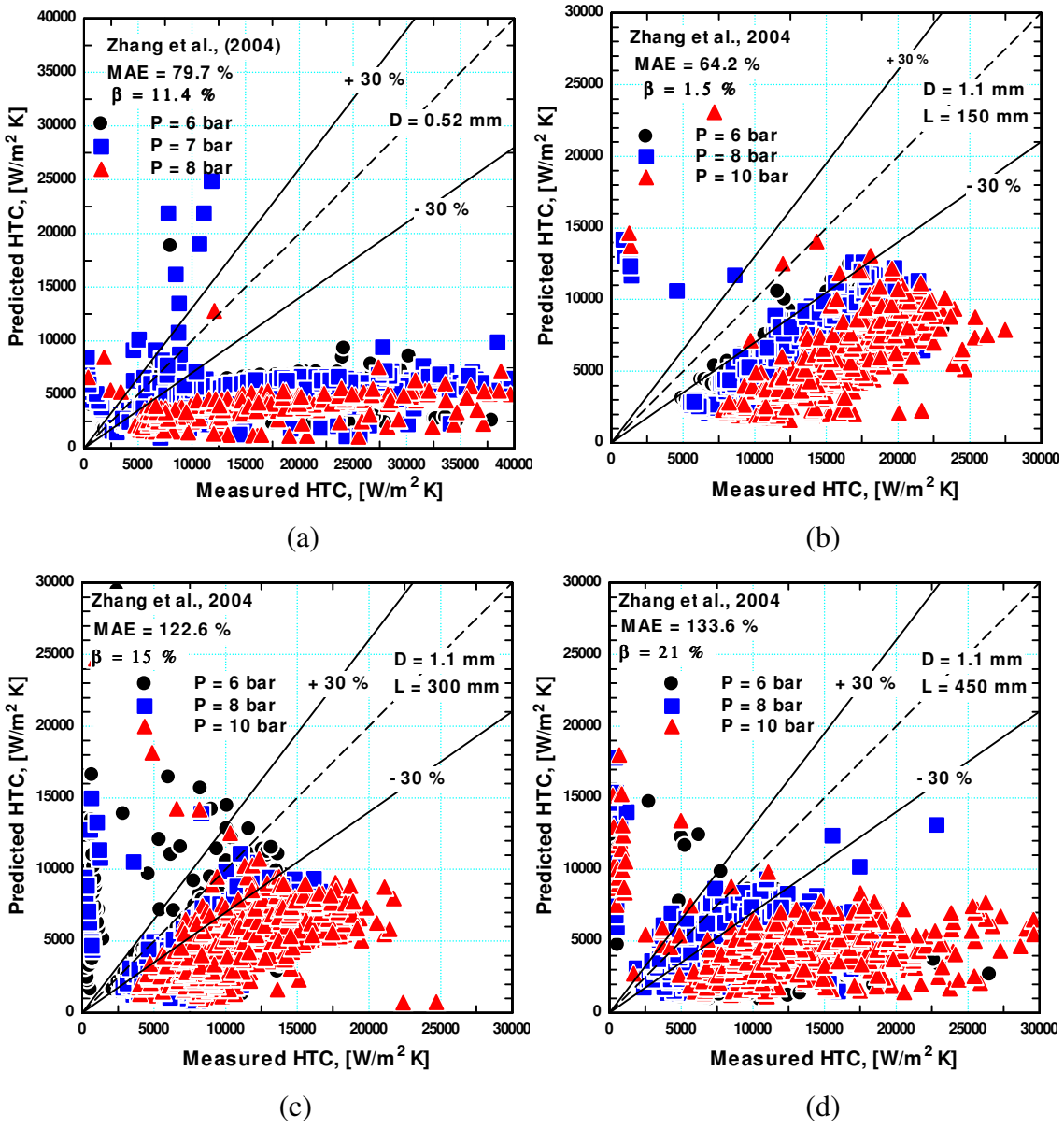

Figure 5.14 Comparison with the Zhang et al. (2004) correlation for (a) D = 0.52 mm, L = 100 mm, (b) D = 1.1 mm, L = 150 mm, (c) D = 1.1 mm, L = 300 mm and (d) D = 1.1 mm, L = 450 mm.

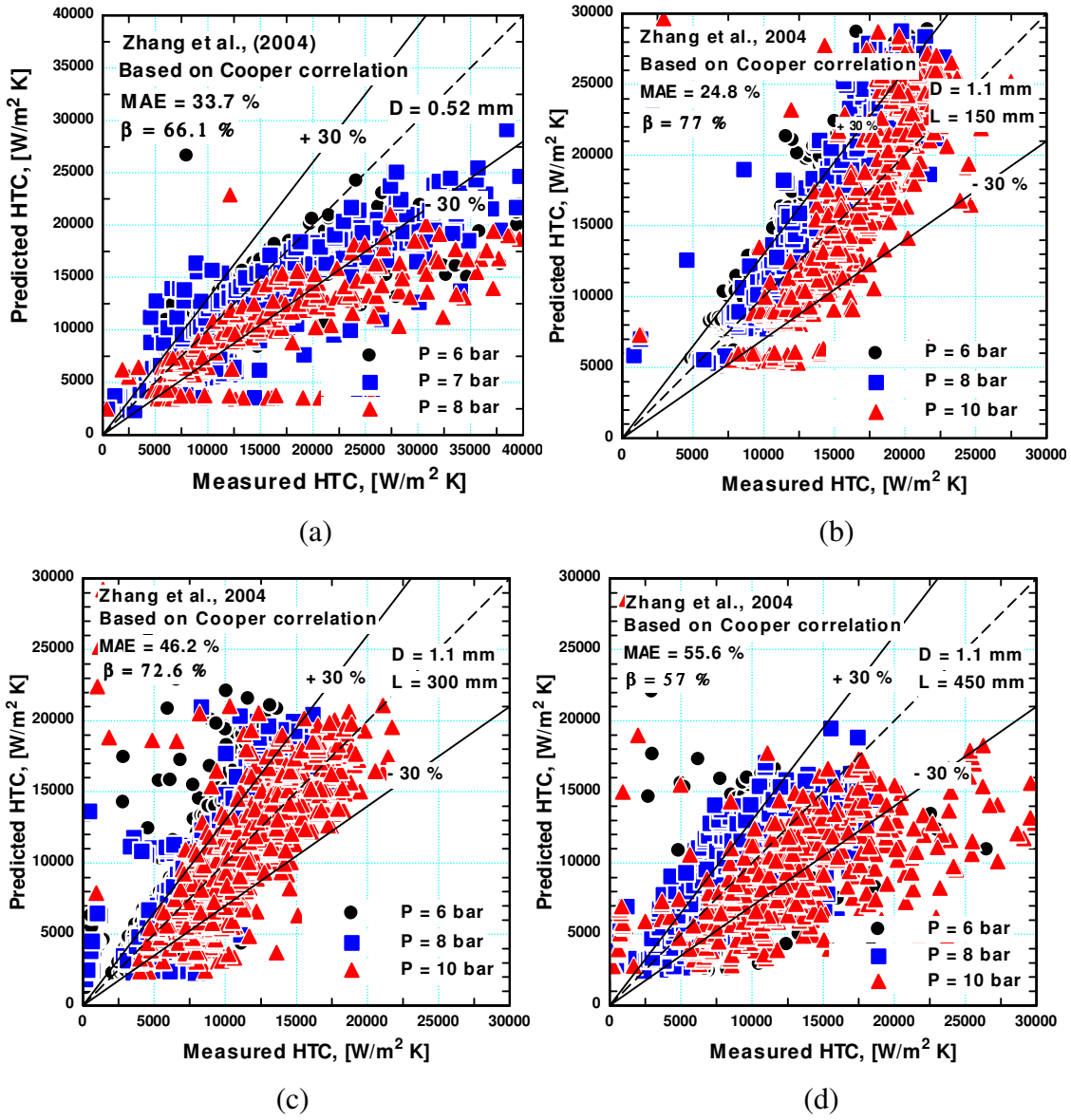

Figure 5.15 Comparison with the Zhang et al. (2004) correlation modified by the Cooper correlation instead of the Forster-Zuber correlation for (a) D = 0.52 mm, L = 100 mm, (b) D = 1.1 mm, L = 150 mm, (c) D = 1.1 mm, L = 300 mm and (d) D = 1.1 mm, L = 450 mm.

The Lee and Mudawar (2005) correlation

Lee and Mudawar (2005) investigated flow boiling heat transfer of R134a in a micro-channel heat sink with hydraulic diameter of 0.35 mm. Since the macro and microscale correlations failed to predict their experimental data, they proposed a new correlation for saturated flow boiling in microchannels. The correlation was developed based on 318 data points of which 111 data points for R134a and the remaining was for water. It is worth mentioning that they calculated the local quality at one location in the middle

of the channel and the inlet quality was varied from 0.001 to 0.25 using an expansion device. Additionally, the R134a experiments were conducted by varying the mass flux for a constant heat flux value whilst the water experiments were conducted in an opposite way. To correlate the data of water and R134a, they found that Boiling number and the liquid Weber number are the important dimensionless parameters to be included in the correlation plus the Martinelli parameter. To achieve accurate predictions, they divided the quality domain into three ranges based on the dominant mechanism and proposed a correlation for each range. In the first range ($x < 0.05$), the dominant mechanism was nucleate boiling whereas convective boiling dominated at intermediate quality range ($x = 0.05 - 0.55$) and high quality range ($x > 0.55$). Although nucleate boiling was the prevailing mechanism at very low quality, the heat transfer coefficient was correlated as a function of Martinelli parameter only which is a flow parameter without including any term for the heat flux effect in this region.

Figure 5.16 shows the global comparison with the Lee and Mudawar (2005) correlation. The figure indicates that the correlation predicts poorly the experimental values with a large scatter. This scatter is arising from the fact that, the correlation is not capable of predicting the correct experimental trend as presented previously in Fig. 5.8. The local heat transfer coefficient behaves according to N-shape trend, which is completely different from the measured experimental trends in all tubes. So, the correlation has captured only a few number of experimental points and either under-predicted or over-predicted the others. The failure of this correlation to predict the current experimental data may be attributed to the fact that the correlation was developed for rectangular multi-micro-channels using a few number of data points for R134a. Another reason could be the difference in experimental methodology. The current experimental data were collected through increasing the heat flux gradually at constant pressure and mass flux. In the study of Lee and Mudawar (2005), the mass flux was varied while the pressure and the heat flux were kept constant.

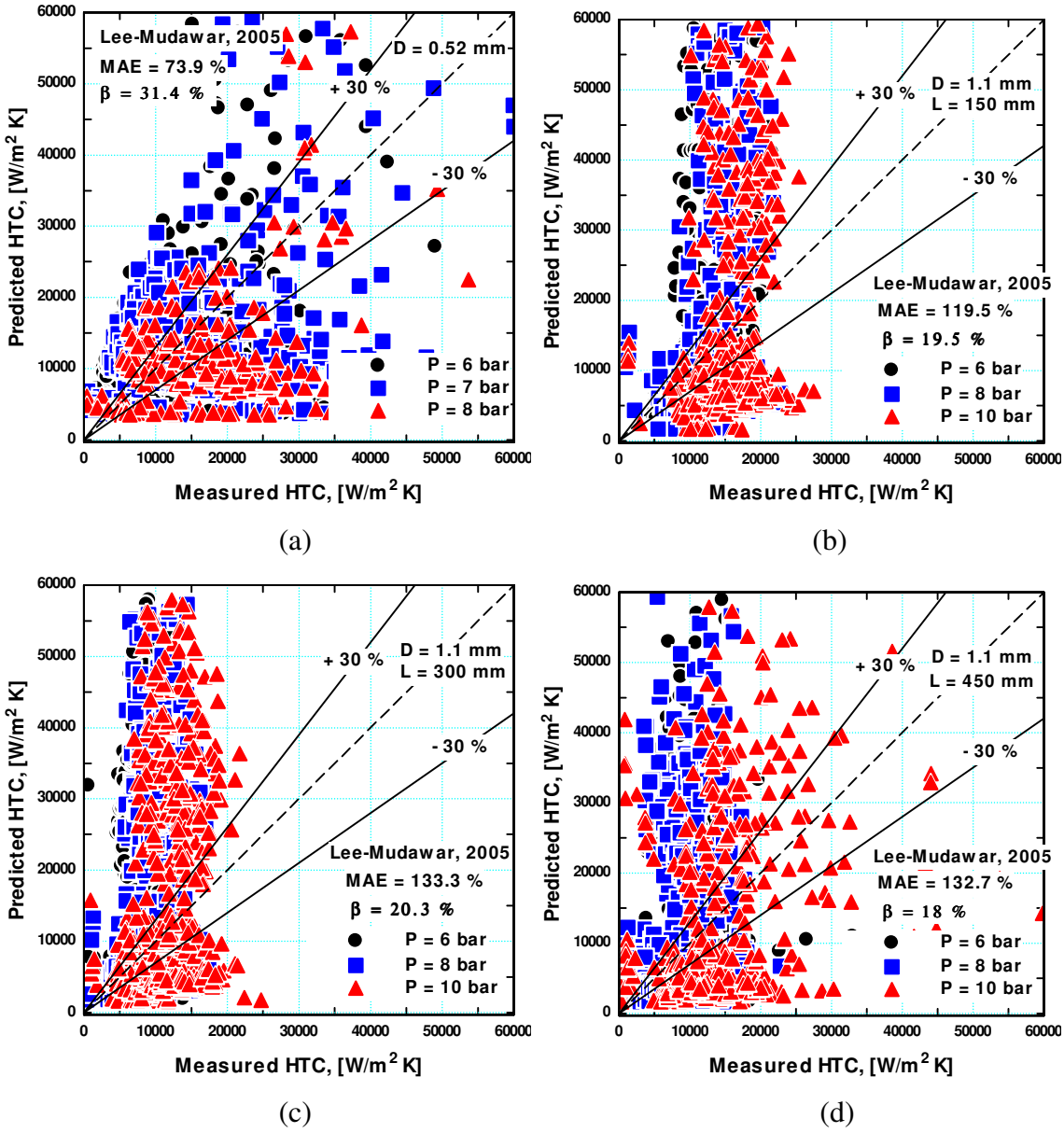

Figure 5.16 Comparison with the Lee and Mudawar (2005) correlation for (a) D = 0.52 mm, L = 100 mm, (b) D = 1.1 mm, L = 150 mm, (c) D = 1.1 mm, L = 300 mm and (d) D = 1.1 mm, L = 450 mm.

The Saitoh et al. (2007) correlation

Saitoh et al. (2007) proposed a correlation of the Chen type taking into account the effect of channel diameter. The correlation was based on a 2224 data points collected for R134a in horizontal tubes of diameters ranging from 0.51 to 11 mm. The effect of diameter was taken into consideration through incorporating the gas phase Weber number into the enhancement factor. The nucleate boiling suppression factor *S* was correlated in the same functional form proposed by Chen. For the nucleate boiling part,

they suggested using the nucleate pool boiling correlation of Stephan-Abdelsalam (1980) that was developed for refrigerants instead of using Forster-Zuber (1955) correlation.

The correlation was globally compared with the current experimental data in Fig. 5.17. It is obvious that, the correlation works better than the aforementioned correlations. It predicts 45.3 % of the micro-tube data within the error bands with an error value of 39.1 %. The correlation predicted the data of the shortest mini-tube reasonably well where 73.9 % of the data were predicted with an error value of 27.7 %. Similar to the abovementioned correlations, the performance of Saitoh et al. (2007) correlation gets worse as the heated length increases. However, the prediction in the longer tubes is still much better compared to the above correlations. The correlation succeeded to predict 54 – 63.3 of the longest tubes data (Fig. 5.17c and Fig. 5.17d), which is better than the other correlations.

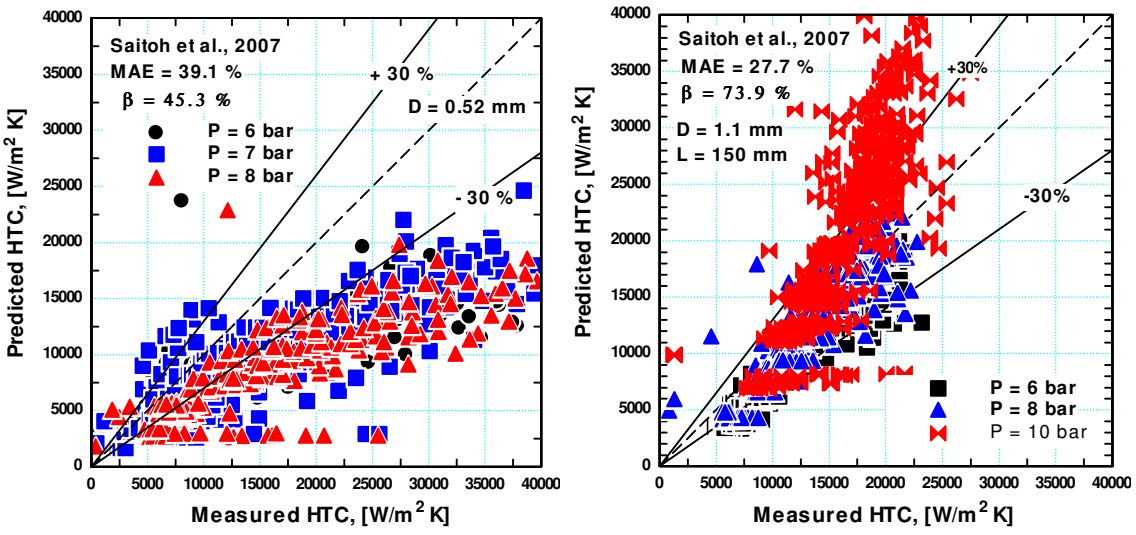

(a) (b)

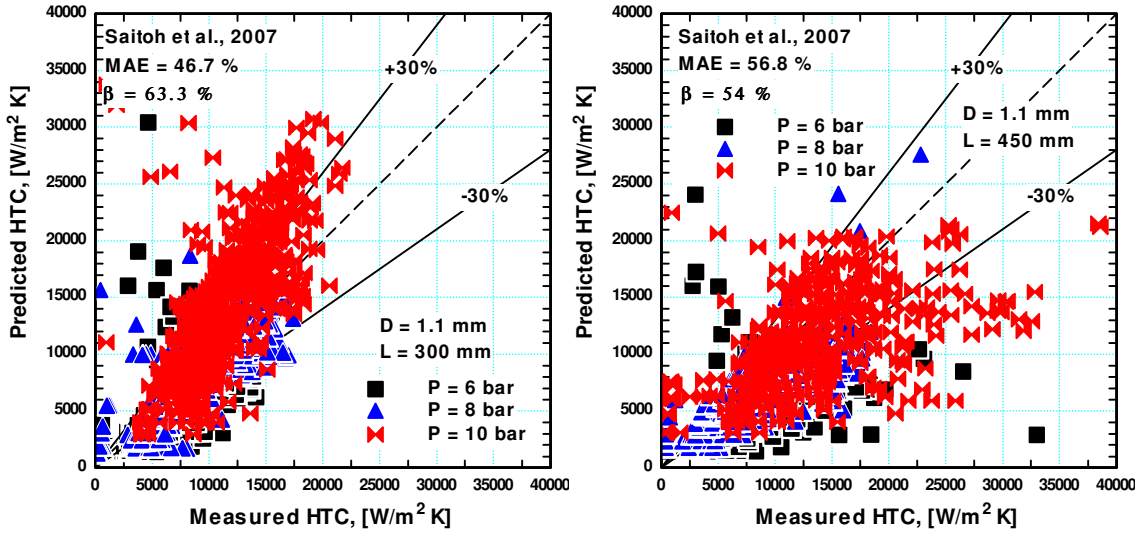

(c) (d)

Figure 5.17 Comparison with the Saitoh et al. (2007) correlation for (a) D = 0.52 mm, L = 100 mm, (b) D = 1.1 mm, L = 150 mm, (c) D = 1.1 mm, L = 300 mm and (d) D = 1.1 mm, L = 450 mm.

The Bertsch et al. (2009b) correlation

Bertsch et al. (2009b) proposed a correlation for predicting saturated flow boiling heat transfer coefficient in mini and microchannels. This correlation was developed based on a large experimental data base consisting of 3899 data points which were collected from 14 different experimental studies and included 12 different fluids including refrigerants and diameters ranging from 0.16 to 2.92 mm. The correlation was developed based on the Chen correlation. The Cooper correlation was recommended for the nucleate pool boiling term. The single phase heat transfer coefficient in the convective boiling term was calculated as the average of the single phase liquid heat transfer coefficient and single phase vapour heat transfer coefficient as given by Eq. (5.10). They have modified the convective boiling enhancement factor and correlated it as a function of vapour quality and the confinement number. The nucleate boiling suppression factor was found to be dependent on vapour quality only rather than Reynolds number. Thus they simply used the term $(1-x)$ as a nucleate boiling suppression factor.

$$h_{sp} = (1-x)h_{sp,L} + xh_{sp,g} \tag{5.10}$$

Figure 5.18 depicts the global comparison with the correlation of Bertsch et al. (2009b). The correlation predicts only about 55 % of the micro-tube data within the error bands with an error value of 37.6 %. For the mini-tube with L = 150 and 300 mm, the performance of the correlation was almost similar where about 60 % of the data were predicted within the error bands. As the heated length increased to 450 mm, the prediction gets worse where only 45.1 % of the data were predicted within the error bands. Looking at Fig. 5.8a for the micro tube, the correlation predicted heat transfer coefficient that increases with vapour quality towards the exit, which is similar to the experimental trend. For the mini tube, the correlation predicted heat transfer coefficient that sharply decreases with quality (Fig. 5.8b) or slightly decreases with vapour quality (Fig. 5.8c and Fig. 5.8d). This behaviour may be attributed to the functional form selected for the nucleate boiling suppression factor and the convective boiling enhancement factor. Though the convective boiling enhancement factor was correlated using the confinement number, it gives values that contradict the confinement principle. Confinement effects are significant when the confinement number is in excess of 0.5. So, it is expected that the higher the confinement number, the higher the enhancement in convective boiling. However, the proposed correlation for the convective boiling gives values that increase with decreasing the confinement number. Also, for a fixed value of the confinement number, the enhancement factor reaches a peak value at $x \approx 0.78$ after which it rapidly decreases with increasing vapour quality. Additionally, introducing the nucleate boiling suppression factor as a function of vapour quality only may not be enough. This is because nucleate boiling suppression seems to be strongly influenced by other parameters such as flow velocity and fluid properties that strongly influence the characteristics of the boundary layer next to the wall. The rapid decrease in the heat transfer coefficient with increasing vapour quality that was observed only in the shortest mini-tube (L = 150 mm) is attributed to the operation at much higher heat flux values compared to the other tubes. This high heat flux results in much higher nucleate pool boiling heat transfer coefficient according to the Cooper correlation, which when it is multiplied by the suppression factor $(1-x)$ results in the rapid decrease with quality.

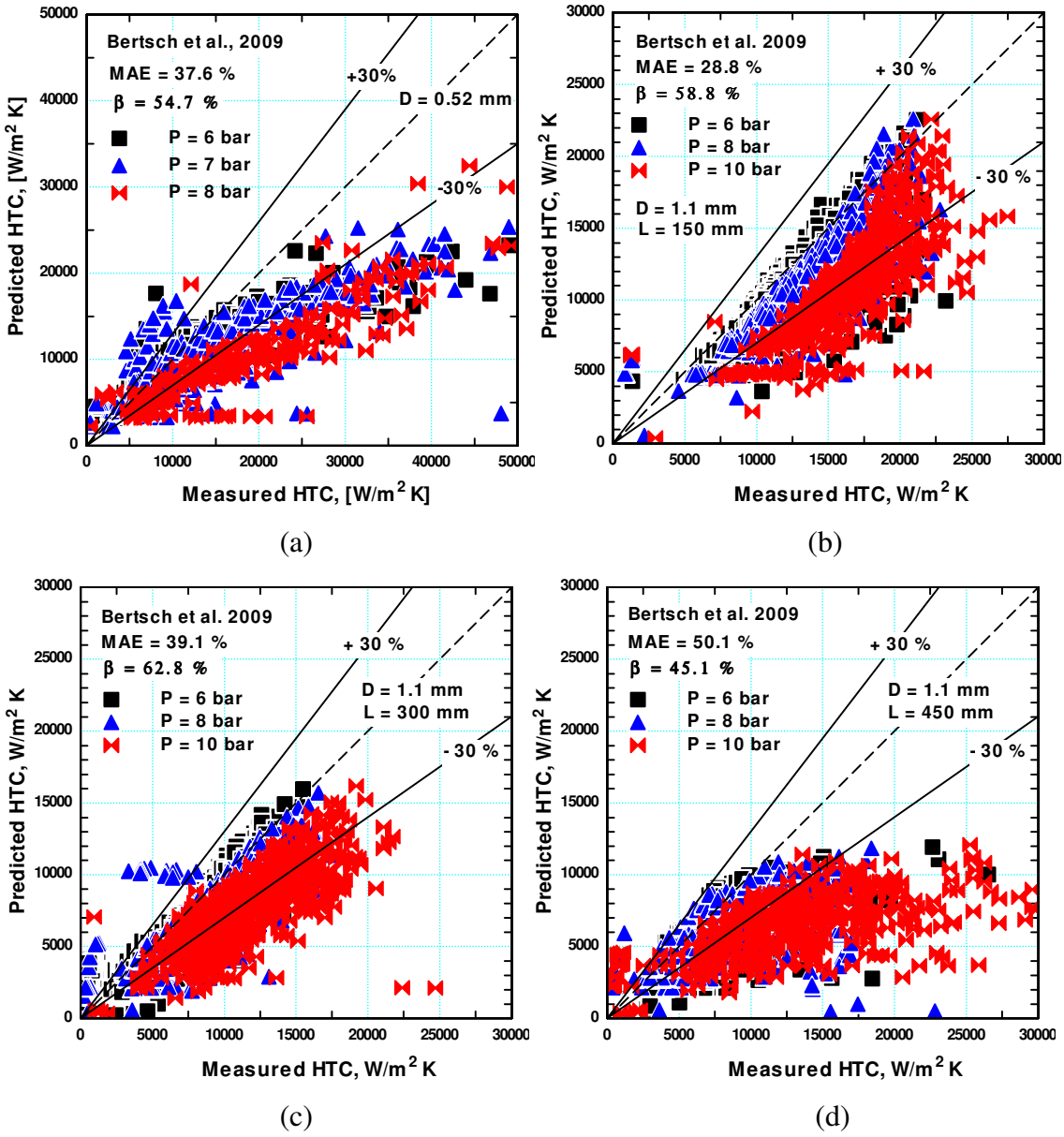

Figure 5.18 Comparison with the Bertsch et al. (2009) correlation for (a) D = 0.52 mm, L = 100 mm, (b) D = 1.1 mm, L = 150 mm, (c) D = 1.1 mm, L = 300 mm and (d) D = 1.1 mm, L = 450 mm.

The Mikielewicz (2010) correlation

Mikielewicz (2010) proposed a model based on the analogy between momentum transfer and energy transfer. The model started with the premise that the total energy dissipation in the flow is the sum of the energy dissipation due to shearing flow without nucleation and the energy dissipation due to nucleation as given by Eq. (5.11). Under steady state conditions in two phase flow, the energy dissipation was approximated by the viscous energy dissipation per unit volume in the boundary layer as given by Eq.

(5.12). Using the analogy between momentum and energy transfer, the two phase heat transfer coefficient was written in a form similar to Eq. (5.14). This equation is similar in form to the asymptotic model of Liu and Winterton (1991) with an exponent n = 2 but this exponent was obtained based on theoretical analysis rather than empirical adjustments. The convective heat transfer coefficient in Eq. (5.14) was expressed in terms of the frictional two phase multiplier as recommended by the Műller-Steinhagen and Heck (1986) correlation. The Cooper pool boiling correlation was recommended for the nucleate boiling term corrected by a factor that depends on the Reynolds number, Boiling number and the frictional two phase multiplier. The final functional of the correlation is given by Eq. (5.15) with the exponent $n = 0.9$ for turbulent flow and $n = 2$ for laminar flow.

$$E_{Total} = E_{Shear} + E_{Nucleation} \tag{5.11}$$

$$\frac{f_{Total}^2 \rho_L^2 U^4}{64\mu_L} = \frac{f_{Shear}^2 \rho_L^2 U^4}{64\mu_L} + \frac{f_{Nucleation}^2 \rho_L^2 U^4}{64\mu_L} \tag{5.12}$$

$$f_{Total}^2 = f_{Shear}^2 + f_{Nucleation}^2 \tag{5.13}$$

$$h_{tp}^2 = h_{Conv}^2 + h_{Nucleat}^2 \tag{5.14}$$

$$\frac{h_{tp}}{h_{sp,f}} = \sqrt{\phi_{MSH}^n + \frac{1}{1+P}\left(\frac{h_{Coop}}{h_{sp,L}}\right)^2} \tag{5.15}$$

$$P = 2.53\times10^{-3}\,\mathrm{Re}^{1.17}\,Bo^{0.6}\left(\phi_{MSH}-1\right)^{-0.65}$$

Figure 5.19 shows the global comparison with the correlation of Mikielewicz (2010). It is clear that the correlation could not predict more than 50 % of the micro-tube data within the error bands. On the other hand, the performance of the correlation is significantly influenced by the variation of the heated length of the mini-tube. For the shortest tube, Fig. 5.19b indicates that the correlation predicted reasonably 76.3 % of the data with a MAE value of 21.8%. For L = 300 mm, the correlation predicted only 65.3 % of the data within the error bands (Fig. 5.19c) and this value decreased to 45.8 % when the heated length increased to 450 mm (Fig. 19d). Figure 5.8 illustrates that the correlation predicts that the heat transfer coefficient increases moderately with increasing vapour quality. This may explain the success of the correlation in predicting

the data of the shortest tube where the heat transfer coefficient was independent of vapour quality.

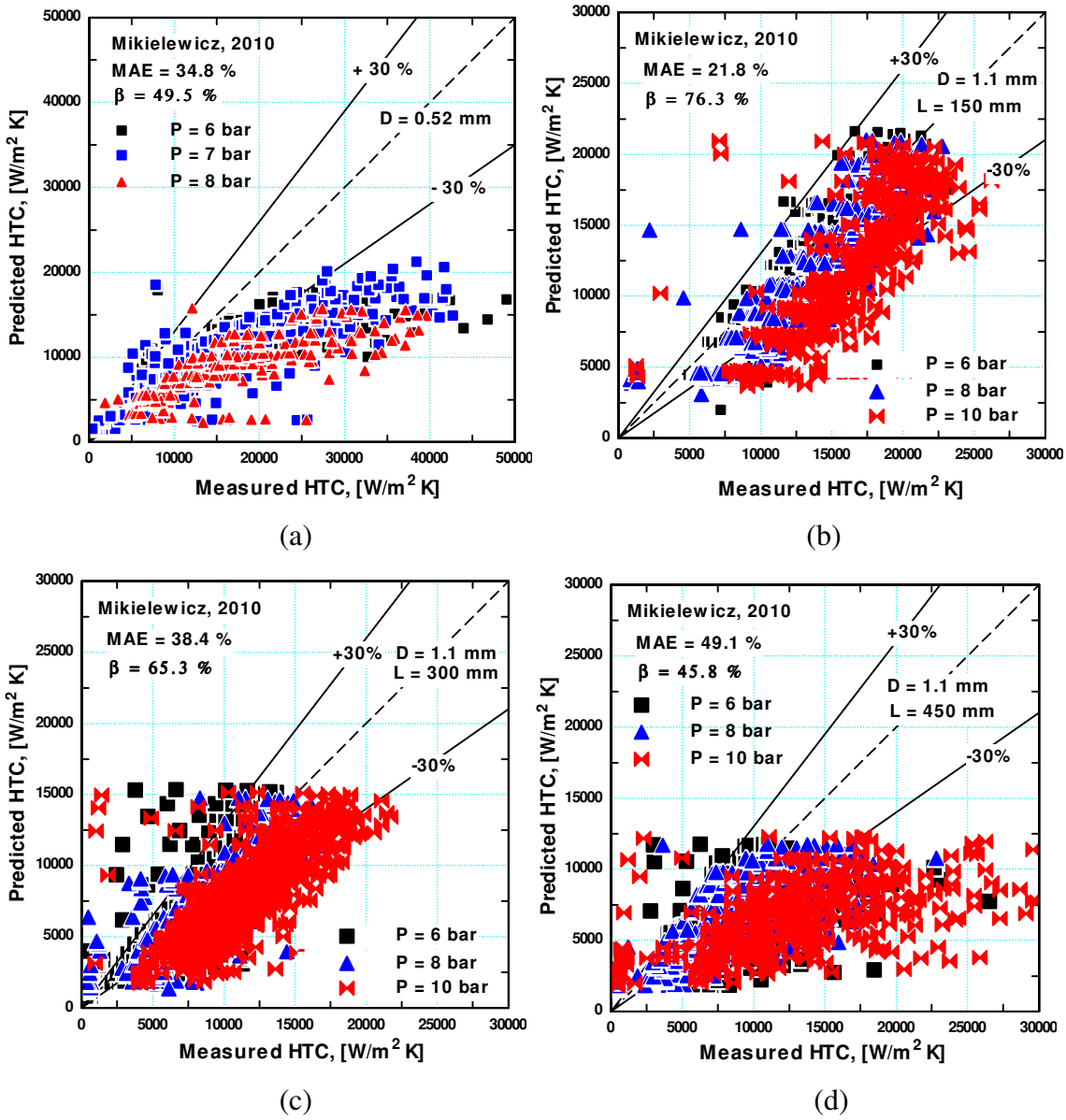

Figure 5.19 Comparison with the Mikielewicz (2010) correlation for (a) D = 0.52 mm, L = 100 mm, (b) D = 1.1 mm, L = 150 mm, (c) D = 1.1 mm, L = 300 mm and (d) D = 1.1 mm, L = 450 mm.

The Li and Wu (2010a) correlation

Li and Wu (2010a) collected a large number of experimental data points from the open literature covering saturated flow boiling heat transfer in mini/micro-channels. The database consists of 3744 data points and covers hydraulic diameters ranging from 0.16

to 3.1 mm with most data located in the laminar regime (Re < 2000). The difference between conventional channels and micro-channels arises from the relative significance of gravity, inertia, viscous and surface tension forces. Accordingly, they have correlated the data as a function of three dimensionless parameters namely boiling number, bond number and Reynolds number. The boiling number accounts for the heat and mass flux effects, Reynolds number accounts for inertia and viscous effects and Bond number accounts for gravity and surface tension effects. The final form of the correlation is given by Eq. (5.16).

$$\begin{aligned} h_{tp} &= 334 Bo^{0.3}\left(Bd\,\mathrm{Re}_L^{0.36}\right)^{0.4}\left(k_L/D\right) \\ &= 334 q^{0.3} G^{-0.3} h_{fg}^{-0.3} D^{0.4}\left[\sigma/g\Delta\rho\right]^{-0.2}(1-x)^{0.144} G^{0.144} D^{0.144}\mu_L^{0.144} D^{-1} k_L \\ &= 334 q^{0.3} G^{-0.156} D^{-0.456} h_{fg}^{-0.3}(1-x)^{0.144}\mu_L^{0.144}\left[\sigma/g\Delta\rho\right]^{-0.2} k_L \end{aligned} \quad (5.16)$$

The above equation predicts heat transfer coefficient that decreases very slowly with vapour quality in the low quality region and decreases with a higher rate in the high quality region; see Fig. 5.8. Figure 5.20 presents the global comparison with the above equation. For the micro-tube, Fig. 5.20a shows that the correlation predicts only 43 % of the data within the error bands with a high MAE value of 58.4 %. The performance of the correlation has improved in the mini-tube with heated lengths of 150 and 300 mm where about 70 % of the data were predicted within the error bands. However, the MAE value in the mini-tube with L = 150 mm was less than 30 % compared to 64.4 % for L = 300 mm. As mentioned before, the value of the MAE is usually influenced by the heat transfer coefficient value at the first location in the very low quality region and the delay in boiling incipience. As the heated length increased to 450 mm, the correlation predicted only 52.3 % of the data within the error bands with MAE value of 70.6 %. It can be concluded that, the correlation highly under-predicts the experimental values in the high quality region particularly when the measured heat transfer coefficient increases with vapour quality. Analysing Eq. (5.16) indicates that the heat transfer coefficient depends on heat flux, mass flux, tube diameter, vapour quality, surface tension, liquid viscosity, liquid-gas density difference, liquid thermal conductivity and latent heat. The exponents of the heat flux and the mass flux are 0.3 and - 0.156 respectively which reflects the small effect of theses two parameters on the heat transfer coefficient. The correlation predicts that the heat transfer coefficient increases with

decreasing tube diameter where the exponent of D is 0.456. Some investigators such as Saitoh et al. (2007), Karayiannis et al. (2008) and Consolini and Thome (2009) reported that the heat transfer coefficient increases with decreasing tube diameter.

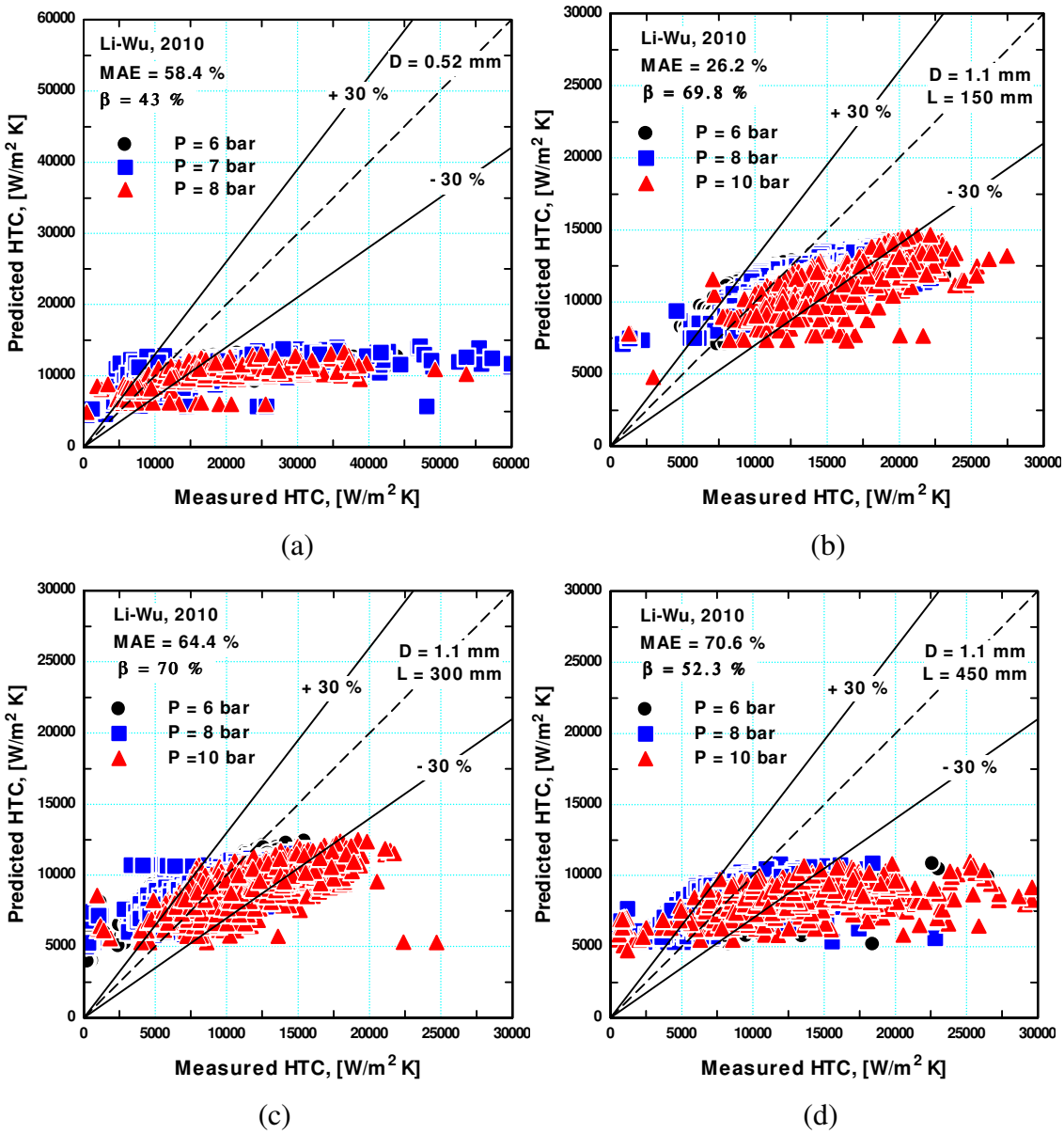

Figure 5.20 Comparison with the Li and Wu (2010) correlation for (a) D = 0.52 mm, L = 100 mm, (b) D = 1.1 mm, L = 150 mm, (c) D = 1.1 mm, L = 300 mm and (d) D = 1.1 mm, L = 450 mm.

The Cooper (1984) correlation

The Cooper correlation is one of the widely used pool boiling correlation. It takes into account the effects of fluid, reduced pressure, heat flux and surface roughness. The comparison of the flow boiling data with this correlation may assist in understanding the dominant heat transfer mechanism. If the experimental data agree totally with this correlation then it may be deduced that nucleate boiling is dominating. Figure 5.21 shows the global comparison with the Cooper correlation. Although the correlation was developed for nucleate pool boiling, the figure indicates that it predicts the experimental data much better than the evaluated macro and micro scale correlations. It predicted 51.5 % of the micro tube data within the ± 30 % error bands and with a MAE value of 34.4 %. For the shortest mini tube, the correlation performed very well where it predicted 85 % of the data within the ± 30 % error bands and with a MAE value of 19.3 %. As the heated length increased, the performance of the correlation gets worse compared to the shortest tube (see Fig. 5.21c and Fig. 5.21d). The performance of this correlation looks very consistent with the experimental results for each tube. In the micro tube, nucleate boiling dominated up to vapour quality value of about 0.4. This means that about 50 % of the data in this tube are located in the nucleate boiling regime, which agrees with the correlation where 51.5 % of the data were predicted very well. By contrast, the experiment indicated that all data before dryout (see Table 5.1) of the shortest mini tube (L = 150 mm) located in the nucleate boiling regime. Therefore the correlation performed very well with this tube (Fig. 5.21b). As the heated length of the mini tube was increased, both nucleate and convective boiling exists, which makes the performance of the correlation worse.

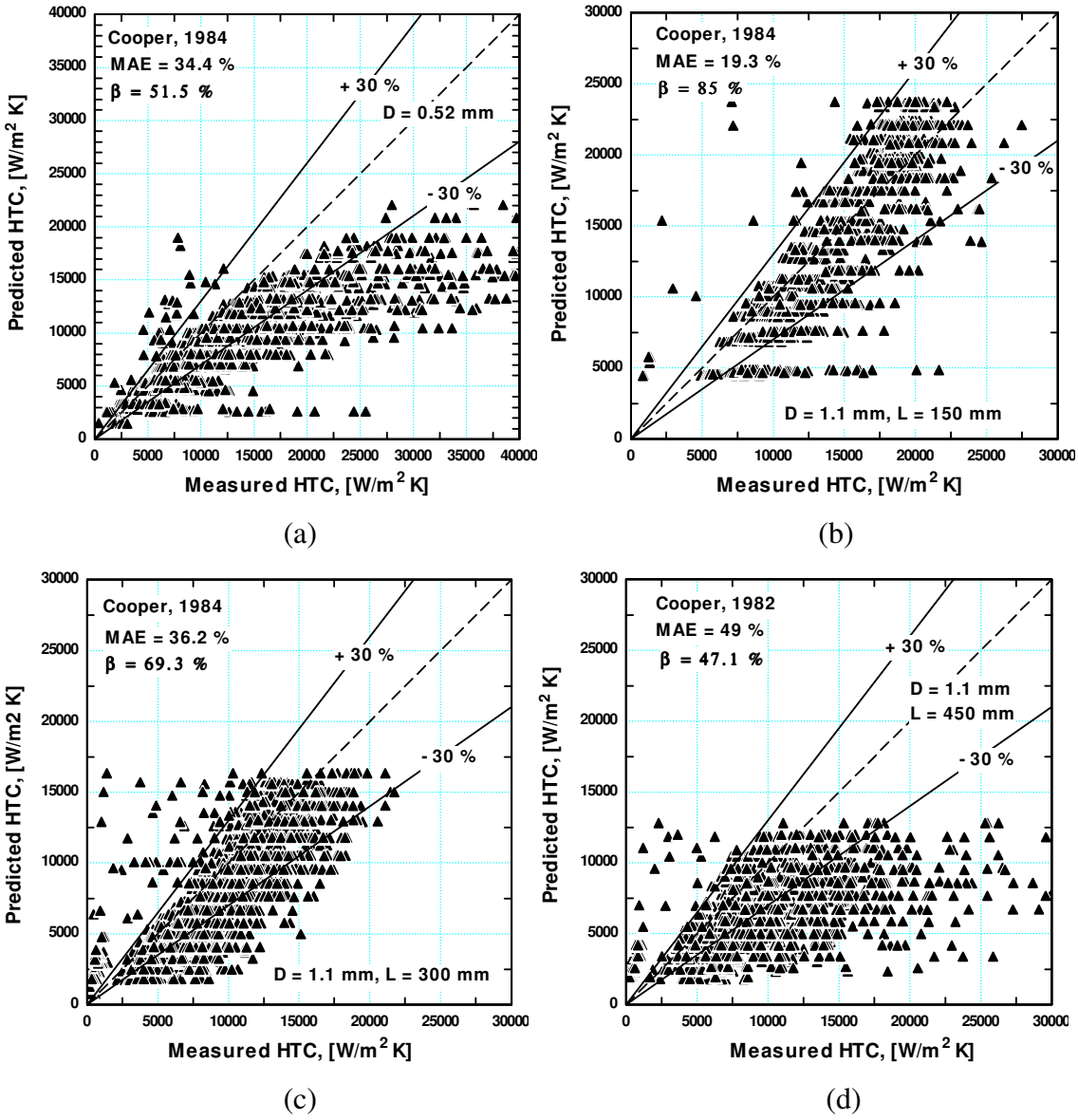

Figure 5.21 Comparison with Cooper (1984) correlation for (a) D = 0.52 mm, L = 100 mm, (b) D = 1.1 mm, L = 150 mm, (c) D = 1.1 mm, L = 300 mm and (d) D = 1.1 mm, L = 450 mm.

5.4 Heat transfer models

This section presents a comparison between the experimental data and two mechanistic models developed for flow boiling heat transfer in micro-channels. The two selected models include the three zone film evaporation model proposed by Thome et al. (2004) and the recent coalescing bubble evaporation model proposed by Consolini and Thome (2010). The annular flow models proposed by Qu and Mudawar (2003b) and Boye et al. (2007) were excluded from the comparison since these two models were developed for water. Water has different properties compared to refrigerants which affects the

characteristics of the liquid film plus annular flow develops too early at very low vapour quality values in case of water. Qu and Mudawar (2003b) included liquid droplet entrainment in their model which was believed to explain the decreasing trend of the heat transfer coefficient with vapour quality. In the current study, liquid droplet entrainment was not clearly observed. The model of Boye et al. (2007) was a one dimensional model that predicts the variation in film thickness as a function of vapour quality. The predicted heat transfer coefficient using this model slightly increases with quality without any heat flux effect which is not the case in the current study.

5.4.1 The three zone evaporation model

Jacobi and Thome (2002) proposed a heat transfer model (two-zone model) based on the premise that thin-film evaporation is the most important mechanism in microchannels. At a fixed location, a pair composed of elongated bubble and liquid slug was assumed to pass with a velocity equal to the homogeneous velocity. Principally, this model is based on the idea that during elongated bubble flow a thin liquid film of uniform thickness forms around the bubble and the film becomes thinner as evaporation starts until the arrival of the next liquid slug. This model requires the knowledge of the critical nucleation radius or effective wall superheat in order to estimate the frequency of the pairs and also requires the knowledge of initial film thickness. When Jacobi and Thome (2002) compared the model with the experimental data with initial film thickness in the order of 10 – 20 μm, the model managed to predict the data very well. Thome et al. (2004) extended this model to include the passage of a vapour slug when dryout occurs and called it "three-zone model". In this version, a cyclic passage of liquid slug, elongated bubble and vapour slug was considered. The model assumptions were: (i) homogeneous flow, uniform and constant heat flux, (ii) all energy entering the fluid was consumed in vaporizing the liquid, (iii) thermal inertia of channel wall is neglected, (v) the film remains smooth and attached to the wall. Based on the work of Moriyama and Inoue (1996) and applying an asymptotic approach, they got a continuous relation for calculating the initial film thickness. Dupont et al. (2004) assessed the model against a large experimental database and optimised the pair generation frequency, the minimum film thickness and the adjustable constant in the initial film thickness correlation. The model predicts the local time averaged heat

transfer coefficient over the three zones (liquid slug, elongated bubble and dryout) and the equations used in the calculations are presented as follows:

$$h_{tp}(z) = \frac{t_L}{\tau_b} h_L(z) + \frac{t_{film}}{\tau_b} h_{film}(z) + \frac{t_{dry}}{\tau_b} h_v(z) \tag{5.17}$$

The period τ_b was calculated from the bubble generation frequency f_b which was optimized by Dupont et al. (2004) using a large database.

$$\tau_b = \frac{1}{f_b}, \quad f_b = \left(\frac{q}{q_{ref}} \right)^{1.74}, \quad q_{ref} = 3328 \left(\frac{P_{sat}}{P_{crit}} \right)^{-0.5} \tag{5.18}$$

The residence time for each zone was deduced from the mass and energy balance with the assumption of homogeneous flow and they are given as:

$$t_L = \frac{\tau_b}{1 + \frac{\rho_L}{\rho_v} \frac{x}{1-x}} \tag{5.19}$$

$$t_v = \frac{\tau_b}{1 + \frac{\rho_v}{\rho_L} \frac{1-x}{x}} \tag{5.20}$$

$$t_{dry\ film}(z) = \frac{\rho_L h_{fg}}{q} \left[\delta_0(z) - \delta_{\min} \right] \tag{5.21}$$

The initial film thickness δ_0 was calculated using the empirical relations given by Moriyama and Inoue (1996) after modifying it by an empirical constant $C_{\delta 0} = 0.29$ and formulating it in a continuous functional form as:

$$\frac{\delta_0}{D} = C_{\delta 0} \left(3 \sqrt{\frac{\upsilon_l}{U_p D}} \right)^{0.84} \left[\left(0.07 Bd^{0.41} \right)^{-8} + 0.1^{-8} \right]^{-1/8} \tag{2.22}$$

The minimum film thickness $\delta_{\min}$ in Eq. (5.21) was taken as 0.3 μm which was recommended by Dupont et al. (2004) based on the optimization analysis. The pair velocity U_p and Bond number *(Bd)* are defined as:

$$U_p = G\left[\frac{x}{\rho_v} + \frac{1-x}{\rho_L}\right] \tag{2.23}$$

$$Bd = \frac{\rho_L D}{\sigma} U_p^2 \tag{2.24}$$

Based on Eqs (5.20 and 5.21), if $t_{dry_{film}} > t_v$ then no dryout will occur. $t_{film} = t_v$ and the end film thickness δ_{end} is calculated as;

$$\delta(z,t) = \delta_0(z) - \frac{q}{\rho_l h_{lg}} t \tag{5.25}$$

If $t_{dry_{film}} < t_v$ then dryout occurs, $t_{film} = t_{dry_{film}}$, $t_{dry} = t_v - t_{film}$ and the end film thickness equal to the minimum film thickness value (0.3 μm). The single phase liquid and vapour heat transfer confidents h_L and h_v were calculated from the local Nusselt number correlations of London and Shah for developing laminar flow and Gnielinski for transition and turbulent flow that were given by VDI (1997). In the evaporating liquid film region, the local heat transfer coefficient was given as:

$$h_{film}(z) = \frac{k_L}{\delta_0 - \delta_{end}} \ln\left(\frac{\delta_0}{\delta_{end}}\right) \tag{5.26}$$

Figure 5.22 depicts the comparison between the measured heat transfer coefficient and the three-zone model on the *h-x* plane at P = 6 bar and G = 300 kg/m^2 s while Fig. 5.23 shows the global comparison. Since the model was developed for elongated bubbles (slug) flow, the transition line from coalescence bubble regime into annular flow regime is shown also on Fig. 5.22. It is clear from the figure that the predicted heat transfer coefficient jumps to a peak value at x ≈ 0 then it decreases continuously with increasing vapour quality. The behaviour of the model at x ≈ 0 agrees with the experimental behaviour but highly under-predicts the values at the first thermocouple location. This could be due to the high pressure drop at the onset of boiling that was not taken into

consideration by the model. Pressure drop significantly influences the local saturation temperature and consequently the heat transfer coefficient. Inspecting Fig. 5.22a for the micro-tube, the model could not predict the increasing trend of the heat transfer coefficient with vapour quality and there is an overall partial agreement over a narrow quality range. This is also clear from the global comparison in Fig. 5.23a where the model predicted only 42 % of the data within the ± 30 % error bands at a MAE value of 39.2 %. It is worth noting that, Fig. 5.22 indicates for all tubes that the model tends to match the experimental values or slightly under-predicts the values at low to intermediate heat fluxes. On the other hand, the model tends to highly over-predict the data at high heat fluxes which is clear in Fig. 5.22b for the shortest mini-tube. However, the model predicted the trend very well in this tube. The performance of the model at high heat flux may be due to the strong effect of heat flux on the pair frequency that is used in the model. The frequency was calculated using an empirical equation based on an optimization study. It is worth mentioning that, the pair frequency significantly affects the magnitudes of the predicted heat transfer coefficient and it shifts the predicted values up or down. Shiferaw et al. (2007) assessed the three zone evaporation model using experimental data for R134a and tubes with diameters of 4.26 mm and 2.01 mm. They reported that the model satisfactorily predicted the data and they referred to the features of the model that require further modifications. Theses features include the bubble frequency, the initial film thickness, considering the local pressure fluctuations and considering nucleation before the location of the onset of confined bubble. The model performed very well in this shortest mini tube where it predicted 76 % of the data within the ± 30 % error bands at MAE value of 24 % (Fig. 5.23b). As the heated length increased (Figs. 5.22c and 5.22d), the heat transfer coefficient exhibited an increasing trend towards the exit, similar to the micro-tube, which the model can not predict. However, the performance of the model in the tube with L = 300 mm was similar to that in the shortest tube where it predicted 75.8 % of the data within the ± 30 % error bands but at higher MAE value of 35.7 % (Fig. 5.23c). On the contrary, the performance of the model decreased in the longest tube where it predicted only 55 % of the data within the ± 30 % error bands at a MAE value of 48 % (Fig. 5.23d).

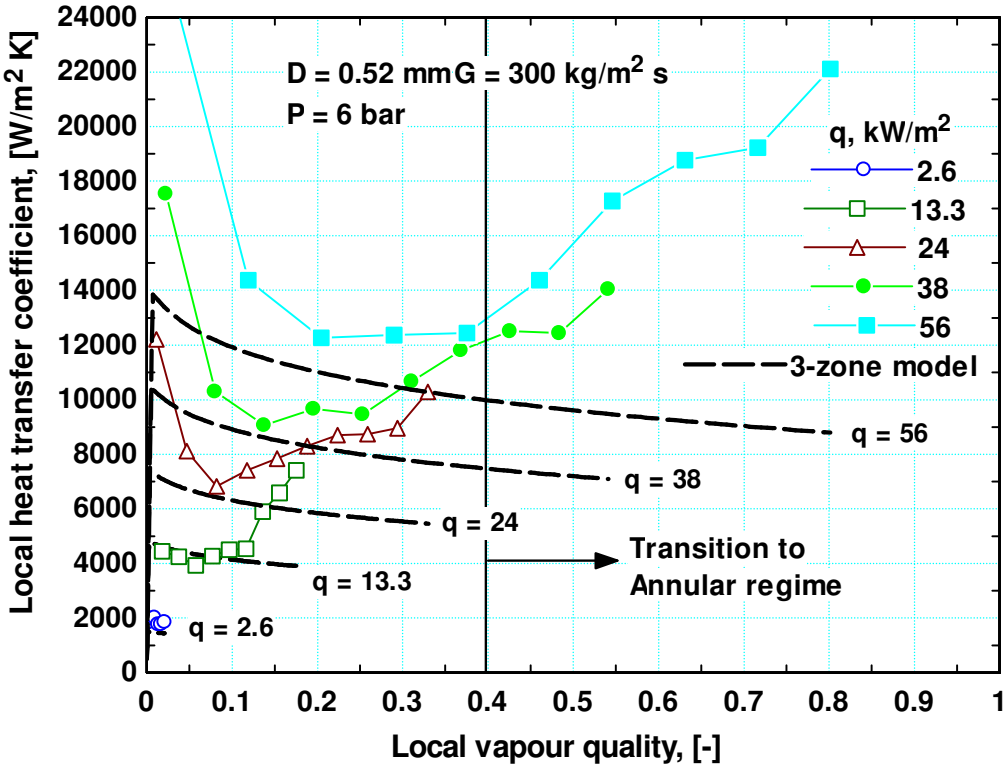
D = 0.52 mm G = 300 kg/m2 s
P = 6 bar
q, kW/m2
2.6
13.3
24
38
56
3-zone model
q = 56
q = 38
q = 24
q = 13.3
q = 2.6
Transition to
Annular regime
Local heat transfer coefficient, [W/m2 K]
Local vapour quality, [-]

(a)

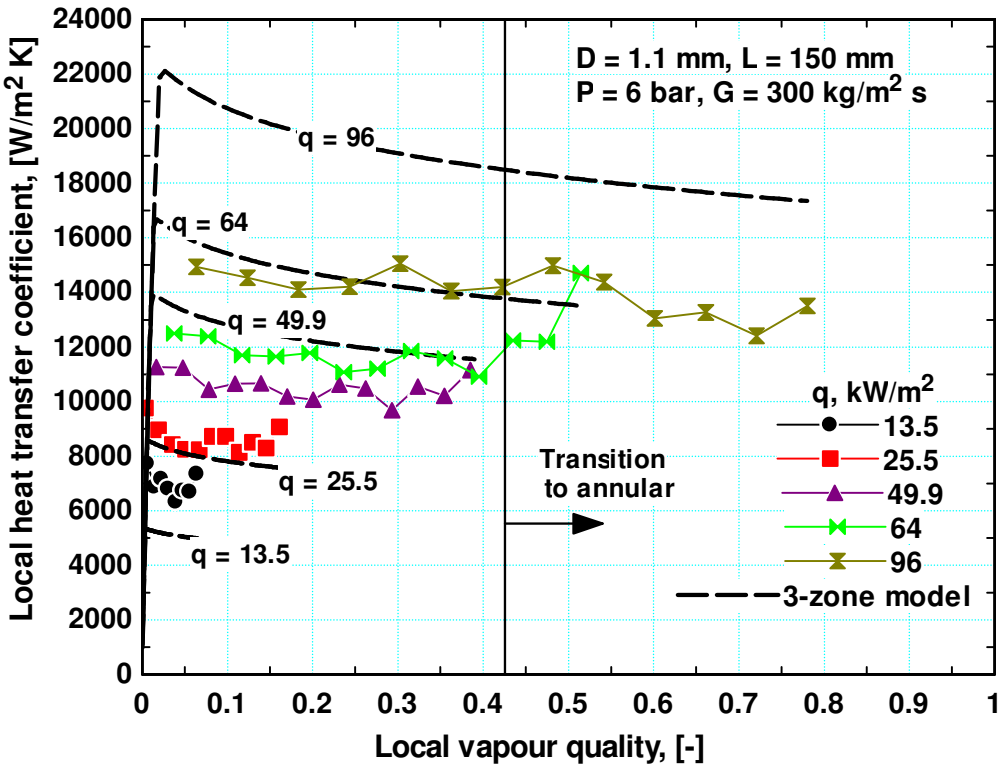
D = 1.1 mm, L = 150 mm
P = 6 bar, G = 300 kg/m2 s
q = 96
q = 64
q = 49.9
q = 25.5
q = 13.5
Transition
to annular
q, kW/m2
13.5
25.5
49.9
64
96
3-zone model
Local heat transfer coefficient, [W/m2 K]
Local vapour quality, [-]

(b)

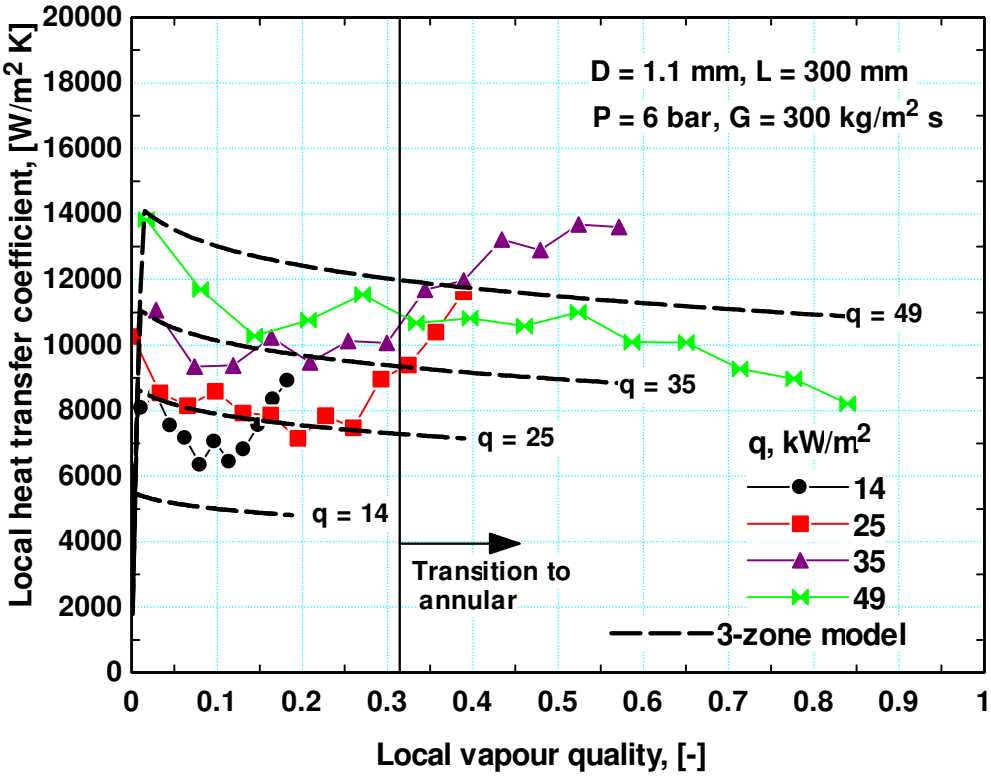

(c)

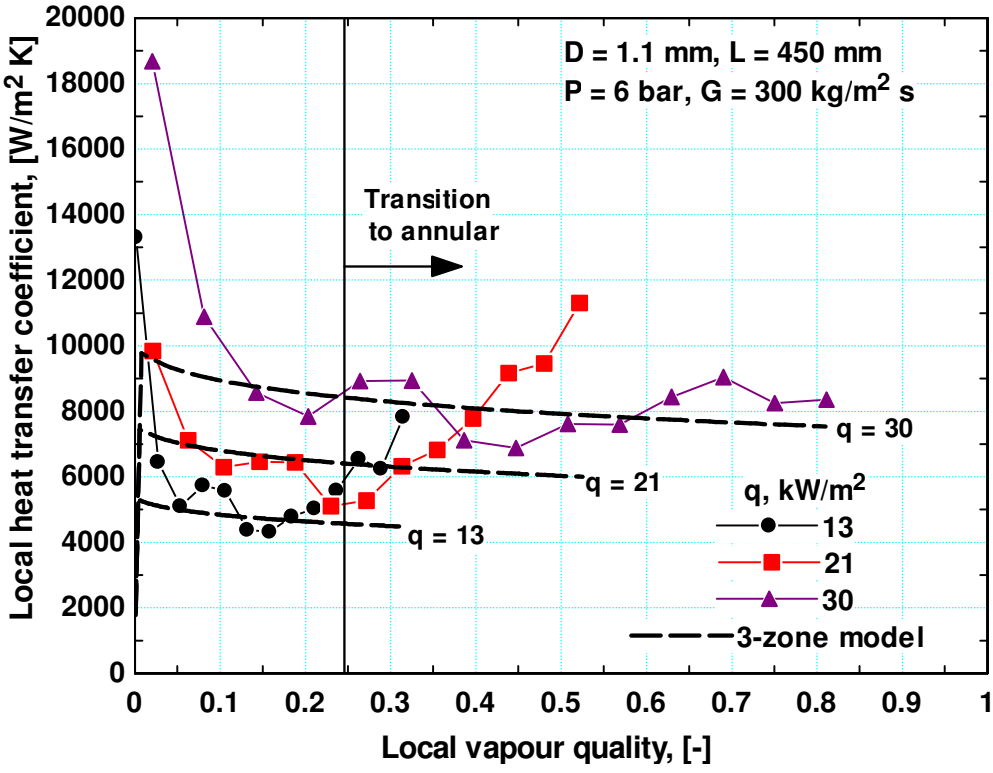

(d)

Figure 5.22 The local comparison with the Thome et al. (2004) three zone model at G = 300 kg/m2 s, P = 6 bar for (a) D = 0.52 mm, L = 100 mm, (b) D = 1.1 mm, L = 150 mm, (c) D = 1.1 mm, L = 300 mm and (d) D = 1.1 mm, L = 450 mm.

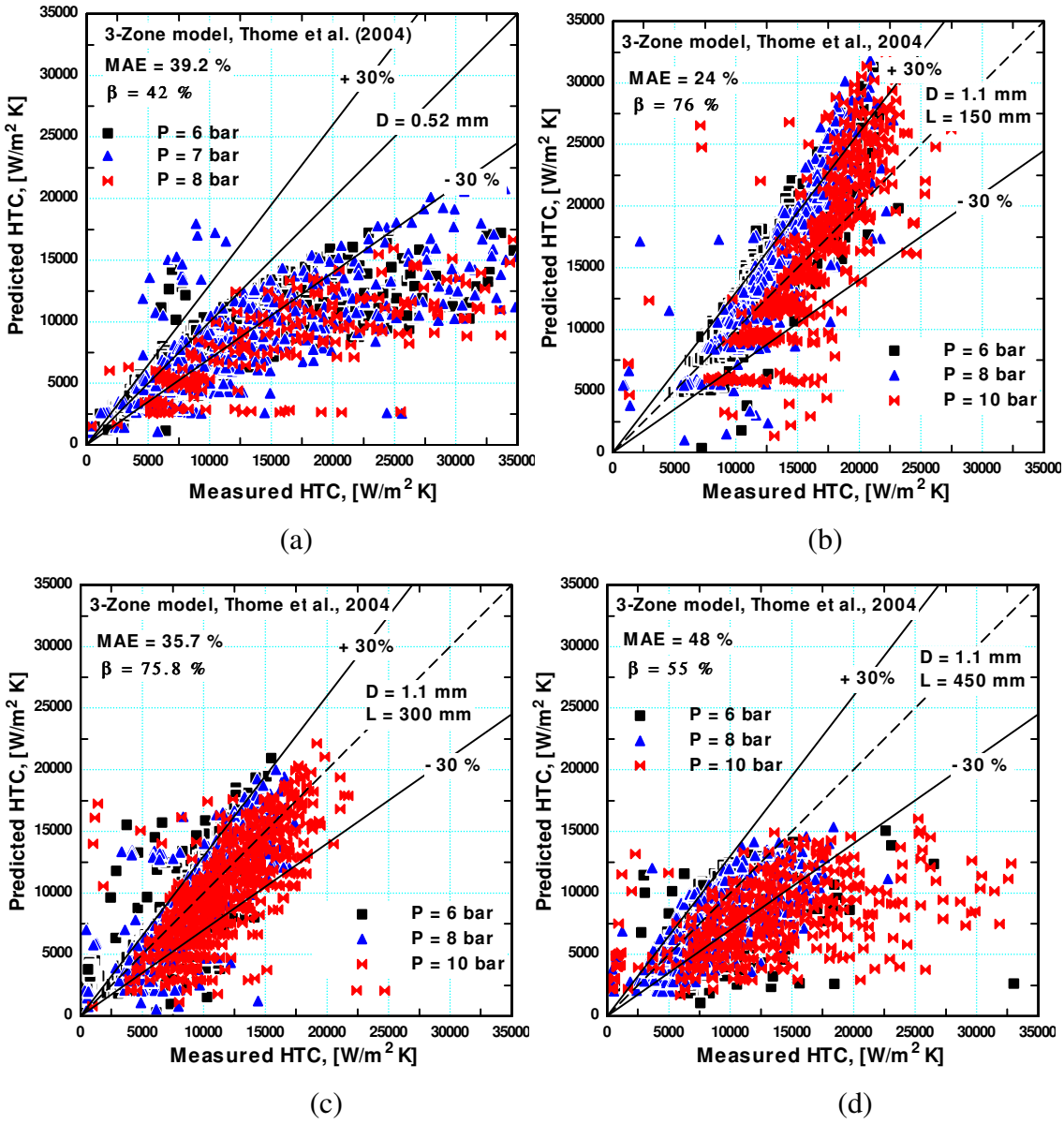

Figure 5.23 Comparison with the Thome et al. (2004) three-zone model for (a) D = 0.52 mm, L = 100 mm, (b) D = 1.1 mm, L = 150 mm, (c) D = 1.1 mm, L = 300 mm and (d) D = 1.1 mm, L = 450 mm.

5.4.2 The coalescing bubbles evaporation model

The three-zone evaporation model presented above did not take into account the coalescence between the consecutive bubbles. So, Consolini and Thome (2010) developed a one dimensional slug flow model that takes bubbles coalescence into consideration. The model assumes that: (i) the two phases are in thermodynamic equilibrium, (ii) the bubbles nucleate periodically only at x = 0, (iii) the bubbles depart

from the heated wall only axially without radial detachment, (iv) the liquid film is laminar and driven only by interfacial shear, (v) the flow is axi-symmetry and the interface of the liquid film varies linearly in the axial direction, (vi) heat transfer to the liquid slug and dry patches is negligible, (vii) pressure drop is negligible, the film thickness is small compared to channel diameter and heat flux is constant. The principle equations of the model that are required only for calculations are presented here whereas the details of the derivations of the equations can be found in the paper. Figure 5.23 illustrates the control volumes used in their analysis in order to understand the model parameters presented here. They selected a control volume such that it has a stationary boundary at channel inlet where all liquid flow enters and a moving boundary with a velocity equal to bubble nose velocity (W_N); see Fig. 5.24a.

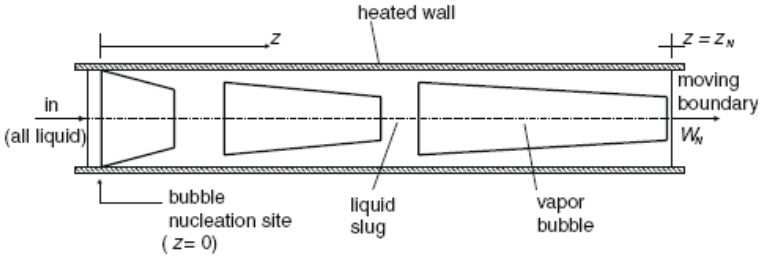

(a)

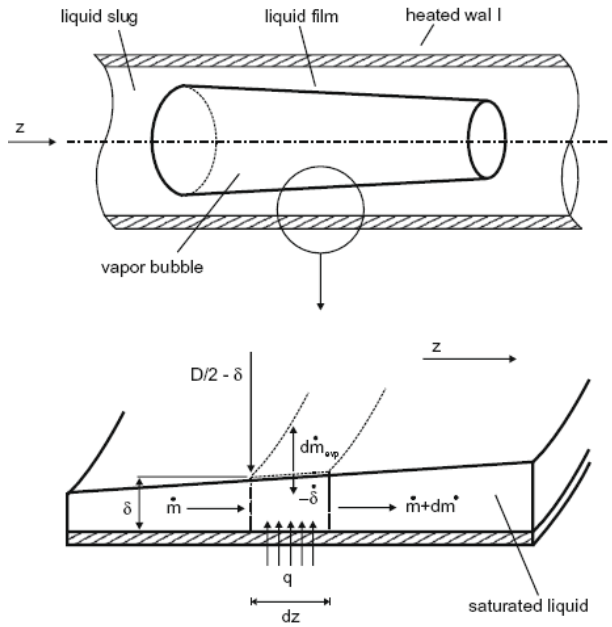

(b)

Figure 5.24 The control volumes used by Consolini and Thome (2010) (a) for the velocity and location of bubble nose and (b) for the film evaporation

Applying mass and energy conservations on this control volume (Fig. 5.24a), the axial position of the bubble nose was expressed as:

$$Z_N(t) = \frac{G}{\rho_L}\frac{\rho_v h_{fg} D}{4q}\left[\exp\left(\frac{4q}{\rho_v h_{fg} D}t\right) - 1\right] \tag{5.27}$$

Applying the conservation equations on the control volume in Fig. 5.24b, the variation of the film thickness with time was expressed as:

$$\delta(t,z) = \frac{\mu_L}{\tau_i}\frac{Z}{t} - \frac{q}{2\rho_L h_{fg}}t \tag{5.28}$$

The above equation represents the behaviour of the liquid film deposited by a liquid slug during its passage through the channel. The film thickness at the nose of the bubble can be calculated by substituting Eq. (5.27) into Eq. (5.28) as follows:

$$\delta_N(t,z) = \frac{\mu_L}{\tau_i}\frac{1}{t}\frac{G}{\rho_L}\frac{\rho_v h_{fg} D}{4q}\left[\exp\left(\frac{4q}{\rho_v h_{fg} D}t\right) - 1\right] - \frac{q}{2\rho_L h_{fg}}t \tag{5.29}$$

The initial film thickness at the instant the bubble forms was deduced from the above equation by taking the limit as time *(t)* approaches zero.

$$\delta_0 = \frac{\mu_L}{\tau_i}\frac{G}{\rho_L} \tag{5.30}$$

The above equations are for elongated bubbles without coalescence. To take bubbles coalescence into account, the above film thickness equations were modified such that it takes into account the additional liquid mass displaced into the film due to coalescence. Two boundaries of vapour qualities were identified namely the transition into coalescing regime x_c and the transition into annular x_a. These boundaries were calculated using the empirical equations given by Revellin and Thome (2007c). The

new expression for the liquid film thickness after replacing the local position z with the local vapour quality x is given as:

$$\delta\ (t,x) = \frac{\mu_L}{\tau_i}\frac{x}{t}\frac{Gh_{fg}D}{4q} - \frac{q}{2\rho_L h_{fg}}t\left[1-\psi_C\left(\frac{t^2-t_C^2}{t^2}\right)\right] \tag{5.31}$$

where t_C represents the time at which the bubble nose reaches the coalescing bubble mode boundary defined at x $= x_c$. This time was estimated from Eq. (5.27) after substituting Z in terms of quality x_c. The term ψ_C accounts for the incremental mass entered the liquid film due to coalescence and it was expressed as:

$$\psi_C = \varsigma\beta\left(\frac{1-x_C}{x_a-x_C}\right) \tag{5.32}$$

The local heat transfer coefficient was given as:

$$h_{tp}(x) = f_b \int_{1/f} \frac{k_L}{\delta(t,x)}dt \tag{5.33}$$

where f_b is the bubbles frequency proposed in a functional form such that its value equal zero when x = x_a and reaches its maximum when x = x_c as given by Eq. (5.34).

$$\frac{f_b}{f_{\max}} = \left(\frac{x_a-x}{x_a-x_c}\right)^{\beta} \tag{5.34}$$

Integrating Eq. (5.33), the final expression for the local time average heat transfer coefficient was given as:

$$h_{tp}(x) = \frac{k_L}{D}\frac{\left(\frac{\rho_L}{\rho_V}\right)\left[\left(\frac{x_a-x}{x_a-x_c}\right)^{\beta}\right]^{\gamma}\ln\left(\frac{1-\theta_{1C}}{1-\theta_{2C}}\right)}{Bo\left(1-\psi_C\right)} \tag{5.35}$$

$$\gamma = \left(\frac{x_a - x}{x_a - x_c} \right)^{\chi} \tag{5.36}$$

where

$$\theta_{1C} = \frac{(1-\psi_C)\ln^2\left(1+\frac{\rho_L}{\rho_v}x_c\right)}{\theta_{3C}}, \qquad \theta_{2C} = \frac{(1-\psi_C)\left[\ln\left(1+\frac{\rho_L}{\rho_v}x_c\right)+4Bo\right]^2}{\theta_{3C}}$$

$$\theta_{3C} = 8\frac{\mu_L}{\tau_i}\frac{G}{\rho_v D}\frac{\rho_L}{\rho_v}x_c - \psi_C \ln^2\left(1+\frac{\rho_L}{\rho_v}x_c\right), \quad Bo = \frac{q}{\rho_v h_{fg} D f_{\max}}$$

To predict the heat transfer coefficient using Eq. (5.35), five parameters are need to be identified first namely $\tau_i, f_{\max}$, β, ς and χ. The interfacial shear stress τ_i was empirically correlated as given by Eq. (5.37) while the maximum bubble frequency $f_{\max}$ was empirically correlated by Eq. (5.38). The best fit value of the other parameters was found to be $\beta = 1$, $\varsigma = 0.002$, $\chi = 3$.

$$\tau_i = \left(f_q + f_{v,Blasius}\right)\frac{G^2 x_c^2}{2\rho_v} \tag{5.37}$$

$$f_{\max} = 0.004\left(\frac{q}{\sigma}\right)\left(\frac{\sigma^3}{q^2 D^3 \rho_v}\right) \tag{5.38}$$

The friction factor f_q was incorporated to account for the friction due to evaporation and was empirically correlated as:

$$f_q = 304\left(\frac{GD}{\mu_L}\right)^{-1.16}\left(\frac{\rho_L}{\rho_v}\right)^{-1.74}\left(\frac{\mu_L}{\mu_v}\right)^{1.43} x_c^{-2}\left[1-\exp\left(-\frac{qD}{h_{fg}\mu_L}\right)\right] \tag{5.39}$$

The transitional qualities are calculated as follows:

$$x_c = 0.763\left(\frac{q\rho_v\sigma}{\mu_L h_{fg} G^2}\right)^{0.39} \quad \text{and} \quad x_a = 1.4\times10^{-4}\left(\frac{GD}{\mu_L}\right)^{1.47}\left(\frac{G^2 D}{\rho_L \sigma}\right)^{-1.23} \tag{5.40}$$

Figure 5.25 depicts the comparison between the model and the experimental data on the *h-x* plane for the micro-tube and the mini-tube with the shortest heated length at P = 6 bar and G = 300 kg/m^2 s while the global comparison is shown in Fig. 5.26. All data included in the comparison are located within the applicability range of the model, i.e. $x_c < x < x_a$. It is clear from Fig. 5.25a that the model predicted reasonably the trend and magnitudes for some heat fluxes whereas the model highly under-predicted the data of the mini-tube (Fig. 5.25b). The global comparison in Fig. 5.26 indicates that the model predicts poorly the experimental values in all tubes with better performance in the micro-tube. It is worth noting that, the three-zone model performs globally better than this new model though both models assume thin film evaporation. The reason could be the size of the data bank that was used to correlate the empirical parameters in the two models. In the recent model, only data for tubes with diameters 0.51 and 0.79 mm and fluids R134a, R245fa and R236fa were used. In the three-zone model, the empirical parameters were optimized using a large data bank consisting of various fluids and tube diameters.

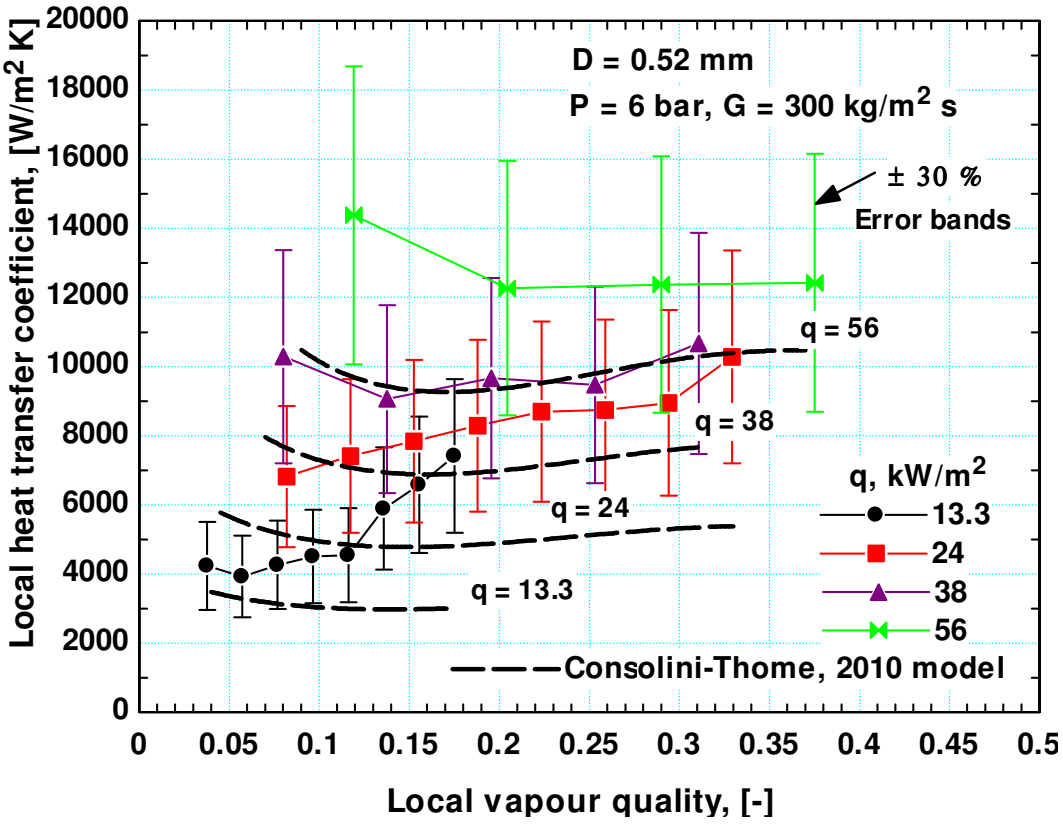

(a)

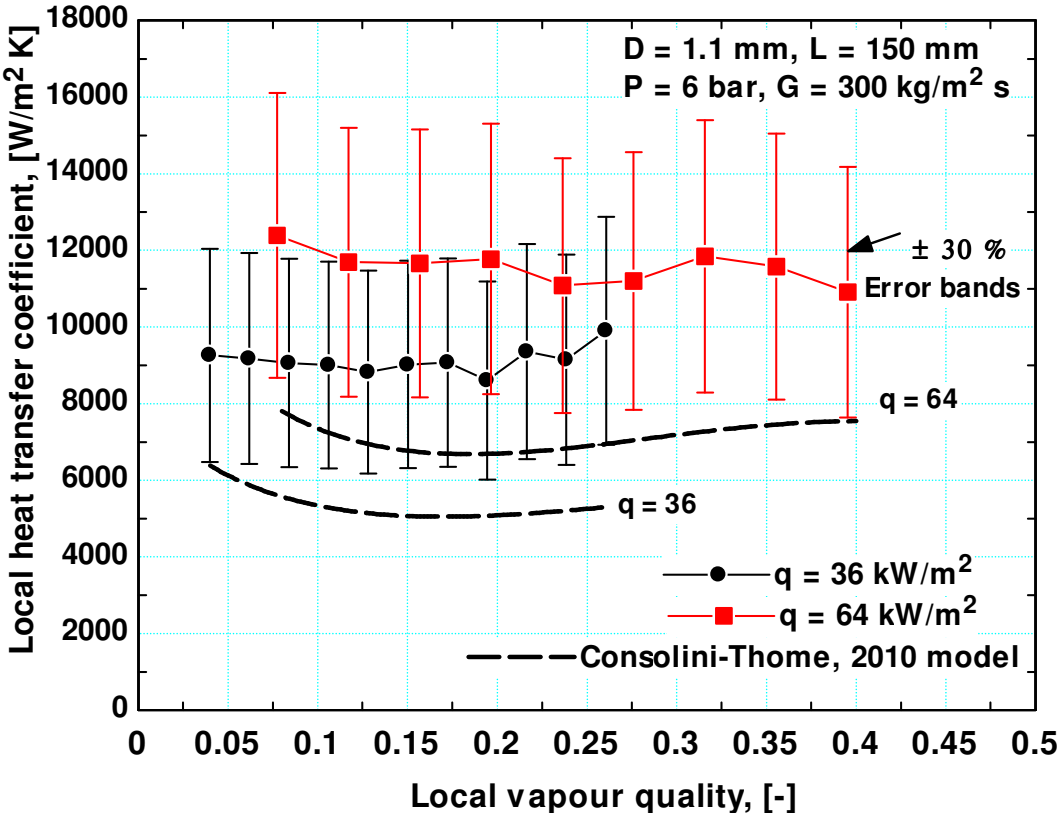

(b)

Figure 5.25 Comparison with the Consolini-Thome (2010) model for (a) D = 0.52 mm, L = 100 mm, (b) D = 1.1 mm, L = 150 mm at P = 6 bar and G = 300 kg/m^2 s.

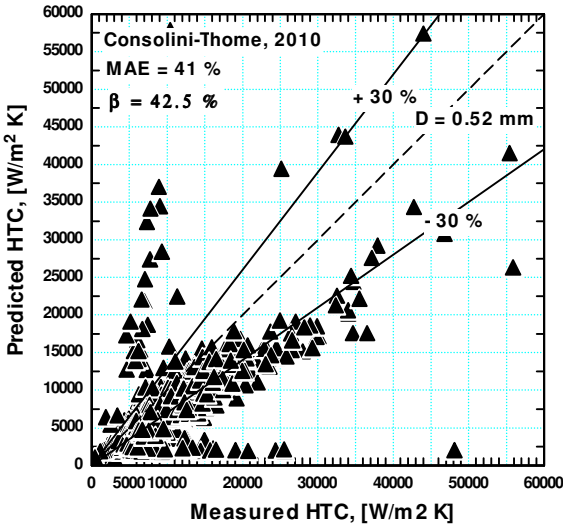

(a)

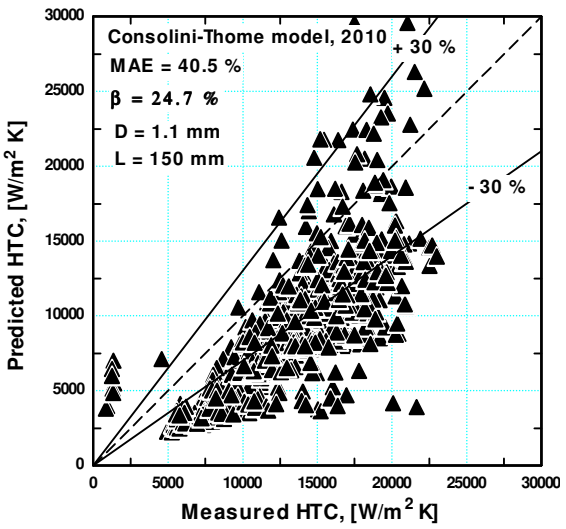

(b)

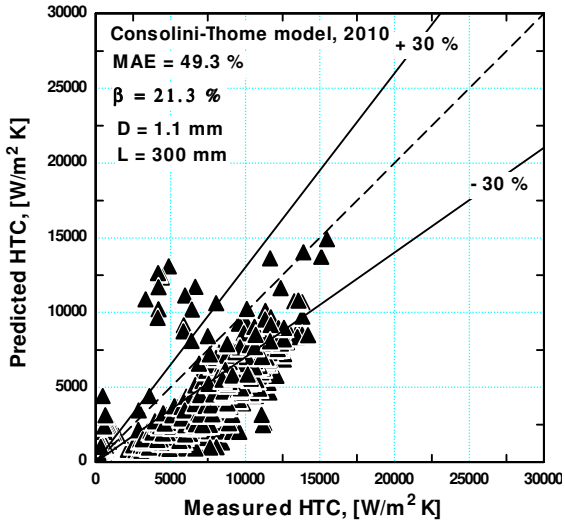

(c)

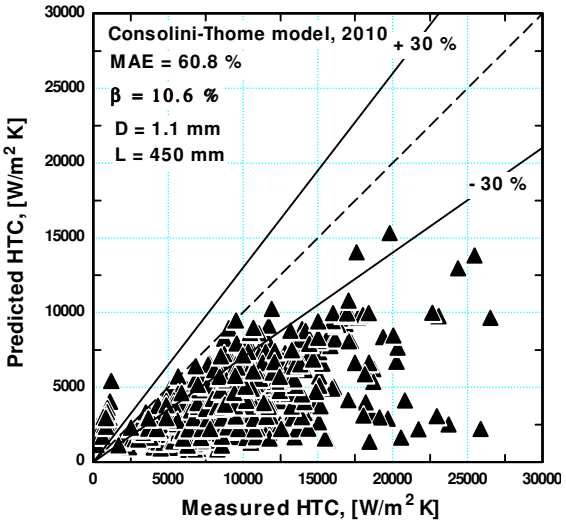

(d)

Figure 5.26 Comparison with the Consolini-Thome (2010) model for (a) D = 0.52 mm, L = 100 mm, (b) D = 1.1 mm, L = 150 mm, (c) D = 1.1 mm, L = 300 mm and (d) D = 1.1 mm, L = 450 mm.

5.5 Proposed new correlations

As presented above, none of the models and correlations could predict the experimental data of all tubes with the same accuracy. For example, for the 0.52 mm diameter tube, the best correlation was that proposed by Bertsch et al. (2009b) where it predicted 54.7 % of the data within the ± 30 % error bands but it predicted the data of the other tubes with less accuracy. For the shortest 1.1 mm tube (L = 150 mm), the Cooper pool boiling correlation was the best one where it predicted about 85 % of the data within the ± 30 % error bands but the performance of the correlation decreased in the other tubes. For the medium 1.1 mm tube (L = 300 mm) and the longest tube (L = 450 mm), the three zone evaporation model of Thome et al. (2004) gave the best predictions where it predicted 75.8 % and 55 % of the data within the ± 30 % error bands, respectively. Owing to the non generality of the above correlations, two new heat transfer correlations are proposed. The first correlation (correlation I) is proposed based on introducing the heat transfer coefficient as a function of the most important dimensionless groups such as boiling number, Weber number, confinement number, liquid Reynolds number and the convection number. The second correlation (correlation II) is based on adopting the superposition model of Chen's (1966) correlation.

5.5.1 Correlation I

The experimental Nusselt number defined by Eq. (5.41) was correlated using the boiling number, the liquid Weber number, the liquid Reynolds number and the confinement number. The boiling number takes into account the heat and mass flux effects, the Weber number takes into accounts the inertia and surface tension effects while Reynolds number accounts for the inertia and viscous forces. The confinement number was considered here to take into accounts the effect of tube diameter. To correlate the experimental data of the current study (D = 0.52 and 1.1 mm) as well as the experimental data of Huo (2005) and Shiferaw (2008) for D = 4.26 – 2.01 mm, the function form given by Eq. (5.42) was proposed. The constant and the exponents in Eq. (5.42) are determined using the multi-parameters non linear least square fitting (Multi-X NLSF) and the final form of the correlation is given by Eq. (5.43).

$$Nu_{\exp} = \frac{h_{tp,\exp} D}{k_L} = f\left(Bo, We_L, \mathrm{Re}_L, Co\right) \tag{5.41}$$

$$Nu_{\exp} = CBo^{a} We_L^{b} \mathrm{Re}_L^{c} Co^{d} \tag{5.42}$$

$$h_{tp} = 3414 \frac{Bo^{0.625} We_L^{0.2} \mathrm{Re}_L^{0.1}}{Co^{0.6}} \frac{k_L}{D} \tag{5.43}$$

The above equation was developed based on 8561 data points and is valid for R134a, D = 4.26 – 0.52 mm, G = 100 – 500 kg/m^2 s, P = 6 – 14 bar and $x < x_{dryout}$, i.e. the correlation is valid as long as there is no dryout. It is interesting to note that the exponent of the boiling number in Eq. (5.43) obtained using the NLSF method is very close to that in the Cooper pool boiling correlation (0.67). Figure 5.27 illustrates how the above dimensionless groups managed to correlate the current experimental data with insignificant scattering.

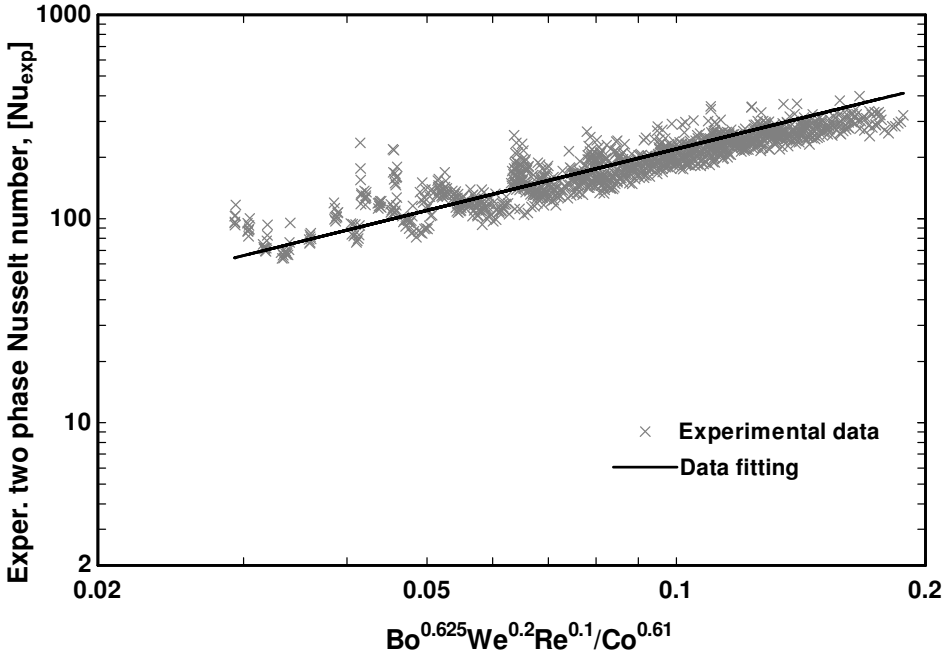

Figure 5.27 The experimental two phase Nusselt number versus the dimensionless groups.

Equation (5.43) fitted the data of all tubes very well while it fitted the data of the 0.52 mm tube up to x = 0.3. As presented and discussed previously in Chapter 4, the *h-x* plot indicated that the heat transfer coefficient increases rapidly with increasing vapour quality after x = 0.3 – 0.4 and all heat flux lines merged together into one line. Accordingly, the data of the 0.52 mm tube for x > 0.3 were segregated and the dependence of the experimental Nusselt number on the different dimensionless groups was assessed. The effect of the liquid Reynolds number and the confinement number were found to be insignificant compared to the effects of Weber and boiling numbers. Additionally, the convection number (*Nco*) (given by Eq. (5.45)) proposed by Shah (1982) was found to have a significant effect. It is worth mentioning here that the effect of the convection number in the 1.1 mm tubes was also assessed and the exponent was found to be very close to zero, which means that its effect is insignificant. Consequently, for the 0.52 mm tube with x > 0.3, the following correlation is recommended:

$$h_{tp} = 5324\left[\frac{Bo^{0.3}We_L^{0.25}}{N_{Co}^{0.25}}\right]^{1.79}\frac{k_L}{D} \qquad (5.44)$$

$$N_{Co} = \left(\frac{1-x}{x}\right)^{0.8}\left(\frac{\rho_L}{\rho_g}\right)^{0.5} \tag{5.45}$$

Figure 5.28 depicts the comparison between the current experimental data and the proposed new correlation (correlation I). It is obvious that the correlation predicts 86.1 – 92.8 % of the data within the ± 30 % error bands at MAE values ranging from 14 – 17.1 %.

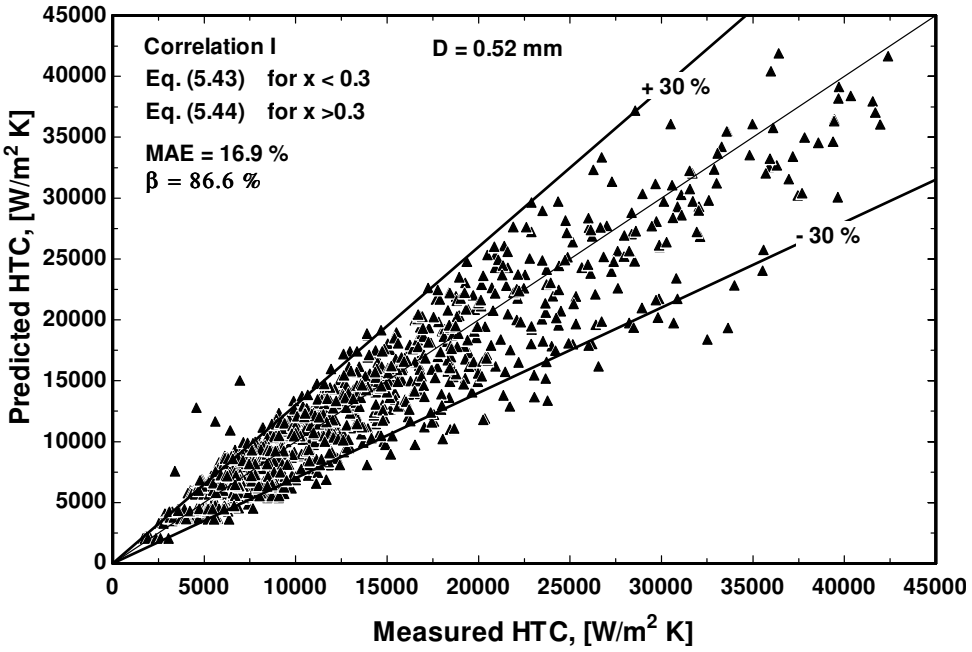

(a)

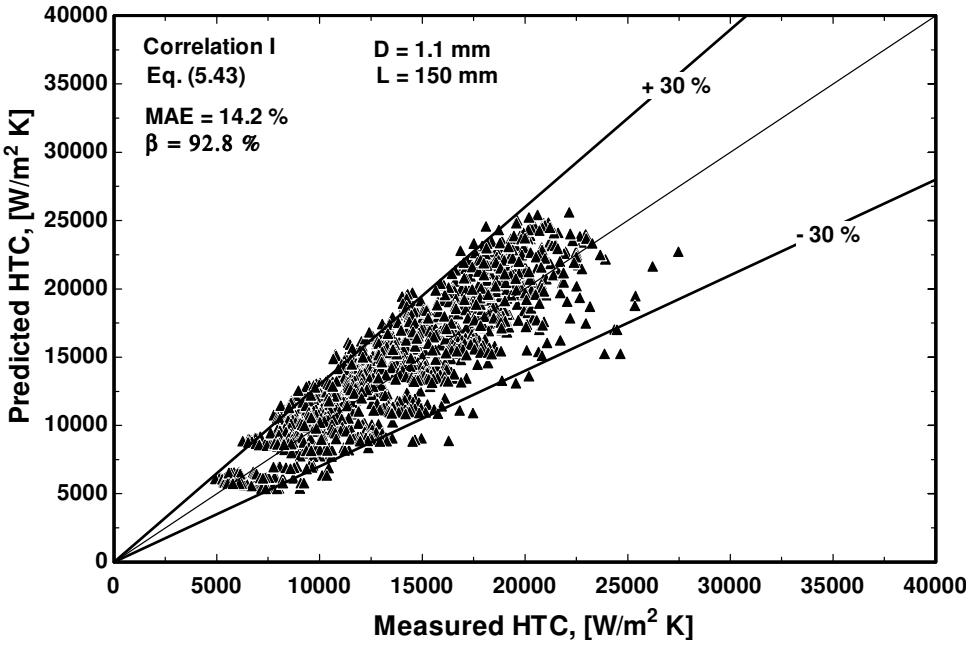

(b)

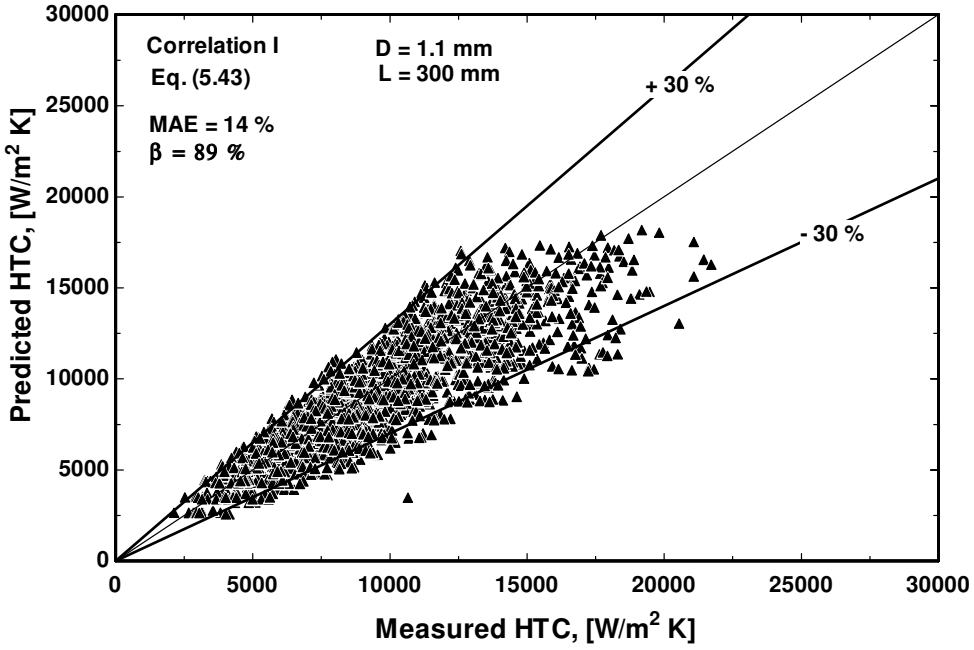

(c)

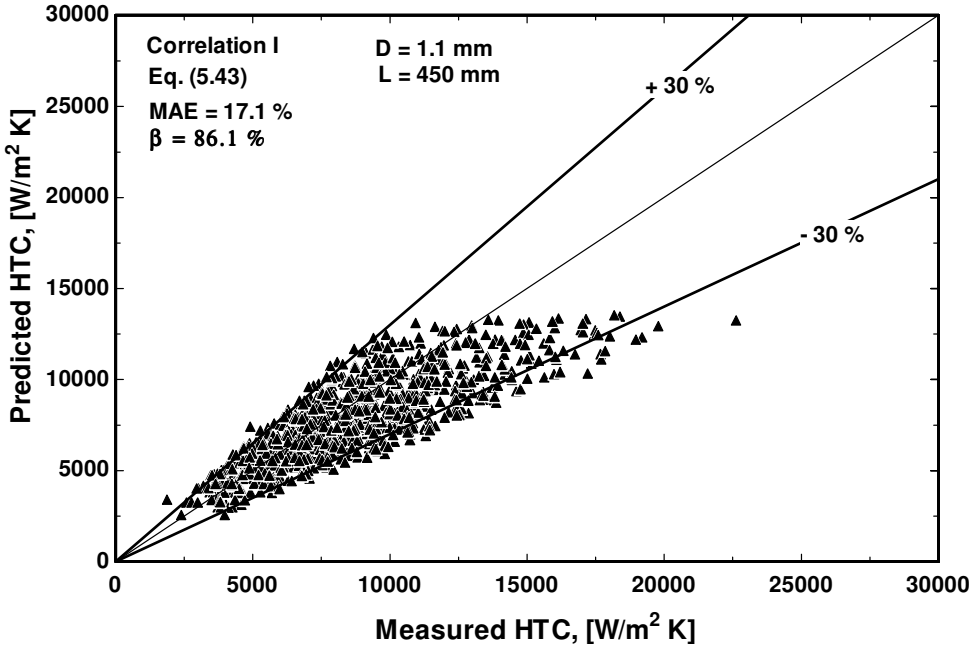

(d)

Figure 5.28 Comparison between the experimental data and the new correlation (correlation I) for (a) D = 0.52 mm, (b) D = 1.1 mm, L = 150 mm, (c) D = 1.1 mm, L = 300 mm and (d) D = 1.1 mm, L = 450 mm.

The correlation was also compared with the experimental data of X. Huo (2005) for D = 4.26 and 2.01 mm and the experimental data of D. Shiferaw (2008) for D = 2.88 mm as seen in Fig. 5.29. The correlation managed to predict 88.4 – 94.4 % of the data within the ± 30 % error bands at MAE values of 12.8 – 17.1 %.

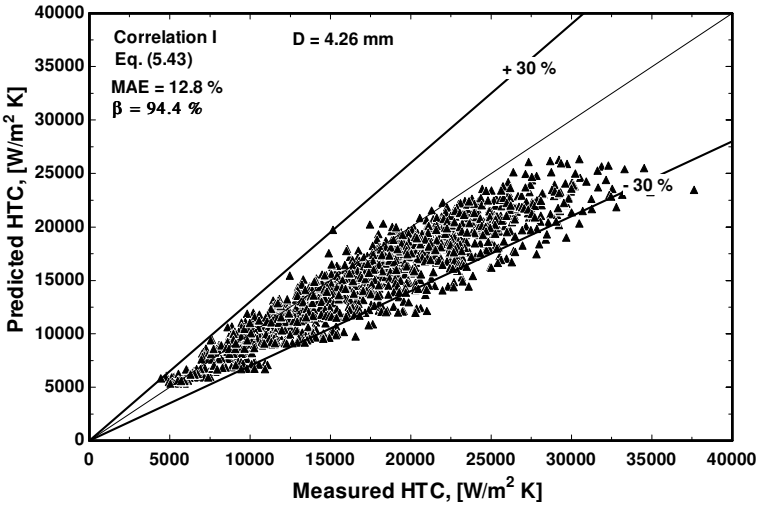

(a)

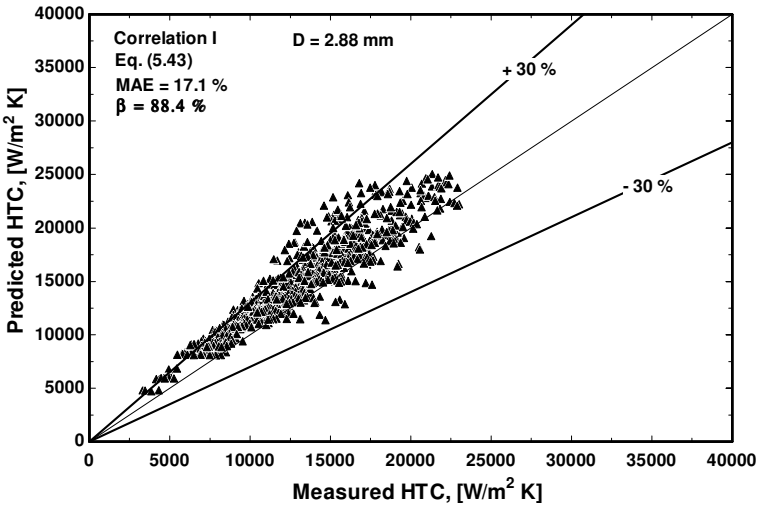

(b)

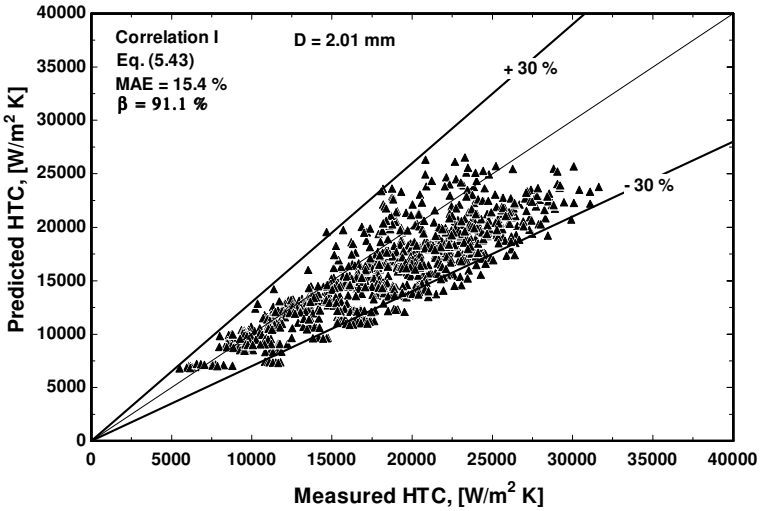

(c)

Figure 5.29 Comparison between the new correlation (correlation I) and the experimental data of X. Huo (2005) and D. Shiferaw (2008) for (a) D = 4.26 mm, (b) D = 2.88 mm and (c) D = 2.01 mm.

5.5.1 Correlation II

The second proposed approach to correlate the current experimental data is to follow the superposition model of Chen (1966). The form of the new correlation is given by Eq. (5.46). In the new correlation, the Cooper pool boiling correlation given by Eq. (5.47) is used instead of the Forster and Zuber (1955) correlation, which was used in the original Chen correlation. The single phase liquid heat transfer coefficient in the correlation is calculated using the conventional single phase equations for laminar and turbulent flows as given by Eq. (5.48) based on the liquid Reynolds number defined by Eq. (5.49). For the transition region, an interpolation was conducted between the laminar and turbulent heat transfer coefficients.

$$h_{tp} = S_{new} h_{Cooper} + F_{new} h_L \tag{5.46}$$

$$h_{Cooper} = 55 P_r^{(0.12-0.4343\ln e)} \left(-\log P_r\right)^{-0.55} MW^{-0.5} q^{0.67} \tag{5.47}$$

$$h_L = \begin{cases} 4.36 \dfrac{k_L}{D} & \mathrm{Re}_L < 2000 \\ 0.023\,\mathrm{Re}_L^{0.8}\,\mathrm{Pr}_L^{0.4}\,\dfrac{k_L}{D} & \mathrm{Re}_L > 3000 \end{cases} \tag{5.48}$$

$$\mathrm{Re}_L = \frac{(1-x)GD}{\mu_L} \tag{5.49}$$

The remaining unknowns in the correlation (Eq. (5.46)) are the nucleate boiling suppression factor S_{new} and the convective boiling enhancement factor F_{new}. Chen (1966) determined these two parameters empirically using experimental data for convective boiling of water and hydrocarbons in large diameter tubes. Accordingly, the correlations proposed by Chen for these two parameters are not expected to work properly with refrigerants and consequently new correlations are required. To propose a new correlation for the enhancement factor F_{new}, the experimental values of the enhancement factor should be determined first. Chen (1966) proposed two approaches to determine the enhancement factor from the experimental data. The first approach was by a certain kind of iteration whilst the second was theoretical by the analogy between heat and momentum transfer in the boundary layer. Chen (1966) did not find any significant difference between the values of the enhancement factors calculated using the two methods as seen in Fig. 5.30. So, in the current study, the second approach was

selected to determine the experimental values of the enhancement factor. In this approach, the enhancement factor was deduced theoretically and introduced as a function of the two phase frictional multiplier as:

$$F = \left(\phi_L^2\right)^{0.444} \tag{5.50}$$

Equation (5.50) is valid as long as the value of the liquid Prandtl number is about one. Bennet and Chen (1980) modified Eq. (5.50) to be extended for Prandtl number values greater than one as cited in Collier and Thome (1994). The new modified equation is given by Eq. (5.51).

$$F = \left[\left(\frac{\mathrm{Pr}_L + 1}{2}\right)\phi_L^2\right]^{0.444} \tag{5.51}$$

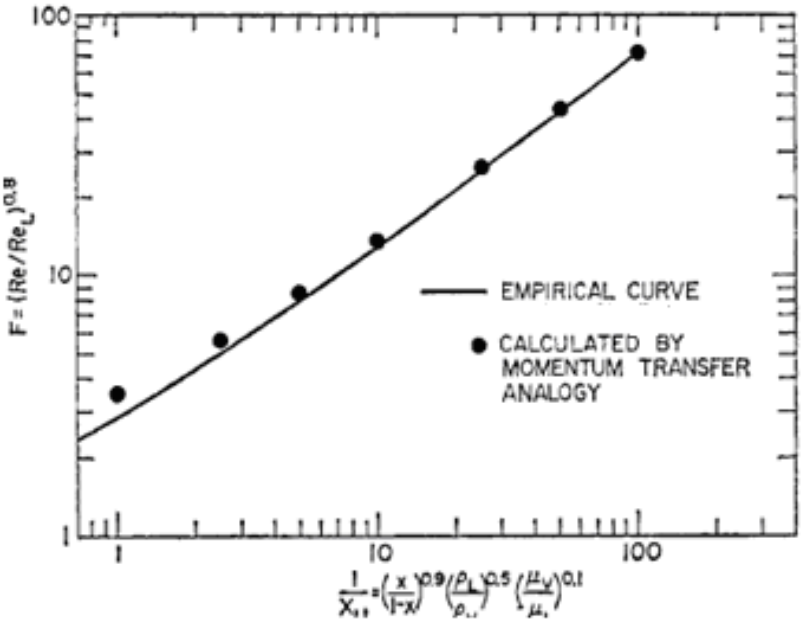

Figure 5.30 Comparison of *E* function calculated by heat-momentum transfer analogy to the empirical curve, Chen (1966).

The two phase frictional multiplier proposed by Mishima and Hibiki (1996) was used in this thesis since it was developed for small to mini diameter tubes and also it predicted the current experimental pressure drop data well as will be presented later in the next chapter. The determined enhancement factor *F* was plotted against the reciprocal of Martinelli parameter as seen in Fig. 5.31. In this figure, 1249 data points for the shortest

1.1 mm diameter tube covering system pressure range of 6 – 10 bar, mass flux range of 100 – 500 kg/m^2 s and x up to 0.6 – 0.8. It is very obvious that, all data points collapsed into one single line without any scatter which confirms the success of the reciprocal of the Martinelli parameter to correlate the enhancement factor. It is interesting to note that, the trend for the other tubes was similar to that in Fig. 5.31 but the slope of the curve was found to be dependent on the tube diameter. Therefore, the data of X. Huo (2005) and D. Shiferaw (2008) for D = 2.01 – 4.26 mm tube were included in the analysis to correlate the effect of diameter on the new enhancement factor. The proposed function for the enhancement factor that was found to fit all experimental data (D = 4.26 – 0.52 mm) is given by Eq. (5.52).

$$F_{New} = \left(1 + \frac{A}{\mathrm{X}}\right)^{0.64} \tag{5.52}$$

The constant A in the above equation was found to depend strongly on the confinement number as shown in Fig. 5.32 and was fitted by Eq. (5.53). As the confinement number increases (diameter decreases), the value of *A* decreases and consequently the enhancement factor. This may be attributed to the damping of turbulence, which enhances the convective heat transfer, as the diameter decreases. This should not contradict with Karayiannis et al. (2008) and Consolini and Thome (2009) who reported that the flow boiling heat transfer coefficient increases as the diameter decreases. This is because they were talking about the average heat transfer coefficient versus heat flux. Reducing tube diameter (increasing confinement number) may significantly increase the nucleate boiling heat transfer coefficient in the very low vapour quality region and make the total average value too big.

$$A = 2.812 Co^{-0.408} \tag{5.53}$$

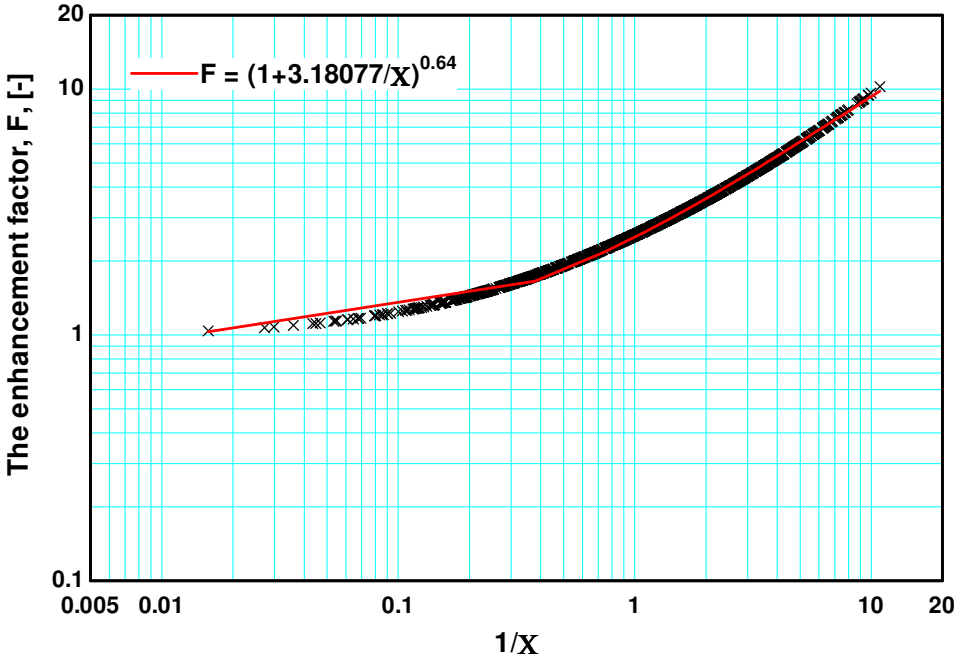

Figure 5.31 The experimental enhancement factor versus the reciprocal of Martinelli's parameter.

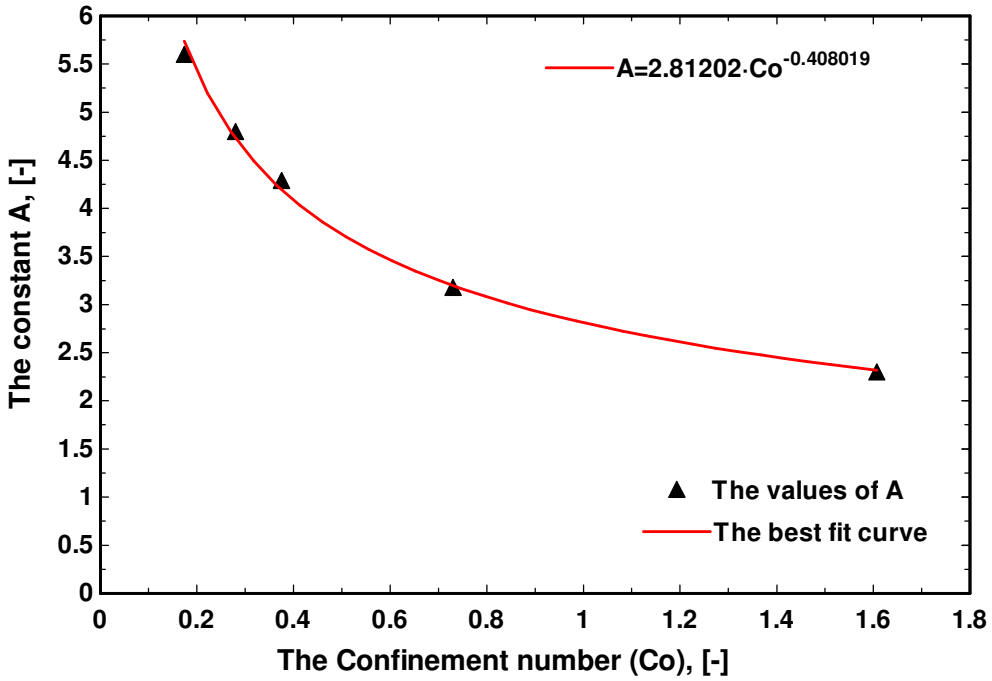

Figure 5.32 the constant A in Eq. (5.52) as a function of the confinement number, [-]

Figure 5.33 depicts a comparison between the new proposed enhancement factor and the original one proposed by Chen (1966). It is very obvious that, the two curves approach a value of one as $1/X$ decreases, i.e. as the vapour quality decreases. This is

consistent with the fact that bubbly flow dominates at very small vapour quality values and consequently nucleate boiling dominates over convective boiling and the enhancement factor should be one. On the other hand, the two curves tend to merge at very high values of $1/X$ whereas for values between about 0.01 and 2, large deviations are observed. It is worth mentioning here that Chen used the Martinelli parameter for turbulent liquid and turbulent vapour but in the current study the Martinelli parameter was calculated based on the actual flow conditions, i.e. laminar or turbulent. Based on the determined enhancement factor, the experimental suppression factor was calculated using Eq, (5.54). The result was plotted against the two phase Reynolds number defined by Eq. (5.55) for all tubes including those of Huo and Shiferaw (D = 4.26, 2.88, 2.01 mm) as seen in Fig. 5.34. To correlate the data in this figure, the same function proposed by Chen (1966) was used but modified by the new enhancement factor as given by Eq. (5.56).

$$S_{Exp} = \frac{h_{tp,Exp} - F_{New} h_L}{h_{Cooper}} \tag{5.54}$$

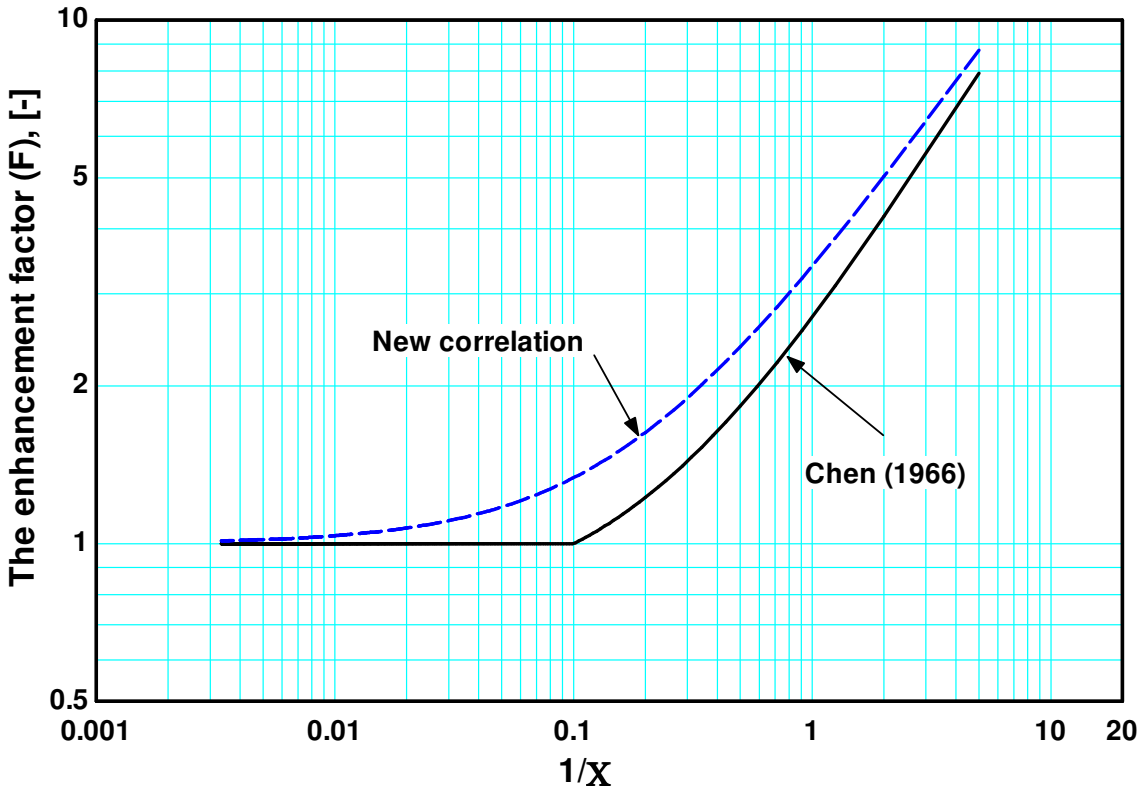

Figure 5.33 A comparison between the new enhancement factor and the enhancement factor proposed by Chen (1966).

$$\mathrm{Re}_{tp} = \mathrm{Re}_L \, F_{New}^{1.25} \tag{5.55}$$

$$S_{New} = \frac{1}{1 + 2.56 \times 10^{-6} \left(\mathrm{Re}_L \, F_{New}^{1.25} \right)^{1.17}} \tag{5.56}$$

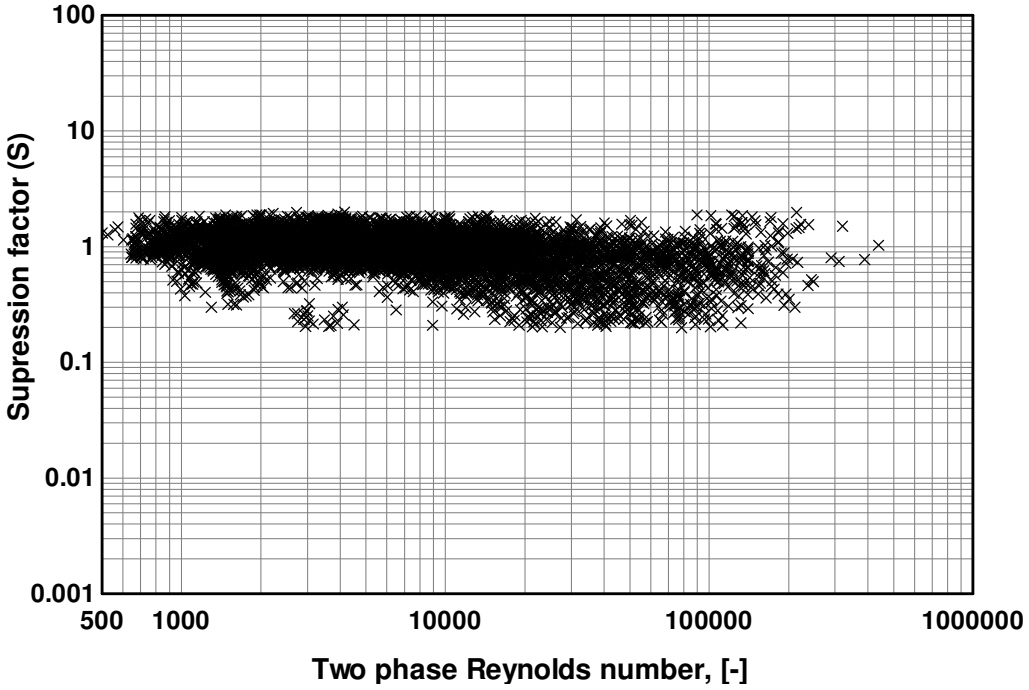

Figure 5.34 The experimental suppression factor versus the two phase Reynolds number

Figure 5.35 depicts a comparison between the new suppression factor and the original one proposed by Chen (1986). This figure explains why the original Chen correlation highly under-predict the current experimental data as previously presented in Fig. 5.2. The figure indicates that the nucleate boiling suppression factor of Chen decreases rapidly with the two phase Reynolds number. This makes the nucleate boiling term in the original correlation very small and consequently the total value of the heat transfer coefficient. On the contrary, the new modified suppression factor remains equal to one up to Reynolds number value of about 5×10^4 then it decreases slowly with increasing Reynolds number.

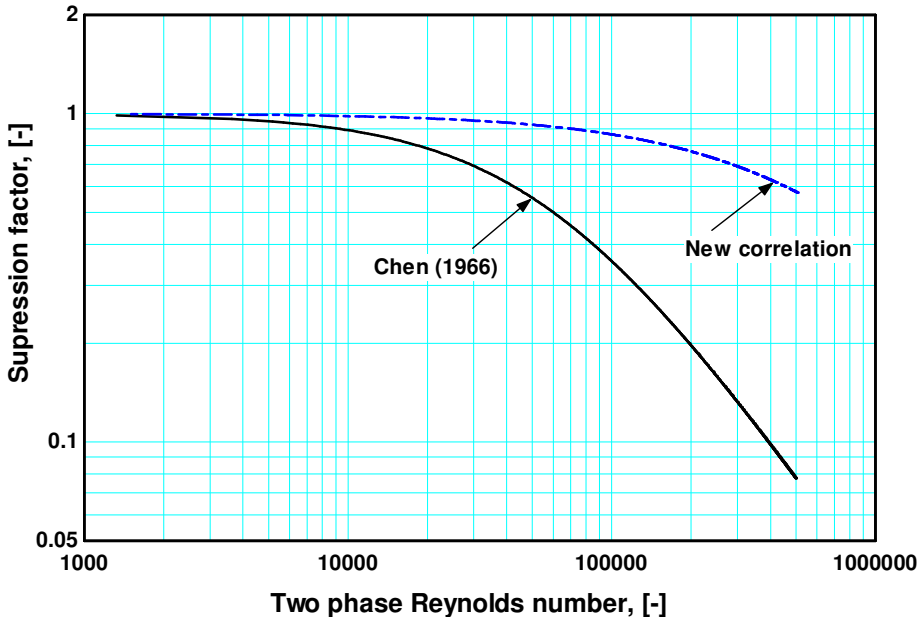

Figure 5.35 A comparison between the new correlation of the nucleate boiling suppression factor and the original one proposed by Chen (1966).

Figures 5.36 depicts the global comparison between the new correlation and the current experimental data while Fig. 5.37 compares the correlation with the data of X. Huo (2005) and D. Shiferaw (2008). For the current experimental data, the correlation predicted 85.9 – 93.4 % within the error bands at MAE values of 14 – 17.9 %. For the data of X. Huo and D. Shiferaw, the correlation predicted 92.2 – 95.3 % of the data within the error bands at MAE values of 10.8 – 16.5 %.

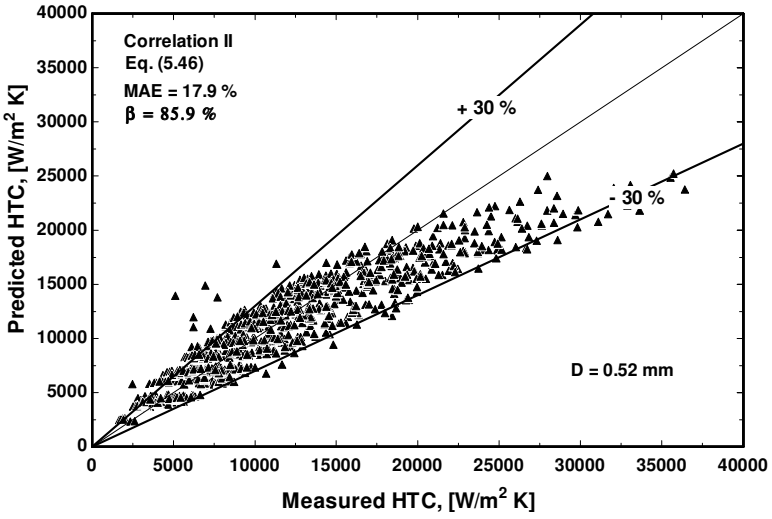

(a)

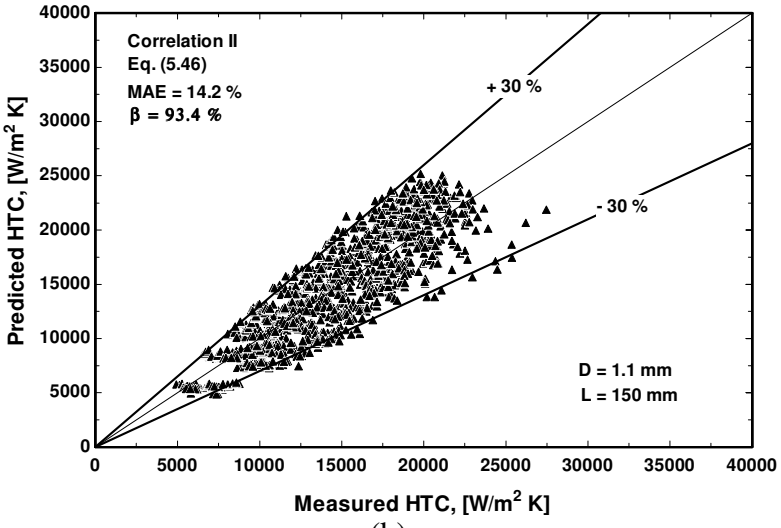

(b)

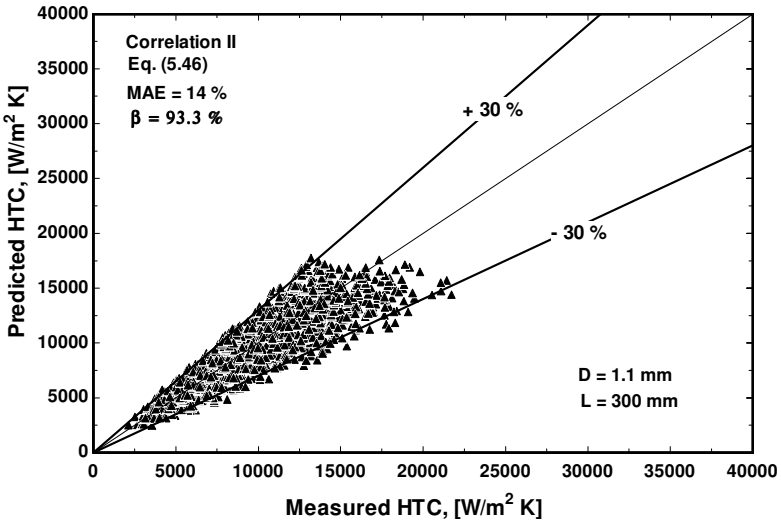

(c)

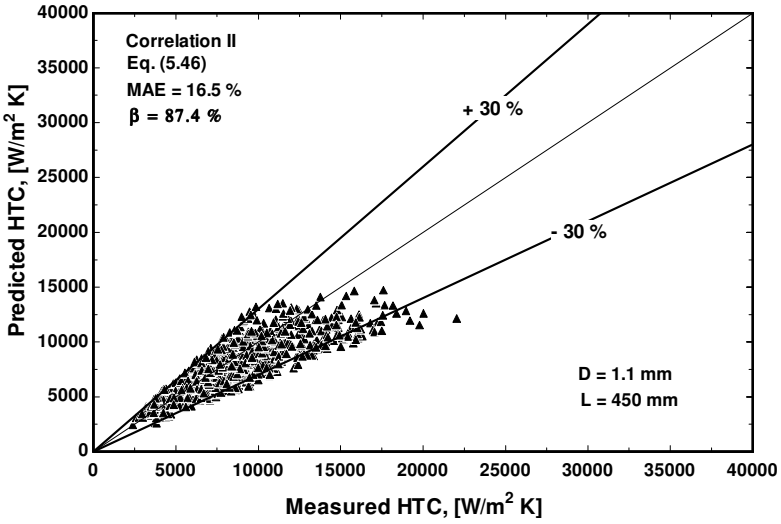

(d)

Figure 5.36 Comparison between the new correlation (correlation II) and the current experimental data for (a) D = 0.52 mm, (b) D = 1.1 mm, L = 150 mm, (c) D = 1.1 mm, L = 300 mm and (d) D = 1.1 mm, L = 450 mm

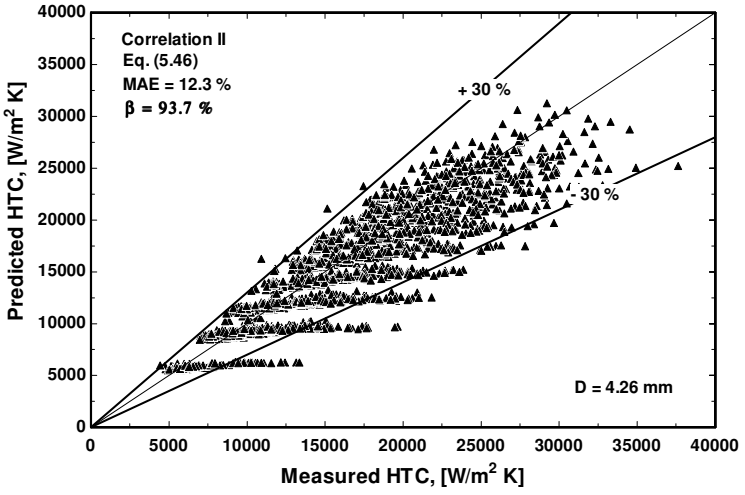

(a)

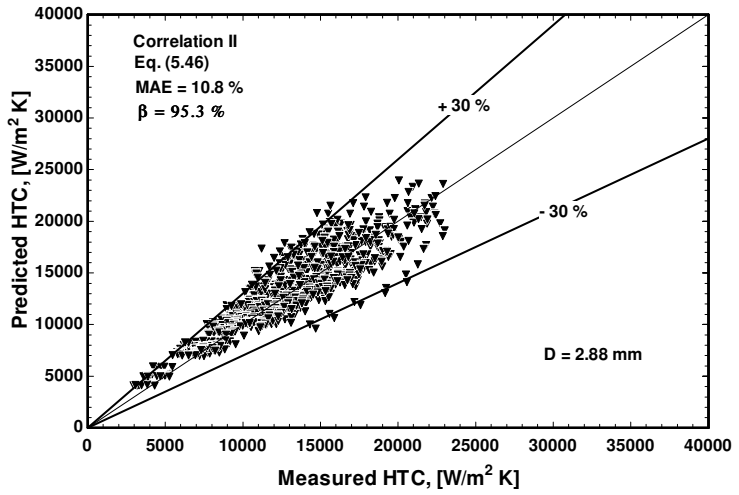

(b)

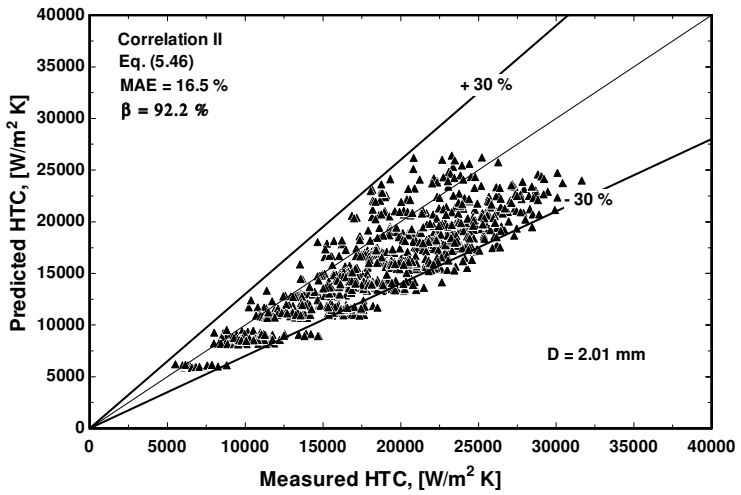

(c)

Figure 5.37 Comparison between the new correlation (correlation I) and the experimental data of X. Huo (2005) and D. Shiferaw (2008) for (a) D = 4.26 mm, (b) D = 2.88 mm and (c) D = 2.01 mm.

Figure 5.38 shows an example for the comparison between correlation I and correlation II for D = 4.26, 2.01, 1.1 mm tubes as an example. The figure indicates that the mean deviation between the two correlations is very small and ranges from 4.4 to 7.8 %. The small deviation between the two correlations is expected to occur at high vapour quality. This is because, correlation I gives heat transfer coefficient that slightly decreases with quality towards the tube exit whilst correlation II gives heat transfer coefficient that slightly increases with quality towards the tube exit. .

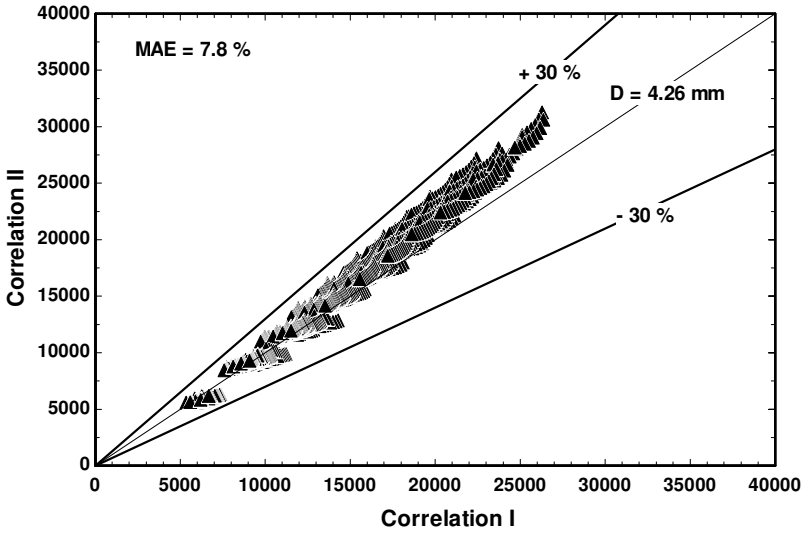

(a)

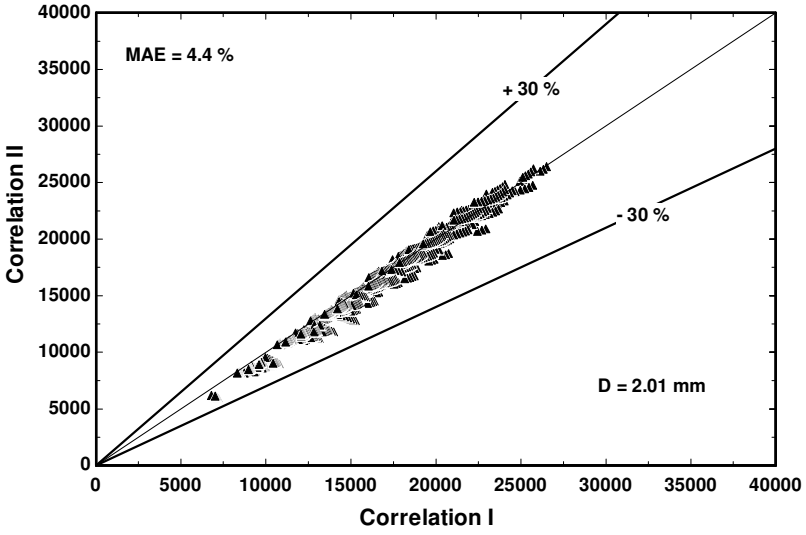

(b)

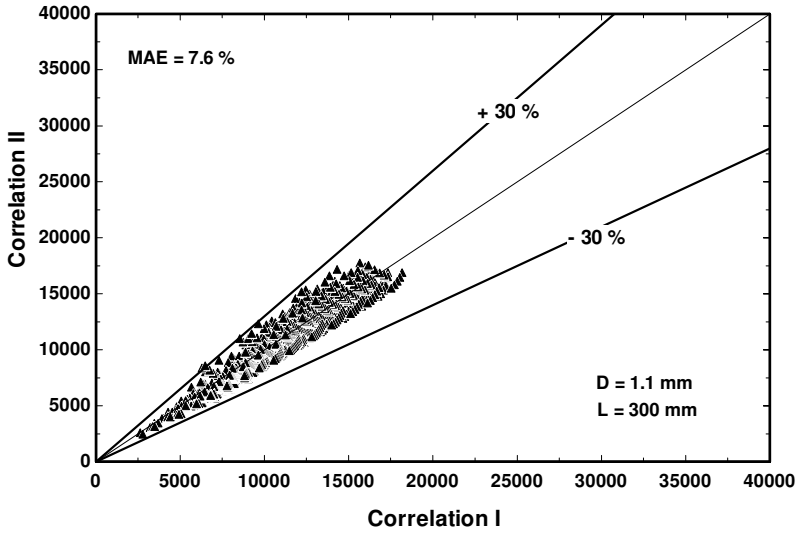

(c)

Figure 5.38 Comparison between correlation I and correlation II for (a) D = 4.26 mm, (b) D = 2.01 mm and (c) D = 1.1 mm, L = 300 mm.

5.6 Summary

This chapter presented a detailed evaluation for macro and microscale heat transfer correlations as well as two existing mechanistic models. Some researchers correlated the heat transfer coefficient as a function of dimensionless groups whilst some others followed the commonly used superposition or asymptotic models. However, none of theses models and correlations could predict the current experimental data with a reasonable accuracy. Also, the mechanistic models failed to predict the current experimental data of all tubes. This is because these models are not totally based on theory and depend on empirical correlations, i.e. they are semi mechanistic models. The MAE values and the percentage of data *(β)* within the ± 30 % error bands for all examined correlations and models are summarized in Table 5.2. This table indicates that there is no generality for the correlations where the performance of the correlations changed with changing tube diameter and heated length. For the 0.52 mm diameter tube, all correlations predicted poorly the data with MAE values greater than 30 %. For the 1.1 mm tube with L = 150 mm, The Cooper pool boiling correlation, Thome et al. (2004), Mikielwicz (2010) and Saitoh et al. (2007) predicted reasonably the data with MAE less than 30 % and β = 76 – 85 %. However, the performance of these correlations gets worse as the heated length increased. It is worth mentioning that, most

microscale heat transfer correlations were developed based on experimental data collected using too short channels. This may explain why the accuracy of the correlations varies with variation in the heated length. For too short channels, the applied heat flux is too high for the same exit quality compared to the long channels. Accordingly, there is a possibility for the nucleate boiling mechanism to dominate in short microchannels, i.e. the local heat transfer coefficient does not vary with local quality. So, it is expected for the microscale correlations to work better in short tubes with nucleate boiling as a dominant heat transfer mechanism. This explains why some correlations managed to predict reasonably the data of the shortest 1.1 mm tube. For the 0.52 mm tube and the longer 1.1 mm tubes, the heat transfer coefficient increase with vapour quality toward the exit over a wide range of quality, which explains why the predictions get worse in these tubes.

Owing to the none generality of the evaluated models and correlations, two new correlations were proposed in this study. The first correlation was based on the dimensionless groups such as boiling number, Weber number, liquid Reynolds number, confinement number and convection number. Due to the term (1-x) in the liquid Reynolds number (see Eq. (5.43)), the predicted heat transfer coefficient using the dimensionless correlation slightly decreases with vapour quality which is not consistent with the experimental trends that were found in all tubes. Accordingly a second correlation was proposed based on the superposition model of Chen (1966) such that it can capture the experimental trend. Since the new correlations were validated using experimental data collected for tubes with different heated lengths, the effect of heated length, which was not considered before, is incorporated in the correlation parameters. It is clear from Table 5.2 that the two new correlations predicted 85.9 to 93.4 % of the experimental data within the ± 30 % error bands at MAE values of 14 – 17.9 %, which is much better than the other correlations.

Table 5.2 The MAE values and the percentage of data within the ± 30 % error bands (β) for all evaluated models and correlations

Correlation	0.52 mm		D = 1.1 mm					
			L = 150 mm		L = 300 mm		L = 450 mm	
	MAE	β	MAE	β	MAE	β	MAE	β
Chen (1966)	69.8	27.2	66.1	0.2	102.6	10.6	70.7	21
Shah (1982)	60.1	11.8	56.8	15	47.3	12.5	60.4	10.4
Gungor and Winterton (1986)	62.8	36.7	33.4	50.2	58.7	47.2	66.5	47
Kandlikar (1990)	40.1	45.2	32.3	68	49.6	45.5	50.3	45.5
Liu and Winterton (1991)	54.4	18.7	60.3	0.3	60.6	0.4	60.6	15.6
Stiener-Taborek (1992)	237	1.1	48.4	4.3	52.8	15.8	54.4	27
Lazarek and Black (1982)	51.6	43.7	32.15	65.8	42	38.4	45.2	23.8
Tran et al. (1996)	69.3	2.4	50.7	3.5	54.6	3.1	56.8	2.7
Kew and Cornwell (1997)	32.5	52.7	25.7	69.1	44.2	49.7	53.2	34.2
Warrier et al. (2002)	76.8	7	77.4	1.8	88	0.4	84.7	0.6
Kandlikar and Balasubramanian (2004)	68.9	2	62.3	7.8	65.2	2	69	1.8
Zhang et al. (2004) (original)	79.7	11.4	64.2	1.5	122.6	15	133.6	21
Zhang et al. (2004) (modified by Cooper correlation)	33.7	66.1	24.8	77	46.2	72.6	55.6	57
Lee and Mudawar (2005)	73.9	31.4	119.5	19.5	133.3	20.3	132.7	18
Saitoh et al. (2007)	39.1	45.3	27.7	73.9	46.7	63.3	56.8	54

Bertsch et al. (2009)	37.6	54.7	28.8	58.8	39.1	62.8	50.1	45.1
Mikielewicz (2010)	34.8	49.5	21.8	76.3	38.4	65.3	49.1	45.8
Li and Wu (2010)	58.4	43	26.2	69.8	64.4	70	70.6	52.3
Cooper (1984)	34.4	51.5	19.3	85	36.2	69.3	49	47.1
Thome et al. (2004)	39.2	42	24	76	35.7	75.8	48	55
Consolini and Thome (2010)	41	42.5	40.5	24.7	49.3	21.3	60.8	10.6
New correlation (correlation I)	16.9	86.6	14.2	92.8	14	89	17.1	86.1
New correlation (correlation II)	17.9	85.9	14.2	93.4	14	93.3	16.5	87.4

Chapter 6

Pressure Drop Results and Prediction Methods

6.1 Introduction

Pressure drop is one of the key parameters that should be estimated accurately for the proper design of mini/microchannels evaporators. In the present study, the pressure drop was directly measured across the heated section simultaneously with the heat transfer measurements. Thus, the measured pressure drop in the current study represents the flow boiling pressure drop, i.e. it is not diabatic or adiabatic pressure drop which is measured by several researchers in the open literature. This chapter presents and discusses the characteristics of the measured flow boiling pressure drop in the 0.52 mm diameter tube and the three investigated heated lengths of the 1.1 mm diameter tube. Additionally, a detailed evaluation of the existing macro- and micro-scale pressure drop models and correlations is presented. The evaluation covered five macro-scale models and correlations and thirteen micro-scale models and correlations. The chapter is organised as follows: section 6.2 presents and discusses the characteristics of the measured pressure drop; section 6.3 presents the comparison with the existing macro-scale models and correlations; section 6.4 compares the experimental data with the existing micro-scale correlations; section 6.5 compares the experimental data with two mechanistic pressure drop models developed for slug flow in micro-channels; Section 6.6 gives a summary and conclusions for the chapter.

6.2 The measured pressure drop

This section presents the effect of different parameters such as heat flux, mass flux, system pressure, tube diameter and heated length on the measured flow boiling pressure drop. It is worth mentioning here that the test sections in the current study do not have any inlet or outlet restrictions. In other words, the total flow boiling pressure drop was

directly measured across the heated section without any inlet or outlet pressure losses. Also, since the flow enters the heated section as a sub-cooled liquid, the single phase pressure drop part was subtracted from the total measured value. Additionally, the pressure drop results presented here are corresponding to stable boiling conditions as presented and discussed previously in Chapter 4. Figures 6.1 to 6.3 depict the effect of heat and mass fluxes, system pressure and tube diameter respectively on the total measured two phase pressure drop. It is obvious from Fig. 6.1 that the total measured two phase pressure drop increases almost linearly with increasing heat flux (exit quality) due to the increase in the contribution of the acceleration pressure drop component. The same figure demonstrates also that the measured pressure drop increases with increasing mass flux with higher mass flux effect at high heat flux values compared to the low heat flux values. This mass flux effect is understood from the momentum equation where the frictional and acceleration pressure gradients are proportional to the term G^2.

Figure 6.2 shows the effect of system pressure on the total measured pressure drop. The figure shows that the measured pressure drop decreases with increasing system pressure due to the effect of pressure on fluid properties. For R134a, as the pressure increases, the liquid density slightly decreases whereas the vapour density significantly increases. For example, increasing the pressure from 6 to 10 bar resulted in 6 % reduction in the liquid density and 69 % increase in the vapour density. This means that the vapour superficial velocity will decrease significantly as the pressure increases resulting in a reduction in the acceleration component of the pressure drop. Additionally, the increase in system pressure reduces the liquid and vapour viscosities and consequently the frictional component of the pressure drop. The effect of fluid properties on pressure drop can be quantified using the homogeneous flow model (for example) at G = 300 kg/m^2 s, D = 1.1 mm, L = 0.15 mm, x = 0.5 when the pressure increases from 6 – 10 bar as follows. As the pressure increased from 6 – 10 bar, the liquid to vapour density ratio decreased by about 44 % and the liquid to vapour viscosity ratio decreased by about 25.5 %. This resulted in a decrease in the acceleration component by about 42 %, a decrease in the frictional component by about 50 % and an increase in the gravitational component by about 40.5 %.

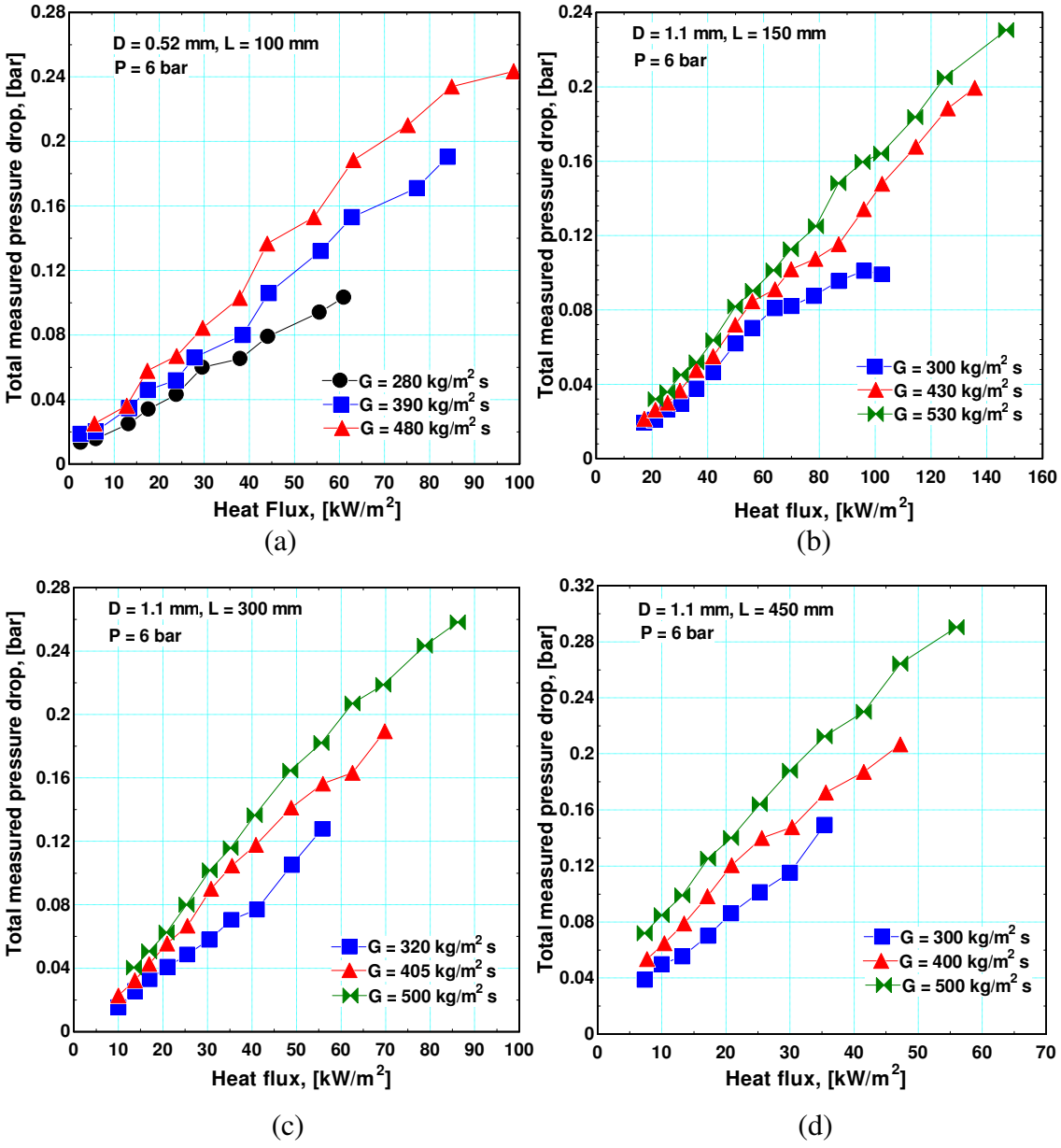

Figure 6.1 The total measured two phase pressure drop versus heat flux at different mass fluxes for (a) D = 0.52 mm, (b) D = 1.1 mm, L = 150 mm, (c) D = 1.1 mm, L = 300 mm, (d) D = 1.1 mm, L = 450 mm.

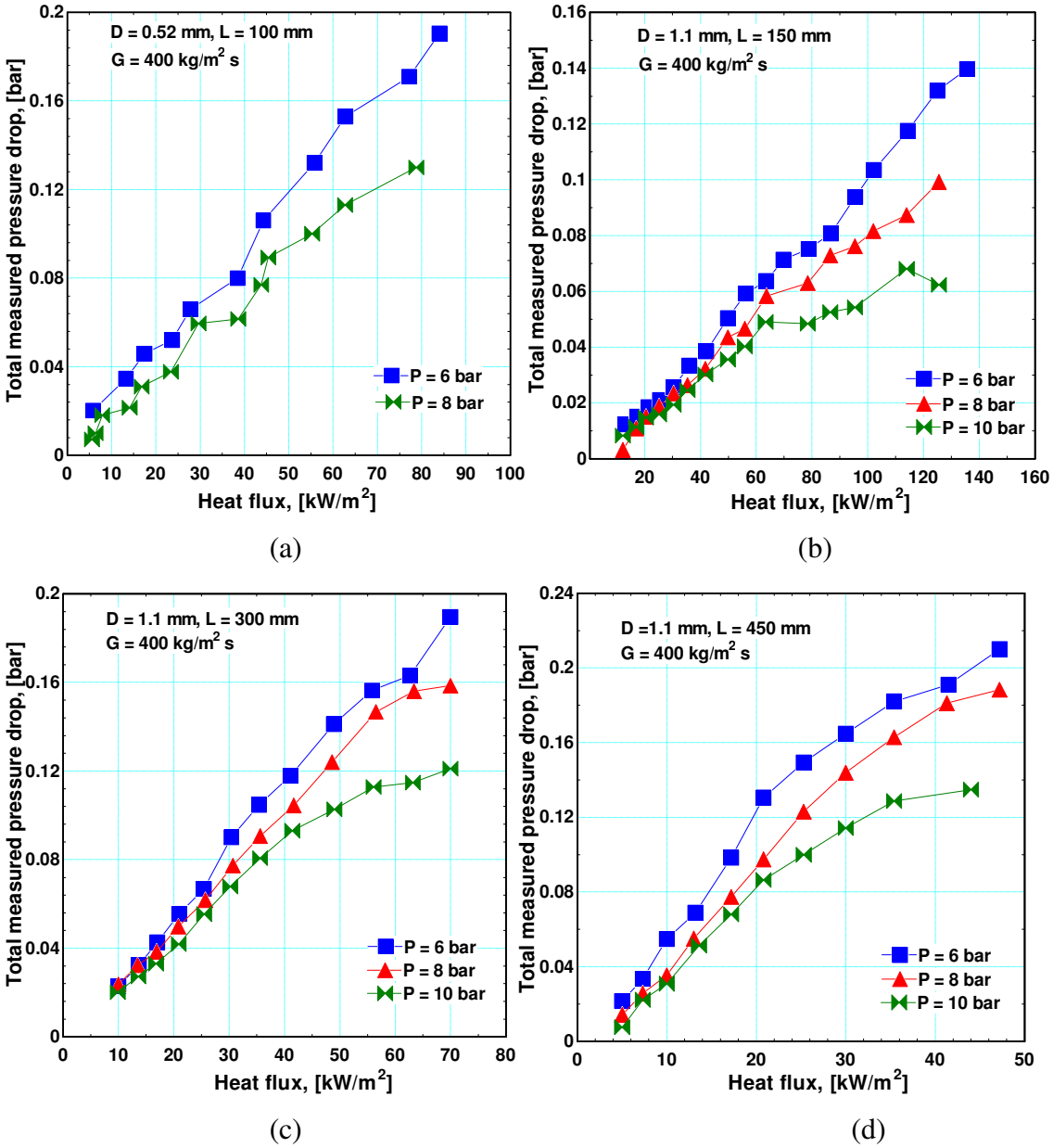

Figure 6.2 The effect of system pressure on the total measured two phase pressure drop at G = 400 kg/m^2 s (a) D = 0.52 mm, L = 100 mm, (b) D = 1.1 mm, L = 150 mm, (c) D = 1.1 mm, L = 300 mm, (d) D = 1.1 mm, L = 450 mm.

Figure 6.3 depicts the effect of tube diameter on the total measured two phase pressure drop per unit length at 6 bar system pressure and 400 kg/m^2 s mass flux. It is obvious that as the diameter was decreased from 1.1 to 0.52 mm (about 50 % reduction), the measured pressure drop increased by about 300 %. The increase in pressure drop as the diameter decreases may be attributed to the large velocity gradient in the boundary layer next to the wall arising from the thinning of the liquid film as the diameter decreases. This may significantly increase the wall shear stress and consequently the frictional

pressure drop. The contribution of the frictional pressure drop to the total measured two phase pressure drop is the largest compared to the gravitational and acceleration contributions as seen in Fig. 6.4. This figure illustrates the contributions of the three pressure drop components (acceleration, gravitation and friction) to the total measured two phase pressure drop at 6 bar system pressure and 300 kg/m^2 s mass flux. The void fraction correlation of Lockhart-Martinelli (1949) (see Appendix A) was used to calculate the gravitational and acceleration components presented in Fig. 6.4. Figure 6.4a shows, for the 0.52 mm tube, that the contribution of the gravitational component decreased from about 43 to 2 % whereas the contribution of the acceleration component increased from about 7 to 22 %. The contribution of the frictional component increased rapidly from about 50 to about 80 % up to exit quality value of about 0.25 after which it remained approximately constant with a tendency to decrease at very high exit quality. Figure 6.4b, for the 1.1 mm tube, shows similar behaviour to that found in the 0.52 mm tube. The gravitational contribution dropped rapidly from about 60 % to less than 5 % whereas the acceleration contribution increased from about 19 to 37 %. The high gravitational contribution at the lowest exit quality observed in the 1.1 mm tube compared to the 0.52 mm is due to the longer heated length. The heated length of the 0.52 mm tube is 100 mm while that of the 1.1 mm tube is 150 mm. The frictional contribution increased rapidly from about 18 to 70 % up to exit quality value of about

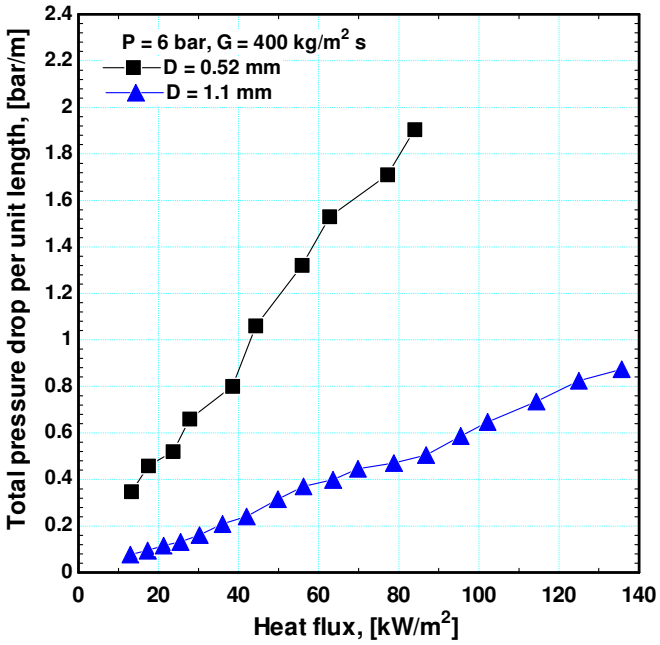

Figure 6.3 The effect of tube diameter on the total measured pressure drop at G = 400 kg/m^2 s and P = 6 bar.

0.4 after which it remained constant over a narrow range of quality before it decreases at high exit quality values. It is obvious also from Figs. 6.4a and 6.4b that as the diameter increases, the contribution of the frictional component decreases which may support the previous explanation of the boundary layer thinning.

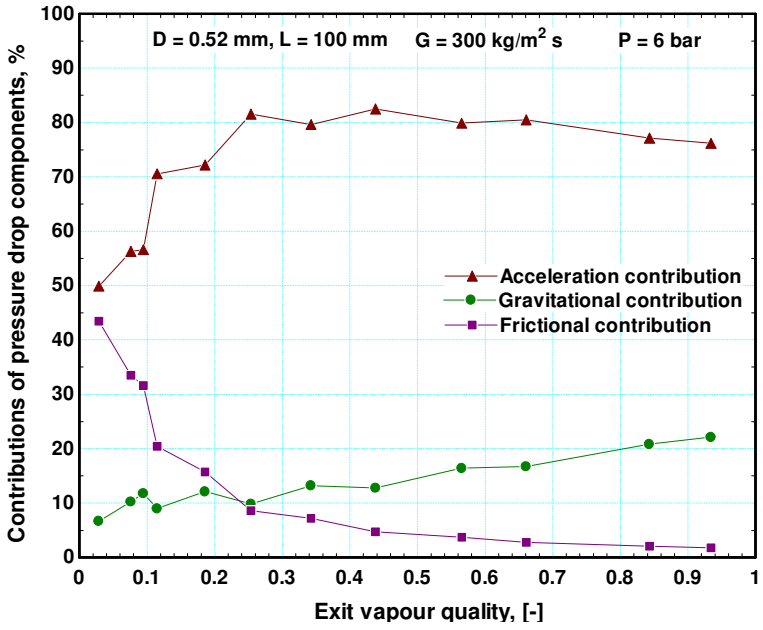

(a)

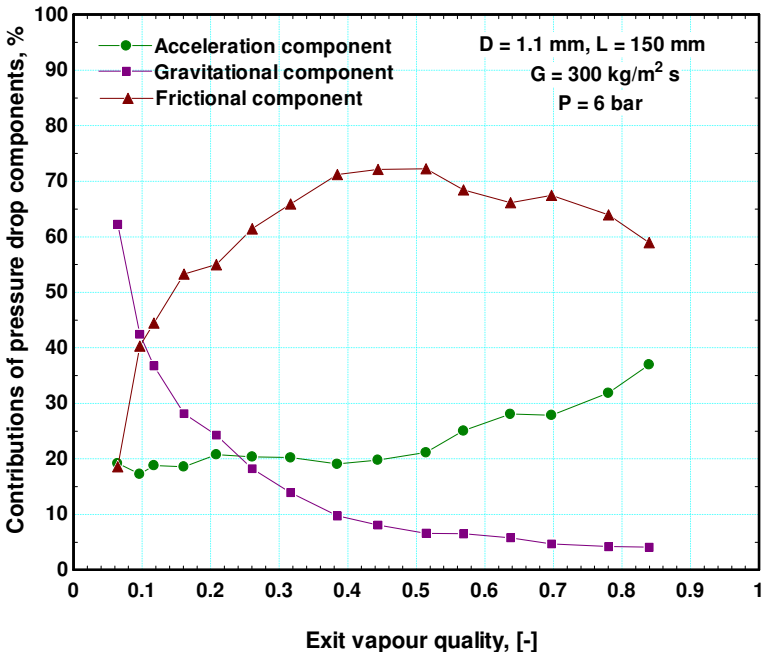

(b)

Figure 6.4 The contributions of the acceleration, gravitational and frictional components to the total measured two phase pressure drop at G = 300 kg/m^2 s and p = 6 bar for (a) D = 0.52 mm and (b) D = 1.1 mm, L = 150 mm.

Figure 6.5 depicts the effect of the heated length on the total measured pressure drop per unit length for D = 1.1 mm, P = 6 bar and G = 500 kg/m^2 s. Each curve in Fig. 6.5 represents the slope of the *P(z)* line at each exit quality value. In other words, each point was calculated as the total measured pressured drop divided by the total length of the tube. It is clear from Fig. 6.5 that, at the same exit quality value, the total measured pressure drop per unit length increases as the heated length decreases. This means that the slope of the *P(z)* line in the shortest tube is much higher than that in the longer tubes for the same exit quality. This behaviour may be explained as follows: at the same exit quality, the applied heat flux in the shortest tube is much higher than that in the longer tubes. As a result of that high heat flux (high wall superheat), nucleate boiling was the dominant heat transfer mechanism in the shortest tube as previously presented in Chapter 4. Accordingly, the possibility of having small nucleating bubbles next to the wall in the shortest tube may increase the frictional pressure drop due to the additional interaction between the phases in the liquid film region next to the wall. This point is clarified further by plotting the frictional pressure drop per unit length versus exit quality in Fig. 6.6. It is worth mentioning here that the total measured pressure drop (bar) was found to increase with increasing the tube heated length, which is expected.

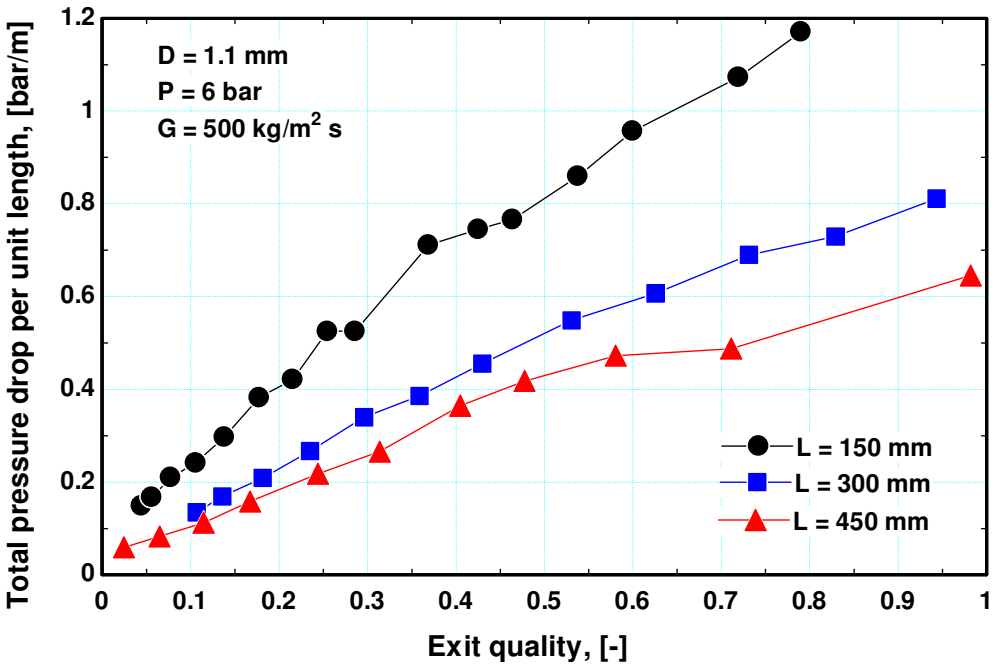

Figure 6.5 The effect of tube heated length on the total measured pressure drop per unit length for D = 1.1 mm at P = 6 bar and G = 500 kg/m^2 s

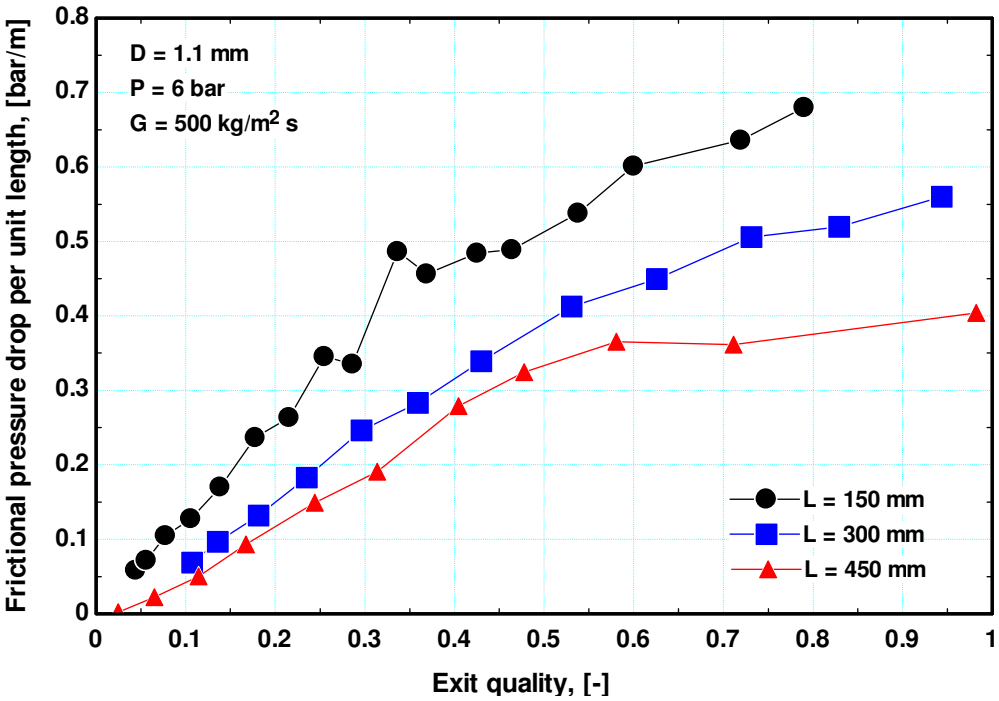

Figure 6.6 The frictional pressure drop per unit length versus exit quality for the three heated lengths for D = 1.1 mm, G = 500 kg/m^2 s and P = 6 bar.

6.3 Evaluation of macroscale models and correlations

Generally, there are two approaches to predict the two phase pressure drop. The first approach is to use the homogeneous flow model whilst the second is to use the separated flow model. The homogeneous flow model assumes that the two phases travel with the same velocity. It is more applicable for cases in which the two phases are mixed very well such as bubbly and dispersed flows. On the other hand, the separated flow model assumes that the two phases are separated and travel with different velocities. It is a more general approach compared to the homogeneous flow model. The problem with the separated flow model compared to the homogeneous model is that it requires very accurate correlation for the void fraction in order to estimate the acceleration and gravitational components. Additionally, it requires an accurate method for estimating the frictional pressure drop component. Lockhart and Martinelli (1949) were the first who proposed the principle of the two phase frictional multiplier for calculating the two phase frictional pressure gradient. This multiplier accounts for the friction coming from the interaction between the phases. Based on that, the two phase frictional pressure gradient was given as:

$$\left(\frac{dP}{dz}\right)_{tp,f} = \phi_L^2 \left(\frac{dP}{dz}\right)_L \tag{6.1}$$

$$\phi_L^2 = 1 + \frac{C}{X} + \frac{1}{X^2} \tag{6.2}$$

The value of *C* in Eq. (6.2) ranges from 5 – 20 depending on whether the regimes of the gas and liquid are laminar or turbulent. This section compares the experimental data with the existing macro-scale models and correlations. The data include those of the 0.52 mm and 1.1 mm diameter tubes at system pressure of 6 – 10 bar, mass flux range of 200 – 500 kg/m^2 s and exit quality up to about 0.9. It is worth mentioning that, the void fraction correlation that was used in the original pressure drop model with which the current data are compared was also used here. For example, the void fraction correlation of Chisholm et al. (1983) was used with their pressure drop correlation instead of using Zivi (1964) or Lockharat-Martinelli (1949) void fraction correlations. The current experimental data are compared with the homogeneous flow model and several separated flow models including those proposed by Lockharat and Martinelli (1949), Friedel (1979), Chisholm et al. (1983) and Muller-Steinhagen and Heck (1986). These models and correlations are evaluated here based on the mean absolute error (*MAE*) defined by Eq. (6.3) and the percentage of data within ± 30 % error bands (β). The details of these correlations and models will be summarized in Appendix A.

$$MAE = \frac{1}{N}\sum_{i=1}^{N}\left[\frac{\left|\Delta P_{measured} - \Delta P_{\Pr edicted}\right|}{\Delta P_{measured}}\right]_i \tag{6.3}$$

The homogeneous flow model

In the present study, the homogeneous frictional pressure gradient was calculated based on all liquid Reynolds number (GD/μ_L). Figure 6.7 depicts the global comparison between the total measured pressure drop and the homogeneous flow model for the 0.52 and 1.1 mm diameter tubes. It is clear from the figure that the homogeneous flow model predicts the experimental data in all tubes very well. In Fig. 6.6a, for the 0.52 mm tube, the model predicted the data with MAE/β values of 18.5/83.4 %. In Figs. 6.6b-d, for the

1.1 mm tubes, the performance of the model does not change significantly where it predicted about 80 % of the data with a MAE value of about 20 %. Figure 6.6 demonstrates also that the model tends to slightly over-predict the experimental values for pressure drop values less than about 0.05 bar, which corresponds to low heat flux values. This may be attributed to the fact that the pressure drop at the lowest heat fluxes may be influenced by the onset of nucleate boiling, which is not taken into account by any model or correlation. In microchannels, due to the incipience of boiling at high wall superheat, the pressure drop remains at its single phase value then it jumps to a higher value at the onset of nucleate boiling. Figure 6.8 shows the experimental pressure drop versus exit quality compared to the homogeneous flow model at P = 6 bar and G = 300 kg/m^2 s for the 0.52 and 1.1 mm tubes. The figure shows that the homogeneous flow model predicts the experimental trend very well. The success of the homogeneous flow model in predicting the experimental data in the 0.52 and 1.1 mm diameter tubes may indicate that there is a good mixing between the phases in theses micro-sizes and thus the slip ratio (u_g / u_L) approaches unity. Serizawa et al. (2002), Hayashi et al. (2007) and Saisorn and Wongwises (2008) measured the void fraction in micro-diameter tubes and found that the measured void fraction is in good agreement with the homogeneous void fraction. Additionally, some researchers such as Mishima and Hibiki (1996), Chen et al. (2002), Kawahara et al. (2002), Serizawa et al. (2002), Chung and Kawaji (2004), Xiong and Chung (2007), Hayashi et al. (2007) and Fu et al. (2008) reported that the drift velocity in micro-diameter tubes can be ignored. Another possible explanation could be the stable versus unstable flow. When the flow is unstable with large oscillations at the liquid/vapour interface, there is a possibility for the axial flow velocities to decrease due to the possible momentum transfer in the traverse direction. This will influence the local velocities and the slip ratio and consequently improve the performance of the homogenous flow model. In the current study, the flow visualization indicated that there are no disturbances at the liquid/vapour interface.

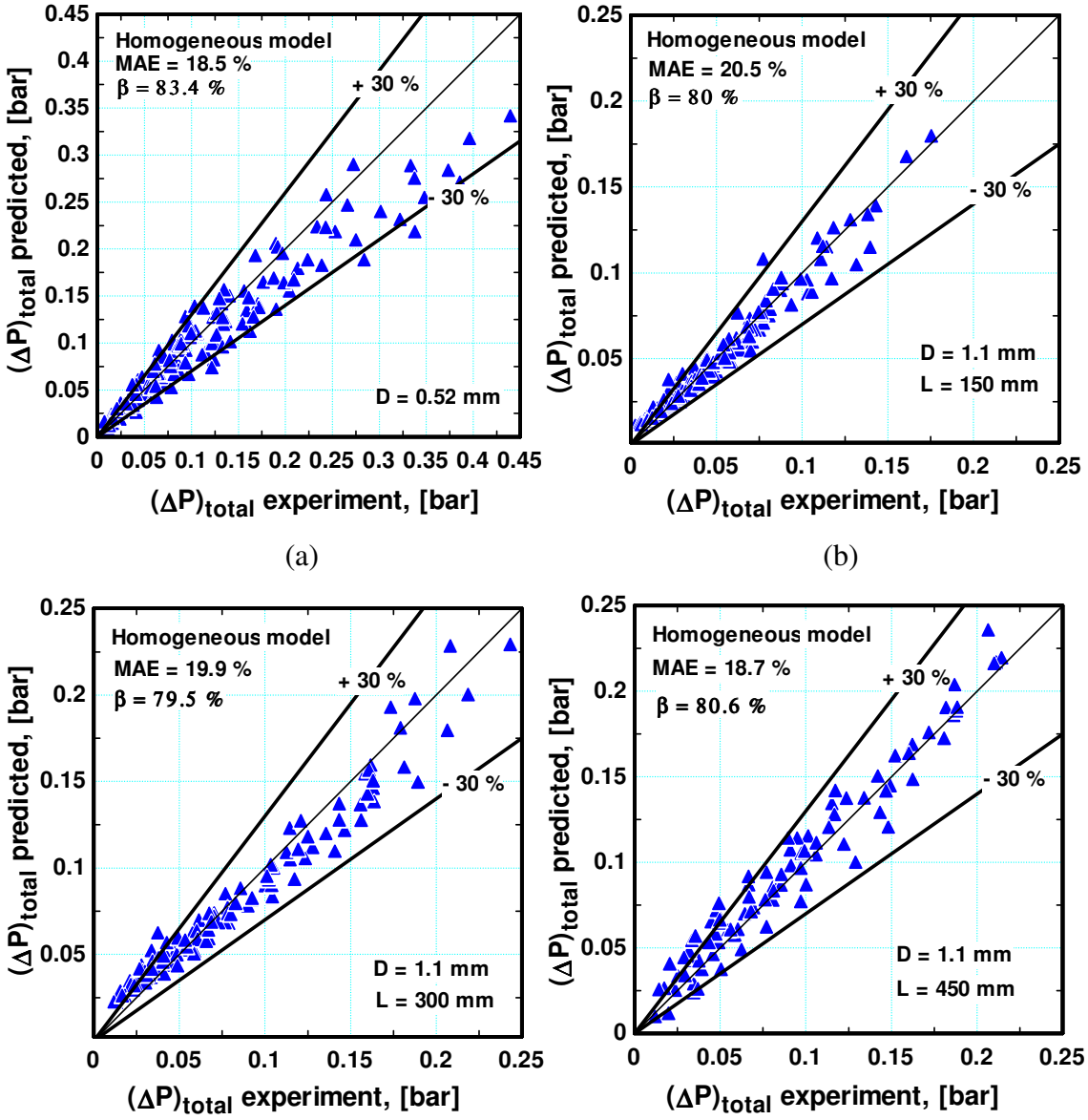

Figure 6.7 The comparison with the homogeneous flow model for (a) D = 0.52 mm, L = 100 mm, (b) D = 1.1 mm, L = 150 mm, (c) D = 1.1 mm, L = 300 mm and (d) D = 1.1 mm, L = 450 mm.

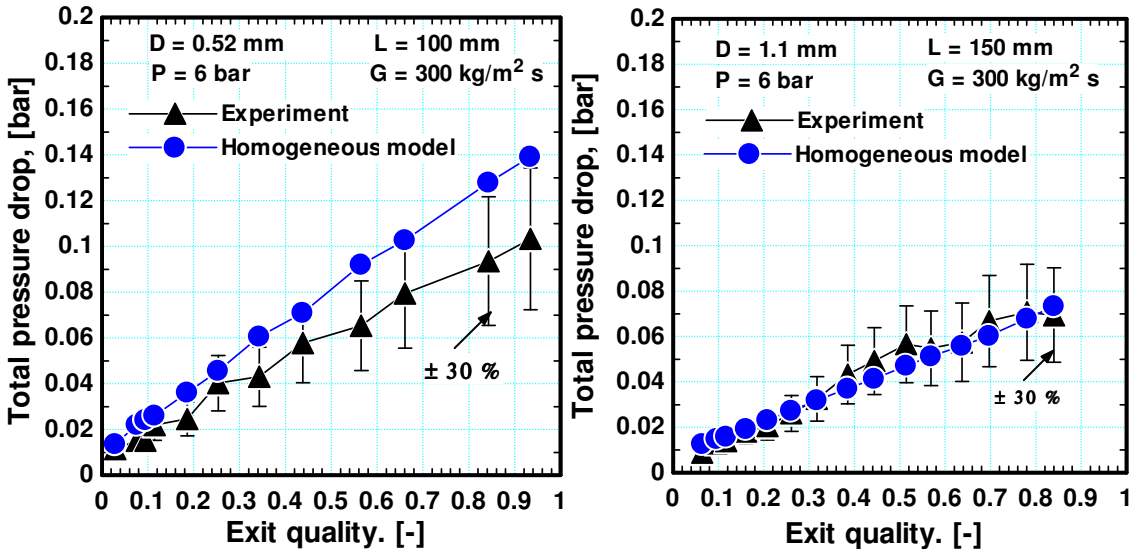

(a) (b)

Figure 6.8 The total measured pressure drop versus exit quality compared to the homogeneous flow model at P = 6 bar and G = 300 kg/m^2 s for (a) D = 0.52 mm and (b) D = 1.1 mm.

The Lockhart-Martinelli model

Figure 6.9 shows the comparison between the experimental data and the separated flow model of Lockhart and Martinelli (1949). The correlation predicted the data of the 0.52 mm diameter tube very well where 85.4 % of the data were predicted within the ± 30 % error bands with a MAE value of 16.5 %. On the contrary, the correlation failed to predict the data of the 1.1 mm diameter tubes and the predictions become worse as the heated length of the 1.1 mm tube increases an the reasons are not clear. Figure 6.10 depicts the experimental pressure drop versus exit quality compared to the Lockhart-Martinelli's model at some mass fluxes. This figure explains why the model predicts the data of the 0.52 mm tube much better than the other 1.1 mm tubes. In the 0.52 mm diameter tube (Fig. 6.10a) at G = 300 kg/m^2 s and P = 6 bar, the experimental trend was perfectly linear even at very high exit qualities, i.e. the pressure drop increases constantly with almost a constant rate. Similar behaviour was also found at all mass fluxes and system pressures. Accordingly, the separated flow model deviated from the experimental values at few data points. On the contrary, the trend of the measured pressure drop in the 1.1 mm tubes was not perfectly linear at all experimental conditions. For example, in Fig. 6.10b for D = 1.1 mm, L = 150 mm, G = 300 kg/m^2 s,

the model and the experiment exhibited excellent agreement with a tendency to deviate at the last data point. For the same tube at higher mass flux and system pressure (Fig. 6.10c), the model predicted exactly a similar trend to the experiment (non-linear) but over-predicted about 50 % of the data points by more than 30%. Figure 6.9d, for the longest 1.1 mm diameter tube, shows that the trends are almost linear but the slope of the experimental line is less than that of the predicted line. This means that there is only partial agreement with the model at very low exit quality values and the deviation increases with increasing exit quality. The reason why the trend of the measured pressure drop in the 0.52 mm diameter tube was a perfect linear at all mass fluxes compared to the 1.1 mm diameter tube may be attributed to the laminar nature of the flow in the 0.52 mm tube. See for example Figs. 6.10a and b where Reynolds number is less than 2000 in both cases and the trends are perfectly linear. In Fig. 6.9c, the value of Reynolds number is greater than 3000 and the trend is not perfect linear. When the flow is turbulent, the liquid film may be distorted at high heat fluxes (exit quality) and consequently the wall shear stress may decrease. In the 0.52 mm tube due to the strongest effect of surface tension compared to the 1.1 mm tube and the laminar flow in the liquid film, the liquid film stay in contact with the wall even at high heat fluxes. This may result in a higher wall shear stress (frictional pressure drop), which prevents the pressure drop from decreasing at high heat fluxes. The fact that the homogeneous flow model predicted the data of all tubes very well whereas the separated flow model predicted only the data of the 0.52 mm tube needs a comment. The reason may be due to the void fraction correlation in both models. The void fraction correlation of Lockhart and Martinelli is developed mainly based on the annular flow regime, which agrees with the dominant flow regimes in the 0.52 mm tube (elongated bubble and annular flow). On the other hand, bubbly, slug, churn and annular flow regimes were observed in the 1.1 mm diameter tube.

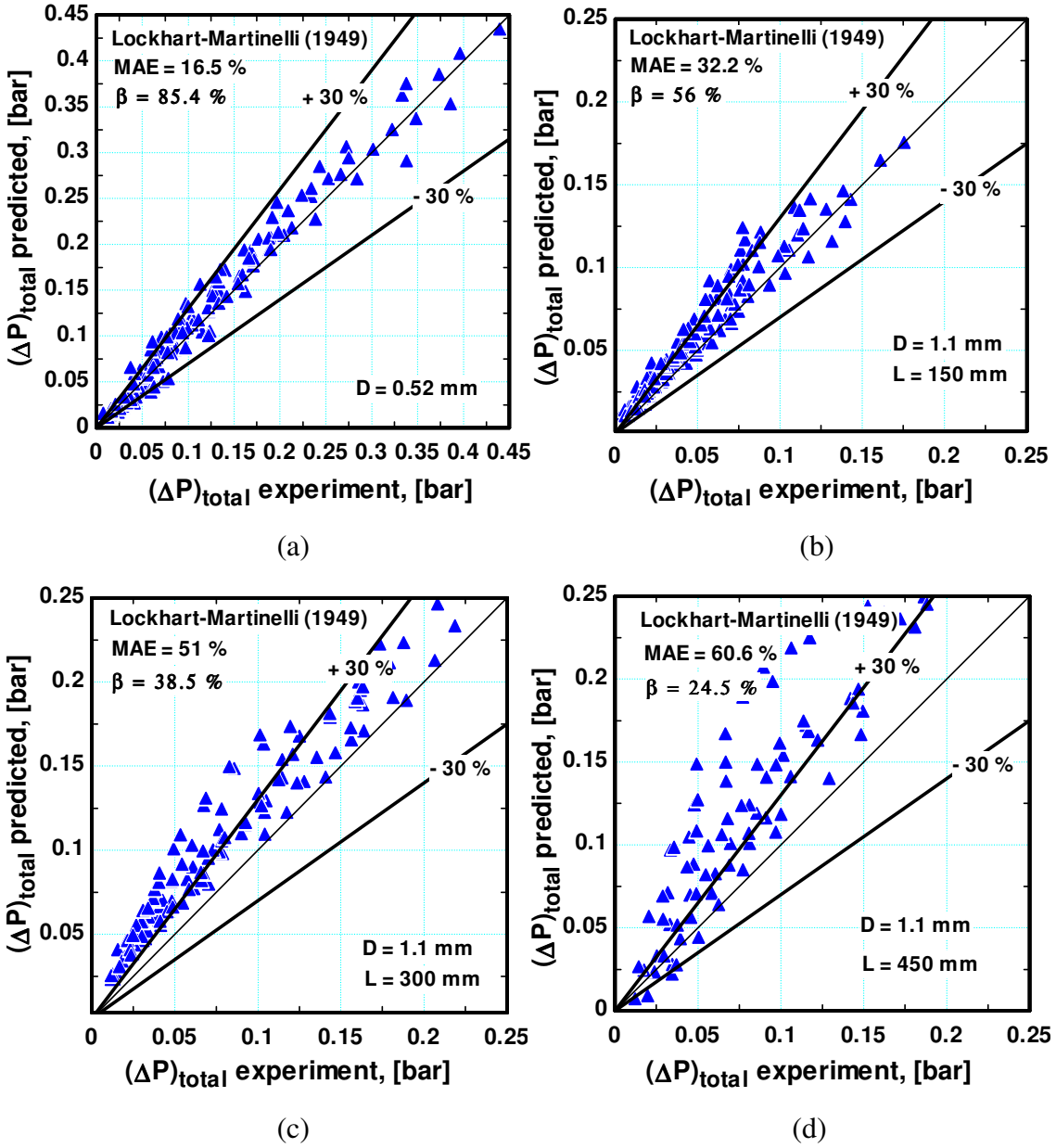

Figure 6.9 The comparison with the Lockhart-Martinelli (1949) model for (a) D = 0.52 mm, L = 100 mm, (b) D = 1.1 mm, L = 150 mm, (c) D = 1.1 mm, L = 300 mm and (d) D = 1.1 mm, L = 450 mm.

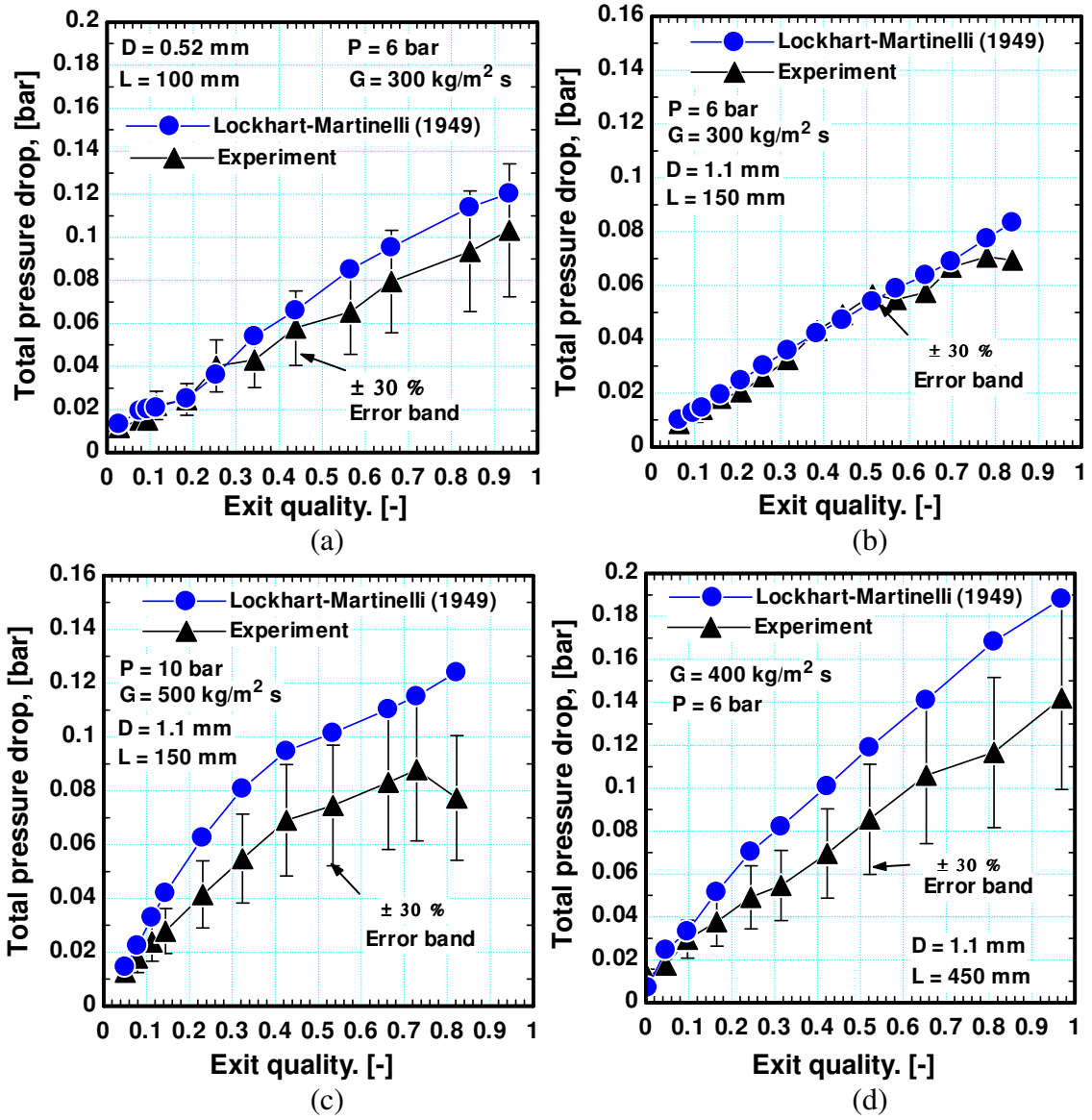

Figure 6.10 The total measured pressure drop versus exit quality compared to the model of Lockhart-Martinelli (1949) for (a) D = 0.52 mm and (b), (c) D = 1.1 mm, L = 150 mm and (d) D = 1.1 mm, L = 450 mm.

The Chisholm correlation

Chisholm (1973) proposed a correlation for the two phase frictional multiplier based on all liquid flow. The Chisholm multiplier was introduced as a function of vapour quality and the ratio between the all gas and all liquid pressure gradients. Also, Chisholm incorporated a factor *B* into the correlation that depends on the total mass flux and consequently the correlation was called Chisholm B-coefficient correlation. Figure 6.11 depicts the global comparison between the experimental data and the correlation of Chisholm (1973). It is obvious from the figure that, the correlation predicts poorly the

experimental data in all tubes. In Figs. 6.11a and b the correlation predicted only 15.9 % and 18.8 % of the data for the 0.52 mm tube and the shortest 1.1 mm tube respectively. When the heated length of the 1.1 mm tube was increased, the prediction gets worse as seen in Figs. 6.11c and d. Figure 6.12 compares the trend of the measured pressure drop versus exit quality with that predicted by the Chisholm correlation. It is obvious that, the correlation did not capture the linear trend in the 0.52 mm tube as seen in Fig. 6.12a and there is some agreement with very few data points particularly at the lowest and highest exit qualities. The same behaviour is seen in the 1.1 mm tube results depicted in Fig. 6.12b. Generally, the correlation highly over-predicts the experimental data in both tubes.

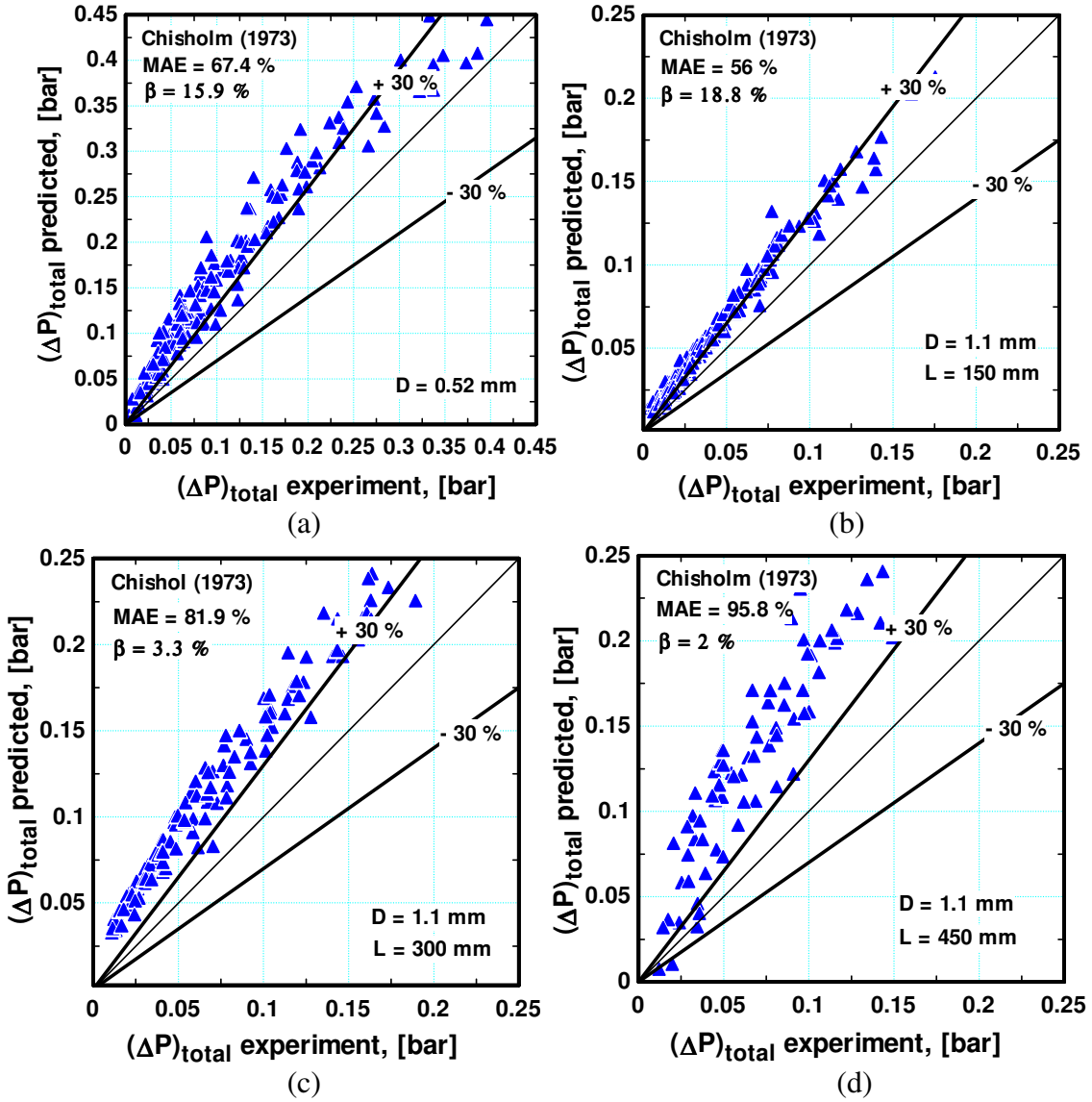

Figure 6.11 The comparison with the Chisholm (1973) model for (a) D = 0.52 mm, L = 100 mm, (b) D = 1.1 mm, L = 150 mm, (c) D = 1.1 mm, L = 300 mm and (d) D = 1.1 mm, L = 450 mm.

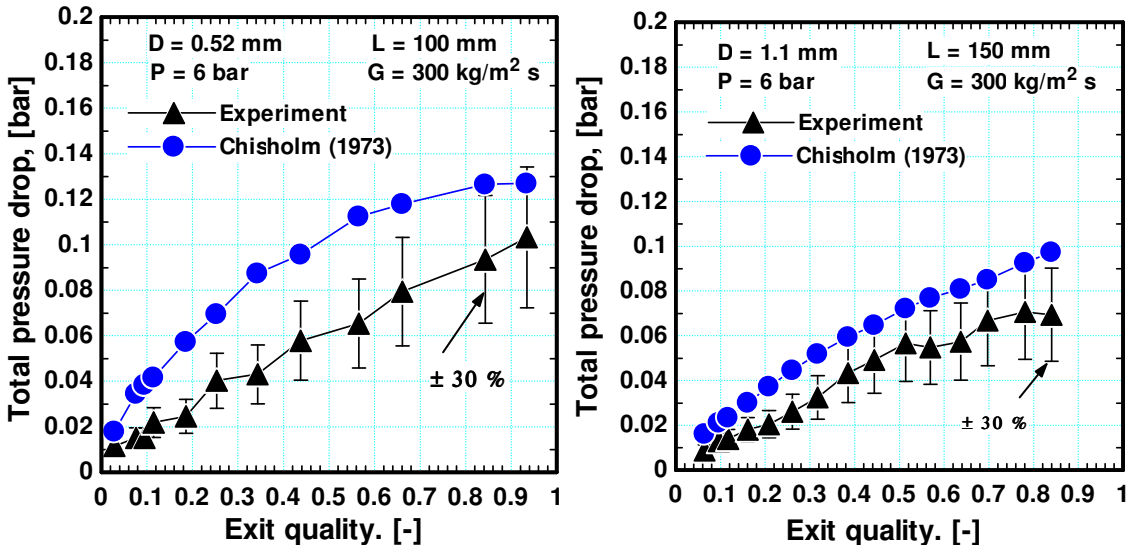

Figure 6.12 The total measured pressure drop versus exit quality compared to the model of Chisholm (1973) for (a) D = 0.52 mm and (b) D = 1.1 mm.

The Friedel correlation

In the Lockhart-Martinelli correlation, the two phase frictional multiplier was calculated based on the premise that the liquid fraction is flowing alone and the single phase friction factor was calculated based on the liquid Reynolds number $(1-x)GD/\mu_L$. However, Friedel (1979) proposed a correlation for the two phase frictional multiplier but based on all liquid Reynolds number GD/μ_L. The correlation was introduced as a function of the Weber and Froude number as well as vapour quality and fluid properties and it is applied to both vertical and horizontal tubes. Figure 6.13 compares the current experimental data with the correlation of Friedel (1979). In Fig. 6.13a, for the 0.52 mm tube, the correlation predicted 69 % of the data at a MAE value of 20.6 %. In Fig. 6.13b for the shortest 1.1 mm tube, the correlation predicted 79 % of the data at a MAE value of 21.5 %. For the two longest 1.1 mm diameter tubes, the performance slightly decreased where the correlation predicted 63 and 60 of the data at MAE values of 28.5 and 31.9 respectively as seen in Figs. 6.13c and d. From Fig. 6.13, the correlation slightly over-predicts the data at very low pressure drop values. Figure 6.14 illustrates the experimental pressure drop versus exit quality compared to the Friedel correlation at G = 300 kg/m^2 s and P = 6 bar for D = 0.52 and 1.1 mm. It is obvious that the correlation predicts the experimental trend and magnitudes very well. For the two longest 1.1 mm diameter tubes, the performance of the correlation was similar to that

shown in Fig. 6.14 and the correlation tends to slightly over-predict the experimental values at very low exit qualities.

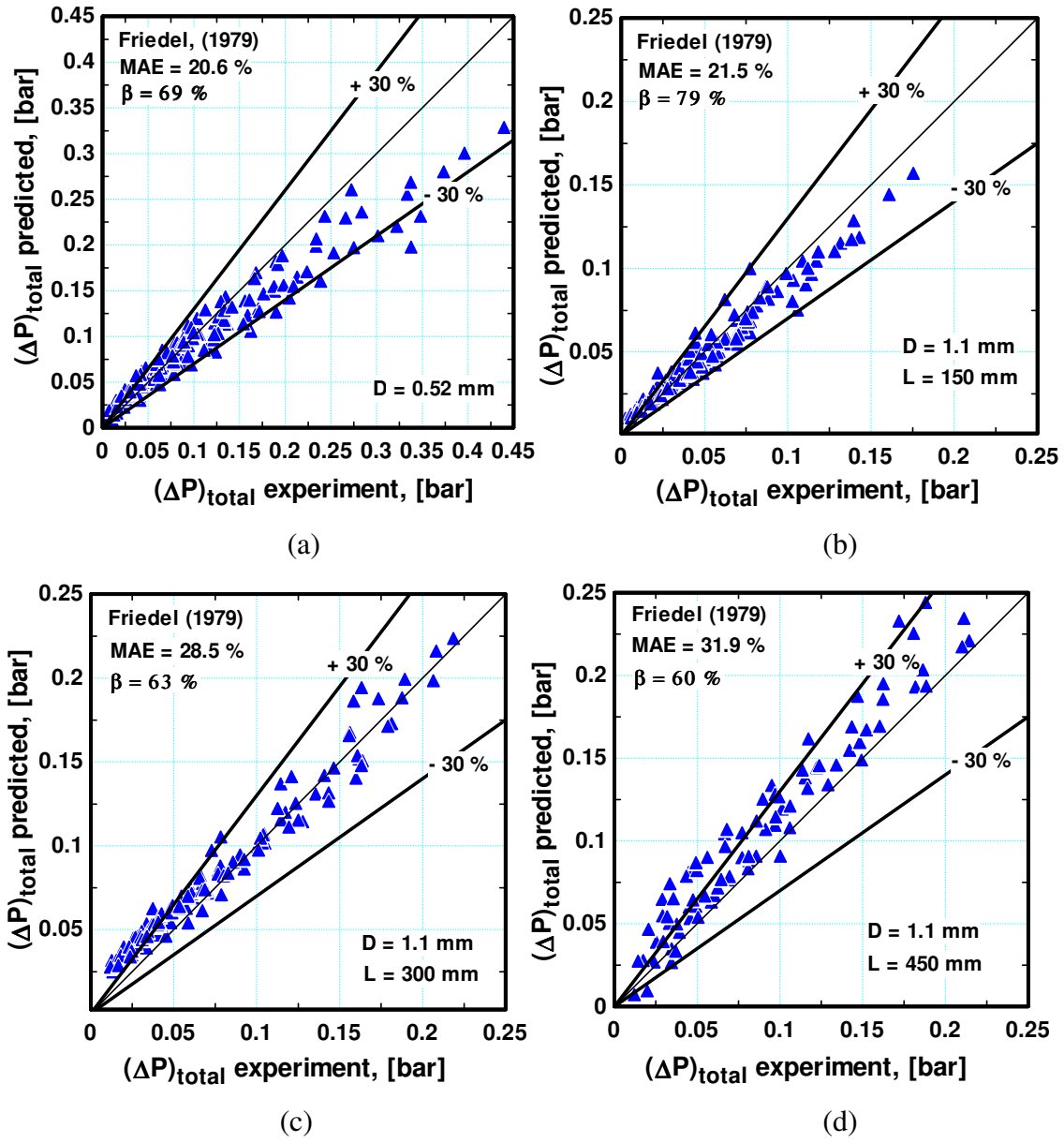

Figure 6.13 The comparison with the Friedel (1979) correlation for (a) D = 0.52 mm, L = 100 mm, (b) D = 1.1 mm, L = 150 mm, (c) D = 1.1 mm, L = 300 mm and (d) D = 1.1 mm, L = 450 mm.

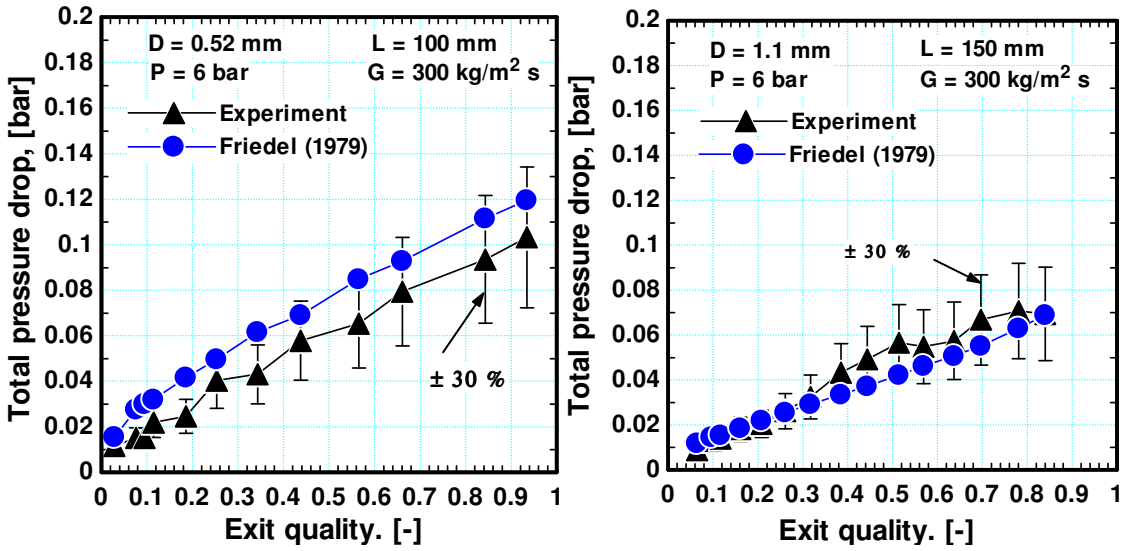

(a) (b)

Figure 6.14 The total measured pressure drop versus exit quality compared to the correlation of Friedel (1979) for (a) D = 0.52 mm and (b) D = 1.1 mm.

The Muller-Steinhagen and Heck correlation

Muller-Steinhagen and Heck (1986) proposed a correlation for the two phase frictional multiplier using interpolation between all liquid flow and all vapour flow. This correlation was developed based on data for air-water, steam-water and several refrigerants. Figure 6.15 compares the experimental data with the correlation of Muller-Steinhagen and Heck. As seen in Figs. 6.15a and b for the 0.52 mm and the shortest 1.1 mm tube, the correlation predicts the experimental data very well and better than the above correlations. For the two longest 1.1 mm diameter tubes, the performance of the correlation was similar to the homogeneous flow model where it predicted 81.1% and 78.6 % of the data within the ± 30 % error bands. Again Fig. 6.16 demonstrates that the correlation predicts the trend of the experimental pressure drop versus exit quality very well. Similar behaviour was obtained for the two longest 1.1 mm tubes. The performance of the Muller-Steinhagen and Heck correlation in the current study agrees with the conclusions of Ribataski et al. (2006). They found that Muller-Steinhagen and Heck correlation is the best examined one followed by the homogeneous model and the Mishima and Hibiki correlation.

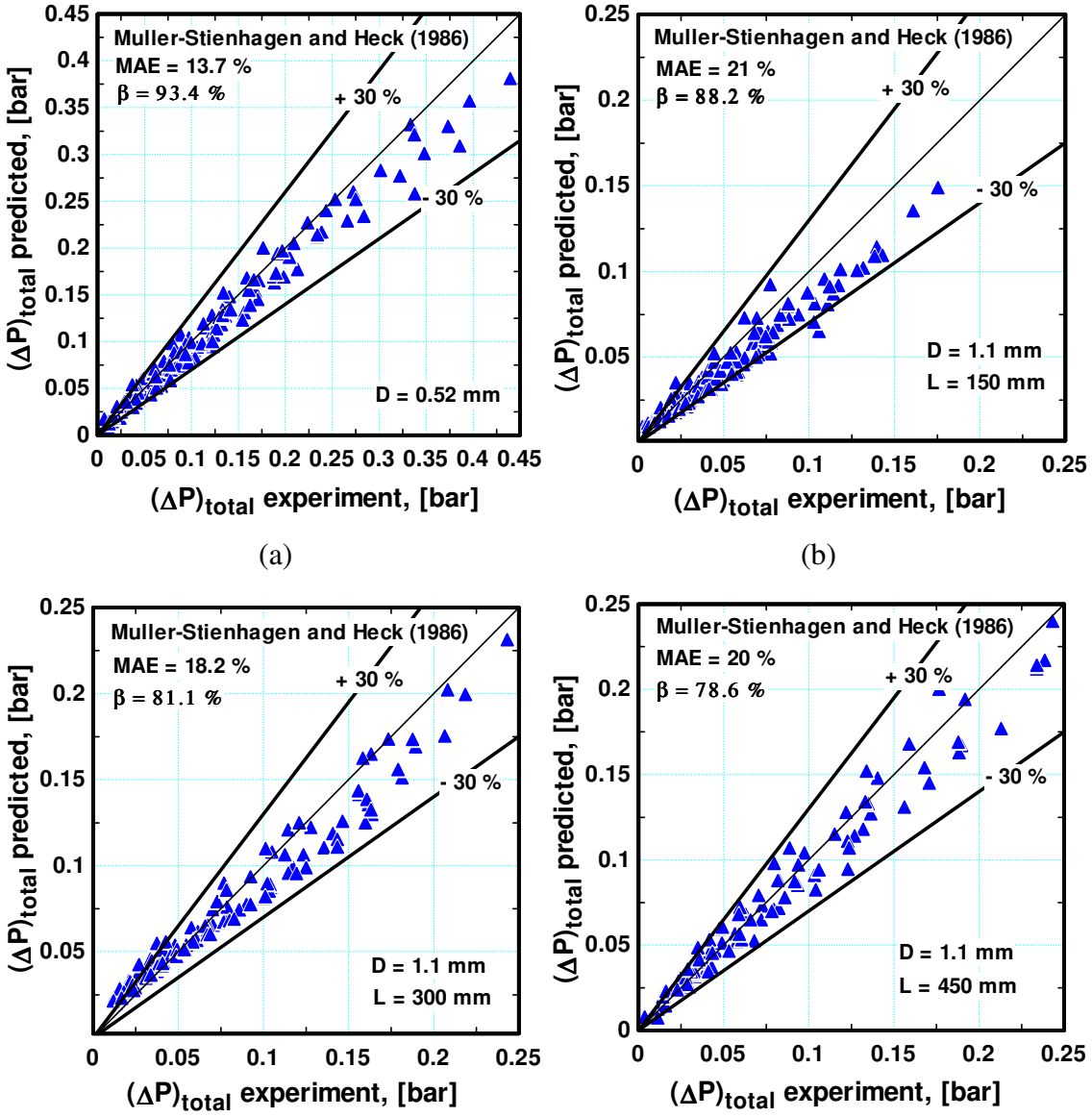

Figure 6.15 The comparison with the correlation of Muller-Stienhagen and Heck (1986) for (a) D = 0.52 mm, L = 100 mm, (b) D = 1.1 mm, L = 150 mm, (c) D = 1.1 mm, L = 300 mm and (d) D = 1.1 mm, L = 450 mm.

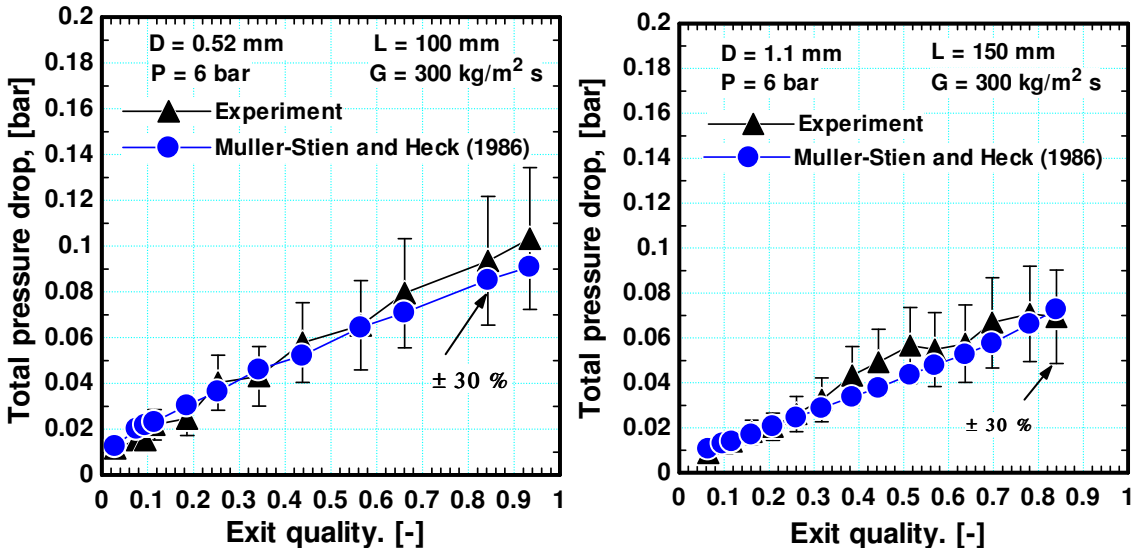

Figure 6.16 The total measured pressure drop versus exit quality compared to the correlation of Muller-Stienhagen and Heck (1986) for (a) D = 0.52 mm and (b) D = 1.1 mm.

6.4 Evaluation of microscale correlations

Several correlations were proposed in the past fifteen years for predicting the two phase flow pressure drop in small to micro diameter channels. Most researchers adopted the separated flow model of Lockhart-Martinelli and modified the Chisholm's constant in Eq. (6.2). This section presents a comparison between the experimental data and eleven micro-scale correlations including those proposed by Mishima and Hibiki (1996), Tran et al. (2000), Lee and Lee (2001), Warrier et al. (2002), Yu et al. (2002), Qu and Mudawar (2003a), Lee and Mudawar (2005), Lee and Garimella (2008), Zhang et al. (2010), Li and Wu (2010) and Lee et al. (2010).

The Mishima and Hibiki correlation

Mishima and Hibiki (1996) measured the two phase pressure drop for air-water flow in capillary tubes with diameters ranging from 1 to 4 mm. They have found that the Chisholm's constant depends on tube inner diameter where it decreases when the diameter decreases. They proposed a correlation for this parameter given by Eq. (6.4), which is applicable for vertical, horizontal, circular and rectangular channels.

$$C = 21\left(1 - e^{-0.319 d_h}\right) \tag{6.4}$$

Figure 6.17 depicts the global comparison between the experimental data and the correlation of Mishima and Hibiki (1996). Figure 6.17a shows, for the 0.52 mm tube, that the correlation under-predicts the experimental data by values slightly greater than 30 %. Although the MAE value is 24.5%, the correlation predicted only 69 % of the data within the error bands. The performance of the correlation has improved in the 1.1 mm diameter tubes compared to the 0.52 mm tube as seen in Figs. 6.17b-d where it predicted 77 – 83.7 % of the data within the error bands. Figure 6.18 illustrates the experimental pressure drop versus exit quality compared to the trend predicted by the correlation. It is seen from the figure that the correlation predicts the experimental trend properly but tends to under-predict the experimental values in the 0.52 mm tube (Fig. 6.18a) at high exit qualities. The relatively less performance of the correlation in the 0.52 mm tube, compared to the 1.1 mm tube, may be due to the fact that the smallest diameter in the study of Mishima-Hibiki was 1 mm. Also, it is clear from Eq. (6.4) that the smaller the diameter, the smaller the Chisholm's constant and consequently the two phase frictional multiplier. In other words, the correlation can not be extrapolated to work in tubes with size much less than 1 mm as it will highly under-predict the experimental values.

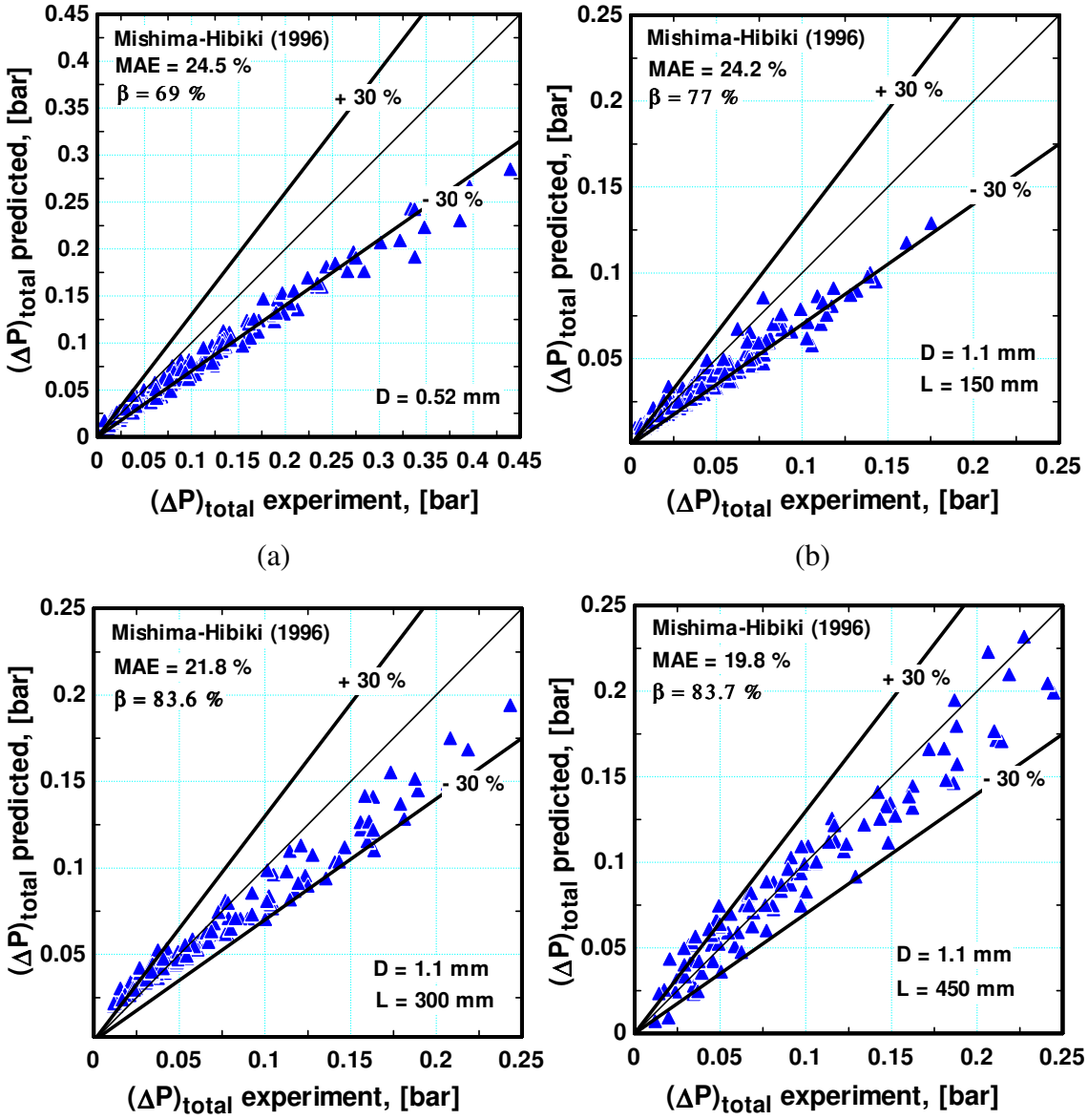

Figure 6.17 The comparison with the Mishima and Hibiki (1996) correlation for (a) D = 0.52 mm, L = 100 mm, (b) D = 1.1 mm, L = 150 mm, (c) D = 1.1 mm, L = 300 mm and (d) D = 1.1 mm, L = 450 mm.

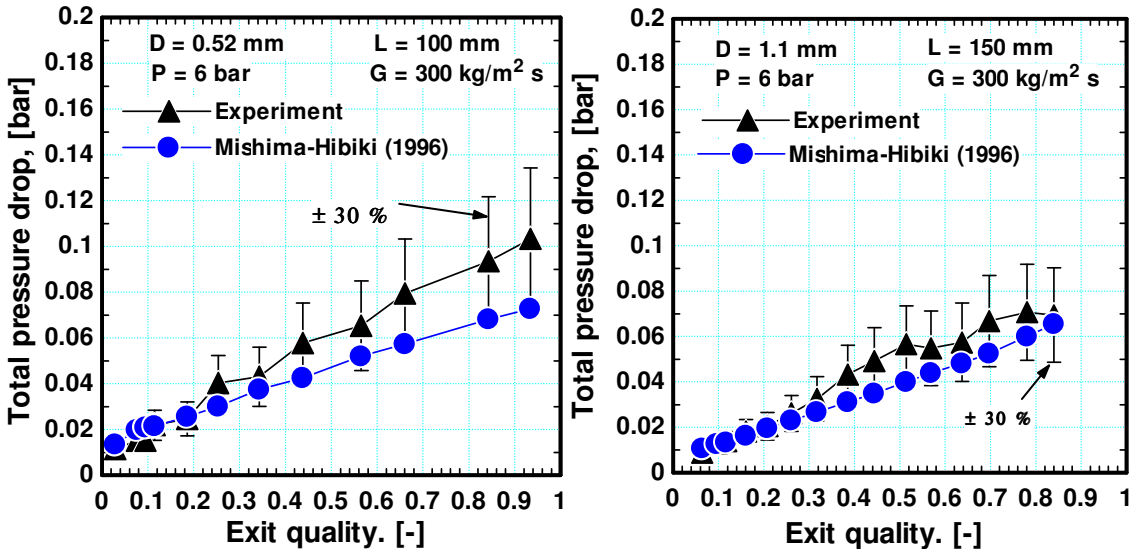

(a) (b)

Figure 6.18 The total measured pressure drop versus exit quality compared to the correlation of Mishima and Hibiki (1996) for (a) D = 0.52 mm and (b) D = 1.1 mm.

The Tran et al. correlation

Tran et al (2000) investigated flow boiling of three refrigerants (R134a, R12, R113) in two circular channels with diameters of 2.46 and 2.92 mm and a rectangular channel with hydraulic diameter of 2.4 mm. They have found that the macro-scale correlations could not predict their measured two phase pressure drop. They believed that the failure of these correlations was due to an additional frictional component resulting from the deformation of the elongated bubbles in small diameter channels, which makes the pressure drop in micro-channels too high. Accordingly, they proposed a correlation for the two phase frictional multiplier based on 610 data points. Their correlation was basically a modified version of the Chisholm (1983) B-coefficient correlation. They replaced the coefficient *B* in the original correlation with the confinement number (*Co*) proposed by Kew and Cornwell (1997) to account for the effect of tube diameter and surface tension as given by:

$$\phi_{Lo}^2 = 1 + \left(4.3\Gamma^2 - 1\right)\left[\left(Cox^{0.875}(1-x)^{0.875} + x^{1.75}\right)\right] \qquad (6.5)$$

Figure 6.19 compares the experimental data with the correlation of Tran et al. (2000). It is clear from the figure that the correlation highly over-predicts the experimental data with MAE values ranging from 66.5 to 168 % and percentage of data within the error

bands ranging from 0 to 16.5 %. Although the correlation is a modified version of the conventional Chisholm et al. correlation, it predicted poorly the data in the 0.52 mm diameter tube compared to the original correlation. Figure 6.20 shows the experimental pressure drop versus exit quality compared to Tran et al. correlation. The figure demonstrates that the correlation over-predicts the data of the 0.52 mm diameter tube (Fig. 6.20a) to a much higher degree compared to the 1.1 mm diameter tube (Fig. 6.20b). It is obvious from Eq. (6.5) that as the diameter decreases, the frictional two phase multiplier increases due to the increase in the confinement number (Co). This is consistent with the current experimental results presented in Fig. 6.3 where the measured pressure drop increased when the diameter decreased. The reason why the correlation highly over-predicts the current experimental data may be due to the fact that they did not investigate a wide range of tube diameters to determine the proper exponent of the confinement number in their correlation. They only investigated one diameter value of 2.92 mm at which the confinement number value is about 0.25 for R134a at 6 bar system pressure. This value is 3 times less than the value for D = 1.1 mm and 6 times less than the value for D = 0.52 mm tube.

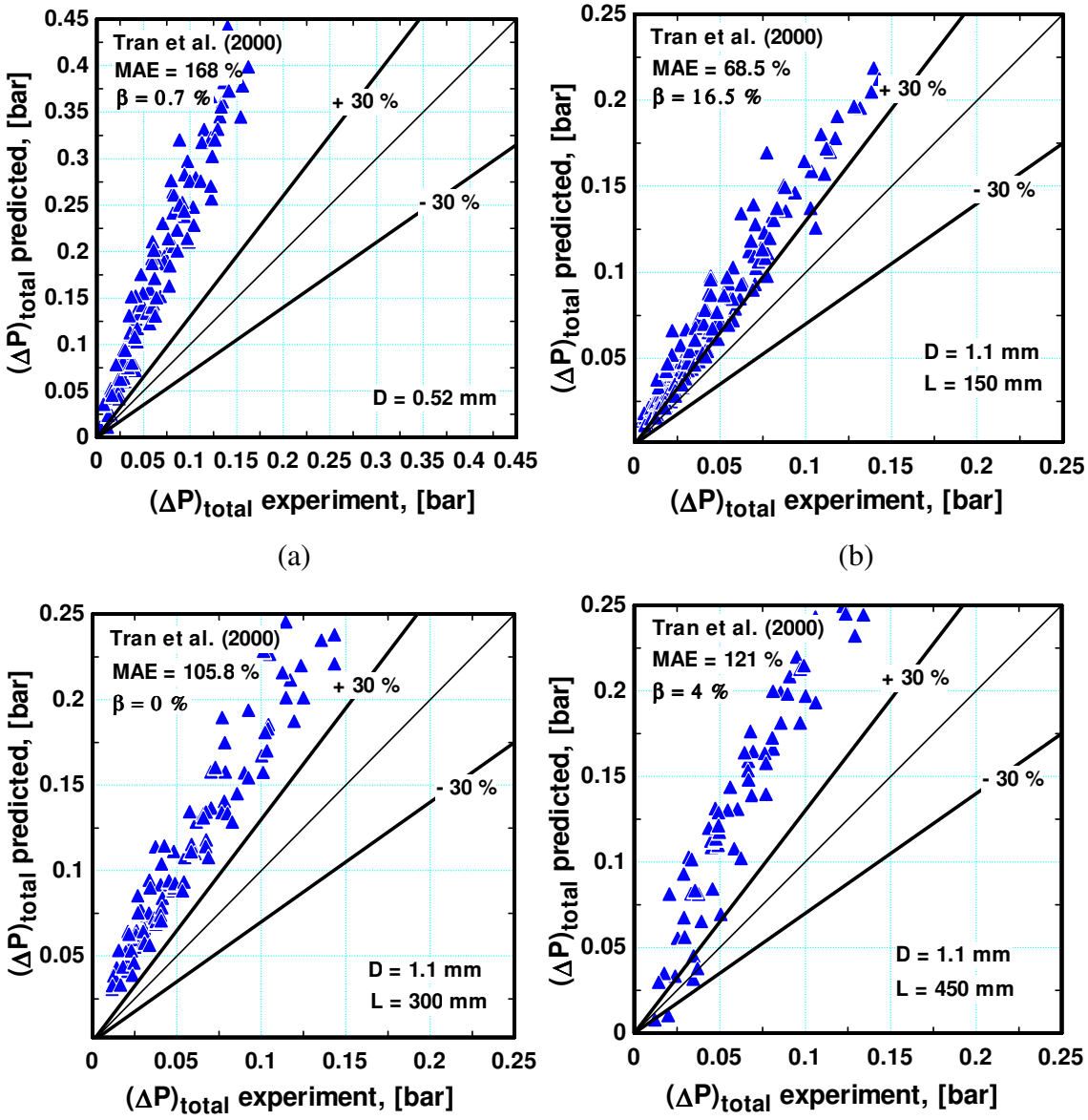

Figure 6.19 The comparison with the Tran et al. (2000) correlation for (a) D = 0.52 mm, L = 100 mm, (b) D = 1.1 mm, L = 150 mm, (c) D = 1.1 mm, L = 300 mm and (d) D = 1.1 mm, L = 450 mm.

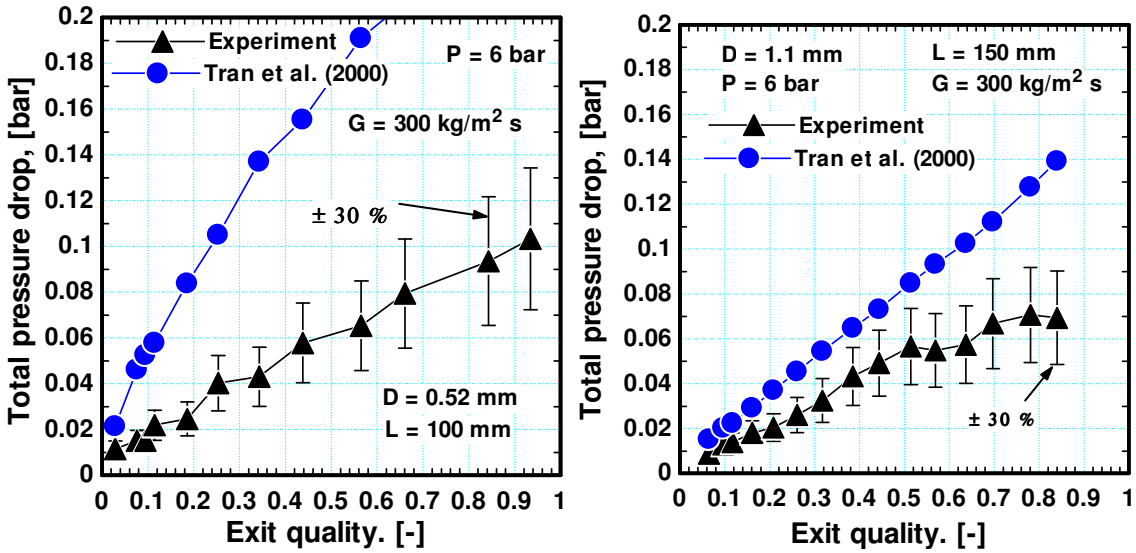

Figure 6.20 The total measured pressure drop versus exit quality compared to the correlation of Tran et al. (2000) for (a) D = 0.52 mm and (b) D = 1.1 mm.

Figure 6.19 indicates that the Tran et al. (2000) correlation has a fixed bias that makes the correlation predicts poorly the current experimental data. The constant 4.3 in Eq. (6.5) was determined experimentally by Tran et al. (2000). It is interesting to note that, when this constant was changed in the current study to 1.75, the correlation performed much better compared to the original version of the correlation. Figure 6.21 shows the global comparison between the current experimental data and the modified Tran et al. correlation. For the 0.52 mm diameter tube (Fig. 5.21a), the MAE value decreased from 168 % to 23.1% and the percentage of data within the ± 30 % error bands increased from 0.7 % to 74 %. For the shortest mini diameter tube (Fig. 6.21b), the MAE value decreased from 68.5 % to 22.3 % and the percentage of data within the ± 30 % error bands increased from 16.5 % to 86 %. For the mini diameter tube with L = 300 mm (Fig. 6.21c), the MAE value decreased from 105.8 % to 20.8 % and the percent of data within the ± 30 % error bands increased from 0 % to 80 %. For the longest mini diameter tube (Fig. 6.21d), the MAE value decreased from 121 % to 22.9 % and the percent of data within the ± 30 % error bands increased from 4 % to 76.5 %.

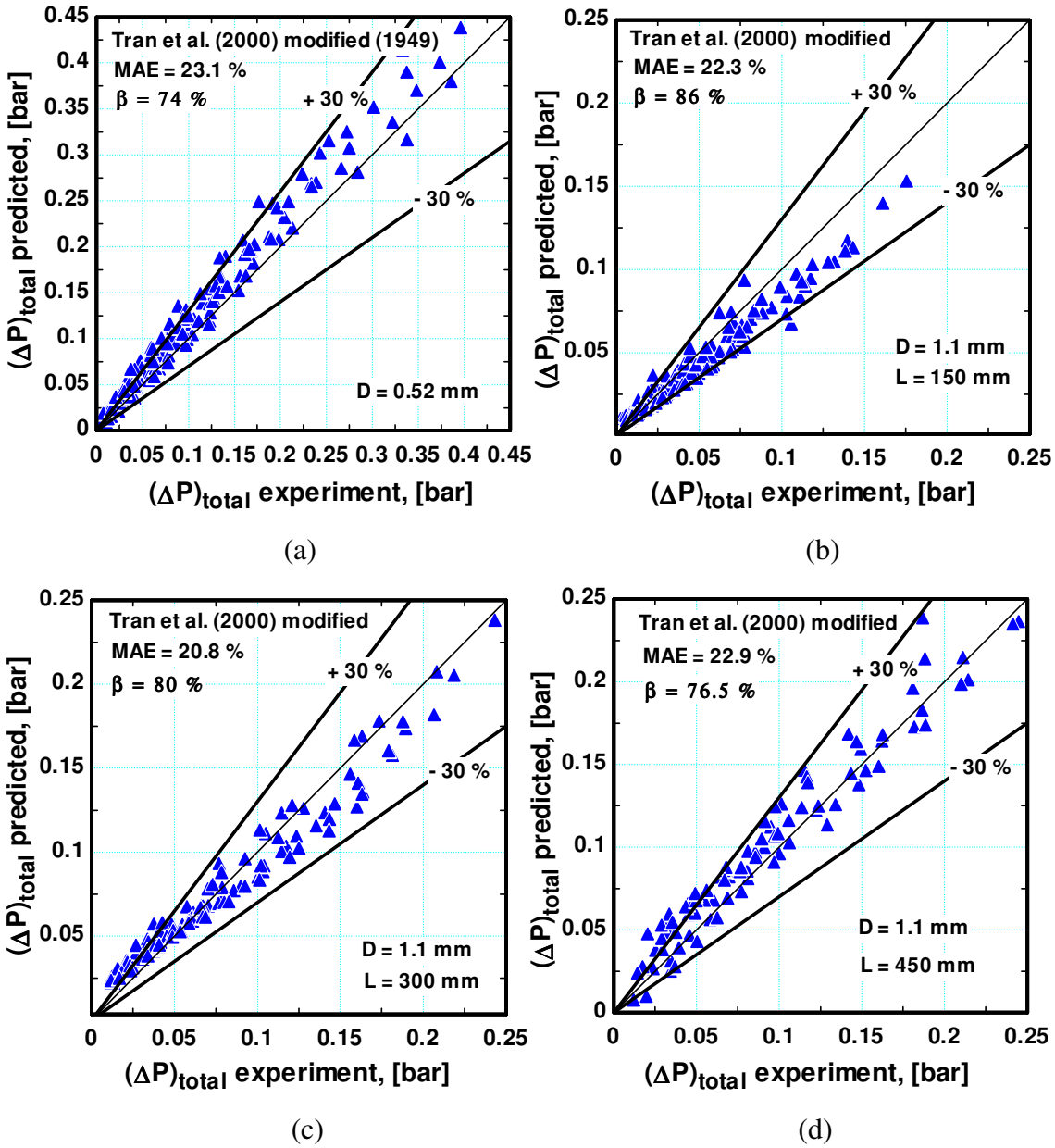

Figure 6.21 The comparison with the modified Tran et al. (2000) correlation for (a) D = 0.52 mm, L = 100 mm, (b) D = 1.1 mm, L = 150 mm, (c) D = 1.1 mm, L = 300 mm and (d) D = 1.1 mm, L = 450 mm.

The Yu et al. correlation

Yu et al. (2002) investigated flow boiling heat transfer and pressure drop of water in a 2.98 mm diameter tube with 910 mm heated length. In their study, the flow regime of the liquid and vapour flowing alone was laminar and turbulent respectively. They compared the experimental two phase frictional multiplier against the classical Lockhart-Martinelli multiplier (Eq. 6.2) and found that the correlation over-predicts the experimental values. They attributed this to the occurrence of slug flow over a wide

range of qualities in small diameter tubes, which reduces the pressure gradients compared to the annular flow regimes that dominates in large diameter tubes. This explanation may be suitable for refrigerants but in their study they used water and it is known that annular flow is the dominant flow regime. Due to this overestimation, they fitted their experimental two phase frictional multiplier data as a power function given by:

$$\phi_L^2 = \frac{1}{\mathrm{X}^{1.9}} \tag{6.6}$$

Figure 6.22 compares the experimental data with the correlation of Yu et al. (2002). The correlation predicts about 27.8 % of the 0.52 mm tube data particularly for very low pressure drop values as seen in Fig. 6.22a. For the 1.1 mm tubes, the data are scattered as seen in Figs. 6.22b-d and the correlation predicted only 30.3 – 38.2 % of the data within the error bands. Again, Fig. 6.22 shows the experimental pressure drop versus exit quality compared to the correlation. As seen in the figure, the correlation predicted very few data points at very low exit quality values. Additionally, there is a change in trend after $x \approx 0.3$, which is very clear in Fig. 6.22a. This change in trend is attributed to the fact that at very low exit qualities both liquid and vapour are laminar and the pressure drop was predicted using the original Lockhart-Martinelli correlation, i.e. based on C = 5 in Eq. (6.2). As the quality increases, the vapour becomes turbulent and the new correlation of Yu et al. was used. Since the new correlation ignored the term C/X in the laminar liquid/turbulent vapour regime, it is expected that the correlation under-predicts the experimental values at high vapour qualities. The Chisholm's constant seems to be very important in the correlation since it takes into account the frictional contributions resulting from the interaction between the phases.

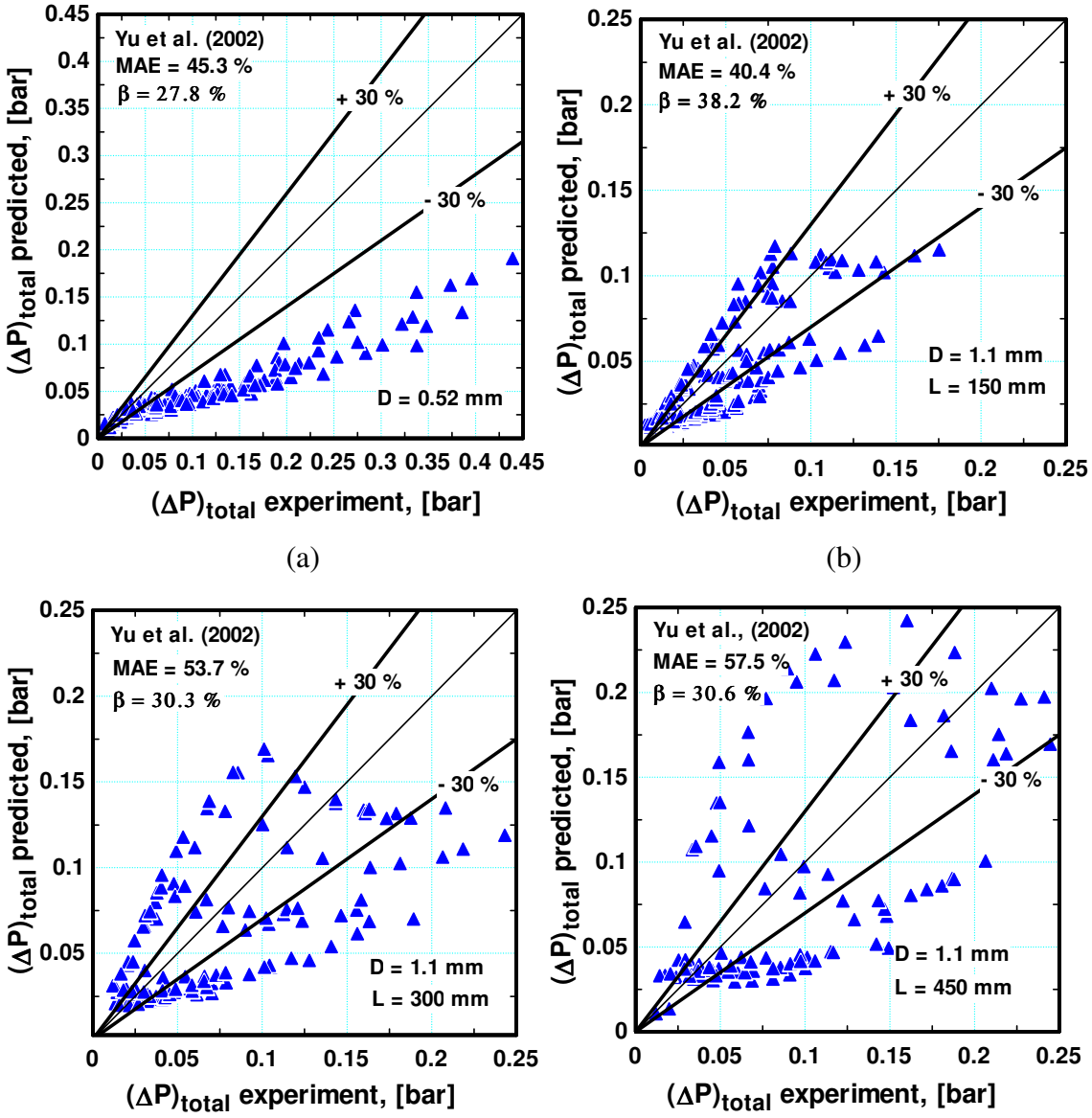

Figure 6.22 The comparison with the Yu et al. (2002) model for (a) D = 0.52 mm, L = 100 mm, (b) D = 1.1 mm, L = 150 mm, (c) D = 1.1 mm, L = 300 mm and (d) D = 1.1 mm, L = 450 mm.

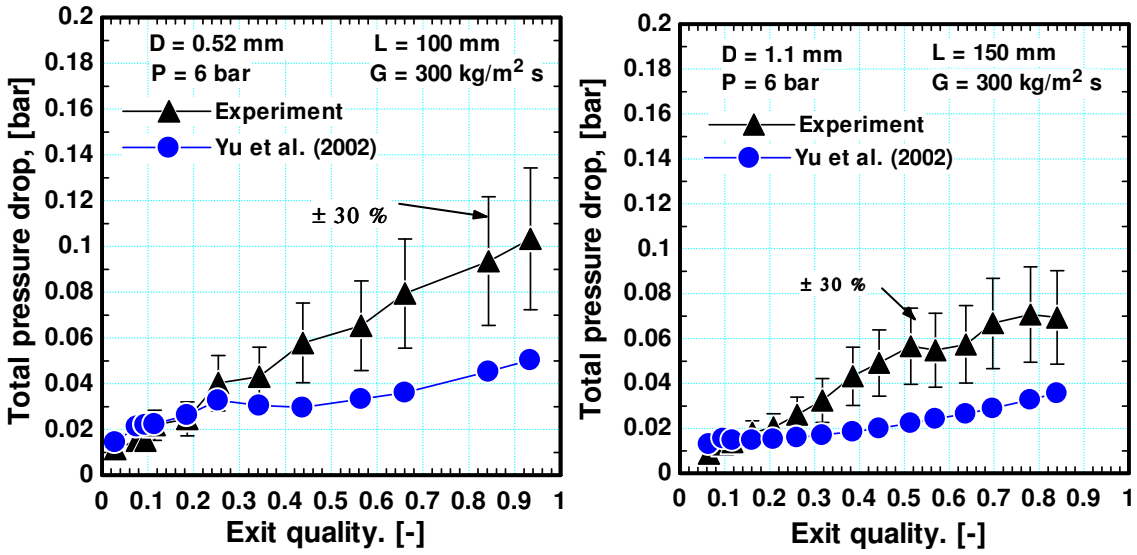

(a) (b)

Figure 6.23 The total measured pressure drop versus exit quality compared to the correlation of Yu et al. (2002) for (a) D = 0.52 mm and (b) D = 1.1 mm.

The Lee and Lee correlation

Lee and Lee (2001) investigated two phase flow pressure drop of air-water flow through narrow rectangular channels. The dimensions of the channels were 20 mm width, 640 mm length, and different depths of 0.4, 1, 2, and 4 mm. They proposed a correlation for the Chisholm's constant as a function of the all liquid Reynolds number and two other dimensionless groups to account for the effects of surface tension, viscosity and liquid slug velocity as given by Eq. (6.7).

$$C = A\lambda^{q}\psi^{r}\,\mathrm{Re}_{Lo}^{s} \tag{6.7}$$

$$\psi = \frac{\mu_L j_L}{\sigma} \tag{6.8}$$

$$\lambda = \frac{\mu_L^2}{\rho_L \sigma D_h} \tag{6.9}$$

The constant A and the exponents in Eq. (6.7) depend on whether the liquid and gas are laminar or turbulent and their values are summarized in Appendix A. Figure 6.24 shows the comparison between the experimental data and the correlation of Lee and Lee (2001). The correlation predicted only about 50 % of the 0.52 mm tube data within the error bands as seen in Fig. 6.24a. For the 1.1 mm tube, the correlation predicted only 14

– 25.9 % of the data within the error bands as seen in Figs. 6.24b-d. Generally, the correlation over-predicts the experimental data in both sizes of tubes. Examining the ability of the correlation to predict the experimental trend, Fig. 6.25 shows that correlation managed to predict the trend of the measured pressure drop versus exit quality in the 0.52 mm tube at the specified mass flux in Fig. 6.25a. At higher mass fluxes, few data located within the ± 30 % error bands. On the contrary, the correlation failed to predict the correct trend in the 1.1 mm tube where the pressure drop increased very slowly up to x ≈ 0.2 after which it rapidly increased with exit quality.

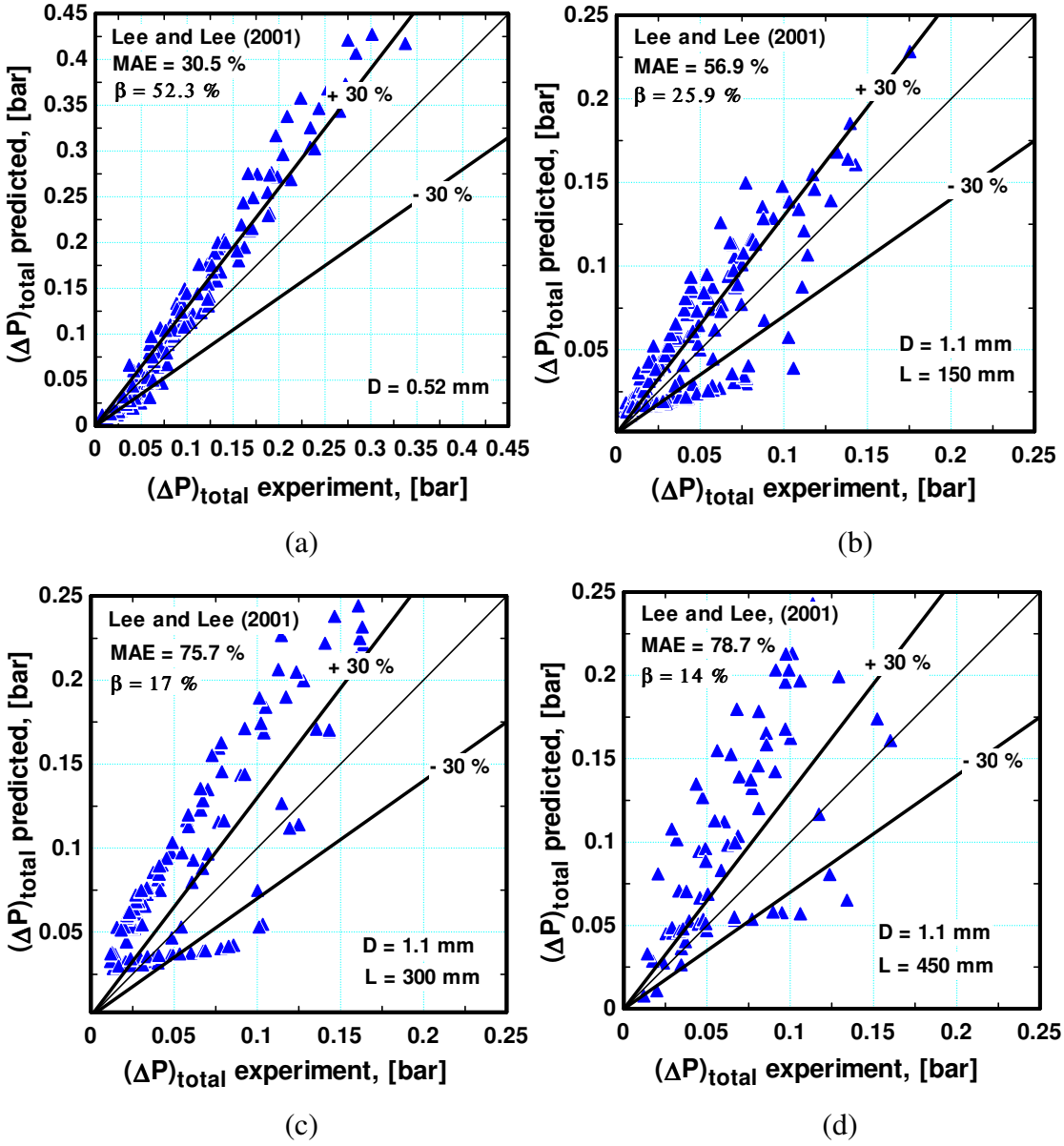

Figure 6.24 The comparison with the Lee and Lee (2001) correlation for (a) D = 0.52 mm, L = 100 mm, (b) D = 1.1 mm, L = 150 mm, (c) D = 1.1 mm, L = 300 mm and (d) D = 1.1 mm, L = 450 mm.

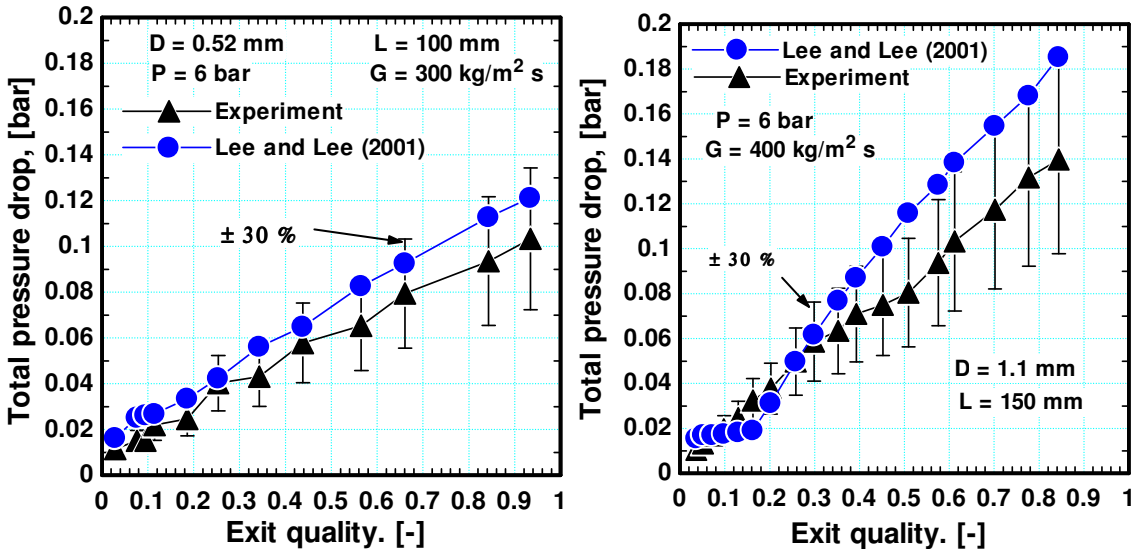

(a) (b)

Figure 6.25 The total measured pressure drop versus exit quality compared to the correlation of Lee and Lee (2001) for (a) D = 0.52 mm and (b) D = 1.1 mm.

The Warrier et al. correlation

Warrier et al. (2002) investigated flow boiling of FC-84 in an aluminium multi-channels heat sink with hydraulic diameter of 0.75 mm and heated length of 307.4 mm. They proposed using a fixed value of 38 for the Chisholm's constant irrespective of the flow regimes. They attributed this to the rapid development into annular flow in narrow channels with liquid mostly confined to the corners of the rectangular channel. It is worth mentioning that, some of the physical properties of the FC-84 vapour were not known such as density and viscosity. They calculated the density of the vapour from the perfect gas law and they assumed that the viscosity of FC-84 is the same as that of R113. Figure 6.26 depicts the global comparison between the experimental data and the correlation of Warrier et al. (2000). It is obvious from the figure, for all tubes, that the correlation predicts poorly the current experimental data. It highly over-predicts the data with MAE values ranging from 175 to 264 %. Figure 6.27 indicates that the slope of the predicted pressure drop curve versus exit quality is much higher than the experimental one. The reason behind this high over-estimation could be due to fixing the Chisholm's constant at a value of 38, which may not be correct. The value of Chisholm's constant should vary according to the variation in the interaction between the phases. Additionally, in their experiment, the dominant flow regime in micro-channels is

laminar liquid-laminar vapour and the Chisholm's constant should be much smaller than 38.

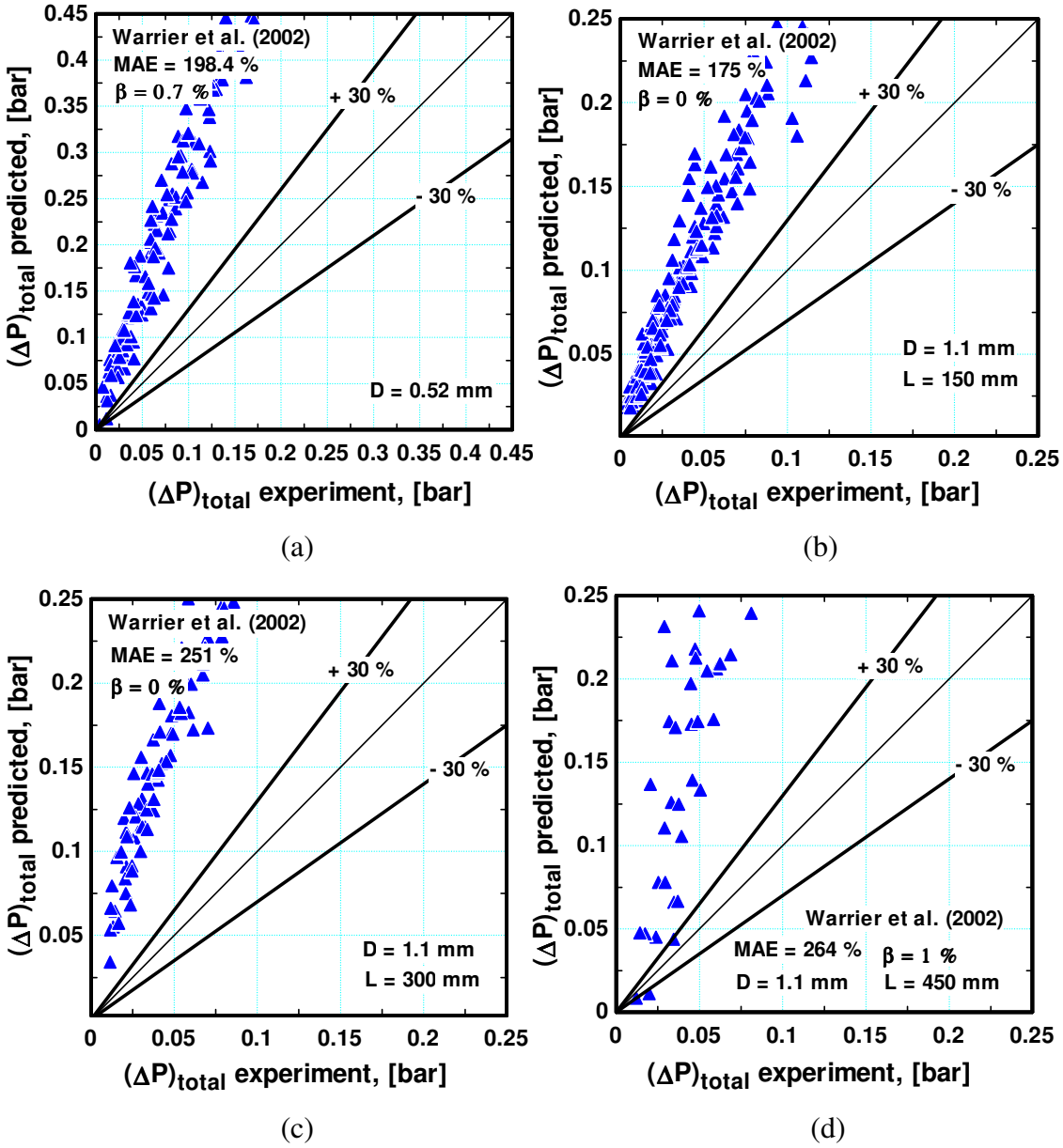

Figure 6.26 The comparison with the Warrier et al. (2002) correlation for (a) D = 0.52 mm, L = 100 mm, (b) D = 1.1 mm, L = 150 mm, (c) D = 1.1 mm, L = 300 mm and (d) D = 1.1 mm, L = 450 mm.

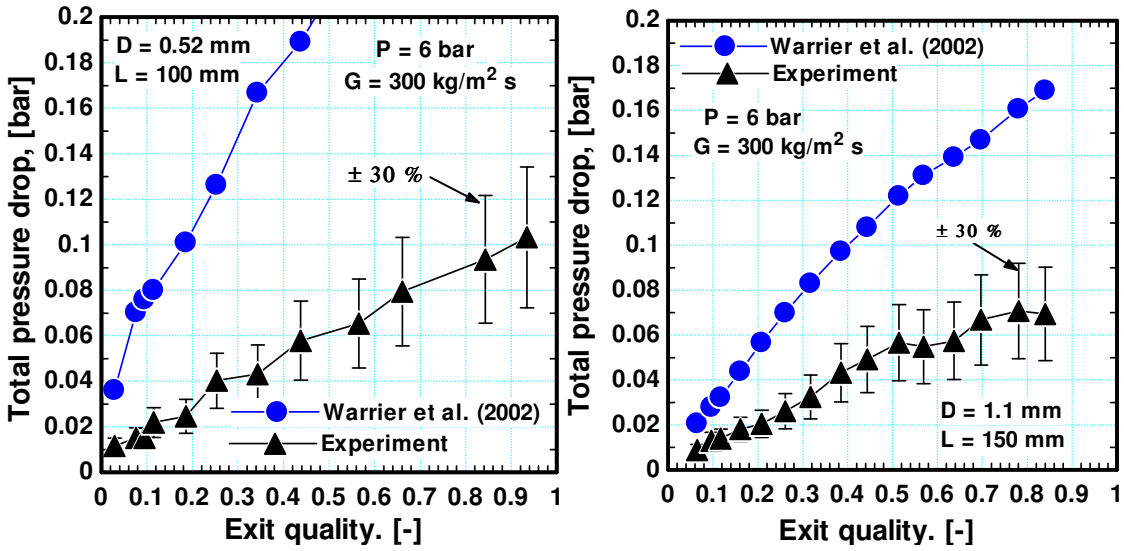

(a) (b)

Figure 6.27 The total measured pressure drop versus exit quality compared to the correlation of Warrier et al. (2002) for (a) D = 0.52 mm and (b) D = 1.1 mm.

The Qu and Mudawar correlation

Qu and Mudawar (2003) investigated flow boiling pressure drop of water in a multi-channel heat sink with hydraulic diameter of 0.35 mm. They modified the correlation of Mishima and Hibiki (1996) defined by Eq. (6.4) in order to take into account the mass flux effect as given by Eq. (6.10).

$$C = 21\left(1 - e^{-3190 D_h}\right)\left(0.00418G + 0.0613\right) \tag{6.10}$$

Figure 6.28 depicts the global comparison with the correlation of Qu and Mudawar (2003) whereas Fig. 6.29 shows the experimental pressure drop versus exit quality compared to the correlation at the mass flux value specified on the figure. For the 0.52 mm tube (Fig. 6.28a), the correlation predicts only 41.7 % of the data within the error bands and also it exhibited similar performance in the shortest 1.1 mm tube (Fig. 6.28b). Examining Figs. 6.29a and b, the correlation over-predicts the data at low exit quality values (low pressure drop values). For the two longest 1.1 mm diameter tubes (Figs. 6.28c and d), the performance of the correlation became worse where the percentage of data within the error bands has decreased. Looking at Fig. 6.29c, the correlation over-predicts the experimental values for all vapour quality values. It is worth mentioning that, when Qu and Mudawar (2003) compared their experimental data with the new

correlation, they obtained similar performance as the original Mishima and Hibiki (1996) correlation. In other words, the incorporation of mass flux effect into the Chisholm's constant did not significantly improve the predictability of the correlation.

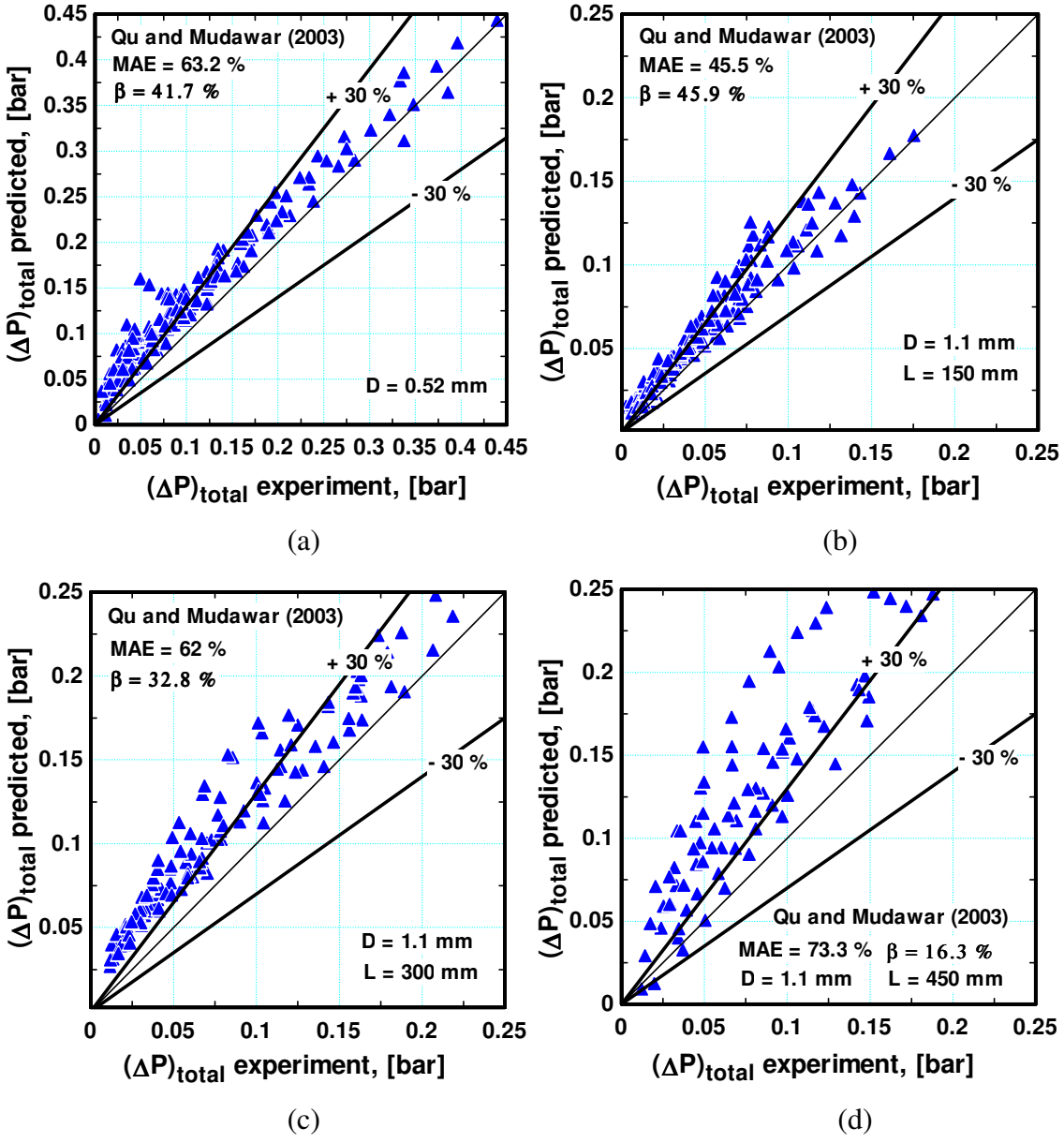

Figure 6.28 The comparison with the Qu and Mudawar (2003) correlation for (a) D = 0.52 mm, L = 100 mm, (b) D = 1.1 mm, L = 150 mm, (c) D = 1.1 mm, L = 300 mm and (d) D = 1.1 mm, L = 450 mm.

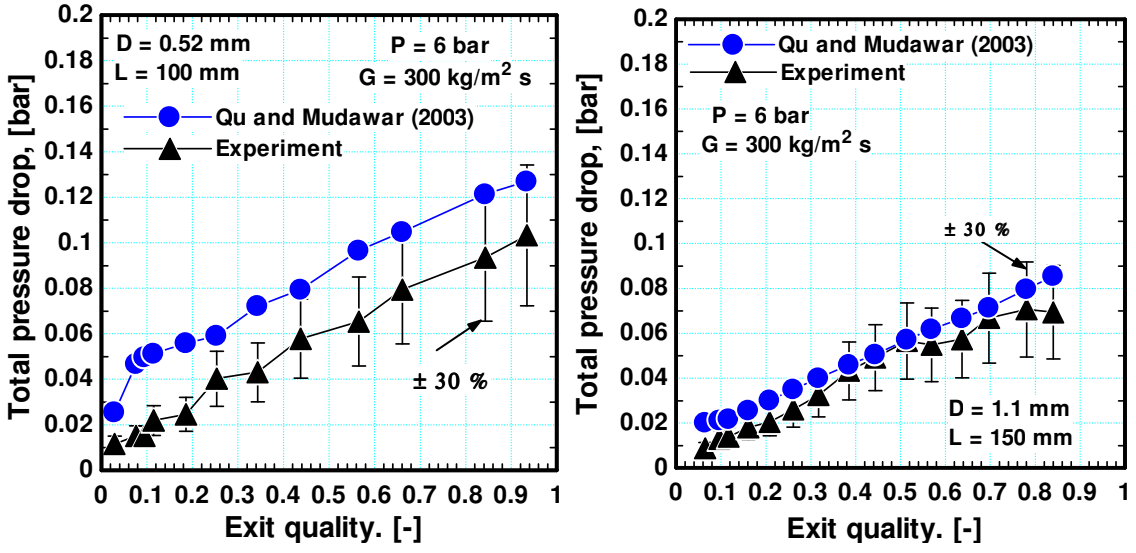

Figure 6.29 The total measured pressure drop versus exit quality compared to the correlation of Qu and Mudawar (2003) for (a) D = 0.52 mm, (b) D = 1.1 mm, L = 150 mm and (c) D = 1.1 mm, L = 450 mm.

The Lee and Mudawar correlation

Lee and Mudawar (2005) measured the two phase pressure drop of R134a in a multi-channel heat sink with channel dimensions of 231 × 713 μm. They compared their data with the homogeneous flow model, separated flow model based correlations and some of the existing micro scale correlations. They found that the macro scale correlations were not as poor as expected. Based on the premise that slug and annular flow regimes

are the most dominant regimes at high heat fluxes, they proposed a new correlation based on the separated flow model by modifying the Chisholm constant. The new constant takes into account the effects of liquid inertia, liquid viscous force and liquid surface tension and it was expressed as:

$$C = \begin{cases} 2.16\,\mathrm{Re}_{Lo}^{0.047}\,We_{Lo}^{0.6} & la\min ar\ \ liquid - la\min ar\ \ vapour \\ 1.45\,\mathrm{Re}_{Lo}^{0.25}\,We_{Lo}^{0.23} & la\min ar\ \ liquid - turbulent\ vapour \end{cases} \qquad (6.11)$$

Figure 6.30 depicts the global comparison with the Lee and Mudawar (2005) correlation. The correlation predicts only 31.8 % of the 0.52 mm tube data within the error bands and the predictions became worse in the 1.1 mm diameter tubes where the percentage of data within the error bands ranged from 2.4 to 8.8 %. Figure 6.31 indicates that this correlation is similar to that proposed by Qu and Mudawar (2003) where it over-predicts the data at low vapour qualities particularly at low mass fluxes.

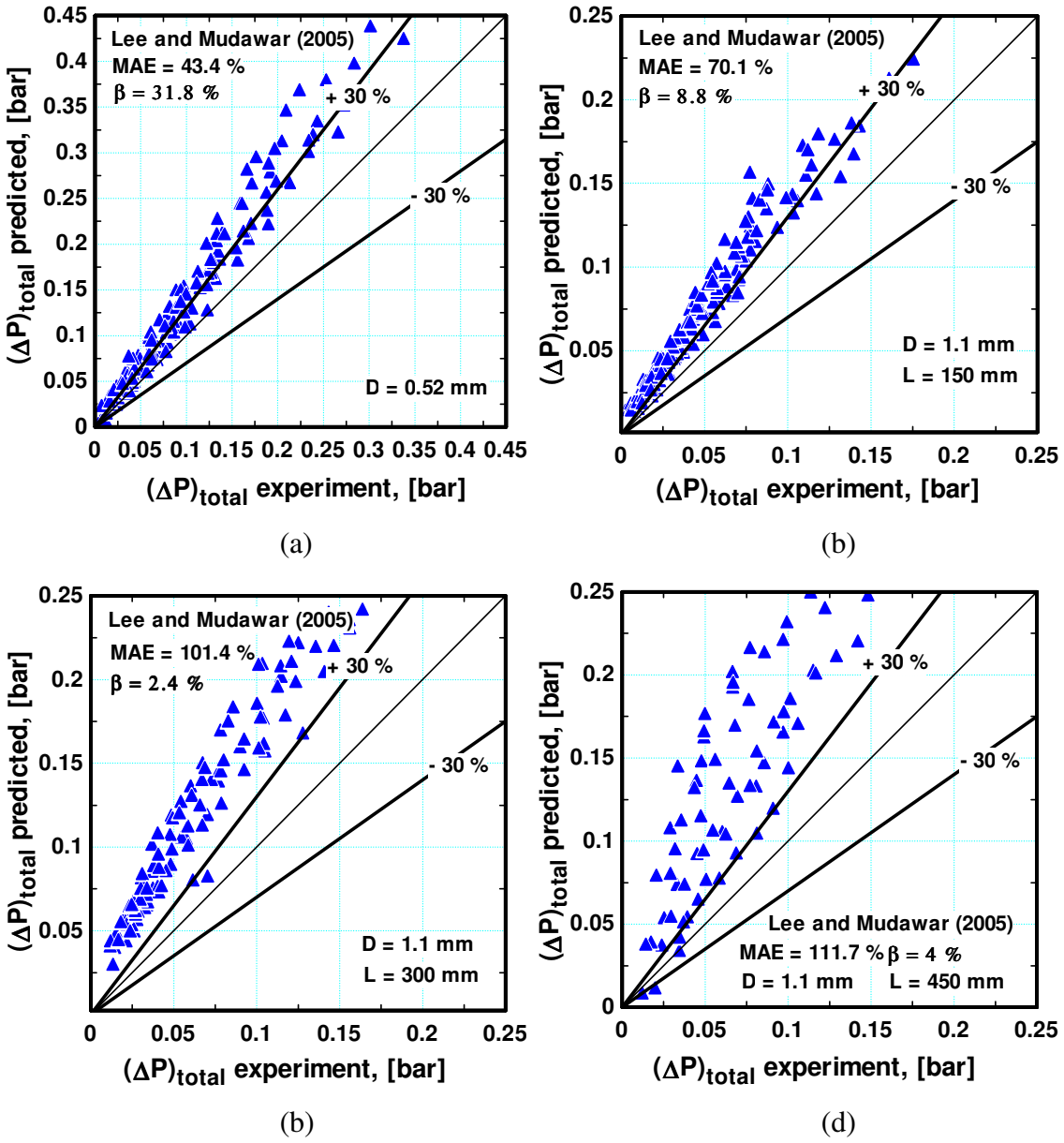

Figure 6.30 The comparison with the Lee and Mudawar (2005) model for (a) D = 0.52 mm, L = 100 mm, (b) D = 1.1 mm, L = 150 mm, (c) D = 1.1 mm, L = 300 mm and (d) D = 1.1 mm, L = 450 mm.

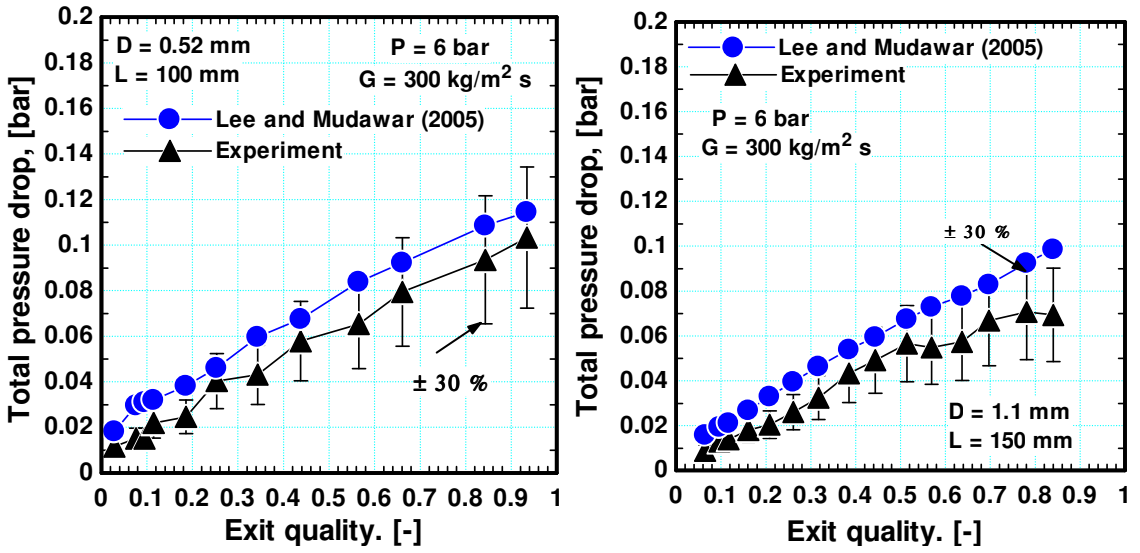

(a) (b)

Figure 6.31 The total measured pressure drop versus exit quality compared to the correlation of Lee and Mudawar (2005) for (a) D = 0.52 mm, (b) D = 1.1 mm.

The Lee and Garimella correlation

Lee and Garimella (2008) investigated flow boiling heat transfer and pressure drop of deionised water in parallel micro-channels with fixed channel depth of 400 µm and channel width ranging from 102 to 997 µm. They proposed a correlation for the Chisholm's constant in the laminar liquid/laminar vapour regime such that it takes into account the effect of hydraulic diameter and mass flux as given by Eq. (6.12).

$$C = 2566 G^{0.5466} D_h^{0.8819} (1 - e^{-319 D_h}) \tag{6.12}$$

Figures 6.32 and 6.33 depict the comparison between the experimental data and the correlation of Lee and Garimella (2008). Figure 6.32a for the 0.52 mm tube indicates that the correlation predicts reasonably the experimental data with a MAE value of 20.3% and 74.8 % of the data within the error bands. The performance of the correlation in the 1.1 mm tubes decreased particularly when the heated length increased as seen in Figs. 6.32b-d. Figure 6.33b shows that the correlation over-predicts the data of the shortest 1.1 mm tube particularly at high system pressure and mass fluxes although it predicts the correct experimental trend. For the 0.52 mm tube, Fig. 6.33a shows that the correlation predicts the experimental trend and values very well.

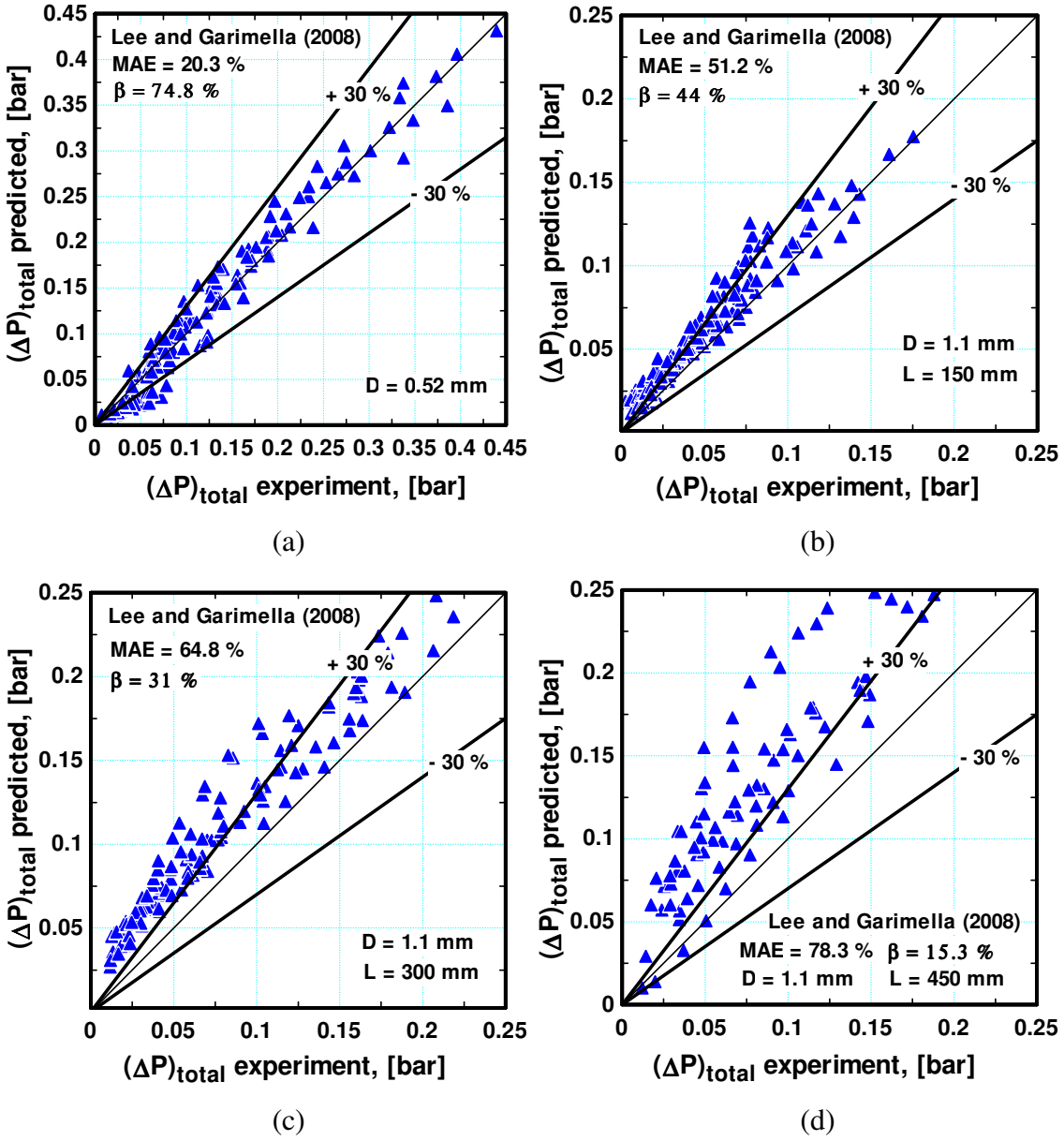

Figure 6.32 The comparison with the Lee and Garimella (2008) correlation for (a) D = 0.52 mm, L = 100 mm, (b) D = 1.1 mm, L = 150 mm, (c) D = 1.1 mm, L = 300 mm and (d) D = 1.1 mm, L = 450 mm.

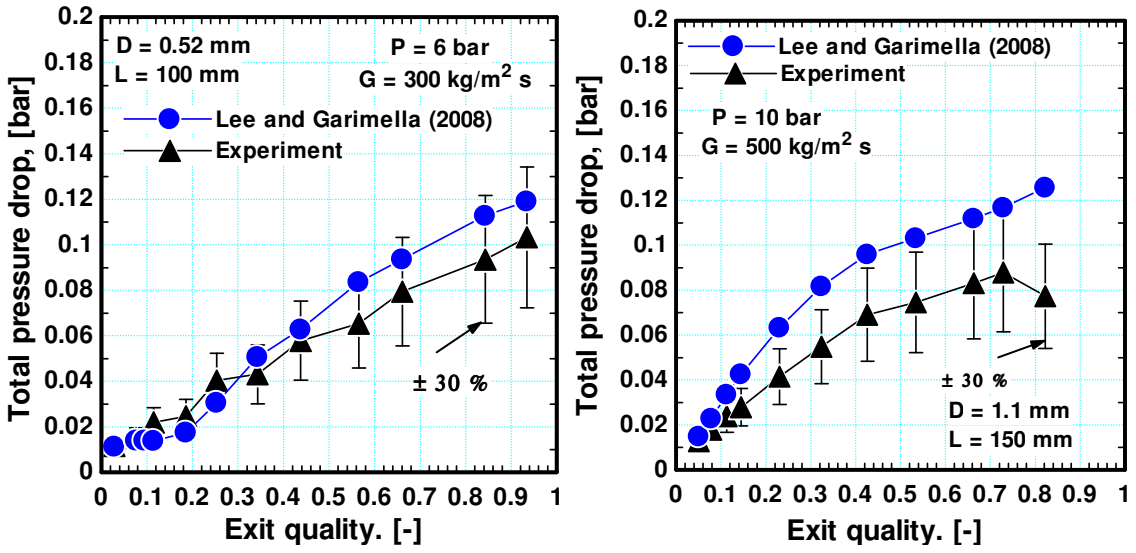

(a) (b)

Figure 6.33 The total measured pressure drop versus exit quality compared to the correlation of Lee and Garimella (2008) for (a) D = 0.52 mm, (b) D = 1.1 mm.

The Zhang et al. Correlation

Zhang et al. (2010) conducted an extensive analysis using the artificial neural network (ANN) to find the most important parameters that significantly influence the frictional pressure drop. They have found that mass flux, system pressure and vapour quality have minor effects whereas the hydraulic diameter and the dimensionless Laplace constant defined below have the strongest effects. Based on that, they modified the correlation of Mishima and Hibiki (1996) and proposed the following correlation for the Chisholm constant in the laminar liquid and laminar vapour regimes. This correlation is valid for channels with diameters ranging from 0.014 to 6.25 mm.

$$C = 21\left(1-\exp\left(-\frac{0.358}{La}\right)\right) \tag{6.13}$$

where

$$La = \frac{\left[\dfrac{\sigma}{g(\rho_L-\rho_v)}\right]^{0.5}}{D}$$

Figure 6.34 shows the global comparison between the experimental data and the correlation of Zhang et al. (2010) while Fig. 6.35 compares the measured and predicted trend of pressure drop versus exit quality. The correlation under-predicts the data of the

0.52 mm tube and predicts only 45 % of the data within the error bands as seen in Fig. 6.34a. This under-prediction occurs particularly at high exit qualities as seen in Fig. 6.35a for the 0.52 mm tube. The correlation performed much better in the 1.1 mm diameter tubes as seen in Figs. 6.34b-d where 71.4 – 81.2 % of the data were predicted within the error bands at MAE values ranging from 22.9 to 24 %. Also, it is obvious from Fig. 6.35 that the correlation predicts the experimental trend very well.

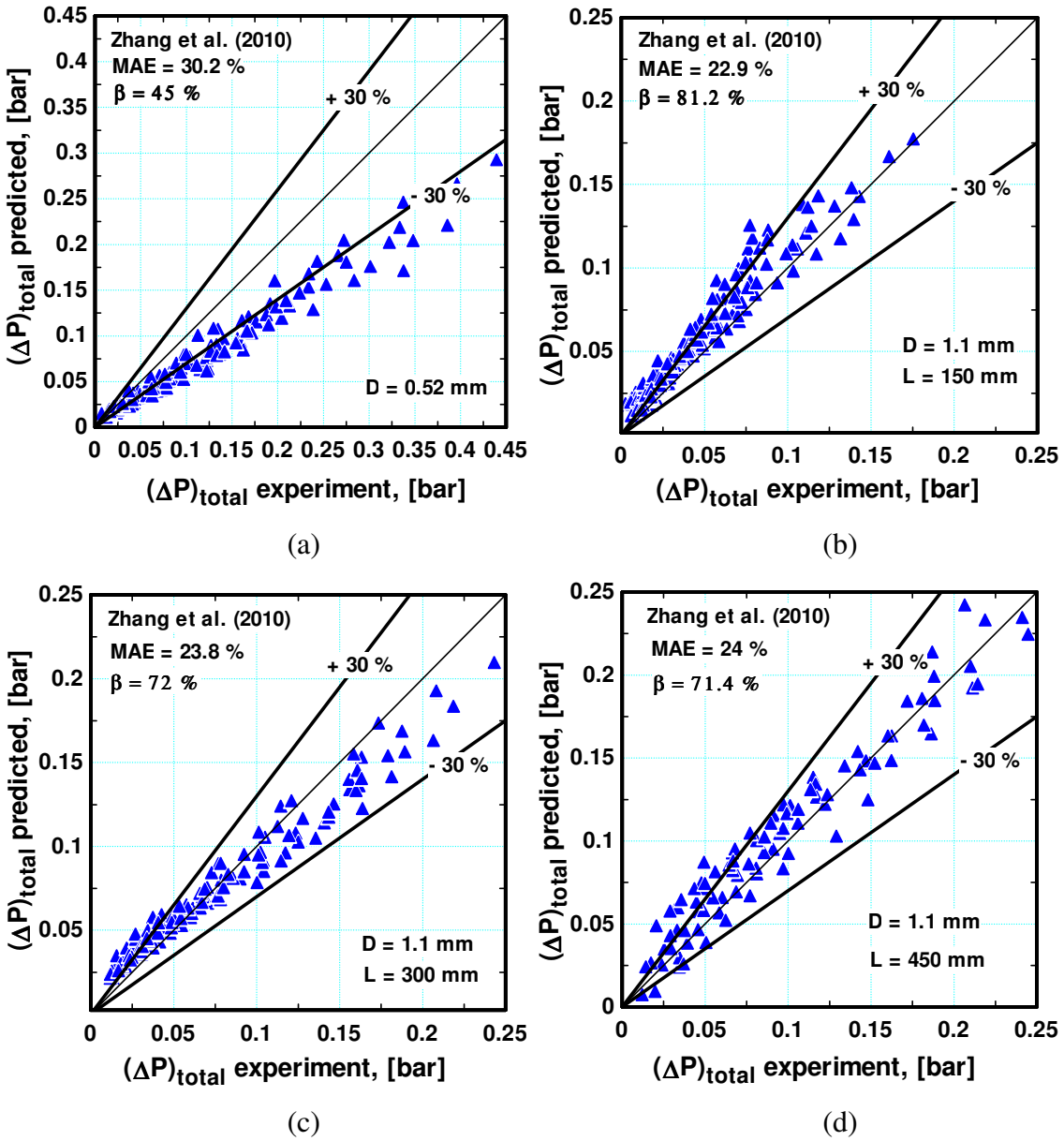

Figure 6.34 The comparison with the Zhang et al. (2010) correlation (a) D = 0.52 mm, L = 100 mm, (b) D = 1.1 mm, L = 150 mm, (c) D = 1.1 mm, L = 300 mm and (d) D = 1.1 mm, L = 450 mm.

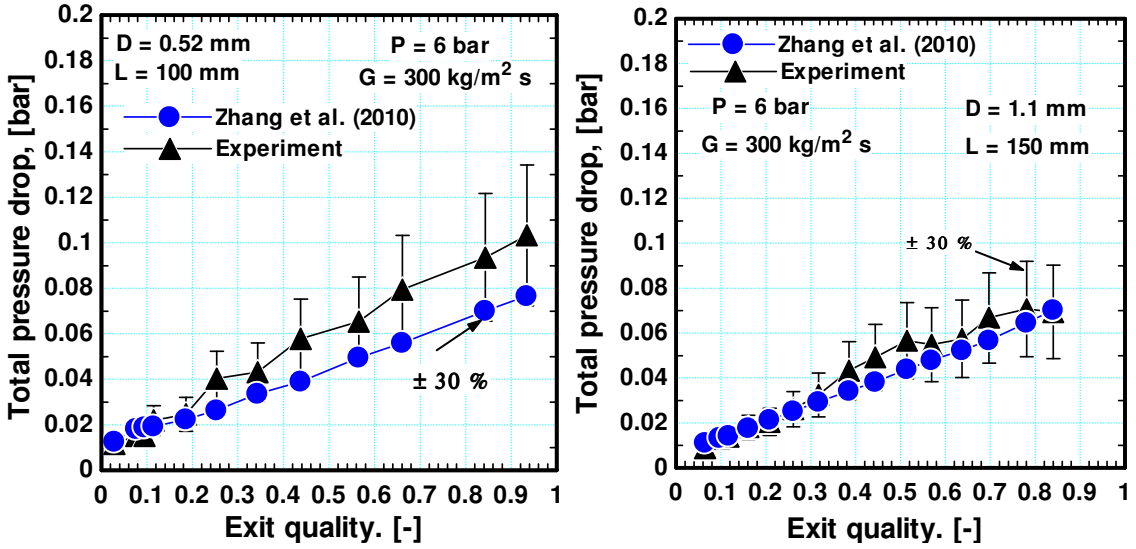

(a) (b)

Figure 6.35 The total measured pressure drop versus exit quality compared to the correlation of Zhang et al. (2010) for (a) D = 0.52 mm, (b) D = 1.1 mm.

The Li and Wu correlation

Li and Wu (2010) collected a large number of experimental data from the open literature for adiabatic two phase flow in micro/mini-channels and proposed a pressure drop correlation using regression analysis. They have modified the Chisholm's constant in the two phase multiplier using Bond number and Reynolds number. The proposed new correlation was given as:

$$C = \begin{cases} 11.9 Bd^{0.45} & Bd \le 1.5 \\ 109.4\left(Bd\,\mathrm{Re}^{0.5}\right)^{-0.56} & 1.5 < Bd \le 11 \end{cases} \qquad (6.14)$$

Figure 6.36 depicts the global comparison with the correlation of Li and Wu (2010) while Fig. 6.37 shows the trend of the experimental pressure drop versus exit quality compared to that predicted by the correlation. The correlation gives excellent prediction for the data of the 0.52 mm tube (Fig. 6.36a) where 92 % of the data were predicted within the error bands. This is also clear from Fig. 6.37a where the correlation captured the trend and values very well. On the contrary, the performance of the correlation in the shortest 1.1 mm tube was lower but still reasonable and the performance gets worse as the heated length increases as seen in Figs. 6.37b-d. It is clear that the deviation occurs at pressure drop values less than 0.05 bar (low heat flux or exit quality) where it

tends to under-predict the data. For the longest 1.1 mm tube (Fig. 6.36d), the correlation predicted only 48 % of the data and over-predicted the other remaining data. This over-prediction can be explained by Fig. 6.37b where the slope of the measured pressure drop curve is less than that predicted by the correlation and thus the percentage deviation increases as the quality increases.

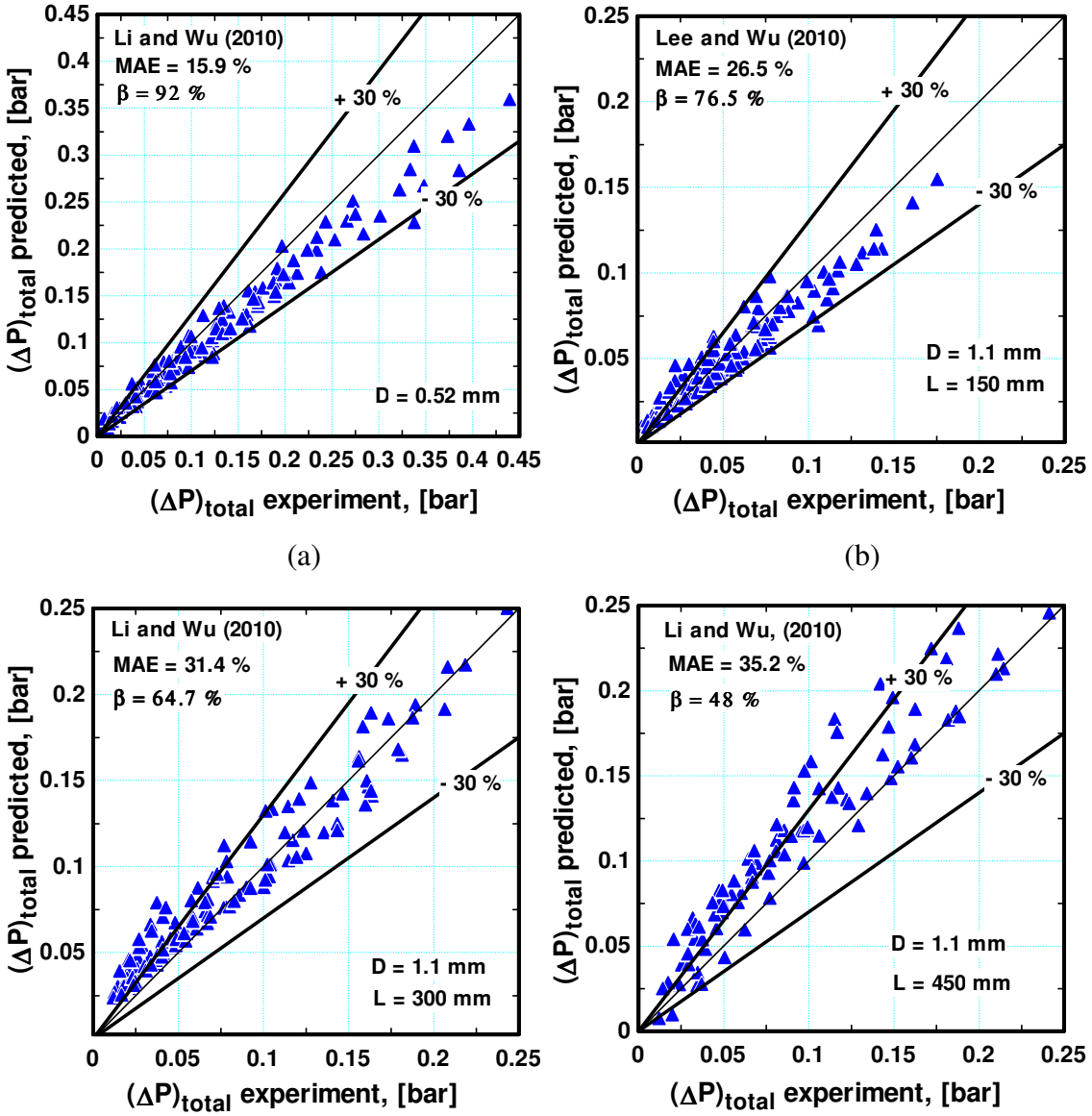

Figure 6.36 The comparison with the Li and Wu (2010) correlation for (a) D = 0.52 mm, L = 100 mm, (b) D = 1.1 mm, L = 150 mm, (c) D = 1.1 mm, L = 300 mm and (d) D = 1.1 mm, L = 450 mm.

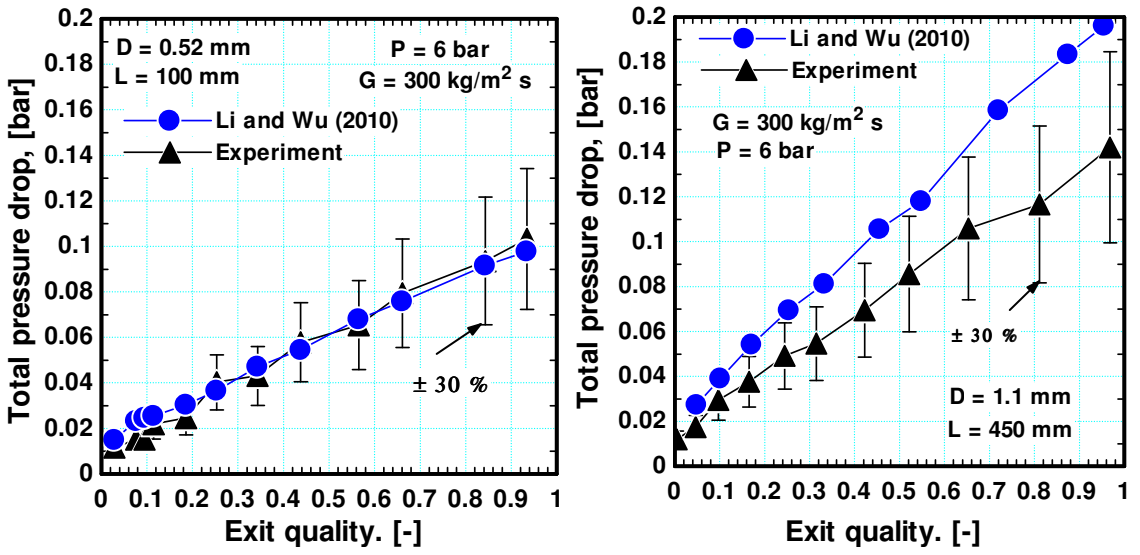

(a) (b)

Figure 6.37 The total measured pressure drop versus exit quality compared to the correlation of Li and Wu (2010) for (a) D = 0.52 mm, (b) D = 1.1 mm.

The Lee et al. Correlation

Lee et al. (2010) collected 484 data points for flow boiling pressure drop in mini/micro-channels with diameters < 3 mm and covered seven working fluids including water, n-pentane, ammonia, CO_2, R410a, R134a and R12. It is worth mentioning that, most of the data were for rectangular multi-channels configurations. These data were collected from nine different experimental studies. They found that, the Chisholm constant depends on the Bond number and the exit quality. As the Bond number increases, the Chisholm constant was found to increase until it reaches an asymptotic value of about 30 at Bond number values greater than about 2. They attributed this to the presence of large number of bubbles at high values of Bond number and consequently high interfacial interactions between the phases. On the other hand, at small values of Bond number, one confined bubble fills the channel with less interaction between the phases. As the exit quality increases, the Chisholm constant was found to increase rapidly according to a polynomial trend where its value exceeded 100, which is much greater than the original values in the Lockhart-Martinelli model. The new proposed correlation was given as:

$$C = 121.6(1 - e^{-22.7\,Bd})\,x_e^{1.85} \tag{6.15}$$

Despite the fact that this above correlation was developed based on a database including refrigerants, it predicted their refrigerant data with high mean absolute error values. Figure 6.38 depicts the global comparison between the current experimental data and Lee et al. (2010) correlation. As seen in the figure, the correlation predicts poorly the experimental data in all tubes with a tendency to highly over-predict the data. From Fig. 6.39 that shows the pressure drop versus exit quality, the correlation does not predict the correct trend compared to the experimental data. The reason may be due to the use of exit quality in the Chisholm constant correlation with exponent 1.85, which may not be correct. The flow boiling pressure drop seems to be strongly influenced by the local vapour qualities (flow patterns) rather than exit quality. The correlation seems to predict the low pressure drop values, which are corresponding to low exit quality values. It is interesting to note that, when the exit quality term was excluded from their correlation and the best fit equation for Chisholm constant as a function of Bond number was used, the correlation performed much better. For example, in the 0.52 mm tube, the MAE % value decreased from 152.5 % to 28.5% and the data within the error bands increased from 25 to 65.5 %. This confirms that, exit quality is not the correct parameter to correlate the Chisholm constant.

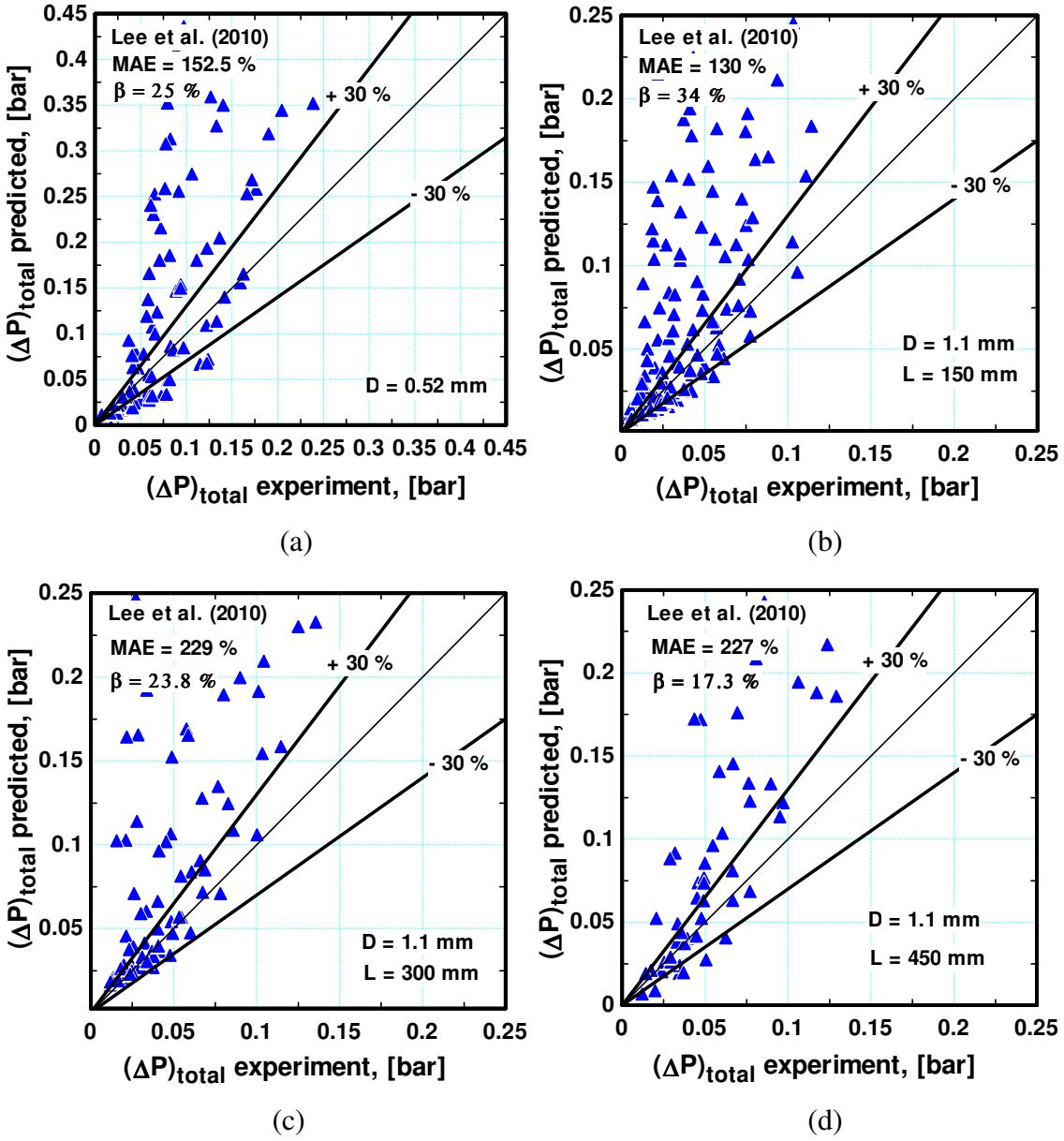

Figure 6.38 Comparison with the correlation of Lee et al. (2010) for (a) D = 0.52 mm, (b) D = 1.1 mm, L = 150 mm, (c) D = 1.1 mm, L = 300 mm and (d) D = 1.1 mm, L = 450 mm.

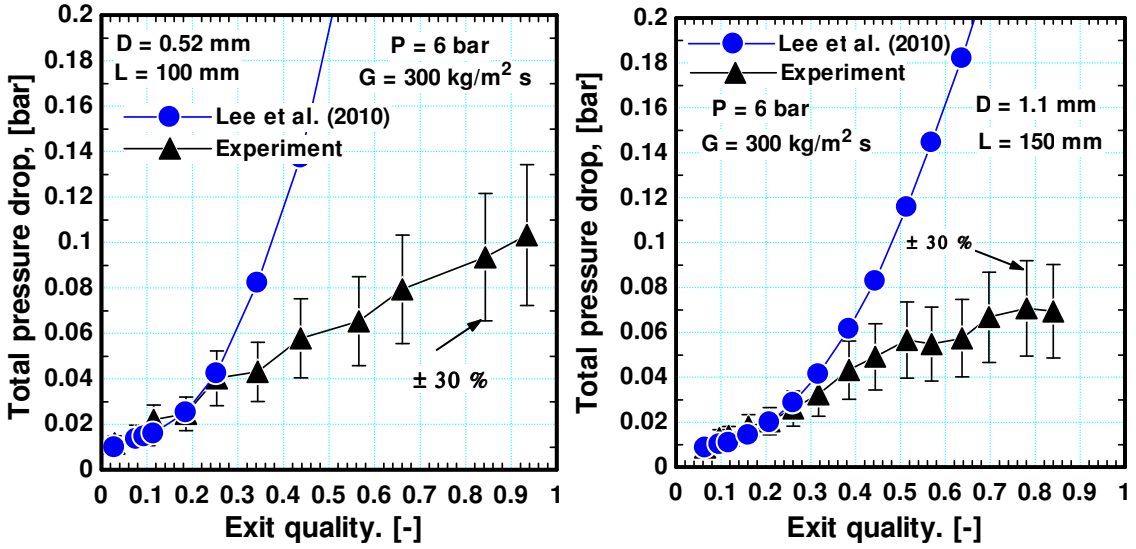

(a) (b)

Figure 6.39 The total measured pressure drop versus exit quality compared to the correlation of Lee et al. Wu (2010) for (a) D = 0.52 mm, (b) D = 1.1 mm.

6.5 Pressure drop mechanistic models

This section evaluates two mechanistic models developed for slug flow in micro-channels. The first one was proposed by Garimella et al. (2002) for condensation while the second was proposed by Shiferaw et al. (2009) for evaporation. It is worth mentioning here that in the current study the transition to annular flow occurred at exit qualities ranging from 0.3 to 0.4 and bubbly flow appeared only at very small quality values. Accordingly, these two mechanistic models are compared with the current experimental data up to vapour quality value of 0.4, i.e. the data in the annular flow regime were excluded. The two models are presented and compared with the current experimental data in the following subsections.

6.5.1 The model of Garimella et al. (2002)

Garimella et al. (2002) presented a pressure drop model for slug flow in circular microchannels during condensation of R134a. The model assumes that the bubble is cylindrical in shape, the liquid film around the bubble is uniform and moves very slowly compared to the vapour and liquid slugs, no entrained vapour in the liquid slug and the bubble flows somewhat faster than the liquid slug. Figure 6.40 depicts a unit cell consisting of liquid slug and bubble/film, which was used in the model developments.

According to this model, the total pressure drop was given as the sum of the frictional pressure drop in the slug and bubble/film regions plus the losses due to the film flow behind the bubble. The frictional pressure gradient in the liquid slug region was calculated as follows:

$$U_{Slug} = j_V + j_L \tag{6.16}$$

$$\mathrm{Re}_{Slug} = \frac{\rho_L U_{Slug} D}{\mu_L} \tag{6.17}$$

$$\left(\frac{dP}{dz}\right)_{Slug} = \frac{0.3164}{\mathrm{Re}_{slug}} \frac{\rho_L U_{Slug}^2}{2D} \tag{6.18}$$

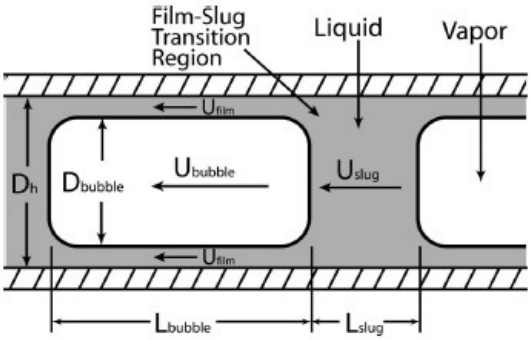

Figure 6.40 The unit cell and model parameters of Garimella et al. (2002).

where j_L and j_V are the superficial velocities of liquid and vapour respectively. The frictional pressure gradient in the bubble/film region was calculated by applying momentum and mass conservation and using iteration between the following equations:

$$U_{bubble} = 1.2 U_{Slug} \tag{6.19}$$

$$\mathrm{Re}_{Film} = \frac{\rho_L U_{Film} (D - D_{bubble})}{\mu_L} \tag{6.20}$$

$$U_{Interface} = \frac{-(dP/dz)}{4\mu_L}\left(R^2 - R_b^2\right) \tag{6.21}$$

$$U_{Film} = \frac{-(dP/dz)_{film/bubble}}{8\mu_L}\left(R^2 - R_b^2\right) \tag{6.22}$$

$$\left(\frac{dP}{dz}\right)_{film/bubble} = \frac{0.3164}{\mathrm{Re}_{bubble}^{0.25}} \frac{\rho_v \left(U_{bubble} - U_{Interface}\right)^2}{4R_b} \tag{6.23}$$

$$U_{Slug} = U_{bubble}\left(\frac{R_{bubble}}{R}\right)^2 + U_{Film}\left[1 - \left(\frac{R_{bubble}}{R}\right)^2\right] \tag{6.24}$$

After calculating the pressure gradient in each region, the total pressure drop was given as follows:

$$\Delta P = L\left[\left(\frac{dP}{dz}\right)_{film/bubble}\left(1 - \frac{L_{slug}}{L_{slug} + L_{bubble}}\right) + \left(\frac{dP}{dz}\right)_{slug}\left(\frac{L_{slug}}{L_{slug} + L_{bubble}}\right)\right] + \Delta P_{trans} \tag{6.25}$$

$$\frac{L_{slug}}{L_{slug} + L_{bubble}} = \left[0.7228 + 0.4629\exp\left(-0.9604D\right)\right]\frac{j_L}{j_L + j_V} \tag{6.26}$$

$$\Delta P_{trans} = \Delta P_{one\,transition} N_{cell} \tag{6.27}$$

$$\Delta P_{one\ transition} = \rho_L\left[1 - \left(\frac{R_b}{R}\right)^2\right]\frac{\left(U_{slug} - U_{film}\right)\left(U_{bubble} - U_{Film}\right)}{2} \tag{6.28}$$

$$N_{cell} = 2436.9\,\mathrm{Re}_s^{-0.5601} \tag{6.29}$$

Figure 6.41 depicts the global comparison between the current experimental data and the model of Garimella et al. (2002) while Fig. 6.42 compares the trend of the measured pressure drop versus exit quality with that predicted by the model. Figure 6.41a shows, for the 0.52 mm diameter tube, that the model predicts poorly the experimental data where the MAE value is 71.8 % and only 14 % of the data were located within the error bands. For the shortest 1.1 mm diameter tube (Fig. 6.41b), the model predicts reasonably the data with a MAE value of 29 % and 69 % of the data within the error bands. As the heated length was increased (Figs. 6.41c and d), the model predicted poorly the experimental data. Looking at Figs. 6.42a and c, the slope of the predicted pressure drop is much higher that the experimental one which explains the poor performance of the correlation in the 0.52 mm tube and the longest 1.1 mm tubes. On the other hand, there is a good agreement between the measured and predicted trend in the shortest 1.1 mm tube as seen in Fig. 6.42b. Revellin and Thome (2007) evaluated this model using the measured pressure drop data of R134a and R245fa and found that only 20.4% of the data fall within ± 20 % error bands with a mean deviation of 51.7 %.

They attributed this high deviation to the fact that the break down of annular flow into intermittent flow in condensation is different from the coalescence mechanism in boiling. Another possible reason for the failure of the model to predict data for all tubes with the same accuracy may be the difference in flow patterns in the four test sections. In the 0.52 mm tube, elongated bubble regime (similar in features to annular flow) was dominating at low exit qualities whereas annular flow developed earlier at lower exit qualities in the longer tubes compared to the shortest one. Generally, the failure of the model to predict the current experimental data may be attributed to the dependence of the model on several empirical relations such as Eq. (6.19) for the bubble velocity, Eq. (6.26) for the relative length of the liquid slug, and Eq. (6.29) for the number of unit cells occurring over tube length.

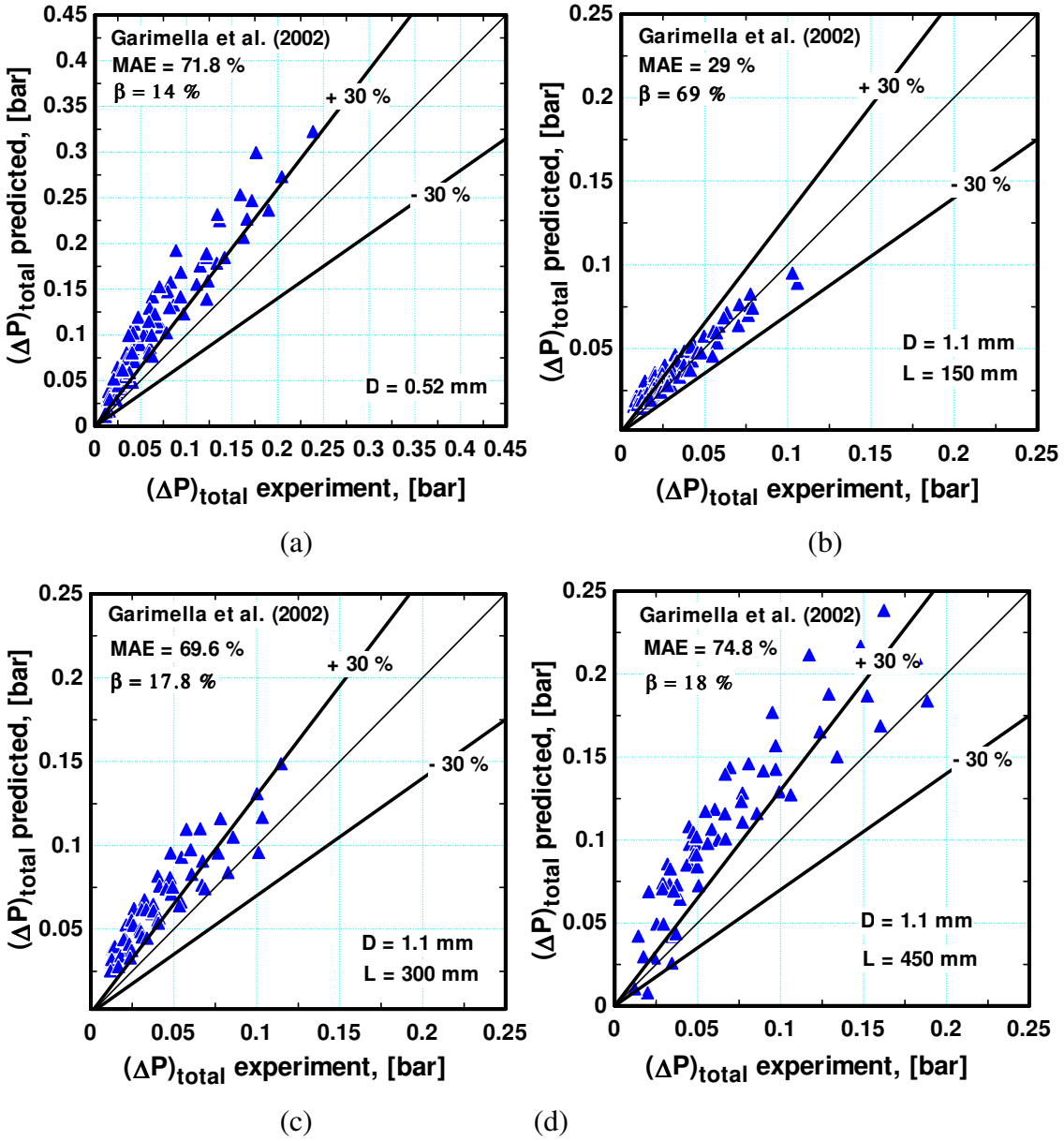

Figure 6.41 Comparison with the model of Garimella et al. (2002) for (a) D = 0.52 mm, (b) D = 1.1 mm, L = 150 mm, (c) D = 1.1 mm, L = 300 mm and (d) D = 1.1 mm, L = 450 mm.

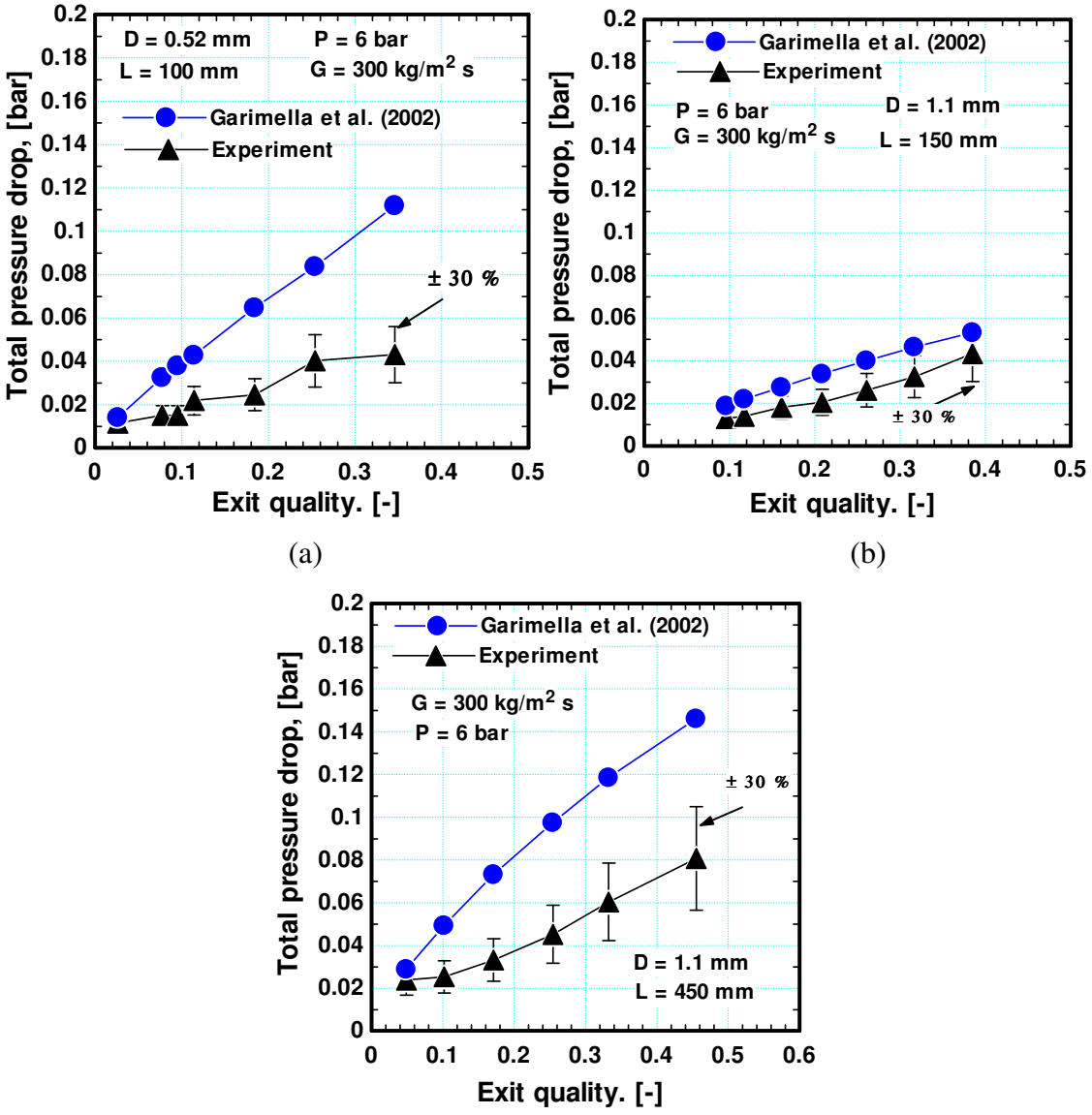

Figure 6.42 The total measured pressure drop versus exit quality compared to the model of Garimella et al. (2002) for (a) D = 0.52 mm, (b) D = 1.1 mm, L = 150 mm and (c) D = 1.1 mm, L = 450 mm.

6.5.2 The Shiferaw et al. (2009) model

Shiferaw et al. (2009) presented a one dimensional semi-mechanistic pressure drop model for flow boiling of R134a in narrow passages based on the premise that slug flow is the dominant flow pattern. The model was developed based on the three zone heat transfer model of Thome et al. (2004) presented in section 5.4. The total pressure drop was calculated in a way similar to Eq. (5.17) through the time averaging of wall shear

stress for single phase liquid, bubble with a liquid film and single phase vapour as given by Eq. (6.30).

$$\tau_w = \tau_l \frac{t_l}{t_b} + \tau_{film} \frac{t_{film}}{t_b} + \tau_v \frac{t_{dry}}{t_b} \tag{6.30}$$

The time averaged pressure gradient is the sum of the three time averaged contributions:

$$\frac{dp}{dz} = \frac{dp_g}{dz} + \frac{dp_a}{dz} + \frac{dp_f}{dz} \tag{6.31}$$

$$\frac{dp_g}{dz} = -\frac{\rho_l g}{\left(1 + \frac{4qv_{lv}}{DGh_{lv}v_l} z\right)}, \quad \frac{dp_a}{dz} = -\frac{4Gqv_{lv}}{Dh_{lv}}, \quad \frac{dp_f}{dz} = -\frac{4\tau_w}{D} \tag{6.32}$$

The frictional pressure gradients of single phase liquid and single phase vapour in Eq. (6.31) are calculated from the well known single phase relations as:

$$\tau_{lorv} = \begin{cases} \dfrac{0.0791}{\mathrm{Re}_{lorv}^{1/4}} \dfrac{\rho_{lorv} U_p^2}{2} & \text{turbulent} \\ \dfrac{16}{\mathrm{Re}_{lorv}} \dfrac{\rho_{lorv} U_p^2}{2} & \text{laminar} \end{cases}, \quad \mathrm{Re}_{lorv} = \frac{\rho_{lorv} U_p D}{\mu_{lorv}} \tag{6.33}$$

In the bubble with liquid film region, the interfacial shear stress is given by:

$$\tau_i = \begin{cases} \dfrac{0.0791}{\mathrm{Re}^{1/4}} \dfrac{\rho_v (U_p - u_i)^2}{2} & \text{turbulent} \\ \dfrac{16}{\mathrm{Re}} \dfrac{\rho_v (U_p - u_i)^2}{2} & \text{laminar} \end{cases}, \quad \mathrm{Re} = \frac{\rho_v (U_p - u_i) D}{\mu_v} \tag{6.34}$$

In a vertical tube, the film is subjected to the same total pressure gradient *dp/dz* as the adjacent gas phase, a gravitational body force $\rho_L g$, a wall shear stress τ_f and an interfacial shear stress τ_i, as seen in Fig. 6.41. Consistent with the steady-flow

approximation, the changes in momentum of the film are assumed negligible. For a planar approximation consistent with $\delta_m << 1$, the velocity distribution for laminar flow in the film is given by:

$$u_i = \frac{\tau_i}{\mu_l}\delta_m - \left[\frac{dp}{dz} + \rho_l g\right]\frac{\delta_m^2}{2\mu_l} \tag{6.35}$$

$$\tau_f = \tau_i - \left[\frac{dp}{dz} + \rho_l g\right]\delta_m \tag{6.36}$$

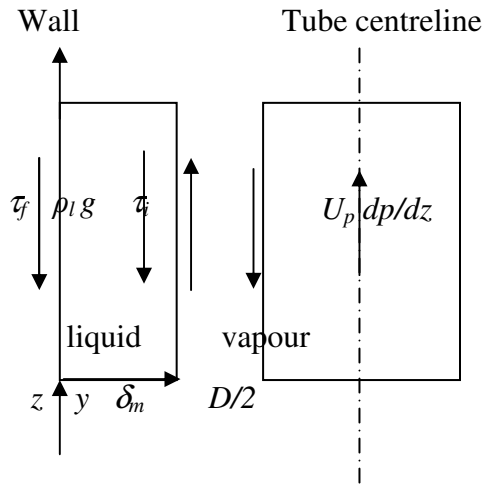

Figure 6.43 The thin film model

The pressure gradient in the vapour during the thin-film period is not equal to the time-averaged pressure gradient and is given by:

$$\begin{aligned}\frac{dp}{dz} &= -\rho_v\left[g + U_p\frac{dU_P}{dz}\right] - \frac{4\tau_i}{D\left(1-\frac{\delta_m}{D}\right)} \\ &\approx -\rho_V\left[g + U_p\frac{dU_p}{dz}\right] - \frac{4\tau_i}{D}\end{aligned} \tag{6.37}$$

The wall shear stress in the bubble + film region is calculated by solving Eqns. (6.34 – 6.37) simultaneously. As stated above, the model is based on the assumption that the dominant flow pattern is slug flow with smooth vapour-liquid interfaces.

Figure 6.44 depicts the global comparison with the three zone pressure drop model of Shiferaw et al. (2009) while Fig. 6.45 shows the measured pressure drop versus exit quality compared to the model. Both figures show that the model predicts reasonably the experimental trend and values with MAE values ranging from 20.9 to 24.8 %. The percentage of data within the error bands ranged from 64 to 81.8 %. The reason behind the variation in the model performance from tube to tube may be due to the variation in vapour quality at which transition to annular flow occurs. As previously mentioned, the model was compared with the experimental data up to x = 0.4. At high mass fluxes, the slug flow region becomes narrow and transition to annular flow occurs at qualities less than 0.4. Also, as the heated length increases, annular flow appeared earlier at qualities lower than 0.4. Accordingly, the small deviations between the model and the experimental data may occur due to the fact that the model is working outside its validity range. It is worth mentioning here that, all model parameters used in the three zone heat transfer evaporation model were also used in the three zone pressure drop model such as the end film thickness value of 0.3 μm. The model strongly depends on the initial and final film thicknesses which influence the predictability of the model as well.

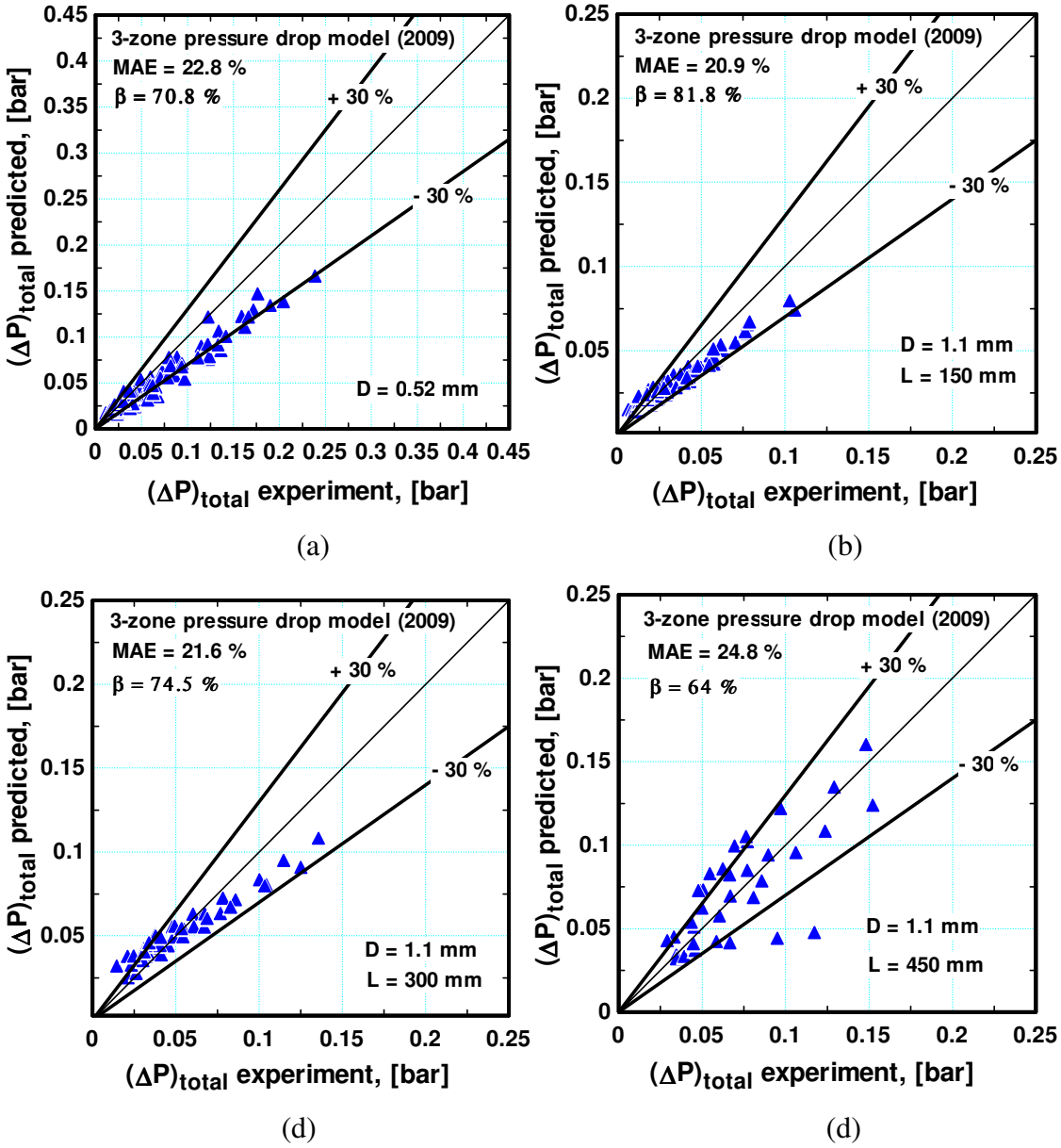

Figure 6.44 Comparison with the model of Garimella et al. (2002) for (a) D = 0.52 mm, (b) D = 1.1 mm, L = 150 mm, (c) D = 1.1 mm, L = 300 mm and (d) D = 1.1 mm, L = 450 mm.

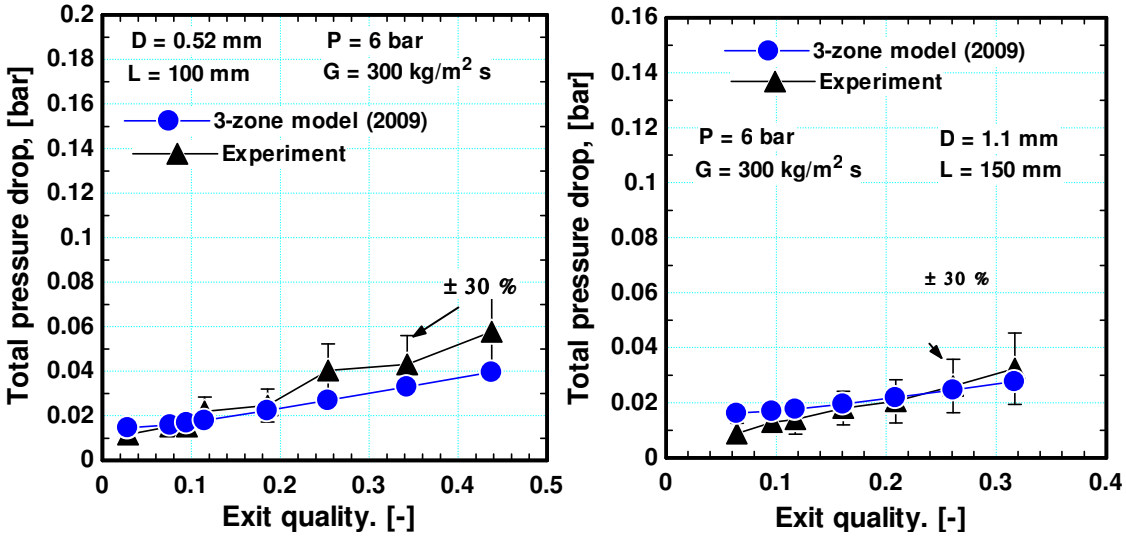

(a) (b)

Figure 6.45 The total measured pressure drop versus exit quality compared to the three zone pressure drop model of Shiferaw et al. (2002) for (a) D = 0.52 mm, (b) D = 1.1 mm, L = 150 mm and (c) D = 1.1 mm, L = 450 mm.

6.6 Summary

The experimental results of the total measured flow boiling pressure drop in 0.52 and 1.1 mm diameter tubes were presented and discussed in this chapter at mass flux range of 200 – 500 kg/m^2 s and system pressure range of 6 – 10 bar. The results indicated that the two phase pressure drop increases with increasing heat flux (exit quality), increasing mass flux, decreasing system pressure and decreasing tube diameter. The contribution of the frictional pressure drop component to the total measured two phase pressure drop was found to be the largest compared to the contribution of the gravitational and acceleration components. Its value reached about 70 % in the 1.1 mm diameter tube and about 80 % in the 0.52 mm diameter tube. This indicates that the contribution of the frictional component to the total measured two phase pressure drop increases as the diameter decreases. This may be attributed to the thinning of the boundary layer in micro-tubes resulting in higher velocity gradients and consequently higher wall shear stress. However, the contribution of the acceleration component to the total measured pressure drop can not be ignored in flow boiling studies compared to adiabatic studies. Its value reached about 22 % in the 0.52 mm tube at exit quality value of about 0.9 whilst the corresponding value in the 1.1 mm tube was about 37 %. The higher

contribution of the acceleration component in the 1.1 mm tube compared to the 0.52 mm tube is due to the higher values of Reynolds number. Also, the experimental results indicated that the heated length has a significant effect on the measured pressure drop per unit length. At the same exit quality, the shorter the heated length, the higher the measured pressure drop per unit length. At the same exit quality, the applied heat flux to the shortest tube is much higher compared to the longer tubes. This results in the dominance of nucleate boiling in the shortest tube as presented and discussed previously in Chapter 4. Accordingly, with the premise that there are small nucleating bubbles next to the wall, the additional interaction between the phases in the liquid film due to nucleation may explain why the pressure drop per unit length in the shortest tube is high. This result is important in explaining why the performance of some correlations gets worse as the heated length increases as summarized below.

The experimental two phase pressure drop results were compared with eighteen macro- and micro-scale models and correlations. The performance of each model and correlation was discussed in details through global comparison and also through comparing the experimental trend of the measured pressure drop versus exit quality with predicted one at a certain mass flux value and system pressure. The results of the comparison are summarized in Table 6.1.

Table 6.1 The mean absolute error (MAE) and the percentage of data within the ± 30 % error bands for all evaluated models and correlations

Model/Correlation	D = 0.52 mm		D = 1.1 mm					
			L = 150 mm		L = 300 mm		L = 450 mm	
	MAE %	β %	MAE %	β %	MAE %	β %	MAE %	β %
Homogeneous model	18.5	83.4	**20.5**	80	19.9	79.5	**18.7**	80.6
Lockhart-Martinelli (1949)	16.5	85.4	32.2	56	51	38.5	60.6	24.5
Chisholm (1973)	67.4	15.9	56	18.8	81.9	3.3	95.8	2
Friedel (1979)	20.6	69	21.5	79	28.5	63	31.9	60
Muller-Steinhagen and Heck (1986)	**13.7**	***93.4***	21	***88.2***	**18.2**	81.1	20	78.6
Mishima and Hibiki (1996)	24.5	69	24.2	77	21.8	***83.6***	19.8	***83.7***
Tran et al. (2000)	168	0.7	68.5	16.5	105.8	0	121	4
Modified Tran et al. (2000)	23.1	74	22.3	86	20.8	80	22.9	76.5
Yu et al. (2000)	45.5	27.8	40.4	38.2	53.7	30.3	57.5	30.6
Lee and Lee (2001)	30.5	52.3	56.9	25.9	75.7	17	78.7	14
Warrier et al. (2002)	198.4	0.7	175	0	251	0	264	1
Qu and Mudawar (2003)	63.2	41.7	45.5	45.9	62	32.8	73.3	16.3
Lee and Mudawar (2005)	43.4	31.8	70.1	8.8	101.4	2.4	111.7	14
Lee and Garimella (2008)	20.3	74.8	51.2	44	64.8	31	78.3	15.3
Zhang et al. (2010)	30.2	45	22.9	81.2	23.8	72	24	71.4
Li and Wu (2010)	15.9	92	26.5	76.5	31.4	64.7	35.2	48
Lee et al. (2010)	152.5	25	130	34	229	23.8	227	17.3
Garimella et al. (2002)	71.8	14	29	69	69.6	17.8	74.8	18
Shiferaw et al. (2009)	22.8	70.8	20.9	81.8	21.6	74.5	24.8	64

Table 6.1 indicates that few correlations predicted the current experimental data in all tubes fairly well. These correlations are the Muller-Stienhagen and Heck (1986) correlation, the homogeneous flow model and the correlation of Mishima and Hibiki (1996). In addition to that, the three zone pressure drop model of Shiferaw et al. (2009) predicted the slug flow data fairly well in all tubes. On the other hand, some correlations predicted the data of one tube only whereas failed to predict the data of the others. For example, the correlations of Li and Wu (2010) and Lockhart-Martinelli (1949) predicted the data of the 0.52 mm diameter tube very well while the performance of these correlations is worse in the other tubes. Also, it is interesting to note that the correlations which were developed for multi-channels configurations such as those proposed by Lee and Lee (2001), Warrier et al. (2002), Qu and Mudawar (2003), Lee and Mudawar (2005) and Lee and Garimella (2008) predicted poorly the current experimental data.

Chapter 7

Conclusions and Recommendations

7.1 Conclusions

Flow boiling heat transfer and pressure drop in mini/micro diameter tubes were investigated experimentally in the current study. Five test sections were investigated including (i) one seamless cold drawn tube with D = 0.52 mm and L = 100 mm, (ii) three seamless cold drawn tubes with D = 1.1 mm and L = 150, 300, and 450 mm, and (iii) one welded tube, i.e. manufactured by welding technique, with D = 1.16 mm and L = 150 mm. Parallel to the heat transfer and pressure drop measurements, the flow patterns observed at the exit of the heated section were recoded using a high speed camera to assist on understanding and explaining the heat transfer results. Additionally, a detailed evaluation for the existing heat transfer and pressure drop models and correlations was also conducted in the current study. The important conclusions that can be drawn from the present study are summarized below in the following subsections.

7.1.1 Flow patterns

The flow patterns were recorded in the present study for mass flux range G = 100 – 500 kg/m^2 s, system pressure range P = 6 – 10 bar and exit quality x ≅ 0.01 – 0.9. The results demonstrated the following points:

1. The flow patterns observed in the 0.52 mm diameter tube are slug, transition to annular and annular flow regimes. The flow patterns observed in the 1.1 mm diameter tubes are slug, churn and annular flow regimes.
2. The features of the observed flow regimes in the 0.52 mm tube are completely different compared to those observed in the 1.1 mm tubes. The differences include the following:

a. The vapour slug was too long in the 0.52 mm diameter tube with a very smooth thin liquid film and features similar to annular flow. In the 1.1 mm tubes, the vapour slugs were shorter in length with a relatively thicker and unstable liquid film.
b. Bubble coalescence appeared in a considerable number of pictures at low heat fluxes (low exit quality) in the 0.52 mm diameter tube which was not the case in the 1.1 mm tube.
c. The conventional churn flow with a large distortion at the liquid/vapour interface did not appear in the 0.52 mm tube. Instead, a smooth transition from slug to annular flow regime occurred. This transition regime was created by the coalescence of the elongated bubbles and was characterized by the presence of rings at the merging locations. The liquid film was only disturbed at the merging stations whilst it remained smooth at locations away from the merging area. In the 1.1 mm tubes, churn flow was observed with highly unstable liquid/vapour interface.
d. In the 0.52 mm tube, at very low heat fluxes (low exit qualities), the flow patterns were observed to fluctuate between single phase liquid, bubbly, slug and elongated bubbles. This did not occur in the 1.1 mm tubes. This observation indicates that the nucleation sites seem unstable in the 0.52 mm tube compared the 1.1 mm tube at very low heat fluxes.
e. The annular flow regime in the 0.52 mm tube did not show liquid droplet entrainment into the gas core whilst the pictures of the 1.1 mm tube did show.
f. Very small bubbles were observed trapped in the liquid film surrounding the vapour slug. These small bubbles disappeared after about 10 ms and fully merged with the main vapour slug. This point is very important in that it may open the door to think about the possibility of nucleation in the liquid film.

3. The comparison with the flow maps indicated that there is a reasonable agreement with the map of Revellin and Thome (2007c) and Chen (2006). The transition to annular flow regime observed in the 0.52 mm tube is corresponding to the coalescing bubble regime in the Revellin and Thome map whilst is corresponding to churn flow in the Chen map.

4. As the heated length increases, the transition to annular flow occurs at lower vapour qualities. For example, at mass flux value of 300 kg/m^2 s and 6 bar system pressure increasing the length from 150 to 450 mm decreased the transition quality from 0.44 to 0.25.
5. There is no clear effect for system pressure on the transition boundaries from the *G-x* map whilst there is a tendency for the transition boundaries to shift left on the U_{GS}-U_{LS} map.

7.1.2 Heat transfer characteristics

The local flow boiling heat transfer coefficient was determined experimentally for all tubes (D = 0.52 mm and 1.1 mm) at G = 100 – 500 kg/m^2 s, P = 6 – 10 bar, $\Delta T_{sub} \approx 5$ K and vapour quality up to ≈ 0.9. All measurements were recorded under steady and stable conditions. The following conclusions can be drawn:

1. There is a significant effect for tube diameter on the local behaviour of the heat transfer coefficient. This effect is very obvious from comparing the results of the 0.52 mm tube with that of the 1.1 mm tube. Both tubes are seamless cold drawn and have approximately similar heated lengths (100 mm for the 0.52 mm tube and 150 mm for the 1.1 mm tube). The differences are summarized in the following table:

Table 7.1 Comparison between the heat transfer results in the 0.52 mm tube (L = 100 mm) and the 1.1 mm tube (L = 150 mm).

Parameter	0.52 mm tube	1.1 mm tube
Trend	For most heat fluxes, the HTC dropped from a very high value at x ≈ 0, then it remained approximately constant with x up to the intermediate quality region then it increased rapidly with quality.	The large drop in the HTC at x ≈ 0 did not occur and the HTC exhibited little dependence of x for all x values before the occurrence of dryout
Heat flux	• The HTC increases with q for x < 0.4 with little dependence on x after the first thermocouple location.	The HTC increases with q with small dependence on x for all quality values except the dryout region.

	• For x > 0.4, there is no heat flux effect and the HTC increased with x.	
Mass flux	For x < 0.4, there is insignificant mass flux effect whilst the HTC increased with G for x > 0.4.	There is insignificant mass flux effect.
System pressure	The HTC increases with increasing pressure	The HTC increases with increasing pressure
Mechanism (s)	Nucleate – convective boiling	Nucleate boiling
Diameter effect	As presented in Fig. 4.52, the average heat transfer coefficient in the 0.52 mm tube is much higher that in the 1.1 mm tube. The HTC in the 0.52 mm tube is a bout 1.53 times that in the 1.1 mm tube.	

The differences in the heat transfer results between the 0.52 mm and the 1.1 mm tube are very consistent with the differences in the flow patterns characteristics summarized above. The presence of the short vapour slugs in the 1.1 mm tube may increase the chance of nucleation in the liquid slugs between the consecutive bubbles whilst the elongation of the bubbles in the 0.52 mm tube with the presence of few liquid slugs may suppress nucleation towards the tube exit. This may explain the dominance of nucleate boiling in the 1.1 mm tube compared to the 0.52 mm tube. Additionally, the large instability at the liquid vapour interface observed in the 1.1 mm tube may result in the partial dryout observed in this tube for $x \approx 0.5 - 0.6$. On the contrary, no partial dryout was observed in the 0.52 mm tube even at very high qualities due to the very smooth and stable liquid/vapour interface.

2. The hysteresis analysis for the 0.52 mm tube and all 1.1 mm tubes demonstrated that, there is boiling hysteresis in the 0.52 mm tube for $q < 18$ kW/m^2 whilst the hysteresis in the 1.1 mm tubes were observed at lower heat fluxes ($q < 10$ kW/m^2), i.e. in the region of boiling incipience. This point indicates that possibly there are few active nucleation sites in the 0.52 mm tube which are unstable at low heat fluxes. This result is also consistent with the fluctuations in

flow patterns observed at low heat fluxes in the 0.52 mm tube as previously mentioned.

3. The tube inner surface characteristics significantly influence the local heat transfer behaviour. The effect of different parameters such as mass flux, heat flux and system pressure was is not clear in a tube with a very smooth surface (the welded tube). On the contrary, there is a clear effect for these parameters in a rough tube (the seamless cold drawn tube). The heat transfer coefficient in the smooth tube was not uniform along the tube as was the case in the rough tube. This point is very important and should be clarified first before the design of the micro-evaporators. Most researchers did not consider this parameter in their studies and they did not report any information about the manufacturing process of the investigated tubes. This parameter can contribute in explaining the various conclusions reported in the open literature on the local heat transfer trends and the dominant heat transfer mechanism.
4. The heated length significantly affected the local heat transfer behaviour. In the shortest (L = 150 mm), the heat transfer coefficient increases with increasing heat flux with little dependence of quality except the dryout region. As the heated length increased, the trend of the local heat transfer coefficient versus local quality changed. The coefficient exhibited increasing trend towards the exit at low to intermediate heat flux values. After this intermediate heat flux value, the increasing trend with vapour quality disappeared and the dependence on vapour quality became small.
5. The mass flux effect was insignificant in the shortest tube for all quality values whilst in the longer tubes the heat transfer coefficient increased with mass flux at high qualities towards the exit. In the low to intermediate quality region, the mass flux effect was insignificant for the longer tubes.
6. Applying the conventional criterion to infer the dominant heat transfer mechanism, nucleate boiling is dominant in the shortest tube while both nucleate and convective boiling are contributing in the longer tubes.
7. Plotting the local heat transfer coefficient versus axial distance rather than the local vapour quality demonstrated interesting points. The *h-z* plot indicated that there is a clear heat flux effect all along the tube although the *h-x* plot did not show significant effect towards the tube exit for the 0.52 mm tube and the two longest 1.1 mm tubes. Additionally, the *h-z* plots at different mass fluxes did not

show a clear mass flux effect whereas the h-x plots indicated mass flux effect towards the exit. This point raises the question: which parameter should be used to predict or infer the mechanism(s)? Is it local quality or axial position? It is very interesting to note that, the heat transfer coefficient in the 0.52 mm tube at location near the tube exit (where convective boiling is believed to dominate according to the conventional criterion) exhibited similar trend as the Cooper (1984) nucleate pool boiling correlation. The agreement with the Cooper correlation at location near the tube exit increases the doubt about the dominant heat transfer mechanism in this region.

7.1.3 Heat transfer prediction

In the current study, six macroscale correlations, eleven microscale correlations and two mechanistic models were evaluated using the current experimental data. The results of the comparison demonstrated that:

1. For the 0.52 mm diameter tube, the best examined correlations are the correlation of Bertsch et al. (2009) and Kew and Cornwell (1997). Both correlations predicted about 52 % of the data within the ± 30 % error bands.
2. For the 1.1 mm diameter tubes, the Cooper (1984) correlation was the best one for the shortest tube (MAE = 19.3 % and β = 85 %) followed by the Thome et al. (2004) model, the Mikielewicz (2010) model and the Saitoh et al. (2007) correlation. For the longer tubes, the predictions get worse.
3. The mechanistic models still require many improvements. These models performed globally in a similar way to the correlations, i.e. no big difference between the models and correlations, although they predict the experimental trend fairly well. This is because these models are not totally based on theory and depend on empirical parameters, i.e. they are semi mechanistic models.
4. Due to the failure of the evaluated models and correlations in predicting the current experimental data, two new correlations were proposed in this study. The first correlation was based on the dimensionless groups such as boiling number, Weber number, liquid Reynolds number, confinement number and convection number. The second correlation was a modified version of the Chen (1966) correlation. Since the new correlations were validated using experimental data collected for tubes with different heated lengths, the effect of heated length,

which was not considered before, is incorporated in the correlation parameters. The two new correlations predicted 85.9 to 93.4 % of the experimental data within the ± 30 % error bands at MAE values of 14 – 17.9 %, which is much better than the other evaluated correlations.

7.1.4 Pressure drop

The total measured flow boiling pressure drop in 0.52 and 1.1 mm diameter tubes was measured at mass flux range of 200 – 500 kg/m^2 s and system pressure range of 6 – 10 bar. The results indicated that:

1. The two phase pressure drop increases with increasing heat flux (exit quality), increasing mass flux, decreasing system pressure and decreasing tube diameter.
2. The contribution of the frictional pressure drop component to the total measured pressure drop was found to be the largest compared to the contribution of the gravitational and acceleration components. Its value reached about 70 % in the 1.1 mm diameter tube and about 80 % in the 0.52 mm diameter tube. This indicates that the contribution of the frictional component to the total measured two phase pressure drop increases as the diameter decreases. This may be attributed to the thinning of the boundary layer in micro-tubes resulting in higher velocity gradients and consequently higher wall shear stress. However, the contribution of the acceleration component to the total measured pressure drop can not be ignored in flow boiling studies compared to adiabatic studies. Its value reached about 22 % in the 0.52 mm tube at exit quality value of about 0.9 whilst the corresponding value in the 1.1 mm tube was about 37 %. The higher contribution of the acceleration component in the 1.1 mm tube compared to the 0.52 mm tube is due to the higher values of Reynolds number.
3. The heated length has a significant effect on the measured pressure drop per unit length. At the same exit quality, the shorter the heated length, the higher the measured pressure drop per unit length.
4. The evaluation of eighteen macro- and micro-scale models and correlations indicated that, the Muller-Stienhagen and Heck (1986) correlation, the homogeneous flow model and the correlation of Mishima and Hibiki (1996) predict the current experimental data very well. Also, it is interesting to note

that the correlations which were developed for multi-channels configurations poorly predicted the current experimental data.

7.2 Recommendations

Based on the experiments conducted in the present study, the issues that require further investigations include the following:

- According to the current study, there is an argument about the dominant heat transfer mechanism(s) in mini/micro-diameter tubes. This fundamental point needs further investigation to clarify whether nucleate boiling is very important in microchannels or not. One recommendation to study this point is to conduct the test in a tube which is partially smooth and partially rough, i.e. the entry section of the tube is rough whilst the remaining section of the tube is very smooth as shown in the schematic below. A seamless cold drawn tube with L = 150 mm (similar to the shortest one in the current study) is a good option for this test. This is because nucleate boiling was found to dominant everywhere in this tube (before dryout), according to the result of the current study. Making one part of the tube very smooth may be done by the electro-polishing technique where one end of the tube can be immersed into the electrolyte with the required depth. The difference between this experiment and the one conducted in the current study using a welded tube is that, the welded tube looks smooth everywhere.

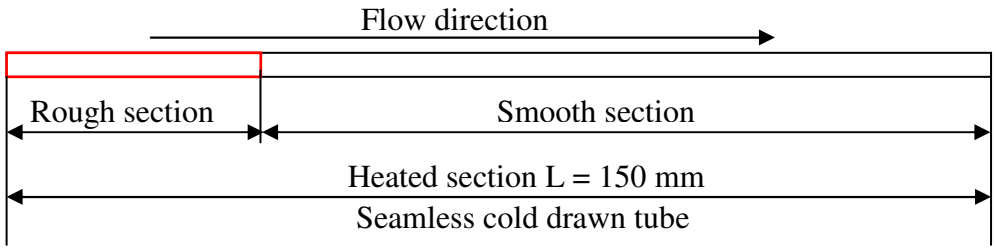

- The effect of surface tension on the flow boiling heat transfer characteristics was not quantified at microscale although many researchers reported that there is a strong effect for surface tension. This may be investigated by testing new refrigerants that has higher surface tension compared to R134a.
- The above point (testing many fluids) is also needed for the purpose of developing new empirical correlations based on a wide range of experimental

conditions. As found in the current study, the existing microscale correlations are not general due possibly to the lack of wide and accurate experimental data.

- Modelling is one of the topics that represent a big challenge in flow boiling. The existing mechanistic models, which are few, still need further modifications.

REFERENCES

Adams, T. M., Abdel-khalik, S. I., Jeter, S. M. and Qureshi, Z. H. An experimental investigation of single phase forced convection in microchannels. *Int. J. Heat Mass Transfer*, 41, 6-7: 851 – 857, 1998.

Agostini, B., Watel, B., Bontemps, A., and Thonon, B. Friction factor and heat transfer coefficient of R-134a liquid flow in minichannels. *Applied Thermal Engineering*, 22:1821 – 1834, 2002.

Agostini, B. and Bontemps, A. Vertical flow boiling of refrigerant R134a in small channels. *International Journal Heat Fluid Flow*, 26(2):296-306, 2005.

Agostini, B. and Thome, J.R. Comparison of an extended database for flow boiling heat transfer coefficients in multi-microchannels: Elements with the three-zone model. *ECI Heat Transfer and Fluid Flow in Microscale*, Castelvecchio Pascoli, Italy, Sept. 25–30, 2005.

Agostini, B., Thome, J.R., Fabri, M. and Michel, B. High heat flux two phase cooling in silicon multi-microchannels. *IEEE Transactions on Components and Packaging Technologies, Vol. 31, No.3, September 2008a.*

Agostini, B., Revellin, R., Thome, J.R., Fabbri, M., Michel, B., Calmi, D., Kloter, U. High heat flux flow boiling in silicon multi-microchannels - Part III: Saturated critical heat flux of R236fa and two-phase pressure drops**.** *International Journal of Heat and Mass Transfer* 51 (21-22), pp. 5426-5442, 2008b.

Agostini, B., Revellin, R., Thome, J.R. Elongated bubbles in microchannels. Part I: Experimental study and modeling of elongated bubble velocity**.** *International Journal of Multiphase Flow* 34 (6), pp. 590-601, 2008c.

Agostini, B., Thome, J.R., Fabbri, M., Michel, B. Calmi, D., Kloter, U., High heat flux flow boiling in silicon multi-microchannels Part II: Heat transfer characteristics of

refrigerant R245fa**.** *International Journal of Heat and Mass Transfer* 51 (21-22), pp. 5415-5425, 2008d.

Akbar, M.K., Plummer, D.A. and Ghiaasiaan, S.M. On gas-liquid two-phase flow regimes in microchannels. *International Journal of Multiphase Flow*, 29:855-865, 2003.

Aligoodarz, M. R., Yan, Y. and Kenning, D.B.R.. Wall temperature and pressure variations during flow boiling in narrow channels. In *Proceedings of 11th International Heat Transfer Conference (IHTC),* August 23-28, 2:225-230, 1998.

Bao, Z.Y., Fletcher, D.F. and Haynes, B.S. Flow boiling heat transfer of Freon R11 and HCFC123 in narrow passages. *International Journal Heat Mass Transfer*, 43: 3347-3358, 2000.

Bang, K-H, Hong, K-E and Hwang, I-S. Flow boiling of water in minichannels: Effect of pressure. *Proceedings of the 5th International Conference on Nanochannels, Microchannels and Minichannels, ICNMM2007* , pp. 35-40, 2007.

Barnea, D., Luninski, Y. and Taitel, Y. Flow pattern in horizontal and vertical two phase flow in small diameter pipes. *The Canadian Journal of Chemical Engineering*, 61(5):617-620, 1983.

Blasius, H. Das Ähnlichkeitsgesetz bei Reibungsvorgängen in Flüssigkeiten, *Forchg. Arb. Ing.-Wes.*, No. 131, Berlin, 1913.

Boye, H., Staate, Y. and Schmidt, J. Experimental investigation and modelling of heat transfer during convective boiling in a minichannel. *International Journal Heat Mass Transfer*, 50:208-215, 2007.

Bowers, M.B. and Mudawar, I. High flux boiling in low flow rate, low pressure drop minichannel and microchannel heat sinks. *International Journal Heat Mass Transfer*, 37(2):321-332, 1994.

Bennet, D. L. and Chen, J. C. Forced convection boiling in forced tubes for saturated pure fluids and binary mixtures. AIChE J. 26(3): 454 – 464, 1980.

Bergles, A. E., Collier, J. G., Delhaye, J.M., Hewitt, G.F., Mayinger, F. Two phase flow and heat transfer in the power and process industries. *Hemisphere Publishing Corporation, New York, 1981.*

Bergles, A.E., Kandlikar, S.G.. Critical heat flux in microchannels: Experimental issues and guidelines for measurement**.** *International Conference on Microchannels and Minichannels* 1, pp. 141-147, 2003.

Bertsch, S.S., Groll, E.A., Garimella, S.V.. Refrigerant flow boiling heat transfer in parallel microchannels as a function of local vapor quality**.** *International Journal of Heat and Mass Transfer* 51 (19-20), pp. 4775-4787, 2008a.

Bertsch, S.S., Groll, E.A., Garimella, S.V. Review and comparative analysis of studies on saturated flow boiling in small channels**.** *Nanoscale and Microscale Thermophysical Engineering* 12 (3), pp. 187-227, 2008b.

Bertsch, S.S., Groll, E.A. & Garimella, S.V., Effects of heat flux, mass flux, vapour quality, and saturation temperature on flow boiling heat transfer in microchannels. International Journal of Multiphase Flow, 35 (2), pp. 142-154, 2009a.

Bertsch, S.S., Groll, E.A., Garimella, S.V.. A composite heat transfer correlation for saturated flow boiling in small channels**.** *International Journal of Heat and Mass Transfer* 52 (7-8), pp. 2110-2118, 2009b.

Brauner, N. and Barnea, D. Slug/churn transition in upward gas-liquid flow, *Chemical Engineering Science*, 41(1):159-163, 1986.

Brauner, N. and Moalem-Maron, D. Identification of the range of small diameter conduits regarding two-phase flow pattern transitions. *International Communications Heat Mass Transfer*, 19:29-39, 1992.

Brutin, D., Topin, F., Tadrist, L. Experimental study of unsteady convective boiling in heated minichannels**.** *International Journal of Heat and Mass Transfer* 46 (16), pp. 2957-2965, 2003.

Cavallini, A., Col, D.D., Doretti, L., Matkovic, M., Rossetto, L. and Zilio, C. Two-hase frictional pressure gradient of R-236ea, R-134a and R-410a inside multi-port minichannels. *Experimental Thermal Fluid Science*, 29:861–870, 2005.

Celata, G.P. Cumo, M., Guglielmi, M. and Zummo, G. Experimental investigation of hydraulic and single phase heat transfer in 0.13 mm capillary tube. Microscale Thermophysical Engineering, 6(2): 85 – 97, 2002.

Celata, G.P., Cumo, M., Marconi, V., McPhail, S.J., Zummo, G.. Microtube liquid single-phase heat transfer in laminar flow. *International Journal of Heat and Mass Transfer* 49 (19-20), pp. 3538-3546, 2006.

Chen, J.C. A correlation for boiling heat transfer to saturated fluids in convective flow. *Industrial and Engineering Chemistry*, 5:322-329, 1966.

Chen, W.L., Twu, M.C., and Pan, C. Gas-liquid two phase flow in microchannels. International Journal of Multiphase Flow, 28, pp. 1235 – 1247, 2002.

Chen, L. Flow patterns in upward two-phase flow in small diameter tubes, PhD thesis, Brunel University, UK, 2006.

Chen, L., Tian, Y.S., and Karayiannis, T.G. The effect of tube diameter on vertical two-phase flow regimes in small tubes. *International Journal Heat Mass Transfer*, 49: 4220-4230, 2006.

Chen, I.Y., Chen, Y-M., Liaw, J-S., Wang, C.-C. Two-phase frictional pressure drop in small rectangular channels. *Experimental Thermal and Fluid Science* 32 (1), pp. 60-66, 2007.

Chen, T., Garimella, S.V. Measurements and high-speed visualizations of flow boiling of a dielectric fluid in a silicon microchannel heat sink. *International Journal of Multiphase Flow* 32 (8), pp. 957-971

Chin L. O. and Thome J. R. Flow boiling heat transfer of R134a, R236fa and R245fa in a horizontal 1.03 mm circular channel. Experimental Thermal and Fluid Science, 33:651 – 663, 2009.

Chisholm, D. A theoretical basis for the Lockhart–Martinelli correlation for two-phase flow. *International Journal of Heat Mass Transfer*, 10:1767–1778, 1967.

Chisholm, D. Pressure gradients due to friction during the flow of evaporating two-phase mixtures in smooth tubes and channels. *International Journal Heat Mass Transfer*, 16:347-358, 1973.

Chisholm, D. *Two-Phase Flow in Pipelines and Heat Exchangers*. Longman, New York, 1983.

Chang, K.H., Pan, C.. Two-phase flow instability for boiling in a microchannel heat sink**.** *International Journal of Heat and Mass Transfer* 50 (11-12), pp. 2078-2088, 2007.

Choi, S. B., Barron R. F., and Warrington, R. O. Fluid flow and heat transfer in microtubes. *DSC-Vol. 32, Micromechanical Sensors, Actuators, and Systems, ASME, 1991*.

Choi, K.-I., Pamitran, A.S., Oh, C.-Y., Oh, J.-T. Two-phase pressure drop of R-410A in horizontal smooth minichannels**.** *International Journal of Refrigeration* 31 (1), pp. 119-129, 2008

Choi, K., Pamitran, A.S., Oh, J-T & Saito, K., Pressure drop and heat transfer during two-phase flow vaporization of propane in horizontal smooth minichannels. International Journal of Refrigeration, 32, pp. 837-845, 2009.

Chung, P. M-Y. and M. Kawaji. The effect of channel diameter on adiabatic two-phase flow characteristics in microchannels. *International Journal of Multiphase Flow*, 30:735-761, 2004.

Coleman, J.W. and S. Garimella. Characterization of two-phase flow patterns in small diameter round and rectangular tubes. *International Journal of Heat and Mass Transfer*, 42:2869-2881, 1999.

Coleman, H. W. and W.G. Steele. *Experimentation and uncertainty analysis for engineers*, John Wiley & Sons Inc. Second edition, New York, 1999.

Collier, J.G. and J.R. Thome. *Convective Boiling and Condensation*. Oxford University Press, Oxford, UK, third edition, 1994.

Consolini, L. and Thome, J. R., Micro-channel flow boiling heat transfer of R-134a, R-236fa, and R-245fa. *Microfluidics and Nanofluidics, 6 (6), pp. 731-746, 2009*.

Consolini, L., Thome, J.R.. A heat transfer model for evaporation of coalescing bubbles in micro-channel flow**.** *International Journal of Heat and Fluid Flow* 31 (1), pp. 115-125, 2010.

Cornwell, K. and P.A. Kew. Boiling in small parallel channels. In: Proc CEC Conf. on energy Efficiency in Process Technology, Athens. Elsevier Applied Science, 1993 p. 624-638.

Cooper, M. G. Saturated nucleate pool boiling – a simple correlation. In *first UK National Heat Transfer Conference, IChemE Symposium*, Series 86, 2:785-793, 1984.

Damianides, C. A. and J.W. Westwater. Two-phase flow patterns in a compact heat exchanger and in small tubes. In *Second UK National Conference on Heat Transfer*, 11:1257-1268, 1988.

Davis, E. J. and G.H. Anderson. The incipience of nucleate boiling in forced convection flow. *AIChE Journal*, 12(4):774–780:1966.

De-Cachard, F., Delhaye, J.M. A slug-churn flow model for small-diameter airlift pumps**.** *International Journal of Multiphase Flow* 22 (4), pp. 627-649, 1996.

Del Col, D., Cavallini, A., Bortolin, S., Matkovic, M., and Rosseto L., Heat transfer coefficient during flow boiling of R134a in a circular minichannel. *5th European Thermal Sciences Conference, the Netherland, 2008*.

Díaz, M.C., Boye, H., Hapke, I., Schmidt, J., Staate, Y., Zhekov, Z.. Investigation of flow boiling in narrow channels by thermographic measurement of local wall temperatures**.** *Microfluidics and Nanofluidics* 2 (1), pp. 1-11, 2006.

Dittus, F.W. and Boelter, L.M.K., 1930. Heat transfer in automobile radiators of tubular type, Univ. California Berkeley, Publ. Eng. 2/13, pp. 443–461.

Dupont, V., J.R. Thome, A.M. Jacobi, Heat transfer model for evaporation in microchannels, Part II: comparison with the database, *International Journal Heat Mass Transfer*, 47:3387-3401, 2004.

El-Genk, M.S., and Bostanci, H. Saturation boiling of HFE-7100 from a copper surface simulating a microelectronic chip. *Int. J. of Heat and Mass Transfer, 46 (10):1841 – 1854, 2003.*

Fabbri, M. and Dhir, V.K. Optimized heat transfer for high power electronic cooling using arrays of microjets. Journal of Heat Transfer 127 (7): 760 – 769, 2005.

Faulkner, D., Khotan, M. and Shekharriz, R. Practical design of 1000 W/cm^2 cooling system. *19th IEEE SEMI-THERM Symposium, 2003.*

Forster, H. K. and N. Zuber, Dynamics of vapour bubbles and boiling heat transfer, AIChe J. 1, pp. 531-535, 1955.

Friedel, L. (1979). Improved friction pressure drop correlations for horizontal and vertical two-phase pipe flow. Presented at the European Two-phase Flow Group Meeting, Ispra, Italy, Paper E2, June.

Fukano, T., A. Kariyasaki, M. Kagawa. Flow patterns and pressure drop in isothermal gas–liquid concurrent flow in a horizontal capillary tube. In *ANS Proceedings National Heat Transfer Conference*, 4:153–161, 1989.

Fukano, T. and A. Kariyasaki. Characteristics of gas-liquid two-phase flow in a capillary tube. *Nuclear Engineering and Design*, 141:59-68, 1993.

Fu, X., Qi, S.L., Zhang, P., Wang, R.Z. Visualization of flow boiling of liquid nitrogen in a vertical mini-tube**.** *International Journal of Multiphase Flow* 34 (4), pp. 333-351, 2008.

Garimella, S., J.D. Killion, and J.W. Coleman. An experimental validated model for two-phase pressure drops in the intermittent flow regime for circular channel. *Journal of Fluid Engineering*, 124:205–214, 2002.

Geisler, K.J.L, Straznicky, I. and Bar-Cohen, A. Immersion cooling module for military COTS applications. Proceedings – Ninth Intersociety Conference on Thermal and Thermomechanical Phenomena in Electronic Systems, Las Vegas, NV, USA, 2, 67 – 74, 2004.

Ghiaasiaan, S. M. and R.C. Chedester. Boiling incipience in microchannels. *International Journal of Heat and Mass Transfer* 45:4599-4606, 2002.

Gnielinski, V. New equations for heat transfer in turbulent pipe and channel flow. *International Chemical Engineering*, 16:359–368, 1976.

Gnielinski, V. *VDI-Wärmeatlas*, Springer-Verlag, Berlin, Heidelberg, 1997.

Guo, Z-Y., and Li, Z-X. Size effect on microscale single phase flow and heat transfer. *Int. J. of Heat and Mass Transfer, 46:149 – 159, 2003.*

Gungor, K. E., Winterton, R.H.S.. A general correlation for flow boiling in tubes and annuli. *International Journal Heat Mass Transfer*, 29:351-358, 1986.

Gungor, K. E. Winterton, R.H.S. Simplified general correlation for saturated and comparisons of correlations with data. The Canadian Journal of Chemical Engineering, Vol. 65, No. 1: 148 – 156, 1987.

Hall, D.D., Mudawar, I.. Ultra-high critical heat flux (CHF) for subcooled water flow boiling-II: High-CHF database and design equations**.** *International Journal of Heat and Mass Transfer* 42 (8), pp. 1429-1456, 1999.

Han, Y., Shikazono, N.. Measurement of the liquid film thickness in micro tube slug flow**.** *International Journal of Heat and Fluid Flow* 30 (5), pp. 842-853, 2009.

Hao, P-F., Zhang, X-W., Yao, Z-H., and He F. Transitional and turbulent flow in a circular microtube. Experimental Thermal and Fluid science, 32: 423 – 431, 2007.

Hapke, I., Boye, H. and Schmidt, J. Onset of nucleate boiling in minichannels. *International Journal Thermal Science*, 39:505–513, 2000.

Harirchian, T., Garimella, S.V.. Microchannel size effects on local flow boiling heat transfer to a dielectric fluid**.** *International Journal of Heat and Mass Transfer* 51 (15-16), pp. 3724-3735, 2008.

Harirchian, T. & Garimella, S.V., Effects of channel dimension, heat flux, and mass flux on flow boiling regimes in microchannels. International Journal of Multiphase Flow, 35 (4), pp. 349-362, 2009a.

Harirchian, T., Garimella, S.V. The critical role of channel cross-sectional area in microchannel flow boiling heat transfer**.** *International Journal of Multiphase Flow* 35 (10), pp. 904-913, 2009b

Hayashi, S., Kasagi, N. & Suzuki, Y., The effects of inlet flow conditions on gas liquid two phase flow in a micro tube. Proceedings of HT2007, 2007 ASME-JSME Thermal Engineering Summer Heat Transfer Conference, Vancouver, British Columbia, Canada, July 8 – 12, 2007.

Hegab, H. E., Bari, A. and Ameel, T. A. Experimental investigation of flow and heat transfer characteristics of R-134a in microchannels. *Proc. Of SPIE* Vol. 4560, 2001.

Hewitt, G.F. and N.S. Hall-Taylor. *Annular two-phase flow*. Pergamon Press, Oxford, UK, 1970.

Hetsroni, G., Klein, D., Mosyak, A., Segal, Z., Pogrebnyak, E.. Convective boiling in parallel microchannels**.** *Microscale Thermophysical Engineering* 8 (4), pp. 403-421, 2004.

Hetsroni, G., Mosyak, A., Pogrebnyak, E., and Yarin, L.P. Fluid flow in microchannels. Int. J. of Heat and Mass Transfer, 48: 1982 – 1998, 2005.

Hewitt, G. F. and N.S. Hall-Taylor. *Annular two-phase flow*. Pergamon Press, Oxford, UK, 1970.

Hrnjak, P. and Tu, X. Single phase pressure drop in microchannels. *Int. J. Heat Fluid Flow*, 28:2 – 14, 2007.

Holt, A.J., Azzopardi, B.J. and Biddulph, M.W. Two phase pressure drop and void fraction in narrow channels. 5th UK National Heat Transfer Conference , Imperial College, London, Uk, 17 – 18 September, 1997.

Holt, A.J., Azzopardi, B.J. and Biddulph, M.W. Calculation of two phase pressure drop for vertical upflow in narrow passages by means of a flow pattern specific model. Trans. IChemE, vol. 77, part A, January 1999.

Hrnjak, P. and Litch, A.D. Microchannel heat exchangers for charge minimization in air-cooled ammonia condensers and chillers. *Int. J. of Refrigeration, 31(4):658 – 668, 2008.*

Hsieh, S-S., Lin, C-Y., and Huang, C-F. Liquid flow in a micro-channel. *J. of Micomech. And Microeng., 14, pp. 436 – 445. 2004.*

Huo, X., Chen, L., Tian, Y. S. and Karayiannis, T. G. Flow boiling and flow regimes in small diameter tubes. *Applied Thermal Engineering*, 24:1225-1239, 2004.

Huo, X. Experimental study of boiling heat transfer in small diameter tubes, PhD thesis, London South Bank University, London, UK, 2005.

Huo, X., Tian, Y.S. and Karayiannis, T. G. R134a Flow boiling heat transfer in small diameter tubes. *Advances in compact heat exchangers*, R.T. Edwards, Inc., 5: 95-111, 2007.

Huh, C., Kim, M.H. Two-phase pressure drop and boiling heat transfer in a single horizontal microchannel**.** *Proceedings of the 4th International Conference on Nanochannels, Microchannels and Minichannels, ICNMM2006* 2006 B, pp. 1097-1104

Hwang, Y. W. and Kim, M. S. The pressure drop in microtubes and the correlation development. *Int. J Heat Mass Transfer*, 49:1804 – 1812, 2006.

In, S., Jeong, S. Flow boiling heat transfer characteristics of R123 and R134a in a micro-channel**.** *International Journal of Multiphase Flow* 35 (11), pp. 987-1000, 2009.

Incropera, F. P. and DeWitt, D. P. (2007) Fundamentals of Heat and Mass Transfer, Fourth Edition, John Wiley & Sons.

International Technology Roadmap for Semiconductors, 2001, www.itrs.net

Ide, H., Fukano, T.. Experimental research on the correlations of holdup and frictional pressure drop in air-water two-phase flow in a capillary rectangular channel**.** *Experimental Thermal and Fluid Science* 29 (7 SPEC. ISS.), pp. 833-841, 2005.

Jacobi, A. M. and J.R. Thome. Heat transfer model for evaporation of elongated bubble flows in microchannels. *Journal Heat Transfer*, 124(6):1131-1136, 2002.

Jang, Y., Park, C., Lee, Y., Kim, Y. Flow boiling heat transfer coefficients and pressure drops of FC-72 in small channel heat sinks**.** *International Journal of Refrigeration* 31 (6), pp. 1033-1041, 2008.

Jiang, L. Mikkelsen, J., Koo, J-M, Huber, D., Yao, S., Zhang, L., Zhou, P., Goodson, K.E. Closed-loop electroosmotic microchannel cooling system for VLSI circuits. IEEE Transactions on Components and Packaging Technologies 25(3):347 – 355, 2002.

Jeglic, F. A. An analytical determination of temperature oscillations in a wall heated by alternating current. Technical not, D-1286, National Aeronautics and Space Administration, Washington, July, 1962.

Jeong, S. How difficult is it to make a micro refrigerator. *Int. J. of Refrigeration. 27(3):309 – 313.*

Jung, D. S. & Radermacher, R. 1991 Prediction of heat transfer coefficient of various refrigerants during evaporation. *ASHRAE Trans.* 97(2), Paper No. 3492.

Kaminaga, F. Sumith, B. and Matsumura, K. Pressure drop in a capillary tube in boiling two phase flow. In *Proceedings of First International Microchannels and Minichannels*, April 24-25, New York, ICMM2003- 1080, 2003.

Kaew-On, J., Wongwises, S.. Experimental investigation of evaporation heat transfer coefficient and pressure drop of R-410A in a multiport mini-channel**.** *International Journal of Refrigeration* 32 (1), pp. 124-137, 2009.

Kandlikar, S. G. A general correlation for saturated two-phase flow boilingheat transfer inside horizontal and vertical tubes. *Journal of Heat Transfer, Transactions of the ASME*, 112:219-228, 1990.

Kandlikar, S. G. 1991 A model for correlating flow boiling heat transfer in augmented tubes and compact evaporators. *ASME J. Heat Transfer* 113, 966-972.

Kandlikar, S. G., Cartwright, M. D. and Mizo, V.R. A photographic study of nucleation characteristics of cavities in flow boiling. In *Proceedings of the International Conference on Convective Flow Boiling*, Banff, Canada, United Engineering Foundation, NY, 11-1, 1995.

Kandlikar, S. G., Joshi, S., and Tian, S. Effect of channel roughness on heat transfer and fluid flow characteristics at low Reynolds numbers in small diameter tubes. *Proc. Of NHTC'01 35th National Heat Transfer Conference, June 10 – 12, Anaheim, California, 2001*.

Kandlikar S. G. Two-phase flow patterns, pressure drop, and hear transfer during boiling in minichannel flow passages of compact evaporators. *Heat Transfer Engineering*, 23, Issue 1:5-23, 2002.

Kandlikar, S.G. and W.J. Grande. Evolution of microchannel flow passages—thermo hydraulic performance and fabrication technology. *Heat Transfer Engineering*, 25 (1): 3-17, 2003.

Kandlikar S. G. and P. Balasubramanian. An extension of the flow boiling correlation to transition, laminar, and deep laminar flows in minichannels and microchannels. *Heat Transfer Engineering*, 25(3): 86-93, 2004.

Kang, S., Miller, D., and Cennamo, J. Closed loop liquid cooling for high performance computer systems. Proceedings of the ASME InterPack Conference, IPACK, (2):509 – 515, 2007.

Karayiannis, T.G., Shiferaw D., and Kenning, D.B.R., Flow boiling in small- to micro-diameter tubes: experimental results and modelling, *ECI International Conference on Heat Transfer and Fluid Flow in Microscale*, Whistler, pp. 21-26, September 2008.

Kariyasaki, A., Fukano, T., Qusaka, A. and Kagawa, M. Isothermal air-water two phase flow up and downward flows in a vertical capillary tube (1st report, Flow pattern and void fraction. Trans. JSME (Ser. B) 58, 2684 – 2690. 1992.

Kawahara, A., P.M-Y. Chung, and M. Kawaji. Investigation of two-phase flow patterns, void fraction and pressure drop in a micro-channel. *International Journal Multiphase Flow*, 28(9):1411–1435, 2002.

Kawahara, A., Sadatomi, M., Nei, K. & Matsuo, H., Experimental study on bubble velocity, void fraction and pressure drop for gas-liquid two-phase flow in a circular microchannel. International Journal of Heat and Fluid Flow, 30 (5), pp. 831-841, 2009.

Kasza, K.E., Didascalou, T. & Wambsganss, M.W., Microscale flow visualization of nucleate boiling in small channels: mechanisms influencing heat transfer. Conference on Compact Heat Exchangers for Process Industries, Snowbird, Utah, June 22-27, 1997.

Katto, Y. A generalized correlation of critical heat flux for the forced convection boiling in vertical uniformly heated round tubes. *International Journal Heat Mass Transfer,* 21:1527–1542, 1978

Katto, Y. Critical heat flux Of Forced Convection Boiling In Uniformly Heated Vertical Tubes (Correlation Of CHF In Hp-Regime and determination of CHF-Regime Map). *International Journal of Heat and Mass Transfer* 23 (11), pp. 1573-1580, 1980.

Katto Y. and H. Ohno. An improved version of the generalized correlation of critical heat flux for the forced convection boiling in uniformly heated vertical tubes. *International Journal Heat and Mass Transfer* 27:1641–1648, 1984.

Kelly K. W., Harris C., Stephens L. S., Marques C., and Foley D., 2001. Industrial applications for LIGA-fabricated micro-heat exchangers. *Proc. Of SPIE Vol. 4559.*

Kenning, D.B.R. and Y. Yan. Saturated flow boiling of water in a narrow channel: experimental investigation of local phenomena. *IChemE Transaction A, Chemical Engineering Res. and Design*, 79: 425-436, 2001.

Kew, P. A. and K. Cornwell. Correlations for the prediction of boiling heat transfer in small diameter channels. *Applied Thermal Engineering*, 17(8-10):705-715, 1997.

Koşar, A., Kuo, C.-J., Peles, Y. Suppression of boiling flow oscillations in parallel microchannels by inlet restrictors**.** *Journal of Heat Transfer* 128 (3), pp. 251-260, 2006.

Koşar, A., Peles, Y. Critical heat flux of R-123 in silicon-based microchannels**.** *Journal of Heat Transfer* 129 (7), pp. 844-851, 2007.

Koşar, A.. A model to predict saturated critical heat flux in minichannels and microchannels**.** *International Journal of Thermal Sciences* 48 (2), pp. 261-270, 2009.

Kuan, W.K., Kandlikar, S.G.. Experimental study on the effect of stabilization on flow boiling heat transfer in microchannels**.** *Heat Transfer Engineering* 28 (8-9), pp. 746-752, 2007.

Kureta, M., Kobayashi, T., Mishima, K. and H. Nishihara. Pressure drop and heat transfer for flow boiling of water in small diameter tubes, *JSME International Journal, Series B*, 41(4):871-879, 1998.

Kuo, C.-J., Peles, Y.. Local measurement of flow boiling in structured surface microchannels**.** *International Journal of Heat and Mass Transfer* 50 (23-24), pp. 4513-4526, 2007.

Kuznestov, V. V. and A.S. Shamirzaev. Two phase flow pattern and flow boiling heat transfer in non-circular channel with a small gap. In *proceedings of Two-Phase Flow Modelling and Experimentation*, Pisa, 249-253, 1999.

Lazarek, G.M. and S.H. Black. Evaporative heat transfer, pressure drop and critical heat flux in a small vertical tube with R-113. *International Journal Heat Mass Transfer*, 25(7):945-960, 1982.

Lee, H. J. and S.Y. Lee. Heat transfer correlation for boiling flows in small rectangular horizontal channels with low aspect ratios. *International Journal Multiphase Flow*, 27:2043-2062, 2001.

Lee, M., Wong, Y.Y., Wong, M., Zohar, Y. Size and shape effects on two-phase flow patterns in microchannel forced convection boiling. *Journal of Micromechanics and Microengineering* 13 (1), pp. 155-164, 2003.

Lee, J. and Mudawar, I. 2005a. Two-phase flow in high heat flux microchannel heat sink for refrigeration cooling applications: Part II-heat transfer characteristics. *Int. J. Heat Mass Transfer*, 48, pp. 941 – 955.

Lee, J., Mudawar, I. Two-phase flow in high-heat-flux micro-channel heat sink for refrigeration cooling applications: Part I - Pressure drop characteristics. *International Journal of Heat and Mass Transfer* 48 (5), pp. 928-940, 2005b.

Lee, J. and Mudawar, I. Low-temperature two phase microchannel cooling for high heat flux thermal management of Defense electronics. IEEE Transactions on Components and Packaging Technologies, Vol. 32, No.2, June 2009.

Lee, P-S., Garimella, S. V., and Liu, D. Investigation of heat transfer in rectangular microchannels. *Int. J. Heat Mass Transfer*, 48:1688 – 1704, 2005.

Lee, P.-S., Garimella, S.V.. Saturated flow boiling heat transfer and pressure drop in silicon microchannel arrays. *International Journal of Heat and Mass Transfer* 51 (3-4), pp. 789-806, 2008.

Lee, H.J., Liu. D.Y., Alyousef, Y., Yao, S-C., Generalized two phase pressure drop and heat transfer correlations in evaporative micro/mini-channels. Journal of Heat Transfer, vol. 132, 041004-1 – 041004-9, 2010.

Lelea, D., Nishio, S., and Takano, K. The experimental research on microtube heat transfer and fluid flow of distilled water. *Int. J. Heat Mass Transfer*, 47: 2817 – 2830, 2004.

Li, W. and Wu, Z. A general correlation for evaporative heat transfer in micro/mini-channels. Int. J. of Heat and Mass Transfer, (53):1778 – 1787, 2010a.

Li, W. and Wu, Z. A general correlation for adiabatic two phase pressure drop in micro/mini-channels. Int. J. of Heat and Mass Transfer, (53):2732 – 2739, 2010b.

Li, Z-X., Du, D-X, Guo, Z-Y. Experimental study on flow characteristics of liquid in circular microtubes. *Microscale Thermophysical Engineering*, 7: 253 – 265, 2003.

Li, Z-H., and Cui, H-H. Experiments about simple liquid flows in microtubes. 1st International Conference on Microchannels and Mininchannels, April 21 – 23, Rochester, New York, USA, 2003.

Li, Z., He, Y-L, Tang, G-H, and Tao, W-Q. Experimental and numerical studies of liquid flow and heat transfer in microtubes. Int. J. Heat Mass Transfer, 50: 3447 – 3460, 2007.

Lie, Y.M., Lin, T.F. Subcooled flow boiling heat transfer and associated bubble characteristics of R-134a in a narrow annular duct. *International Journal of Heat and Mass Transfer* 49 (13-14), pp. 2077-2089, 2006.

Lin, S., Kew, P.A. and K. Cornwell. Flow boiling of refrigerant R141b in small tubes. *Chemical Engineering Research and Design*, 79(4):417-424, 2001a.

Lin, S., Kew, P.A. and K. Cornwell. Two-phase heat transfer to a refrigerant in a 1 mm diameter tube. *International Journal of Refrigeration*, 24:51–56, 2001b.

Lin, S., Kew, P.A.. Pressure fluctuation and flow regimes of air-water flow in a small tube. *Experimental Heat Transfer* 14 (2), pp. 135-144, 2001.

Lin, T-W. and Yang, C-Y. An experimental investigation on forced convection heat transfer performance in microtubes by the method of liquid crystal thermography. *Int. J. Heat Mass Transfer*, 50, pp. 4736 – 4742, 2007.

Liu, Z. and R.H.S. Winterton. A general correlation for saturated and subcooled flow boiling in tubes and annuli, based on a nucleate pool boiling equation. *International Journal Heat Mass Transfer*, 34(11):2759-2766, 1991.

Liu, D., Lee, P-S and S.V. Garimella. Prediction of the onset of nucleate boiling in microchannel flow. *International Journal Heat Mass Transfer,* 48:5134- 5149, 2005.

Liu, Z., Zhang, C., Huo, Y. and Zhao, X. Flow and heat transfer in rough micro steel tubes. Experimental Heat Transfer, 20: 289 – 306. 2007.

Liu, D., Garimella, S.V.. Flow boiling heat transfer in microchannels. *Journal of Heat Transfer* 129 (10), pp. 1321-1332, 2007.

Lu, C.T., Pan, C. Stabilization of flow boiling in microchannel heat sinks with a diverging cross-section design. *Journal of Micromechanics and Microengineering* 18 (7), art. no. 075035, 2008.

Lockhart, R.W. and R.C. Martinelli. Proposed correlation of data for isothermal two-phase two-component flow in pipes. *Chemical Engineering Progress*, 45-39, 1949.

McQuillan, K.W., Whalley, P.B. Flow patterns in vertical two-phase flow. *International Journal of Multiphase Flow* 11 (2), pp. 161-175, 1985.

Mala, G. M., Li, D., and Dale, J. D., Heat transfer and fluid flow in microchannels. *Int. J. Heat Mass Transfer*, 40, 13, pp. 3079 – 3088, 1997.

Mala, G. M., Li, D., and Dale, J. D. Heat transfer and fluid flow in microchannels. *Int. J. Heat Mass Transfer*, 40 (13): 3079 – 3088, 1999.

Maranzana. G. Perry. I. and Maillet, D., Mini and microchannels: influence of axial conduction in the walls. *Int. J. Heat Mass Transfer*, 47, pp. 3993 – 4004, 2004.

Martín-Callizo, C., Palm, B., and Owhaib, W., Subcooled flow boiling of R134a in vertical channels of small diameters. *Int. J. of Multiphase Flow*, 33, pp. 822 – 832, 2007a.

Martin-Callizo, C., Ali, R. & Palm, B. New experimental results on flow boiling of r-134a in a vertical microchannel. UK. Heat Transfer Conference Proceedings, Edinburgh 10-11 September, 2007b.

Martin-Callizo, C., Palm, B., Owhaib, W., and Ali, R. Flow boiling visualization of R134a in a vertical channel of small diameter. Journal of Heat Transfer, vol. 132 (3):1 – 8, 2010.

Mehendale, S.S., A. M. Jacobi, and R. K. Shah. Fluid flow and heat transfer at micro- and meso-scales with application to heat exchanger design. *Applied Mechanics Reviews*, 53(7):175–193, 2000.

Mikielewicz, D. A new method for determination of flow boiling heat transfer coefficient in conventional-diameter channels and minichannels. Heat transfer Engineering, 31 (4), pp. 276-287, 2010

Mishima, K. and M. Ishii. Flow regime transition criteria for two-phase flow in vertical tubes. *International Journal Heat Mass Transfer*, 27:723-734, 1984.

Mishima, K. and T. Hibiki, Some characteristics of air-water two-phase flow in small diameter vertical tubes, Int. J. Multiphase flow, Vol. 22, No. 4, pp. 703-712, 1996.

Muwanga, R., Hassan, I.. A flow boiling heat transfer investigation of FC-72 in a microtube using liquid crystal thermography**.** *Journal of Heat Transfer* 129 (8), pp. 977-987, 2007.

Muller-Steinhagen, H. and K. Heck. A simple friction pressure drop correlation for two-phase flow in pipes. In *Proceedings of Chemical Engineering,* 20:297–308, 1986.

Moriyama, K., and Inoue, A. Thickness of the liquid film formed by a growing bubble in a narrow gap between two horizontal plates. *Journal Heat Transfer*, 118:132-139, 1996.

Mudawar I. Assessment of high heat flux thermal management schemes. *Transactions on Components and Packaging Technologies*, 24(2):122-140, 2001.

Natarajan, G. and Bezama, R.J. Microject cooler with distributed returns. Heat Transfer Engineering 28 (8-9): 779 – 787, 2007.

Nnanna, A.G.A. Application of refrigeration system in electronics cooling. Applied Thermal Engineering 26(1):18 – 27, 2006.

Nnanna, A.G.A., Rutherford, W., Elomar, W. And Sankowski, B. Assessment of thermoelectric module with nanofluid heat exchanger. Applied Thermal Engineering, 29(2-3):491 – 500, 2009.

Ohta, H., Inoue, K., Ando, M., & Watanabe, K. (2009). Experimental investigation on observed scattering in heat transfer characteristics for flow boiling in small diameter tube. *Heat Transfer Engineering, **30** (1-2), 19 – 27.*

Owahib, W. and Palm, B. Experimental investigation of single phase convective heat transfer in circular microchannels. *Exp. Thermal and Fluid Science*, 28, pp. 105 – 110, 2004.

Owhaib, W., Martin-Callizo, C. and B. Palm. Evaporative heat transfer in vertical circular microchannels. *Applied Thermal Engineering,* 24:1241-1253, 2004.

Owhaib, W., Palm, B., Martn-Callizo, C. A visualization study of bubble behavior in saturated flow boiling through a vertical mini-tube**.** *Heat Transfer Engineering* 28 (10), pp. 852-860. 2007.

Owhaib, W., Palm, B. and C. Martin-Callizo. Flow boiling visualization in a vertical circular microchannel at high vapour quality. *Experimental Thermal Fluid Science*, 30(8): 755-763, 2006.

Park, C.Y. and Hrnjak, P. Experimental and numerical study on microchannel and round tube condensers in a R410A residential air-conditioning system. International Journal of Refrigeration, 31(3):822 – 831, 2008.

Park, J.E., Thome, J.R. Critical heat flux in multi-microchannel copper elements with low pressure refrigerants**.** *International Journal of Heat and Mass Transfer* 53 (1-3), pp. 110-122, 2010.

Peng, X.F., Hu, H.Y., Wang, B.X. Flow boiling through V-shape microchannels**.** *Experimental Heat Transfer* 11 (1), pp. 87-100, 1998a

Peng, X**.** F., Hu, H. Y. and B. X. Wang. Boiling nucleation during liquid flow in microchannels. *International Journal Heat Mass Transfer*, 41:101-106, 1998b.

Peng, X.F., Tian, Y., Lee, D.J. Arguments on microscale boiling dynamics**.** *Microscale Thermophysical Engineering* 6 (1), pp. 75-83, 2002.

Pettersen, J., Hafner, A., Skaugen, G. and Rekstad H. Development of compact heat exchangers for CO_2 air conditioning systems. International Journal of Refrigeration, 21(3):180 – 193, 1998.

Petukhov, B. S., 1970, Heat transfer and friction in turbulent pipe flow with variable physicalproperties, In Advances in Heat Transfer Vol. 6, Academic Press, New York, pp. 503–564.

Pehlivan, K., Hassan, I., Vaillancourt, M. Experimental study on two-phase flow and pressure drop in millimeter-size channels. *Applied Thermal Engineering* 26 (14-15), pp. 1506-1514, 2006.

Piasecka M. and M. Poniewski. Hysteresis phenomena at the onset of subcooled nucleate flow boiling in microchannels. *Heat Transfer Engineering*, 25(3):441-451, 2004.

Poggi, F., Macchi-Tejeda, H., Leducq, D., and Bontemps, A. Refrigerant charge in refrigeration systems and strategies of charge reduction. International Journal of Refrigeration, 31:353 – 370, 2008.

Prasher, R.S., Chang, J-Y, Sauciuc, I., Narasimhan, S., Chau, D., Chrysler, G., Myers, L., Prstic, S. and Hu, C. Nano and micro technology-based-next generation package-level cooling solutions. Intel Technology Journal, Vol. 9, Issue 4:285 - 296, 2005

Pua Lee M. and Rumbold S.O. Industrial microchannel devices-where are we today? 1st International Conference on Microchannels and Minichannels, April 24 – 25, 2003, Rochester, New York, USA

Qi, Z., Zhao, Y., and Chen, J. Performance enhancement study of mobile air conditioning system using microchannel heat exchanger. International Journal of Refrigeration, 33(3):301 – 312, 2010.

Qi, S.L., Zhang, P. Wang, R.Z. & Xu, L.X., Flow boiling of liquid nitrogen in micro-tubes: Part I - The onset of nucleate boiling, two-phase flow instability and two-phase flow pressure drop. International Journal of Heat and Mass Transfer, 50 (25-26), pp. 4999-5016, 2007a.

Qi, S.L., Zhang, P., Wang, R.Z., Xu, L.X.. Flow boiling of liquid nitrogen in micro-tubes: Part II - Heat transfer characteristics and critical heat flux. *International Journal of Heat and Mass Transfer* 50 (25-26), pp. 5017-5030, 2007b.

Qu, W., Mala, M. Gh., and Li, D. Heat transfer for water flow in trapezoidal silicon microchannels. Int. J. of Heat and Mass Transfer, 43: 3925 – 3936, 2000.

Qu, W. and I. Mudawar. Prediction and measurement of incipient boiling heat flux in microchannel heat sinks. *International Journal Heat and Mass Transfer*, 45:3933-3945, 2002.

Qu, W., Mudawar, I. Measurement and prediction of pressure drop in two-phase micro-channel heat sinks. *International Journal of Heat and Mass Transfer* 46 (15), pp. 2737-2753, 2003a.

Qu, W. and I. Mudawar. Flow boiling heat transfer in two phase microchannel heat sinks – II. Annular two phase flow model. *International Journal Heat Mass Transfer*, 46:2773-2784, 2003b.

Qu, W. and I. Mudawar. Flow boiling heat transfer in two phase microchannel heat sinks: I. Experimental investigation and assessment of correlation methods. *International Journal Heat Mass Transfer*, 46:2755-2771, 2003c.

Qu, W. and I. Mudawar. Measurement and correlation of critical heat flux in two phase microchannel heat sinks. *International Journal Heat Mass Transfer*, 47:2045–2059, 2004.

Reay, D. A. Compact heat exchangers, enhancement and heat pumps. International Journal of Refrigeration, 25(4):460 – 470, 2002.

Revellin, R., Dupont, V., Ursenbacher, T., Thome, J.R. and Zun. I. Characterization of diabatic two phase flows in microchannels: Flow parameter results for R134a in a 0.5 mm channel. *International Journal Multiphase Flow* 32:755-774, 2006.

Revellin, R. and J.R. Thome. Experimental investigation of R134a and R245fa two-phase flow in microchannels for different flow conditions. *International Journal of Heat and Fluid Flow,* 28(1):63-71, 2007a.

Revellin, R. and J.R. Thome. A new type of diabatic flow pattern map for boiling heat transfer in microchannels. *Journal of Micromechanics and Microengineering*, 17(4):788-796, 2007b.

Revellin, R. and J.R. Thome. Adiabatic two-phase frictional pressure drops in microchannels. *Experimental Thermal Fluid Science*, 31(7):673-685, 2007c.

Revellin, R., Agostini, B., Thome, J.R.. Elongated bubbles in microchannels. Part II: Experimental study and modeling of bubble collisions. *International Journal of Multiphase Flow* 34 (6), pp. 602-613, 2008a.

Revellin, R., Agostini, B., Ursenbacher, T., Thome, J.R.. Experimental investigation of velocity and length of elongated bubbles for flow of R-134a in a 0.5 mm microchannel. *Experimental Thermal and Fluid Science* 32 (3), pp. 870-881, 2008b.

Revellin, R., Thome, J.R.. A theoretical model for the prediction of the critical heat flux in heated microchannels. *International Journal of Heat and Mass Transfer* 51 (5-6), pp. 1216-1225, 2008c

Revellin, R., Mishima, K., Thome, J.R.. Status of prediction methods for critical heat fluxes in mini and microchannels. *International Journal of Heat and Fluid Flow* 30 (5), pp. 983-992, 2009a.

Revellin, R., Thome, J.R.. Critical heat flux during flow boiling in microchannels: A parametric study. *Heat Transfer Engineering* 30 (7), pp. 556-563, 2009b.

Ribatski, G., Wojtan, L., & Thome, J. R. (2006). An analysis of experimental data and prediction methods for two-phase frictional pressure drop and flow boiling heat transfer in micro-scale channels. *Experimental Thermal and Fluid Science, **31**, 1 – 19.*

Rosa, P., Karayiannis, T. G., and Collins, M. W., Single-phase heat transfer in microchannels: the importance of scalling effects. *Applied Thermal Engineering*, 29(17-18):3447 – 3468, 2009.

Rohsenow, W. M., A method of correlating heat-transfer data for surface boiling of liquids, *Trans. ASME,* 74,969-975, 1952

Simons, R.E. and Chu, R.C. Application of thermoelectric cooling to electronic equipment: a review and analysis. 16th IEEE SEMI-TERM Symposium: pp. 1 – 9, 2000.

Saisorn, S. and Wongwises, S. Flow pattern, void fraction and pressure drop of two phase air-water flow in a horizontal circular microchannel. Experimental Thermal and Fluid Science, 32:748-760, 2008.

Saisorn, S. and Wongwises, S. The effects of channel diameter on flow pattern, void fraction and pressure drop of two phase air-water flow in circular microchannels. Experimental Thermal and Fluid Science, 34(4):454-462, 2010.

Saitoh S., H. Daiguji and E. Hihara. Effect of tube diameter on boiling heat transfer of R134a in horizontal small-diameter tubes. *International Journal of Heat Mass Transfer*, 48:4973-4984, 2005.

Saitoh, S., Daiguji, H. and E. Hihara. Correlation for boiling heat transfer of R134a in horizontal tubes including effect of tube diameter. *International Journal of Heat Mass Transfer*, 50:5215-5225, 2007.

Serizawa, A., Z. Feng, and Z. Kawara. Two phase flow in microchannels. *Experimental Thermal Fluid Science*, 26:703-714, 2002.

Shah, M. M. (1 976). A new correlation for heat transfer during boiling flow through pipes. ASHRAE Trans., 82(2), 66-86.

Shah, R.K. and London, A. L. (1978). Laminar flow forced convection in ducts. In: Irvin TF, Hartnett JP (eds) *Advances in Heat Transfer*. Academic , New York, 51 – 52, 124 – 128.

Shah, M.M.. Chart correlation for saturated boiling heat transfer: equations and further study. ASHRAE *transactions* 88 (pt 1), pp. 185-196, 1982.

Shah, M.M. Improved general correlation for critical heat flux during up flow in uniformly heated vertical tubes. *Heat and Fluid Flow* 84: 326–335, 1987.

Shah, R.K. and Sekulić, D.P. Fundamentals of heat exchanger design. John Wiley & Sons Inc., 2003.

Shao, L.L., Yang, L. and Zhang, C. L. comparison of heat pump performance using fin and tube and microchannel heat exchangers under frost conditions. *Applied Energy, 87(4):1187 – 1197.*

Shiferaw, D., Huo, X., Karayiannis, T.G. & Kenning, D.R.K., Examination of heat transfer correlations and a model for flow boiling of R134a in small diameter tubes. International Journal of Heat and Mass Transfer, 50, pp. 5177-5193, 2007.

Shiferaw, D. Two phase flow boiling in small- to micro-diameter tubes, PhD thesis, Brunel University, UK, 2008.

Shiferaw, D., Karayiannis, T.G. & Kenning, D.B.R., Flow boiling in a 1.1 mm tube with R134a: experimental results and comparison with model. International Journal of Thermal Sciences, 48, pp. 331-341, 2009.

Shiferaw, D., Mahmoud, M.M., Karayiannis, T.G. & Kenning, D.B.R., One dimensional mechanistic model for flow boiling pressure drop in small to micro passages. 2nd Micro and Nano Flows Conference, West London, UK, 1-2 September, 2009.

Shuai, J., Kulenovic, R., and Groll, M. Heat transfer and pressure drop for flow boiling of water in narrow vertical rectangular channels. International Conference on Microchannels and Minichannels, 1: 667 – 673, 2003.

Singh, R., Akbarzadeh, A., Dixon, C., and Mochizuki, M. Novel design of a miniature loop heat pipe evaporator for electronic cooling. Journal of Heat Transfer 129(10):1445 – 1452, 2007.

Sobierska, E., Kulenovic, R., Mertz, R., Groll, M. Experimental results of flow boiling of water in a vertical microchannel**.** *Experimental Thermal and Fluid Science* 31 (2), pp. 111-119

Sobierska, E., Kulenovic, R., Mertz, R. Heat transfer mechanism and flow pattern during flow boiling of water in a vertical narrow channel-experimental results**.** *International Journal of Thermal Sciences* 46 (11), pp. 1172-1181

Steiner, O. and J. Taborek. Flow boiling heat transfer in vertical tubes correlated by an asymptotic model. *Heat Transfer Engineering*, 13(2):43-69, 1992.

Stephan, K., and Abdelsalam, M. (1980). Heat Transfer Correlations for Natural Convection Boiling, *Int. J. Heat Mass Transfer,* 23, 73–87.

Sturgis, J.C., Mudawar, I.. Critical heat flux in a long, rectangular channel subjected to one-sided heating-I. flow visualization**.** *International Journal of Heat and Mass Transfer* 42 (10), pp. 1835-1847, 1999a.

Sturgis, J.C., Mudawar, I.. Critical heat flux in a long, rectangular channel subjected to one-sided heating-II. Analysis of critical heat flux data**.** *International Journal of Heat and Mass Transfer* 42 (10), pp. 1849-1862, 1999b.

Sumith, B., F. Kaminaga, and K. Matsumura. Saturated flow boiling of water in a vertical small diameter tube. *Experimental Thermal Fluid Science,* 27:789–801, 2003.

Su, S., Huang, S., Wang, X.. Study of boiling incipience and heat transfer enhancement in forced flow through narrow channels**.** *International Journal of Multiphase Flow* 31 (2), pp. 253-260, 2005.

Sudo, Yukio, Miyata, Keiichi, Ikawa, Hiromasa, Kaminaga, Masanori, Ohkawara, Masami. Experimental Study of Differences In DNB Heat Flux Between Upflow And Downflow In Vertical Rectangular Channel**.** *Journal of Nuclear Science and Technology* 22 (8), pp. 604-618, 1985.

Sun, L. & Mishima, K., Evaluation analysis of prediction methods for two-phase flow pressure drop in mini-channels. International Journal of Multiphase Flow, 35 (1), pp. 47-54, 2009.

Sung, M.K., and Mudawar, I. Single phase and two phase hybrid cooling schemes for high heat flux thermal management of defense electronics. J. of Electronic Packaging, Transactions of the ASME 131 (2):0210131 – 02101310, 2009.

Taitel, Y. and A. E. Dukler. A model for predicting flow regime transitions in horizontal and near-horizontal flow. *AIChE Journal*, 22:47-55, 1976.

Taitel, Y. Barnea, D. and A. E. Dukler. Modelling flow pattern transitions for steady upward gas-liquid flow in vertical tubes. *AIChE Journal,* 26:345-354, 1980.

Taitel, Y. (1990) Flow pattern transition in two phase flow, Keynote lecture, 9th International Heat Transfer Conference, Jerusalem, Israel, 19-24 Aug., pp. 237-254.

Tang, G.H., Zhuo, L., He, Y.L. and Tao, W.Q. Experimental study of compressibility, roughness and rarefaction influences on microchannel flow. *Int. J. of Heat and Mass Transfer, 50: 2282 – 2295, 2007.*

Suo, M. and T. Griffith. Two-phase flow in capillary tubes. *Journal Basic Engineering,* 86:576-582, 1964.

Thome J. R. Boiling in microchannels: a review of experiment and theory. *International Journal of Heat and Fluid Flow*, 25, Issue 2:128-139, 2004.

Thome, J. R., Dupont, V. and A.M. Jacobi. Heat transfer model for evaporation in microchannels, Part I: presentation of the model. *International Journal Heat Mass Transfer*, 47:3375-3385, 2004.

Tong, W., Bergles, A.E.and M.K. Jensen. Pressure drop with highly subcooled flow boiling in small-diameter tubes. *Experimental Thermal and Fluid Science*, 15:202–212, 1997.

Tran, T.N., M.W. Wambsganss, and D.M. France. Small circular- and rectangular-channel boiling with two refrigerants. *International Journal Multiphase Flow*, 22(3): 485-498, 1996.

Tran, T.N., M.W. Wambsganss, Chyu, M, -C, and D.M. France. A correlation for nucleate flow boiling in small channels. Compact Heat Exchangers for the Process Industries Conference, Snowbird, Utah, June 22 – 27, 1997.

Tran, T. N., Chyu, M. C., Wambsganss, M. W. and D. M. France. Two-phase pressure drop of refrigerants during flow boiling in small channels: an experimental investigation and correlation development. *International Journal Multiphase Flow*, 26:1739 -1754, 2000.

Triplett, A.K., S.M. Ghiaasiaan, S.I. Abdel-Khalik, and D.L. Sadowski. Gas-liquid two-phase flow in microchannels, Part I: Two-phase flow patterns. *International Journal of Multiphase Flow*, 25:377-394, 1999.

Truttasanawin, S., Groll, E.A., Garimella, S.V., and Cremaschi, Experimental investigation of a miniature-scale refrigeration system for electronics cooling. IEEE Transactions on Components and Packaging Technologies, Vol. 29, No.3, September 2006.

Tuckerman, D.B., and R.F.W. Pease. High performance heat sink for VLSI. *IEEE Electronic Device Letters*, 2:126-129, 1981.

Wallis. G.B., *One Dimensional Two-phase Flow*. McGraw-Hill, New York, 1969.

Whalley, B.P.. *Boiling, condensation, and gas – liquid flow*. Oxford University press, 1987.

Wang H. and Wang Y. Influence of three-dimensional wall roughness on the laminar flow in microtube. Int. J. of Heat and Fluid flow, 28:220 – 228, 2007.

Wang, G., Cheng, P., Wu, H. Unstable and stable flow boiling in parallel microchannels and in a single microchannel**.** *International Journal of Heat and Mass Transfer* 50 (21-22), pp. 4297-4310, 2007.

Wang, G. and Bao, R. Two phase flow patterns of nitrogen and nanofluids in a vertically capillary tube. International Journal of Thermal Sciences, 48(11); 2074-2079, 2009.

Wang, G., Cheng, P.. Subcooled flow boiling and microbubble emission boiling phenomena in a partially heated microchannel**.** *International Journal of Heat and Mass Transfer* 52 (1-2), pp. 79-91, 2009.

Wambsganss, M. W., D.M. France, J.A. Jendraejczyk, and T.N. Tran. Boiling heat transfer in a horizontal small-diameter tube. *Journal of Heat Transfer*, 115:963-972, 1993.

Woldesemayat, M.A., Ghajar, A.J. Comparison of void fraction correlations for different flow patterns in horizontal and upward inclined pipes. *International Journal of Multiphase Flow* 33 (4), pp. 347-370, 2007.

Warrier, G. R., Dhir, V.K. and L. A. Momoda. Heat transfer and pressure drop in narrow rectangular channels. *Experimental Thermal and Fluid Science*, 26:53-64, 2002.

Watel, B., Review of saturated flow boiling in small passages of compact heat exchangers. *International Journal of Thermal Sciences*, 42, pp. 107 – 140, 2003.

Webb, R. L. Next generation devices for electronic cooling with heat rejection to air. Journal of Heat Transfer, 127 (1): 2 – 10, 2005.

Weinmueller, C., Hotz, N., Mueller, A. and Poulikakos, D. On two phase flow patterns and transition criteria in aqueous methanol and CO2 mixtures in adiabatic, rectangular microchannels. International Journal of Multiphase Flow, 35: 760-772, 2009.

Wei, X., Joshi, Y., and Patterson, M.K. Experimental and numerical study of a stacked microchannel heat sink for liquid cooling of microelectronic devices. Journal of Heat Transfer, vol. 129, 1432 – 1444, 2007.

Wei J. Challenges in cooling Design of CPU packages for high-performance servers. Heat Transfer Engineering, 29(2):178 – 187, 2008

Wen, D.S., Y. Yan and D.B.R. Kenning. Saturated flow boiling of water in a narrow channel: time-averaged heat transfer coefficients and correlations, *Applied Thermal Engineering*, 24:1207-1223, 2004.

Wojtan, L., Revellin, R. and J. R. Thome. Investigation of saturated critical heat flux in a single, uniformly heated microchannel. *Experimental Thermal Fluid Science*, 30(8):765-774, 2006.

Xie, X.L., Liu, Z.J. He, Y.L., and Tao, W.Q. Numirical study of laminar heat transfer and pressure drop characteristics in a water-cooled minichannel heat sink. Applied Thermal Engineering 29:64 – 74, 2009.

Xiong, R. and J. N. Chung. An experimental study of the size effect on adiabatic gas-liquid two-phase flow patterns and void fraction in microchannels. *Physics of Fluids*, 19:033301-1, 2007.

Xu, J.L., Cheng, P., and Zhao, T.S. Gas-liquid two phase flow regimes in rectangular channels with mini/micro gaps. Int. J. of Multiphase flow, 25(3):411 – 432, 1999.

Yan, Y.Y. and T.F. Lin. Evaporation heat transfer and pressure drop of refrigerant R-134a in a small pipe. *International Journal Heat Mass Transfer*, 41: 4183-4194, 1998.

Yan, Y. and D.B.R. Kenning. Pressure and temperature fluctuations during boiling in narrow channel. In *Eurotherm, Heat Transfer in Condensation and Evaporation*, Grenoble, 62:107-1223, 1998.

Yang, C-Y., Wu, J-C., Chien, H-T., and Lu, S-R. Friction characteristics of water, R134a and air in small tubes. Microscale Thermophysical Engineering, 7: 335 – 348, 2003.

Yang B., Wang, P. and Bar-Cohen A. Mini-contact enhanced thermoelectric cooling of hot spots in high power devices. IEEE Transactions on Components and Packaging Technologies, Vol., 30, No.3:432 – 438, 2007.

Yang, C.Y., and C.C. Shieh. Flow pattern of air-water and two-phase R-134a in small circular tubes. *International Journal of Multiphase Flow*, 27:1163-1177, 2001.

Yeom, S., Lee, S.S. and Lee, S.Y. Two phase flow characteristics in a co-flow induced microchannel with microbubble generation. Proceedings of the 5th International Conference on Nanochannels, Microchannels and Minichannels ICNMM2007, June 18-20, 2007, Puebla, Mexico.

Yen, T-H., Kasagi, N. and Y. Suzuki. Forced convective boiling heat transfer in microtubes at low mass and heat fluxes. *International Journal of Multiphase Flow*, 29:1771-1792, 2003.

Yun, R., Kim, Y. Two-phase pressure drop of CO_2 in mini tubes and microchannels**.** *Microscale Thermophysical Engineering* 8 (3), pp. 259-270, 2004.

Yu, W., France, D. M , Wambsganss, M.W. and J.R. Hull. Two-phase pressure drop, boiling heat transfer, and critical heat flux to water in a small-diameter horizontal tube. *International Journal of Multiphase Flow*, 28:927 – 941, 2002.

Yun, R., Kim, Y. and M. S. Kim. Flow boiling heat transfer of carbon dioxide in horizontal mini tubes. *International Journal Heat and Fluid Flow,* 26:801-809, 2005.

Yun, R., Hyeok Heo, J., Kim, Y.. Evaporative heat transfer and pressure drop of R410A in microchannels**.** *International Journal of Refrigeration* 29 (1), pp. 92-100, 2006.

Zhang, H.Y., Pinjala, D., Wong, T.N., and Joshi, Y.K. Development of liquid cooling techniques for flip chip ball grid array packages with high heat flux dissipations. IEEE Transactions on Components and Packaging Technologies, vol. 28, no. 1, March, 2005.

Zhang M. and R.L. Webb. Correlation of two-phase friction for refrigerants in small-diameter tubes. *Experimental Thermal Fluid Science*, 25:131–139, 2001.

Zhang, W., Hibiki, T. and K. Mishima. Correlation for flow boiling heat transfer in mini-channels. *International Journal Heat Mass Transfer*, 47:5749-5763, 2004.

Zhang, W., Hibiki, T., Mishima, K. and Y. Mi. Correlation of critical heat flux for flow boiling of water in minichannels. *International Journal Heat Mass Transfer*, 49(5-6):1058-1072, 2006.

Zhang, W., Hibiki, T., and Mishima, K. Correlations of two-phase pressure drop and void fraction in min-channel. *International Journal Heat Mass Transfer*, 53: 453-465,2010.

Zhao, T.S., and Q.C. Bi. Co-current air-water two-phase flow patterns in vertical triangular microchannels. *International Journal of Multiphase Flow*, 27:765-782, 2001.

Zhirnov, V.V., Cavin lll, R.K., Hutchby, J.A., and Bourianoff, G.l. Limits to binary logic switch scaling-A gedanken model. Proceedings of the IEEE 91 (11): 1934 – 1939.

Zhou P., Hom J., Upadhya G., Goodson K. and Munch M., Electro-kinetic microchannel cooling system for desktop computers. 20th IEEE SEMI-THERM Symposium, 2004.

Zimbeck, W., Slavik, G., Cennamo, J., Kang, S., Yun, J., and Kroliczek, E. Loop heat pipe technology for cooling computer servers. 2008 11th IEEE Intersociety Conference on Thermal and Thermomechanical Phenomena in Electronic Systems, I-THERM , art. no. 4544248, pp. 19-25.

Zivi, S.M., 1964. Estimation of steady state steam void fraction by means of the principle of minimum entropy production. Trans. ASME, J. Heat Transfer 86, 247–252.

Zou, Z.J., North, M.T., and Wert, K.L. High heat flux heat pipe mechanism for cooling of electronics. 2000 Inter Society Conference on Thermal Phenomena, IEEE 2000.

Zuber N. and J. Findlay. Average volumetric concentration in two-phase systems. *Journal of Heat Transfer, ASME,* 86:453-468, 1965.

Appendix A

Two phase pressure drop correlations

A.1 Macroscale pressure drop correlations

Reference	Correlation	Conditions
Homogenous flow model	$\Delta P_f = \frac{2 f_{Lo} L_{tp} G^2}{D \rho_L}\left[1+\frac{x_e}{2}\left(\frac{\rho_L}{\rho_{Lv}}\right)\right]$ $\Delta P_{acc} = \frac{G^2}{\rho_L}\left(\frac{\rho_L}{\rho_{Lv}}\right)$ $\Delta P_g = \rho_{Lv} g \frac{L_{tp}}{x_e}\ln\left[1+x_e\frac{\rho_L}{\rho_{Lv}}\right]$	
Lockhart-Martinelli (1949)	$\Delta P_f = \frac{L_{tp}}{x_e}\int_0^{x_e}\frac{2 f_L G^2}{D\rho_L}\phi_L^2\, dx$ $\phi_L^2 = 1+\frac{C}{\mathrm{X}}+\frac{1}{\mathrm{X}^2}$ $\mathrm{X} = \left(\frac{f_L}{f_g}\right)^{0.5}\left(\frac{\rho_g}{\rho_L}\right)^{0.5}\left(\frac{1-x}{x}\right)$ C = 5 for laminar liquid – laminar gas C = 12 for laminar liquid – turbulent gas C = 10 for turbulent liquid – laminar gas C = 20 for turbulent liquid – turbulent gas	Water, benzene, kerosene, oil D = 1.49 – 25.83 mm.

	$\Delta P_g = g\frac{L_{tp}}{x_e}\int_0^{x_e}\left[\alpha\rho_g + (1-\alpha)\rho_L\right]dx$ $\Delta P_{acc} = \frac{G^2}{\rho_L}\left[\frac{x_e^2}{\alpha_e}\frac{\rho_L}{\rho_g} + \frac{(1-x_e)^2}{(1-\alpha_e)} - 1\right]$ $\alpha = \frac{1}{1+0.28\mathrm{X}_M}, \quad \mathrm{X}_M = \left(\frac{1-x}{x}\right)^{0.64}\left(\frac{\rho_g}{\rho_L}\right)^{0.36}\left(\frac{\mu_L}{\mu_g}\right)^{0.07}$	
Chisholm et al. (1973), B-coefficient method	$\Delta P_f = \frac{2 f_{Lo} G^2}{D\rho_L}\frac{L_{tp}}{x_e}\int_0^{x_e}\phi_{Lo}^2\, dx$ $\phi_{lo}^2(x) = 1 + \left(\Gamma^2 - 1\right)\left[Bx^{0.875}(1-x)^{0.875} + x^{1.75}\right]$ $\Gamma^2 = \left[\frac{(dP/dz)_{go}}{(dP/dz)_{lo}}\right]_f$ $B = \begin{cases} 4.8; \ for\ G \le 500\ \&\ \Gamma \le 9.5 \\ 15000/\left(\Gamma^2 G^{0.5}\right); \ for\ \ \Gamma \ge 9.5 \\ 21/\Gamma; \ for\ G > 600\ \&\ 9.5 < \Gamma < 28 \\ 520/\left(\Gamma G^{0.5}\right); \ for\ G \le 600\ \&\ 9.5 < \Gamma < 28 \\ 2400/G; \ for\ 500 < G < 1900\ \&\ \Gamma \le 9.5 \\ 55/G^{0.5}; \ for\ G \ge 1900, \&\ \Gamma \le 9.5 \end{cases}$ $\Delta P_g = g\frac{L_{tp}}{x_e}\int_0^{x_e}\left[\alpha\rho_g + (1-\alpha)\rho_L\right]dx$ $\Delta P_{acc} = \frac{G^2}{\rho_L}\left[\frac{x_e^2}{\alpha_e}\frac{\rho_L}{\rho_g} + \frac{(1-x_e)^2}{(1-\alpha_e)} - 1\right]$ $\alpha = \left[1 + \left(\frac{1-x}{x}\right)\left(\frac{\rho_g}{\rho_L}\right)\sqrt{1 - x\left(1 - \frac{\rho_L}{\rho_g}\right)}\right]$	G = 500 – 1900 kg/m^{2}s

Friedel (1979)	$\Delta P_f = \frac{2 f_{Lo} G^2}{D \rho_L} \frac{L_{tp}}{x_e} \int_0^{x_e} \phi_{Lo}^2 \, dx$ $\phi_{Lo}^2 = A1 + \frac{3.24 A2 A3}{Fr^{0.045} We^{0.035}}$ $A1 = (1-x)^2 + x^2 \left(\frac{\rho_L f_{go}}{\rho_g f_{Lo}} \right)$ $A2 = x^{0.78} (1-x)^{0.224}$ $\left(\frac{\rho_L}{\rho_g} \right)^{0.91} \left(\frac{\mu_g}{\mu_L} \right)^{0.19} \left(1 - \frac{\mu_g}{\mu_L} \right)^{0.7}$ $Fr = \frac{G^2}{g D \rho_H^2}, \qquad We = \frac{G^2 D}{\rho_H \sigma}$ $\Delta P_g = g \frac{L_{tp}}{x_e} \int_0^{x_e} [\alpha \rho_g + (1-\alpha) \rho_L] dx$ $\Delta P_{acc} = \frac{G^2}{\rho_L} \left[\frac{x_e^2}{\alpha_e} \frac{\rho_L}{\rho_g} + \frac{(1-x_e)^2}{(1-\alpha_e)} - 1 \right]$ $\alpha = \frac{1}{1 + 0.28 \mathrm{X}_M}, \quad \mathrm{X}_M = \left(\frac{1-x}{x} \right)^{0.64} \left(\frac{\rho_g}{\rho_L} \right)^{0.36} \left(\frac{\mu_L}{\mu_g} \right)^{0.07}$	D ≥ 4 mm
Muller- Steinhagen and Heck, (1986)	$\Delta P_f = \frac{L_{tp}}{x_e} \int_0^{x_e} \left(\frac{dP}{dz} \right)_{f,M} dx$ $\left(\frac{dP}{dz} \right)_{f,M} = F (1-x)^{1/3} + B x^3$ $F = A + 2(B - A) x$ $A = \left(\frac{dP}{dz} \right)_{Lo} = f_{lo} \frac{2 G^2}{D \rho_L}$	D = 4 – 392 mm

	$B = \left(\frac{dP}{dz}\right)_{go} = f_{go}\frac{2G^2}{D\rho_g}$ $\Delta P_g = g\frac{L_{tp}}{x_e}\int_0^{x_e}[\alpha\rho_g + (1-\alpha)\rho_L]dx$ $\Delta P_{acc} = \frac{G^2}{\rho_L}\left[\frac{x_e^2}{\alpha_e}\frac{\rho_L}{\rho_g} + \frac{(1-x_e)^2}{(1-\alpha_e)} - 1\right]$ $\alpha = \frac{1}{1+0.28\mathrm{X}_M}, \quad \mathrm{X}_M = \left(\frac{1-x}{x}\right)^{0.64}\left(\frac{\rho_g}{\rho_L}\right)^{0.36}\left(\frac{\mu_L}{\mu_g}\right)^{0.07}$	

A.2 Microscale pressure drop correlations

Reference	Correlation	Conditions
Mishima and Hibiki (1996)	$\Delta P_f = \frac{L_{tp}}{x_e}\int_0^{x_e}\frac{2f_L G^2}{D\rho_L}\phi_L^2\, dx$ $\phi_L^2 = 1 + \frac{C}{\mathrm{X}} + \frac{1}{\mathrm{X}^2}$	D = 1.05 – 4 mm U_{gs} = 0.071- 49.4 m/s U_{ls} = 0.071-2.33

	$\mathrm{X} = \left(\frac{f_L}{f_g}\right)^{0.5}\left(\frac{\rho_g}{\rho_L}\right)^{0.5}\left(\frac{1-x}{x}\right)$ $C = 21\left(1-e^{0.319D}\right)$ $\Delta P_g = g\frac{L_{tp}}{x_e}\int_0^{x_e}\left[\alpha\rho_g + (1-\alpha)\rho_L\right]dx$ $\Delta P_{acc} = \frac{G^2}{\rho_L}\left[\frac{x_e^2}{\alpha_e}\frac{\rho_L}{\rho_g} + \frac{(1-x_e)^2}{(1-\alpha_e)} - 1\right]$ $\alpha = \frac{1}{1+0.28\mathrm{X}_M}, \quad \mathrm{X}_M = \left(\frac{1-x}{x}\right)^{0.64}\left(\frac{\rho_g}{\rho_L}\right)^{0.36}\left(\frac{\mu_L}{\mu_g}\right)^{0.07}$	m/s
Tran et al. (2000)	$\Delta P_f = \frac{2f_{Lo}G^2}{D\rho_L}\frac{L_{tp}}{x_e}\int_0^{x_e}\phi_{Lo}^2\,dx$ $\phi_{lo}^2 = 1 + \left(4.3\Gamma^2 - 1\right)\left[Co\,x^{0.875}\,(1-x)^{0.875} + x^{1.75}\right]$ $\Gamma^2 = \left[\frac{(dP/dz)_{go}}{(dP/dz)_{lo}}\right]_f;\ Co = \frac{\left[\sigma / g\left(\rho_l - \rho_g\right)\right]^{0.5}}{D}$ $\Delta P_g = g\frac{L_{tp}}{x_e}\int_0^{x_e}\left[\alpha\rho_g + (1-\alpha)\rho_L\right]dx$ $\Delta P_{acc} = \frac{G^2}{\rho_L}\left[\frac{x_e^2}{\alpha_e}\frac{\rho_L}{\rho_g} + \frac{(1-x_e)^2}{(1-\alpha_e)} - 1\right]$ $\alpha = \left[1 + \left(\frac{1-x}{x}\right)\left(\frac{\rho_g}{\rho_L}\right)\sqrt{1 - x\left(1 - \frac{\rho_L}{\rho_g}\right)}\right]$	D = 2.46, 2.92 mm D_h = 2.40 mm G = 33 – 832 kg/m^{2}s q = 2.2– 91 kW/m^2 P_R = 0.04 – 0.23 R134a, R12, R113
Lee and Lee (2001)	$\Delta P_f = \frac{L_{tp}}{x_e}\int_0^{x_e}\frac{2f_L G^2}{D\rho_L}\phi_L^2\,dx$ $\phi_L^2 = 1 + \frac{C}{\mathrm{X}} + \frac{1}{\mathrm{X}^2}$	Air-water D = 0.78, 6.67 mm

	$\mathrm{X} = \left(\frac{f_L}{f_g}\right)^{0.5} \left(\frac{\rho_g}{\rho_L}\right)^{0.5} \left(\frac{1-x}{x}\right)$ for laminar liquid – laminar gas $C = 6.833\times10^{-8}\,\lambda^{-1.317}\psi^{0.719}\,\mathrm{Re}_{Lo}^{0.557}$ for laminar liquid – turbulent gas $C = 0.06185\,\mathrm{Re}_{Lo}^{0.726}$ for turbulent liquid – laminar gas $C = 3.627\,\mathrm{Re}_{Lo}^{0.174}$ for turbulent liquid – turbulent gas $C = 0.408\,\mathrm{Re}_{Lo}^{0.451}$ $\psi = \frac{\mu_L U_L}{\sigma}, \quad \lambda = \frac{\mu_L^2}{\rho_L \sigma D}$ $\Delta P_g = g\frac{L_{tp}}{x_e}\int_0^{x_e}\left[\alpha\rho_g + (1-\alpha)\rho_L\right]dx$ $\Delta P_{acc} = \frac{G^2}{\rho_L}\left[\frac{x_e^2}{\alpha_e}\frac{\rho_L}{\rho_g} + \frac{(1-x_e)^2}{(1-\alpha_e)} - 1\right]$ $\alpha = \left[1 + \left(\frac{1-x}{x}\right)\left(\frac{\rho_g}{\rho_L}\right)^{0.67}\right]^{-1}$	
Yu et al. (2002)	$\Delta P_f = \frac{L_{tp}}{x_e}\int_0^{x_e}\frac{2f_L G^2}{D\rho_L}\phi_L^2\,dx$	Water D = 2.98 mm G = 50 – 200 kg/m^2 s P = 1.98 bar

	$\phi_L^2 = \frac{1}{\mathrm{X}^{1.9}}$ for laminar liquid – turbulent gas $\mathrm{X} = \left(\frac{f_L}{f_g}\right)^{0.5}\left(\frac{\rho_g}{\rho_L}\right)^{0.5}\left(\frac{1-x}{x}\right)$ $\Delta P_g = g\frac{L_{tp}}{x_e}\int_0^{x_e}\left[\alpha\rho_g + (1-\alpha)\rho_L\right]dx$ $\Delta P_{acc} = \frac{G^2}{\rho_L}\left[\frac{x_e^2}{\alpha_e}\frac{\rho_L}{\rho_g} + \frac{(1-x_e)^2}{(1-\alpha_e)} - 1\right]$ $\alpha = \left[1 + \left(\frac{1-x}{x}\right)\left(\frac{\rho_g}{\rho_L}\right)^{0.67}\right]^{-1}$	
Warrier et al. (2002)	$\Delta P_f = \frac{2 f_{Lo} G^2}{D\rho_L}\frac{L_{tp}}{x_e}\int_0^{x_e}\phi_{Lo}^2\, dx$ $\phi_L^2 = 1 + \frac{C}{\mathrm{X}} + \frac{1}{\mathrm{X}^2}$ $\mathrm{X} = \left(\frac{f_L}{f_g}\right)^{0.5}\left(\frac{\rho_g}{\rho_L}\right)^{0.5}\left(\frac{1-x}{x}\right)$ C = 38 for all flow regimes $\phi_{Lo}^2 = \phi_L^2\left(\frac{f_L}{f_{Lo}}\right)(1-x)^2$ $\Delta P_g = g\frac{L_{tp}}{x_e}\int_0^{x_e}\left[\alpha\rho_g + (1-\alpha)\rho_L\right]dx$ $\Delta P_{acc} = \frac{G^2}{\rho_L}\left[\frac{x_e^2}{\alpha_e}\frac{\rho_L}{\rho_g} + \frac{(1-x_e)^2}{(1-\alpha_e)} - 1\right]$	FC84, D_h = 0.75 mm

	$\alpha = \frac{1}{1+0.28\mathrm{X}_M}, \quad \mathrm{X}_M = \left(\frac{1-x}{x}\right)^{0.64}\left(\frac{\rho_g}{\rho_L}\right)^{0.36}\left(\frac{\mu_L}{\mu_g}\right)^{0.07}$	
Qu and Mudawar (2003)	$\Delta P_f = \frac{L_{tp}}{x_e}\int_0^{x_e}\frac{2f_L G^2}{D\rho_L}\phi_L^2\, dx$ $\phi_L^2 = 1+\frac{C}{\mathrm{X}}+\frac{1}{\mathrm{X}^2}$ $\mathrm{X} = \left(\frac{f_L}{f_g}\right)^{0.5}\left(\frac{\rho_g}{\rho_L}\right)^{0.5}\left(\frac{1-x}{x}\right)$ for laminar liquid – laminar gas $C = 21\left(1-e^{-3190 d_h}\right)(0.00418G+0.0613)$ $\Delta P_g = g\frac{L_{tp}}{x_e}\int_0^{x_e}[\alpha\rho_g+(1-\alpha)\rho_L]dx$ $\Delta P_{acc} = \frac{G^2}{\rho_L}\left[\frac{x_e^2}{\alpha_e}\frac{\rho_L}{\rho_g}+\frac{(1-x_e)^2}{(1-\alpha_e)}-1\right]$ $\alpha = \left[1+\left(\frac{1-x}{x}\right)\left(\frac{\rho_g}{\rho_L}\right)^{0.67}\right]^{-1}$	D = 0.35 mm Water
Lee and Mudawar (2005)	$\Delta P_f = \frac{L_{tp}}{x_e}\int_0^{x_e}\frac{2f_L G^2}{D\rho_L}\phi_L^2\, dx$ $\phi_L^2 = 1+\frac{C}{\mathrm{X}}+\frac{1}{\mathrm{X}^2}$ $\mathrm{X} = \left(\frac{f_L}{f_g}\right)^{0.5}\left(\frac{\rho_g}{\rho_L}\right)^{0.5}\left(\frac{1-x}{x}\right)$	D = 0.35 mm R134a G = 127 – 654 P = 1.44 – 6.6 bar x_{in} = 0.001 – 0.25 x_{out} = up to 0.49

	for laminar liquid – laminar gas $C = 2.16\,\mathrm{Re}_{Lo}^{0.047}\,We_{Lo}^{0.6}$ For laminar liquid – turbulent gas $C = 1.45\,\mathrm{Re}_{Lo}^{0.25}\,We_{Lo}^{0.23}$ $\Delta P_g = g\frac{L_{tp}}{x_e}\int_0^{x_e}\left[\alpha\rho_g + (1-\alpha)\rho_L\right]dx$ $\Delta P_{acc} = \frac{G^2}{\rho_L}\left[\frac{x_e^2}{\alpha_e}\frac{\rho_L}{\rho_g} + \frac{(1-x_e)^2}{(1-\alpha_e)} - 1\right]$ $\alpha = \left[1 + \left(\frac{1-x}{x}\right)\left(\frac{\rho_g}{\rho_L}\right)^{0.67}\right]^{-1}$	
Lee and Garimella (2007)	$\Delta P_f = \frac{L_{tp}}{x_e}\int_0^{x_e}\frac{2f_L G^2}{D\rho_L}\phi_L^2\,dx$ $\phi_L^2 = 1 + \frac{C}{\mathrm{X}} + \frac{1}{\mathrm{X}^2}$ $\mathrm{X} = \left(\frac{f_L}{f_g}\right)^{0.5}\left(\frac{\rho_g}{\rho_L}\right)^{0.5}\left(\frac{1-x}{x}\right)$ for laminar liquid – laminar gas $C = 2566G^{0.5466}D_h^{0.8819}(1-e^{-319D_h})$ $\Delta P_g = g\frac{L_{tp}}{x_e}\int_0^{x_e}\left[\alpha\rho_g + (1-\alpha)\rho_L\right]dx$ $\Delta P_{acc} = \frac{G^2}{\rho_L}\left[\frac{x_e^2}{\alpha_e}\frac{\rho_L}{\rho_g} + \frac{(1-x_e)^2}{(1-\alpha_e)} - 1\right]$	Water D = 0.162 – 0.571 mm

	$\alpha = \left[1 + \left(\frac{1-x}{x}\right)\left(\frac{\rho_g}{\rho_L}\right)^{0.67}\right]^{-1}$	
Zhang et al. (2010)	$\Delta P_f = \frac{L_{tp}}{x_e}\int_0^{x_e} \frac{2 f_L G^2}{D\rho_L}\phi_L^2 \, dx$ $\phi_L^2 = 1 + \frac{C}{\mathrm{X}} + \frac{1}{\mathrm{X}^2}$ $\mathrm{X} = \left(\frac{f_L}{f_g}\right)^{0.5}\left(\frac{\rho_g}{\rho_L}\right)^{0.5}\left(\frac{1-x}{x}\right)$ $C = 21\left(1 - \exp\left(-\frac{0.358}{La}\right)\right)$ $La = [\sigma / g\Delta\rho]^{0.5} / D$ $\Delta P_g = g\frac{L_{tp}}{x_e}\int_0^{x_e}[\alpha\rho_g + (1-\alpha)\rho_L]dx$ $\Delta P_{acc} = \frac{G^2}{\rho_L}\left[\frac{x_e^2}{\alpha_e}\frac{\rho_L}{\rho_g} + \frac{(1-x_e)^2}{(1-\alpha_e)} - 1\right]$ $\alpha = \frac{1}{1+0.28\mathrm{X}_M}, \quad \mathrm{X}_M = \left(\frac{1-x}{x}\right)^{0.64}\left(\frac{\rho_g}{\rho_L}\right)^{0.36}\left(\frac{\mu_L}{\mu_g}\right)^{0.07}$	D = 0.07 – 6.25 mm. Adiabatic gas-liquid flow, adiabatic liquid-vapour flow and flow boiling
Li and Wu (2010)	$\Delta P_f = \frac{L_{tp}}{x_e}\int_0^{x_e} \frac{2 f_L G^2}{D\rho_L}\phi_L^2 \, dx$ $\phi_L^2 = 1 + \frac{C}{\mathrm{X}} + \frac{1}{\mathrm{X}^2}$ $\mathrm{X} = \left(\frac{f_L}{f_g}\right)^{0.5}\left(\frac{\rho_g}{\rho_L}\right)^{0.5}\left(\frac{1-x}{x}\right)$	769 data points D = 0.148 – 3.25 mm 12 different fluids

	$C=\begin{cases}11.9Bd^{0.45} & Bd\le 1.5\\ 109.4\left(Bd\,\mathrm{Re}^{0.5}\right)^{-0.56} & 1.5<Bd\le 11\end{cases}$ $Bd=g\Delta\rho D^2/\sigma$ $\Delta P_g=g\frac{L_{tp}}{x_e}\int_0^{x_e}\left[\alpha\rho_g+(1-\alpha)\rho_L\right]dx$ $\Delta P_{acc}=\frac{G^2}{\rho_L}\left[\frac{x_e^2}{\alpha_e}\frac{\rho_L}{\rho_g}+\frac{(1-x_e)^2}{(1-\alpha_e)}-1\right]$ $\alpha=\frac{1}{1+0.28\mathrm{X}_M},\quad \mathrm{X}_M=\left(\frac{1-x}{x}\right)^{0.64}\left(\frac{\rho_g}{\rho_L}\right)^{0.36}\left(\frac{\mu_L}{\mu_g}\right)^{0.07}$	
Lee et al. (2010)	$\Delta P_f=\frac{L_{tp}}{x_e}\int_0^{x_e}\frac{2f_LG^2}{D\rho_L}\phi_L^2\,dx$ $\phi_L^2=1+\frac{C}{\mathrm{X}}+\frac{1}{\mathrm{X}^2}$ $\mathrm{X}=\left(\frac{f_L}{f_g}\right)^{0.5}\left(\frac{\rho_g}{\rho_L}\right)^{0.5}\left(\frac{1-x}{x}\right)$ $C=121.6(1-e^{-22.7Bd})x_e^{1.85}$ $Bd=g\Delta\rho D^2/\sigma$ $\Delta P_g=g\frac{L_{tp}}{x_e}\int_0^{x_e}\left[\alpha\rho_g+(1-\alpha)\rho_L\right]dx$ $\Delta P_{acc}=\frac{G^2}{\rho_L}\left[\frac{x_e^2}{\alpha_e}\frac{\rho_L}{\rho_g}+\frac{(1-x_e)^2}{(1-\alpha_e)}-1\right]$	D < 3 mm Water, n-pentane, ammonia, CO_2, R410a, R134a, R12

	$\alpha = \frac{1}{1+0.28\mathrm{X}_M}, \quad \mathrm{X}_M = \left(\frac{1-x}{x}\right)^{0.64}\left(\frac{\rho_g}{\rho_L}\right)^{0.36}\left(\frac{\mu_L}{\mu_g}\right)^{0.07}$	

Appendix B

Boiling Heat Transfer correlations

B.1 Macroscale heat transfer correlations

Reference	Correlation	Applicability range
Chen (1966)	$h_{tp} = h_{mic} + h_{mac}$ $h_{tp} = Sh_{F-Z} + Fh_L$ $h_L = 0.023\,\mathrm{Re}_L^{0.8}\,\mathrm{Pr}_L^{0.4}\,\frac{k_L}{D}$ $\mathrm{Re}_L = \frac{(1-x)GD}{\mu_L}$ $h_{F-Z} = 0.00122\frac{k_L^{0.79} c_{pL}^{0.45} \rho_L^{0.49}}{\sigma^{0.5}\mu_L^{0.29} h_{fg}^{0.24} \rho_v^{0.24}}(\Delta T)^{0.24}(\Delta P)^{0.75}$ $E = \begin{cases} 1 & 1/\mathrm{X}_{tt} \le 0.1 \\ 2.35\left(0.213 + \frac{1}{\mathrm{X}_{tt}}\right)^{0.736} & 1/\mathrm{X}_{tt} > 0.1 \end{cases}$ $\mathrm{X}_{tt} = \left(\frac{1-x}{x}\right)^{0.9}\left(\frac{\rho_v}{\rho_L}\right)^{0.5}\left(\frac{\mu_L}{\mu_v}\right)^{0.1}$ $S = \frac{1}{1 + 0.00000253\mathrm{Re}_{tp}^{1.17}}$ $\mathrm{Re}_{tp} = \mathrm{Re}_L . E^{1.25}$	Water, methanol, cyclohexane, pentane, heptane, benzene representing 594 data points. Vertical upward and downward flow in tubes and annuli. Pressure range of 1 – 34.8 bar. Liquid inlet velocity range of 0.06 – 4.5 m/s. Vapour quality range of 0.01 – 0.71. Heat flux range of 6.2 – 2400 kW/m^2
Shah (1982)	$N_{Co} = \left(\frac{1-x}{x}\right)^{0.8}\left(\frac{\rho_g}{\rho_L}\right)^{0.5}, \qquad Bo = \frac{q}{Gh_{fg}}$ $h_L = 0.023\,\mathrm{Re}_L^{0.8}\,\mathrm{Pr}_L^{0.4}\,\frac{k_L}{D}$ $\frac{h_{cb}}{h_L} = \frac{1.8}{N_{Co}^{0.8}}$ For $N_{Co} > 1$:	Valid over reduced pressure range of 0.004 – 0.8. Based on 780 data points.

	$\frac{h_{nb}}{h_L} = \begin{cases} 230Bo^{0.5} & Bo > 0.0003 \\ 1 + 46Bo^{0.5} & Bo < 0.0003 \end{cases}$ For $0.1 < N_{Co} < 1$: $\frac{h_{nb}}{h_L} = FBo^{0.5} \exp(2.74N_{Co} - 0.1)$ $F = \begin{cases} 14.7 & Bo > 0.0011 \\ 15.43 & Bo < 0.0011 \end{cases}$ For $N_{Co} < 0.1$: $\frac{h_{nb}}{h_L} = FBo^{0.5} \exp(2.74N_{Co} - 0.15)$ $h_{tp} = MAX(h_{cb}, h_{nb})$	
Gungor and Winterton (1986)	$h_{tp} = Eh_L + Sh_{Coop}$ $h_L = 0.023 \mathrm{Re}_L^{0.8} \mathrm{Pr}_L^{0.4} \frac{k_L}{D}$ $h_{Coop} = 55P_r^{0.12-0.434\ln R_p}(-\log P_r)^{-0.55} M^{-0.5} q^{0.67}$ $E = 1 + 24000Bo^{1.16} + 1.37(1/\mathrm{X}_{tt})^{0.86}$ $S = \frac{1}{1 + 1.15\times10^{-6} E^2 \mathrm{Re}_L^{1.17}}$	Water, R11, R12, R22, R113, R114, ethylene glycol. Based on 4800 data points. D = 2.95 – 32 mm. P = 0.08 – 202.6 bar.
Kandlikar (1990)	$h_{tp,conv} = \left[1.136N_{Co}^{-0.9}(25Fr_{lo})^c + 667.2Bo^{0.7}F_{fl}\right]h_L$ $N_{Co} = \left(\frac{1-x}{x}\right)^{0.8}\left(\frac{\rho_v}{\rho_l}\right)^{0.5}$ $h_L = 0.023 \mathrm{Re}_L^{0.8} \mathrm{Pr}_L^{0.4} \frac{k_L}{D}$ $h_{tp,nb} = \left[0.6683N_{Co}^{-0.2}(25Fr_{lo})^c + 1058Bo^{0.7}F_{fl}\right]h_L$ c = 0 for vertical tubes $h_{tp} = MAX(h_{tp,conv}, h_{tp,nb})$	Water, R-11, R-12, R13-B1, R-22, R-113, R-114, R-152a, nitrogen and neon. Based on 5246 data points. D = 4.6 – 32 mm. G = 13 – 8179 kg/m^2 s x = 0.001 – 0.987 P = 0.4 – 64.2 bar N_{Co} = 0.004 – 52.1
Liu and Winterton (1991)	$h_{tp} = \sqrt{(Eh_{LO})^2 + (Sh_{Coop})^2}$ $h_{LO} = 0.023 \mathrm{Re}_{LO}^{0.8} \mathrm{Pr}_L^{0.4} \frac{k_L}{D}$, $\mathrm{Re}_{LO} = \frac{GD}{\mu_L}$	G: 12.4 – 8179.3 kg/m^2 s q: 348.9 - 2.62×10^6 W/m^2 x: 0 – 0.948

	$h_{Coop} = 55 P_r^{0.12-0.434\ln R_p} (-\log P_r)^{-0.55} M^{-0.5} q^{0.67}$ $E = \left[1 + x \Pr_L \left(\frac{\rho_L}{\rho_g} - 1\right)\right]^{0.35}$ $S = \frac{1}{1 + 0.055 F^{0.1} \mathrm{Re}_{LO}^{0.16}}$	D: 2.95 – 32 mm Re: 568.9 – 8.75 × 10^5 P_r: 0.0023 – 0.895 $\Pr_L$: 0.83 – 9.1
Stiener and Taborek (1992)	$h_{tp} = \left[\left(h_{nb,0} F_{nb}\right)^3 + \left(h_L F_{tp}\right)^3\right]^{1/3}$ $h_{nb,0} = 3500$ W/m^2 K for R-134a $F_{nb} = F_{pf} \left(\frac{q}{q_0}\right)^{nf} \left(\frac{D}{D_0}\right)^{-0.4} \left(\frac{R_p}{R_{p,0}}\right)^{0.133} f(M)$ $q_0 = 20000$ W/m^2 for R134a $D_0 = 0.01$m, $R_{P,0} = 1\mu$m R_P is surface roughness $F_{pf} = 2.816 P_r^{0.45} + \left(3.4 + \frac{1.7}{1 - P_r^7}\right) P_r^{3.7}$ $nf = 0.8 - 0.1 \exp(1.75 P_r)$ $f(M) = 0.377 + 0.199 \ln M + 0.000028427 M^2$ M = 102 for R134a $q_{ONB} = \frac{2\sigma T_{sat} h_L}{r_c \rho_g h_{fg}}$, $r_c = 0.3\ \mu m$ $h_L = Nu_{Geniel} \frac{k_L}{D}$ For $q > q_{ONB}$ and $x \le 0.6$: $F_{tp} = \left[(1-x)^{1.5} + 1.9 x^{0.6} \left(\frac{\rho_L}{\rho_g}\right)^{0.35}\right]^{1.1}$ For $q < q_{ONB}$ and all values of x: $F_{tp} = \left\{\left[(1-x)^{1.5} + 1.9 x^{0.6} (1-x)^{0.01} \left(\frac{\rho_L}{\rho_g}\right)^{0.35}\right]^{-2.2} + \left[\frac{h_g}{h_L} x^{0.01} \left(1 + 8(1-x)^{0.7}\right) \left(\frac{\rho_L}{\rho_g}\right)^{0.67}\right]^{-2}\right\}^{-0.5}$	Based on 10262 data points for water and 2345 data points for four refrigerants (R11, R12, R22, R113), seven hydrocarbons (benzene, n-pentane, n-heptane, cyclohexane, methanol, ethanol, n-butanol) and three cryogenics (nitrogen, hydrogen and helium).

B.2 Microscale heat transfer correlations

Reference	Correlation	Comments
Lazarek and Black (1982)	$h_{tp} = 30\,\mathrm{Re}_l^{0.857}\, Bo^{0.714}\left(\lambda_l / D_h\right)$	Based on 728 data points D = 3.1 mm G = 125 – 750 kg/m^{2}s q = 14 – 380 kW/m^2 P = 1.3 – 4.1 bar R113
Tran et al. (1996)	$\alpha_{tp} = 840000\left(Bo^2 We_l\right)^{0.3}\left(\frac{\rho_l}{\rho_g}\right)^{-0.4}$ $We_l = \frac{G^2 D_h}{\rho_l \sigma}$	D = 2.4, 2.92 mm, G = 44 – 832 kg/m^{2}s q = 7.5 – 129 kW/m^2 P_R = 0.045 – 0.2 R12, R113
Kew and Cornwell (1997)	$h_{tp} = 30\,\mathrm{Re}^{0.857}\, Bo^{0.714}\,\frac{k_f}{D}\left(1-x\right)^{-0.143}$	R141b, D = 1.39 – 3.69 mm
Warrier et al. (2002)	$h_{tp} = \left[1 + 6Bo^{1/16} - 5.3x^{0.65}\left(1 - 855Bo\right)\right]\frac{4.36k_L}{D}$	$0.00027 \le Bo \le 0.00089$ $0.03 \le x \le 0.55$ FC84, D_h = 0.75 mm
Kandlikar and Balasubramanian (2004)	$\alpha_{tp} = max\left(E_{CBD}, S_{NBD}\right)\left(1-x\right)^{0.8}\alpha_{lo}$ $S_{NBD} = \left(0.6683\,Co^{-0.2} + 1058\,Bo^{0.7} F_{Fl}\right)$ $E_{CBD} = 1.136\,Co^{-0.9} + 667.2Bo^{0.7} F_{Fl}$ $\alpha_{lo} = \frac{Re_l\, Pr_l (f/2)(\lambda_l / d)}{1 + 12.7(Pr_l^{2/3} - 1)(f_f / 2)^{0.5}}$ $for\ 10^4 \le Re_l \le 5\times 10^6$ $\alpha_{lo} = \frac{(Re_l - 1000)\, Pr_l (f_f / 2)(\lambda_l / d)}{1 + 12.7(Pr_l^{2/3} - 1)(f_f / 2)^{0.5}}$ $for\ 3000 \le Re_l \le 10000,$	Range of data for the original Kandlikar (1990) correlation D = 0.19 – 32.0 mm G = 13 – 8179 kg/m^{2}s q = 0.3 – 2280 kW/m^2

	$Co = \left(\frac{1-x}{x}\right)^{0.8}\left(\frac{\rho_g}{\rho_l}\right)^{0.5}$ For $1600 < Re < 3000$ (transition region), α_{Lo} interpolation at Re = 1600 and 3000 For Re < 1600 (laminar) α_{lo} is calculated from Nu = constant For $Re \le 100$, $\alpha_{tp} = S_{NBD}(1-x)^{0.8}\alpha_{lo}$	P = 0.4 – 64 bar water, refrigerants
Zhang et al. (2004)	$\alpha_{tp} = S\alpha_{nb} + E\alpha_{sp}$ $\alpha_{nb} = 0.00122\left(\frac{\lambda_l^{0.79} Cp_l^{0.45} \rho_l^{0.49}}{\sigma^{0.5} \mu_l^{0.29} h_{lg}^{0.24} \rho_g^{0.24}}\right)\Delta T_{sat}^{0.24} \Delta P_{sat}^{0.75}$ $S = \left(1 + 2.53\times10^{-6}\ Re_l^{1.17}\right)^{-1}$ $E = MAX(E', 1)\ E' = 0.64\phi_l$ $\phi_l^2 = 1 + \frac{C}{X} + \frac{1}{X^2}$ $for\ Re_l < 1000\ and\ Re_g < 1000, X = X_{vv}, C = 5$ $for\ Re_l > 2000\ and\ Re_g < 1000, X = X_{tv}, C = 1$ $for\ Re_l < 1000\ and\ Re_g > 2000, X = X_{vt}, C = 1$ $for\ Re_l > 2000\ and\ Re_g > 2000, X = X_{tt}, C = 2$ For other regions of Re_k (k = l or g) interpolate the above values of C $X = \left[\left(\frac{dP}{dz}\right)_l \Big/ \left(\frac{dP}{dz}\right)_g\right]^{0.5} = \left(\frac{f_f}{f_g}\right)^{0.5}\left(\frac{1-x}{x}\right)\left(\frac{\rho_g}{\rho_l}\right)$ $f_k = \begin{cases} 16/Re_k, for\ tubes, Re_k < 1000 \\ 0.046\ Re_k^{-0.2}, for\ Re_k > 2000 \end{cases}$ $\alpha_{sp} = (\lambda_l / D) Nu_{sp}$ $Nu_{sp} = \begin{cases} max(4.36, Nu_{Collier}), for\ Re \le 2000, \\ 0.023\ Re_l^{0.8}\ Pr_l^{0.4}, for\ Re \ge 2300 \end{cases}$	D = 0.78 – 6.0 mm G = 23.4 – 2939 kg/m^{2}s q = 2.95 – 2511 kW/m^2 P = 1.01 – 8.66 bar Water, refrigerants

	$Nu_{Collier} = 0.17\,Re_l^{0.33}\,Pr_l^{0.43}\left(\frac{Pr_l}{Pr_w}\right)^{0.25} \times \left[\frac{g\beta\rho_l^2 D_h^3 (T_w - T_l)}{\mu_l^2}\right]^{0.1}$	
Lee and Mudawar (2005)	For $0 < x \le 0.05$ $h_{tp} = 3.856 \mathrm{X}^{0.267} h_L$ For $0.05 < x \le 0.55$ $h_{tp} = 436.48 Bo^{0.522} We^{0.351} \mathrm{X}^{0.665} h_L$ For $0.55 < x \le 1$ $h_{tp} = MAX\left(108.6 \mathrm{X}^{1.665} h_g, h_g\right)$ h_g is single phase gas heat transfer coefficient	Water, R134a D_h = 0.35 mm
Saitoh et al. (2007)	$\alpha_{tp} = S\alpha_{nb} + E\alpha_{sp}$ $\alpha_{nb} = 207 \frac{\lambda_l}{D_b}\left(\frac{qD_b}{\lambda_l T_l}\right)^{0.745}\left(\frac{\rho_g}{\rho_l}\right)^{0.581} Pr_l^{0.533}$ $D_b = 0.512\left[\sigma / g(\rho_l - \rho_g)\right]^{0.5}$ $S = \left(1 + 0.4\, Re_l \times 10^{-4}\right)^{1.4}$ $E = 1 + \left[\left(\frac{1}{X}\right)^{1.05} \Big/ 1 + We_g^{-0.4}\right]$ $\alpha_{sp} = \begin{cases} 0.023\frac{\lambda_l}{D}\left(\frac{G_l D}{\mu_l}\right)^{0.8}\left(\frac{Cp_l \mu_l}{\lambda_l}\right)^{1/3}, Re > 100 \\ \frac{4.36\lambda_l}{D}, Re < 1000 \end{cases}$ $X = \left(\frac{1-x}{x}\right)^{0.9}\left(\frac{\rho_g}{\rho_l}\right)^{0.5}\left(\frac{\mu_l}{\mu_g}\right)^{0.1}$, $for\ Re_l > 1000\ \&\ Re_g > 1000$ $X = \left(\frac{f_l}{f_g}\right)^{0.5}\left(Re_g^{-0.4}\right)\left(\frac{G_l}{G_g}\right)^{0.5}\left(\frac{\rho_g}{\rho_l}\right)^{0.5}\left(\frac{\mu_l}{\mu_g}\right)^{0.5}$ $for\ Re_l < 1000\ \&\ Re_g > 1000$	D = 0.5 – 11 mm G = 150 – 450 kg/m^{2}s q = 5 – 39 kW/m^2 P = 3.5 – 5 bar R134a
Bertsch et al. (2009)	$\alpha_{tp} = Sh_{nb} + Fh_{conv}$	3899 data points D = 0.16 – 2.92 mm

	$h_{np} = 55P_r^{0.12-0.434\ln R_p}(-\log P_r)^{-0.55} M^{-0.5} q^{0.67}$ $h_{conv} = (1-x)h_L + xh_v$ For turbulent flow h_L and h_v are calculated from the Dittus-Boelter equation For laminar flow: $h = \frac{k_L}{D}\left[3.66 + \frac{0.0668\frac{D}{L}\mathrm{Re}\,\mathrm{Pr}}{1+0.04\left(D\,\mathrm{Re}\frac{\mathrm{Pr}}{L}\right)^{2/3}}\right]$ $S = (1-x)$ $F = 1+80\left(x^2 - x^6\right)\exp(-0.6Co)$ $Co = \left\|\sigma/g\Delta\rho\right\|^{0.5}/D$	Co = 0.3 – 4 G = 20 – 3000 kg/m^2 s x = 0 – 1 12 fluids including cryogens and refrigerants
Mikielewicz (2010)	$\frac{h_{tp}}{h_L} = \sqrt{\phi_{MS}^n + \frac{1}{1+P}\left(\frac{h_{nb}}{h_L}\right)^2}$ $P = 0.00253\,\mathrm{Re}^{1.17} Bo^{0.6}(\phi_{MS}-1)^{-0.65}$ $\phi_{MS} = \left[1+2\left(\frac{1}{f_1}-1\right)xCo^{-1}\right](1-x)^{1/3} + \frac{x^3}{f_2}$ For laminar flow: $f_1 = \frac{\rho_g}{\rho_L}\frac{\mu_L}{\mu_g}, \qquad f_2 = \frac{\mu_g}{\mu_L}\frac{c_{pL}}{c_{pg}}\left(\frac{k_L}{k_g}\right)^{1.5}$ For turbulent flow: $f_1 = \frac{\rho_g}{\rho_L}\left(\frac{\mu_L}{\mu_g}\right)^{0.25}, \qquad f_2 = \left(\frac{k_g}{k_L}\right)$ $h_{np} = 55P_r^{0.12-0.434\ln R_p}(-\log P_r)^{-0.55} M^{-0.5} q^{0.67}$	Applicable for conventional and small diameter channels.
Li and Wu (2010)	$h_{tp} = 334\,Bo^{0.3}\left(Bd\,\mathrm{Re}_L^{0.36}\right)^{0.4}\frac{k_L}{D}$ $\mathrm{Re}_L = \frac{(1-x)GD}{\mu_L}$	769 data points D = 0.148 – 3.25 mm 12 different fluids

Appendix C

Oscillations in wall temperature due to AC heating

The analysis presented here was first presented by Jeglic (1962) for a flat plate. The oscillations in wall temperature due to AC heating can be determined by solving the one dimensional transient energy equation.

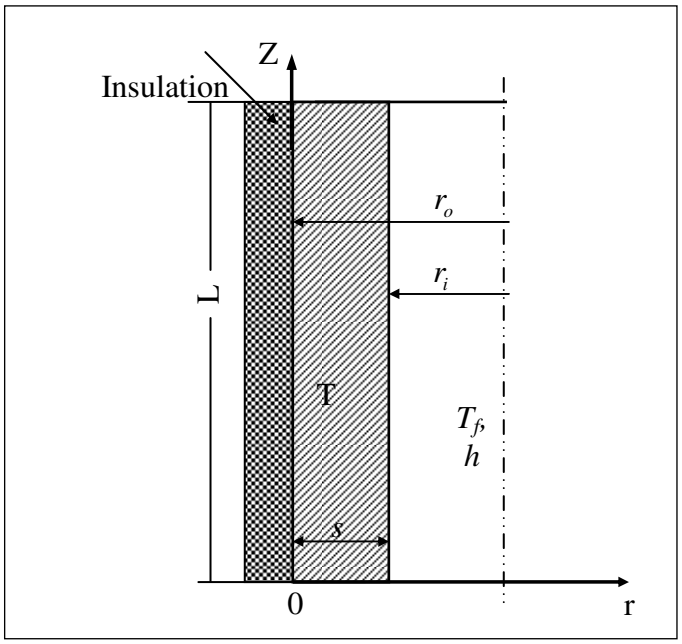

Assumptions:

1. Heat flows only in the radial direction and the end losses are neglected.
2. The tube outer surface is insulated very well.
3. The thermo-physical and electrical properties of the tube material are constant.

Governing Equations:

a. Heat generation per unit volume

$$i = I_m \sin \omega t = \sqrt{2} I_{eff} \sin \omega t$$

$$p = i^2 R = 2 I_{eff}^2 R \sin^2 \omega t = 2 P_m \sin^2 \omega t$$

$$\dot{q}_g = \frac{p}{V} = \frac{2 P_m \sin^2 \omega t}{\pi (r_o^2 - r_i^2) L} = \frac{2 P_m \sin^2 \omega t}{\pi (r_o - r_i)(r_o + r_i) L} = \frac{2 P_m \sin^2 \omega t}{s \pi r_i L (1 + r_o / r_i)}$$

$$= \frac{4 P_m \sin^2 \omega t}{s (2 \pi r_i L)(1 + r_o / r_i)} = \left(\frac{4}{s} \right) \left(\frac{P_m}{2 \pi r_i L} \right) \left(\frac{1}{1 + r_o / r_i} \right) \sin^2 \omega t$$

the second paranthes is the heat flux and the third one is constant

$$\dot{q}_g = B \left(\frac{4}{s} \right) q \sin^2 \omega t, \quad \text{where} \quad B = \left(\frac{1}{1 + r_o / r_i} \right)$$

b. One dimensional energy equation

$$k \frac{\partial^2 T}{\partial r^2} + \dot{q}_g = \rho c \frac{\partial T}{\partial t}$$

$$\frac{\partial^2 T}{\partial r^2} - \frac{\rho c}{k} \frac{\partial T}{\partial t} = -\frac{\dot{q}_g}{k}$$

$$\frac{\partial^2 T}{\partial r^2} - \frac{\rho c}{k} \frac{\partial T}{\partial t} = -\frac{B}{s} \frac{4q}{k} \sin^2 \omega t \qquad \text{(A1)}$$

To solve this equation two boundary conditions are required and one initial condition.

$$B.C = \begin{cases} \dfrac{\partial T}{\partial r} = 0, & r = 0 \\ -k \dfrac{\partial T}{\partial r} = h (T - T_f), & r = s \end{cases} \qquad \text{(A2)}$$

$$I.C: \quad T - T_f = 0, \quad \text{at} \quad t = 0, \quad \text{thermal equlibrium}$$

It is better to write Eq. (A1) in a dimensionless form using the following dimensionless parameters.

$$r^* = r / s, \quad t^* = \omega t, \quad T^* = \frac{(T - T_f) k}{q s}, \quad h^* = \frac{h s}{k}, \quad \omega^* = \frac{\omega \rho c s^2}{k}$$

$$T = \frac{qs}{k}T^* + T_f \;\Rightarrow \frac{\partial^2 T}{\partial r^2} = \frac{qs}{k}\frac{\partial^2 T^*}{s^2 \partial r^{*2}} = \left(\frac{q}{ks}\right)\frac{\partial^2 T^*}{\partial r^{*2}}$$

$$\Rightarrow \frac{\partial T}{\partial t} = \frac{qs}{k}\frac{\omega \partial T^*}{\partial t^*} = \left(\frac{q\omega s}{k}\right)\frac{\partial T^*}{\partial t^*}$$

$$\left(\frac{q}{ks}\right)\frac{\partial^2 T^*}{\partial r^{*2}} - \frac{\rho c}{k}\left(\frac{q\omega s}{k}\right)\frac{\partial T^*}{\partial t^*} = -\frac{B}{s}\frac{4q}{k}\sin^2 \omega t$$

$$\frac{\partial^2 T^*}{\partial r^{*2}} - \left(\frac{\omega \rho c s^2}{k}\right)\frac{\partial T^*}{\partial t^*} = -4B\sin^2 t^*$$

$$\frac{\partial^2 T^*}{\partial r^{*2}} - \omega^* \frac{\partial T^*}{\partial t^*} = -4B\sin^2 t^* \qquad \text{(A3)}$$

The new boundary and initial conditions are:

$$B.C = \begin{cases} \dfrac{\partial T^*}{\partial r^*} = 0, & r^* = 0 \\ \dfrac{\partial T^*}{\partial r^*} = -h^* T^*, & r^* = 1 \end{cases} \qquad \text{(A4)}$$

The initial conditions become:

$$T^* = 0, \qquad at \quad t^* = 0$$

The above equation can be solved analytically by superposition method in which the solution is a sum of a steady part and a transient part.

$$T^*\left(r^*, t^*\right) = steady\ part\ +\ transient\ part$$

The steady solution represents the solution of the above equation with constant heat generation. In that case the heat generation term can be calculated and substituted into the energy equation using the above methodology.

$$\dot{q}_g = \frac{I_{eff}^2 R}{V} = B\frac{q}{s}$$

The new equation will be like this:

$$\frac{\partial^2 T_c^*}{\partial r^{*2}} - \omega^* \frac{\partial T_c^*}{\partial t^*} = -B \qquad \text{(A5)}$$

At steady state the second term vanishes, then

$$\frac{\partial^2 \theta_c^*}{\partial r^{*2}} = -B \qquad \text{With the same boundary conditions (A4)}$$

$$\theta_c^*(r^*) = -\frac{B}{2} r^{*2} + C_1 r^* + C_2$$

$$0 = \left[B r^* + C_1 \right]_{r^*=0} \Rightarrow \; C_1 = 0$$

$$-h^* \left[-\frac{B}{2} r^{*2} + C_1 r^* + C_2 \right]_{r^*=1} = \frac{\partial}{\partial r^*} \left[-\frac{B}{2} r^{*2} + C_1 r^* + C_2 \right]_{r^*=1}$$

$$-h^* \left[-\frac{B}{2} + C_2 \right] = -B \quad \Rightarrow C_2 = B/h^* + B/2$$

$$\theta_c^*(r^*) = -\frac{B}{2} r^{*2} + \frac{B}{h^*} + \frac{B}{2} = \frac{B}{2h^*} \left[2 + h^* - h^* r^{*2} \right]$$

$$\theta_c^*(r^*) = \frac{B}{2h^*} \left[2 + h^* - h^* r^{*2} \right] \tag{A6}$$

$$T_c^* = \theta_c^* + V^* = \frac{B}{2h^*} \left[2 + h^* - h^* r^{*2} \right] + V^*$$

$$\frac{\partial T_c^*}{\partial r^*} = -B r^* + \frac{\partial V^*}{\partial r^*}, \quad \frac{\partial^2 T_c^*}{\partial r^{*2}} = -B + \frac{\partial^2 V^*}{\partial r^{*2}} \tag{A7}$$

$$\frac{\partial T_c^*}{\partial t^*} = \frac{\partial V^*}{\partial t^*}$$

From Eq. (A7) substitute into Eq. (A5), then

$$-B + \frac{\partial^2 V^*}{\partial r^{*2}} - \omega^* \frac{\partial V^*}{\partial t^*} = -B$$

$$\frac{\partial^2 V^*}{\partial r^{*2}} - \omega^* \frac{\partial V^*}{\partial t^*} = 0 \tag{A8}$$

Eq. (A8) has the same boundary conditions but the initial condition is the steady state solution;

$$at \;\; t^* = 0, \quad V^* = -\frac{B}{2h^*} \left[2 + h^* - h^* r^{*2} \right]$$

Eq. (A8) can be solved by separation of variables as follows:

$$V^*(r^*, t^*) = M(r^*) N(t^*)$$

$$\frac{\partial^2 V^*}{\partial r^{*2}} = N \frac{\partial^2 M}{\partial r^{*2}}, \quad \frac{\partial V^*}{\partial t^*} = M \frac{\partial N}{\partial t^*}$$

$$N \frac{\partial^2 M}{\partial r^{*2}} - \omega^* M \frac{\partial N}{\partial t^*} = 0 \;\; \Rightarrow \quad \frac{1}{M} \frac{\partial^2 M}{\partial r^{*2}} = \frac{\omega^*}{N} \frac{\partial N}{\partial t^*} = \beta$$

$$\frac{\partial N}{\partial t^*} - \frac{\beta}{\omega^*} N = 0$$

$$\frac{\partial^2 M}{\partial r^{*2}} - \beta M = 0$$

The value of β should be less than zero to have a physical meaning. Accordingly, let $\beta = -\lambda^2$ then the above equations can be written as follow:

$$\frac{\partial N}{\partial t^*} + \frac{\lambda^2}{\omega^*} N = 0 \qquad \text{(A9)}$$

$$\frac{\partial^2 M}{\partial r^{*2}} + \lambda^2 M = 0 \qquad \text{(A10)}$$

Eq. (A9) can be solved as follow:

$$\frac{dN}{N} = -\frac{\lambda^2}{\omega^*} dt^*$$

$$\ln N = -\frac{\lambda^2}{\omega^*} t^* + C$$

$$N = e^{-\frac{\lambda^2}{\omega^*} t^* + C} = C_1 e^{-\frac{\lambda^2}{\omega^*} t^*}$$

Eq. (A10) can be solved by the characteristic equation as follow:

$$\left(m^2 + \lambda^2\right) = 0 \;\Rightarrow m^2 = -\lambda^2, \quad m = \pm \lambda i$$

$$M = C_2 e^{\lambda i r^*} + C_3 e^{-\lambda i r^*}$$

$$M = C_2 \cos \lambda r^* + C_3 \sin \lambda r^*$$

Applying the first boundary condition:

$$\frac{dM}{dr^*} = 0, \; at \; r^* = 0, \quad 0 = \left[-\lambda C_2 \sin \lambda r^* + \lambda C_3 \cos \lambda r^* \right]_{r^*=0}$$

$$\lambda C_3 = 0, \quad \Rightarrow \quad C_3 = 0$$

$$\therefore M = C_2 \cos \lambda r^*$$

$$V^*(r^*, t^*) = C_1 C_2 e^{-\frac{\lambda^2}{\omega^*} t^*} \cos \lambda r^* = A e^{-\frac{\lambda^2}{\omega^*} t^*} \cos \lambda r^*$$

Applying the second boundary condition:

$$\left.\frac{\partial V^*}{\partial r^*}\right|_{r^*=1} = N(t^*) \left.\frac{\partial M}{\partial r^*}\right|_{r^*=1} = -h^* * V^*(1, t^*) = -h^* M(1) N(t^*)$$

$$M'(1) = -h^* M(1)$$

$$-\lambda C_2 \sin(\lambda) = -h^* C_2 \cos(\lambda)$$

$$\lambda C_2 \sin \lambda = h^* C_2 \cos \lambda, \;\; \Rightarrow \;\; \lambda \tan \lambda = h^*$$

$$\lambda \tan \lambda = -h^* \tag{A11}$$

Eq. (A11) has infinite number of roots but as assumed before for the physical meaning the value of β to be less than zero the roots of Eq. (A11) should be positive.

$$V^*(r^*,t^*) = \sum_{n=1}^{\infty} A_n e^{-\frac{\lambda_n^2}{\omega^*}t^*} \cos \lambda_n r^* \tag{A12}$$

At the moment, the constants should be determined by applying the initial conditions:

$$V^*(r^*,0) = -\frac{B}{2h^*}\left[2 + h^* - h^* r^{*2}\right]$$

$$\sum_{n=1}^{\infty} A_n \cos \lambda_n r^* = -\frac{B}{2h^*}\left[2 + h^* - h^* r^{*2}\right]$$

Multiply both sides by $\cos \lambda_j r^*$ and integrate from 0 to -1

$$\sum_{n=1}^{\infty} A_n \int_0^{-1} \cos \lambda_n r^* \cos \lambda_j r^* dr^* = -\frac{B}{2h^*} \int_0^{-1} \left[2 + h^* - h^* r^{*2}\right] \cos \lambda_j r^* dr^*$$

Integrating the left hand side by parts:

$$I = \int_0^{-1} \cos \lambda_n r^* \cos \lambda_j r^* dr^*, \qquad u = \cos \lambda_j r^*, \qquad dv = \cos \lambda_n r^* dr^*$$

$$du = -\lambda_j \sin \lambda_j r^* dr^* \qquad v = \frac{1}{\lambda_n} \sin \lambda_n r^*$$

$$I = \frac{1}{\lambda_n} \sin \lambda_n r^* \cos \lambda_j r^* + \frac{\lambda_j}{\lambda_n} \int \sin \lambda_n r^* \sin \lambda_j r^* dr^*$$

Intergating the sec*ond term by parts again*

$$u = \sin \lambda_n r^*, \qquad dv = \sin \lambda_j r^* dr^*$$

$$du = \lambda_n \cos \lambda_n r^* dr^*, \qquad v = -\frac{1}{\lambda_j} \cos \lambda_j r^*$$

$$I = \frac{1}{\lambda_n} \sin \lambda_n r^* \cos \lambda_j r^* - \frac{1}{\lambda_j} \sin \lambda_n r^* \cos \lambda_j r^* + \frac{\lambda_j}{\lambda_n} \frac{\lambda_n}{\lambda_j} \int \cos \lambda_n r^* \cos \lambda_j r^* dr^*$$

$$I = \frac{1}{\lambda_n} \sin \lambda_n r^* \cos \lambda_j r^* - \frac{1}{\lambda_j} \sin \lambda_n r^* \cos \lambda_j r^* + \frac{\lambda_j}{\lambda_n} \frac{\lambda_n}{\lambda_j} \int \cos \lambda_n r^* \cos \lambda_j r^* dr^*$$

$$I = \frac{1}{\lambda_n} \sin \lambda_n r^* \cos \lambda_j r^* - \frac{1}{\lambda_j} \sin \lambda_n r^* \cos \lambda_j r^* + I \quad \Rightarrow \quad \lambda_n = \lambda_j$$

Accordingly, the left hand side to have a definite value λ_n should equal λ_j otherwise all the terms in the above series will be zero.

$$A_n\int_0^1\cos^2\lambda_n r^*dr^*=-\frac{B}{2h^*}\int_0^1\left[2+h^*-h^*r^{*2}\right]\cos\lambda_n r^*dr^*$$

$$A_n\left[\frac{r^*}{2}+\frac{1}{4\lambda_n}\sin 2\lambda_n r^*\right]_0^1=-\frac{B}{2h^*}\left\{\begin{array}{l}\left(\frac{2}{\lambda_n}\sin\lambda_n r^*\right)+\left(\frac{h^*}{\lambda_n}\sin\lambda_n r^*\right)-\\ \frac{h^*r^{*2}}{\lambda_n}\sin\lambda_n r^*+\frac{2h^*}{\lambda_n^3}\sin\lambda_n r^*-\frac{2h^*r^*}{\lambda_n^2}\cos\lambda_n r^*\end{array}\right\}_0^1$$

$$A_n\left[\frac{1}{2}+\frac{1}{4\lambda_n}\sin 2\lambda_n\right]=-\frac{B}{2h^*}\left\{\frac{2}{\lambda_n}\sin\lambda_n+\frac{h^*}{\lambda_n}\sin\lambda_n-\frac{h^*}{\lambda_n}\sin\lambda_n+\frac{2h^*}{\lambda_n^3}\sin\lambda_n-\frac{2h^*}{\lambda_n^2}\cos\lambda_n\right\}$$

$$A_n\left[\frac{1}{2}+\frac{1}{4\lambda_n}\sin 2\lambda_n\right]=-\frac{B\sin\lambda_n}{2h^*}\left\{\frac{2}{\lambda_n}+\frac{h^*}{\lambda_n}-\frac{h^*}{\lambda_n}+\frac{2h^*}{\lambda_n^3}-\frac{2h^*}{\lambda_n^2\tan\lambda_n}\right\}$$

$$A_n\left[\frac{1}{2}+\frac{1}{4\lambda_n}\sin 2\lambda_n\right]=-\frac{B\sin\lambda_n}{2h^*}\left\{\frac{2h^*}{\lambda_n^3}\right\}=-\frac{B\sin\lambda_n}{\lambda_n^3},\quad note\quad \tan\lambda_n=h^*/\lambda_n$$

$$A_n=\frac{-2B\sin\lambda_n}{\lambda_n^2\left(\frac{1}{2}\sin 2\lambda_n+\lambda_n\right)}$$

Substitute into equation 12 we can get:

$$V^*(r^*,t^*)=-2B\sum_{n=1}^{\infty}\frac{\sin\lambda_n}{\lambda_n^2\left(\frac{1}{2}\sin 2\lambda_n+\lambda_n\right)}e^{-\frac{\lambda_n^2}{\omega^*}t^*}\cos\lambda_n r^* \qquad \text{(A13)}$$

$$T_c^*(r^*,t^*)=\frac{B}{h^*}+\frac{B}{2}-\frac{B}{2}r^{*2}-2B\sum_{n=1}^{\infty}\frac{\sin\lambda_n}{\lambda_n^2\left(\frac{1}{2}\sin 2\lambda_n+\lambda_n\right)}e^{-\frac{\lambda_n^2}{\omega^*}t^*}\cos\lambda_n r^* \qquad \text{(A14)}$$

Equation (A14) represents the steady solution of the energy equation with constant heat generation. If the heat generation is not constant as we guess from alternating current the solution can be obtained using Duhamel's theorem. The theorem states that:

$$T^*(r^*,t^*)=-\int_0^{t^*}F(t_0^*)\frac{\partial}{\partial t^*}T_c^*(r^*,t^*-t_0^*)\partial t_0^*$$

$$F(t^*)=-4B\sin^2 t^*,\quad \Leftrightarrow\ F(t_0^*)=-4B\sin^2 t_0^*=-2B\left[1-\cos 2t_0^*\right]=-2B+2B\cos 2t_0^*$$

$$\frac{\partial T_c^*}{\partial t^*} = -2B\sum_{n=1}^{\infty} -\frac{\lambda_n^2}{\omega^*}\frac{\sin\lambda_n}{\lambda_n^2\left(\frac{1}{2}\sin 2\lambda_n + \lambda_n\right)} e^{-\frac{\lambda_n^2}{\omega^*}t^*}\cos\lambda_n r^* = \frac{2B}{\omega^*}\sum_{n=1}^{\infty}\frac{\sin\lambda_n}{\left(\frac{1}{2}\sin 2\lambda_n + \lambda_n\right)} e^{-\frac{\lambda_n^2}{\omega^*}t^*}\cos\lambda_n r^*$$

$$\left.\frac{\partial T_c^*}{\partial t^*}\right|_{r^*,t^*-t_0^*} = \frac{2B}{\omega^*}\sum_{n=1}^{\infty}\frac{\sin\lambda_n}{\left(\frac{1}{2}\sin 2\lambda_n + \lambda_n\right)} e^{-\frac{\lambda_n^2}{\omega^*}(t^*-t_0^*)}\cos\lambda_n r^*$$

$$T^{*`}(r^*,t^*) = -\int_0^{t^*} -2B(1-\cos 2t_0^*) * \frac{2B}{\omega^*}\sum_{n=1}^{\infty}\frac{\sin\lambda_n}{\left(\frac{1}{2}\sin 2\lambda_n + \lambda_n\right)} e^{-\frac{\lambda_n^2}{\omega^*}(t^*-t_0^*)}\cos\lambda_n r^*$$

$$= \frac{4B^2}{\omega^*}\sum_{n=1}^{\infty}\int_0^{t^*}(1-\cos 2t_0^*)\frac{\sin\lambda_n}{\left(\frac{1}{2}\sin 2\lambda_n + \lambda_n\right)} e^{-\frac{\lambda_n^2}{\omega^*}(t^*-t_0^*)}\cos\lambda_n r^*\partial t_0^*$$

$$T^*(r^*,t^*) = \frac{4B^2}{\omega^*}\sum_{n=1}^{\infty}\int_0^{t^*}\frac{\sin\lambda_n}{\left(\frac{1}{2}\sin 2\lambda_n + \lambda_n\right)} e^{-\frac{\lambda_n^2}{\omega^*}(t^*-t_0^*)}\cos\lambda_n r^*\partial t_0^*$$

$$-\int_0^{t^*}\frac{\cos 2t_0^*\sin\lambda_n}{\left(\frac{1}{2}\sin 2\lambda_n + \lambda_n\right)} e^{-\frac{\lambda_n^2}{\omega^*}(t^*-t_0^*)}\cos\lambda_n r^*\partial t_0^*$$

$$T^*(r^*,t^*) = \frac{4B^2}{\omega^*}\sum_{n=1}^{\infty}\left[\frac{\omega^*\sin\lambda_n\cos\lambda_n r^*}{\lambda_n^2\left(\frac{1}{2}\sin 2\lambda_n + \lambda_n\right)} e^{-\frac{\lambda_n^2}{\omega^*}(t^*-t_0^*)}\right]_0^{t^*}$$

$$-\left[\frac{\sin\lambda_n\cos\lambda_n r^* e^{-\frac{\lambda_n^2}{\omega^*}(t^*-t_0^*)}}{\left(\frac{1}{2}\sin 2\lambda_n + \lambda_n\right)\left(\frac{\lambda_n^4}{\omega^{*2}}+4\right)}\left\{\frac{\lambda_n^2}{\omega^*}\cos 2t_0^* + 2\sin 2t_0^*\right\}\right]_0^{t^*}$$

$$T^*(r^*,t^*) = \frac{4B^2}{\omega^*}\sum_{n=1}^{\infty}\left[\frac{\omega^*\sin\lambda_n\cos\lambda_n r^*}{\lambda_n^2\left(\frac{1}{2}\sin 2\lambda_n + \lambda_n\right)} - \frac{\omega^*\sin\lambda_n\cos\lambda_n r^*}{\lambda_n^2\left(\frac{1}{2}\sin 2\lambda_n + \lambda_n\right)} e^{-\frac{\lambda_n^2}{\omega^*}t^*}\right] -$$

$$\left[\frac{\sin\lambda_n\cos\lambda_n r^*}{\left(\frac{1}{2}\sin 2\lambda_n + \lambda_n\right)\left(\frac{\lambda_n^4}{\omega^{*2}}+4\right)}\left\{\frac{\lambda_n^2}{\omega^*}\cos 2t^* + 2\sin 2t^*\right\} - \frac{\sin\lambda_n\cos\lambda_n r^* e^{-\frac{\lambda_n^2}{\omega^*}t^*}}{\left(\frac{1}{2}\sin 2\lambda_n + \lambda_n\right)\left(\frac{\lambda_n^4}{\omega^{*2}}+4\right)}\left\{\frac{\lambda_n^2}{\omega^*}\right\}\right]$$

$$T^*(r^*,t^*)=\frac{4B^2}{\omega^*}\sum_{n=1}^{\infty}\frac{\omega^*\sin\lambda_n\cos\lambda_n r^*}{\lambda_n^2\left(\frac{1}{2}\sin 2\lambda_n+\lambda_n\right)}\left[(1-e^{-\frac{\lambda_n^2}{\omega^*}t^*})-\left\{\frac{\omega^*\lambda_n^2}{\lambda_n^4+4\omega^{*2}}\left(\begin{array}{l}\frac{\lambda_n^2}{\omega^*}\cos 2t\\ +2\sin 2t-\frac{\lambda_n^2}{\omega^*}e^{-\frac{\lambda_n^2}{\omega^*}t^*}\end{array}\right)\right\}\right]$$

$$T^*(r^*,t^*)=\frac{4B^2}{\omega^*}\sum_{n=1}^{\infty}\frac{\omega^*\sin\lambda_n\cos\lambda_n r^*}{\lambda_n^2\left(\frac{1}{2}\sin 2\lambda_n+\lambda_n\right)}\left[(1-e^{-\frac{\lambda_n^2}{\omega^*}t^*})-\left\{\frac{\lambda_n^4}{\lambda_n^4+4\omega^{*2}}\left(\begin{array}{l}\cos 2t\\ +\frac{2\omega^*}{\lambda_n^2}\sin 2t-e^{-\frac{\lambda_n^2}{\omega^*}t^*}\end{array}\right)\right\}\right]$$

$$=4B^2\sum_{n=1}^{\infty}\frac{\sin\lambda_n\cos\lambda_n r^*}{\lambda_n^2\left(\frac{1}{2}\sin 2\lambda_n+\lambda_n\right)}\left[(1-e^{-\frac{\lambda_n^2}{\omega^*}t^*})-\frac{\lambda_n^4}{\lambda_n^4+4\omega^{*2}}\left(\begin{array}{l}\cos 2t\\ +\frac{2\omega^*}{\lambda_n^2}\sin 2t-e^{-\frac{\lambda_n^2}{\omega^*}t^*}\end{array}\right)\right]$$

Publications

[1] M.M. Mahmoud, D.B.R. Kenning and T.G. Karayiannis. Single and two phase heat transfer and pressure drop in a 0.52 mm vertical metallic tube. 7th International Conference on Enhanced, Compact and Ultra-compact Heat Exchangers: From Microscale Phenomena to Industrial Applications, September 13 – 18, 2009, Heredia, Costa Rica.

[2] M. Mahmoud, T. Karayiannis and D. Kenning Surface effects in flow boiling of R134a in microtubes. Proceedings of the 2nd European Conference on Microfluidics – Microfluidics 2010, Toulouse, France, December 8 – 10, 2010.

[3] M. M. Mahmoud, T.G. Karayiannis and D.B.R. Kenning. Surface effects in flow boiling of R134a in microtubes. Submitted for the International Journal of Heat and Mass Transfer.

[4] M.M. Mahmoud, D. Shiferaw, T.G. Karayiannis and D.B.R. Kenning. Flow boiling in vertical small to micro tubes with refrigerant R134a. A book chapter in "Emerging Topics in Heat Transfer Enhancement and Heat Exchangers".

[5] D. Shiferaw, M. Mahmoud, T.G. Karayiannis and D.B.R. Kenning. One-dimensional mechanistic model for flow boiling pressure drop in small- to micro-passages. 2nd Micro and Nano Flows Conference, West London, Uk, 1 – 2 September, 2009.

[6] D. Shiferaw, M. Mahmoud, T.G. Karayiannis and D.B.R. Kenning. One-dimensional semi-mechanistic model for flow boiling pressure drop in small- to micro-passages. Submitted for Heat Transfer Engineering Journal.